11th Electromagnetic & Light Scattering Conference

Extended Abstracts

7-12 September 2008

de **Havilland Campus**

University of Hertfordshire

University of Hertfordshire

Table of Contents

THEORETICAL STUDIES

MINERAL DUST AEROSOLS

COSMIC PARTICLES

LIGHT SCATTERING PROPERTIES OF CIRRUS

AEROSOLS (REMOTE SENSING FROM GROUND, AIRCRAFT AND SPACE)

SCATTERING FROM BIOLOGICAL PARTICLES

PARTICLE LEVITATION AND LABORATORY SCATTERING

INDUSTRIAL AND ENVIRONMENTAL APPLICATIONS

THEORETICAL STUDIES

A Closer Look at the Extinction Paradox

Matthew J. Berg, Christopher M. Sorensen,
and Amit Chakrabarti

Kansas State University, Department of Physics,
Manhattan, Kansas 66502-2601 USA
tel: +1 (785) 532-1626 , fax: +1 (785) 532-6806, e-mail: mberg@phys.ksu.edu

Abstract

The extinction paradox is usually described as the large-particle size limit of the extinction efficiency factor as it approaches a value of twice the particle's geometric projection in the forward direction. This effect is paradoxical because geometrical optics, valid for such large particles, predicts that the efficiency factor equal the particle's projection in this limit. The paradox has received much attention since its discovery and is now generally understood as being due to a combination of geometrical optics and particle edge diffraction. We report new work that identifies problems with the traditional explanations of the paradox, and we present a different way of describing a particle's extinction behavior.

1 Introduction

One of the remarkable predictions of Mie theory is that the extinction cross section C^{ext} of a spherical particle approaches an asymptotic value of twice the area of its geometric shadow G as the size parameter of the sphere becomes large. This so-called extinction paradox is an unexpected result in the sense that geometrical optics should apply in the large size parameter limit, in which case one would expect that the sphere extincts only as much power as is incident across G. A very intuitive explanation of the paradox was quickly developed, most notably by van de Hulst, that attributes one factor of G in the cross section to scattering and absorption by the sphere's illuminated profile, and the other factor to diffraction of the incident light from the sphere's edge where the shadow begins [1]. Since its initial description, the paradox has been shown to be a general behavior of extinction by particles of any shape and is now widely regarded as a well-understood phenomenon [2].

In this presentation, we review the details of the popular edge diffraction explanation of the paradox and describe the subtle problems associated with it. We present a different way of describing the extinction process, which ties C^{ext} directly to the fields inside of a particle, and discuss our recent computational and analytical results. We show that these new results call for a more critical look at the extinction paradox and its traditional explanations.

2 The paradox

A particle's extinction efficiency Q^{ext} is defined as the ratio of the extinction cross section to the particle's geometric projection G in the forward direction. The efficiency curves for spheres of vastly different size R and complex-valued refractive index m show remarkably similar structure when plotted as a function of the so-called phase shift parameter ρ, given by

$$\rho = 2kR(m_{re} - 1) \tag{1}$$

where k is the vacuum wave number and m_{re} is the real part of the refractive index. Typical efficiency curves for spherical particles generated by Mie theory are shown in Fig. (1). One can see that the curves oscillate together with ρ and asymptotically approach the (paradoxical) value of $Q^{ext} \to 2$ for large ρ.

The large scale oscillations in the curves have been attributed to the interference of the diffracted and forward scattered light, and the finer structures in the curves are attributed to the sphere's internal resonances [1]. Similar qualitative behavior has recently been found in inhomogeneous and nonspherical particles, e.g., see [3].

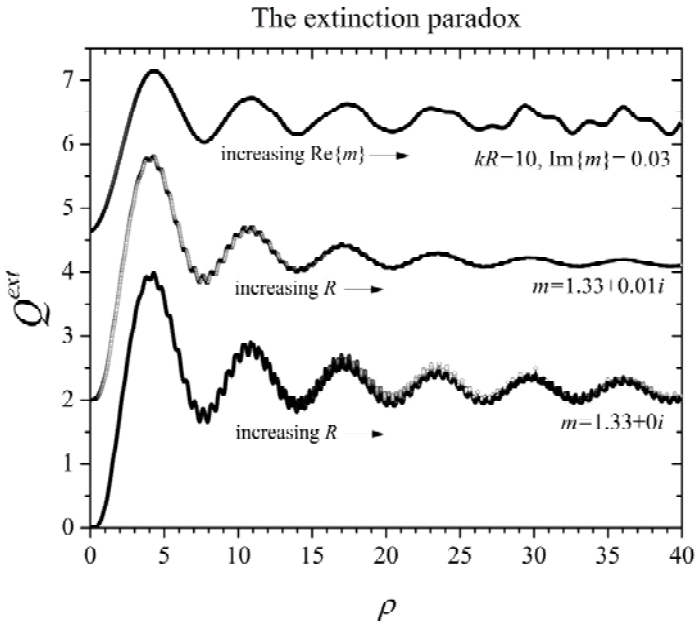

Figure 1: Extinction efficiency curves Q^{ext} for spheres plotted as a function of the phase shift parameter ρ of Eq. (1). The bottom two curves correspond to refractive indices of $m = 1.33 + 0i$ and $m = 1.33 + 0.01i$, respectively. For these curves, ρ is increased by increasing the sphere size R with k held constant. The top curve corresponds to a sphere of fixed size $kR = 10$ where ρ is increased by increasing the real part of the refractive index m_{re} form 1.001 to 3.0 and with constant k and imaginary part $m_i = 0.03$. The curves are displaced by factors of two vertically for clarity. Notice the common oscillation in ρ and limit $Q^{ext} \to 2$.

3 Edge diffraction?

The edge diffraction explanation of the paradox is well established in the literature. Investigators like van de Hulst, Bohren and Huffman, and Born and Wolf, to name a few, elegantly apply the concept to explain nearly every major feature of the extinction behavior of large particles [1,2,4]. However, the edge diffraction explanation is not the only one that has been proposed. Brillouin and others explain the paradox by separating the total external wave into a part that accounts for scattering and another part, called the shadow forming wave, which cancels out the incident wave within geometrical shadow in the near-field zone [5-7]. Recent theoretical work by Lai *et al.* adopted this explanation and showed that the edge diffraction concept is inconsistent with the behavior of C^{ext} for a sphere illuminated by a narrow Gaussian beam [8]. In addition, Fu *et al.* did not see the paradox occur for a sphere embedded in an absorbing medium [9].

Following our recent work with extinction and the optical theorem [10,11], we examined the various explanations of the paradox and identified problems with each of them. For example, the primary assumptions involved in the edge diffraction explanation are that the scattered light at all angles is regarded as being removed from the incident wave (i.e., extinction) and that the observation of a particle's cross section is made in the far-field zone where no sharp shadow exists [1]. However, one would expect that the cross section of a particle in vacuum should be independent of the distance at which it is calculated or observed. This means that the extinction paradox must occur in the near-field zone *arbitrarily* close to a particle's surface where the concept of a far-field edge-diffraction pattern loses its meaning. Using Mie theory, we have verified that that the paradox does indeed occur in the near-field zone by calculating C^{ext} directly from the near-field energy flow around a spherical particle. In addition, we have derived the typical expression relating C^{ext} to the expansion coefficients of an arbitrary

particle's scattered wave represented in terms of the vector spherical wave functions, e.g. see [12]. We carry out this calculation however, without invoking the far-field limit or using the optical theorem, which demonstrates that the cross section is independent of distance for *any* particle.

Another problem with the edge diffraction explanation is that it tacitly assumes that the particle is much larger than the wavelength. This is because the edge diffraction concept requires that the wave outside of the particle can be meaningfully separated into rays incident on G and rays that pass by the particle's edge undeflected [1]. However, inspection of the efficiency curves in Fig. (1) reveals that the paradox is not just a large kR effect, but rather is a large ρ effect. The top curve in Fig. (1) asymptotically approaches two with increasing ρ even though $kR = 10$. For a sphere of this size, geometrical optics does not apply and hence the total wave near the particle cannot be resolved into rays intercepted by G and rays passing by undeflected.

The shadow forming wave explanation of the paradox mentioned above has been developed only for large perfectly conducting particles. Jackson treats the case of a sphere and explicitly shows how the shadow forming wave can account for the extra factor of G present in the cross section [7]. A key element in such calculations is that the external wave is zero immediately behind the particle in its shadow. In the case of dielectric particles, it is uncertain how the shadow forming wave concept can be applied since the wave in the shadow region behind such particles is not necessarily zero. Consequently, the shadow forming wave concept does not appear to provide an acceptable *general* explanation of the paradox.

3 A different view of the paradox

In an attempt to better understand the physical cause of the paradox, we have applied the optical theorem differentially to a spherical particle using the volume integral equation (VIE) expression for the far-field scattering amplitude [12]. The sphere's internal field is integrated with the VIE over the partial volume ∂V, which consist of the region of the sphere's interior extending from $z = -R$ to z, see Fig. (2a). From the optical theorem, the contribution to the total extinction from this region is

$$\partial C^{ext}(z) = \frac{k}{|\vec{E}^{inc}|} \mathrm{Im}\left\{ \int_{\partial V} E_x^{\mathrm{int}}(\vec{r}') \exp(-ikz') dV' \right\} \tag{2}$$

where $\vec{E}^{inc}$ is the incident electric field and E_x^{int} is the component of the internal electric field directed along the polarization of the incident field.

Figure (2b) plots Eq. (2) for a sphere with a size parameter of $kR = 15$ and $m = 1.5 + 0i$ and a total extinction cross section of $C^{ext} = 1.98G$. The curve is normalized by G. One can see that the curve rises from zero to around two once the portion of the sphere's volume corresponding to its illuminated side has been integrated. The flattening-out of the curve as more of its interior is included indicates that the differential contributions to Eq. (2) from the sphere's interior begin to partially cancel each other out resulting in a total cross section that is proportional to the sphere's projected area. One can understand the cause of this cancellation behavior by realizing that the internal field varies greatly in magnitude and phase throughout the particle's interior due to its large (real-valued) refractive index and corresponding large ρ. Had this partial cancellation been absent, as it would be for a much smaller sphere, the curve would continue to rise ending in a cross section proportional to the square of the sphere's volume. The key point here is to notice that this description of the sphere's extinction cross section furnishes the

expected paradoxical result that $C^{ext} \to 2G$ without any need to consider edge diffraction or identify a shadow forming wave.

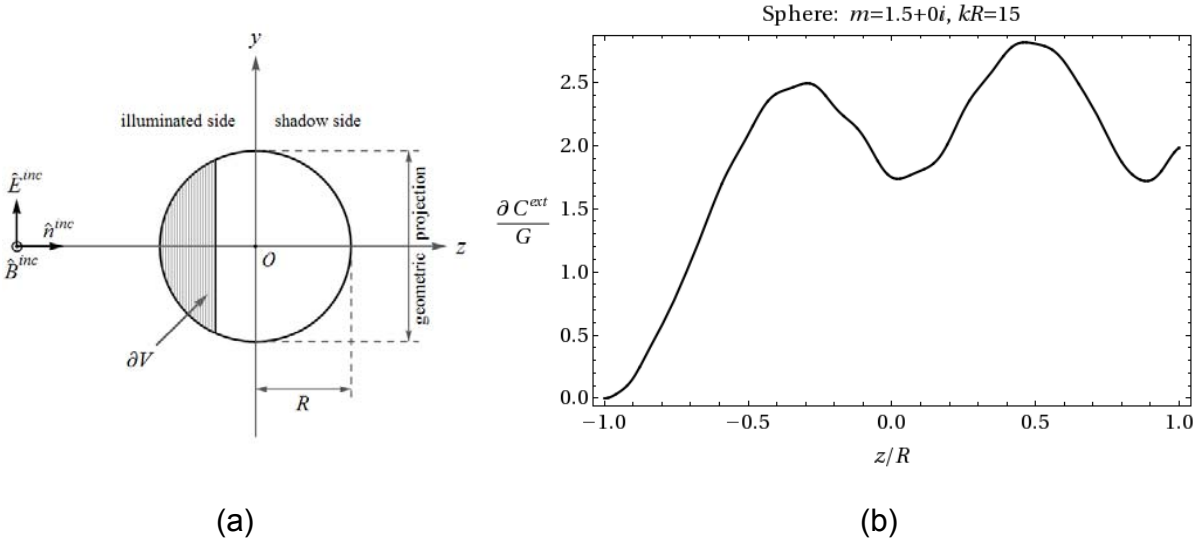

(a) (b)

Figure 2: (a) Sketch showing a spherical particle and the partial volume ∂V. (b) Plot of Eq. (2) normalized by the sphere's geometric projection G. The sphere size parameter is $kR = 15$, $m = 1.5 + 0i$, and has a cross section of $C^{ext} = 1.98G$.

References

[1] H. C. van de Hulst, *Light Scattering by Small Particles* (Dover, New York, 1981).

[2] C. F. Bohren and D. R. Huffman, *Absorption and Scattering of Light by Small Particles* (Wiley, New York, 1983).

[3] S. Asano, "Light scattering properties of spheroidal particles," Appl. Opt. **18**, 712-723 (1979).

[4] M. Born and E. Wolf, *Principles of Optics* (Cambridge University Press, Cambridge, 1999).

[5] L. Brillouin, "The scattering cross section of spheres for electromagnetic waves," J. Appl. Phys. **20**, 110-1125 (1949).

[6] P. M. Morse and H. Feshbach, *Methods of Mathematical Physics* (McGraw Hill, New York, 1953).

[7] J. D. Jackson, *Classical Electrodynamics* (Wiley, New York, 1999).

[8] H. M. Lai, W. Y. Wong, and W. H. Wong, "Extinction paradox and actual power scattered in light beam scattering: a two-dimensional study," J. Opt. Soc. Am. A **21**, 2324-2333 (2004).

[9] Q. Fu and W. Sun, "Mie theory for light scattering by a spherical particle in an absorbing medium," Appl. Opt. **40**, 1354-1361 (2001).

[10] M. J. Berg, C. M. Sorensen, and A. Chakrabarti, "Extinction and the optical theorem. Part I. Single particles," J. Opt. Soc. Am. A **25**, (in press, July 2008).

[11] M. J. Berg, C. M. Sorensen, and A. Chakrabarti, "Extinction and the optical theorem. Part II. Multiple particles," J. Opt. Soc. Am. A **25**, (in press, July 2008).

[12] M. I. Mishchenko, L. D. Travis, and A. A. Lacis, *Scattering, Absorption and Emission of Light by Small Particles* (Cambridge University Press, Cambridge, 2002).

Modeling of light scattering by a nanohole in a noble-metal film in the region of evanescent waves

Elena Eremina [1], Yuri Eremin [2], Natalia Grishina [2] and Thomas Wriedt [3]

[1] *Bremen University, Badgasteiner Str. 3, 28359 Bremen, Germany*
tel: +49-421-218-3583, fax: +49-421-218-5378, e-mail: eremina@iwt.uni-bremen.de
[2]*Moscow Lomonosov State University, Lenin's Hills, 119991 Moscow, Russia*
tel: +7-095-939-1776, fax: +7-095-939-1776, e-mail: eremin@cs.msu.su
[3]*Institute of Materials Science, Badgasteiner Str. 3, 28359 Bremen, Germany*
tel: +49-421-218-3583, fax: +49-421-218-2507, e-mail: thw@iwt.uni-bremen.de

Abstract.

In this work the Discrete Sources Method (DSM) has been applied to analyze the scattering behavior of a cylindrical nanohole in a noble metal film deposited on a glass prism. In contrast to other publications an evanescent wave's field has been taken as an external excitation. The effect of an extreme light transmission in evanescent wave's region has been detected. The dependence of the transmitted intensity on the incident angle, film properties and hole's size and filling has been investigated. Numerical results will be presented on the conference.

1. Introduction

Since the effect of enhanced optical transmission through a subwavelength holes array in a metal screen has been detected by Ebbesen et al. [1], it attracted considerable interest by numerous researchers. The ability to localize light in spots much smaller than the volume predicted by diffraction theory offers multiple practical applications in nanooptics and biophotonics. The effect of enhanced light transmission appears at a certain wavelength of the incident light, which depends on the screen material. In the paper of Wannemacher [2] this effect has been explained by Plasmon excitation. It is now generally agreed that surface plasmon resonances play a key role in enhancement of light transmission through sub-wavelength apertures in noble metal screens. Recently several scientific teams worldwide have examined the transmission properties of sub-wavelength apertures in connection with the development of optical antennas and bionsensors. However, in most of these works conventional incidence is used as an external excitation. At the same time, there are multiple practical applications using an evanescent wave as external excitation. Employing evanescent waves may allow avoiding of the problem of filtering the scattered light from the refracted one.

In our work we concentrated on scattering properties of a single sub-wavelength hole in a noble-metal film filled by a dielectric medium in the range of evanescent waves. DSM [3] has been recently applied to model this problem. The effect of extreme light transmission through the nanohole in a noble metal film on the prism in the range of evanescent waves has been detected [4]. In the oral presentation the influence of the incident angle, hole's size and filling, as well as the material and thickness of the metal film will be demonstrated.

2. Mathematical model

Let the whole space be divided into three areas: air D_0, film D_f and a glass prism D_1. Let the plane Σ_1 separate a film and a glass prism and the plane Σ_f the air and the film. An axially symmetric hole occupying a certain domain D_i with a smooth boundary ∂D is situated inside the film of thickness d, bounded by the planes Σ_1 and Σ_f. We assume that the symmetry axis of the hole coincides with the normal direction to Σ_1. Let us introduce a Cartesian coordinate system Oxyz by choosing its origin O at the prism-surface Σ_1 in the moddle of the hole and let the Oz axis coincide with the symmetry axis of the hole and is directed into D_0. The plane $z = 0$ corresponds to the Σ_1 plane (Figure 1). We assume that

the exciting field $\{\mathbf{E}^0, \mathbf{H}^0\}$ is a plane wave propagating from the prism domain D_1 at the angle θ_1 with respect to the z-axis. First, the plane wave $\{\mathbf{E}^0, \mathbf{H}^0\}$ scattering problem on the layered media is solved.

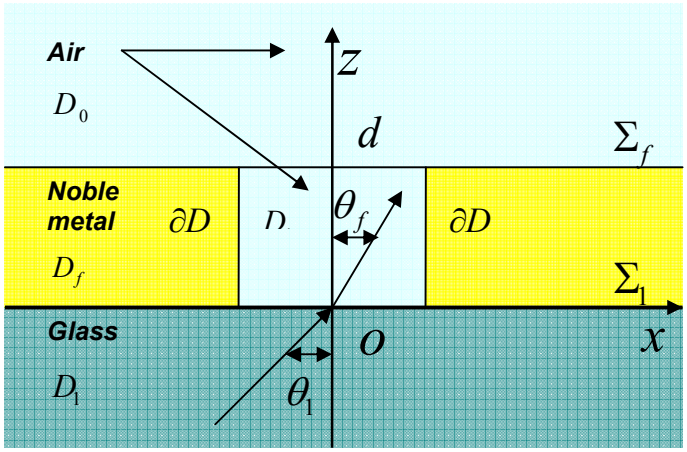

Figure 1. Model geometry.

The result yields external excitation fields $\{\mathbf{E}^0_\zeta, \mathbf{H}^0_\zeta\}, \zeta = 0, f, 1$ in domains $D_{0,f,1}$, which satisfy the transmission conditions at the plane interfaces $\Sigma_{1,f}$. While in $D_{1,f}$ the total field consists of incident and reflected waves, in D_0 the total field includes the transmitted wave which transforms to the evanescent one behind the critical angle.

Then the mathematical statement of the scattering problem for the scattering field outside D_i and total field inside D_i can be formulated as follows:

$$\nabla\times\mathbf{H}_\zeta = jk\varepsilon_\zeta\mathbf{E}_\zeta;\qquad \nabla\times\mathbf{E}_\zeta = -jk\mu_\zeta\mathbf{H}_\zeta \quad \text{in } D_\zeta,\quad \zeta = 0,1,f,i,$$

$$\begin{aligned}
&\mathbf{n}_p\times\big(\mathbf{E}_i(p)-\mathbf{E}_f(p)\big)=\mathbf{n}_p\times\mathbf{E}^0_f(p),\\
&\mathbf{n}_p\times\big(\mathbf{H}_i(p)-\mathbf{H}_f(p)\big)=\mathbf{n}_p\times\mathbf{H}^0_f(p),
\end{aligned}\qquad p\in\partial D; \tag{1}$$

$$\begin{aligned}
&\mathbf{e}_z\times\big(\mathbf{E}_f(p)-\mathbf{E}_1(p)\big)=0,\\
&\mathbf{e}_z\times\big(\mathbf{H}_f(p)-\mathbf{H}_1(p)\big)=0,
\end{aligned}\quad p\in\Sigma_1;\qquad
\begin{aligned}
&\mathbf{e}_z\times\big(\mathbf{E}_0(p)-\mathbf{E}_f(p)\big)=0,\\
&\mathbf{e}_z\times\big(\mathbf{H}_0(p)-\mathbf{H}_f(p)\big)=0,
\end{aligned}\quad p\in\Sigma_f$$

and radiation/attenuation conditions at infinity for the scattered field in $D_{0,1}$ and in D_f.

Here, $\mathbf{e}_z$ is the unit normal vector to the planes $\Sigma_{1,f}$, $\mathbf{n}_p$ is the outward unit normal vector to ∂D, $k = \omega/c$. If $\operatorname{Im}\varepsilon_\zeta, \mu_\zeta \le 0$ (the time dependence for the fields is chosen as $\exp\{j\omega t\}$) and the particle surface is smooth enough: $\partial D \subset C^{(2,\alpha)}$, then the above boundary-value scattering problem is uniquely solvable.

After the plane wave $\{\mathbf{E}^0, \mathbf{H}^0\}$ scattering problem on the interface is solved, the approximate solution of the boundary value problem (1) for the scattered field $\{\mathbf{E}^s_\zeta, \mathbf{H}^s_\zeta\}$ in D_ζ, $\zeta = 0, f, 1$ and the total field in D_i is constructed. Let us remind that the boundary conditions of problem (1) are inhomogeneous at the hole's surface only.

To construct an approximate solution we will employ DSM [3]. In the frame of DSM the approximate solution is constructed by representing the electromagnetic fields as a finite linear combination of the

electric and magnetic fields of multipoles distributed over the axis of symmetry inside the hole. Besides, the fields analytically satisfy the transmission conditions enforced at the plane interfaces $\Sigma_{1,f}$, which provides an opportunity to account for whole interactions between hole and interfaces occuring due to multiple field reflections. Then the approximate solution satisfies Maxwell equations in the domains $D_\zeta, \zeta = 0,1,f,i$, the infinity conditions and the transmission conditions at plane interfaces $\Sigma_{1,f}$. Thus, the scattering problem is reduced to the problem of approximation of the exciting field on the hole's surface ∂D. Finally, the amplitudes of the discrete sources (DS) are to be determined from the boundary conditions at ∂D (see (1)).

For construction of the fields of dipoles and multipoles that analytically satisfy the transmission conditions at the plane interfaces $\Sigma_{1,f}$, the Green's tensor for a layered interface is used [5]. An approximate solution of the scattering problem is constructed taking into account not only the rotational symmetry of the scattering problem geometry (hole together with layered interface) but the polarization of the exciting field [3] as well. The detailed description of the method including all related representations can be found in [4]. The completeness of the system of dipoles and multipoles guarantees the convergence of the approximate solution to the exact one [6].

The approximate solution, based on DSM satisfies all the conditions of the scattering problem (1) except the transmission conditions at the hole's surface ∂D. These conditions are used to determine the unknown amplitudes of discrete sources. Since the scattering problem geometry is axially symmetric with respect to the z-axis and the DS are distributed over the axis of symmetry, fulfilling the transmission conditions (1) at the surface ∂D can be reduced to a sequential set of 1D transmission problems for the Fourier harmonics of the fields. Thus, instead of matching the fields on the scattering surface ∂D, we match their Fourier harmonics separately by reducing the approximation problem on the surface ∂D to a set of 1D problems enforced at the particle surface generatrices $\Im$. By solving these problems one can determine the DS amplitudes. Besides, the DSM numerical scheme provides an opportunity to control the actual convergence of the approximate solution to the exact one by posterior error estimation [3].

After the amplitudes of the DS have been determined, one can calculate the far field pattern $\mathbf{E}_\infty(\theta,\varphi)$ of the scattered field, which is determined at the upper semi-sphere $\Omega = \{0^\circ \le \theta \le 90^\circ,\ 0^\circ \le \varphi \le 360^\circ\}$ and is given by

$$\mathbf{E}_0^s(M) \Big/ \left|\mathbf{E}^0(z=0)\right| = \frac{\exp\{-jk_0 r\}}{r}\mathbf{E}_\infty(\theta,\varphi) + o(r^{-1}), \quad z > d, \quad r = |M| \to \infty.$$

The asymptotical estimation of the Weyl-Sommerfeld integrals [7] allows to present the components of the far field patterns for P/S polarization as finite linear combinations of elementary functions. This circumstance ensures a low costs computer analysis of the scattering characteristics in the far zone.

3. Numerical results and discussion.

The Differential Scattering Cross-Section (DSC) is calculated as:

$$I^{P,S}(\theta_1,\theta,\varphi) = \left|E^{P,S}_{\infty,\theta}(\theta_1,\theta,\varphi)\right|^2 + \left|E^{P,S}_{\infty,\varphi}(\theta_1,\theta,\varphi)\right|^2, \qquad (2)$$

where $E^{P,S}_{\infty,\theta,\varphi}(\theta_1,\theta,\varphi)$ are the components of the far field pattern for a P and S polarized incident wave, in a spherical coordinate system θ,φ [4].

We will consider the Transmission Cross-Section (TCS), which represents the integrated intensity transmitted into the upper semi-sphere $\Omega = \{0^\circ \le \theta \le 90^\circ,\ 0^\circ \le \varphi \le 360^\circ\}$:

$$\sigma^{P,S}(\theta_1) = \int_\Omega I^{P,S}(\theta_1,\theta,\varphi)d\omega. \qquad (3)$$

Next, we will present exemplary numerical results obtained using the DSM model. We consider the scattering properties of the hole excited by a light source with wavelengths in the range of λ=400-700nm. The refractive indices of the film materials were taken from the paper by Lynch and Hunter [8].

In Figure 2 the TCS (3) versus the incident angle is presented for a hole with diameter D=30nm in an Ag film of thickness d=40nm for two different cases: when both the upper half-space and the hole are filled either with water or air. In Figure 3 the TCS versus incident angle is presented for the hole of D=35nm in Ag and Au films of thickness d=50nm for both polarizations under a fixed wavelength λ=532nm.

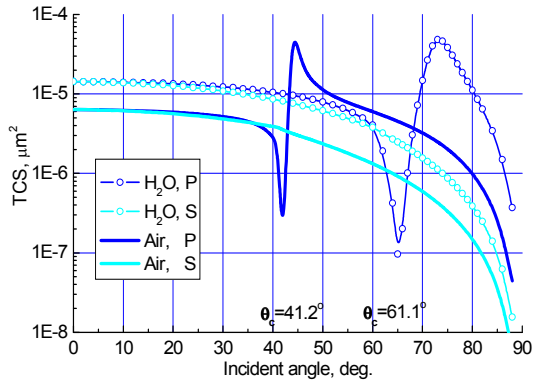

Figure 2. TCS (3) for the hole of diameter D=30nm in silver (Ag) film of thickness d=40nm in cases of air and water inside the hole

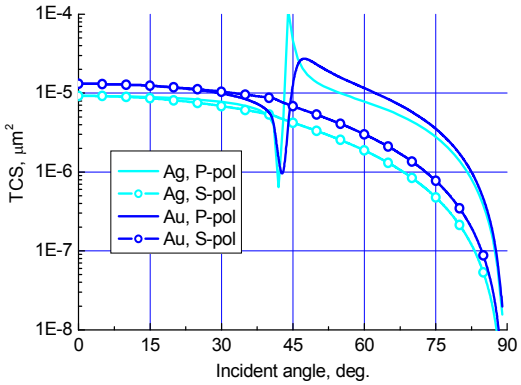

Figure 3. TCS for a hole D=35nm in gold (Au) and silver (Ag) films of d=50nm on glass prism, λ=532nm

Conclusion

In this work the DSM has been adjusted to model the scattering properties of a single nanohole in a noble-metal film deposited on a glass prism. The influence of the film thickness and material as well as the diameter and filling of the hole on this effect was investigated. Detailed numerical results and their discussion will be presented on conference.

Acknowledgement

We gratefully acknowledge funding of this research by Deutsche Forschungsgemeinschaft (DFG) and the Russian Foundation for Basic Research (RFBR).

References:

[1] T.W. Ebbesen, H.J. Lezec, H.F. Ghaemi, T. Thio and P.A. Wolff. Extraordinary optical transmission through sub-wavelength hole arrays. Nature 391 (1998), p. 667.
[2] R. Wannemacher, Plasmon-supported transmission of light through nanometric holes in metallic thin films, Opt. Comm. 195 (2001) 107.
[3] Yu.A. Eremin, The Method of Discrete Sources in electromagnetic scattering by axially symmetric structures, J. Comm. Technology and Electronics. 45 (2) (2000) 269.
[4] E. Eremina, Y. Eremin, N. Grishina, T. Wriedt Analysis of light scattering in the evanescent waves area by a cylindrical nanohole in a noble-metal film. Opt. Comm 281 (2008) 3581.
[5] J.A. Kong, Electromagnetic Wave Theory, EMW Publ., Cambridge, MA, 2000.
[6] A. Doicu, Yu. Eremin, T. Wriedt, Acoustic and Electromagnetic Scattering Analysis using Discrete Sources, Academic Press, London, 2000.
[7] Y. Eremin, N. Orlov and A. Sveshnikov, in: T. Wriedt (Ed.), Generalizes Multipole Techniques for Electromagnetic and Light Scattering. Elsevier Science, Amsterdam, 1999, 39.
[8] D.W. Lynch and W.R. Hunter, Comments on the Optical Constants of Metal and an Introduction to the Data for Several Metals, in Palik ED (ed.): Handbook of Optical Constants of Solids 1, Academic Press, San Diego, 1985.

Light scattering by inhomogeneous concave-hull-transformed clusters of spheres

Hannakaisa Erkkilä and Karri Muinonen

Observatory, Kopernikuksentie 1, P.O. Box 14, FI-00014 University of Helsinki, Finland
e-mail: hannakaisa.erkkila@helsinki.fi

Abstract

Light scattering by coated aggregates of spheres is studied using the discrete-dipole approximation. The coatings are formed by a concave-hull transformation, which proves to be highly applicable in particle inhomogeneity studies. The scattering results for depolarization yield an intriguing double-lobe feature near backscattering direction. Intensity and polarization results are compared to light scattering by concave-hull-transformed Gaussian random particles.

1 Introduction

Small particles in nature, e.g., atmospheric particles or interplanetary dust particles, have often inhomogeneous internal composition in addition to nonspherical shapes. In fact, nonsphericity can encourage for inhomogeneity, because material is easily collected in the surface concavities of a particle.

The previously introduced concave-hull-transformation method [1] is here utilized to model the inhomogeneities by rolling a generating sphere over a cluster of spheres. The inner surface formed by the generating sphere defines the resulting shape of the particle, and the volume added by the transformation is treated as a coating which makes the particle inhomogeneous. Example shapes generated using clusters of 10 spheres and 100 spheres are presented in Fig. 1.

The only parameter of the concave-hull transformation is the scale radius h which, for the clusters of spheres, denotes the ratio of the generating-sphere radius to the radius of a sphere of equal volume than the cluster. The example shapes in Fig. 1 were generated using a scale radius $h = 2$.

2 Scattering by concave-hull-transformed clusters of spheres

The random ballistic clusters were studied using 10 and 100 spheres, and three sample clusters were generated in both cases to obtain a tentative average over the results. Two complex refractive indices were used to model silicate and slightly absorbing ice: $m_s = 1.55 + 0.001i$ and $m_i = 1.31 + 0.001i$.

Light-scattering characteristics by the inhomogeneous, coated clusters of spheres were computed using the discrete-dipole approximation code DDSCAT [2]. Random orientation was mimicked by computing the scattering properties in 1296 orientations. The equal-volume-sphere size parameters for the clusters of 10 spheres are, for uncoated and coated particles, $x = 5.0 \pm 0.2$ and $x = 6.1 \pm 0.2$, respectively. For clusters of 100 spheres, the size parameters are $x = 4.0 \pm 0.1$ and $x = 6.1 \pm 0.3$.

The results of the computations are shown in Fig. 2 for all the combinations of cluster and coating compositions, when refractive indices of ice and silicate are used. In addition to intensity and the degree of linear polarization for unpolarized incident light, depolarization results $1 - S_{22}/S_{11}$ are also considered. For spheres, S_{22}/S_{11} is equal to unity and, therefore, depolarization can indicate particle-shape deviations from spherical, although the effect is not systematic.

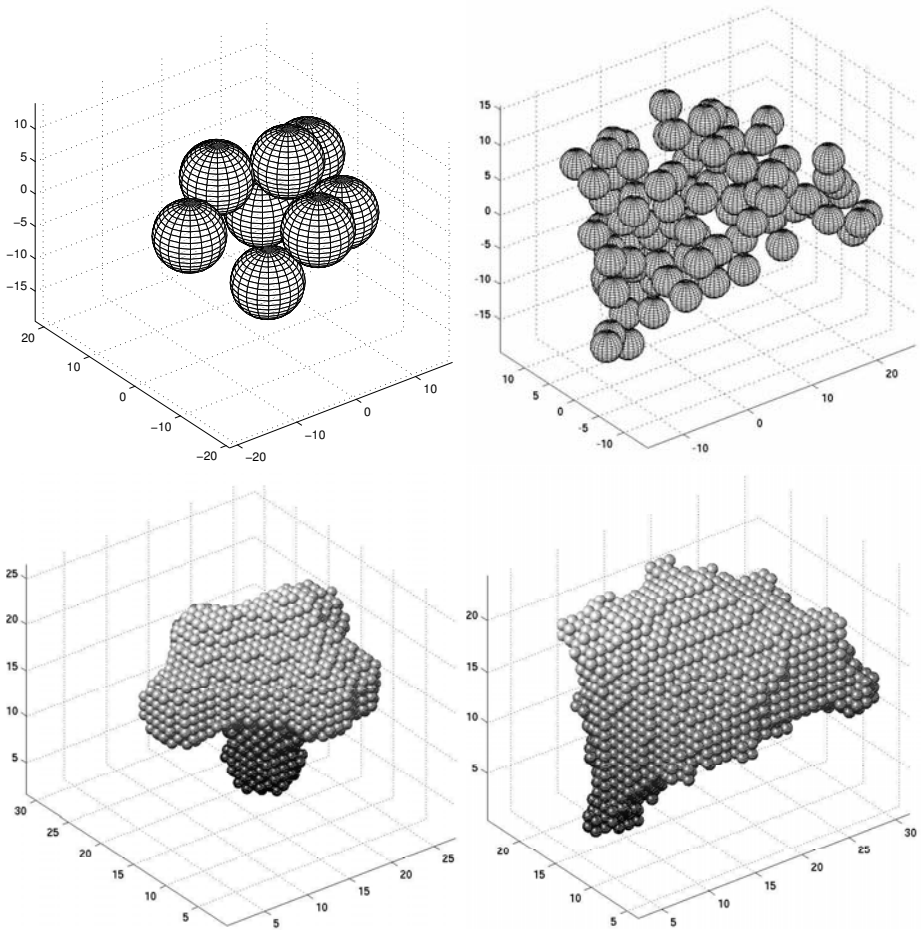

Figure 1: Ballistic clusters of spheres (top) with 10 (left) and 100 (right) equal-size spheres and their concave hulls (bottom) generated with a sphere of scale radius $h = 2$. The concave-hull-transformed particles are shown in a form discretized for DDA computations.

For the clusters of 10 spheres, the cluster composition clearly dominates the scattering characteristics whereas, for the clusters of 100 spheres, the results are grouped according to the coating composition. As a material, silicate scatters effectively more than ice. Light scattered by the coated clusters of 10 spheres is more positively polarized than observed for clusters without the coating. On the contrary, the uncoated clusters of 100 spheres have a polarization profile quite similar to the entirely positive Rayleigh polarization, probably because the spheres in the clusters are small enough compared to the wavelength of incident light. With the coatings, the polarization decreases, which is most prominently seen in the particles with silicate coatings. Near the backscattering direction, the intensity increases nonlinearly and polarization has negative values as explained in [3] and [4].

A comparison between the light scattering results obtained here for the coated clusters and the results for the concave-hull-transformed Gaussian random particles in [1] yields that, although the intensity of the scattered light varies quite similarly as a function of the scattering angle, there are major differences in polarization behaviour. The Gaussian-random-particle geometry is generated by deforming a sphere [5], which is probably the reason for the resonant oscillations observed in the polarization curves of the Gaussian particles. These resonances are not as pronounced for the clusters of spheres, as seen in Fig. 2.

One yet unexplained feature is observed in the depolarization results: for large scattering-angle values,

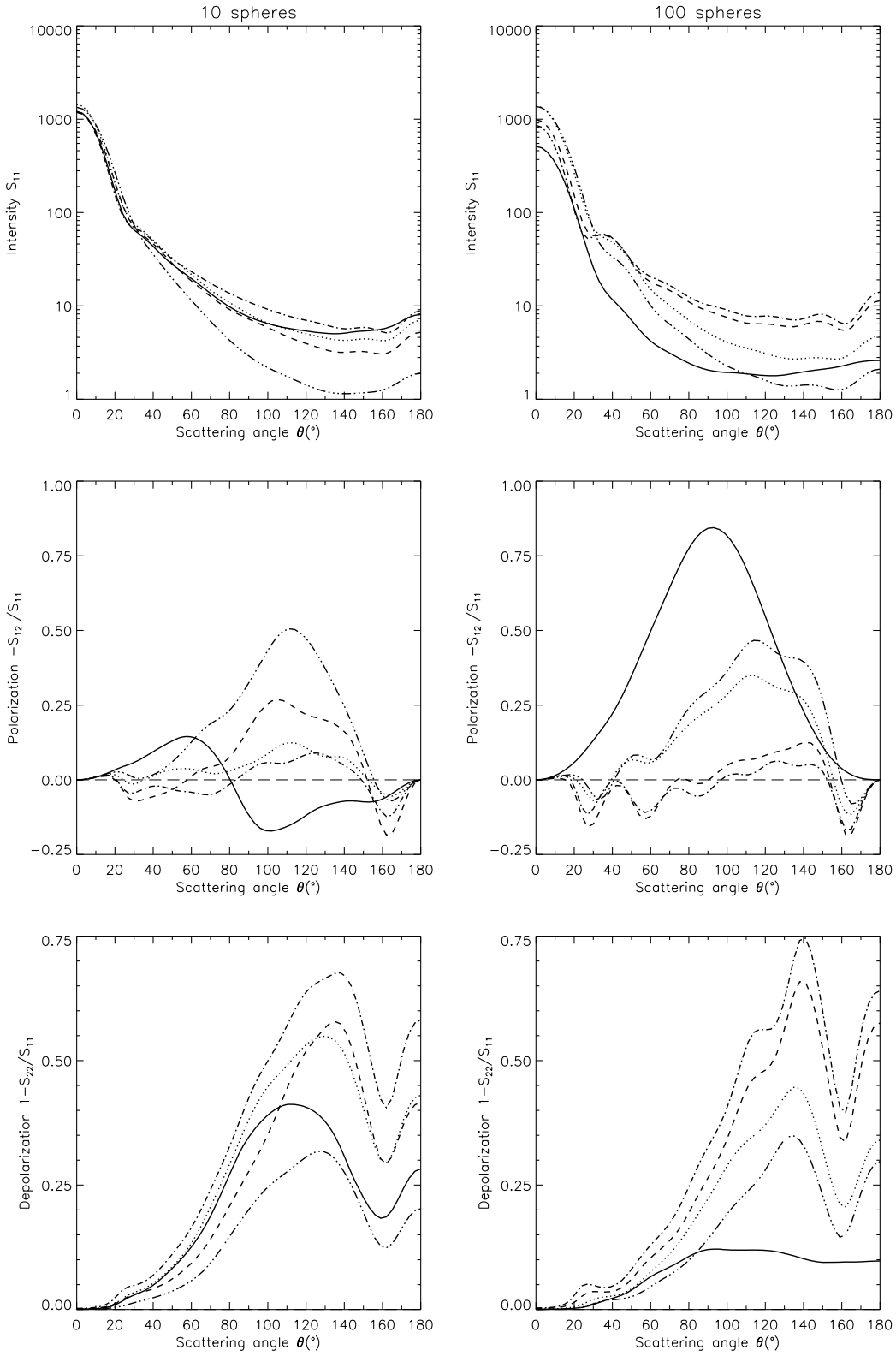

Figure 2: DDA results for inhomogeneous particles. The solid line denotes the silicate-composed cluster of spheres, while the dotted line refers to a silicate cluster with an icy coating, and the dashed line represents an icy cluster with a silicate coating. Dash-dot line is used for silicate particles and dash-triple-dot for icy particles.

depolarization performs systematically a double-lobe feature. The minimum between the two peaks occurs at approximately a constant angle, $\theta \approx 160°$, for every particle, despite the composition or the number of spheres in the original cluster. Particle composition affects the height of the maxima and the depth of the minimum, but the phenomenon is, nevertheless, similar in all cases studied. The double-lobe feature has been observed previously in light-scattering computations, e.g., in [3] and [6], and also in laboratory measurements [7]. Note that depolarization is not observed if the incident light is unpolarized (e.g., sunlight).

3 Discussion

The concave-hull transformation presented in [1] has been developed further and applied to clusters of spheres. In all, the concave hull proved to be an efficient tool in modelling particle inhomogeneity: the coatings added on the homogeneous particles appear realistic and offer a promising method in the studies of, e.g., atmospheric mineral aerosols that easily collect inhomogeneities in their grooves, or interplanetary dust particles which possess an aggregate-like structure and are often inhomogeneous due to the space environment exposure. For practical applications, the simulations could be repeated using realistic size distributions for the particles.

In light-scattering computations, a common feature was observed for the particles despite the composition or shape: a double-lobe structure of depolarization near the backscattering direction. The mechanism behind this intriguing feature has not yet been uncovered, but in all likelihood, it has a connection to the mechanisms causing the backscattering phenomena for intensity and polarization, because the maxima and minima were seen to mostly coincide. Definitely, the effects seen in depolarization call for an in-depth mechanism study in the future.

References

[1] Muinonen, K. and Erkkilä, H. (2007).“Scattering of light by concave-hull-transformed Gaussian particles”, *Tenth Conference on Electromagnetic & Light Scattering*, Videen, G., Mishchenko, M., Mengüc, M. P. and Zakharova, N. Eds. (Bodrum, Turkey, June 17-22, 2007), 125-128.

[2] Draine, B. T. and Flatau, P. J. (2004). “User guide to the discrete-dipole approximation code DDSCAT 6.1”, http://arxiv.org/abs/astro-ph/0409262v2.

[3] Muinonen, K., Zubko, E., Tyynelä, J., Shkuratov, Y. G., and Videen, G. (2007). “Light scattering by Gaussian random particles with discrete-dipole approximation”, *JQSRT*, **106**, 360-377.

[4] Tyynelä, J., Zubko, E., Videen, G., and Muinonen, K. (2007). “Interrelating angular scattering characteristics to internal electric fields for wavelength-scale spherical particles”, *JQSRT*, **106**, 520-534.

[5] Muinonen, K., Nousiainen, T., Fast, P., Lumme, K., and Peltoniemi, J. I. (1996). “Light scattering by Gaussian random particles: ray optics approximation”, *JQSRT*, **55**, 577-601.

[6] Zubko, E., Muinonen, K., Shkuratov, Y., Videen, G., and Nousiainen, T. (2007). “Scattering of light by roughened Gaussian random particles”, *JQSRT*, **106**, 604-615.

[7] Volten, H., Muñoz, O., Brucato, J. R., Hovenier, J. W., Colangeli, L., Waters, L. B. F. M., and van der Zande, W. J. (2006). “Scattering matrices and reflectance spectra of forsterite particles with different size distributions”, *JQSRT*, **100**, 429-436.

Unified Approach to the Methods Using Single Field Expansions

Victor Farafonov[1], Evgeny Farafonov[1], Vladimir Il'in[2], Alexander Vinokurov[1]

[1] *University of Aerocosmic Instrumentation, Bol. Morskaya 67, St. Petersburg, 190000 Russia*
[2] *St. Petersburg University, Universitetskij pr., 28, St. Petersburg, 198504 Russia*
tel: +7 (812) 783-2236, fax: +7 (812) 428-7129, e-mail: ilin55@yandex.ru

Abstract

We present a unified approach to the separation of variables (SVM), extended boundary condition (EBCM) and point-matching (PMM) methods based on expanding the electromagnetic fields in terms of some wave functions. Because of essential difference in the light scattering problem formulation used by these methods, earlier they were developed independently. We demonstrate that the *same* 10 integrals of the radial and angular functions and their first derivatives are to be computed within each of the methods to find the unknown scattered and internal field expansion coefficients in the case of axisymmetric scatterers. These integrals are shown to be similar for different (spherical, cylindrical, spheroidal) coordinates (and corresponding functions) applied. So, the methods are unexpectedly tightly related.

1 Introduction

The exact light scattering methods based on expanding the fields in terms of wave functions (EBCM, SVM, and to less extend PMM) are widely applied due to their high efficiency for simple shape and structure scatterers [1,2].

In this paper we first describe the methods under consideration and emphasize their essential difference, and then outline the suggested approach to the methods and the main result of the work.

2 Methods under consideration

The SVM, EBCM and PMM solve the light scattering problem by using the expansions of the harmonic fields $\vec{E}, \vec{H}(\vec{r})$ in terms of some wave functions $\vec{F}_\nu(\vec{r})$

$$\vec{E}(\vec{r}) = \sum_\nu \alpha_\nu \vec{F}_\nu(\vec{r}), \qquad \vec{H}(\vec{r}) = \sum_\nu \beta_\nu \vec{F}_\nu(\vec{r}). \tag{1}$$

In the *SVM* the classic light scattering problem formulation is used, i.e. for the electric field

$$\Delta\vec{E}(\vec{r}) + k^2\vec{E}(\vec{r}) = 0, \qquad \left(\vec{E}^0(\vec{r}) + \vec{E}^{\rm s}(\vec{r})\right) \times \vec{n}(\vec{r}) = \vec{E}^{\rm i}(\vec{r}) \times \vec{n}(\vec{r}) \quad \text{for} \quad \vec{r} \in S, \tag{2}$$

where $\vec{E}^0, \vec{E}^{\rm s}, \vec{E}^{\rm i}$ denote the incident, scattered and internal fields respectively, $\vec{n}$ is the external normal to the scatterer boundary S, the wavenumber $k = \frac{2\pi m}{\lambda}$ with λ and m being the wavelength of radiation and the refractive index. Further, one substitutes the first N terms of the expansions (1) in the boundary condition (2), multiplies both projections of this condition by the angular part of the functions $\vec{F}_{\nu'}$ for $\nu' = 0, 1, ..., N$ and integrates the result over the scatterer surface [1,3]. So, one gets $2(N+1)$ equations relative to $2(N+1)$ unknown coefficients of the scattered ($\alpha^{\rm s}_\nu$) and internal ($\alpha^{\rm i}_\nu$) field expansions

$$\begin{pmatrix} A & B \\ C & D \end{pmatrix} \vec{x}^{\rm s,i} = \begin{pmatrix} E \\ F \end{pmatrix} \vec{x}^0, \tag{3}$$

where $A, B, ..., F$ are matrices whose elements are integrals of the wave functions, $\vec{x}^{\,\mathrm{s,i}} = \{\alpha_\nu^{\mathrm{s}}, \alpha_\nu^{\mathrm{i}}\}_{\nu=0}^{N}$, $\vec{x}^{\,0} = \{\alpha_\nu^{0}\}_{\nu=0}^{N}$ is a vector with known coefficients of the incident field expansion. Solution of the system (3) gives the unknown coefficients which allow one to calculate any light scattering characteristics.

In the *EBCM* an equivalent surface integral formulation of the problem is applied

$$\vec{\nabla} \times \int_S \vec{n}(\vec{r}\,') \times \vec{E}^{\mathrm{i}}(\vec{r}\,') G(\vec{r}, \vec{r}\,') \mathrm{d}s' - \frac{1}{ik_0\varepsilon} \vec{\nabla} \times \vec{\nabla} \times \int_S \vec{n}(\vec{r}\,') \times \left(\vec{\nabla} \times \vec{E}^{\mathrm{i}}(\vec{r}\,')\right) G(\vec{r}, \vec{r}\,') \mathrm{d}s' = \\ = -\vec{E}^{0}(\vec{r}), \quad \vec{r} \in D \quad \text{or} \quad \vec{E}^{\mathrm{s}}(\vec{r}), \quad \vec{r} \in R \setminus \bar{D}, \qquad (4)$$

where $G(\vec{r}, \vec{r}\,')$ is the Green function of the wave equation (2) for free space (the wavenumber is $k_0 = \frac{2\pi}{\lambda}$), D means the interior of the scatterer. The first $N+1$ terms of the field expansions (1) and the known Green function expansion in terms of the same wave functions are substituted in the extended boundary conditions (4) [1-3]. Completeness of the basis functions used allows one to equal the expansion coefficients for each of $N+1$ functions $\vec{F}_\nu$ involved. Two equations provided by (4) give two matrix equations

$$-Q_1 \vec{x}^{\,\mathrm{i}} = \vec{x}^{\,0}, \qquad -\vec{x}^{\,\mathrm{s}} + Q_2 \vec{x}^{\,\mathrm{i}} = 0, \qquad (5)$$

where the matrices Q_1, Q_2 have elements being integrals of the wave functions, $\vec{x}^{\,\mathrm{s}} = \{\alpha_\nu^{\mathrm{s}}\}_{\nu=0}^{N}$, and $\vec{x}^{\,\mathrm{i}} = \{\alpha_\nu^{\mathrm{i}}\}_{\nu=0}^{N}$.

In the *PMM* one uses minimization of the residual Δ describing fulfilment of the boundary conditions (2) at the scatterer surface S

$$\Delta = \int_S \left| \left(\vec{E}^{0}(\vec{r}\,') + \vec{E}^{\mathrm{s}}(\vec{r}\,')\right) \times \vec{n}(\vec{r}\,') - \vec{E}^{\mathrm{i}}(\vec{r}\,') \times \vec{n}(\vec{r}\,') \right|^2 \mathrm{d}s' \longrightarrow \min. \qquad (6)$$

The first $N+1$ term of the field expansions are substituted in the residual (6). The derivatives of the residual $\Delta(\vec{x}^{\,\mathrm{s}}, \vec{x}^{\,\mathrm{i}})$ with respect to the unknown coefficients $\alpha_\nu^{\mathrm{s}}, \alpha_\nu^{\mathrm{i}}, \nu = 0, 1, ..., N$ are made equal to 0, which gives $2(N+1)$ linear algebraic equations relative to these coefficients [2,3]. As a result one gets a system like (3) but with other elements being obtained here from relaxing (6).

Thus, the way of solution of the problem essentially differs in three considered methods.

3 Approach to the methods and the main result

Instead of the fields and their usual expansions (1) in terms of vector wave functions we utilized scalar potentials and their expansions in terms of scalar functions (see Appendix for some details).

In our approach the potentials V, U are combined for axisymmetric scatterers as follows:

$$\vec{E}^{\mathrm{tm}} = \vec{\nabla} \times (V_{\mathrm{m}} \vec{r} + U_{\mathrm{m}} \vec{i}_{\mathrm{z}}), \quad \vec{E}^{\mathrm{te}} = -\frac{1}{ik\varepsilon} \vec{\nabla} \times \vec{\nabla} \times (V_{\mathrm{e}} \vec{r} + U_{\mathrm{e}} \vec{i}_{\mathrm{z}}), \qquad (7)$$

where the superscripts (tm, te) denote two kinds of the incident plane wave polarization [3].

The potentials are expanded in the functions (19) or (20) depending on the coordinates selected

$$\begin{matrix} V_{\mathrm{m}} \\ V_{\mathrm{e}} \end{matrix} = \sum_{m=0}^{\infty} \sum_{l=m}^{\infty} \begin{matrix} a_{ml}^{\mathrm{v}} \\ b_{ml}^{\mathrm{v}} \end{matrix} \varphi_{ml}, \qquad \begin{matrix} U_{\mathrm{m}} \\ U_{\mathrm{e}} \end{matrix} = \sum_{m=0}^{\infty} \sum_{l=m}^{\infty} \begin{matrix} a_{ml}^{\mathrm{u}} \\ b_{ml}^{\mathrm{u}} \end{matrix} \varphi_{ml}. \qquad (8)$$

Such expansions are completely equivalent to the field expansions in terms of the corresponding vector functions

$$\vec{E}^{\mathrm{tm}} = \sum_{m=0}^{\infty} \sum_{l=m}^{\infty} \left(a_{ml}^{\mathrm{v}} \vec{M}_{ml}^{\mathrm{r}} + a_{ml}^{\mathrm{u}} \vec{M}_{ml}^{\mathrm{z}}\right), \quad \vec{E}^{\mathrm{te}} = \sum_{m=0}^{\infty} \sum_{l=m}^{\infty} \left(b_{ml}^{\mathrm{v}} \vec{N}_{ml}^{\mathrm{r}} + b_{ml}^{\mathrm{u}} \vec{N}_{ml}^{\mathrm{z}}\right), \qquad (9)$$

where $\vec{M}^{\rm r} = \vec{\nabla} \times (V\vec{r})$, ..., $\vec{N}^{\rm z} = -\frac{1}{ik\varepsilon}\vec{\nabla} \times \vec{\nabla} \times (U\vec{i}_{\rm z})$.

We also extract an axisymmetric (independent of φ) part of the fields, e.g.

$$\vec{E}^{\rm tm} = \vec{E}^{\rm tm}_{\rm A}(r,\theta) + \vec{E}^{\rm tm}_{\rm N}(r,\theta,\varphi), \quad \vec{E}^{\rm tm}_{\rm N} = \sum_{m=1}^{\infty}\sum_{l=m}^{\infty}\left(a^{\rm v}_{ml}\vec{M}^{\rm r}_{ml} + a^{\rm u}_{ml}\vec{M}^{\rm z}_{ml}\right). \tag{10}$$

Extraction of $\vec{E}_{\rm A}$ has some advantages discussed, e.g., in [3]. To treat $\vec{E}_{\rm A}$, we introduce an original scalar potential p that is expanded as follows:

$$p = \sum_{l=1}^{\infty} a^{\rm p}_l \varphi_{1l}. \tag{11}$$

Another important feature of our approach is the use of specially normalized angular functions in the expansions (8), (11): $\bar{P}^m_l = P^m_l/N^{\rm s}_{ml}$ and $\bar{S}_{ml} = S_{ml}/N^{\rm sp}_{ml}$ and definition of 10 integrals of the radial and angular functions and their first derivatives $a_{nl}, b_{nl}, ...$ (for each azimuthal number m) like the following one:

$$\text{for the spherical coordinates :} \qquad a_{nl} = \int_0^{\frac{\pi}{2}} j_l(kr(\theta))\,\bar{P}^m_l(\cos\theta)\,\bar{P}^m_n(\cos\theta)\,\sin\theta\,{\rm d}\theta, \tag{12}$$

$$\text{for the prolate spheroidal ones :} \qquad a_{nl} = \int_{-1}^{1} R^{(1)}_{ml}(kc,\xi(\eta))\,\bar{S}_{ml}(kc,\eta)\,\bar{S}_{mn}(c,\eta)\,{\rm d}\eta. \tag{13}$$

One needs to calculate all these integrals to obtain $\vec{E}_{\rm N}$, but only 6 of them are necessary to derive $\vec{E}_{\rm A}$. The latter case is used below for illustration.

The main result of our work is that **these and only these** *matrix blocks (integrals) are required to derive the systems matrices in all three methods. And this holds for* **any** *(spherical, cylindrical, spheroidal, etc.) coordinates for which the separation of variables (19),(20) is possible.*

The integrals form the matrix blocks of the systems (3) arising in the SVM

$$A^{\rm svm} = A = \{a_{nl}\}^{\infty}_{n,l=1}, \quad B^{\rm svm} = B = \{b_{nl}\}^{\infty}_{n,l=1}, \quad ..., \quad F^{\rm svm} = F = \{f_{nl}\}^{\infty}_{n,l=1}. \tag{14}$$

For the EBCM, we have (the superscript T denotes the transposed matrices)

$$Q_1 = i[C^{\rm T}B - A^{\rm T}D], \quad Q_2 = -i[F^{\rm T}B - E^{\rm T}D]. \tag{15}$$

For the PMM, it was obtained that (the asterisk means the complex conjugation)

$$A^{\rm pmm} = (A^{\rm T})^*A + (C^{\rm T})^*C, \quad B^{\rm pmm} = -[(A^{\rm T})^*B + (C^{\rm T})^*D], \ ... \tag{16}$$

In Table 1 we give just a few values of the extinction ($C_{\rm ext}$) and scattering ($C_{\rm sca}$) cross-sections calculated by different methods. Excellent agreement of the results confirms the correctness of the ansatz suggested. More numerical examples will be presented at the conference.

Thus, we find an elegant independent of the coordinates used formulation of three essentially different methods: SVM, EBCM, and PMM. Our SVM solution to the light scattering problem for axisymmetric particles needs calculation of 10 integrals. We demonstrate that the same integrals allow one to get the EBCM and PMM solutions. This shows an unexpectedly tight relation of the methods and gives a ground for creation of a code being not more complex than that for any of the methods, but combining their advantages.

The work was supported by the grants RFFI 07-02-00831, RNP 2.1.1.2852 and NSh 1318.2008.2.

References

[1] Mishchenko MI, Hovenier J, and Travis LD (eds), Light Scattering by Nonspherical Particles (San Diego: Academic Press, 2000).

[2] Kahnert FM, JQSRT, v.79, p. 775-824 (2003).

[3] Farafonov VG, Il'in VB, In: Kokhanovsky A (ed), Light Scattering Reviews (Berlin: Springer-Praxis, 2006), p. 125-77.

Appendix: Scalar potentials

The wave equation (1) has three general solutions, but only two of them satisfy the equation $\vec{\nabla} \cdot \vec{E} = 0$ and can be used for the field expansions

$$\vec{M}_\nu^{\rm a} = \vec{\nabla} \times (\varphi_\nu \, \vec{a}) \,, \quad \vec{N}_\nu^{\rm a} = \frac{1}{k} \vec{\nabla} \times \vec{\nabla} \times (\varphi_\nu \, \vec{a}) \,, \tag{17}$$

where $\vec{a}$ is a vector, φ_ν a scalar potential being solution to the scalar Helmholtz equation

$$\Delta \varphi_\nu(\vec{r}) + k^2 \varphi_\nu(\vec{r}) = 0. \tag{18}$$

In several coordinate systems this equation can be solved by *separation of variables*. For example, in spherical coordinates (r, θ, φ), one has

$$\varphi_{ml}(r, \theta, \varphi) = z_l(kr) \, P_l^m(\cos\theta) \, \cos m\varphi, \tag{19}$$

where the radial functions $z_l(kr)$ are the spherical Bessel ($j_l(kr)$) or first kind Hankel ($h_l^{(1)}(kr)$) functions, $P_l^m(\cos\theta)$ the associated Legendre functions. In spheroidal coordinates (ξ, η, φ)

$$\varphi_{ml}(\xi, \eta, \varphi) = R_{ml}(c, \xi) \, S_{ml}(c, \eta) \, \cos m\varphi, \tag{20}$$

where $R_{ml}(c, \xi)$ are the first or third kind prolate radial spheroidal functions, $S_{ml}(c, \eta)$ the prolate angular spheroidal functions, c is a parameter defining the system.

When one solves the light scattering problem for a sphere in spherical coordinates or for a cylinder in cylindrical ones, in fact a pair of scalar potentials $V_{\rm e}, V_{\rm m}$ or $U_{\rm e}, U_{\rm m}$ are introduced. For instance, for one kind of the incident wave polarization one has

$$\text{sph}: \vec{E} = \vec{\nabla} \times (V_{\rm m} \vec{r}) - \frac{1}{ik\varepsilon} \vec{\nabla} \times \vec{\nabla} \times (V_{\rm e} \vec{r}), \quad \text{cyl}: \vec{E} = \vec{\nabla} \times (U_{\rm m} \vec{i}_{\rm z}) - \frac{1}{ik\varepsilon} \vec{\nabla} \times \vec{\nabla} \times (U_{\rm e} \vec{i}_{\rm z}), \tag{21}$$

where $\varepsilon = m^2$, $\vec{i}_{\rm z}$ is the unit vector along the infinite cylinder axis (z-axis).

Table 1: Cross-sections computed for a spheroid ($a/b = 1.5$) and a Chebyshev particle ($n = 5$, $\epsilon = 0.07$) by three methods with $N = 20$ terms kept ($m = 1.5, x_{\rm v} = 1, \alpha = 45°$, spherical basis)

	Spheroid		Chebyshev particle	
	$C_{\rm ext}$	$C_{\rm sca}$	$C_{\rm ext}$	$C_{\rm sca}$
SVM	0.4062428581	0.4062428585	0.334616303	0.334616301
EBCM	0.4062428589	0.4062428585	0.334616303	0.334616305
PMM	0.4062428581	0.4062428585	0.334616303	0.334616301

Modeling of surface phonon-polaritons coupling in thin films for near-field thermal radiation

Mathieu Francoeur,[1] M. Pinar Mengüç,[1] and Rodolphe Vaillon[2]

[1] University of Kentucky, Department of Mechanical Engineering, Radiative Transfer Laboratory, 322 RGAN bldg., Lexington, KY 40506, USA
e-mails: mfran0@engr.uky.edu, menguc@engr.uky.edu
[2] Centre de Thermique de Lyon (CETHIL, CNRS-INSA Lyon-UCBL), Bât. Sadi Carnot, 20 av. A. Einstein, 69621 Villeurbanne Cedex, France, e-mail: rodolphe.vaillon@insa-lyon.fr

Abstract

We investigate near-field thermal radiation between a thin (10-100 nm) film emitter and a bulk SiC using Maxwell's equations and fluctuational electrodynamics. Results obtained via a modified T-matrix approach show a narrow spectral band enhancement of the radiative flux for nanometric emitters due to a coupling of surface phonon-polaritons inside the film.

1 Introduction

Near-field effects of thermal radiation lead to an increase of radiant energy exchanges beyond Planck's blackbody distribution (due to tunneling) taking place in a narrow spectral band if surface polaritons are thermally excited. While thermal emission from bulk materials in the near-field and from thin films for far-field control has been studied during the past years, little attention has been paid to near-field radiative heat transfer involving a thin film emitter.

It was shown recently that the near-field energy density above a 10 nm thick emitting film of SiC is more than an order of magnitude higher than for a bulk SiC around the resonant frequency of surface phonon-polaritons (SPhP) [1]. Biehs et al. [2,3] studied near-field energy density of thin metallic emitters and materials coated with metallic films, and explained the enhancements by the coupling of surface plasmon-polaritons (SPP) inside the films. In general, SPhP are easier to excite thermally than SPP since their resonance is in the infrared region; for example, resonance of SPhP for a SiC-vacuum interface is around 10.55 μm (1.786×10^{14} rad/s).

In this work, we study near-field radiative heat transfer from thin SiC film emitters submerged in vacuum, and show that the coupling of SPhP inside the emitting thin film is responsible for the enhancement of the radiative flux.

2 Theory

2.1 Near-field radiative heat transfer in 1D layered medium

We consider radiative transfer between a SiC emitter of finite thickness t (medium 1) and a bulk SiC (medium 3) spaced by a vaccum gap d, as shown in Fig. 1. The near-field radiative heat flux between media 1 and 3 is derived starting from Maxwell's equations and using fluctuational electrodynamics (FE), where the source of thermal radiation is modeled as a stochastic current density vector in Ampère's law [4]. Derivation of a solution for the time-averaged Poynting vector (i.e., radiative heat flux) for non-magnetic and isotropic media defined by a dielectric constant local in space [4] in the z-direction at location z_2^+ in medium 3 leads to:

$$q_{13}(z_2^+,\omega)=\frac{k_v^2\Theta(\omega,T_1)}{\pi^2}\mathrm{Re}\left\{i\varepsilon''_{r1}(\omega)\int_0^\infty k_x dk_x\int_{z_0}^{z_1}dz'\begin{pmatrix} g^E_{13x\alpha}(k_x,z_2^+,z',\omega)g^{H*}_{13y\alpha}(k_x,z_2^+,z',\omega)\\ -g^E_{13y\alpha}(k_x,z_2^+,z',\omega)g^{H*}_{13x\alpha}(k_x,z_2^+,z',\omega)\end{pmatrix}\right\} \quad (1)$$

where k_v is the magnitude of the wavevector in vacuum, ω the angular frequency, ε''_{r1} the imaginary part of the dielectric function (ε_r = ε'_r + $i\varepsilon''_r$) of the source medium 1, k_x the wavevector parallel to the surfaces, and Θ the mean energy of a Planck oscillator in thermal equilibrium. Terms $g^{E/H}_{13j\alpha}$ (j = x or y) are the scalar electric/magnetic Wejl components of the Green's tensor relating the fields observed at z_2^+ due to a source located at z' [5]; the subscript α in Eq. (1) implies a summation over the three orthogonal components x, y, and z. When deriving Eq. (1), local thermodynamic equilibrium (LTE) of the emitting medium is assumed for the application of the fluctuation-dissipation theorem (linking the ensemble average of the spatial correlation function of stochastic current density and temperature of the medium). The fields in each layer are solved using a modified T-matrix approach to avoid numerical instabilities appearing when dealing with thick layers and/or evanescent waves [6]. The dielectric function of SiC is approximated by a damped harmonic oscillator model ε_r = $\varepsilon_\infty[1+(\omega_{LO}^2-\omega_{TO}^2)/(\omega_{TO}^2-\omega^2-i\gamma\omega)]$ with ε_∞ = 6.7, ω_{LO} = 1.825 × 10^{14} rad/s, ω_{TO} = 1.494 × 10^{14} rad/s, and γ = 8.966 × 10^{11} s^{-1} [7].

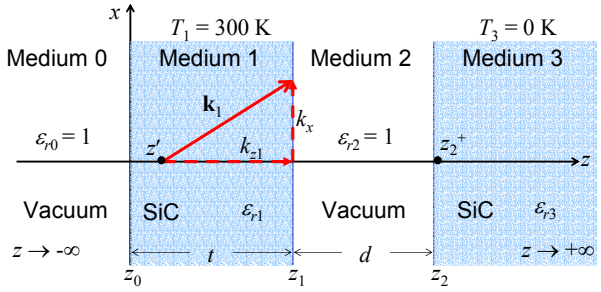

Figure 1: Geometry for near-field radiative heat transfer simulations between a SiC film (thickness t) and a bulk SiC spaced by a vacuum gap d.

2.2 Surface phonon-polaritons coupling in thin films

Transverse optical phonons (TO) generate SPhP at a polar crystal-dielectric interface, with evanescent fields in both media, due to out-of-phase oscillations of opposite charges. SPhP are excited via random thermal motion of charges inside the medium; note that these SPhP exist only in TM-polarization for non-magnetic materials. In thin films surrounded by dielectric materials, the evanescent field of SPhP associated with each interface can interact with each other inside the film. In that case, the dispersion relation of SPhP (i.e., ω as a function of k_x) splits into anti-symmetric and symmetric modes. Here, the terms anti-symmetric and symmetric refer to the distribution of the tangential electric field inside the film with respect to the middle plane of the layer [8]. The dispersion relation of SPhP for a film of thickness t (medium 1) surrounded by a dielectric material (medium 2) with the origin of the z-axis centered in the film leads to two possible resonances [8] :

$$L^+ : \varepsilon_{r1}k_{z2}+\varepsilon_{r2}k_{z1}\tanh\left(\frac{-ik_{z1}t}{2}\right)=0 \text{ and } L^- : \varepsilon_{r1}k_{z2}+\varepsilon_{r2}k_{z1}\coth\left(\frac{-ik_{z1}t}{2}\right)=0 \quad (2)$$

where L^+ and L^- refers to anti-symmetric and symmetric modes, respectively. Equations (2) are transcendental and solutions of the complex wavevectors for each mode are found using a Newton method for a system of two equations (i.e., real and imaginary parts). The dispersion relation of a SiC film, as a function of its thickness t, is shown in Fig. 2 and compared with the dispersion relation obtained for a single SiC-vacuum interface. For the single interface, resonance of SPhP occurs around 1.786 × 10^{14} rad/s where k_x becomes very large. On the other hand, two distinct branches (i.e., one for each mode) develop for thin films due to the coupling of SPhP, and this splitting becomes more pronounced as the film thickness decreases. Therefore, the splitting of the dispersion relation into two distinct branches for thin films increases the number of channels (i.e., k_x) available for radiative heat transfer, and can be

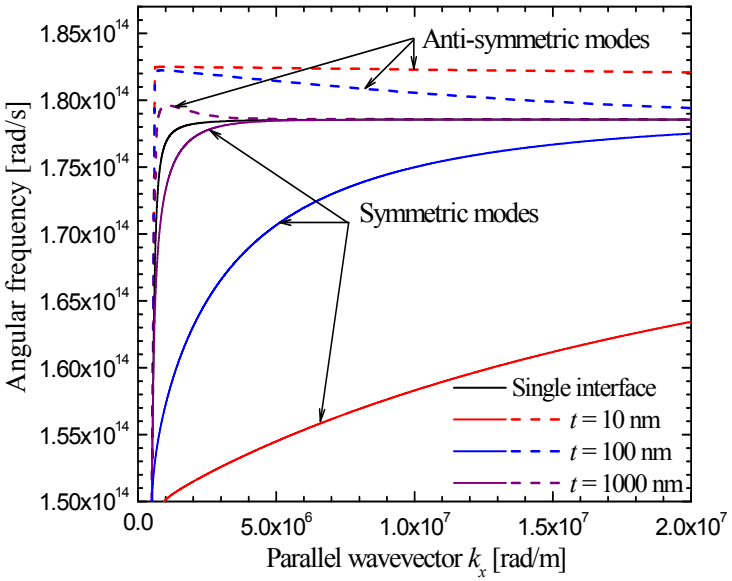

exploited to increase the radiative heat flux between closely spaced bodies. For large values of k_x, dispersion relations of both modes approach asymptotically the dispersion curve of a single interface; for large films, coupling of SPhP becomes impossible, and the anti-symmetric and symmetric branches merge into the curve for a single interface.

Figure 2: Dispersion relations for surface phonon-polaritons on a thin film of SiC submerged in vacuum; comparison with the dispersion relation on a single SiC-vacuum interface.

3 Results

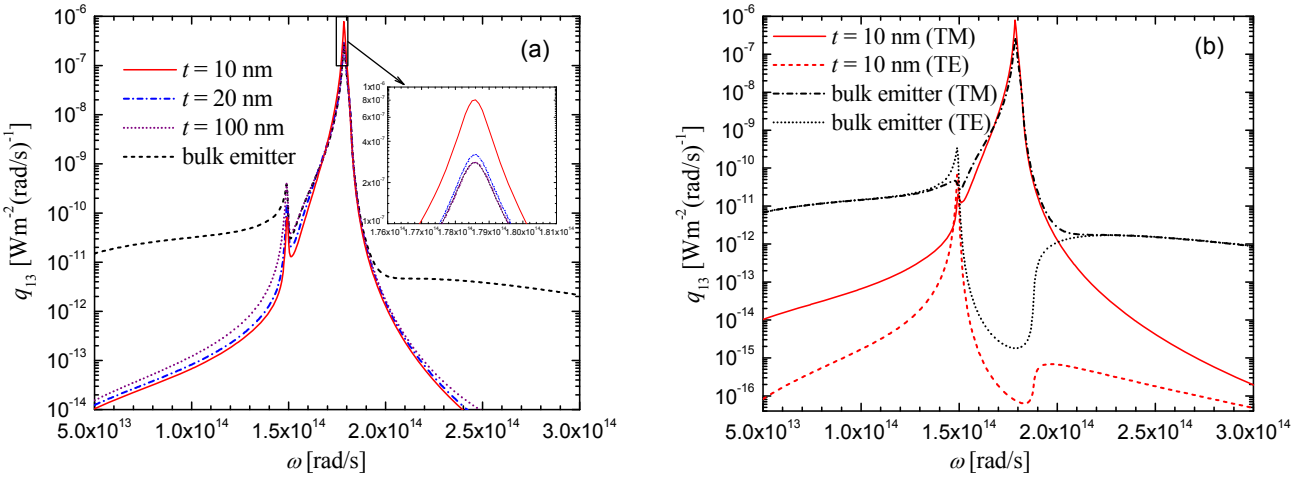

Figure 3: Monochromatic radiative heat flux between a SiC film of thickness t (at 300 K) and a bulk SiC (at 0 K) spaced by a vacuum gap of 10 nm. (a) Comparisons are shown for t = 10, 20, 100 nm and a bulk SiC emitter. (b) TE and TM evanescent contributions for t = 10 nm and a bulk SiC emitter.

Figure 3(a) shows the monochromatic radiative heat flux between media 1 and 3 for T_1 = 300 K, d = 10 nm, and t = 10, 20, 100 nm; results are compared with those obtained for a bulk SiC emitter. The radiative flux around the resonant frequency (ω_{res}) of SPhP increases as the thickness of the film decreases. On the other hand, the flux decreases for other frequencies because of the diminishing emitter source volume. The enhancement around ω_{res} for the film is due to SPhP coupling since the number of k_x available for radiative heat transfer increases at t decreases. This statement is confirmed by results depicted in Fig. 3(b), which show that only the TM evanescent contribution to the radiative heat flux is higher at ω_{res} for a 10 nm film emitter compared to a bulk emitter. This SPhP coupling enhancement quickly decreases as the film thickness increases; for t = 100 nm, the radiative heat flux at ω_{res} is identical to that for a bulk emitter. Note that the smaller peak of radiative heat flux (at 1.490 × 10^{14}

rad/s) for TE-polarization is due to the tunneling of regular evanescent waves which can lead to a maximum radiative heat flux proportional to ε'_{r1} times blackbody radiation. At this frequency, ε'_{r1} of SiC is very large, and consequently the contribution from this secondary peak to the radiative heat flux, not due to SPhP, decreases as the volume of the emitter decreases. For a bulk emitter, the total radiative heat flux (i.e., integrated over all angular frequencies) is 6.130 $\times 10^5$ W/m^2, where 6.079 $\times 10^5$ W/m^2 is concentrated within the spectral band between 1.500 $\times 10^{14}$ to 1.900 $\times 10^{14}$ rad/s. For an emitter of 10 nm submerged in vacuum, the total radiative heat flux increases substantially to a value of 1.3369 $\times 10^6$ W/m^2, with 1.3367 $\times 10^6$ W/m^2 within the band 1.500 $\times 10^{14}$ to 1.900 $\times 10^{14}$ rad/s.

4 Concluding Remarks

We have shown that near-field radiative heat transfer is enhanced around resonance of SPhP for nanometric film emitters due to SPhP coupling. As a consequence, the total radiative flux increases in a narrow spectral range which could potentially be exploited for nanoscale thermophotovoltaic power generation devices.

One may question the validity of applying FE to media as thin as 10 nm. Indeed, for nanometric films, we expect some deviations from FE where LTE has to be assumed. Despite the fact that the absolute values of radiative heat fluxes might contain a systematic error, the underlying physics of SPhP coupling in thin film and the associated enhancement of radiant energy exchanges caused by an increase of k_x is still valid; the trends and comparisons between thin films and bulk emitters reported here are consequently physically realistic.

Acknowledgments

MF is grateful to the NSERC (ES D3 scholarship), to the Graduate School of University of Kentucky (Dissertation year fellowship), and to the organization committee of ELS XI for covering travel and conference expenses.

References

[1] J. Drevillon, “Design ab-initio de matériaux micro et nanostructurés pour l’émission thermique cohérente en champ proche et en champ lointain,” PhD thesis, Université de Nantes (2007).

[2] S.-A. Biehs, D. Reddig, and M. Holthaus, “Thermal radiation and near-field energy density of thin metallic films,” Eur. Phys. J. B **55**, 237–251 (2007).

[3] S.-A. Biehs, “Thermal heat radiation, near-field energy density and near-field radiative heat transfer of coated materials,” Eur. Phys. J. B **58**, 423–431 (2007).

[4] M. Francoeur, and M. P. Mengüç, “Role of fluctuational electrodynamics in near-field radiative transfer” J. Quant. Spectrosc. Radiat. Transfer **109**, 280–293 (2008).

[5] J. E. Sipe, “New Green-function formalism for surface optics” J. Opt. Soc. Am. B **4**(4), 481–489 (1987).

[6] M. Auslender, and S. Hava, “Scattering-matrix propagation algorithm in full-vectorial optics of multilayer grating structures” Opt. Lett. **21**(21), 1765–1767 (1996).

[7] E. D. Palick, *Handbook of Optical Constants of Solids* (Vol.1, Academic Press, San Diego, 1998).

[8] J. A. Dionne, L. A. Sweatlock, H. A. Atwater, and A. Polman, “Planar metal plasmon waveguides: frequency-dependent dispersion, propagation, localization, and loss beyond the free electron model” Phys. Rev. B **72**, 075405 (2005).

On Green's function for cylindrically symmetric fields of polarized radiation

Juris Freimanis[1,2]

[1] *Ventspils University College, Ventspils International Radio Astronomy Center, Inzenieru iela 101, Ventspils, LV-3600, Latvia*
[2] *University of Latvia, Institute of Astronomy, Raina bulv. 19, Riga, LV-1586, Latvia*
tel: +371-29144160, fax: +371-63629660, e-mail: jurisf@venta.lv, freima@latnet.lv

Abstract

Analytic expressions for Green's function of stationary polarized radiative transfer equation in case of cylindrically symmetric radiation field are found, assuming that the medium is homogeneous, isotropic, infinite, with scalar extinction law and monochromatic nonconservative scattering.

1 Introduction

In the framework of the classical theory of polarized radiative transfer, Green's function for the inhomogeneous radiative transfer equation (RTE) has been considered by several authors. Domke investigated stationary monochromatic radiation fields with plane-parallel symmetry in homogeneous isotropic medium with scalar extinction if the phase matrix can be represented as a finite sum of generalized spherical functions [1, 2]. Freimanis extended these results to phase matrices obeying only some regularity conditions, and to the case if the homogeneous RTE has adjoint functions [3, 4]. Poutanen et al. [5] explored Green's function in case of Compton effect. Closed expressions were obtained for Green's function in case of spherically symmetric radiation field in homogeneous isotropic infinite medium with nonconservative scattering [6]. In this study analytic expressions for Green's function of the stationary RTE in homogeneous isotropic infinite medium with scalar extinction, monochromatic nonconservative scattering and cylindrically symmetric radiation field are found.

2 The physical conditions

In order to describe partially polarized radiation, in this section, Eq. (1), we use Stokes - Poincare (SP) representation where the radiation is characterized by Stokes vector consisting of Stokes parameters $(I, Q, U, V)^{\mathrm{T}}$, the latter being defined as in [7]. But for convenience of derivations, everywhere further only circular polarization (CP) representation is used, with Stokes vector $\boldsymbol{I} = (I_2, I_0, I_{-0}, I_{-2})^{\mathrm{T}} = ½(Q\text{-i}U,\ I\text{-}V,\ I\text{+}V,\ Q\text{+i}U)^{\mathrm{T}}$ (see [1]).

It is assumed that the medium obeys the following conditions:

- The medium is homogeneous, isotropic and infinite, and the extinction matrix is scalar.
- The scattering (and extinction) process is monochromatic.
- The scattering matrix is physically valid accordingly to Konovalov [8] almost everywhere on the interval $z \equiv \cos\theta \in [-1, 1]$, where θ is the scattering angle, and block-diagonal in SP representation (assuming the scattering plane as the plane of reference):

$$\boldsymbol{\Gamma}(z) = \begin{Vmatrix} a_1(z) & b(z) & 0 & 0 \\ b(z) & a_2(z) & 0 & 0 \\ 0 & 0 & a_3(z) & c(z) \\ 0 & 0 & -c(z) & a_4(z) \end{Vmatrix}. \qquad (1)$$

- In CP representation, all the functions

$$u_{mn}(z) = \left[\boldsymbol{\Gamma}(z)\right]_{mn}(1-z)^{-\frac{|m-n|}{2}}(1+z)^{-\frac{|m+n|}{2}}, \qquad m, n = 2, 0, -0, -2, \tag{2}$$

  are entire functions.

- Single scattering albedo λ satisfies the inequalities $0 < \lambda < 1$.
- The dispersion matrix $\boldsymbol{\Lambda}_s(z)$ defined as in [1, 3, 6] is nonsingular on the sides of the cut $z \in [-1, 1]$ for all azimuthal harmonics $s = 0, \pm1, \pm2, \ldots$:

$$\lim_{z\to\eta\pm i0} \det \boldsymbol{\Lambda}_s(z) = \lim_{z\to\eta\pm i0} \det\left[\boldsymbol{E} + \frac{z}{2}\boldsymbol{\pi}_s^{-1}(z)\int_{-1}^{1}\frac{\boldsymbol{\pi}_s(\mu)\boldsymbol{\psi}_s(\mu,z)}{\mu - z}d\mu\right] \neq 0, \qquad \eta \in [-1,\ \ 1]. \tag{3}$$

3 Main ideas and results

The cylindrically symmetric radiation field is assumed to be stationary. It depends on single radial spatial coordinate r, or equivalently on the optical distance $\tau = \alpha r$ from the axis of cylindrical symmetry, as well as two angles ($\cos^{-1}\mu$, φ) characterizing the direction of propagation $\boldsymbol{S}$ (see Fig. 1):

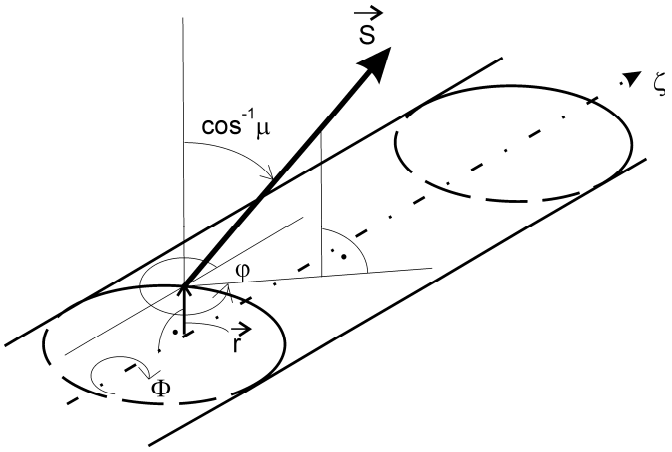

Figure 1: Coordinate system for the description of cylindrically symmetric radiation field.

The Green's function $\boldsymbol{G}(\tau, \mu, \varphi; \tau', \mu', \varphi')$ obeys the transfer equation

$$\mu\frac{\partial \boldsymbol{G}(\tau,\mu,\varphi;\tau',\mu',\varphi')}{\partial\tau}+\frac{(1-\mu^2)\sin^2\varphi}{\tau}\frac{\partial \boldsymbol{G}(\tau,\mu,\varphi;\tau',\mu',\varphi')}{\partial\mu}-\frac{\mu\sin 2\varphi}{2\tau}\frac{\partial \boldsymbol{G}(\tau,\mu,\varphi;\tau',\mu',\varphi')}{\partial\varphi}$$
$$=-\boldsymbol{G}(\tau,\mu,\varphi;\tau',\mu',\varphi')+\frac{1}{4\pi}\int_0^{2\pi}\sum_{s=-\infty}^{+\infty}e^{-is(\varphi-\varphi'')}d\varphi''\int_{-1}^{1}\boldsymbol{p}_s(\mu,\mu'')\boldsymbol{G}(\tau,\mu'',\varphi'';\tau',\mu',\varphi')d\mu''$$
$$+\boldsymbol{E}\delta(\tau-\tau')\delta(\mu-\mu')\delta(\varphi-\varphi'). \qquad (4)$$

In order to obtain its solution, we construct an auxiliary plane-parallel transfer problem which is a superposition of cylindrical problems, namely, with primary sources distributed inside slab $|\tau_z| \le \tau_0$. The solution of the auxiliary problem in kind of expansion in generalized spherical functions [9],

$$\boldsymbol{I}^{pl}(\tau_z,\nu,\beta;\tau_0)=\sum_{s=-\infty}^{\infty}\sum_{l=|s|}^{\infty}e^{-is\beta}\boldsymbol{P}_s^l(\nu)\boldsymbol{D}_s^l(\tau_z,\tau_0), \qquad (5)$$

is obtained analytically using plane-parallel Green's function [3]. The expressions are of kind

$$\boldsymbol{D}_s^l(\tau_z,\tau_0)=\int_0^1 e^{-\frac{\tau_z}{\eta}}\sum_{j=|s|}^{\infty}\sum_{m=-\left[\frac{j+s}{2}\right]}^{\left[\frac{j-s}{2}\right]}\boldsymbol{f}_{jm(1)}^{ls}(\tau_0,\eta)\boldsymbol{b}_{s+2m}^{j}d\eta+\sum_{\mathrm{Re}\,\eta_i>0}e^{-\frac{\tau_z}{\eta_i}}\sum_{j=|s|}^{\infty}\sum_{m=-\left[\frac{j+s}{2}\right]}^{\left[\frac{j-s}{2}\right]}\boldsymbol{f}_{jm(2)}^{ls}(\tau_z,\tau_0,\eta_i)\boldsymbol{b}_{s+2m}^{j} \qquad (6)$$

for $\tau_z \ge \tau_0$, and similar but twice longer expression for $\tau_z \le \tau_0$. Here functions $\boldsymbol{f}(\ldots)$ are some lengthy expressions, and $\boldsymbol{b}_s^j$ are arbitrary constant coefficients.

The cylindrical Green's function is expanded as series in generalized spherical functions; it is shown that the expansion coefficients as functions of τ obey systems of Abel integral equations, with generalized spherical functions in their nuclei, and functions $\boldsymbol{D}_s^l(\ldots)$ given by Eq. (6) and an analog formula for $\tau_z \le \tau_0$ on the right hand side. These systems of integral equations are transformed to a set of mutually independent Abel integral equations, each with only one integral, one unknown function and one Chebyshev polynomial of the first kind in the nucleus. Finally, Abel integral equations are solved analytically using formula given in [10], and the result is as follows:

$$\boldsymbol{G}(\tau,\mu,\varphi;\tau',\mu',\varphi')$$
$$=-\frac{1}{\pi}\sum_{s=-\infty}^{\infty}\sum_{l=|s|}^{\infty}e^{-is\varphi}\boldsymbol{P}_s^l(\mu)\sum_{m=-\left[\frac{l+s}{2}\right]}^{\left[\frac{l-s}{2}\right]}(-1)^m\int_1^{\infty}P_{s,s+2m}^l(x)\frac{d}{dy}\boldsymbol{D}_{s+2m}^l(y,\tau')\Big|_{y=\tau x}\frac{dx}{\sqrt{x^2-1}}, \qquad (7)$$

where $\boldsymbol{b}_s^l$ must be replaced by $(-1)^s(2l+1)\boldsymbol{P}_s^l(\mu')\,e^{is\varphi'}/(4\pi)$ when substituting Eq. (6) into Eq. (7).

Acknowledgments

The author is grateful to Dr. I.Shmeld and Dr. J.Zhagars for continuing financial support of this work.

References

[1] H. Domke, “Transfer of polarized light in an isotropic medium. Singular eigensolutions of the transfer equation,” Journ. Quant. Spectrosc. & Rad. Transfer **15**, 669–679 (1975).

[2] H. Domke, “Transfer of polarized light in an isotropic medium. Biorthogonality and the solution of transfer problems in semi infinite media,” Journ. Quant. Spectrosc. & Rad. Transfer **15**, 681–694 (1975).

[3} J. Freimanis, “On the completeness of system of eigenfunctions and adjoint functions of transfer equation of polarized radiation,” Investigations of the Sun and Red Stars **32**, 20-116 (1990) (in Russian).

[4] J. Freimanis, “Transfer of polarized light in homogeneous isotropic semi infinite medium if the generalized eigenfunctions of transfer equation exist,” Investigations of the Sun and Red Stars **36**, 18-84 (1993).

[5] J. Poutanen, K. N. Nagendra, R. Svensson, “Green’s matrix for Compton reflection of polarized radiation from cold matter,” Mon. Not. Roy. Astron. Soc. **283**, 892-904 (1996).

[6] J. Freimanis, “On Green’s function for spherically symmetric problems of transfer of polarized radiation,” Journ. Quant. Spectrosc. & Rad. Transfer **96**, 451–472 (2005).

[7] J. W. Hovenier, C. V. M. van der Mee, “Fundamental relationships relevant to the transfer of polarized light in a scattering atmosphere,” Astron. and Astrophys. **128**, 1-16 (1983).

[8] N. V. Konovalov, “Polarization matrices corresponding to transformations within Stokes cone,” Preprint No. 171, Institute of Applied Mathematics of the USSR Academy of Sciences (1985).

[9] I. M. Gelfand, R. A. Minlos and Z. Ya. Shakiro, *Representations of the Rotation and Lorentz Groups and their Applications* (Pergamon Press, New York, 1963).

[10] R. Gorenflo and S. Vessella, *Abel Integral Equations* (Springer, Berlin et al., 1991).

Generalized Lorenz-Mie: the third decade

Gérard Gouesbet and Gérard Gréhan

LESP, UMR CNRS 6614, CORIA,
Université de Rouen et INSA de Rouen,
76 801, Saint Etienne du Rouvray, FRANCE

Abstract

The generalized Lorenz-Mie stricto sensu is the theory of interaction between an arbitrary shaped beam (typically a laser beam) and a homogeneous sphere (with other additional assumptions that are not required to be discussed here). As indicated by its name, this theory is a generalization of the Mie's theory (that we prefer to name Lorenz-Mie theory) which is now exactly one century old, after the famous paper by Mie, in 1908, that we are currently commemorating. The present paper provides a review of the work accomplished during the past decade in this generalized field.

1 Introduction

The first paper on generalized Lorenz-Mie from Rouen (GLMT) has been published in 1982 [1]. It dealt with the case of a "Mie's sphere" (a terminology used here for convenience, although it has been criticized) illuminated on-axis by a circularly symmetric beam (such as a Gaussian laser beam). In 1988, we published what we consider as the "pivot" paper on GLMT, dealing with light scattering from a "Mie's sphere" arbitrarily located in a Gaussian beam [2]. Although this paper is somewhat specified for the case of a Gaussian beam, it actually provides an arbitrary beam theory as discussed in [3]. As a whole, the building of the formulation has typically taken a decade before the possibility of effective applications being possible.

An overall exposition of the GLMT can be found in a manuscript which has been available from www.coria.fr [4], since 1996. Three review papers have also been published. The first one, in 1991 [5], dealt with about one decade of GLMT. It essentially contains, under a single roof, various aspects of the formalism. The second review paper, in 1994 [6], three years later, could discuss applications of GLMT to phase-Doppler anemometry, more specifically to what has been a troublesome feature of this measurement technique, known as the trajectory ambiguity effect (or defect). A few other applications are also briefly mentioned. The third review paper, dated 2000 [7], could contain the discussion of extensions of the theory (generalized Lorenz-Mie theories for various other shapes of scatterers) and of applications (radiation pressure, rainbow refractometry, imaging, morphology-dependent resonances, phase-Doppler instrument, miscellaneous).

2 The past decade

GLMT is now about 3 decades old. Simplifying a bit, it is correct to state that the first decade has essentially been devoted to the development of the theory, to its numerical implementation, and to various ramifications of it, as obvious from [5], in 1991. The second decade has been devoted to the development of various applications (although further theoretical advances were still of interest), as can been seen from [7]. In the ninth section of this reference [7], we provided some recommendations for future research (more GLMTs, more applications, irregular scattering, optical chaos). It is interesting to examine how these prospects have been developed during the past (third) decade.

2.1 More GLMTs.

The headline of this sub-section was already a headline in [7]. The formalism of a GLMT for a sphere with an eccentrically located spherical inclusion has been published in [8]. This GLMT has not yet been numerically implemented but the associated Hamiltonian problem has been thoroughly investigated [9], and references therein, exhibiting Hamiltonian (optical) chaos. We may also forecast the possibility of irregular (chaotic) scattering [7], in connection with a GLMT for assemblies of spheres and aggregates [10].

There has been also a vigorous effort devoted to the development and applications of GLMT for spheroids [11]-[12], and references therein, which, in particular, can serve as models for deformed droplets. But one of the more interesting prospects has been the development of a GLMT for unsteady electromagnetic processes, more specifically for laser pulses [13], and references therein. Movies showing the interaction between various kinds of scatterers and femtosecond pulses are available. GLMT for laser pulses has also been used in the case when the scatterer is a spheroid [14], to suggest the possibility of Cerenkov-based radiation from supra-luminic excitation in microdroplets by ultra-short pulses [15], or even to investigate a two-photons processes in a microcavity [16].

2.2 More applications, and miscellaneous

The headline of this sub-section has essentially also been used in [7]. More studies have been devoted to phase-Doppler instruments, to particle imaging sizing, to the laboratory determination of beam shape coefficients, to a GLMT-Debye series formulation with the Bromwich method and to the theoretical evaluation of a shadow Doppler velocimeter (references omitted to save room).

2.3 Out of Rouen

The above part of this abstract has been devoted to the results obtained by the Rouen-group. We would like now to discuss a bit the use of GLMT out of this group. However, Rouen-papers on GLMT have received nearly 2000 citations (ISIweb of knowledge) and, on the first of may 2008, searching for generalized Lorenz Mie theory (with upper case letters for Lorenz and Mie, and a blank between the two names) on Google returned 49400 pages. Therefore, we shall report only a sample (from 2000 on), without pretending to exhaustivity.

A first set in the sample is made of theoretical papers related to mathematics or to physics such as by Koumandos discussing a certain integral, motivated by force evaluations in optical tweezers, Lu Bai et al devoted to cluster spheres scattering, Han et al dealing with the expansion coefficients of arbitrary shaped beams, Zhang and Han for the scattering by a confocal multilayered spheroidal particle, or for the scattering by an infinite cylinder, Nieminen et al discussing vector spherical wavefunction expansion by laser beams, Zhang et al dealing with the description of shaped beams in terms of cylindrical vector wave functions or Matoko et al reviewing whispering-gallery modes (references omitted).

A second set in the sample is devoted to optical particle sizing (the original motivation for the development of GLMTs), and more generally to optical particle characterization, particularly to phase-Doppler instruments or particle image velocimetry. Relevance of GLMTs to optical particle characterization and to the science of particulates and aerosols is well illustrated by textbooks such as by R. Xu [17], Davis and Schweiger [18], Albrecht et al [19].

A third set in the sample is devoted to radiation forces and torques, optical trapping, optical tweezers and optical stretchers, to trap and manipulate particles e.g. [20]-[21], among many others. I would like to end this brief review by mentioning two fantastic and fascinating applications of GLMT-like theories for optical trapping and manipulation.

The first one concerns a new concept of earth-based satellites, as discussed in a NASA report, explicitly referring to GLMT [22]. A shepherd satellite is proposed, based on the use of electromagnetic radiation forces to position and hold a large number of small, specialized spacecrafts in a precise array. The

concept derives from well-known optical scattering and gradient force techniques, which have been used to trap and manipulate microscopic objects using laser radiation. Although the presumed physical dimensions of the satellites will exclude the use of optical wavelengths, it is proposed that a technique similar to laser optical trapping can be used at millimeter or microwave frequencies more appropriate to larger object sizes.

The second one originates from a dream of A. Labeyrie who would like to photograph exo-planets details, such as possibly mountains, forests, oceans, deserts, many light years away from Earth. This would be achieved by using hypertelescopes (made out from many small telescopes) ranging over hundreds of kilometers across, with elementary telescopes positioned and held by using radiation forces produced by a laser operating in space, e.g. [23]. The relevance of GLMT-like approaches to such a project is known to us via a personal communication.

3 Conclusion

The famous Mie's paper, one hundred years ago, remains continuously cited and is still a benchmark reference for light scattering theories and applications. Mie, as far as we know, could not predict the advent of lasers, and the associated necessity to produce generalized Lorenz-Mie theories. We are now living the end of the third decade of GLMTs. We have taken the opportunity of the commemoration of Mie's paper to provide a brief review of what happened with GLMTs in the past (and third) decade.

References

[1] G. Gouesbet and G. Gréhan. Sur la généralisation de la théorie de Lorenz-Mie. J. of Optics, 13(2):97--103, 1982.

[2] G. Gouesbet, B. Maheu, and G. Gréhan. Light scattering from a sphere arbitrarily located in a Gaussian beam,using a Bromwich formulation.J. Opt. Soc. Amer. A., 5(9):1427--1443, 1988.

[3] B. Maheu, G. Gouesbet, and G. Gréhan. A concise presentation of the generalized Lorenz-Mie theory for arbitrary location of the scatterer in an arbitrary incident profile. J. Optics (Paris), 19(2):59--67, 1988.

[4] G. Gouesbet, G. Gréhan, B. Maheu, and K.F. Ren. Electromagnetic Scattering of Shaped Beams (generalized Lorenz-Mie theory). Manuscript available on request or on www.coria.fr.

[5] G. Gouesbet, G. Gréhan, and B. Maheu. In Combustion measurements edited by N. Chigier, chapter 10, Generalized Lorenz-Mie theory and applications to optical sizing, pages 339--384. Hemisphere Publishing Corporation, 1991.

[6] G. Gouesbet. Generalized Lorenz-Mie theory and applications. Part. Part. Syst. Charact., 11:22--34, 1994.

[7] G. Gouesbet and G. Gréhan. Generalized Lorenz-Mie theories, from past to future. Atomization and Sprays, 10(3-5):277--333, 2000.

[8] G. Gouesbet and G. Gréhan. Generalized Lorenz-Mie theory for a sphere with an eccentrically located spherical inclusion.J. of Modern Optics, 47(5):821--837, 2000.

[9] G. Gouesbet, S. Meunier-Guttin-Cluzel, and G. Gréhan. Morphology-dependent resonances and/or whispering gallery modes for a two-dimensional dielectric cavity with an eccentrically located circular inclusion, a Hamiltonian point of view with Hamiltonian (optical) chaos. Optics Communications, 201:223--242, 2002.

[10] G. Gouesbet and G. Gréhan. Generalized Lorenz-Mie theory for assemblies of spheres and aggregates.J. of Optics A: Pure and Applied Optics, 1:706--712, 1999.

[11] Y.P. Han, L. Méès, G. Gouesbet, Z. Wu, and G. Gréhan. Resonant spectra of a deformed spherical microcavity. J. Optical Society of America B, 23:1390--1397, 2006.

[12] F. Xu, K.F. Ren, G. Gouesbet, X. Cai, and G. Gréhan. Theoretical prediction of radiation pressure force exerted on a spheroid by an arbitrary shaped beam. Physical Review, E 75, 026613:1--14, 2007.

[13] L. Méès, G. Gouesbet, and G. Gréhan. Numerical predictions of microcavity internal fields created by femtosecond pulses with emphasis on whispering gallery modes. J. Opt. A: Pure Appl. Opt., (4):8150--8153, 2002.

[14] Y.P. Han, L. Méès, K.F. Ren, G. Gréhan, Z.S. Wu, and G. Gouesbet. Far scattered field from a spheroid under a femtosecond pulsed illumination in a generalized Lorenz-Mie theory framework. Optics Communications, 231:71--77, 2004.

[15] M. Brunel, L. Méès, G. Gouesbet, and G. Gréhan. Possibility of Cerenkov-based radiation from supra-luminic excitation in microdroplets by ultra-short pulses. Optics Letters, 26(20):1621--1623, 2001.

[16] L. Méès, J.P. Wolf, G. Gouesbet, and G. Gréhan. Two-photons absorption in a spherical microcavity by using two lasers pulses: numerical simulations.Optics Communications, pages 371--375, 2002.

[17] R. Xu. Particle characterization: light scattering methods. Kluwer Academic, 2000.

[18] E.J. Davis and G. Schweiger. Airborne microparticle, its physics, chemistry, optics and transport phenomena . Springer, 2002.

[19] H.E. Albrecht, M. Borys, N. Damaschke, and C. Tropea. Laser Doppler and phase Doppler measurement. Springer, 2003.

[20] J.A. Lock. Calculation of the radiation trap force for laser tweezers by use of generalized Lorenz-Mie theory I. localized model description of an on-axis tightly focused laser beam with spherical aberration. Applied Optics, 43:2532--2544, 2004.

[21] J.A. Lock. Calculation of the radiation trap force for laser tweezers by use of generalized Lorenz-Mie theory II. on-axis trap force. Applied Optics, 43:2545--2554, 2004.

[22] M.R. La Pointe. Formation flying with shepherd satellites. Technical report, Ohio Aerospace Institute, Cleveland, Final report, NASA institute for advanced concepts, grant 07600-072.

[23] S. Gillet, P. Riaud, O. Lardiere, J. Dejongle, J. Schmitt, L. Arnold, A. Bocealetti, D. Horville, and A. Labeyrie. Imaging capabilities of hypertelescopes with a pair of micro-lens arrays. Astronomy and astrophysics, 400:393--396, 2003

Modelling light reflection from flat particles with rough surfaces

Ye. Grynko[1] and S. Pulbere[2]

[1]*BASF SE, Carl-Bosch-Str. 38, 67056, Ludwigshafen, Germany*
[2]*BASF Coatings AG, Glasuritsr. 1, 48165, Münster, Germany*
tel: +49 173 3796946, e-mail: Yevgen.Grynko@basf.com

Abstract

We study light reflection from flat particles with rough surfaces and fractal statistics of topography. Discrete Dipole Approximation method is used to solve the problem of light scattering. Refractive indices corresponding to dielectric and metallic materials are taken. The sizes of particles are much larger than the wavelength of incident light and the roughness scales are larger, comparable to and smaller than the wavelength. The influence of the fractal dimension parameter and the amplitude of heights of random topography on reflectance and on the profile of the specular reflection peak is considered.

1 Introduction

Natural and artificial light scattering objects often have irregular shapes and rough surfaces. The natural examples are ocean surface, terrains and soils at scales down to the rough surface of constituent particles. The industrial light scattering applications deal with surfaces of metals and dielectrics of various structures and composition. The interaction of electromagnetic waves with such objects is strongly influenced by degree of surface roughness, i.e. the amplitude of heights and the slope statistics. Both for scientific and industrial applications the knowledge of the optics of rough interfaces is required [e.g., 1-3]. In this paper we use numerical experiments to study light reflection from flat metallic and dielectric particles with the surface roughness scales larger, comparable to and smaller than the wavelength of light.

2 Numerical method

We use discrete-dipole approximation (DDA) [4, 5] method as it provides full flexibility for the geometry of the scatterer (e.g., [6]). In the DDA continuous object is approximated with an array of dipoles. The dipoles and spaces between them are much smaller than the wavelength of incident light. A system of equations is required to describe basic interaction of each dipole with the total field. The solution of the problem is the sum of the incident wave and the contribution from all the dipoles in the array [4]. The disadvantage of this method is that computer memory requirements quickly increase with the size of the scatterer as large objects must be approximated with large enough number of dipoles. Among the publicly available computer codes we chose ADDA code [7] which is capable of parallel multi-processor calculation for a single orientation of the particle.

The scattering object in our simulations is a thin square slab consisting of a substrate of constant thickness and a layer representing random rough surface (Fig. 1). Fractal statistics of heights is used to model the surface. In this case the standard deviation σ in all points follows the power law [8]

$$\sigma(\vec{r}) = \sqrt{\left\langle \left[h(\vec{r}) - h(0)\right]^2 \right\rangle} = \sigma_0 \left(\frac{|\vec{r}|}{r_0} \right)^{3-D},$$

where D is fractal dimension ($2 < D < 3$) and r_0 is topothesy which influences to certain extent the horizontal scale of roughness [8].

Horizontal size of the slab is 512x512 dipoles and the substrate layer thickness is 10 dipoles. The thickness of the rough layer τ varies between 0 and 50 dipoles and is further expressed in the fractions of

the wavelength λ. The slab is illuminated at incidence angle of i=45° to the average surface normal. The result of the calculation is the full scattering matrix $F_{ik}(\theta, \varphi)$ obtained in the entire range of scattering and azimuthal angles.

3 Results and discussion

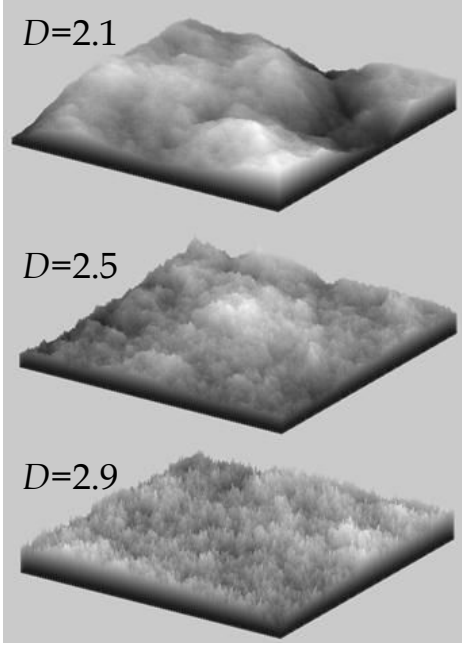

Figure 1: Samples of particles with different surface fractal dimensions D.

Here we present examples of DDA calculations of phase functions of particles with fractal surfaces. The scattered intensity is detected in the principal scattering plane. We consider two materials: aluminum in a resin with relative refractive index m = 0.8 + 4.8i and an arbitrary absorbing dielectric m = 1.5 + 1.0i. The simulation of an infinite surface is impossible in the frame of pure DDA therefore we simulate as large particles as possible. For both cases we took maximal size parameters ($X=\pi d/\lambda$) for the horizontal dimensions of the particles allowed by the DDA condition of discretization (number of dipoles per wavelength dpl) [4, 5] and our computer recources, X = 47 for the metal and X = 94 for the dielectric. To study the quality of discretization at such large refractive indices as that of metal or dielectric with high absorption we made a separate experiment. Comparison of the DDA results for spheres with Mie theory solution gave some discrepancies even at very large values of dpl. However, the calculations for flat particles both with smooth and rough surfaces showed that for the region of specular reflection which is of interest for us DDA gives stable solution in intensity already at dpl=10|m|.

Figs. 2 and 3 show phase functions of dielectric and metallic particles with different fractal dimensions of surfaces near the direction of specular reflection θ=90°. The thickness

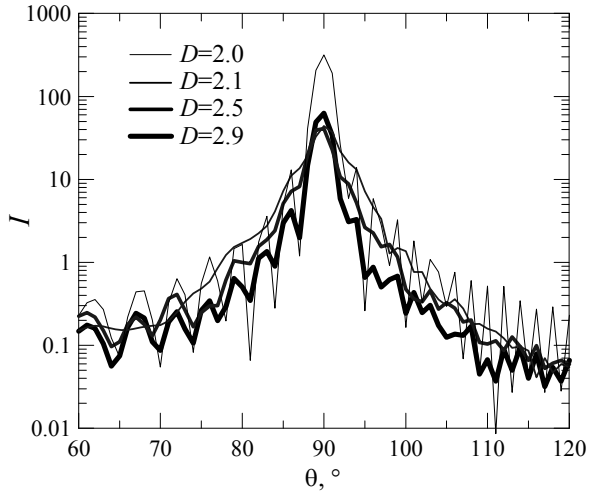

Figure 2: Phase functions of dielectric particles with different surface fractal dimensions D near specular direction (m=1.5+1.0i, X=94, τ=1λ).

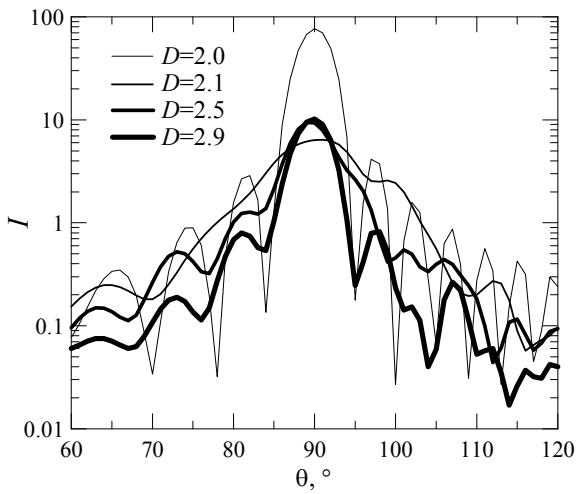

Figure 3: Phase functions of metallic particles with different surface fractal dimensions D near specular direction (m=0.8+4.8i, X=47, τ=1λ).

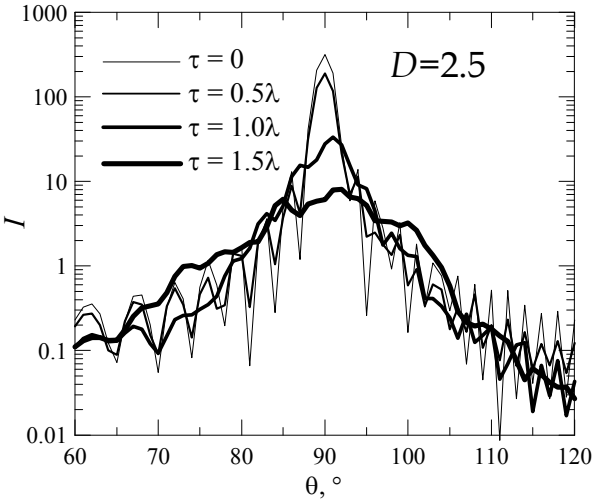

Figure 4: Phase functions of dielectric particles with different amplitude of topography heights τ and *D*=2.5 near specular direction (*m*=1.5+1.0*i*, *X*=94).

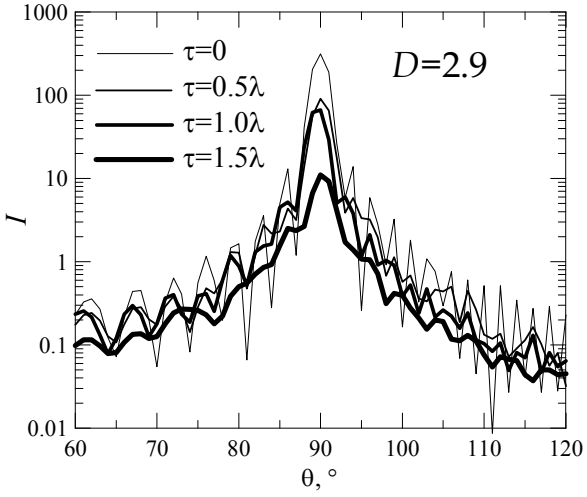

Figure 5: Phase functions of dielectric particles with different amplitude of topography heights τ and *D*=2.9 near specular direction (*m*=1.5+1.0*i*, *X*=94).

of the rough layer, i. e. the amplitude of heights is fixed ($\tau = 1\lambda$) and we study the influence of the parameter *D* on the reflection peak profile. The case of smooth surface *D*=2.0 is used as a reference. The most of the reflected energy is distributed in the peak. Its width is equal to that of the forward scattering peak as they both are determined by diffraction law and depend on the dimensions of the projection of the slab in the direction of incidence. The degree of surface roughness at *D* > 2 is shown at the example pictures in Fig. 1. *D*=2.1 produces large scale topography elements. At *D*=2.9 the scales smaller than the wavelength prevail, the surface is flat in average but has a porous structure. *D*=2.5 is an intermediate case where all scales are equally present. The plots show that for all the types of roughness reflectance is decreased significantly in comparison to ideal surface. However, intensity at θ=90° remains approximately at the same level. The width of the peak is different. It is wider for *D*=2.1 where large scale areas act like finite mirrors and produce dispersion of the scattered intensity. Small scale roughness at *D*=2.9 leads only to the drop of reflectance.

In Figs. 4 and 5 we present phase functions for dielectrics with the same fractal dimensions of the their surfaces, *D*=2.5 and *D*=2.9, correspondingly, and different amplitude of heights of random topography τ. The plots show that τ has strong influence on the reflectance of the surface. This influence depends on the fractal dimension, i.e. on the surface slope distribution. At *D*=2.9 reflectance progressively drops. At *D*=2.5 the decrease of reflectance is followed by the peak broadening.

3 Conclusions

From the results of our simulations we can conclude the following.

1. Fractal dimension changes surface slope distribution law and therefore angular dispersion of the reflection peak. Prevailing topography features of high spatial frequencies which are smaller than the wavelength does not produce broadening of the specular reflection peak and only decreases reflectivity. Presence of roughness pattern at all scales with amplitude of heights comparable to or larger than the wavelength leads to broadening of the reflection peak profile. Fractal dimension only slightly influences reflectance.

2. The amplitude of heights of random topography appears to be much more important for the surface reflectance.

References

[1] F. G. Bass, and I. M. Fuks, *Wave Scattering from Statistically Rough Surfaces* (Pergamon Press, Oxford, 1979).

[2] T. M. Elfouhaily, and C. A. Guérin, "A critical survey of approximate scattering wave theories from random rough surfaces," Waves in Random Media **14**, R1–R40 (2004).

[3] Yu. Shkuratov, D. Petrov, and G. Videen, “Classical photometry of prefractal surfaces,” J. Opt. Soc. Am. A, **20**, 2081–2092 (2003).

[4] E. M.Purcell, and C. R. Pennypacker, “Scattering and absorption of light by non-spherical dielectric grains,” Astrophys. J. **186**, 705–714 (1973).

[5] B. T.Draine, “The discrete dipole approximation and its application to interstellar graphite grains,” Astrophys. J. **333**, 848–872 (1988).

[6] E. Zubko, K. Muinonen, Yu. Shkuratov, G. Videen, and T. Nousiainen, “Scattering of light by roughened Gaussian random particles,” J. Quant. Spec-trosc. Radiat. Transfer. **106**, 604-615 (2007).

[7] M. A. Yurkin, and A. G.Hoekstra, http://www.science.uva.nl/research/scs/Software/adda/index.html.

[8] R. F.Voss, In: *Fundamental Algorithms in Computer Graphics* (Springer-Verlag, Berlin, 1985) 805-835.

Scattering of typical particles by shaped beam in oblique illumination

Yiping Han, [1] Yang Zhang, [2] Huayong Zhang, [1] Guoxia Han, [1]

[1]*School of Science, Xidian University, Xi'an, 710071, P. R. China, yphan@xidian.edu.cn*
[2]*Department of Mechanical, Aerospace and Manufacturing Engineering, PO Box 88, UMIST, Manchester M60 1QD, UK*

Abstract

The expansions of the incident arbitrary shaped beam in spherical, spheroidal and cylindrical coordinates in the general case of oblique illumination is presented. Based on the generalized Lorenz-Mie theory (GLMT), the scattered electromagnetic fields of typical particles of arbitrary orientation illuminated with a shaped beam are provided. The numerical results of the normalized scattering cross section are evaluated.

1. Introduction

A strong effort has recently been devoted by us to the study of shaped beam scattering by typical particles, such as multilayered spheroids, cylinder, eccentric sphere, due to the fact that a large number of real objects can be modeled by those particles and to the possibility of subsequent applications of exact analytical methods. One fundamental problem in the generalized Lorenz-Mie theory (GLMT) is to expand of the incident shaped beam as a series of vector wave functions[1,2]. Once the beam-shape coefficients are determined, the solution of scattering for shaped beam in oblique illumination by a spherical, spheroidal and cylindrical particle can be obtained by means of the method of separation of variables. It also has been extended to the case of multilayered particle.

The paper is organized as follows. Section 2 provides representations of the beam shape coefficients corresponding to spherical, spheroidal and cylindrical coordinates respectively, in oblique illumination. In section 3, the numerical results of scattering properties for a spheroid and cylinder in oblique shaped beam illumination are given. Section 4 is a conclusion.

2. Expansion of incident shaped beam with respect to spherical, spheroidal and cylindrical coordinates

We expand the incident beam in terms of the spherical vector wave functions $\mathbf{m}_{\substack{e\\o}mn}^{r(1)}(kr,\theta,\phi)$ and $\mathbf{n}_{\substack{e\\o}mn}^{r(1)}(kr,\theta,\phi)$ as follows (TE Mode):[3]

$$\mathbf{E}^i = E_0 \sum_{m=-\infty}^{\infty} \sum_{n=|m|}^{\infty} \left[iG_{n,TE}^{m,spher} \mathbf{m}_{mn}^{r(1)}(kR,\theta,\phi) + G_{n,TM}^{m,spher} \mathbf{n}_{mn}^{r(1)}(kR,\theta,\phi) \right] \tag{1}$$

where $G_{n,TE}^{m,spher}$ and $G_{n,TM}^{m,spher}$ are shaped beam coefficients in spherical coordinates (R,θ,ϕ)

$$G_{n,TE}^{m,spher} = \sum_{s=-n}^{n} \rho(s,m,n) C_{ns} g_{n,TE}^{s}$$

$$G_{n,TM}^{m,sphere} = \sum_{s=-n}^{n} \rho(s,m,n) C_{ns} g_{n,TM}^{s}$$

$$\rho(m,s,n)=(-1)^{s+m}e^{is\gamma}[\frac{(n+m)!(n-s)!}{(n-m)!(n+s)!}]^{1/2}\mathrm{u}_{sm}^{(n)}(\beta)e^{im\alpha}$$

$$\mathrm{u}_{sm}^{(n)}(\beta)=\left[\frac{(n+s)!(n-s)!}{(n+m)!(n-m)!}\right]^{1/2}\sum_{\sigma}\binom{n+m}{n-s-\sigma}\binom{n-m}{\sigma}(-1)^{n-s-\sigma}(\cos\frac{\beta}{2})^{2\sigma+s+m}(\sin\frac{\beta}{2})^{2n-2\sigma-s-m} \quad (2)$$

And $g_{n,TE}^{s}$, $g_{n,TM}^{s}$ are the beam shape coefficients in spherical coordinates for the incident shaped beam propagating parallel to the z' axis. They can be derived from those results obtained by the three computational methods given by Gouesbet et al, which are quadratures, finite series technique and localized approximations [2],

The expansion of the incident beam in terms of spheroidal vector wave functions attached to an arbitrarily oriented spheroid can be written as follows (TE Mode):

$$\begin{aligned}\mathbf{E}^{i}=E_0\sum_{m=0}^{\infty}\sum_{n=m}^{\infty}i^{n}[&G_{n,TE}^{m,ellip}\mathbf{M}_{emn}^{r(1)}(c,\zeta,\eta,\phi)-G_{n,TE}^{\prime m,ellip}\mathrm{M}_{omn}^{r(1)}(c,\zeta,\eta,\phi)\\&+iG_{n,TM}^{m,ellip}\mathbf{N}_{omn}^{r(1)}(c,\zeta,\eta,\phi)+iG_{n,TM}^{\prime m,ellip}\mathbf{N}_{emn}^{r(1)}(c,\zeta,\eta,\phi)]\end{aligned} \quad (3)$$

where $G_{n,TE}^{m,ellip}$, $G_{n,TE}^{\prime m,ellip}$, $G_{n,TM}^{m,ellip}$ and $G_{n,TM}^{\prime m,ellip}$ are the expansion coefficients for arbitrary shaped beam at oblique incidence in the spheroidal coordinates.

$$\begin{bmatrix}G_{n,TE}^{m,ellip}\\G_{n,TE}^{\prime m,ellip}\\G_{n,TM}^{m,ellip}\\G_{n,TM}^{\prime m,ellip}\end{bmatrix}=\sum_{r=0,1}^{\infty}{}'\sum_{s=0}^{r+m}\frac{2(r+2m)!}{(2r+2m+1)r!}\frac{i^{-r-m}}{N_{mn}}d_{r}^{mn}(c)\begin{bmatrix}g_{r+m,TE}^{sm}\\g_{r+m,TE}^{\prime sm}\\g_{r+m,TM}^{sm}\\g_{r+m,TM}^{\prime sm}\end{bmatrix} \quad (4)$$

The expansion of the incident shaped beam in terms of the cylindrical vector wave functions $\mathbf{m}_{m\lambda}^{(1)}e^{ihz}$ and $\mathbf{n}_{m\lambda}^{(1)}e^{ihz}$ is described in the following[4].

$$\mathbf{E}^{i}=E_0\sum_{m=-\infty}^{\infty}\int_{0}^{\pi}[I_{m,TE}(\zeta)\mathbf{m}_{m\lambda}+I_{m,TM}(\zeta)\mathbf{n}_{m\lambda}]e^{ihz}\sin\zeta d\zeta \quad (5)$$

where $I_{m,TE}(\zeta)$ and $I_{m,TM}(\zeta)$ are the shaped beam coefficients in cylindrical coordinates (r,ϕ,z)

$$\begin{aligned}I_{m,TE}&=\sum_{n=|m|}^{\infty}[iG_{n,TE}^{m,sphere}c_{mn}(\zeta)+G_{n,TM}^{m,sphere}a_{mn}(\zeta)]\\I_{m,TM}&=\sum_{n=|m|}^{\infty}[iG_{n,TE}^{m,sphere}a_{mn}(\zeta)+G_{n,TM}^{m,sphere}c_{mn}(\zeta)]\\c_{mn}(\zeta)&=\frac{i^{m-n+1}}{2k}\frac{dP_{n}^{m}(\cos\zeta)}{d(\cos\zeta)}\\a_{mn}(\zeta)&=\frac{mk}{\lambda^{2}}\frac{i^{m-n-1}}{2}P_{n}^{m}(\cos\zeta)\end{aligned} \quad (6)$$

Once the beam-shape coefficients in oblique illumination are determined in spherical, spheroidal and cylindrical coordinates, the incident, scattered and internal fields can be expanded in terms of corresponding vector wave functions. For spheroidal particle, as an example, incident fields are given in Eq.(3) for TE mode, and the internal and scattered fields can be expressed as following[17]:

$$\mathbf{E}^w = E_0 \sum_{m=0}^{\infty} \sum_{n=m}^{\infty} i^n [\delta_{mn} \mathbf{M}_{emn}^{r(1)}(c',\zeta,\eta,\phi) + i\gamma_{mn} \mathbf{N}_{omn}^{r(1)}(c',\zeta,\eta,\phi) + \delta'_{mn} \mathbf{M}_{omn}^{r(1)}(c',\zeta,\eta,\phi) + i\gamma'_{mn} \mathbf{N}_{emn}^{r(1)}(c',\zeta,\eta,\phi)]$$

$$\mathbf{E}^s = E_0 \sum_{m=0}^{\infty} \sum_{n=m}^{\infty} i^n [\beta_{mn} \mathbf{M}_{emn}^{r(3)}(c,\zeta,\eta,\phi) + \beta'_{mn} \mathbf{M}_{omn}^{r(3)}(c,\zeta,\eta,\phi) + i\alpha_{mn} \mathbf{N}_{omn}^{r(3)}(c,\zeta,\eta,\phi) + i\alpha'_{mn} \mathbf{N}_{emn}^{r(3)}(c,\zeta,\eta,\phi)] \quad (7)$$

The unknown coefficients (γ_{mn} , δ_{mn} , γ'_{mn} , δ'_{mn} α_{mn}, β_{mn}, α'_{mn} β'_{mn}) are determined by applying the boundary conditions of continuity of the tangential electromagnetic fields over the surface of the particle. Thus, the solution of scattering for arbitrary shaped beam by a homogeneous spheroidal particle can be obtained

3. NUMERICAL RESULTS

We have the scattering cross section which is defined by

$$\sigma(\theta,\phi) = 4\pi r^2 \left| \frac{\mathbf{E}^s}{E_0} \right|^2$$

Fig.1 show the angular distributions of the normalized scattering cross sections of a non-confocal two-layered dielectric prolate spheroid with $ka_1 = 4, ka_2 = 6$ in two scattering planes of $\phi = 0^0, 90^0$, as a function of the scattering angle θ, for $\alpha = \pi/4, \beta = \pi/6, \gamma = 0$. The spheroid is illuminated by the Gaussian beam of $w_0 = 2\lambda$. Fig.2 shows the normalized differential scattering cross section $k^2\sigma(\phi)/4$ for incidence of the Gaussian beam with $s = 0.15$ on an infinite cylinder with different cross-sectional radii.

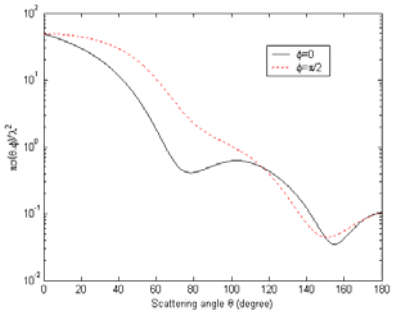

Fig.1. Normalized scattering cross sections $\pi\sigma(\theta,0)/\lambda^2$ (solid curves) and $\pi\sigma(\theta,\pi/2)/\lambda^2$ (dashed curves) for a concentric non-confocal two-layered spheroid $(\alpha = \pi/4, \beta = \pi/6, \gamma = 0)$ with $ka_i = 4,6,\quad \tilde{n}_i = 1.5, 1.33,\quad a_i/b_i = 2\ (i = 1, 2)$ for incidence of a Gaussian beam with $w_0 = 2\lambda$.

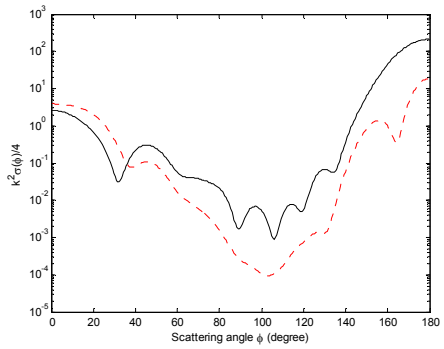

Fig.2. Normalized differential scattering cross section $k^2\sigma(\phi)/4$ for an infinite cylinder ($\widetilde{n}=1.33$, $kr_0=12.57$, $z_0=0$) (solid line) and that for another one ($\widetilde{n}=1.33$, $kr_0=18.85$, $z_0=0$) (dotted line), all with Euler angles $\alpha=\gamma=0, \beta=\pi/2$, illuminated by the Gaussian beam (TE mode) with $s=0.15$

4 Conclusion

The representations of the beam shape coefficients by oblique illumination in different coordinates are provided. By virtue of the Generalized Lorenz-Mie theory, the numerical results of normalized scattering cross section for a non-confocal two-layered dielectric prolate spheroid and cylinder are evaluated.This study is suggestive and useful for interpretation of electromagnetic scattering phenomena from arbitrarily oriented spherical and nonspherical particles.

Acknowledgements
This work is supported by The Royal Society International Joint Project (grant no: 2006/R4-UP) and by Nation Nature Science Foundation of China (grant no: 60771039).

References

[1] G. Gouesbet, B. Maheu, and G. Gréhan, “Light scattering from a sphere arbitrarily located in a Gaussian beam, using a Bromwich formulation,” J. Opt. Soc. Am. A **5**, 1427-1443 (1988).
[2] G. Gouesbet, G. Gréhan, and B. Maheu, “Computations of the g_n coefficients in the generalized Lorenz-Mie theory using three different methods,” Appl. Opt. **27**, 4874-4883 (1988).
[3] Yiping Han, Huayong Zhang and Guoxia Han，The expansion coefficients of arbitrary shaped beam in oblique illumination, Optics Express， **15**, p735-746, (2007)
[4] Huayong Zhang, Yiping Han and Guoxia Han，Expansion of the electromagnetic fields of a shaped beam in terms of cylindrical vector wave functions，Journal of the Optical Society of America B, **24**, p. 1383-1391, (2007),

New Scattering Information Portal for the light scattering community – an update

Jens Hellmers,[1] Thomas Wriedt,[2]

[1] *Universität Bremen, FB4 / IWT, Badgasteiner Str. 3, 28359 Bremen, Germany*
tel: +49 421-218-5418, fax: +49 421-218-5378, e-mail: hellmers@iwt.uni-bremen.de
[2] *Institut für Werkstofftechnik, Badgasteiner Str. 3, 28359 Bremen, Germany*
tel: +49 421-218-2507, fax: +49 421-218-5378, e-mail: thw@iwt.uni-bremen.de

Abstract

The internet is an important tool for the gathering and exchange of information for scientists. In this paper we describe the current stage of development of a new light scattering internet information portal and outline the upcoming technical realization for the web pages as well as the benefits for the users. We also invite the members of the light scattering community to participate in the development of the portal.

1 Introduction

Light scattering is a subject of interest for different research fields like physics, geophysics, astronomy, meteorology, biology, particle measurement, etc. Due to this multidisciplinarity an effective exchange of information is of high importance for the scientific community. The internet allows sharing information easily, on the other side needed information might be distributed over several web pages and difficult to find.

In a current project funded by the German Research Foundation DFG our research group is working on a new internet information portal for the light scattering community. This new portal will be loosely based on the existing internet pages “List of Electromagnetic Scattering Programs” [1]. It will offer news like conference announcements or latest books as well as a comprehensive list of computer programs to calculate light scattering together with tools to help users finding fitting software to their scattering problems.

The main difference to the existing page will be the possibility to integrate users into the publishing process by enabling them to provide own content to the web page. By this users will no longer be ‘passive consumers’ of a given information offer but active clients.

The paper by Wriedt and Hellmers [2] describes the general motivation and structure of such an information portal. At this point we would like to go more into the details and to present the project’s current stage.

2 Realization of the new webpage

The main idea of the new information portal is to integrate the members of the science community as active contributors into the process of keeping the information updated.

Core of the new information portal will be a Content Management System (CMS) for the administration of the content. The use of a CMS enables to separate the content from the presentation, for example the design of the web pages can be changed or expanded easily without loosing the current content.

A CMS also simplifies adding new information. It will be possible to provide users with own accounts so they can create and edit own articles and use the page independently. For this no knowledge of HTML is necessary as a CMS provides an easy to understand interface usually consisting of a text editor and an upload tool for pictures.

Using a CMS on the other hand might lead to some problems. As in principle everybody could use the CMS to publish problems may arise if there is no careful selection of users with access to the system. The

access should be limited strictly to people from the light scattering community. Otherwise there might be companies that will try to use the portal as platform for product placement or such called ‘internet trolls’ who will just try to provoke and bring disorder.
To protect against such unwanted disturbance selected users can be provided with special supervisor accounts. These administrators will have the option to activate or delete user accounts as well as new content. These supervisors not necessarily have to be from the Bremen research group as a CMS can be administrated remotely.

2.1 Current development

The current development for testing purposes uses the free *Joomla* CMS which is developed in an open source project. This CMS by default offers multiple options that improve the usefulness of the web page, like a search interface, the generation of lists of latest news and most popular topics or a printer-friendly layout for articles. It can be expanded by more useful extensions like a discussion board or a page access counter. Another benefit is a ‘frontend’ user interface for registered editors. If one wants to create a new article or edit some existing content all he has to do is using a login interface with his username and password. After that the pages of the information portal are shown in the same way as for unregistered users but with the accessible topics marked by a special symbol. For example if an user has the right to publish articles in the area ‘News’ he will be offered an ‘add news’ button which is not available for unregistered users. A logged in user will also see an ‘edit’ symbol behind his previously published articles. Clicking such a symbol opens an easily usable text editor. So an author doesn’t have to learn the usage of a special ‘backend’ interface; the whole process is intuitive. Also no special HTML knowledge is necessary. By saving the new content the article is ready. The CMS can be configured to hold this new article back until a supervisor checked it and gives clearance for its publication.
The supervisors on the other hand will have to use a special ‘backend’ interface for their work due to the amount of possibilities of administration which can not be integrated into a ‘frontend’ interface. But also the backend of the Joomla CMS is highly intuitive and can be learned fast and easily.
Figure 1 outlines the basic elements of the publication process for a registered user.

3 Computer programs

Another focus is on the revision of the list of computer programs to simulate light scattering [1]. The existing list is going to be revised and updated. The list will consist of links to the software; additionally we would like to invite authors of programs to upload their codes to the new portal. Placing the software on the new portal is advantageous in cases authors change their working facilities or retire as the programs will stay and be available. Of course this wouldn’t affect the intellectual property rights of the authors of light scattering programs; they will keep full access to their work and can update, change or remove their programs anytime.
Additionally we plan to develop a scheme to classify the software. This classification scheme then should be used to program an internet tool that can help users to find fitting programs for solving their scattering problems.
Such a classification has to consider several (different) aspects. Every program is based on a specific scattering theory like Mie Theory, Discrete Dipole Approximation (DDA), Finite Difference Time Domain (FDTD), T-Matrix Method (TMM), etc. So at the first sight it seems to be reasonable to base a classification on the underlying scattering theories. But a closer look shows that all these theories have significant advantages or disadvantages that affect different program attributes that might be of interest for a user. For example a Mie code is suitable only for spherical particles but on the other hand is very fast while DDA can be used for irregular particle shapes but is slow compared to a Mie program.

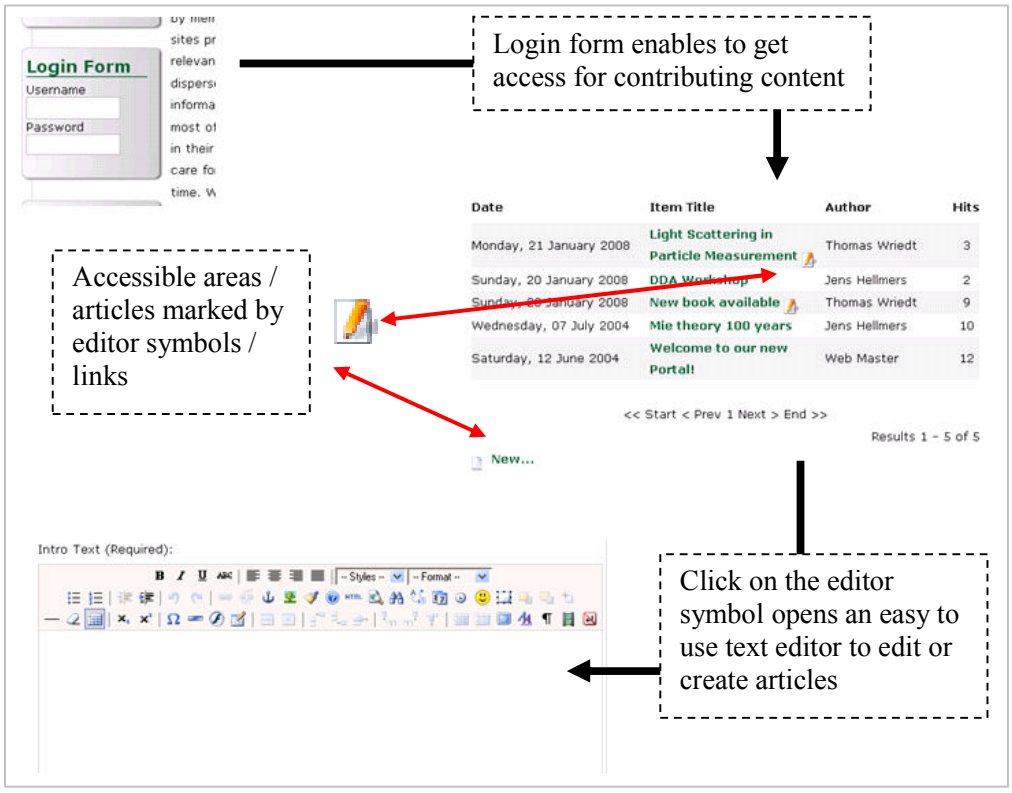

Figure 1: Procedure for the work with a CMS.

So in practice it seems to be more reasonable to argue the other way round: for a user who wants to calculate light scattering by a specific particle the explicit scattering theory is not the main issue as long as he can find a program suitable for his scattering problem. A classification also must consider the particle shapes and dimensions that can be handled by a program. Furthermore it might be of interest if a program is available as source code (so modifications can be made) or as pre-compiled executable file (which can restrict the use of the program to particular operating systems or hardware). This also should be taken into account.
Because of these multiple attributes the development of an appropriate classification scheme is not a trivial task. Therefore it will be done in cooperation with researchers working on the field of information technology.

4 Outlook

A test system based on the CMS described above is currently in development. It should go online as testbed soon. We will then invite the scattering community for tests, content and further suggestions. By this feedback we plan to improve the portal further step by step.

5 Summary

A new internet information portal for the light scattering community is recently in development. Compared to other existing offers we plan an interactive approach which will allow the users to become active members who can contribute own content to the portal. At this point we would like to invite the members of the scientific community to provide us with their ideas and suggestions for such an information portal. Especially welcome would be the active contribution of information like news, conferences, open positions, etc. Please feel free to contact us if you are interested in becoming an editor and get your own account for the CMS.

Acknowledgments

We would like to acknowledge support of this work by Deutsche Forschungsgemeinschaft DFG.

References

[1] T. Wriedt, “List of Electromagnetic Scattering Programs,” http://www.iwt-bremen.de/vt/laser/wriedt/index_ns.html.

[2] T. Wriedt and J. Hellmers, “New Scattering Information Portal for the light scattering community,” JQSRT **109**, 1536-1542 (2008).

Solution of electromagnetic waves scattering problems from inhomogeneously layered scatterers using pattern equation method

Alexander G. Kyurkchan, Dmitrii B. Demin

Moscow Technical University of Communication and Informatics,
Aviamotornaya Street 8A, Moscow, 111024, Russia
tel: +7 (499) 192-80-29, e-mail: kyurkchan@yandex.ru

Abstract

In this paper the generalization of the pattern equation method for solving the problems of electromagnetic waves scattering on inhomogeneously layered scatterers is presented. Numerical results are presented to demonstrate the accuracy and efficiency of the method. A comparison of the results obtained by the present method and other methods are shown and the restrictions on applicability of method are established.

1 Introduction

The scattering problem of electromagnetic waves from three-dimensional (3D) conducting inhomogeneously layered scatterers is of great scientific interest in radiophysics, theory of antennas, radioastronomy etc. To solve this problem in rigorous statement the integral equation method is extensively used. In solving the diffraction problem by this method the required characteristic is the current distributed either inside of volume of the object, or on its surface. For objects of arbitrary shapes it leads to great calculation expenses, therefore this method is used for the objects with simple shape.

In this paper, we extended the pattern equation method (PEM) to solution of the problems of electromagnetic waves scattering from inhomogeneously layered scatterers. Earlier, this method was already applied to the solution of the scattering problems for impedance and dielectric scatterers, and also for conducting objects coated with dielectric materials [1-3].

Using the standard scheme of PEM (see [1-3]) the initial boundary problem is reduced to the system of algebraic equations with respect to the coefficients of the expansion of the scattering pattern (spectral function of a wave field) in terms of vector angular spherical harmonics.

Under the certain restrictions on geometry of the problem, which can be strictly established [1-2], the received infinite linear system of the algebraic equations is solved by the method of a reduction, i.e. truncation. Thus the expansion of the scattering pattern in terms of vector angular spherical harmonics contains the finite amount of addends, which is determined by the maximal number of a harmonic N. The restrictions of the method have been specified earlier by consideration of the electromagnetic scattering problem for conducting objects.

The PEM is one of the most effective methods for solving the problem considered here. So, it has been earlier established [1-2] that under the solution of the scattering problems for impedance scatterers the rate of the algorithm convergence is mainly governed by the scatterer size and weekly depends on its geometry.

In present work we consider the elementary kind of the inhomogeneously layered scatterer, namely, a magneto-dielectric object coated with a magneto-dielectric layer with other parameters (other than the core characteristics).

2 Problem Statement

Consider the problem of electromagnetic scattering of incident primary monochromatic ($e^{i\omega t}$) field $\vec{E}^0$, $\vec{H}^0$ by an arbitrarily shaped 3D compact magneto-dielectric obstacle bounded by surface S_1 and coated with a magneto-dielectric covering with external surface S_2.

Let the following boundary conditions be met at S_1 and S_2:

$$(\vec{n}\times\vec{H})\big|_{S_2} = (\vec{n}\times\vec{H}_1)\big|_{S_2}, \quad (\vec{E}\times\vec{n})\big|_{S_2} = (\vec{E}_1\times\vec{n})\big|_{S_2}, \tag{1}$$

$$(\vec{n}\times\vec{H}_1)\big|_{S_1} = (\vec{n}\times\vec{H}^i)\big|_{S_1}, \quad (\vec{E}_1\times\vec{n})\big|_{S_1} = (\vec{E}^i\times\vec{n})\big|_{S_1}, \tag{2}$$

where $\vec{n}$ is the outward unit normal to S_1 and S_2; $\vec{E} = \vec{E}^0 + \vec{E}^1, \vec{H} = \vec{H}^0 + \vec{H}^1$ is the total external field; $\vec{E}_1, \vec{H}_1$ is the unknown field inside the dielectric covering (V_1); $\vec{E}^i, \vec{H}^i$ is the unknown field inside the region V_i, bounded by surface S_1; $\vec{E}^1, \vec{H}^1$ is the secondary (diffracted) field, which satisfies the system of homogeneous Maxwell equations elsewhere outside S_2 (inside the medium V_e) and the Sommerfeld radiation condition at infinity.

Let's input the following notations: $k_0 = \omega\sqrt{\varepsilon_0\mu_0}$ is the free-space wave number; $\varsigma_0 = \sqrt{\mu_0/\varepsilon_0}$ is the characteristic impedance of the external medium V_e; $\varsigma_1 = \varsigma_0\sqrt{\mu_1/\varepsilon_1}$, $\varsigma_i = \varsigma_0\sqrt{\mu_i/\varepsilon_i}$ are the characteristic impedances, and $k_1 = k_0\sqrt{\varepsilon_1\mu_1}$, $k_i = k_0\sqrt{\varepsilon_i\mu_i}$ are the wave numbers inside the media V_1 and V_i with related permittivities ε_1, ε_i and permeabilities μ_1, μ_i, respectively. Let the outer (V_e) and inner (V_1, V_i) media be homogeneous, linear, and isotropic.

3 Reduction of Boundary-Value Problem to System of Algebraic Equations

According to the PEM standard scheme [1-3], we search the scattering pattern function, that is, the function that defines the dependence of the diffracted field on the angles (θ,φ) in spherical coordinates (r,θ,φ) for the far zone (for $k_0 r >> 1$). The following asymptotic relations are valid:

$$\vec{E}^1 = \frac{\exp(-ik_0 r)}{r}\vec{F}^E(\theta,\varphi) + O\left(\frac{1}{(kr)^2}\right), \quad \vec{H}^1 = \frac{\exp(-ik_0 r)}{r}\vec{F}^H(\theta,\varphi) + O\left(\frac{1}{(kr)^2}\right),$$

Here $\vec{F}^E$, $\vec{F}^H$ are the patterns for electrical and magnetic fields, respectively.

Under solution of the initial problem, the basic point of the PEM is to obtain the infinite system of algebraic equations with respect to unknown coefficients of the expansion of the scattering pattern in terms of vector angular spherical harmonics [4], which compose the orthogonal basis in the spherical coordinates. These series of the patterns for electrical and magnetic fields have the following form

$$\vec{F}^E(\theta,\varphi) = -\sum_{n=1}^{\infty}\sum_{m=-n}^{n} a_{nm} i^n \left(\vec{i}_r \times \vec{\Phi}_n^m(\theta,\varphi)\right) - \sum_{n=1}^{\infty}\sum_{m=-n}^{n} b_{nm} i^n \varsigma_0 \vec{\Phi}_n^m(\theta,\varphi), \tag{3}$$

$$\vec{F}^H(\theta,\varphi) = \sum_{n=1}^{\infty}\sum_{m=-n}^{n} a_{nm} i^n \frac{1}{\varsigma_0}\vec{\Phi}_n^m(\theta,\varphi) - \sum_{n=1}^{\infty}\sum_{m=-n}^{n} b_{nm} i^n \left(\vec{i}_r \times \vec{\Phi}_n^m(\theta,\varphi)\right), \tag{4}$$

where

$$\vec{\Phi}_n^m(\theta,\varphi) = \vec{r} \times \nabla P_n^m(\cos\theta)\cdot\exp(im\varphi), \tag{5}$$

and a_{nm}, b_{nm} are the unknown expansion coefficients of the scattering pattern. In Eq. (5) P_n^m are the associated Legendre functions.

By analogy with [1-2] using Maxwell equations and boundary conditions (1)-(2) one can get the required expressions of the coefficients a_{nm}, b_{nm}. Then using decompositions of the fields $\vec{E}^1, \vec{H}^1$, $\vec{E}_1, \vec{H}_1$, and $\vec{E}^i, \vec{H}^i$ in terms of the vector spherical harmonics and representations of coefficients a_{nm}, b_{nm} in terms of the boundary values of the fields, we obtain the following system of PEM:

$$\begin{cases} a_{nm} = \sum\limits_{q=1}^{\infty}\sum\limits_{p=-q}^{q}\left(G^{13}_{nm,qp}a^1_{qp} + G^{14}_{nm,qp}b^1_{qp} + G^{15}_{nm,qp}a^2_{qp} + G^{16}_{nm,qp}b^2_{qp}\right), \\ b_{nm} = \sum\limits_{q=1}^{\infty}\sum\limits_{p=-q}^{q}\left(G^{23}_{nm,qp}a^1_{qp} + G^{24}_{nm,qp}b^1_{qp} + G^{25}_{nm,qp}a^2_{qp} + G^{26}_{nm,qp}b^2_{qp}\right), \end{cases}$$

$$\begin{cases} a^1_{nm} = \sum\limits_{q=1}^{\infty}\sum\limits_{p=-q}^{q}\left(G^{37}_{nm,qp}a^i_{qp} + G^{38}_{nm,qp}b^i_{qp}\right), \\ b^1_{nm} = \sum\limits_{q=1}^{\infty}\sum\limits_{p=-q}^{q}\left(G^{47}_{nm,qp}a^i_{qp} + G^{48}_{nm,qp}b^i_{qp}\right), \end{cases} \tag{6}$$

$$\begin{cases} a_{nm}^2 = a_{nm}^0 + \sum_{q=1}^{\infty} \sum_{p=-q}^{q} \left(G_{nm,qp}^{51} a_{qp} + G_{nm,qp}^{52} b_{qp} \right), \\ b_{nm}^2 = b_{nm}^0 + \sum_{q=1}^{\infty} \sum_{p=-q}^{q} \left(G_{nm,qp}^{61} a_{qp} + G_{nm,qp}^{62} b_{qp} \right), \end{cases}$$

In this system a_{nm}^1, b_{nm}^1 и a_{nm}^2, b_{nm}^2 are the unknown expansion coefficients of the field $\vec{E}_1, \vec{H}_1$ inside the covering (V_1); a_{nm}^i, b_{nm}^i are the unknown expansion coefficients of the field $\vec{E}^i, \vec{H}^i$. The field $\vec{E}_1, \vec{H}_1$ represents the sum of a field, past through a surface S_2 and a field caused by the equivalent surface current at S_1. $G_{nm,qp}^{ij}$ ($i, j = 1...8$) and a_{nm}^0, b_{nm}^0 are the matrix elements and the coefficients of the right part of system (6), which are represented in surface integrals on S_1 and S_2.

The system of PEM (6) is applicable for calculation of scattering characteristics of the arbitrary shape covered scatterers which have not the axial symmetry. When the scatterer is an axially symmetric object, i.e. the surface equation $\rho(\theta, \varphi) = \rho(\theta)$, the algebraic system (6) is significantly simplified and becoms similar to the system for dielectric scatterers [2]: the sum of the index " p " disappears, and the index " p " is replaced by " m "; the index " q " in the sum changes from $|m|$ to ∞; and the matrix elements of system (6) are expressed in terms of single integrals.

For the verification of applicability of the method of the reduction to the received infinite system (6), the estimations of the matrix elements and the right part of the system for large values n and q can be made (see, for example, [1-2]). It allows us to specify rigorous restrictions on geometry of the scatterers. So, if the incident field is a plane wave, the method of a reduction is applicable provided that the geometry of the scatterer belongs to a class of weakly nonconvex bodies [1-2]. In particular, this class contains all convex bodies.

4 Numerical results

Under the developed numerical algorithm of PEM, we carried out researches of accuracy of numerical calculations for scattering characteristics. Moreover, we carried out comparisons of our results with the results obtained by PEM for impedance and dielectric scatterers, and also by other methods. If we restrict ourselves by the scatterers in the form of the bodies of revolution then it significantly simplifies the numerical algorithm and reduces the surface integrals for matrix elements in the system of PEM to single integrals. Some of the results are shown here.

We consider the axial incidence of a plane wave directed along the symmetry axis of the scatterer, which coincides with the z-axis.

In the first example, we consider a dielectric sphere coated with a dielectric covering. Then S_1 and S_2 are concentric spheres with a common center located in the origin of coordinate system, and $\rho_1(\theta) = a_1$, $\rho_2(\theta) = a_2$, where a_1 and a_2 are the radiuses of inner and outer spheres, respectively ($a_2 > a_1$). In the case of sphere, from system of PEM it is possible to receive explicit expressions for a_{nm}, b_{nm}, which correspond to the analytical solution of the scattering problem for sphere as in the theory of Mie series.

The bistatic RCS σ/λ^2 of the dielectric sphere coated with a dielectric spherical layer with size parameters $k_0 a_1 = 2\pi$, $k_0 a_2 = 2.1\pi$ is shown in Fig.1. Parameters of a material of a core and covering: $\varepsilon_i = 4$, $\mu_i = 1$ (relative permeability), $\varepsilon_1 = 1$, $\mu_1 = 3 - 6i$. The geometry of the sphere coincides with those, which is presented in [5].

The quantity σ/λ^2 was calculated under the formula

$$\frac{\sigma}{\lambda^2} = \frac{k_0^2}{\pi} \left(\left| F_\theta^E(\theta, \varphi) \right|^2 + \left| F_\varphi^E(\theta, \varphi) \right|^2 \right)$$

in the plane $\varphi = 0$ (E-plane).

There are two curves presented: curve 1 is the solution obtained by the proposed method, and curve 2 is the result taken from [5]. In [5] the volume integral equation method is used for the solution of the given above scattering problem. In the same work the result of calculation of the scattering pattern for the dielectric sphere is presented. The result completely coincides with that received by using the PEM for magneto-dielectric objects.

In the next example we consider the dielectric prolate spheroid coated by dielectric material. One consists of two concentric spheroids with the semiaxes of the internal spheroid $ka_1 = 1.5$, $kc_1 = 3$ and the

semiaxes of the external spheroid $ka_2 = 3,\ kc_2 = 6$. The regions in internal spheroid and its coating layer are purely dielectric with the relative permittivities $\varepsilon_i = 3.24$ and $\varepsilon_1 = 2.25$, respectively. The result plotted in Fig.2 for the coated spheroid shows the bistatic RCS's σ/λ^2 normalized by πc_2^2. The scattering cross-section is computed in the planes $\varphi = 0$ (curve 1: E-plane) and $\varphi = \pi/2$ (curve 2: H-plane). Our numerical results agree very well with the results obtained by using the null-field method with discrete sources [6].

Calculations of scattering characteristics were carried out at $N \approx 1.5k_0 d$ for spheroid and $N \approx k_0 d$ for sphere, thus the two correct meaningful decimal digits were established in the solution for spheroid, and four – for sphere. Here N is the upper limit of summation in (6), and d is the maximal diameter of the scatterer.

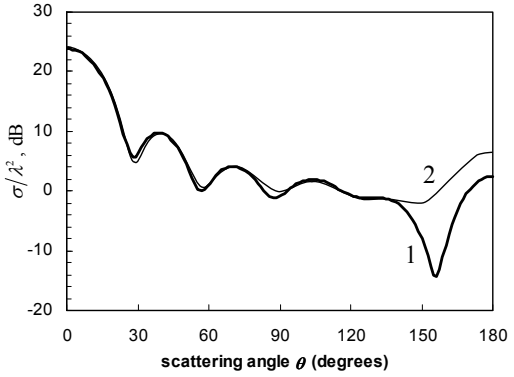

Fig.1. Scattering pattern for sphere

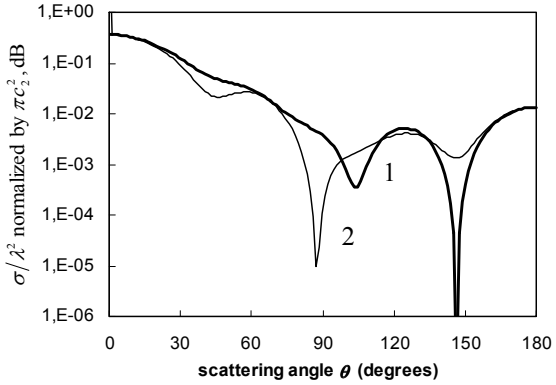

Fig.2. Scattering pattern for spheroid

3 Conclusion

The generalization of PEM for the problems of wave diffraction by inhomogeneously layered scatterers has been proposed. In all examples considered, high accuracy and convergence rate of the method were demonstrated. The proposed method will be extended to the solution of the problems of electromagnetic wave scattering by multilayered scatterers.

Acknowledgments

This work was supported by Russian Foundation for Basic Research, Project no. 06-02-16483.

References

[1] A.G. Kyurkchan and D.B. Demin, "Electromagnetic wave diffraction from impedance scatterers with piecewise-smooth boundaries", Journal of Commun. Techn. and Electron., **47**, 856-863 (2002).

[2] A. Kyurkchan, D. Demin, "Pattern equation method for solving problems of diffraction of electromagnetic waves by axially dielectric scatterers", JQSRT, **89**, 237-255 (2004).

[3] A.G. Kyurkchan, D.B. Demin, and N.I. Orlova, "Solution based on the pattern equation method for scattering of electromagnetic waves by objects coated with dielectric materials", JQSRT, **106**, 192-202 (2007).

[4] Papas C.H., *Theory of Electromagnetic Wave Propagation* (McGraw–Hill Book Comp. New York, London, Sydney, 1965).

[5] X.C. Nie, N. Yuan, L.W. Li, Y.B. Gan, and T.S. Yeo, // IEEE Trans. Antennas Propag., **54**, 961-969, (2006).

[6] A. Doicu, T. Wriedt. Null-field method with discrete sources to electromagnetic scattering from layered scatterers. Comput. Phys. Commun. 2001; 138: 136-142.

Solution of diffraction problems by null field method with accounting for analytical continuation singularities

Alexander G. Kyurkchan,[1] Nadezhda I. Smirnova,[1]

[1] *Moscow Technical University of Communication and Informatics,*
Aviamotornaya street, 8a, 111024, Moscow, Russia
tel: +7 (495) 236-1627, fax: +7 (495) 274-0032, e-mail: kyurkchanl@yandex.ru

Abstract

It is shown that the correct use of the null field condition for obtaining integral equation requires that the surface, on which null field condition is satisfied, covers the set of singularities of wave field analytical continuation into interior of the scatterer. Moreover, it is demonstrated, that solution algorithm of the obtained integral equation is fastest and most stable if the above mentioned surface is constructed by analytical deformation of scatterer boundary.

1 Introduction

The wave field in the source-free domain is the solutions of Maxwell homogeneous equation system (homogeneous Helmholtz equation) and thus are real-analytical functions [1]. Therefore, the correct solution of a direct and inverse problems is possible only if an a priori information about wave field singularities is taken into account [2]. In this work the importance of using such information is demonstrated by applying it to the popular null field method. Null field method (NFM), as well as one of its modification – T-matrix method – is the most widely used methods for solution of wave diffraction problems [4, 5].

2 Scalar diffraction problem

First let's consider the scalar diffraction problem. The following expression is true [1]

$$\int_S \left\{ u(\vec{r}') \frac{\partial G_0}{\partial n'} - \frac{\partial u(\vec{r}')}{\partial n'} G_0(\vec{r},\vec{r}') \right\} ds' = \begin{cases} u^1(\vec{r}), & \vec{r} \in \mathbf{R}^3 \setminus \bar{D}, \\ -u^0(\vec{r}), & \vec{r} \in D, \end{cases} \tag{1}$$

where $u(\vec{r}) = u^1(\vec{r}) + u^0(\vec{r})$ is the total field, $u^0(\vec{r})$ - the incident wave field, $u^1(\vec{r})$ - the scattered wave field, $G_0(\vec{r},\vec{r}') = \exp(-ik\,|\,\vec{r}-\vec{r}'\,|)/4\pi\,|\,\vec{r}-\vec{r}'\,|$ - the fundamental solution of Helmholtz equation. As is well known, the second line in Eq.°(1) is a null field condition. If impedance boundary condition is satisfied on boundary *S* of scatterer

$$\left[u(\vec{r}) - \frac{Z}{ik\zeta} \frac{\partial u(\vec{r})}{\partial n} \right]_S = 0\,, \tag{2}$$

then on the basis of Eq.°(1) the following null field integral equation can be written

$$u^0(\vec{r}) + \int_S \frac{\partial u(\vec{r}')}{\partial n'} \left\{ \frac{Z}{ik\zeta} \frac{\partial G_0(\vec{r},\vec{r}')}{\partial n'} - G_0(\vec{r},\vec{r}') \right\} ds' = 0, \quad M(\vec{r}) \in \Sigma\,, \tag{3}$$

where Σ - some closed surface inside *S*.

It's a traditional to think, that the only requirement is the non-resonance (see below) of surface Σ. Let's show that it is not true.

Consider integral equation of auxiliary currents method [6] in case of Dirichlet condition on *S* (i.e. in Eq.°(2) $Z = 0$)

$$\int_\Sigma \nu(\vec{r}') G_0(\vec{r},\vec{r}')\, ds' \big|_S = u^0(\vec{r})\big|_S\,, \tag{4}$$

In Eq.°(4) Σ is a carrier of auxiliary current inside *S*.

The following theorem is true:

Let Σ be an arbitrary closed non-resonance Lyapunov surface (i.e. inner homogeneous Dirichlet problem for domain inside Σ has only trivial solution). Equation Eq.°(4) is solvable if and only if Σ encloses set $\overline{A}$ of singularities of wave field $u^1(\vec{r})$ analytical continuation into domain inside S.

Eq.°(4) has a single solution if theorem conditions are fulfilled.

If set $Z = 0$ in Eq.°(3) and choose the same surface as Σ in Eq.°(3) and in Eq.°(4), then both equation kernels will be allied and therefore obviously Eq.°(3) will have a solution also only when Σ encloses set $\overline{A}$.

Let's illustrate the above statement by concrete examples of solution of diffraction problems on bodies of revolution, when surface S can be expressed in spherical coordinates (r,θ,φ) as $r = \rho(\theta)$. Surface Σ is constructed by three different methods: (1) by analytical deformation of *S* [7] enclosing set $\overline{A}$, by displacement *S* on the same value Δ for all θ with (2) and without (3) enclosing set $\overline{A}$. Unknown function in Eq.°(3) was approximated by piecewise constant function. Values of integrals of equation kernel on fragmentation interval was replaced by values of integrands taken in the middle of intervals multiplied by lengths of corresponding intervals, i.e. the simplest discrete sources method technique was used to solve Eq.°(3) [5]. The $u^0(\vec{r})$ was a plane wave propagating at angles $\varphi_0 = 0$, $\theta_0 = \pi/2$.

Figure 1 shows the scattering pattern for the impedance spheroid with parameters *ka*=1, *kc*=5, $Z = 1000\zeta i$ at $N=N_1=128$, where *N* is approximation level, N_1 is the number of nodes used for Fourier inversion of Green function. Figure legend: 1 – surface Σ obtained by analytical deformation of S enclosing singularities, 2 – surface Σ obtained by non analytical deformation enclosing singularities (the distance $k\Delta$ from Σ to set of singularities is equal to 10^{-3}). Results obtained in case of singularities not enclosed are not shown here, because even in case of enclosing singularities (at non analytical deformation) obtained result is incorrect. Correct result for non analytical deformation enclosing singularities can be obtained only at $N=N_1=512$.

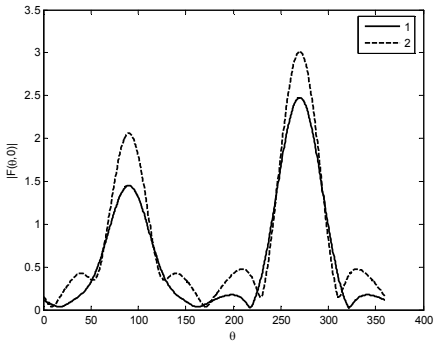

Figure 1: Scattering patterns.

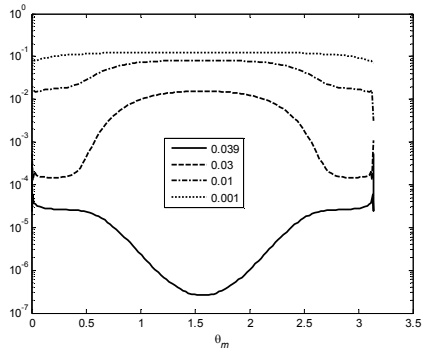

Figure 2: Residuals.

Figure 2 shows residuals on different surfaces inside spheroid with $ka = 1, kc = 5$ for the case when the surface Σ was obtained by analytical deformation of S. The lowest curve – residuals on surface Σ (calculated at points between collocation points); the upper curve – residuals on surface nearest to S. It is clear that zero field condition is satisfied with high precision everywhere. Figure 3 shows residuals for similar calculations, when surface Σ was obtained by non analytical deformation of S with enclosing singularities ($N=N1=512$).

As seen, residuals are small enough, but this was achieved by four-fold increase in the number of the discrete sources. When surface Σ does not enclose set $\overline{A}$ correct results could not be obtained at any *N*.

Figures 4 show scattering patterns for 2-foil of revolution (body produced by rotation of curve $\rho(\theta) = b + a\cos 2\theta$) with *ka*=2, *kb*=3, $N=N_1=256$, *Q*=4, $Z = 0$. To illustrate the point, the diagram 1 was calculated for the surface Σ obtained by analytical deformation until enclosing singularities, while

diagram 2 was calculated for the surface Σ constructed as a sphere with the radius 0.999, as it would be done in T-matrix method. In the last case, singularities located at 3.62 distance from the center of the body are not enclosed.

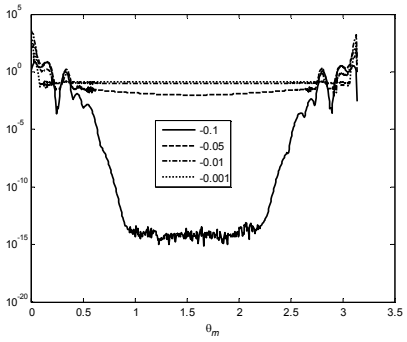

Figure 3: Residuals.

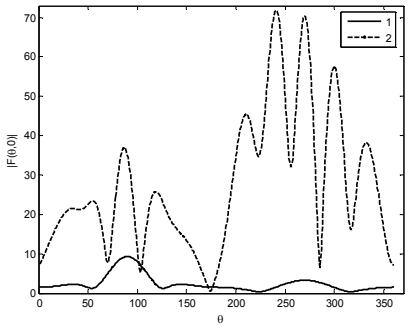

Figure 4: Scattering patterns.

3 Vector diffraction problem

Let's now evaluate the vector model. Specifically, consider diffraction problem on perfectly conducting scatterer. Using zero field condition the boundary problem can be reduced to the following equation:

$$\left\{\vec{n}\times\frac{\zeta}{4\pi ik}\int_S\left[k^2\vec{J}^e(\vec{r}')G_0(\vec{r};\vec{r}')-(\vec{J}^e\cdot\nabla')\nabla G_0(\vec{r};\vec{r}')\right]ds'\right\}\Big|_\Sigma=-\left(\vec{n}\times\vec{E}^0(\vec{r})\right)\Big|_\Sigma, \quad (5)$$

where $\vec{J}^e=\left(\vec{n}\times\vec{H}\right)\Big|_S$, $\vec{H}=\vec{H}^0+\vec{H}^1$, $\vec{H}^0,\vec{E}^0$ -primary, $\vec{H}^1,\vec{E}^1$ - diffracted (secondary) magnetic and electric fields, S – scatterer surface, Σ – surface where zero field condition is set. As mentioned above, at the surface of the scatterer the boundary condition is met: $\left(\vec{n}\times\vec{E}(\vec{r})\right)\Big|_S=0$, where $\vec{E}=\vec{E}^0+\vec{E}^1$.

As in scalar case, the equation (5) is correct only if surface Σ encloses set $\overline{A}$ of analytical continuation singularities

Let's illustrate the above statement with the concrete example.

Consider diffraction problem for a plane incident wave propogating at angles $\varphi_0=0$, $\theta_0=\pi/2$ on perfectly conducting spheroid with axes *ka*=1, *kc*=5. Figure 5 shows the scattering pattern for Σ constructed by analytical deformation of S with N=N_1=256. Figure 6 shows scattering pattern for non analytical deformation of boundary surface with enclosing singularities with the same N=N_1=256. As we can see both diagrams in figure 6 are wrong. An accurate diagrams can be only obtained with N=N_1=1024. Figure 7 shows the residuals for the solution when surface Σ was obtained by analytical deformation of S until enclosing singularities of the wave field. Here again the lowest curve is for residuals at the surface Σ (calculated for the points between collocation points), and the upper curve – at the surface adjacent to S. Thus, in the vector case the null field condition is also satisfied with good precision.

Conclusion

It is shown that the correct reduction of null field condition to the corresponding integral equation is only possible if the surface, where zero field condition is satisfied, covers the set of singularities of wave field analytical continuation into interior of the scatterer. The rational for this requirement is that integral equation solution is based on analytical representations of the wave field, which exist only outside of the field singularities. As a bonus, the obtained integral equation solution algorithm turns out to be the fastest and most stable, when the above mentioned surface is constructed by analytical deformation of the scatterer's boundary.

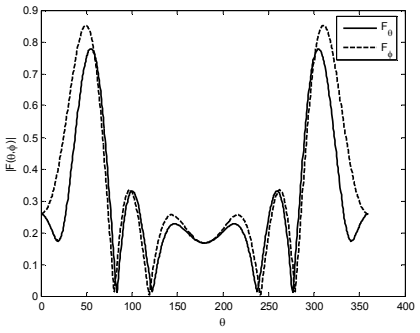

Figure 5: Scattering pattern.

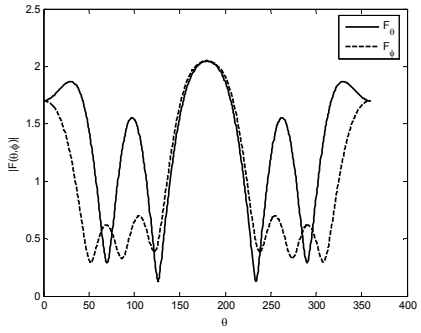

Figure 6: Scattering pattern.

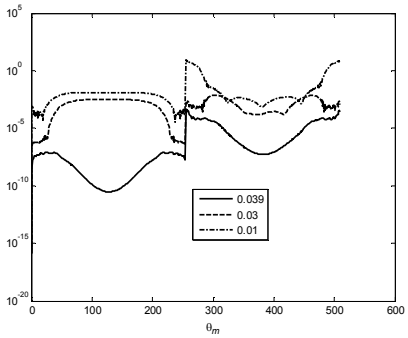

Figure 7: Residuals.

Acknowledgments

This work was supported by the Russian foundation of basic researches, project № 06-02-16483.

References

[1] D. Colton, R. Kress, *Integral Equation Methods in Scattering Theory* (John Wiley&Sons, New York 1983).

[2] A. G. Kyurkchan, B. Yu. Sternin, V. E. Shatalov, “The singularities of continuation of wave fields,” Physics-Uspekhi, V. **39,** 1221-1242 (1996).

[3] P. C. Waterman, “Matrix formulation of electromagnetic scattering,” Proc. IEE, V. **53**, 805-812 (1965).

[4] M. I. Mishchenko, L. D. Travis, A. A. Lacis, *Scattering, absorption and emission of light by small particles* (Cambridge University Press, Cambridge, 2002).

[5] T. Wriedt, “Review of the null-field method with discrete sources,” Journal of Quantitative Spectroscopy & Radiative Transfer, V. **106,** 535-545 (2007).

[6] A. G. Kyurkchan, “Representation of diffraction fields by wave potentials and the method of auxiliary currents in problems of the diffraction of electromagnetic waves,” Soviet Journal of Communications Technology and Electronics, V. **31,** No 5, 20-27 (1986).

[7] A. G. Kyurkchan, S. A. Minaev, “Using of the wavelet technique for the solution of the wave diffraction problems,” Journal of Quantitative Spectroscopy & Radiative Transfer, V. **89,** 219-236 (2004).

Solving of Problems of Electromagnetic Waves Scattering by complex-shaped dielectric bodies via the Pattern Equations Method

Alexander G. Kyurkchan,[1] Elena A. Skorodumova[1]

[1] *Moscow Technical University of Communication and Informatics, Aviamotornaya Street 8a, 111024, Moscow, Russian Federation,*
tel: +7 (495) 236-2267, e-mail: kyurkchan@yandex.ru

Abstract

An efficient method is proposed for solving the problem of diffraction on complex-shaped dielectric bodies. The initial problem is reduced to a system of algebraic equations by expanding the scattering patterns in vector angular spherical harmonics. It is shown that the method offers a high rate of convergence that weakly depends on the distances between them. Examples of modeling of the scattering characteristics of complex-shaped bodies are considered.

1 Introduction

The problem of diffraction on dielectric bodies of arbitrary shapes is one of the most complicated problems of scattering, but, solving of this problem is urgent in a number of scientific and engineering applications. The results of modeling the scattering characteristics for complex-shaped dielectric bodies is of a great practical-purpose interest in such disciplines as medicine, meteorology, radio physics, radio astronomy, astrophysics, and others.

The most efficient approach for solving of such problems consists in using scattering patterns of the bodies as the quantities to be found. On the one hand, those characteristics are integral and therefore smooth out the local disturbances of the equivalent currents arising in localities of a sharp modification of the geometry of the boundary. On the other hand, those characteristics are often just what to be determined in practice.

Such an idea is used in the pattern equation method (PEM), which has appeared to be a high efficient technique for modeling scattering characteristics of groups of bodies and of the complex-shaped bodies with impedance boundary conditions [1–2]. In this work, the developed approach is extended to solving the problem of diffraction on on complex-shaped dielectric bodies.

2 Statement of the problem and it's solution

Let's consider the problem of diffraction of the primary monochromatic field $\vec{E}^0, \vec{H}^0$ on the complex-shaped dielectric body bounded by surface S. To define the scattering characteristics of this object we shall replace it with a combination of simpler scatterers. We shall discuss the algorithm of the PEM for the case of two bodies, but it can be easily extended for any number of objects.

Let the following boundary conditions be met at boundaries S_j, $j = 1, 2$ of the bodies:

$$\vec{n}_j \times \left(\vec{H}^0 + \vec{H}_1^1 + \vec{H}_2^1\right)\Big|_{S_j} = \vec{n}_j \times \vec{H}_j^i\Big|_{S_j}, \quad \left(\vec{E}^0 + \vec{E}_1^1 + \vec{E}_2^1\right) \times \vec{n}_j\Big|_{S_j} = \vec{E}_j^i \times \vec{n}_j\Big|_{S_j}.$$

Here, $\vec{H} = \vec{H}^0 + \vec{H}_1^1 + \vec{H}_2^1$ and $\vec{E} = \vec{E}^0 + \vec{E}_1^1 + \vec{E}_2^1$ – are the total external fields, $\vec{E}_j^i, \vec{H}_j^i$ – are the unknown fields within the volumes of the scatterers explored; $\vec{n}_j$ – is the outward unit normal to S_j. The diffraction fields $\vec{E}_j^1, \vec{H}_j^1$ satisfy the system of homogeneous Maxwell equations elsewhere outside

surfaces S_j, and the Sommerfeld's condition on infinity. Let the outer and inner media be homogeneous, linear and isotropic.

In the PEM, the main characteristics to be found are the aforementioned scattering patterns of bodies. Reduction of the initial boundary problem to the infinite algebraic system of the PEM is based on expansions of these characteristics and the outer and inner fields $\vec{E}_j^1, \vec{H}_j^1, \vec{E}_j^i, \vec{H}_j^i$ into series of vector spherical harmonics [3].

3 Results of calculations

Examination of the convergence rate of the calculation realization of the PEM for the problem of diffraction on two dielectric bodies has shown, that in the case of bodies with a simple geometry (spheres) the algorithm ensures 7–8 significant figures already when the parameter of reduction of the algebraic system $N = kd$ even for the case of minimal distance $k\Delta = 0.02$ between the objects. Here d – is the maximum size of the scatterer. For the superellipsoids, the axial cross-section of which is given by the following equation:

$$\left(\frac{x}{a}\right)^{2m} + \left(\frac{z}{c}\right)^{2m} = 1$$

(see fig. 1), the rate of convergence is noticeably lower. Here to have the results obtained with an acceptable accuracy we need to take the value of the parameter $N \approx (1.5 \div 2)kd$. It can be explained by the fact, that the singularities of an analytic continuation of the diffracted field inward the scatterers [4] are located close enough to their boundaries.

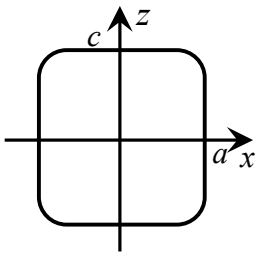

Figure 1: Axial cross-section of a superellipsoid

We tested the possibility of replace the complex-shaped body by the combination of more simple objects based on comparison of the scattering pattern of two close located superellipsoids and the scattering pattern of a single body with the corresponding size. The results obtained have shown that the differences between the corresponding patterns are very small.

Let's consider some examples of modeling of the scattering characteristics of the complex-shaped bodies.

Figure 2 illustrates the scattering problem on the object, having the shape of a "grenade". This figure shows the scattering pattern calculated for two superellipsoids which are located one over the other. The parameters of the upper superellipsoid ($ka_1 = kc_1 = 4$) are smaller than the lower one ($ka_2 = 6,\ \ kc_2 = 4$).

Further, let's consider the scattering problem on the object, having the shape of an "inverted mushroom", i.e. the body, composed of a hemisphere ($ka_{hs} = 5$) and a superellipsoid ($ka_{se} = kc_{se} = 2.5$). Fig. 3 shows the scattering pattern of such a body for various values of material parameters of components. Calculations are carried out for the case of the longitudinal (along the rotation axis) incidence of the primary wave.

Thus, it is advantageous to present the complex-shaped object as a combination of more simple ones. It allows modeling of the scattering characteristics of objects, which components have various material parameters as in our example.

In all the examples of modeling the scattering characteristics of the objects with a complex geometry given above, the distances between surfaces of their constituent elements were smaller than 0.01% of average sizes of the objects. Thus the minimal distance between the objects practically didn't influence on the operational time of the computation algorithm. It allows one to speak about a high efficiency of the method proposed.

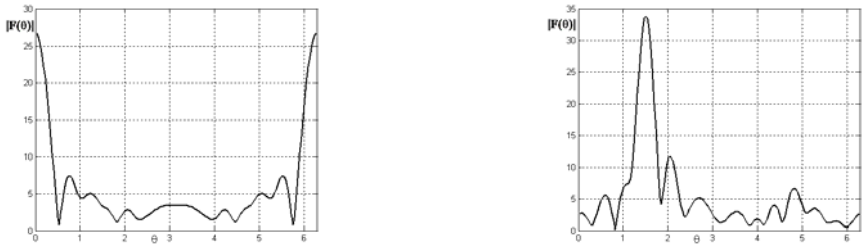

a) b)

Figure 2: Scattering pattern of object composed of two superellipsoids with parameters $ka_1 = kc_1 = 4$, $ka_2 = 6$, $kc_2 = 4$, $k\Delta = 0.01\lambda$, $\varepsilon_{r_{i,2}} = 2.25$, $\mu_{r_{i,2}} = 1$: a) the longitudinal (along the rotation axis) incidence of the wave; b) the perpendicular incidence of the wave

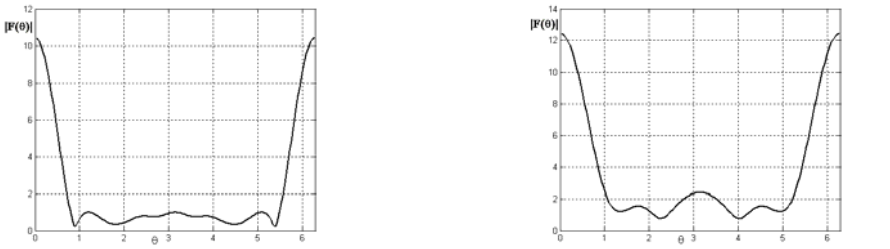

a) $\varepsilon_{rse} = 2.25,\ \mu_{rse} = 1,\ \varepsilon_{rhs} = 1 - 4i,\ \mu_{rhs} = 1 - 4i$ b) $\varepsilon_{rse} = \varepsilon_{rhs} = 2.25,\ \mu_{rse} = 1,\ \mu_{rhs} = 1$

Figure 3: Scattering pattern of an "inverted mushroom" – a hemisphere with radius $ka_{hs} = 5$ and a superellipsoid with parameters $ka_{se} = kc_{se} = 2.5$, located at the minimal distance $k\Delta = 0.01\lambda$, the longitudinal (along the rotation axis) incidence of the wave

To verify our investigations we checked out fulfillment of the Optical Theorem [5], accordicg to which:

$$-\operatorname{Im}\left\{\vec{F}^{E}(\theta = \theta_0,\ \varphi = \varphi_0)\cdot\vec{p}\right\} = \frac{1}{2\lambda}\int_0^{2\pi}\int_0^{\pi} |\vec{F}^{E}(\theta,\ \varphi)|^2 \sin\theta d\theta d\varphi .$$

The results are presented in Table 1. As one can see from the table, its accuracy is quite acceptable irrespective the complexity of shapes of the bodies explored.

4 Conclusion

It is demonstrated the high rate of convergence of the calculation algorithm of the PEM that weakly depends on the complexity of boundaries of the bodies. Examples of modeling of the scattering characteristics of the complex-shaped bodies are considered even for the case when the components of

the researched object have various material parameters. The validity of calculations is confirmed with checkout of fulfillment of the Optical Theorem, which showed the good accuracy independent of the complexity of boundaries of the bodies.

Table 1: Verification of the validity of the optical theorem for various complex-shaped objects ($\varepsilon_{r_{1,2}} = 2.25,\ \mu_{r_{1,2}} = 1$)

Objects	Parameters	$-\mathrm{Im}\left\{\vec{F}^E(\theta=\theta_0,\ \varphi=\varphi_0)\cdot\vec{p}\right\}$	$\frac{1}{2\lambda}\int_0^{2\pi}\int_0^{\pi}\lvert\vec{F}^E(\theta,\ \varphi)\rvert^2\ \sin\theta d\theta d\varphi$
2 superellipsoids (a «grenade») the incidence of the wave is perpendicular to the rotation axis	$ka_1 = 4$ $kc_1 = 4$ $ka_2 = 6$ $kc_2 = 4$	30,3547	30,0580
2 superellipsoids (a «grenade») the incidence of the wave is along the rotation axis	$ka_1 = 4$ $kc_1 = 4$ $ka_2 = 6$ $kc_2 = 4$	26,0003	26,1011
a superellipsoid and a hemisphere (a «mushroom»)	$ka_{se} = 2$ $kc_{se} = 2$ $ka_{hemisph} = 4$	12,2080	12,5100

Acknowledgments

This work was supported by the Russian Foundation for Basic Research, Project No. 06-02-16483.

References

[1] A. G. Kyurkchan and E. A. Skorodoumova, “Modeling the characteristics of the waves scattering by a group of scatterers”, Journal of Quantitative Spectroscopy and Radiative Transfer, **100**, 207-219 (2006).

[2] A. G. Kyurkchan, E. A. Skorodumova, “Solving the diffraction problem of electromagnetic waves on objects with a complex geometry by the pattern equations method”, Journal of Quantitative Spectroscopy and Radiative Transfer, **109**, 1417-1429 (2008).

[3] C. H. Papas, Theory *of Electromagnetic Wave Propagation* (McGraw–Hill Book Comp, New York, London, Sydney, 1965).

[4] A.G. Kyurkchan, B.Yu. Sternin, V.E. Shatalov. “Singularities of continuation of wave fields”, Physics-Uspekhi, **166**, 1221-1242 (1996).

[5] C. F. Bohren and D. R. Huffman, *Absorption and Scattering of Light by Small Particles* (New York, Wiley-Interscience, 1983).

Light scattering by a layer with a high concentration of optically soft particles

Valery Loiko,[1] and Vladimir Berdnik[2]

[1] *Stepanov Institute of Physics, Nezavisimosti avenue 68, 220072, Minsk, Belarus*
[2] *Institute of Aerospace Instrumentation, Lipatova str. 2, 420075, Kazan, Russia*
tel: +375 (017) 284-2894, fax: +375 (017) 284-0879, e-mail: loiko@dragon.bas-net.by

Abstract

A method to describe light propagation in concentrated disperse media with optically soft particles is developed. Interference effects in scattering by unit volume of partially ordered particles are taken into account. The radiative transfer theory is used to describe the light propagation in a thick layer. The radiative transfer equation is solved by the doubling method. Spline approximation of the phase function approximation is used. The analysis of the angular structure on the direction of layer illumination, its optical thickness, concentration, and size of particles is carried out.

1 Introduction

A rigorous description of scattering in close-packed media requires the use of the theory of multiple scattering of waves. There are a number of effects that cannot be described by the conventional radiation transfer theory based on summation of intensities. Because of the complexity and cumbersomeness of the mathematical apparatus of the multiple scattering theory, complete solutions can be obtained in extremely rare situations.

We consider a model of radiation transfer in a layer of disperse medium with a high concentration of optically soft particles [1]. The results of analysis of the angular structure of radiation scattered in the forward and backward hemispheres, depending on the direction of illumination of the layer, its optical thickness, concentration, and size of particles are presented.

2 Model of light transport in a layer

Let an azimuthally symmetric wide radiation beam with intensity I_0 be incident at an angle θ_0 to the normal of a layer of a scattering medium confined from above and below by planes $z = 0$ and $z = z_0$. The scattering medium is a matrix with suspended monodisperse particles with radius R_p and a relative refractive index n_p. The refractive index n_m of the matrix is equal to the refractive index of the surrounding medium and hence there are no reflections at the boundaries. The radiation is scattered inside the layer, is partially absorbed and emerges from the layer through confining surfaces.

In order to describe the propagation of light in the layer, we use the radiative transfer equation (RTE) [2] which can be presented in the following form for an azimuth-averaged scattered light intensity when the layer is illuminated by a parallel beam:

$$\mu\frac{\partial I(z,\mu)}{\partial z}+\varepsilon I(z,\mu)=\sigma\int_{-1}^{1}p(\mu,\mu')I(z,\mu')d\mu'+$$
$$+I_{1n}^{+}\sigma p(\mu,\mu_0)e^{-\frac{\varepsilon z}{\mu_0}}+I_{2n}^{-}\sigma p(-\mu,\mu_0)e^{-\frac{\varepsilon(z_0-z)}{\mu_0}}, \qquad (1)$$

where $I(z,\mu)$ is the azimuth-averaged intensity of scattered radiation propagating inwards along the z axis at an axial angle $\theta=\arccos\mu$ to the direction of incident light; σ and ε are the scattering and attenuation coefficients; $\mu_0=\cos\theta_0$; $p(\mu,\mu')$ is the azimuth-averaged phase function (redistribution

function); $p(\cos\gamma)$ is the phase function in a unit volume, normalised by the condition $\int_{-1}^{1} p(\cos\gamma)d\cos\gamma = 1$; $\cos\gamma = \mu\mu' + \sqrt{1-\mu^2}\sqrt{1-\mu'^2}\cos\varphi$, γ is the scattering angle; $\mu = \cos\theta$; $\mu' = \cos\theta'$; φ is the azimuthal scattering angle; I_{1n}^{+} and I_{2n}^{-} are the intensities of the directional radiation propagating into the layer, at the upper and lower boundaries respectively.

We solve the RTE with the following boundary conditions:

$$\begin{aligned} I(z=0,\mu>0) &= I(z=0,\mu<0), \\ I(z=z_0,\mu<0) &= I(z=z_0,\mu>0). \end{aligned} \tag{2}$$

3 Calculation of the unit volume parameters

We begin the simulation of the parameters of close-packed media with their calculation in the low-concentration limit. In order to calculate the parameters of a unit volume in this limit, we use the theory for spherical particles [3].

To calculate the attenuation coefficient and the phase function of a medium with a high particle concentration, we must solve the problem of diffraction of light from a many body system. A rigorous solution of this problem has not been found so far, and hence various approximation methods are used to calculate the attenuation coefficient and the phase function. For weakly scattering particles, the interference approximation is the most convenient. According to this approach, the expressions for differential scattering coefficient $\sigma_h(\gamma)$, scattering coefficient σ_h, and the attenuation coefficient ε_h for a medium consisting of identical spherical particles have the form

$$\sigma_h(\gamma) = w\sigma_{0l}p_l(\gamma)S_3(\gamma,w), \tag{3}$$

$$\sigma_h = w\sigma_{0l}u, \tag{4}$$

$$\varepsilon_h = w(\varepsilon_{0l} - \sigma_{0l} + \sigma_{0l}u), \tag{5}$$

where

$$u = \int_0^{\pi} p_l(\gamma)S_3(\gamma,w)\sin\gamma d\gamma, \tag{6}$$

$w = Nv/V$ is the volume concentration of the particles, N is the number of particles with volume v, contained in volume V of the medium; $\sigma_h(\gamma)$ is the differential scattering coefficient of a medium with a volume concentration w of particles; σ_h and ε_h are the scattering and attenuation coefficients of a medium with a volume concentration w of particles; $\sigma_{0l} = \Sigma_s/v$; $\varepsilon_{0l} = \alpha_{0l} + \sigma_{0l} = \Sigma_e/v$; $\alpha_0 = \Sigma_a/v$; Σ_a, Σ_s and Σ_e are the absorption, scattering and attenuation cross sections of an individual particle; and $p_l(\gamma)$ is the phase function of an individual particle normalised by the condition $\int_0^{\pi} p_l(\gamma)\sin\gamma d\gamma = 1$.

Parameter u characterises the degree of optical interaction of particles. For independent scattering, its value is equal to unity. The stronger the correlation of particles in space, the more the difference of the u-value from unity. The structural factor $S_3(\gamma,w)$ takes into account the effect of light interference processes occurring in a system of correlated scatterers. For a system of hard spheres, the structural factor is calculated in the Percus -Yevick approximation [1].

Figure 1 illustrates the variation of the phase function upon a change in the concentration of the particles. The intensity of forward-scattered radiation decreases with increasing w and for quite high concentrations, the indicatrix acquires a characteristic maximum for a nonzero scattering angle. Upon an

increase in the value of w, the maximum is displaced towards large angles, while an increase in the particle size displaces it towards small angles. Note that for certain values of the particle radius and concentration, the asymmetry parameter $g = \int_{-1}^{1} p(\mu)\mu d\mu$ can be equal to zero, or even attain negative values (Fig. 2).

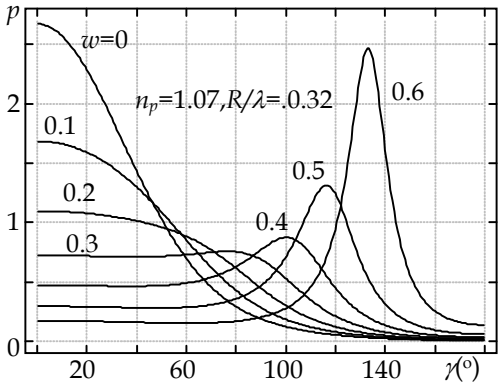

Figure 1: Dependence of the phase function of a unit volume on the concentration w.

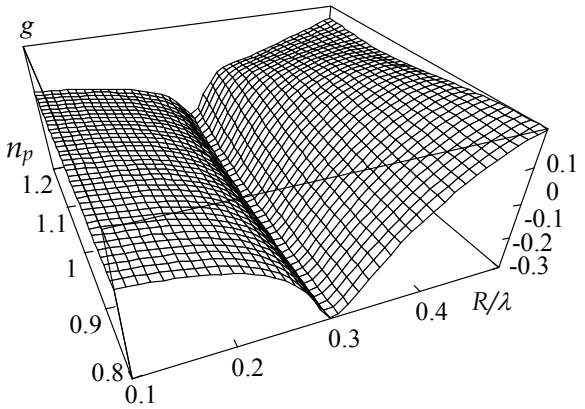

Figure 2: Dependence of the asymmetry parameter g on the refractive index n_p and radius R_p of the particles at w = 0.6

4 Angular structure of scattered light

In order to determine the luminance factors in the backward $\rho(\mu,\mu')$ and forward $\sigma(\mu,\mu')$ hemispheres, we used a calculation approach based on the layer doubling technique. In this method, the computations are started by choosing a layer of a quite small optical thickness τ_m so that $\tau_0 = \tau_m 2^K$, where K is an integer. For a layer with an optical thickness tm, the luminance factors are determined

approximately. The initial optical thickness was assumed to be equal to $\tau_m = 10^{-6}$, which ensured a fairly high precision of the results of calculations.

Angular dependences of the luminance factors $\sigma(\mu, \mu')$ are displayed in Fig. 3 for various angles of incidence. Upon an increase in the incidence angle (decrease in μ'), the characteristic peak in the angular dependence of scattered light becomes blurred. Two peaks can be formed. The separation between them increases with μ' decreasing. An analogous peak, but strictly in the backward direction, can be formed if the phase function of the unit volume has a peak at an angle of 90°.

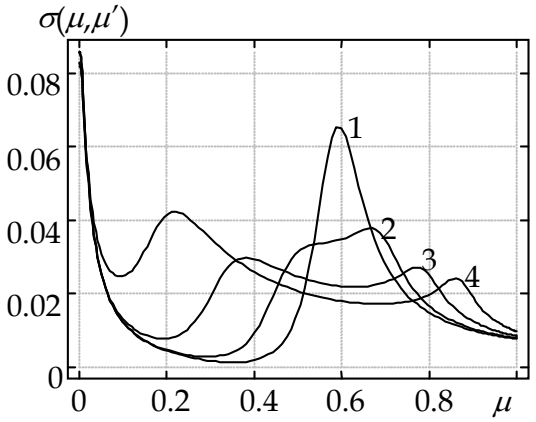

Figure 3: Angular dependences of the luminance factors $\sigma(\mu, \mu')$ of a layer formed by particles with $R_p = 0.3\mu m$, $n_p = 1.1$ ($\lambda = 0.5\mu m$) and $w = 0.5$, for $\mu' = 1$ (curve 1), 0.99 (curve 2), 0.96 (curve 3), and 0.91 (curve 4).

5 Conclusion

We developed a method to describe propagation of light in layers of a close-packed medium formed by optically soft particles. It is based on the interference approximation (to describe the collective scattering effects), and the radiative transfer theory (to describe the light field in the multiple scattering mode).

A numerical calculation method based on the layer-doubling technique and spline approximation of the phase function approximation is used for solving the radiative transfer equation in a high-concentrated layer.

The variation of the angular structure of scattered light is analysed for an azimuth-symmetric illumination of the layer in a wide range of optical thicknesses. We have determined the salient features of the angular structure of the intensity of light scattered in the forward and backward hemispheres in dispersed layers with the phase function having a typical interference peak at nonzero scattering angle.

References

[1] V. A. Loiko and V. V. Berdnik, “Features in the angular structure of light scattered by a layer of partially ordered soft particles,” *J. Quant. Spectrosc. Radiat. Transfer*, **88**, 111-123 (2004).

[2] H. C. Van de Hulst, *Multiple Light Scattering: Tables, Formulas and Applications* (New York, 1980).

[3] V. A. Babenko, L. G. Astafyeva, and V. N. Kuzmin, *Electromagnetic Scattering in Disperse Media* (Springer, Berlin, 2003).

Application of Riccati-Bessel Functions in Light Scattering

I K Ludlow

Science and Technology Research Institute, University of Hertfordshire, College Lane, Hatfield, AL10 9AB, UK
E-mail: i.k.ludlow@herts.ac.uk

Abstract

Riccati-Bessel functions, written as combinations of amplitude and phase functions, have been used to re-express Mie theory. This leads to a simple physical explanation of the scattered phase angle as the sum of a phase shift arising from the optical path difference across the particle radius and an interfacial phase difference at the surface of the particle. The mathematical properties of the different phase angles are examined in detail by treating the order as a continuous variable.

1 Introduction

It has been shown that Riccati-Bessel (R-B) functions and their derivatives with respect to the wave variable $z = kr$ can be usefully represented in terms of amplitude and phase functions [1,2]. Thus for spherical R-B functions:

$$\begin{aligned} \varphi_n(z) &= M_n(z)\sin\theta_n(z) & \varphi_n'(z) &= N_n(z)\cos\phi_n(z) \\ \chi_n(z) &= -M_n(z)\cos\theta_n(z) & \chi_n'(z) &= N_n(z)\sin\phi_n(z) \\ \xi_n(z) &= -i\,M_n(z)\exp i\theta_n(z) & \xi_n'(z) &= N_n(z)\exp i\phi_n(z) \end{aligned} \tag{1}$$

in which the spatial phase angles $\theta_n(z)$ and $\phi_n(z)$ have the forms:

$$\begin{aligned} \theta_n(z) &= z - n\,\pi/2 + \gamma_n(z) \\ \phi_n(z) &= \theta_n(z) + \Delta_n(z) \end{aligned} \tag{2}$$

and the amplitudes are related by

$$M_n(z)N_n(z)\cos\Delta_n(z) = 1. \tag{3}$$

Here, $\theta_n(z)$ is fully defined by

$$\theta_n(z) = \tan^{-1}\left[-\frac{\varphi_n(z)}{\chi_n(z)}\right] \tag{4}$$

together with the boundary condition $\theta_n(0) = 0$. Also, the auxiliary phase angle $\gamma_\nu(z)$ and the phase shift $\Delta_n(z)$ (associated with differentiation w.r.t. z) are constrained by $\underset{z=0}{n\,\pi/2} \geq \gamma_n(z) > \underset{z\to\infty}{0}$ and $\underset{z=0}{\pi/2} \geq \Delta_n(z) > \underset{z\to\infty}{0}$.

From Eqs. (1), (2) and (3), three ratio functions can be derived which will be applied later when analysing light scattering. These are

$$\begin{aligned} \frac{\varphi_n(z)}{\chi_n(z)} &= -\tan\theta_n(z) \\ \frac{\varphi_n'(z)}{\varphi_n(z)} &= \frac{1}{M_n^2(z)}\left[\frac{1}{\tan\theta_n(z)} - \tan\Delta_n(z)\right] \\ \frac{\chi_n'(z)}{\chi_n(z)} &= -\frac{1}{M_n^2(z)}\left[\tan\theta_n(z) + \tan\Delta_n(z)\right]. \end{aligned} \tag{5}$$

Note that the definitions given here for spherical R-B functions differ from those given in Handbook of Mathematical Functions [2,3].

2 Re-expression of Mie theory

To apply our treatment to light scattering, we consider the case of a homogeneous sphere of radius a and refractive index m. This has external and internal size parameters $\alpha = ka$ and $\beta = mka$ respectively for light with a propagation constant of k. Hence the Mie scattering coefficients, obtained from the boundary conditions of the electromagnetic fields at the surface of the sphere, are:

$$a_n = \frac{\varphi_n'(\beta)\varphi_n(\alpha) - m\varphi_n(\beta)\varphi_n'(\alpha)}{\varphi_n'(\beta)\xi_n(\alpha) - m\varphi_n(\beta)\xi_n'(\alpha)}$$
$$b_n = \frac{m\varphi_n'(\beta)\varphi_n(\alpha) - \varphi_n(\beta)\varphi_n'(\alpha)}{m\varphi_n'(\beta)\xi_n(\alpha) - \varphi_n(\beta)\xi_n'(\alpha)} \tag{6}$$

for $n = 1, 2, 3, \ldots$. Unfortunately, Eqs. (6) contain no meaningful physics but this can be partially remedied by introducing the scattered phase angles u_n, v_n through the relations: $a_n = \frac{1}{2}(1 - \exp i2u_n)$ and $b_n = \frac{1}{2}(1 - \exp i2v_n)$ to give:

$$\tan u_n = \frac{\varphi_n'(\beta)\varphi_n(\alpha) - m\varphi_n(\beta)\varphi_n'(\alpha)}{\varphi_n'(\beta)\chi_n(\alpha) - m\varphi_n(\beta)\chi_n'(\alpha)}$$
$$\tan v_n = \frac{m\varphi_n'(\beta)\varphi_n(\alpha) - \varphi_n(\beta)\varphi_n'(\alpha)}{m\varphi_n'(\beta)\chi_n(\alpha) - \varphi_n(\beta)\chi_n'(\alpha)}. \tag{7}$$

Moreover, contributions to the scattered phase can arise from only two possible sources which are:

(a) a phase shift $\theta_n(\beta) - \theta_n(\alpha)$ associated with the optical path difference of intrinsic waves across the particle radius, and

(b) an interfacial phase change u_n^i, v_n^i across the particle surface.

Thus, the total scattered phase angles are assumed to have the form

$$\begin{Bmatrix} u_n \\ v_n \end{Bmatrix} = \theta_n(\beta) - \theta_n(\alpha) + \begin{Bmatrix} u_n^i \\ v_n^i \end{Bmatrix}. \tag{8}$$

Eqs.(8) are verified by substituting for u_n and v_n in Eqs. (7) followed by the use of Eqs. (5) to eliminate $\theta_n(\alpha)$ from both sides of the equations so as to derive:

$$\tan\left[\theta_n(\beta) + u_n^i\right] = \frac{1}{\left[\frac{A_n^u}{\tan\theta_n(\beta)} + B_n^u\right]}$$
$$\tan\left[\theta_n(\beta) + v_n^i\right] = \frac{1}{\left[\frac{A_n^v}{\tan\theta_n(\beta)} + B_n^v\right]}, \tag{9}$$

where $A_n^u = \frac{M_n^2(\alpha)}{mM_n^2(\beta)}$, $B_n^u = \tan\Delta_n(\alpha) - A_n^u \tan\Delta_n(\beta)$ and $A_n^v = \frac{mM_n^2(\alpha)}{M_n^2(\beta)}$, $B_n^v = \tan\Delta_n(\alpha) - A_n^v \tan\Delta_n(\beta)$. Finally, u_n^i and v_n^i are completely separated as

$$\tan u_n^i = \frac{\left[1 - A_n^u - B_n^u \tan\theta_n(\beta)\right]\tan\theta_n(\beta)}{A_n^u + B_n^u \tan\theta_n(\beta) + \tan^2\theta_n(\beta)}$$
$$\tan v_n^i = \frac{\left[1 - A_n^v - B_n^v \tan\theta_n(\beta)\right]\tan\theta_n(\beta)}{A_n^v + B_n^v \tan\theta_n(\beta) + \tan^2\theta_n(\beta)}. \tag{10}$$

3 Results

Although the treatment above was for spherical R-B functions, it may now be generalized to all R-B functions having the form:

$$\tan u_\nu = \frac{c\,\varphi_\nu'(\beta)\varphi_\nu(\alpha) - \varphi_\nu(\beta)\varphi_\nu'(\alpha)}{c\,\varphi_\nu'(\beta)\chi_\nu(\alpha) - \varphi_\nu(\beta)\chi_\nu'(\alpha)} \tag{11}$$

in which c is a constant for all orders and $\nu = n + x$ for $0 \le x < 1$; $n = 0, 1, 2, \ldots$. Relations (8), (9) and (10) are still valid and so:

$$u_\nu = \theta_\nu(\beta) - \theta_\nu(\alpha) + u_\nu^i \tag{12}$$

$$\tan\left[\theta_\nu(\beta) + u_\nu^i\right] = \frac{1}{\left[\frac{A_\nu}{\tan\theta_\nu(\beta)} + B_\nu\right]} \tag{13}$$

$$\tan u_\nu^i = \frac{\left[1 - A_\nu - B_\nu \tan\theta_\nu(\beta)\right]\tan\theta_\nu(\beta)}{A_\nu + B_\nu \tan\theta_\nu(\beta) + \tan^2\theta_\nu(\beta)}, \tag{14}$$

where $A_\nu = c\dfrac{M_\nu^2(\alpha)}{M_\nu^2(\beta)}$, $B_\nu = \tan\Delta_\nu(\alpha) - A_\nu \tan\Delta_\nu(\beta)$.

Eqs. (7) have, however, been previously examined by van de Hulst [4] and this analysis too can be extended for general R-B functions so as to yield the following results.

(a) Nodes of the first kind

These occur when $\theta_\nu(\beta) = p\pi$ since then $\varphi_\nu(\beta) = 0$ and

$$\tan\begin{Bmatrix} u_\nu \\ v_\nu \end{Bmatrix} = \frac{\varphi_\nu(\alpha)}{\chi_\nu(\alpha)} = -\tan\theta_\nu(\alpha) \tag{15}$$

to give $u_\nu^i, v_\nu^i = 0$ and $u_\nu, v_\nu = \theta_\nu(\beta) - \theta_\nu(\alpha)$. It may also be shown that $v_{\nu-1}$ and $v_{\nu+1}$ have the same phase as v_ν, hence all four modes satisfy the conditions

$$v_{\nu-1}, v_\nu, v_{\nu+1}, u_\nu = \theta_\nu(\beta) - \theta_\nu(\alpha) \tag{16}$$

and

$$v_{\nu-1}^i, v_\nu^i, v_{\nu+1}^i, u_\nu^i = 0. \tag{17}$$

(b) Nodes of the second kind

These are present when $\phi_\nu(\beta) = (p + 1/2)\pi$ corresponding to $\varphi_\nu'(\beta) = 0$ and

$$\tan\begin{Bmatrix} u_\nu \\ v_\nu \end{Bmatrix} = \frac{\varphi_\nu'(\alpha)}{\chi_\nu'(\alpha)} = \frac{1}{\tan\phi_\nu(\alpha)}. \tag{18}$$

Thus,

$$v_\nu, u_\nu = \phi_\nu(\beta) - \phi_\nu(\alpha) = \theta_\nu(\beta) - \theta_\nu(\alpha) + \Delta_\nu(\beta) - \Delta_\nu(\alpha) \tag{19}$$

and

$$u_\nu^i, v_\nu^i = \Delta_\nu(\beta) - \Delta_\nu(\alpha). \tag{20}$$

Such generalized expressions are valuable when investigating scattering since, by treating the order as a continuous variable, quasi-continuous graphs can be plotted of the various phase angles rather than the sparse sets of discrete points associated with spherical results alone. It should however be remembered that in the notation of general R-B functions, spherical R-B functions correspond to the orders $\nu = n + 1/2$.

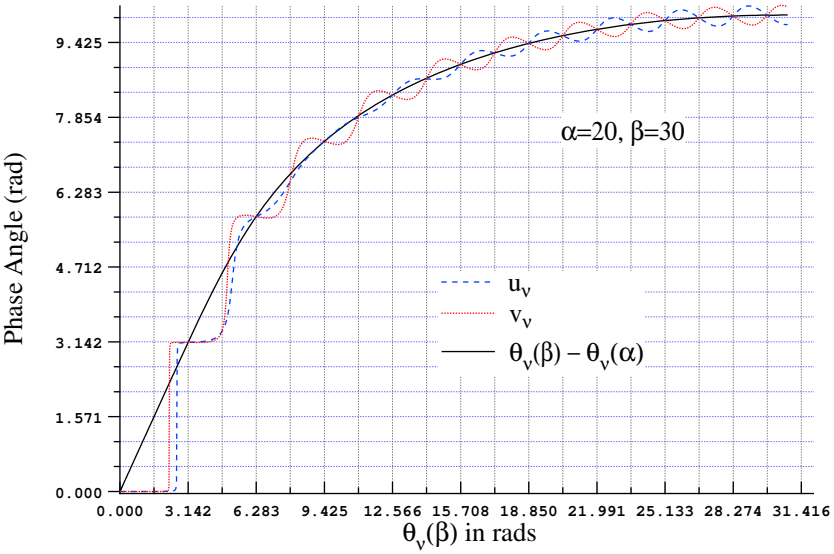

Figure 1: Display of van de Hulst's nodes of the first kind at $\theta_\nu(\beta) = p\pi$ and the second kind at $\theta_\nu(\beta) = (p + 1/2)\pi$.

Plots of the various contributions to the scattered phase angles are presented in figures 1-3 for a hypothetical R-B particle having external and internal size parameters of 20 and 30 respectively. In figure 1, nodes of the first kind are indicated by the crossing of all three traces at $\theta_\nu(\beta) = p\pi$ while for nodes of the second kind only the u_ν and v_ν curves cross at $\theta_\nu(\beta) = (p + 1/2)\pi$. The nodes are similarly recognized in figure 2 where they are displayed as a function of order and the positions of the $v_{\nu-1}$ and $v_{\nu+1}$ modes obtained. Finally figure 3 presents the interfacial phase difference as a function of order. Other features of interest are:

(a) modes make a maximum contribution to scattering whenever $u_\nu, v_\nu = (p + 1/2)\pi$ and the "half-power points" are obtained from $u_\nu, v_\nu = (p + 1/4)\pi$ and $(p + 3/4)\pi$, (b) the two step edges of height π between

orders 25 and 26 are characteristic of resonance scattering and (c) an effective cut-off order exists for the model sphere at $v:\ 26$.

4 Discussion

General R-B functions have been shown to play a crucial role in understanding the physical principals underlying light scattering from a homogeneous sphere. As a consequence, the scattered phase angles u_v, v_v of a hypothetical R-B particle can be fully explained in terms of the optical phase associated with the optical path difference $\theta_v(\beta)-\theta_v(\alpha)$ of intrinsic waves across the particle radius and an interfacial phase difference u_v^i, v_v^i at the surface of the sphere. The latter functions can be calculated directly from Eqs. (10).

Furthermore, the present analysis provides a physical rationale for the sequence of steps in the form of a descending staircase reported in Ref. [1] for anomalous diffraction at a large sphere. Other applications are light scattering from:
(i) multi-layered spheres and (after some modification)
(ii) infinite homogeneous circular cylinders, but also
(iii) acoustic scattering at a homogeneous elastic sphere and
(iv) nuclear scattering at a spherical square well.

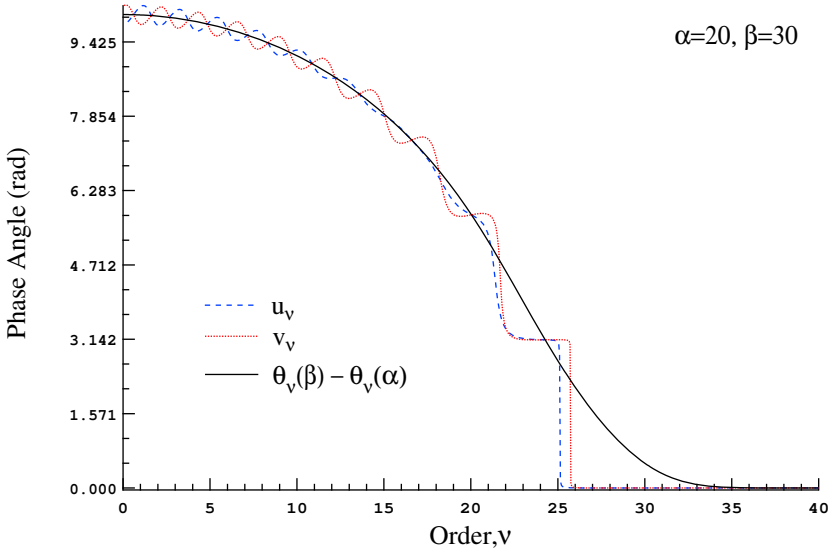

Figure 2. Comparison of the scattered phase angles u_v, v_v with $\theta_v(\beta)-\theta_v(\alpha)$.

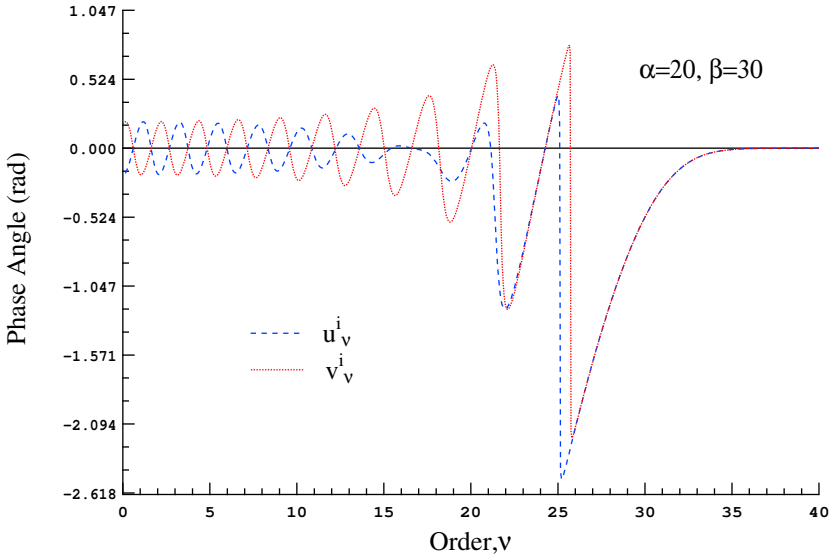

Figure 3. Interfacial phase difference at the surface of the sphere.

References:

[1] I. K . Ludlow and J. Everitt, “Systematic behavior of the Mie scattering coeficients of spheres as a function of order,” Phys. Rev. E **53** 2909-2924 (1995).
[2] I. K. Ludlow, “Intrinsic cylindrical and spherical waves,” J. Phys. A. Math. Theor. **41** 065401-22 (2008).
[3] M. Abramowitz and I. A. Stegun, *Handbook of Mathematical Functions* (Dover, New York, 1972).
[4] H. C. van de Hulst, *Light Scattering by Small Particles* (Dover, New York, 1957).

A generalization of image theory to predict the interaction of multipole fields with plane surfaces

Daniel W. Mackowski
Department of Mechanical Engineering
Auburn University, AL 36849, USA
tel: +1 (334) 844-3334, e-mail: mackodw@auburn.edu

Abstract

A derivation and computational scheme, based on exact image theory, for the field produced by the interaction of an outgoing vector wave harmonic with an infinite–extent plane surface is presented. The method represents the angular–dependent Fresnel reflection coefficients of the surface as Laplace transforms of a spatially–dependent function, which results in the reflected field appearing as a superposition of image sources located at complex points along the normal axis within the surface medium.

1. Introduction

Different scientific communities often come up with different methodologies to describe a particular physical phenomenon. A case in point is the problem of describing an outgoing wave, emanating from a source, that has reflected from a plane, infinite–extent surface. The light scattering community is interested in this problem in the context of predicting the scattering and absorption properties of particles that are on or near a surface. Examples of applications in this area include surface contaminant detection, the effects of soot on the albedo of snow, and prediction of pigment layer reflectivity. On the other hand, the radio and antenna community has long been engaged in the design of antennas for broadcast of microwave and radio radiation, and a key part of this process is the prediction of the reflection of the radiation from the earth's surface.

For both groups, the derivation for the scattered–reflected field begins at the same starting point, that being the integral relation of Sommerfeld for the field produced by a radiating dipole in the half–space above a plane, reflecting surface [1]. This formula was extended by Bobbert and Vlieger [2], and later by Fucile et al. [3] and Wriedt and Doicu [4], to predict the field produced by reflection of vector wave harmonics (VWH), of arbitrary order/degree/mode, that radiate outward from a source point above the surface. Since the scattered–reflected field does not emanate from a source above the surface (i.e., the mathematical description of the field has no singularities in the half–space), the field can be represented by an expansion of regular (or plane–wave) VWH that are centered about some point in the half–space. This derivation, which was the objective of [2–4] and which will be reviewed in the following section, provides an exact description of the field coupling between a particle and a surface. However, the regular VWH description will have a finite radius of convergence; it will not, in general, be able to predict the scattered–reflected field at all points in the half space. The formulation is also quite difficult to implement numerically as it can involve numerical integration of highly oscillating functions over a complex path – which is an aspect of the Sommerfeld integral from which the multipole formulations began.

The numerical challenges posed by the Sommerfeld integral motivated other groups – mostly in the radio and antenna field – to develop the image theory formulation to the dipole half–space problem. This exact approach makes use of the Laplace transform to represent the reflected field, in the half–space above the surface, as that produced by a superposition of image sources located below the surface [5, 6]. This method eliminates many of the stiff numerical integration problems associated with the Sommerfeld integral, and thus can provide an efficient algorithm for calculating the reflected field at any point above the surface.

By use of the addition theorem for vector harmonics, it should be possible to represent the image fields, predicted by image theory, as regular VWH expansions about some point above the surface. By doing so, the

image theory would provide a route to the particle–surface interaction problem. Such an application was performed by Lindell et al. [7] and Muinonen et al. [8] for the case of a particle in the dipole limit.

To this author's knowledge, an extension of the image theory to multipole fields has not been performed. This extension is the objective of the paper – with emphasis given to the spherical particle–surface coupling problem for spheres of arbitrary size/wavelength ratio. The image theory will be shown to provide a significantly more efficient – and more reliable – method of computing the exact scattering and absorption properties of a sphere/plane surface system. In addition, image theory appears to offer improved physical insight into the mechanisms by which the surface affects the scattering behavior of the sphere.

2. Formulation

The detailed mathematical formulation of the multipole image theory cannot be presented in four pages; a much–condensed version will be delivered here and the reader is requested to contact the author for the detailed formulas. The geometry of the problem consists of a surface in the $x-y$ plane at $z=0$, and the positive z axis points towards free space. The surface medium is characterized by a refractive index of $\mathrm{m}=n_m+\mathrm{i}k_m$. A time–harmonic field (of factor $\exp(-\mathrm{i}\omega t)$) is generated from a source centered at position $\mathbf{r}_S=\hat{x}\,x_S+\hat{y}\,y_S+\hat{z}\,z_S$, with $z_S>0$. This source, for example, could represent the scattered field from a particle that is centered at $\mathbf{r}_S$. In the most general sense, this field is described at all points in the $z>0$ half space, except $\mathbf{r}=\mathbf{r}_S$, as an expansion of outgoing vector wave harmonic (VWH) functions, i.e.,

$$\mathbf{E}_S=\sum_{\nu} a_\nu\,\mathbf{N}_\nu^{(3)}(\mathbf{r}-\mathbf{r}_S) \tag{1}$$

with ν being shorthand for degree, order, and mode, i.e., $\nu=(mnp)$ with $p=1,2$ denoting TM and TE modes. The source field will interact with the surface, and a portion of the energy of the source will be reflected back into the free space. Via the principle of superposition, the total field in the $z>0$ half space can be split into the source field and the reflected field.

The issue at hand is how to represent the reflected field, in a way that exactly satisfies the continuity conditions at the plane surface. This will require that the outgoing VWH be represented in a functional form that corresponds to the cartesian frame of the surface, and this can be performed via the multipole generalization of the Sommerfeld integral [2–4]. For all points $\mathbf{r}-\mathbf{r}_S$ such that $z-z_S<0$, an outgoing VWH can be represented by

$$\mathbf{N}_\nu^{(3)}(\mathbf{r}-\mathbf{r}_S)=\frac{1}{2\pi}\int_{\Omega^-}\mathbf{\Pi}_\nu(\Omega)\,\exp\left[\mathrm{i}\,\mathrm{k}(\omega)\cdot(\mathbf{r}-\mathbf{r}_S)\right]\,d\Omega \tag{2}$$

in which $d\Omega=\sin\beta\,d\beta\,d\alpha$, the integration domain Ω^- is $(\alpha,\beta)=((0,2\pi),(\pi/2+\mathrm{i}\infty,\pi))$, $\mathbf{\Pi}_\nu$ is the transverse vector harmonic,

$$\mathbf{\Pi}_{mn2}=(-\mathrm{i})^n\,\left(n(n+1)\right)^{-1/2}\,\mathbf{r}\times\nabla\,Y_{mn},\quad \mathbf{\Pi}_{mn1}=-\mathrm{i}\,\mathbf{\Pi}_{mn2}\times\hat{\mathbf{r}} \tag{3}$$

with Y_{mn} being the normalized spherical harmonic, and

$$\mathbf{k}\cdot(\mathbf{r}-\mathbf{r}_S)=\mathrm{k}\Big[((x-x_S)\cos\alpha+(y-y_S)\sin\alpha)\,\sin\beta+(z-z_S)\cos\beta\Big] \tag{4}$$

Equation (2) can be viewed as a representation of the outgoing VWH by a plane–wave spectrum, in which the spectrum of propagation directions β covers both real and imaginary (i.e., evanescent) angles. Along the surface at $z=0$, each plane–wave component – both real and imaginary – will be reflected according to the Fresnel relations. Accordingly, the reflected field produced by the outgoing VWH will be

$$\mathbf{N}_\nu^{(3)}(\mathbf{r}-\mathbf{r}_S)\Big|_r=\frac{C_\nu}{2\pi}\int_{\Omega^+}\mathcal{R}\cdot\mathbf{\Pi}_\nu\,\exp\left[\mathrm{i}\,\mathrm{k}\cdot(\mathbf{r}-\mathbf{r}_R)\right]\,d\Omega \tag{5}$$

in which Ω^+ now has $\beta : 0 \rightarrow \pi/2 - \mathrm{i}\infty$, $C_\nu = (-1)^{m+n+p}$, $\mathbf{r}_R = (x_S, y_S, -z_S)$ denotes the location of the image point for the source and $\mathcal{R}$ is a 2×2 diagonal matrix having the parallel and perpendicular Fresnel reflection coefficients as diagonal elements. Note that $\mathcal{R}$ will be a function of β.

The integral in Eq. (5) will converge for all points $z > -z_S$; this formally covers the entire half space above the surface. However, Eq. (5) is not an especially workable representation for the reflected field. The approach adopted in Refs. [3, 4, 9] involves representing the phase factor as an expansion of regular VWHs centered about some secondary origin $\mathbf{r}_j$ in the half space (this could be the source origin). This results in a regular VWH description of the reflected field, via

$$\mathbf{N}_\nu^{(3)}(\mathbf{r} - \mathbf{r}_S)\Big|_r = \sum_\mu R_{\mu\,\nu}^{j-S}\, \mathbf{N}_\mu^{(1)}(\mathbf{r} - \mathbf{r}_j) \tag{6}$$

with

$$R_{\mu\,\nu}^{j-S} = \frac{C_\nu}{8\pi} \int_{\Omega^+} (\mathcal{R} \cdot \mathbf{\Pi}_\nu) \cdot \mathbf{\Pi}_\mu^*\, \exp\left[\mathrm{i}\,\mathrm{k} \cdot (\mathbf{r}_j - \mathbf{r}_R)\right]\, d\Omega \tag{7}$$

The expansion in Eq. (6) is still constrained by the convergence conditions of Eq. (5). Specifically, Eq. (6) will converge only for $|\mathbf{r} - \mathbf{r}_j| < z_j + z_S$. This constraint is not an issue if the objective is to represent, via a VWH basis, the reflected field on the surface of a sphere, centered on $\mathbf{r}_j$, which is external to the plane surface. Such a representation is needed to close the sphere–plane surface scattering problem. However, Eq. (6) cannot be used to describe the reflected field in the far–field zone. An additional issue is that the integrations in Eq. (7) – which must be performed numerically – can be difficult due to the highly oscillatory nature of the integrand.

An alternative approach to the representation of the reflected field – which circumvents the problems discussed above – involves the use of image theory. Equation (5) shows that the reflected field can be represented by an integral transformation of a vector product of the Fresnel coefficients and the transverse vector harmonic function, with the kernel of the transform being the phase factor $\exp(i\,\mathbf{k} \cdot \mathbf{r})$. In this sense, Eq. (5) can be viewed as transforming between the directional coordinates $\Omega = (\beta,\ \alpha)$ and the spacial coordinates $\mathrm{k}\,\mathbf{r}$. The objective of image theory is to represent the Fresnel coefficients as as inverse transformation, involving the same kernel of Eq. (5), of a spatially–dependent function. By substituting this relation back into Eq. (5), switching the order of directional and spatial integration, and employing Eq. (2), one should arrive at a formula which gives the scattered–reflected field as a superposition of VWH sources that lie on the spacial domain representing the inverse–transformed Fresnel coefficients.

Equation (5) actually offers two distinct choices for the integral transformation employed in the analysis. The first method, which is adopted here, employs a Laplace transformation of the reflection coefficients and results in a superposition of image sources at complex–valued points along the negative z axis. This route, which is based on that taken in the previous dipole–based formulations [5, 6], will yield a distributed–source, outgoing VWH representation of the scattered–reflected field that is exact at all points above the surface. A second transform method – which is only mentioned in passing – would employ a Fourier transform of the reflection coefficients and would lead to a distribution of image sources in the $x-y$ plane at $z = z_R$. Such a description would not appear to have the same utility as the Laplace transform method, since it would involve a surface integration of sources as opposed to a line integration. As opposed to the Laplace transform source points, however, the Fourier transform image points would be real–valued, which would allow subsequent image translation operations using the VWH addition theorem. In addition, the Fourier transform method would be better suited for azimuthally–dependent reflection coefficients.

Although the basic concepts of the image theory are straightforward, a relatively complicated effort is required to derive the formulation for the multipole VWH case. The key steps in the derivation are 1) expanding Eq. (5) so that the integral appears as products of the individual Fresnel coefficients and inverse–transformed VWH functions, and 2) performing the Laplace transforms on the Fresnel coefficients. In performing the first step,

one encounters a new class of VWH functions, which are defined by

$$\mathbf{P}^{(3)}_{mn2}(\mathrm{k}\mathbf{r}) = \frac{m}{(n(n+1))^{1/2}} \nabla \times (\hat{\mathbf{z}}\, h_n(\mathrm{k}\, r)\, Y_{mn}(\cos\theta, \phi))\,, \qquad \mathbf{P}^{(3)}_{mn1}(\mathrm{k}\mathbf{r}) = \frac{1}{\mathrm{k}} \nabla \times \mathbf{P}^{(3)}_{mn2}(\mathrm{k}\mathbf{r}) \tag{8}$$

Note that these definitions are similar to the standard VWHs, except that $\hat{\mathbf{z}}$ as opposed to $\mathbf{r}$ is used as the pilot vector. The $\mathbf{P}_{mn2}$ function is an interesting quantity in that it has, at all points, an identically zero $\hat{\mathbf{z}}$ component.

By judicious use of the residue theorem, analytical formulas for the Laplace transform pairs for the Fresnel reflection coefficients can be derived. These formulas allow for a relatively simple representation of the reflected field as a distribution of outgoing VWH sources that lie at complex–valued points along the negative z axis (i.e., within the surface medium). This representation, which is valid in the entire half space, avoids the stiff integration problems associated with direct evaluation of Eq. (5). Furthermore, by application of the VWH translation theorem to the image points, a regular VWH expansion of the form in Eq. (6), and associated reflection matrix, can be derived – again avoiding the integration problems in Eq. (7).

An interesting corollary of the image theory, as applied to the multipole VWH case, is that it is impossible to construct a valid representation of the reflected field based on an outgoing VWH expansion centered about a single point – with the sole exception of a perfectly reflecting surface.

References

1. A. Sommerfeld, "ber die ausbreitung der wellen in der drahtlosen telegraphie," Ann. Physik **28**, 665736 (1909).
2. P. A. Bobbert and J. Vlieger, "Light scattering by a sphere on a substrate," Physica **137A**, 209–242 (1986).
3. E. Fucile, P. Denti, F. Borghese, R. Saija, and O. I. Sindoni, "Optical properties of a sphere in the vicinity of a plane surface," J. Opt. Soc. Amer. A **14**, 1505–1514 (1997).
4. T. Wriedt and A. Doicu, "Light scattering from a particle on or near a surface," Opt. Comm. **152**, 376–384 (1998).
5. I. V. Lindell and E. Alanen, "Exact image theory for the sommerfeld half-space problem, part iii: General formulation," IEEE Trans. Antennas Propagat. **AP-32**, 1027–1032 (1984).
6. K. Sarabandi, M. D. Casciato, and I.-S. Koh, "Efficient calculation of the fields of a dipole radiating above an impedance surface," IEEE Trans. Antennas Propagat. **50**, 1222–1235 (2002).
7. I. V. Lindell, A. H. Sihvola, K. O. Muinonen, and P. W. Barber, "Scattering by a small object close to an interface. i. exact-image theory formulation," J. Opt. Soc. Amer. A **8**, 472–476 (1991).
8. K. O. Muinonen, A. H. Sihvola, I. V. Lindell, and K. A. Lumme, "Scattering by a small object close to an interface. ii. study of backscattering," J. Opt. Soc. Amer. A **8**, 477–482 (1991).
9. D. W. Mackowski, "Exact solution for the scattering and absorption properties of sphere clusters on a plane surface," J. Quant. Spectroscopy Radiat. Trans. **109**, 770–788 (2007).

Gustav Mie and the evolving discipline of electromagnetic scattering by particles

Michael I. Mishchenko

NASA Goddard Institute for Space Studies, 2880 Broadway, New York, NY 10025, U.S.A,
e-mail: mmishchenko@giss.nasa.gov

Abstract

The year 2008 marks the centenary of the seminal paper by Gustav Mie on electromagnetic scattering by homogeneous spherical particles. Having been cited in almost 4,000 journal articles since 1955, Mie's paper has been among the more influential scientific publications of the twentieth century. It has affected profoundly the development of a great variety of natural science disciplines including atmospheric radiation, meteorological optics, remote sensing, astrophysics, and biomedical optics. Mie's paper represented a fundamental advancement over the earlier publications by Ludvig Lorenz in that it was explicitly based on the Maxwell equations, gave the final solution in a convenient form suitable for practical computations, and imparted physical reality to the abstract concept of electromagnetic scattering. The Mie solution anticipated such general concepts as far-field scattering and the Sommerfeld–Silver–Müller boundary conditions at infinity as well as paved the way to such important extensions as the separation of variables method for spheroids and the *T*-matrix method. Key ingredients of the Mie theory are quite prominent in the superposition *T*-matrix method for clusters of particles and even in the recent microphysical derivation of the radiative transfer equation. Among the most illustrative uses of the Mie solution have been the explanation of the spectacular optical displays caused by cloud and rain droplets, the identification of sulfuric acid particles in the atmosphere of Venus from Earth-based polarimetry, and optical particle characterization based on measurements of morphology-dependent resonances. Yet it is clear that the full practical potential of the Mie theory is still to be revealed.

Mie's paper under the title "Beiträge zur Optik trüber Medien, speziell kolloidaler Metallösungen" (Contributions to the optics of turbid media, particularly colloidal metal solutions) appeared in 1908 as part of the third issue of the 25th volume of the renowned German physics journal *Annalen der Physik* [1]. At that time Gustav Mie considered it to be a rather trivial application of Maxwell's electromagnetics aimed at a theoretical explanation of the beautiful coloration of metals in a colloidal state. He simply did not anticipate the eventual phenomenal success of this paper and universal acceptance of his exercise in mathematical physics as "the Mie theory." Mie's 1908 paper has been cited in almost 4,000 journal articles since 1955, and the citation rate appears to increase rather than decrease with time. This magnitude of success is highly unusual for a seemingly dry, abstract, and specialized article on physics and definitely places Mie's paper in the category of one of the more influential scientific publications of the twentieth century. In particular, one cannot even imagine the modern-day functioning of such disciplines as atmospheric radiation and remote sensing without the Mie theory. It thus appears highly appropriate to celebrate the centenary of the seminal Mie paper by analyzing its virtues and importance and by placing it in a broader evolving context of electromagnetic scattering by particles.

The fundamental nature of Maxwell's electromagnetics is now universally recognized. In a recent poll of scientists the Maxwell equations have been voted to be the greatest equations ever [2]. However, the situation in the late 19th and early 20th century was somewhat different. While one of the great "continental" physicists Ludwig Boltzmann had immediately recognized the universal importance of the Maxwell equations and was even quoted: "Was it god who wrote these lines…", the stance of many other continental and even British physicists had not been so unequivocal.

One of the decisive virtues of the Mie paper happened to be its explicit reliance on Maxwell's electromagnetics. As such, this paper would eventually be recognized as one of the great triumphs of the

Maxwell theory. It is now widely acknowledged that the brilliant Danish physicist Ludvig Valentin Lorenz (1829–1891) developed a theory of light scattering by spherical particles which is mathematically very similar to the Mie theory. Yet he based his memoir on his own theory of light, which was at variance with the Maxwell theory. This made the physical interpretations of the scattering theories of Mie and Lorenz radically different and has ultimately led to the (largely unjust) neglect of Lorenz's contribution.

In modern physical terms, the Mie theory belongs in the realm of so-called frequency-domain macroscopic electromagnetics. This means, in particular, that all sources and fields are assumed to vary in time harmonically (i.e., are proportional to the common factor $\exp(i\omega t)$, where $i = (-1)^{1/2}$, ω is the angular frequency, and t is time). The fundamental concept of electromagnetic scattering used by Mie can be summarized as follows. A plane electromagnetic wave propagates in an infinite nonabsorbing medium without a change in its intensity or polarization state. However, the presence of a particle modifies the electromagnetic field that would otherwise exist in the unbounded homogeneous space. It is this modification that is called *electromagnetic scattering*. The difference between the total field in the presence of the particle and the original field that would exist in the absence of the particle can be thought of as the field scattered by the particle. In other words, the total field in the presence of the particle is represented as the vector sum of the respective incident (original) and scattered fields: $\mathbf{E}(\mathbf{r})=\mathbf{E}^{inc}(\mathbf{r})+\mathbf{E}^{sca}(\mathbf{r})$, where $\mathbf{r}$ is the position vector, and the common factor $\exp(i\omega t)$ is omitted. It should be recognized that the division of the total field into the incident and scattered parts is a purely mathematical procedure. This means that classical frequency-domain electromagnetic scattering is not a physical process *per se* but rather an abbreviated way to state that the total field computed in the presence of a particle is different from that computed in the absence of the particle. In other words, frequency-domain electromagnetic scattering is a physical phenomenon, but not a physical process.

This concept of electromagnetic scattering by a particle remains as valid now as it was 100 years ago. Yet it is truly remarkable how many confusing and even plainly wrong definitions of scattering have appeared in the literature since the publication of Mie's paper. Despite the purely classical character of scattering of *waves* in the framework of macroscopic frequency-domain Maxwell's electromagnetics, one may frequently encounter the assertion that upon *collision* with an atmospheric particle, the incident *photon* can be either absorbed or scattered. Scattering is then defined as a random choice of new direction of propagation for the photon *according to the Mie theory*. The neo-Newtonian visualization of scattering as a "collision" of a light corpuscle with a cloud droplet followed by the corpuscle changing the direction of flight appears to be intuitively appealing and is rather common. However, this artificial association of photons and the Mie theory invariably falls apart upon a closer look at what is actually meant by a "photon" without an explicit quantization of the electromagnetic field in the presence of a material body (such as the cloud droplet) consisting of an enormous number of elementary particles.

The discipline of radiative transfer has been subject to even more confusion in the frequent reliance on an intuitive perception of *successive* scattering *events* caused by a sequence of particles. For example, van de Hulst [3] defines the subject of the radiative transfer theory as "the play of radiation by *repeated* scattering in a cloud layer or any other slab of particles." Thomas and Stamnes [4] discuss probabilistic aspects of radiative transfer in terms of a "photon" executing a multiple-scattering trajectory, depending upon the random nature of the angular scattering process. As such, multiple scattering by particles is presented as a process unfolding in time.

In truth, however, the classical concept of frequency-domain electromagnetic scattering is as applicable to a group of particles as to a single particle. This means that *multiple scattering* by a particle group is not a physical process per se but rather a purely mathematical expansion of the total electromagnetic field into a Neuman series [5]. It is remarkable that the Neuman series alone (i.e., without attributing to it any specific physical meaning) is sufficient for the derivation of the radiative transfer equation (RTE) directly from the frequency-domain Maxwell equations [5]. In other words, although the RTE has the formal mathematical structure of a kinetic equation describing collisional particle diffusion, it follows directly from the electromagnetic *wave* theory and the classical definition of electromagnetic scattering.

The Mie solution was intentionally constructed in such a way that the scattered field transforms into an outgoing spherical wave in the so-called far-field zone (i.e., as the product kr tends to infinity, where r is the distance from the center of the sphere and k is the wave number in the host medium). Although this was done largely on "physical grounds," the behavior of the scattered field at infinity later turned out to be at the very heart of the problem of uniqueness of solution of the Maxwell equations in an unbounded space. In fact, in constructing his solution Mie anticipated what is now called the Sommerfeld–Silver–Müller radiation condition at infinity applicable to electromagnetic scattering by an arbitrary finite object imbedded in a nonabsorbing unbounded homogeneous medium. This condition requires the transverse components of the electric and magnetic fields to decrease at infinity as $1/r$ and the longitudinal components to decrease faster than $1/r$. Then it can be proven mathematically that the Maxwell equations have a unique (and hence physically relevant) solution. This fundamental aspect of electromagnetic scattering is discussed thoroughly in [6].

Another important ingredient of the Mie solution differentiating it from the Lorenz theory was the explicit assumption of a potentially absorbing host medium. Interestingly enough, discussions of practical implications of the Mie theory have often been intentionally simplified by using the assumption of a nonabsorbing host medium and hence a real-valued k. However, many natural and artificial bulk media are absorbing (e.g., water and water ice at infrared wavelengths). As a consequence, the issue of a complex-valued k has caused a lasting controversy about how to define in the most appropriate way the corresponding optical cross sections and scattering and extinction matrices for particles imbedded in an absorbing host. It appears that the best way to address this problem is to adhere to actual optical observables rather than attempt the generalization of quantities that cannot be measured directly. Recent studies show that this approach also yields the correct generalized form of the radiative transfer equation [7].

The Mie theory belongs to the class of separation-of-variables solutions in that it explicitly exploits the separability of the vector Helmholtz equation for the time-harmonic electric field in polar spherical coordinates. A seminal theoretical development was the reformulation of the Mie theory by Stratton [8] in terms of special so-called vector spherical wave functions (VSWFs) possessing very convenient analytical properties. In the framework of Stratton's formulation, the electromagnetic scattering problem is solved by expanding the incident, internal, and scattered fields in appropriate sets of VSWFs. The expansion coefficients of the incident plane wave are computed analytically, while the unknown expansion coefficients of the internal and scattered fields are then determined through the requirement of the standard boundary conditions on the sphere surface as well as the radiation condition at infinity. Because the VSWFs are orthogonal on the sphere surface, the resulting formulas have the utmost simplicity.

The separation-of-variables approach affords a rather straightforward extension to concentric core-mantle spheres, concentric multilayered spheres, radially inhomogeneous spheres, and even optically active (chiral) spheres. Furthermore, one can solve the scattering problem for a homogeneous or layered spheroid in spheroidal coordinates, although in this case the expansion of the scattered field is a double series, and the solution turns out to be rather complicated analytically and time-consuming when implemented on a computer.

Stratton's reformulation paved the way to several direct generalizations of the Mie theory, all of which were proposed in the late 1960s – early 1970s and contain the original Mie theory as a particular case. Conceptually the simplest of them is the point-matching method (PMM), in which the expansion coefficients of the internal and scattered fields are determined through the requirement of the boundary conditions on the surface of a nonspherical scatterer. In principle, this technique is applicable to an arbitrarily shaped and sized particle. However, convergence problems have imposed a rather severe practical limit on the possible range of particle shapes in the simple original form of the PMM. These problems may have been ameliorated, at least partially, with more advanced and complex versions of the PMM.

The so-called extended boundary condition method (EBCM) is also quite general in principle, although it has been mostly applied to axially symmetric particles. Nevertheless, it has a wide practical range of particle sizes and aspect ratios and has been one of the most frequently used numerically-exact techniques based on a direct solution of the Maxwell equations.

The multi-sphere or superposition *T*-matrix method is explicitly based on the so-called translation-addition theorem for VSWFs and was developed to treat electromagnetic scattering by clusters of spheres. Like EBCM, it has been used in a wide range of practical applications. Similar mathematical properties of vector spheroidal wave functions permitted the development of a technique analogous to the superposition *T*-matrix method but intended to treat electromagnetic scattering by a cluster of spheroids in spheroidal coordinates. Specific information about all the above techniques and further references can be found in the collective monograph [9] as well as in the review [10].

The Mie theory is explicitly based on the assumption that the incident field is a plane electromagnetic wave. However, some types of illumination (e.g., a focused and/or very narrow laser beam) may substantially violate this assumption. Still the Mie solution can be applied provided that the incident field is mathematically expandable in plane waves. A thorough review of this generalization of the Mie theory was given in [11].

Besides Statton's book of 1941, far the greatest impact in the dissemination and popularization of the Mie theory has had the monograph by van de Hulst [12], which in itself is one of the classical scientific treatises of the twentieth century. The great efficiency of modern desktop workstations and PCs coupled with the development of efficient algorithms for the computation of special functions entering the Mie solution has made numerical Mie codes an everyday tool for a large and rapidly expanding body of scientists and engineers. Furthermore, the Mie theory is now firmly established as a fundamental aspect of graduate and even undergraduate courses on atmospheric radiation and remote sensing. The remarkable reach of the Mie solution is well illustrated by its recent implementation on a mobile phone [13].

References

[1] G. Mie, "Beiträge zur Optik trüber Medien, speziell kolloidaler Metallösungen," *Ann. Physik*, **25**, 377–445 (1908).

[2] R. P. Crease, "The greatest equations ever," *Phys. World*, **17**(10), 14–15 (2004).

[3] H. C. van de Hulst, *Multiple Light Scattering* (Academic Press, New York, 1980).

[4] G. E. Thomas and K. Stamnes, *Radiative Transfer in the Atmosphere and Ocean* (Cambridge University Press, Cambridge, 1999).

[5] M. I. Mishchenko, "Multiple scattering, radiative transfer, and weak localization in discrete random media: unified microphysical approach," *Rev. Geophys*., **46**, RG2003 (2008).

[6] C. Müller, *Foundations of the Mathematical Theory of Electromagnetic Waves* (Springer-Verlag, Berlin, 1969).

[7] M. I. Mishchenko, "Multiple scattering by particles embedded in an absorbing medium. 1. Foldy–Lax equations, order-of-scattering expansion, and coherent field," Opt. Express, **16**, 2288–2301 (2008).

[8] J. A. Stratton, *Electromagnetic Theory* (McGraw-Hill, New York, 1941).

[9] M. I. Mishchenko, J. W. Hovenier, and L. D. Travis, Eds., *Light Scattering by Nonspherical Particles* (Academic Press, San Diego, 2000).

[10] M. Kahnert, "Numerical methods in electromagnetic scattering theory," *J. Quant. Spectrosc. Radiat. Transfer*, **79–80**, 775–824 (2003).

[11] G. Gouesbet and G. Gréhan, "Generalized Lorenz–Mie theories, from past to future," *Atomiz. Sprays*, **10**, 277–333 (2000).

[12] H. C. van de Hulst, Light Scattering by Small Particles (Wiley, New York, 1957).

[13] T. Wriedt, "Mie theory 1908, on the mobile phone 2008," *J. Quant. Spectrosc. Radiat. Transfer*, **109**, 1543–1548 (2008).

Computational scattering methods: a comparative study

S K Mishra[1], and S N Tripathi[1]

[1]*Indian Institute of Technology Kanpur,Department of Civil Engineering, Kanpur, India*
tel: +91 (512) 259-7845, e-mail: snt@iitk.ac.in

Abstract

Various numerical methods are available for computing electromagnetic scattering by non-spherical particles. This paper intends to give a concise introduction to three different types of methods and to emphasize their applicabilities and shortcomings for calculating concerned optical properties efficiently. The methods considered are Discrete Dipole Approximation (DDA) which is a special form of the Volume Integral Equation Method (VIEM); T-matrix method which is applicable to axisymmetric particles and extended T-matrix (Tsym) with particle geometric symmetries and modified quadrature scheme applicable to non-axisymmetric particle. The optical properties as the outcome of the codes, mentioned above are compared for hexagonal column and cylindrical shaped atmospheric particles to give an idea of the computational demands and numerical accuracy. Tsym code has been found to be the most computationally efficient.

1 Introduction

All exact theories and numerical techniques for computing the scattered field are based on solving Maxwell's equation either analytically or numerically. In contrast with exact analytical solutions, differential equation methods compute the scattering field by solving the vector wave equation in frequency or time domain while integral equation method are based on the volume or surface integral counterparts of Maxwell's equation. Thus a comparison study is required to assess the relative efficiency and accuracy of the various methods for computing optical properties. Some comparison studies have been published earlier for rotational symmetric [1] and non-symmetrical particles [2] using different integration schemes in the same code [3] and comparing with DDA code [4]. Another similar comparative study for different codes for non-spherical particles [5] has also been done. Here, for the first time, T-matrix, DDA and extended T-matrix (Tsym) have been compared with respect to optical properties as the outcome of the codes. T-matrix method is applicable for axisymmetric particles while DDA and extended T-matrix method are for both axi and non- axisymmetric particles. The present study spans over large size parameter range for hexagonal column and cylindrical shaped particles as the representative of non-spherical particles in the atmosphere. The spread of the results from different codes is necessary to be understood while applying these codes in remote sensing, biomedical applications, particle measurement and for telecommunication purposes. Efficient computing of optical properties of the scatterer would be helpful for simulation of optical particle size counters. We compare different codes concerning their computational efficiency and numerical accuracy to find the best one for applying to above simulation.

In the paper, the physics of different methods such as VIEM (Volume Integral Equation Method), T-matrix and extended T-matrix method has been explained. DDA has been considered as a good example of VIEM. Finally, some scattering problems for hexagonal column and cylindrical shape have been solved using three to give a comparative idea of the accuracy and efficiency as the outcome of each code.

2 Volume Integral methods

Vector Helmholtz equation is a homogeneous differential equation with non-constant coefficients that can be transformed into inhomogeneous differential equation with constant coefficients which is much easier to solve by introducing volume current density, J(r) in the equation. The solution to this inhomogeneous differential equation can be obtained in terms of Green's function which is the solution of the corresponding differential equation with Dirac-delta-inhomogeneity subjected to the radiation condition. The volume integral equation, which gives the field everywhere in terms of the incident and

internal fields using finite grid of integration (r_c) and field discretization (r_b), can be discretized to solve the scattering problem by a 3D scatterer in terms of polarization (P) as follows :

$$K_{bb}P(r_b) = E_{inc}(r_b) - \sum_{c,c\neq b} K_{bc}P(r_c) \quad \textbf{(1)}$$

Where K_{bc} and K_{bb} (for c=b) are the matrices and E_{inc} is the incident field. Discrete Dipole Approximation (DDA) is one of the famous volume-integral equation techniques.

2.1 DDA

Drain [6] have reviewed and developed DDA formulation. In DDA, solid particle is defined in terms of finite array of dipoles. A dipole attains dipole moment after interacting with incident field at that dipole and the field scattered by all other dipoles located at other sites in the particle. In DDA, the scattering problem has been formulated as follows:

$$\sum_{c=1}^{M} K_{bc}P_c - E_{inc,b} = 0 \quad \textbf{(2)}$$

where, particle has been defined using array of point dipoles (b=1,….., M), each element K_{bc} is a 3×3 matrix which is function of wavenumber of the medium and position of dipoles while matrix K_{bb} (for c=b) is function of the polarisability of b^{th} dipole, P_c is the polarization of c^{th} dipole (c=1,…,M), $E_{inc,b}$ is the incident field at b^{th} dipole. The system of 3M complex linear equations is solved for unknown polarization P_b (b= 1,…., M) for evaluation of extinction and absorption cross sections C_{ext} and C_{abs} [6].

3 T-matrix method

T-matrix mathematical formulation describes an efficient analytical method for computation of orientationally-averaged light-scattering characteristics for single or ensembles of nonspherical particles. For solving scattering problem a right handed spherical co-ordinate system, with fixed orientation in space, is chosen whose origin lies inside the scatterer. Amplitude scattering matrix (S) is a 2×2 matrix that linearly transforms the incident field components into scattered one. The incident and scattered fields are expanded in terms of spherical vector functions, which work as basis function to expand the fields. Unknown expansion coefficients are determined by enforcing the tangential boundary conditions. Incident and scattered field expansion coefficients are related linearly via T-matrix [7].
It has been shown by Mishchenko [8] that scattering amplitude matrix is function of T-matrix elements. The key feature of the T-matrix is that it does not depend on the incident or scattered direction but on particle shape, size, refractive index and particle orientation with respect to reference frame. Thus, once calculated T-matrix can be used for any direction of incident or scattered field. This beauty of T-matrix reduces the computation burden efficiently. Evaluation of multiple nested summations in T-matrix formulation requires CPU intensive computation which has been reduced by Mishchenko in his analytical computer code [9].

3.1 Calculating T-matrix for axisymmetric particles:

Extended Boundary Condition Method (EBCM) by Waterman [7] leads to the following equation:

$$[T] = -[Rg\,S][S]^{-1} \quad \textbf{(3)}$$

Where scattering matrix S linearly transforms internal field expansion coefficients into incident one and matrix -Rg S transforms internal field expansion coefficients into scattered one. Elements of matrix S and Rg S are surface integral over particle surface. The integrations have been solved using Gauss-Legendre Quadrature scheme.

3.2 Calculating T-matrix for non-axisymmetric particles:

Numerical evaluation of surface integral terms involved in T-matrix computation (using EBCM) makes the computation very CPU intensive which could be reduced by utilizing various symmetries of the particle [10]. In principal, EBCM can be applied to any particle shape but current model [11] gives analytically averaged optical properties of only axially symmetric particles with random orientation. Kahnert [12] has considered a regular N-hedral finite prism shape with N+2 facets; prism has two facets

as top and bottom and N rectangular same size facets at side. An improved quadrature (integration) scheme has been used to evaluate elements of the T-matrix analytically which are surface integrals over the particle surface. The improved quadrature scheme is applicable for top & bottom facets of N-hedral finite prism shaped particle while surface integral over sides of prism has been performed using Gauss-Legendre double-quadrature scheme proposed by Mishchenko et al. [13]. Use of particle geometric symmetries and improved quadrature scheme lead the extended T-matrix method (Tsym code).

4 Results and discussion

T-matrix code of Mishchenko [14] which is applicable to axisymmetric particles, Programme Tsym [3] by Michael Kahnert applicable to randomly oriented polyhedral prisms, and the DDA-code DDSCAT by Drain and Flatau [4] have been used for the inter-comparison of optical properties as the outcome of the codes. Codes have also been compared on the basis of their computational efficiency. The considered scattering targets are axisymmetric particles (cylinder) and non-axisymmetric particles (hexagonal column with sharp edges) of aspect ratio one with random orientation. For low size parameter, the optical properties of a cylinder and a hexagonal column are nearly same so these shapes have been considered in the computational example. In the example the atmospheric particles say ice-crystals and dust have been considered with 3.7 μm sensing wavelength. The refractive indices for ice and dust particles are $m = 1.39 + i0.007$ and $m = 1.5 + i0.012$ respectively at the above wavelength. Inter-comparison of the different codes leads to assess the relative performance of them in calculating optical properties. On the computational efficiency front, the codes have been intercompared to get the idea of a better code in terms of CPU time consumption and memory occupied for solving a scattering problem.

In the study, T-matrix code has been used for cylinder, DDA for hexagonal column and Tsym for both the shapes with varying sizes. Figure 1 shows the scattering cross section calculated using T-matrix, extended T-matrix (Tsym) and DDA codes. The scattering crosssection (C_{sca}) calculated from different codes is nearly same up to size parameter 8, a bifurcation occurs for DDA, T-matrix and Tsym codes for size parameter beyond 8. The deviation in C_{sca} calculated from T-matrix and DDA has been observed with increasing size. The same holds good for Tsym code for the two shapes.

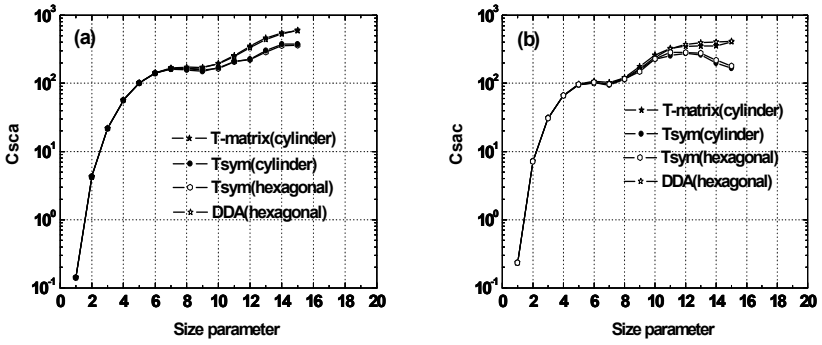

Figure 1: scattering crosssection (C_{sca}) for (a) ice-particles with refractive index $m = 1.39 + i0.007$

(b) dust with refractive index $m = 1.5 + i0.012$

Variation of asymmetry parameter (g) with size parameter has also been studied. Tsym code underestimates the value of g for size parameter range 9-11 while overestimates for size parameter beyond 12 relative to T-matrix and DDA code. The increase in refractive index leads to the increase in deviation between all the codes with increasing size parameter.

Phase function has also been compared for various size parameters. Phase function for size parameter one show fairly good agreement among all the codes and the same is true for size parameter five. For size parameter 10, Tsym showed fluctuating values of phase function compared to those obtained from

DDA and T-matrix for backward scattering angles. The Tsym code overestimates the phase function values for hexagonal column and cylinder for scattering angle beyond 90 degree. Phase function of hexagonal column by Tsym code is found to be flattened for high refractive index compared to that of others. Frequency of the fluctuating phase function for hexagonal column and cylinder is found increased for Tsym code for size parameter 15. Phase function is underestimated by the Tsym code relative to DDA and T-matrix for this size parameter.

Tsym code has been found to be the fastest compared to T-matrix and DDA on machine with specifications X-64 bit and 16 GB RAM. DDA was found to be the slowest among the three.

5. Conclusion

Finally we conclude that all the considered codes show good matching up to size parameter 8 beyond that deviation occurs. T-matrix and DDA code showed good matching compared to Tsym code. Tsym code showed least computation time.

Acknowledgments

This research is supported through a grant from ISRO Meghatropiques project.

References

[1] P. J. Flatau, K. A. Fuller, and D. W. Mackowski, “Scattering by two spheres in contact: comparisons between discrete-dipole approximation and modal analysis,” Appl. Opt. **32,** 3302 (1992).

[2] J. W. Hovenier, K. Lumme, M. I. Mishchenko, N. V. Voshchinnikov, D. W. Mackowski, and J. Rahola, “Computations of scattering of four types of non-spherical particles using diverse methods,” J.Q.S.R.T., **55**(6), 695 (1996).

[3] F. M. Kahnert, J. J. Stamnes, and K. Stamnes, “Application of the extended boundary condition method to particles with sharp edges: a comparison of two surface integration approaches,” Appl. Opt. **40,** 3101 (2001).

[4] B. T. Draine and P. J. Flatau, “User Guide for the Discrete Dipole Approximation Code DDSCAT 6.1,” http://arxiv.org/abs/astro-ph/0409262v2 (2004).

[5] T. Wriedt and U. Comberg, “Comparison of computational scattering methods,” J.Q.S.R.T. **60**, 411-423 (1998).

[6] B. T. Draine, “The Discrete-Dipole Approximation and its application to interstellar graphite grains,” Astrophysical J. **333,** 848-872 (1988).

[7] P. C. Waterman, “Symmetry, Unitarity, and Geometry in Electromagnetic Scattering,” Phys. Rev. D **3**, 825 (1971).

[8] M. I. Mishchenko, L. D. Travis, and D. W. Mackowski, “T-matrix computations of light scattering by nonspherical particles: a review,” J.Q.S.R.T. **55,** 535-575 (1996).

[9] M. I. Mishchenko, “Light scattering by size-shape distributions of randomly oriented axially symmetric particles of size comparable to a wavelength,“ Appl. Opt. **32**, 4652-4666 (1993).

[10] F. M. Schulz, K. Stamnes, and J. J. Stamnes, “Point group symmetries in electromagnetic scattering,” J. Opt. Soc. Am. A **16,** 853–865 (1999).

[11] M. I. Mishchenko, “Light scattering by randomly oriented axially symmetric particles,” J. Opt. Soc. Am. A **8**, 871–882 (1991).

[12] F. M. Kahnert, J. J. Stamnes, and K. Stamnes, “Application of the extended boundary condition method to homogeneous particles with point-group symmetries,” Appl. Opt. **40,** 3110 (2001).

[13] M. I. Mishchenko, L. D. Travis, and A. Macke, “Scattering of light by polydisperse, randomly oriented, finite circular cylinders,” Appl. Opt. **35,** 4927–4940 (1996).

[14] M. I. Mishchenko and L. D. Travis, “Capabilities and limitations of a current FORTRAN implementation of the T-matrix method for randomly oriented, rotationally symmetric scatterers,” J.Q.S.R.T. **60,** 309-324 (1998).

Volume and surface shadowing in particulate random media

Hannu Parviainen and Karri Muinonen

Observatory, P.O. box 14, FIN-00014, University of Helsinki, Finland
e-mail: hannu.p.parviainen@helsinki.fi

Abstract

We use Monte Carlo simulations to study the volume and surface shadowing in rough-surfaced particulate porous random media over the full three-dimensional angle space, and compare the numerical results with the analytical Lumme-Bowell and Hapke models. For the task, we utilise Markov chain Monte Carlo sampling to examine the influence of the analytical model parameters on the quality of the fit. In addition, we compare the behaviour of the relative errors between the numerical and the analytical models for a given set of medium statistics and best-fit parameters over different angles of incidence and emergence.

1 Introduction

Particulate-volume and rough-surface shadowing have a significant impact on the reflectance of atmosphereless planetary surfaces covered by regolith. The volume shadowing arises from the particle-scale porous nature of the regolith, while the rough-surface shadowing originates from roughness in scales larger than the size of the particles [1].

Several analytical models have been presented in order to model the bidirectional reflectance of a regolith-like particulate surface, the Lumme-Bowell [2, 3] and rough-surface-corrected Hapke [4, 5, 3] models being likely the ones most widely utilised. These models pursue to include the effects arising from the volume and rough-surface shadowing, but their functional form is somewhat different due to the divergent approximations taken.

In our study, we compare the results from numerical geometric-optics ray-tracing light scattering simulations with the two aforementioned analytical bidirectional reflectance models. We consider perfectly opaque particles with Lommel-Seeliger reflectance, and concentrate on shadowing. The results show fairly good agreement between the numerical and best-fitting analytical models for most part of the angle space, but differences exist on the distribution of the relative differences between the numerical and analytical models.

2 Lumme-Bowell and Hapke reflectance models

Since our main interest is on the volume and rough-surface shadowing, we consider only the first order scattering and isotropic phase functions. With these simplifications, the Lumme-Bowell model is

$$f_{\mathrm{LB1}}(i,e,\alpha) = \frac{\varpi}{4\pi}\frac{\mu_0}{\mu_0+\mu}\left(1-q+\frac{q}{1+\rho(\mu^2+\mu_0^2-2\mu\mu_0\cos\alpha)^{1/2}/(\mu\mu_0)}\right)S_{LB}(i,e,\alpha), \tag{1}$$

where i is the angle of incidence, e the angle of emergence, $\mu_0 = \cos(i)$, $\mu = \cos(e)$, α the phase angle, ϖ the single scattering albedo, S_{LB} the Lumme-Bowell shadowing function, q the fraction of the surface covered by holes, and ρ is the tangent of the mean surface slope. Likewise, the rough-surface-corrected Hapke model is

$$f_{\mathrm{HR1}}(i,e,\alpha) = \frac{\varpi}{4\pi}\frac{\mu_{0e}}{\mu_{0e}+\mu}\left(1+B_{0,SH}\left[1+\frac{2D\tan(\alpha/2)}{-R\ln(1-D)}\right]^{-1}\right)S_H(i,e,\alpha), \tag{2}$$

where μ_{0e} and μ_e are the effective cosines, and S_H the Hapke shadowing function, all described in more detail by Hapke [4] and Bowell et al. [3]. Also, $B_{0,SH}$ is the amplitude of shadowing opposition effect, D the volume density. and R is the product of the extinction coefficient and mean particle radius, considered to be a free parameter.

3 Numerical methods

3.1 Medium generation

We generate the media, of which an example is shown in Fig. 1, using a dropping-based random-packing method inside a rectangular container with edge width w. The height h of the container depends on the final packing solution. The media packings used in the study consist of 1×10^6 and 2×10^6 spherical particles with mean radii r of $w/500$, and volume densities D of 0.2, 0.35, 0.4, 0.45, 0.5 and 0.55, three realisations for each D. For $D<0.5$, 1×10^6 particles are used, but for larger densities 2×10^6 particles are neces ary to make the packings tall enough to allow for vertical variations in macro-scale surface roughness.

Figure 1: A medium realisation with $D=0.35$. From left to right: no macro-scale roughness, fBm roughness with $H=0.8$, and fBm roughness with $H=0.4$.

In addition to the particle-scale roughness arising from the random packing of the particles, we model larger macro-scale surface roughness of several mean particle diameters and greater using two-dimensional random fields. The packing is intersected with a random field following Gaussian correlation (Gc) or fractional-Brownian-motion (fBm) statistics, and the particles above the random field are ignored in the scattering simulations. The random fields used are functions of two parameters: the standard deviation of heights σ, and a model-specific parameter describing the horizontal roughness statistics. The fBm-fields are parametrised by the Hurst exponent H, and Gc-fields by the correlation length l.

3.2 Light-scattering simulations

We use a numerical geometric-optics light-scattering code implemented to study the reflectance of a regolith-like particulate medium. The code utilises standard Monte-Carlo ray-tracing methods combined with problem-specific optimisations to simulate light scattering in a porous medium consisting of several millions of spherical particles, the reflectance of a single particle following Lommel-Seeliger model with isotropic phase function. The large number of particles was necessitated by the need to model both the volume shadowing due to the medium porosity, and rough-surface shadowing and masking due to macro-scale surface roughness.

The ray-tracing simulation for media with parameters (D,H,σ) (fBm) or (D,l,σ) (Gc) result in a numerical reflectance model that is a function of three angles (i,e,ϕ). The simulation is computed for discrete values of i. For each i, the scattering hemisphere (e,ϕ) is discredised using a simple but efficient scheme that attempts to keep the mean solid angle covered by a single bin constant over the whole hemisphere.

3.3 Model fitting

We apply Markov chain Monte Carlo (MCMC) sampling in the analytical model parameter space to see how different parameters influence the total relative difference Ebetween the numerical and analytical models. Moreover, we use the results of the sampling to derive the best-fit parameters for the analytical model against a numerical model with given medium statistics.

4 Results

Figures 2, 3, and 4 show a subset of the preliminary results of our study. The subset consists of simulations for the case of random porous media with D = 0.2 and 0.5, and no macro-scale roughness.

First, from Fig. 4 we can see that the Lumme-Bowell parameters correspond rather accurately to the medium parameters. In the case of zero macro-scale roughness $q = 0$, the fit for D have minima around 0.2 and 0.5. Next, the Lumme-Bowell models with the best fitting parameters determined from the minimum of E, presented in Fig. 2, show good compatibility for $0^\circ \leq i \lesssim 60^\circ$ over the scattering hemisphere. However, E can be larger than 100% for combinations of $i > 60^\circ$ and $\phi \gtrsim 140^\circ$, i.e., for the largest phase angles. In contrast to the Lumme-Bowell model, E never rises above 100% for the Hapke model, shown in Fig. 3. Nevertheless, $E > 20\%$ for a major part of angle space, and $E < 10\%$ for only slices in the scattering hemisphere.

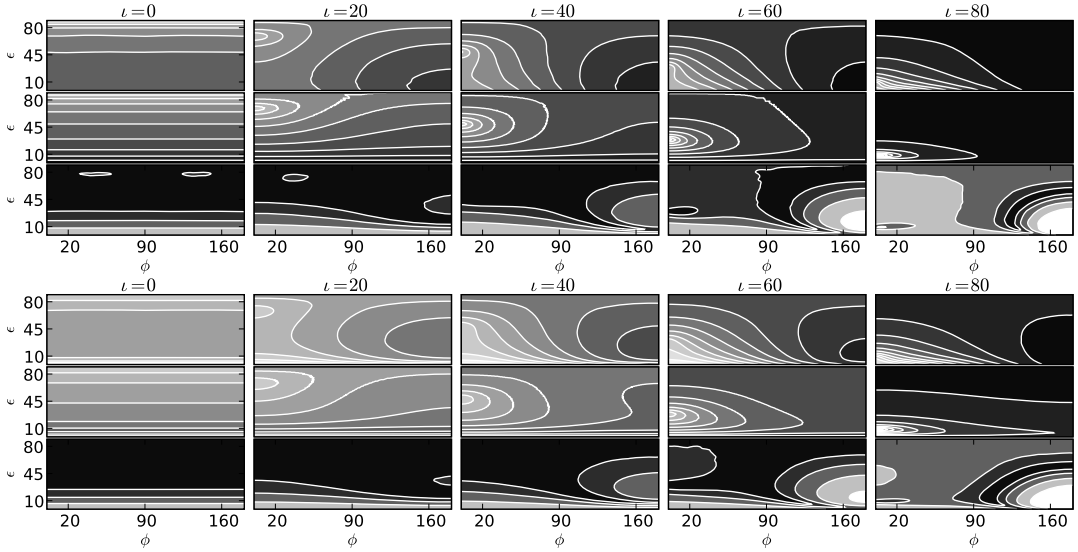

Figure 2: Numerical models for D = 0.2 and 0.5 (up), the corresponding Lumme-Bowell models (middle), and E (bottom). The contour levels are for E = 10, 25, 50, and 100% difference relative to the numerical model. Black and white refer to $E < 10\%$ and $E > 100\%$, respectively.

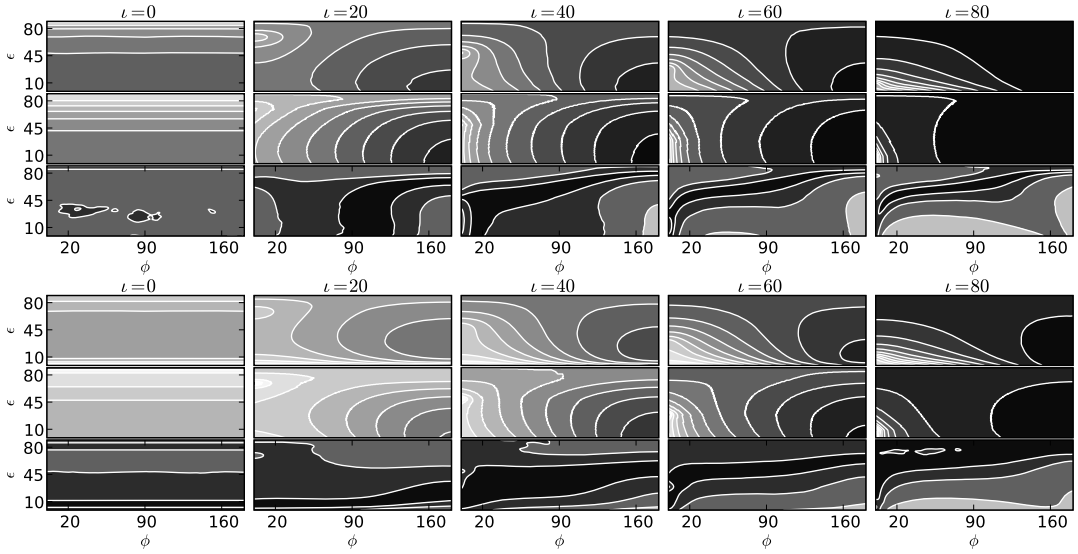

Figure 3: As in Fig. 2, but for the rough-surface-corrected Hapke model.

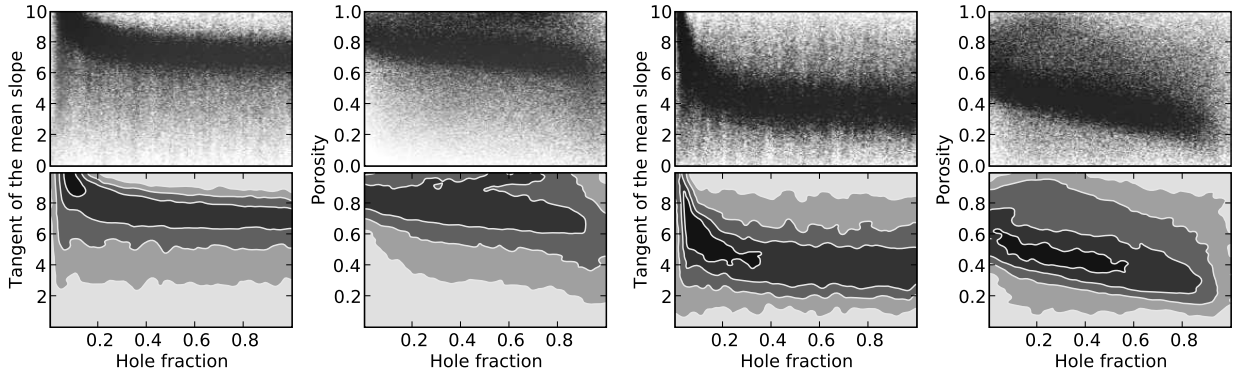

Figure 4: Relative difference E for the numerical models with D = 0.2 and 0.5 and Lumme-Bowell model as a function of q, ρ, and $1 - D$. The upper plots show the actual sampling results, while the lower plots show the smoothed contour levels for E = 15, 25, 50, 75, 100%. Black and white refer to $E < 15\%$ and $E > 100\%$, respectively.

5 Discussion

We compared the results of numerical reflectance modeling with two analytical models. The study concentrated on the first-order particulate-volume and rough-surface shadowing of perfectly opaque particles with Lommel-Seeliger scattering laws for their surface elements. This can be regarded as a special case for the analytical models, both of which can also include physics excluded from our simulations.

Also, the goodness-of-fit estimate chosen for the MCMC sampling has an effect on the best-fit parameters. We tested the effect of this using mean squared residuals as a fit estimate instead of the mean relative absolute difference and the best fit parameters differed somewhat. This was due to the fact that the two estimates emphasise different things. The former gives equal weight to the quality of the fit of areas of high and low reflectance, whereas the latter emphasises the high-reflectance areas. We found the relative absolute difference to yield better correspondence to the analytical model parameters, but more work is needed to study how great impact does the choice of the estimate really have on the inverted parameters.

References

[1] H. Parviainen and K. Muinonen. Rough-surface shadowing of self-affine random rough surfaces. *Journal of Quantitative Spectroscopy and Radiative Transfer*, 106:398–416, July 2007.

[2] K. Lumme and E. Bowell. Radiative transfer in the surfaces of atmosphereless bodies. I - Theory. II - Interpretation of phase curves. *AJ* , 86:1694–1721, November 1981.

[3] E. Bowell, B. Hapke, D. Domingue, K. Lumme, J. Peltoniemi, and A. W. Harris. Application of photometric models to asteroids. In R. P. Binzel, T. Gehrels, and M. S. Matthews, editors, *Asteroids II*, pages 524–556, 1989.

[4] B. Hapke. Bidirectional reflectance spectroscopy. III - Correction for macroscopic roughness. *Icarus*, 59:41–59, July 1984.

[5] B. Hapke. Bidirectional Reflectance Spectroscopy 5. The Coherent Backscatter Opposition Effect and Anisotropic Scattering. *Icarus*, 157:523–534, June 2002.

Computer Modeling of Light Scattering on Separately Spherical Particles, Using Mie Theory

Amin Rikhtehgar, Dimitry Stankevich
Astronomical Observatory of V.N. Kharkov National University, Department of Astronomy, Planetary Remote Sensing Department
35 Sumska St. Kharkov, 61022, Ukraine
tel: *+380 (57) 7075063,* e-mail: *shkuratovl@astron.kharkov.ua*

Abstract

In this present, we have found most effective calculation of light scattering for system of spherical particles used by Mie theory and evaluated floor amount terms of series requisite for calculation scattering characterization by fixed precision.

1 Introduction

As it is known, analytical expressions are found for the derivatives of commonly used Mie scattering parameters, in particular for the absorption and the scattering efficiencies, and for the angular intensity function. They are based on the analytical derivatives of the Mie scattering amplitudes and with respect to the particle size parameter and complex refractive index. These derivatives are given with respect to the total number density, to the medium radius and spread of the distribution, and to the refractive index. In the case of the system of interacting particles - this is a random, but densely packed medium.

It is supposed that it is practically impossible to get an analytical solution to this problem of scattering in a medium, therefore, it is essential to find the solution by using the Mont-Carlo method, i.e. by launching many separate waves in the medium, and calculating the scattering of each wave on each particle and its re-scattering on each subsequent particle. Calculations under the standard Mie formulae undergo two modifications in this case:

a. In contrast to approximation in the far-field zone, which is what is usually done by scientists, we should use a suitable common solution in the near-field zone.

b. Mie formulae should be rearranged in the form most effective for calculations with multiple computations (reducing expenditure of computer computation time).

The final purpose of this modeling of light scattering on spherical particles based on Mie theory is to compute radial and angular intensity dependence and to construct a method for the acceleration of the computation process.

2 Solving the Problem of Light Scattering on Spherical Particles, Based on the Classical Mie Theory

2.1 As is obvious, it follows from Mie theory that the light scattered on a sphere consists of partial waves, emitted by multiple poles of electric charges on the sphere. If amplitude a_n is n- electrical conjugating wave and b_n is n- magnetic partial wave, then:

$$a_n = \frac{\psi_n(x)\psi_n'(mx) - m\psi_n'(x)\psi_n(mx)}{\zeta_n(x)\psi_n'(mx) - m\zeta_n'(x)\psi_n(mx)} \qquad (2.1)$$

$$b_n = \frac{\psi_n'(x)\psi_n(mx) - m\psi_n(x)\psi_n'(mx)}{\zeta_n'(x)\psi_n(mx) - m\zeta_n(x)\psi_n'(mx)} \qquad (2.2)$$

The arguments of these functions are only x and mx, and functions do not depend on other functions. a_n and b_n are only sets of coefficients which may be computed for all particles in advance. We will repeatedly discharge a wave onto each particle, but we will leave a_n and b_n coefficients the same. That is to say that there is no need for multiple, quite compound formulae computations, which include ψ and like Bessel functions, each computation of which increases the computing time. For each particle you may select a_n and b_n coefficients from the table in advance.

Using the computer model, developed at *the Remote sensing department (ГИС – GIS, Geographic Information System) of the Astronomical Institute of Kharkov National University*, it is quite possible to model media, consisting of 256 different types of particles having different refractive indexes m and radii r. This makes it possible to calculate and compile the tables of a_n and b_n coefficients. The size of these tables is relatively small and makes up $256 \times n$. Fig. (2.1).

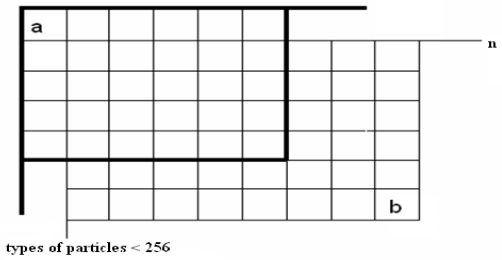

Fig. (2.1): The size of these tables is relatively small and makes up **256 x n**

2.2 Based on the asymptotic expansion analysis of Hankel functions, we may show that the asymptotic representation for spherical Hankel functions has the following forms:

$$h_n^{(1)}(kr) \approx \frac{-i^n e^{ikr}}{ikr} \qquad (2.3)$$

$$h_n^{(2)}(kr) \approx \frac{-i^n e^{ikr}}{ikr} e^{-ikr} \qquad (2.4)$$

The first of these asymptotic forms corresponds to the outgoing spherical wave, but the second corresponds to the ingoing spherical wave. Thus far, from spherical considerations, the scattered field is an outgoing wave at wide intervals between particles. But in generating functions, only $h_n^{(1)}(z)$ should be used. While analyzing the scattered field on a wide interval, we will also need an asymptotic expression for generating $h_n^{(1)}(z)$ functions. Using Fig. (2.2), we may set the dependence of spherical Hankel function hn(2)(z), which is obtained on the basis of the Bessel function of the second kind, on distance r, which is calculated separately for different values of the m refractive index.

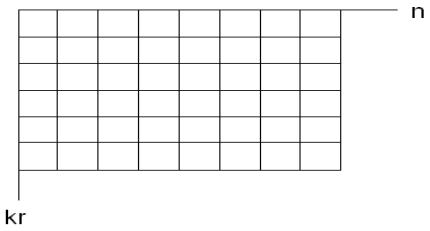

Fig. (2.2): The dependence of spherical Hankel function on distance **r**

2.3 Let's revert to π_n and τ_n, which are described by dint of Legendre polynomial. They depend on the scattering angle and are independent of particle characteristics.

$$\pi_n(\cos\theta) = \frac{1}{\sin\theta} p_n(\cos\theta) \qquad (2.5)$$

$$\tau_n(\cos\theta) = \frac{d}{d\theta} p_n(\cos\theta) \qquad (2.6)$$

Fig. (2.3) demonstrates π_n and τ_n polar curves for $n = 5$. These curves are more visual when changing θ from 0 to 360°. These functions (except π_1, being constant) take on both positive and negative values. For example, τ_2 is positive in the angular range of 0 to 45°, it is negative from 45° to 135°, and again positive from 135° to 180°. All these functions have lobes in the forward direction (i.e. positive in this direction), but in the reverse direction the lobes disappear for alternating n values.

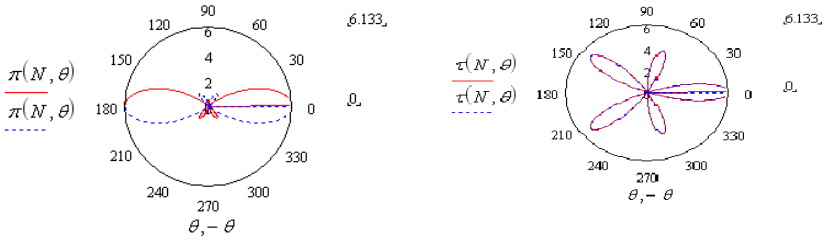

Fig. (2.3): π_n and τ_n polar curves for $n=5$

Fig. (2.4) demonstrates the angular dependence of π_n and τ_n functions for different values of θ scattering angle. The scattering model in medium allows us to calculate the power-angle curve accurately within 1°, which renders doing more detailed calculations of π_n and τ_n angular functions unnecessary.
Thus, the tables of π_n and τ_n functions have moderate sizes $180 \times n$.

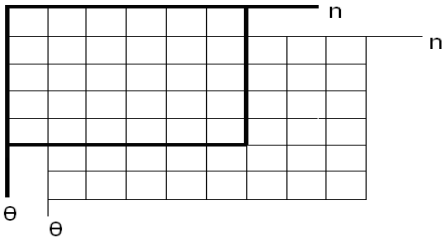

Fig. (2.4): The angular dependence of π_n and τ_n functions for different values of θ scattering angle

For the estimation of a number of terms of a series [ ], indispensable in the achievement of given accuracy, we used the fact that the $\pi_n(\theta)$ and $\tau_n(\theta)$ functions take on values due to order-to-magnitude which do not exceed n.
Therefore, we have the right to cast out the terms of $I_{n,\theta}$ series as soon as A_n and B_n become less than δ/n, where δ is the desired point.

$$I_{n,\theta} = \sum_{n=0}^{N} \frac{2n+1}{n(n+1)} \cdot \left\{ A_n \cdot \pi\left(n, \theta, \frac{\pi}{180}\right) + B_n \cdot \tau\left(n, \theta \frac{\pi}{180}\right) \right\} \qquad (2.7)$$

In Fig. (2.5), (2.6), (2.7), (2.8) at the end of this paper are shown the A_n and B_n coefficients for $x = 1, 3, 10, 30$ in refractive index $m=1.33+0.i$.

Here is represented the angular dependence of scattering amplitude for a particle having $x=10$, calculated to a small point, attainable when computing with the help of a computer and truncated to $n=10$ series of $Z_{n,\theta}$. Fig. (2.9).

In Fig. (2.10), we can see the relative calculation error of the truncated series. You may easily see that the relative calculation error changes sharply against the scattering angle. We will estimate it based on a maximum deviation from 0.
It is clear that when using $n=x$, the relative amplitude error will not exceed 1.5% (it fits with an intensity of $0,0002$). This accuracy is well acceptable for computations of scattering by a medium consisting of randomly packed particles.

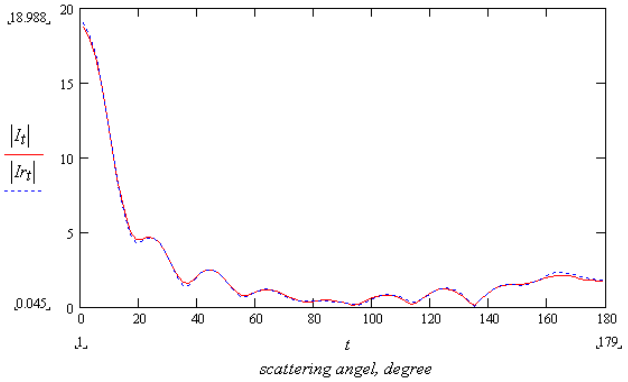

Fig. (2.9): The angular dependence of scattering amplitude for particle having $x=10$

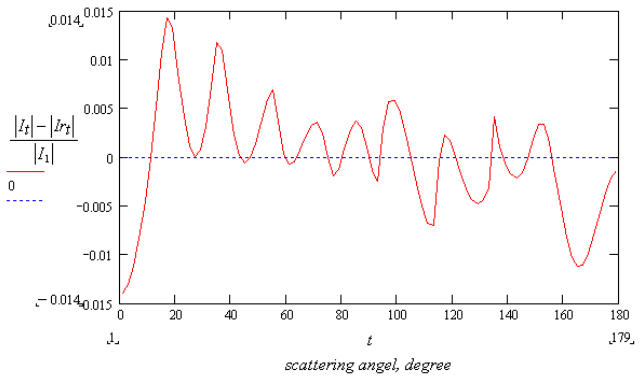

Fig (2.10): The relative calculation error of the truncated series

3 Conclusion

1. Mie formulae for general-case are discussed; (incl. for near-field zone);
2. Mie formulae are reduced to the form permitting the most effective computation; which means that we reduced them to form allowing for convenient and fast computation; i.e. everything that could have been calculated in advance was calculated and written down in tables. A special table for τ and π functions, a special table for A and B coefficients, angular parts of the dependence, characteristics of each type of particles, and a special table of scattering dependence for Hanckel functions which asymptotically converges to 1/r, but in fact, differs in near-field regions.
3. In this paper, there was made an estimation of the minimum number of Mie terms, which is necessary for the detailed calculation of scattering characteristics.

Our specific result is rather larger and not even twice, but let's say ***1.5 x*** times, what is sufficient.

References

[1] M. Born, and E. Wolf, "Principles of Optics", (1999), www.cambridge.org.

[2] C. F. Bohren and D. R. Huffman, Absorption and Scattering of Light by Small Particles (Wiley, New York, 1983).

[3] M. I. Mishchenko, D. W. Mackowski, and L. D. Travis, "Scattering of light by bispheres with touching and separated components," Appl. Opt. 34, 4589–4599 (1995).

[4] R. G. Gainger, J. Lucas, G.E. Thomas, G. B. L. Ewen. Caculation of Mie derivatives. Optical Society of America, 2004.

[5] Mie Scattering. Farside.ph.utexas.edu/teaching/jk/Lectures/node103.html.

[6] Mie theory. wkipedia, en.wikipedia.org/wiki/mie_theory.

[7] Lorenz-Mie Scattering. Nit.colorado.edu/atoc5560/week8.pdf. E. S. Thiele, R. H. French. Light scattering properties of reprehensive, Journal of the American Ceramic, Society, *1998*

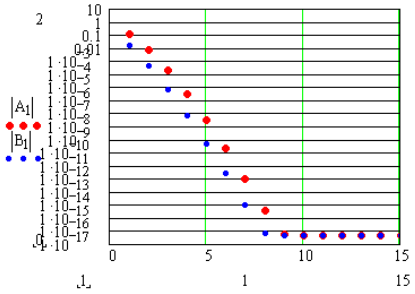

Fig. (2.5): The A_n and B_n coefficients for $x = 1$ in refractive index $m=1.33+0.i$.

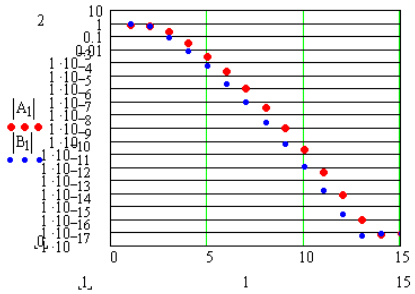

Fig. (2.6): The A_n and B_n coefficients for $x = 3$ in refractive index $m=1.33+0.i$.

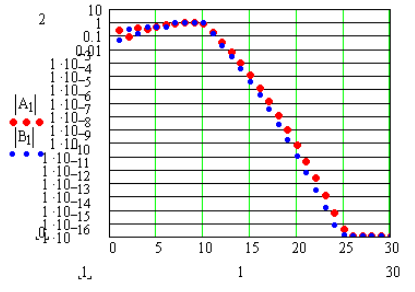

Fig. (2.7): The $\mathbf{A}_n$ and $\mathbf{B}_n$ coefficients for **x = 10** in refractive index **m=1.33+0.i**.

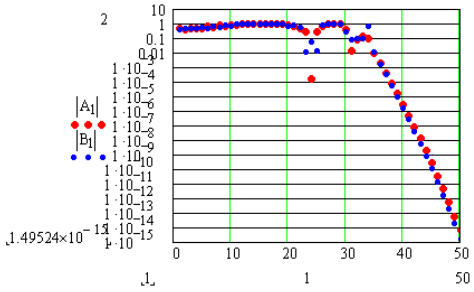

Fig. (2.8): The A_n and B_n coefficients for $x = 30$ in refractive index $m=1.33+0.i$.

Application of the Polar Decomposition Method to Particle Scattering Systems

J.M. Sanz[1], P. Albella, F. Moreno, J. M. Saiz and F. González

[1] *Universidad de Cantabria, Grupo de Óptica, Departmento de Física Aplicada*

Avda de Los Castros SN, 39006, Santander, Spain

tel: +34 (942) 201446, sanzjm@unican.es

Abstract

We have successfully applied the polar decomposition theorem (PDT) to scattering matrix corresponding to simple systems such as isolated metallic or dielectric spheres. The DDA method has been used as an intermediate tool to calculate these matrices. We show how the parameters used by the PDT for describing the scattering by spheres can be easily interpreted. It is also shown that the PDT provides us with a frame in which the systems can be characterized by independent parameters representing magnitudes of simple (virtual) elements constituting an alternative to conventional Mueller Matrix analysis.

1 Introduction

Non-invasive characterization of the size and properties of small particles, either isolated or on substrates as part of a variety of systems, has been focus of the interest of many investigations and discussions over the last twenty years. Since the scattering problem involving cylinders and spheres was analytically solved by Mie, the scattering theory of regular and irregular scattering systems has been broadly developed by many other authors [1-3]. From a practical point of view, different authors have made use of these theoretical approaches for their scattering or polarimetry studies and applied to different experimental systems. Some examples of these are: the study of small changes induced in the backscattering patterns of an irregularity or defect present in a particle located on a substrate by making use of the Extinction Theorem[4]; the analysis of the linear and circular polarization degree of light scattered by asymmetrical particles[5] or the evolution of some system parameters by using a physic interpretation of the Mueller Matrix[6].

Concerning the bulk of the polarimetry information, completely contained in the Mueller matrix, some methods have been proposed over the past few years to simplify the physics interpretation of the information that can be obtained from the matricial formalism. One of these methods is the polar decomposition theorem (PDT). This method, as we will show later on, reduces in a considerable way the number of parameters needed to study different optical systems [7]. Even though, obtaining information from the Mueller Matrix making use of the PDT has not been successfully accomplished yet.

We propose an application of the PDT method to simple systems formed by isolated spheres of size smaller than the incident wavelength. Mueller matrix simulation is carried out by means of the Discrete Dipole Approximation method (DDA). As part of the PDT method, we also present a comparison between some usual magnitudes used in particle systems and the ones obtained from the decomposition of the Mueller Matrix. The aim of this study is to show that we can improve the description of a typical system by analyzing the behavior of PDT parameters (such as the transmission along the axis of a real diattenuator, the phase change induced by an elliptical retarder, etc). These parameters reproduce the evolution of real systems and can be easily understood from a physical point of view.

This study will be completed with other forthcoming experimental works, now under development.

2 System Geometry and Numerical Method

The scattering system we analyze consists of an isolated sphere, of radius ranging from $r=0.1\lambda$ to $r=0.5\lambda$ and two compositions: the first is made of a dielectric material (SiO_2 with refractive index, $n=1.5$ for $\lambda=633nm$) and the second is a metal (Ag, $n=0,135+3,988i$ for $\lambda=633nm$). The sphere is illuminated by a plane wave of λ=633nm.

In this work we employ the discrete dipole approximation (DDA) [8], which is a computational procedure suitable for studying scattering and absorption of EM radiation by particles with sizes of the order or less of the

wavelength of the incident light. The DDA method deals with the object, in our case a nanoparticle, by assuming that it is composed by a high enough number of elements, each one a polarizable dipole. The location and polarizability of each dipole are specified and used to make the calculation of the scattering and absorption efficiencies. The accuracy of the results depends basically on the computational capabilities. The system is handled by assuming an array of N polarizable dipoles located at $\{r_i\}$, $i = 1,2,\ldots,N$; each of them characterized by a polarizability α_i. When a system is excited by a monochromatic incident plane wave $E_{inc}(r, t) = E_0 e^{ikr-wt}$, where r is the position vector, t is time, and ω is the angular frequency of the incident light. Each dipole of the system receives an electric field that can be split in two contributions: (i) the incident radiation field, plus (ii) the field radiated by all the other induced dipoles. The sum of both fields defines the local field at each dipole and is given by

$$E_{loc}(r_j) = E_{j,loc} = E_{j,inc} + E_{j,dip} = E_0 e^{ikr} - \sum_{k \neq j} A_{jk} P_k \qquad [1]$$

where P_k is the dipole moment of the k-th element, and A_{jk} the interaction matrix element jk. Once we solve the $3N$ coupled complex linear equations given by $P_k = \alpha_k E_{k,loc}$, we can find the extinction and absorption cross sections for a target in terms of the dipole moments. By performing these calculations for a set of incident polarizations, we can obtain the elements of the scattering matrix, or Mueller matrix.

The scattering matrices obtained from this method have been post-processed in all cases with an algorithm that performs the PDT. After testing the purity of the matrices [7], it was found that in the cases analayzed, the Mueller matrices obtained were pure, as expected from a system that does not produce any depolarization. Our decompostion algorithm is equivalent to the sum of a diattenuator and an elliptical retarder being its order of crucial importance its order.[9]. Therefore, the system matrix can be decomposed in the following way:

$$M_{4x4} = M_{\Delta}(d_1, d_2, d_3) \cdot M_R(\phi, \varphi, \delta) \cdot M_D(\alpha, t_1, t_2) \qquad [2]$$

where $M_{\Delta}(d_1, d_2, d_3)$ is the depolarization matrix (with d_1, d_2 and d_3 being the depolarizance parameters and equal to 1 in our case), $M_R(\Phi, \varphi, \delta)_R$ is the "retardance matrix" (with Φ, the angle between the fast axis of the retarder and the scattering plane, φ the phase shift and δ the rotation angle induced by the retarder) and $M_D(\alpha, t_1, t_2)$ *is the diattenuation matrix* (with α the azimut or angle between the scattering plane and the first axis of the diattenuator and t_1 and t_2 are the transimissions along the first and second axis of the diattenuator). Due to the simplicity of our system and its symmetry properties, α, Φ and δ are zero. For this reason, we can decompose our problem in an equivalent system composed by an ideal diattenuator aligned with the scattering plane and with the fast axis of a retarder.

The Mueller Matrix of a spherical particle is usually described with four parameters (M_{11},M_{12},M_{33} *and* M_{34}). However, if we examine in detail the polarimetric properties of our system and we make use of the PDT, we can evaluate the behavior of our system by just considering three independent parameters, the total scattered intensity (M_{11}), the transmission along one of the diattenuator axes (t_1) and the phase shift induced by the retarder (φ).

Once the meaning of the PDT parameters is well understood, this polarimetric method provides us with a more handy tool to approach the analysis of the system.

3 Results

The PDT method allows us to extract all the polarimetric information out of a system using less parameters and, what it is more important, being aware of the physics of the problem. Figs. 1 and 2, correspond to the evolution of some polarimetric parameters of a metallic and dielectric sphere respectively. In Figs 1.a and 2.a we have plotted the diattenuator transmission obtained from the PDT as a function of the scattering angle over the range [90º,180º]. Figs 1.b and 2.b show the linear polarization degree ($P_L=-M_{21}/M_{11}$) obtained for the sphere as a function of the scattering angle.

It can be seen how both sets of curves in (b) can be exactly obtained from the correspondig sets (a). This is not a general result but stands for the case of isolated spheres. When the scattered light is linearly polarized ($|P_L|=1$, the transmission along any of the axis of the diattenuator must be maximum ($t_1=0$ *or* $t_1=1$). However, when P_L is zero, the transmission is the same for both attenuator axis ($t_1=0.5$).

Figs 1.c and 2.c, correspond to the direct polarizance (defined as the system capacity to polarize unpolarized light) [7]. These curves also represent the inverse polarizance (that resulting of interchanging the incident and the scattering direction) due to the symmetry of the problem. The polarizance has a strong correlation with parameter t_1 for these systems showing its relationship with the capacity the system to act over the incident light of the diattenuator obtained by applying the PDT method. As expected, Figs. 1c and 2c go to zero when the diattenuator does not have any preference ($t_1=t_2=0.5$), whereas it goes to a maximum value when one of the components is favored over the other.

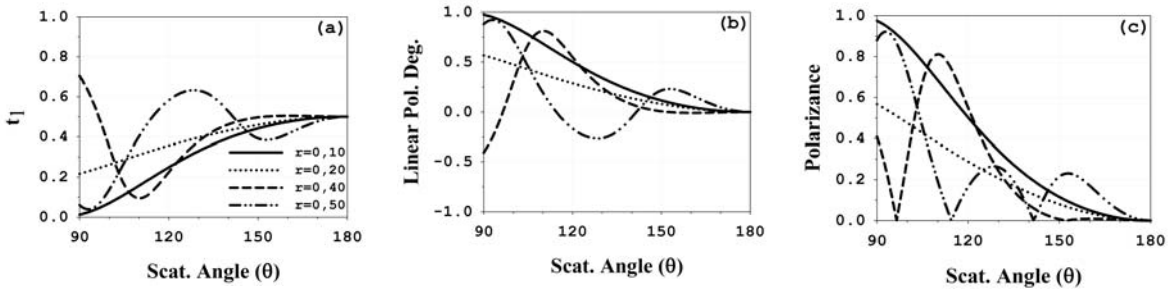

Fig 1. Metallic sphere (Ag) of different radii. a)Transmission coefficient of the diattenuator, b) Linear polarization degree and c) Polarizance vs scattering angle

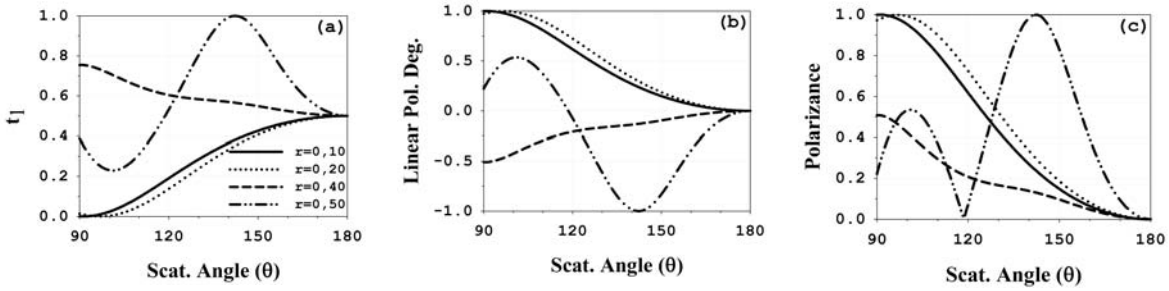

Fig 2. Dielectric sphere (SiO_2) of different radii. a)Transmission coefficient of the diattenuator, b) Linear polarization degree and c) Polarizance vs scattering angle

Finally, in Figs 3.a and 3.b we represent the phase shift introduced by our equivalent retarder. A strong phase shift is observed for those scattering angles that correspond to a maximum in t_1 (also a maximum in the $|P_L|$).

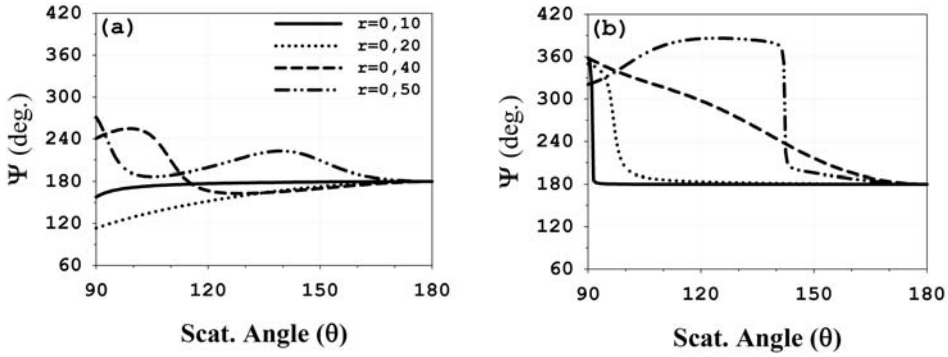

Fig 3. Phase Shift vs Scat. Angle. a) Metallic sphere (Ag) and b) Dielectric sphere (SiO_2)

For an easier visualization of the case $r=0.5\lambda$ we have preserved the continuity of the curve in Fig. 3 by not limiting the phase axis to 360º.

Accordingly to these results, the optical behavior of metal and dielectric spheres can be characterize by the PDT method, that is, by only looking at the diphase, retarder phase and diattenuator parameter t_1.

4 Conclusions

In the present work we have succesfully applied the PDT method to the most simple scattering system: isolated metallic or dielectric sphere of size smaller than the wavelength of the incident light. The original Mueller matrix for our polar decomposition was obtained by means of a conventional DDA technique. We have shown how parameter t_1, the transmission along one of the equivalent diattenuator axis, informs about both the linear degree of polarization and the polarizance of the system. In addition,the diphase introduced by the system in the incident light components appear when we apply the PDT method.

Finally, we must point out that, although we have applied the PDT method to a simple system for the sake of a good comparison, it can be applied to other geometries, no matter its complexity. The sixteen elements of the Mueller Matrix can be reduced to a smaller number of independent ones, never higher than nine. The same number that the PDT method requires as a maximum. These nine parameters are easy to use and also represent magnitudes of simple virtual elements which improve the understanding of the processes involved in complex scattering systems.

Acknowledgments

This research has been supported by the Ministry of Education of Spain under project #FIS2007-60158. The authors thankfully acknowledge the computer resources provided by the Spanish Supercomputing Network (RES) node at Universidad de Cantabria. P. Albella wants to express his gratitude to the Ministry of Education for his FPI grant.

References

[1] H. C. van de Hulst, *Light Scattering by Small Particles* (New York: Dover Publications, Inc., 1981)

[2] C. F. Bohren and D. R. Huffman, *Absorption and Scattering of Light by Small Particles* (New York Wiley, 1983)

[3] J. M. Saiz, J. L. de la Peña, F. González and F. Moreno, “Detection and recognition of local defects in 1D structures,” *Opt. Comms.* 196, (2001), 33-39.

[4] P. Albella, F. Moreno, J.M. Saiz and F. González, “Backscattering of metallic microstructures with small defects located on flat substrates,” *Opt. Express* 15, (2007), 6857-6867.

[5] D. Guirado, J.W. Hovenier and F. Moreno, “Circular polarization of light scattered by asymmetrical particles,” *Journal of Quantitative Spectroscopy and Radiative Transfer* 106, (2007), 63-73.

[6] Gorden Videen and William S. Bickel, “Light-scattering Mueller matrix for a rough fiber,” *Applied Optics* 31, (1992), 3488.

[7] J. J. Gil, “Polarimetric characterization of light and media,” *The European Physical Journal Applied Physics* 40 (2007), 1-47.

[8] Draine, B.T., and Flatau, P.J. (2004), http://arxiv.org/abs/astro-ph/0409262v2.

[9] Shih-Yau Lu and Russell A. Chipman, “Mueller matrices and the degree of polarization,” *Opt. Comm* 146, no. 1-6 (1998), 11-14.

Surface Roughness of Birefringent Slab Alters the Intensity of Light Transmitted Along Orthogonal Directions in the Medium

Sergey N.Savenkov,[1] Ranjan S. Muttiah,[2] Yevgeny A. Oberemok,[1] Viktor V. Yakubchak[1]

[1] *Taras Shevchenko Kiev National University, Department of Radiophysics, 64, Volodymyrska street, 01033 Kyiv, Ukraine, e-mail: sns@univ.kiev.ua*
[2] *Alan Plummer & Associates, 1320 South University Drive, Suite 300, Fort Worth, Texas 76118*

Abstract

We use the Mueller matrix model of inhomogeneous linear birefringent medium in single scattering case derived in previous paper (JQSRT, 106, pp. 475-486, 2007) to study light transmission as a function of the propagation direction in the medium. We show that an inhomogeneous linear birefringent medium can exhibit dichroic behavior depending on direction of propagation of input light. Additionally, we have observed the phenomena of enhancement of the scattered light intensity for input unpolarized light propagated orthogonally to the optical axes relative to one propagated parallel to the optical axes in the medium.

1 Introduction

The geometry of optical problem is shown in Fig. 1. The object is a plane-parallel anisotropic slab, located in a plane defined by $z = 0$. Inhomogeneity of the slab is specified by random variation of its thickness $h(\boldsymbol{\rho})$. Thus, light impinging normally on the slab undergoes single scattering.

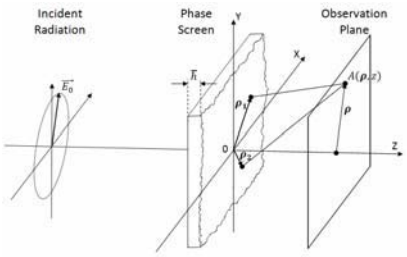

Figure 1: Geometry of light scattering from a slab with roughness $h(\boldsymbol{\rho})$.

The statistical description of the radiation that propagates beyond the slab's surface is determined by the random phase due to surface roughness. Specifically, we assume that the thickness distribution is described by a uniform Gaussian process:

$$f(h) = \left(2\pi\sigma_h^2\right)^{-1/2} \exp\left[-\left(h-\bar{h}\right)^2 / 2\sigma_h^2\right], \tag{1}$$

where, mean thickness is $\bar{h}$, mean-square deviation is σ_h. The correlation coefficient between any two points on the surface of the slab has exponential form:

$$\gamma_h(\boldsymbol{\rho}_-) = \frac{\overline{h(\boldsymbol{\rho}_1)\cdot h(\boldsymbol{\rho}_2)}}{\sigma_h^2} = \exp\left(-\frac{\boldsymbol{\rho}_-^2}{\rho_0^2}\right), \tag{2}$$

where, the distance between the points is $\boldsymbol{\rho}_- = \boldsymbol{\rho}_2 - \boldsymbol{\rho}_1$ (see Fig. 1), and the correlation radius is ρ_0.

The anisotropy of the slab is completely described by the spectrum of the matrix which describes the slab, i.e., by polarization eigenstates and the corresponding eigenvalues [1]. The interaction of radiation with such medium is described by the Jones matrix written in the medium's eigencoordinate system (xoy):

$$\mathbf{J}^{eigen} = \begin{pmatrix} \exp(-i\phi_x) & 0 \\ 0 & \exp(-i\phi_y) \end{pmatrix} = \begin{pmatrix} g_x & 0 \\ 0 & g_y \end{pmatrix} \tag{3}$$

The eigenvalues $g_{x,y}$ are the complex transmittance coefficients of radiation, with polarizations that are determined by the medium's eigenpolarizations. For the rest of our paper, when we use the term "eigen" it denotes the eigencoordinate system built on the medium's eigenpolarizations.

It is known [1] that for a medium characterized by linear birefringence, eigenpolarizations are orthogonal, and linear. Here, we consider the "fast" eigenpolarization on the basis vector x. We assume that the field distribution of the incident radiation is Gaussian in the plane normal to light propagation direction, with the waist of the beam located in plane $z = 0$:

$$\mathbf{E}^{in}(\boldsymbol{\rho}) = \mathbf{E}^{in} \exp(-\boldsymbol{\rho}^2 / a^2), \tag{4}$$

where, $\mathbf{E}^{in}$ denotes Jones vector in the centre of the light beam, and a is the light beam's radius.

After performing mathematics similar to [2], the Mueller matrix in the far zone for inhomogeneous medium with linear birefringence in the eigencoordinate system is:

$$\mathbf{M}^{eigen} = \begin{pmatrix} \Phi_{11}+\Phi_{22} & \Phi_{11}-\Phi_{22} & 0 & 0 \\ \Phi_{11}-\Phi_{22} & \Phi_{11}+\Phi_{22} & 0 & 0 \\ 0 & 0 & \Phi_{12}+\Phi_{21} & i(\Phi_{12}-\Phi_{21}) \\ 0 & 0 & -i(\Phi_{12}-\Phi_{21}) & \Phi_{12}+\Phi_{21} \end{pmatrix}, \tag{5}$$

where,

$$\Phi_{xy} = \Phi_{xy}^{brf}\left((1-\eta_{xy}) \exp\left\{ -\left(\frac{k\boldsymbol{\rho} w}{2z} \right)^2 \right\} + \frac{\eta_{xy}}{\sigma_{xy}^2 w^2 + 1} \exp\left\{ -\frac{1}{\sigma_{xy}^2 w^2 + 1} \left(\frac{k\boldsymbol{\rho} w}{2z} \right)^2 \right\} \right); \tag{6a}$$

$$\Phi_{xy}^{\mathrm{brf}} = \exp\left(ik(n_o - n_e)\bar{h} - k^2 \sigma_h^2 (n_o - n_e)^2 / 2 \right); \tag{6b}$$

$$w = a\left(1 + 4z^2 / a^4 k^2\right)^{1/2}; \tag{6c}$$

$$\sigma_{xy}^2 = k^2 \sigma_h^2 (n_o - 1)(n_e - 1); \tag{6d}$$

$$\eta_{xy} = 1 - \exp(-\sigma_{xy}^2). \tag{6e}$$

2 Simulation results and discussion

Using the matrix model Eq.(5), we examined the features of the transmitted light from inhomogeneous birefringent medium as function of propagation direction for calcite $CaCO_3$. The analysis was carried out for the light propagation direction ranging from 0^0 (parallel to the optical axes) to 90^0 (orthogonal to the optical axes). The geometry for the numerical experiment was as in Fig.1 with slab which is cut in each

numerical experiment orthogonally to the correspondent propagation direction in crystal. Thickness of the slab set to $100\ \mu m$. Wavelength of light was assumed to be $\lambda = 0.63\ \mu m$.

Fig. 2 demonstrates the dependencies of the matrix elements m_{ij} on inhomogeneity σ_h for four directions: 0^0, 25^0, 45^0, 90^0.

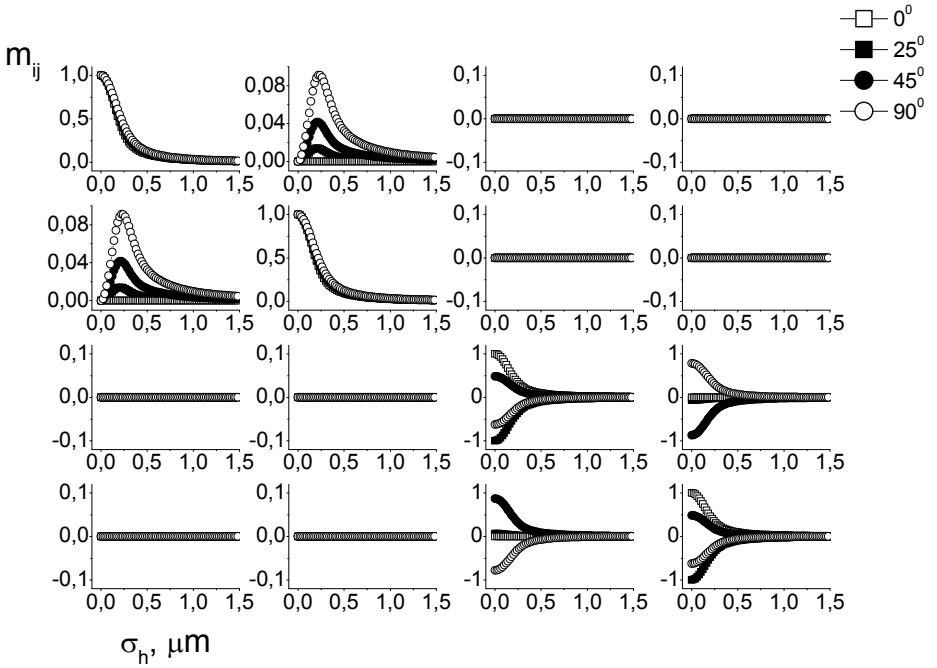

Fig. 2: Dependences of the elements m_{ij} on the value of inhomogeneity.

It can be seen at directions 25^0, 45^0, 90^0 as $\sigma_h \to 0$ perfect phase plates are obtained (with corresponding values of phase shifts). And as expected at direction 0^0, we have an isotropic rough plate for all values of inhomogeneity. While for the case $\sigma_h \neq 0$, at directions of propagation 25^0, 45^0, 90^0, the matrix elements m_{12} and m_{21} are not equal to zero implying the slab exhibits dichroism, i.e. there is dependence of the intensity of scattered light on input polarization. Dichroism is maximum at direction of propagation 90^0 which is orthogonal to optical axes. From Eq (6) it is note worthy that depending on the value of difference of refractive indexes, the matrix Eq.(5) can become singular.

It is interesting to note that there is a difference in behavior of the matrix element m_{11} for different directions of propagation depending on inhomogeneity as presented in Fig. 3a and 3b. From Fig.3b, the difference has its maximum at approximately $\sigma_h = 0.25\ \mu m$. We interpret this to mean that within inhomogeneities dictated by σ_h < 0.5 μm, the slab "enhances" unpolarized light intensity when light propagates orthogonal to the optical axes relative to propagation parallel to the optical axes. To elucidate the physical reasons for this "enhancement" effect, Fig.4 presents the dependences of the intensity of output light for unpolarized input light (the value of m_{11}) for propagation direction 0^0 and 90^0 on observation angle (Fig.1) for peak "enhancement" at roughness value σ_h = 0.25 μm.

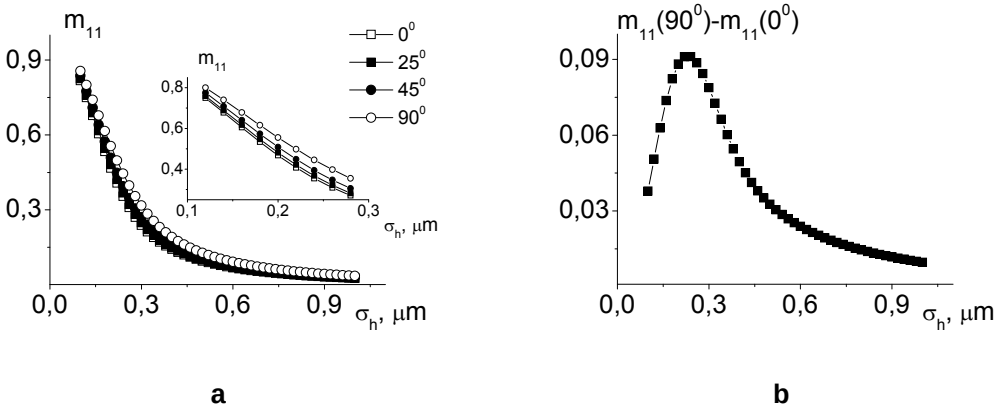

Figure 3: Dependences of the element m_{11} on the value of inhomogeteity.

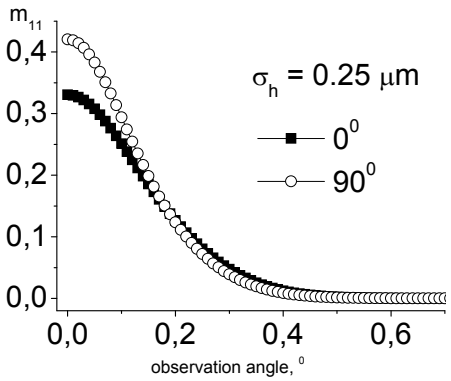

Figure 4: Dependence of the element m_{11} on the observation angle.

Thus, the “enhancement” phenomena presented in Fig.3 results from that the value of m_{11} is a function of the difference in refractive indices of the medium and depends on observation angle (see Fig.1).

References

[1] Ch. Brosseau, *Fundamentals of polarized light* (North-Holland Publishing Company, New York, 1998).

[2] S. N. Savenkov, R. S. Muttiah, K. E. Yushtin, S. A. Volchkov, Mueller-matrix model of an inhomogeneous linear birefringent medium: Single scattering case,” JQSRT **106**, 475-486 (2007)

T-matrix method for biaxial anisotropic particles

Vladimir Schmidt,[1] Thomas Wriedt,[1]

[1] *Bremen Universität, Institut für Werkstofftechnik,*
Badgasteiner Str. 3, 28359 Bremen, Germany
tel: +49 (421) 218-5418, fax: +49 (421) 218-3912, e-mail: vschmidt@iwt.uni-bremen.de

Abstract

Using the T-matrix approach light scattering simulation for biaxial anisotropic non-axisymmetric particles is studied. For the expansion of the electromagnetic field inside the scatterer the basis of quasi-spherical vector wave functions is used that is obtained by inverse Fourier transformation. The calculation results obtained have been compared with results from others light scattering programs such as DDSCAT and ADDA.

1 Introduction

Simulation of optical properties of anisotropic scatterers is very important in different scientific and technology applications. Many industrial materials are anisotropic. Such particles can be found for example as white pigments in paper and color pigments in paint.

A modern and effective numerical tool for exactly solving the scattering problem is the T-matrix approach [1]. At the present time light scattering by anisotropic (permittivity ε and/or permeability μ are tensors) or chiral particles can be simulated by different approximate methods: Discrete Dipole Approximation [2], Methods of Moments [3] and General Multipole Technique [4]. The T-matrix approach is used for very accurate calculations and for the determination of the applicability of various approximations, but it has been applied almost exclusively to isotropic scatterers. Thus the developments of effective light scattering simulation methods for non-axisymmetric anisotropic particles using a T-matrix approach are very important.

T-matrix solutions for anisotropic scatterers are mostly obtained for simple shapes such as uniaxial anisotropic spheres [5], ellipsoids [6] or bianisotropic spheres [7,8]. Liu et al. [9] solved the electromagnetic fields in a rotationally uniaxial medium by using the Separation of Variables Method and used the T-matrix method to solve the scattering problem. In [10] the electromagnetic fields problem is solved in a general bianisotropic medium. Doicu [11] has obtained quasi-spherical vector wave functions (qSVWF) in the case of an anisotropic medium using inverse Fourier transform. The particular solution of the light scattering problem using the T-matrix approach for uniaxial anisotropic (permittivity tensor has $\varepsilon_x=\varepsilon_y$) non-axisymmetric particles is also given in [11].

In this work we extended Doicu's approach [11] to biaxial anisotropic non-axisymmetric particles. Parallelized Fortran code using OpenMP technology for calculating the T-matrix was developed. Convergence of the developed program and comparison of simulation results with other light scattering programs such as DDSCAT [2,12] and ADDA [13,14] are considered.

2 T-matrix approach for biaxial anisotropic medium

The electromagnetic fields in the anisotropic medium are characterized by the stationary Maxwell equations

$$\nabla\times\mathbf{E} = ik\mathbf{B}, \quad \nabla\times\mathbf{H} = -ik\mathbf{D}, \quad k = \omega/c,$$
$$\nabla\cdot\mathbf{B} = 0, \quad \nabla\cdot\mathbf{D} = 0,$$

and the constitutive relations

$$\mathbf{E} = \varepsilon\mathbf{D}, \quad \mathbf{H} = \mu\mathbf{B},$$

where ε – electric permittivity and μ – magnetic permeability tensors. Here we consider the biaxial anisotropic case, in which the permittivity tensor is diagonal and has three different complex components

$$\varepsilon = \begin{pmatrix} \varepsilon_x & 0 & 0 \\ 0 & \varepsilon_y & 0 \\ 0 & 0 & \varepsilon_z \end{pmatrix}, \ \mu = const \ .$$

In general a permittivity tensor can be transformed into this representation by a rotation of the coordinate system. Particularly, this is possible for real-valued permittivity.

In the isotropic case (ε and μ are constants) the T-matrix method is based on an expansion of the total electromagnetic field by spherical vector wave functions (SVWF)

$$M_{mn}^{(i)}(k\mathbf{r}) = \nabla \times [\mathbf{r}\psi_{mn}^{(i)}(k\mathbf{r})], \quad N_{mn}^{(i)}(k\mathbf{r}) = \nabla \times \nabla \times [\mathbf{r}\psi_{mn}^{(i)}(k\mathbf{r})], \quad i \in \{1,3\},$$

where $\psi_{mn}^{(i)}(k\mathbf{r})$ - scalar Helmholz equation solutions containing Bessel or Hankel functions, k - wave number in the medium. In the case of an anisotropic scatterer another basis inside the scatterer is required. This problem is equal to the expansion of the unbounded dyadic Green function by eigenfunctions of the vector Helmholz equation in the anisotropic medium. We use the expansion by qSVWF obtained by Doicu [11]

$$X_{mn}^{e}(k\mathbf{r}), \ Y_{mn}^{e}(k\mathbf{r}), \ X_{mn}^{h}(k\mathbf{r}), \ Y_{mn}^{h}(k\mathbf{r}).$$

For the new basis the formulas of T-matrix calculations are similar to those in the "classical" isotropic case, except that SVWF functions in surface integrals of the Q and RegQ matrices will be exchanged by functions of the new basis.

3 Parallelized code with OpenMP

For the new basis functions it is required to solve the Fourier transform or to calculate two-dimensional integrals over the unit sphere for each point. This makes calculations two times more intensive than in the isotropic case. One effective method to accelerate the program is using parallelism paradigm. There are two well known standards for parallelization of programs: OpenMP, which is mostly used on shared memory systems (multi-processors computers), and MPI, which is mostly used on distributed memory systems (computer clusters). It is difficult to say whether OpenMP or MPI is better. Both have their advantages and disadvantages. We use OpenMP, because it is more convenient and doesn't require modifications for the non-parallel mode.

For the parallelization of the integration process of the Q and RegQ matrixes elements on a computer with *N* processors we divide the particle surface into *N* areas, provide integration separately for each area and then collect the results. We also modified the LU decomposition algorithm for solving of T-matrix linear equation using OpenMP technology. The efficiency of the parallelization $E = I_1/(n \cdot I_n)$, where I_k is the calculation time on a computer with *K* processors, is presented in Fig. 1.

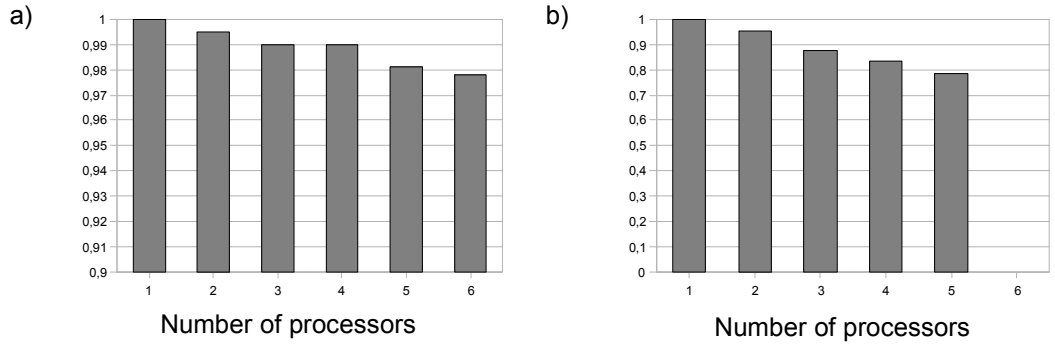

Figure 1: The efficiency of the parallelization of the T-matrix code for biaxial anisotropic particles: a) calculation of Q and RegQ matrixes, b) solving linear equation for matrix T. The size of the T-matrix is bounded by N_{rank}=10, M_{rank}=10, the number of integration points is 50x50.

4 Comparison with DDA

To check our program we compared the simulation results with those obtained from other light scattering programs such as DDSCAT, ADDA. There is good congruence for non-imaginary anisotropic refractive indices as well for imaginary anisotropic refractive indices. There are some small differences in the case of a complex refractive index and for a non-cubic shape. This can be explained by approximation errors for the scatterer volume in the DDA approach.

The comparison of the differential scattering cross sections (DSCS) for biaxial anisotropic cubes and ellipsoidal particles using the T-matrix approach, DDSCAT and ADDA are presented in Fig. 2. The simulation accuracy (absolute change of results by decreasing one parameter of N_{rank}, M_{rank}, N_{theta}, N_{phi} by one) is less than 10^{-4}. The number of points for integration on the ellipsoidal particle surface is N_{theta} x N_{phi} = 55 x 22, the T-matrix is truncated at N_{rank}=9, M_{rank}=7. For cubes these parameters are N_{theta} x N_{phi} = 18 x 18, N_{rank}=11, M_{rank}=9. For the DDA programs the corresponding parameters are the box dimension for the cubic particle 30x30x30 and for the spheroidal particle 30x30x60. In this case, holding of conservative criterion by $|m|2\pi d/\lambda = 0.5$ [2], where m – refractive index, d – dipole box size, λ – wave length, guarantees calculation accuracy less than 1%.

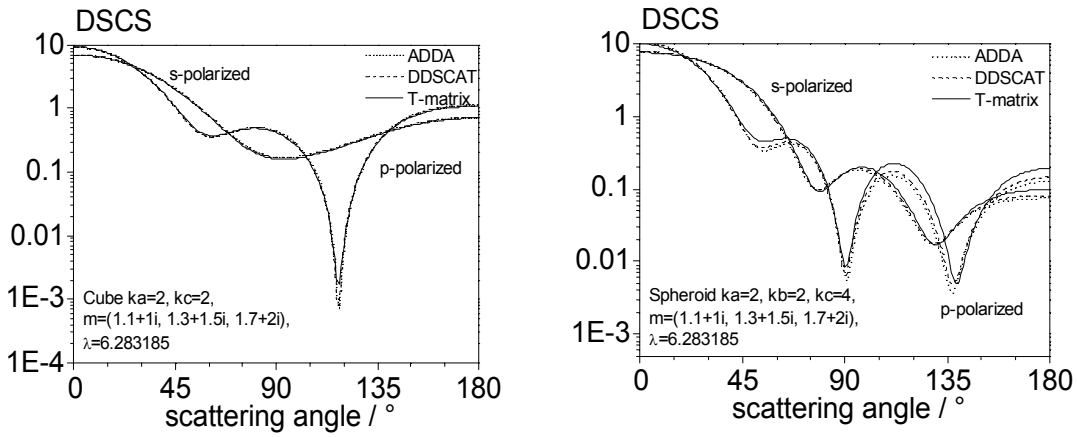

Figure 2: Comparison results of calculation of DSCS for different scattering theory programs: a) cubic particle, b) prolate spheroidal particle, $k = 2\pi/\lambda$ – wave number, a, b, c – semiaxes of corresponding shape.

5 Conclusion

The T-matrix approach has been applied to biaxial anisotropic non-axisymmetric scatterers. A parallelized Fortran code using OpenMP technology for calculating the T-matrix was developed. The efficiency of the parallelization of the developed algorithm for anisotropic particles is sufficiently high. The comparison of simulation results to those using scattering programs based on DDA approach show good congruence.

Acknowledgments

We would like to acknowledge support of this work by Deutsche Forschungsgemeinschaft (DFG).

References

[1] Waterman P.C., “Symmetry, unitary and geometry in electromagnetic scattering,” Phys. Rev. D **3**, 825–839 (1971).

[2] Draine B., Flatau P., “Discrete-dipole approximation for scattering calculations,” J. Opt. Soc. Am. A. **11**, 1491–1499 (1994).

[3] Graglia R.D., Uslenghi P.L.E., Zich R.S., “Moment method with isoparametric elements for three dimensional anisotropic scatterers,” Proc. IEEE **77**, 750–60 (1989).

[4] Piller N.B., Martin O.J.F., “Extension of the generalized multipole technique to the three-dimensional anisotropic scatterers,” Opt. Lett. **23**, 579–81 (1998).

[5] Wong K.-L., Chen H., “Electromagnetic scattering by a uniaxially anisotropic sphere,” IEE Proceedings Microw., Antennas and Propag. **139**, 314–318 (1992).

[6] Papadakis S.N., Uzunoglu N.K., Capsalis C.N., “Scattering of a plane wave by a general anisotropic dielectric ellipsoid,” J. Opt. Soc. Am. A **7**, 991–997 (1990).

[7] Chen H. et al. “The scattering properties of anisotropic dielectric spheres on electromagnetic waves,” Journal of Physics: Condensed Matter **16**, 165–179 (2004).

[8] Stout B., Neviere M., Popov P., “T matrix of the homogeneous anisotropic sphere: applications to orientation-averaged resonant scattering,” J. Opt. Soc. Am. A **24**, 1120–1130 (2007).

[9] Liu S. et al., “Scattering by an arbitrarily shaped rotationally uniaxial anisotropic object: electromagnetic fields and dyadic green’s functions,” PIER **29**, 87–106 (2000).

[10] Tan E.L., Tan S.Y., “On the eigenfunction expansions of the dyadic green’s functions for bianisotropic media,” PIER **20**, 227–247 (1998).

[11] Doicu A., “Null-field method to electromagnetic scattering from uniaxial anisotropic particles,” Optics Comm. **218**, 11–17 (2003).

[12] http://www.astro.princeton.edu/~draine/DDSCAT.html (1 Juni 2008).

[13] Yurkin M.A., Hoekstra A.G., “The discrete dipole approximation: An overview and recent developments,” JQSRT **106**, 558–589 (2007).

[14] http://www.science.uva.nl/research/scs/Software/adda/index.html (1 Juni 2008).

Light scattering by systems of particles. Mutual shielding of particles in the near field

V. P. Tishkovets

Institute of Radio Astronomy of NASU, 4 Chervonopraporna St., Kharkiv, 61002, Ukraine,

e-mail: tishkovets@ri.kharkov.ua

Abstract

One of the manifestations of the near field is a mutual shielding of particles. For simple clusters, consisting of two identical spherical particles (bisphere), the mutual shielding leads to reducing of the intensity of light scattered along the axis of the bisphere. Calculations of the intensity of light scattered by randomly oriented clusters of spherical particles show that for the model ignoring the near field the intensity is significantly larger than for the model with the near field taken into account.

1 Introduction

The classical radiative transfer equation (RTE), which is widely used in many areas of science, may be inapplicable to densely packed random media since the derivation of this equation from the Maxwell equations is explicitly based on the assumption that the scatterers are located in the far-field zones of each other [1]. In this assumption, a number of important peculiarities of light scattering by densely packed scatterers are ignored. In particular, the RTE does not take into account the near field. (In the literature the near field is associated with a field, which amplitude decreases more rapidly than r^{-1}, where r is a distance to a scatterer [2].) Up to now, the influence of the near field on the scattering properties of densely packed media has not been studied adequately. In this paper, the mutual shielding of particles as a phenomenon related to the near field is considered.

2 Shielding of particles by each other in the near field

The mutual shielding of particles can play a significant role when distances between particles of a medium are comparable to their sizes. For particle sizes exceeding the wavelength, this phenomenon is similar to the shadowing as described in [3]. But this phenomenon also reveal itself in systems of particles with sizes much less than the wavelength. Let us consider qualitatively the peculiarities of light scattering by a pair of closely located scatterers of small sizes as compared to the wavelength, which are polarized as dipoles in the external field. Fig.1 shows two pairs of such scatterers illuminated by the external field $\mathbf{E}^{(0)}$, and configuration of charges induced in them. Scatterers are located in the scattering plane (in the picture plane), and the incident radiation is polarized in the scattering plane too. In Fig.1a configuration of charges is shown for the case when the particles do not interact in the near (electrostatic) field. In such configuration of charges the intensity of light scattered by particles along the line *AB* passing through their centers differs from zero. Fig.1b shows the configuration of charges in the scatterers interacting in the electrostatic field. In this case the intensity of light scattered along the line *AB* is equal to zero. In other words, implication of the near field leads to "shielding" of the scatterers by one another in the direction passing through their centers.

Of course, a contribution of the near field in Fig.1b is exaggerated. Angular dependencies of the intensity of scattered light by a pair of identical small scatterers in contact (bisphere) are shown in Fig.2. The size parameter of particles is $X=0.01$, and the refractive index is $m=10.0+i0$. Scatterers are located in the xz plane, and the angle between the z-axis and the axis of the bisphere is 45^0. The scattering angle is measured in the xz plane from the z-axis in the direction of the positive values of x (clockwise in the picture). The dashed curves correspond to the model ignoring the near field components, and the

continuous curves correspond to the model considering the near field. The thick and thin curves correspond to the incident light polarized in the scattering plane and in the perpendicular plane, respectively.

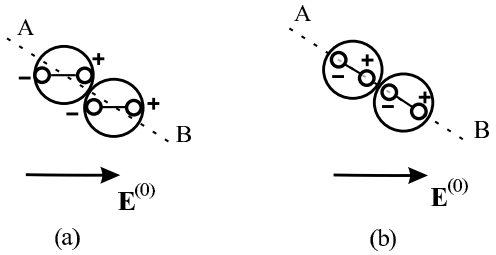

Figure 1: The scheme explaining "shielding" of small scatterers (dipoles) in the near field. The line *AB* passes through the centers of scatterers. If the interaction of the induced charges is ignored, intensity of light scattered by particles along this line differs from zero (a). Intensity of light scattered along the line *AB* by particles interacting in the near field is equal to zero (b)

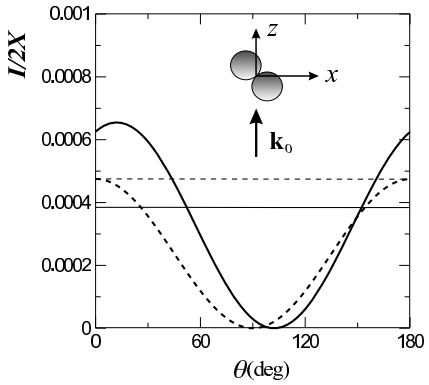

Figure 2: Intensity of light scattered by a bisphere versus scattering angle.

As is seen from the plot, dependence of the intensity on the scattering angle in the model ignoring the near field components is identical to that for a spherical particle in the Rayleigh limit. In the model considering the near field, intensity of light scattered in directions $\theta=0$ and $\theta=180^0$ strongly depends on polarization of the incident light. If the incident light is polarized in the scattering plane, intensity of the scattered light in these directions is much higher than in the previous model. This phenomenon is caused by substantial increase of the dipole moments because of electrostatic interaction of scatterers (Fig.1b). The minimum of the intensity is located at $\theta=105^0$ while the schematic representation in Fig.1b predicts it to be at $\theta=135^0$. At the interval of scattering angles of $100^0<\theta<160^0$, the intensity in the model considering the near field is appreciably less than that in the model ignoring the near field. This diminution of the intensity is caused by "shielding" of scatterers illustrated qualitatively by Fig.1b.

In the previous example the near field is the electrostatic field. Shielding of scatterers arising in the electromagnetic interaction of scatterers with sizes comparable to the wavelength is considered in the following examples. Figures 3a and 3b show the intensity of light scattered by bispheres as a function of the scattering angle. The axis of the bispheres is perpendicular to the direction of propagation of the incident unpolarized light indicated by the wave vector $\mathbf{k}_0$. The size parameter of the constituent particles of bispheres is $X=k_0a=4.0$, where a is the radius of the constituent particles, and their refractive index is $m=1.32+i0.05$. The scattering plane is the picture plane. Two cases of orientation of the bispheres with respect to the scattering plane are considered. (Orientation of bispheres is shown in the right upper

corners of Figs.3a and 3b.) The solid and dashed curves correspond to calculations with the near field components taken into account and ignoring them, respectively.

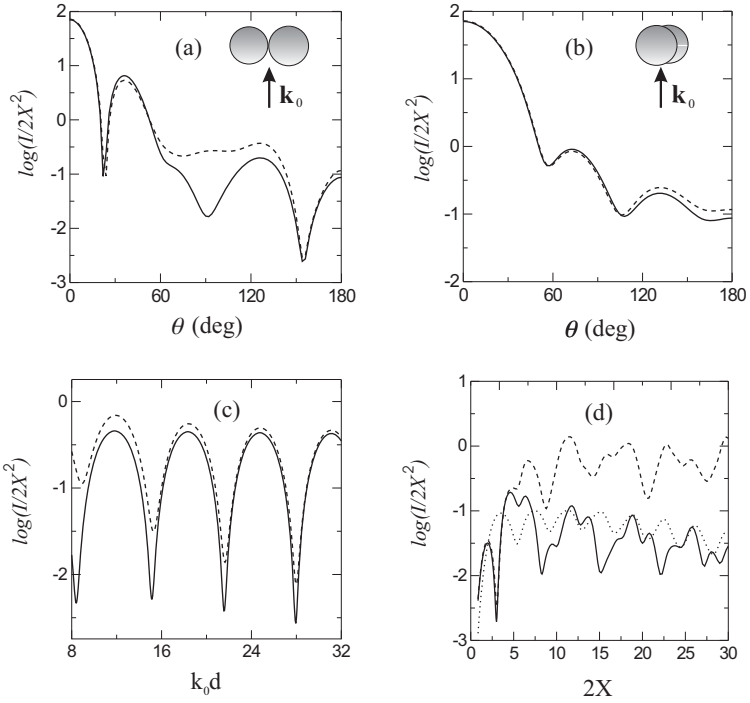

Figure 3: Intensity of light scattered by bispheres versus scattering angle (a, b). The models calculated with the near field components taken into account (continuous curves) and without them (dashed curves) are presented. The constituent particles of the bisphere are in the scattering plane (in the picture plane) (a) and in the perpendicular plane (b). For the orientation (a), intensity of light scattered in the direction of the bisphere axis is shown as a function of distance k_0d between the particles in the plot (c).

The dependence of the intensity of light scattered in the direction of the bisphere axis on the distance between the particles is shown in Fig.3c. As can be seen from the plot, the difference between the models is noticeable up to the distances of about several diameters of the particles. Fig.3d demonstrates the dependence of the intensity of light scattered along the axis of the bisphere with touching components versus size of the components. The dotted line corresponds to the intensity of light scattered at $\vartheta = 90^0$ by a single sphere.

The shielding phenomenon for more complex randomly oriented clusters of spherical particles is considered below. Clusters of identical particles were generated according to the procedure described in [4]. The generated clusters consisting of *50*, *100* and *200* particles are shown in Fig.4. The size parameter of the constituent particles of the clusters is $X=1.5$. The packing density of the clusters is $\xi=N(X/X_0)^3=0.2$, where N is the number of particles in the cluster, $X_0=k_0a_0$, and a_0 is the radius of the smallest circumscribing sphere of the cluster. The intensity of scattered light by these clusters is shown in Fig. 5. As is seen from Fig.5, ignoring of the near field results in a significant increase of the intensity of light scattered by the clusters at all scattering angles. A behavior of the intensity at $\theta>60^0$ attracts a particular attention. For this angle range, the intensity weakly depends on the number of particles N in the models containing the near field. Since the intensity is normalized to the unit of the cross section area of the clusters (more precisely, it is divided by a quantity X_0^2), this behavior of the intensity implies that in this range of scattering angles the intensity is determined mainly by the particles of the upper layer of the clusters. Other particles of the clusters are shielded by the particles of the upper layer. If the near field is ignored, the particles do not shield each other and a large number of particles is involved into multiple

scattering. This results in an increase of contribution from multiple scattering, which, in turn, leads to the much higher intensity of the scattered light in comparison with the models considering the interaction of particles in the near field. For the same reason, in the models ignoring the near field, the intensity depends on the number of particles more significantly.

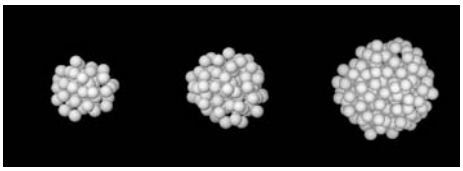

Figure 4: Clusters of 50, 100 and 200 identical spherical particles. For $X=1.5$ the size parameters X_0 of the smallest circumscribing spheres of clusters are 9.25, 11.9 and 14.7, respectively.

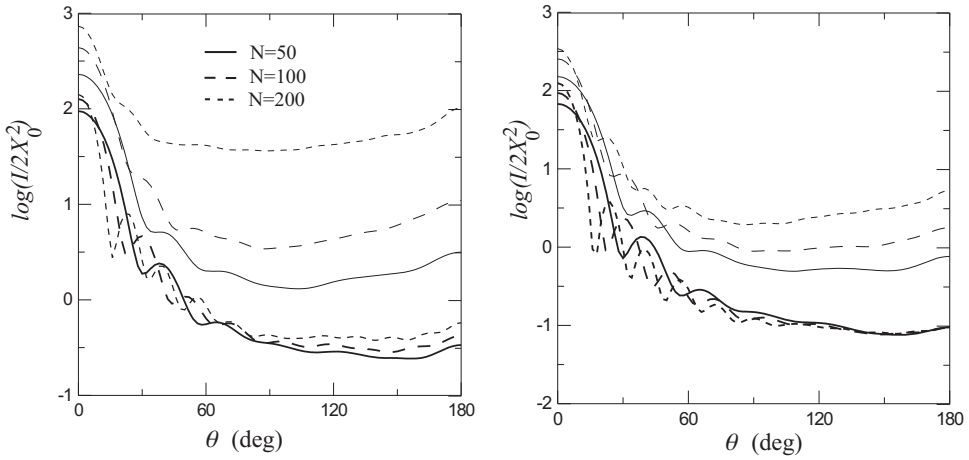

Figure 5: Intensity of light scattered by randomly oriented clusters. The models ignoring the near field (thin lines) produce substantially larger intensity than those taking the near field into account (thick lines). The numbers of particles in the clusters corresponding to the curve types are indicated in the plot. The refractive index of particles is $m=1.5+i0.001$ (left plot) and $m=1.5+i0.1$ (right plot).

References

[1] M. I. Mishchenko, L.D. Travis, and A.A Lacis. *Multiple Scattering of Light by Particles. Radiative Transfer and Coherent Backscattering.* (Cambridge University Press, Cambridge, 2006).

[2] J.-J. Greffet, and R. Carminati, R. “Image formation in near-field optics.” Progr. Surface Sci. **56**, 133-237. (1998).

[3] M. I. Mishchenko, J. W. Hovenier, and D. W. Mackowski. “Single scattering by a small volume element.” JOSA A. **21**, 71-87. (2004).

[4] D. W. Mackowski. “Electrostatics analysis of sphere clusters in the Rayleigh limit: application to soot particles.” Appl Opt. **34,** 3535-3545. (1995).

Angular-scattering, negative-polarization and intensity-enhancement studies of spheroids

Jani Tyynelä,[1,2] Evgenij Zubko,[3,4] Karri Muinonen[1] and Gorden Videen,[5]

[1] *Observatory, P.O. Box 14, FI-00014 University of Helsinki, Finland*
[2] *Department of Physics, P.O. Box 64, FI-00014, University of Helsinki, Finland*
[3] *Center for Atmospheric and Oceanic Studies, Graduate School of Science, Tohoku University, Aoba, Aramakiaza, Aoba-ku, Sendai 980-8578, Japan*
[4] *Astronomical Institute, Kharkov National University, 35 Sumskaya Street, Kharkov, 61022, Ukraine*
[5] *Army Research Laboratory, CI-ES, 2800 Powder Mill Road, Adelphi, Maryland 20783, U.S.A.*
email: jktyynel@mappi.helsinki.fi

Abstract

We study how the internal electric field of oriented spheroids affects the scattered far field. The internal fields have been computed for both oblate and prolate spheroids in a fixed orientation with the incident wave propagating along the symmetry axis in order to study how the deviation from a spherical shape affects both the longitudinal and transverse components of the internal field. We plan to develop a method to analyze the interference inside particles in a general way.

1 Introduction

We study the angular-scattering characteristics and the interrelationship of the internal electric field to the scattered far-field for oriented spheroids. Mechanisms responsible for both the negative polarization branch (NPB) and the intensity enhancement branch (IEB) of single particles have been suggested by, e.g., Muinonen *et al.* [1] and studied for both spherical particles and Gaussian-random-sphere particles by Tyynelä *et al.* [2, 3]. In parallel studies, Zubko *et al.* [4] used phase randomization for single dipoles to investigate interference effects inside irregularly shaped particles.

At least for single particles, the role of the internal electric field in producing far-field scattering characteristics like negative polarization and intensity enhancement near the backward-scattering direction seems to have a two-part mechanism. The longitudinal component, i.e. the component of the internal field parallel to the direction of propagation, seems to affect the overall scattering characteristics at mid-range scattering angles and has little effect near the forward- and backward-scattering directions. This is attributed to the fact that the longitudinal component of the internal field has an odd parity with respect to the central plane perpendicular to the incident polarization.

The transverse component, i.e., the component perpendicular to the direction of propagation, affects the scattering characteristics at all scattering angles, but dominates the longitudinal component close to the backward- and forward-scattering directions, where the contribution from the longitudinal component tends toward zero. The component of the internal field parallel to the incident polarization has an even parity with respect to both the central plane perpendicular to the incident polarization and the central plane defined by the incident polarization and the direction of propagation. The IEB can arise, for example, from constructive interference between the opposing parts of the particle interior with respect to the plane defined by the incident polarization and the direction of propagation near the backward-scattering direction. The NPB arises from the asymmetry of the transverse component. The internal field is structured in a wavelike pattern with alternating maxima and minima, which is analogous to the idea of incident wavefronts refracting into the particle medium, propagating in opposite directions inside the particle, and interfering with each other.

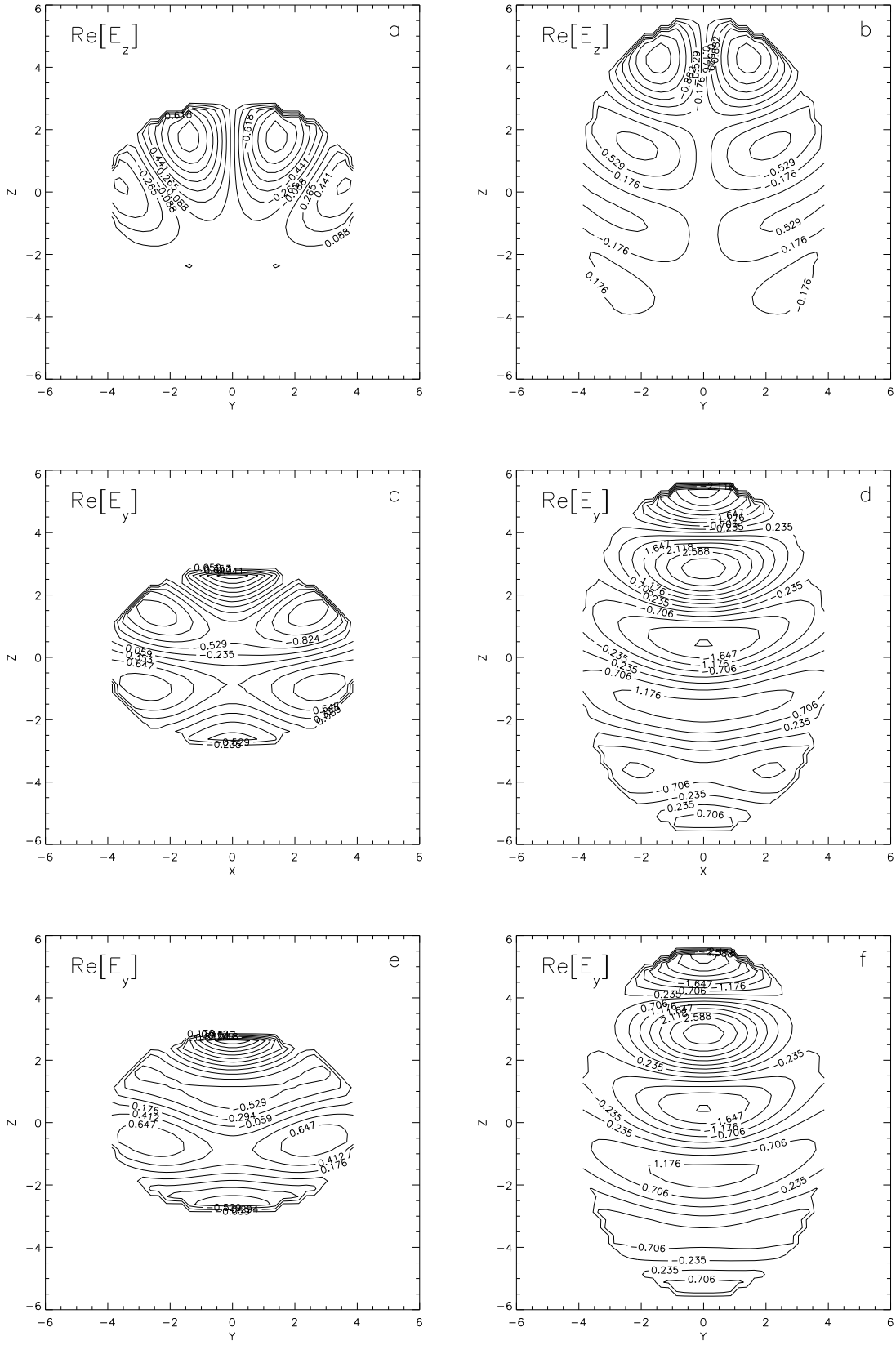

Figure 1: We plot the real part of the Z-component of the internal electric field in the YZ-plane for $c/a = 0.71$ (a) and $c/a = 1.40$ (b). We also plot the real part of the Y-component in the XZ-plane for $c/a = 1/1.4$ (c) and $c/a = 1.40$ (d). Finally, we plot the real part of the Y-component in the YZ-plane for $c/a = 1/1.4$ (e) and $c/a = 1.4$ (f). The incident electromagnetic wave is Y-polarized and propagating in the positive Z-direction. The size parameter is $x = 4$ and the refractive index is $m = 1.55$.

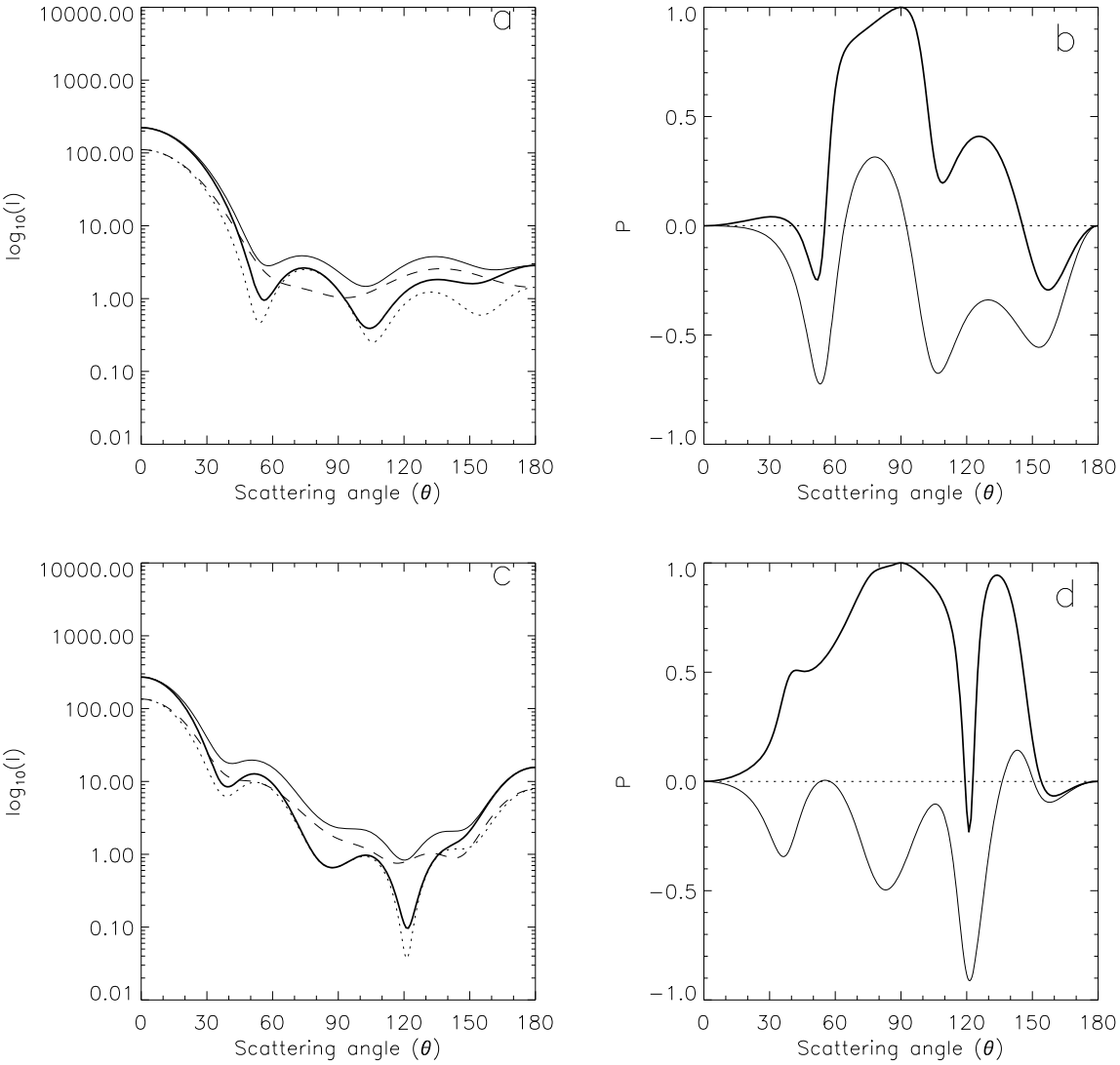

Figure 2: On the left, we plot the parallel intensity $I_{\|}$ (dashed line) and the perpendicular intensity $I_{\perp}$ (dotted line), and also the total intensity $I_{\|} + I_{\perp}$ in the case of the unmodified internal field (thin solid line) and when $E_Z = 0$ (thick solid line). On the right, we plot $P = (I_{\perp} - I_{\|})/(I_{\perp} + I_{\|})$ in the case of the unmodified internal field (thin solid line) and when $E_Z = 0$ (thick solid line). The upper plots are for $c/a = 1/1.4$, and the lower plots are for $c/a = 1.4$. The size parameter is $x = 4$ and the refractive index is $m = 1.55$.

2 Discrete-dipole simulations

We use a fixed orientation with the incident wave propagating along the symmetry axis for the spheroids in order to study how the internal electric field is changed when deviating from the spherical shape. We consider aspect ratios $c/a = 1.05$, 1.1, 1.2, 1.4, 1/1.05, 1/1.1, 1/1.2, and 1/1.4, where c is the vertical axis, and a is the horizontal axis. We define size parameter $x = ka$, where k is the wavenumber, and consider $x = 4$ and 8. Refractive index $m = 1.55$. These parameters are chosen to be consistent with those in our previous studies.

The internal fields are obtained from the ADDA [5]. Two incident polarizations of the incident electromagnetic wave, one along the X-axis and the other along the Y-axis, are used both propagating along the positive Z-axis. Because of rotational symmetry and fixed orientation, only one

scattering plane, the YZ-plane, is used in the DDA computations. The size parameter grid for the internal field is $\Delta x \approx 0.25$. A computational grid of 32^3 dipoles was used in the simulations for $x = 4$, and a grid of 64^3 dipoles for $x = 8$.

3 Results and discussion

In Figs. 1a and 1b, we plot the longitudinal component in the YZ-plane when the incident wave is Y-polarized and propagating in the positive Z-direction, for an oblate ($c/a = 1/1.4$) and prolate ($c/a = 1.4$) spheroid, respectively. The size parameter is $x = 4$ and the refractive index is $m = 1.55$. The two maxima near the forward portion of the particle are clearly visible in both spheroids and separated by a distance nearly half a wavelength ($\Delta x \approx 3$) similar to spherical particles. These dominating maxima seem to be common to all the particles we have studied so far.

In Figs. 1c and 1d, the transverse electric-field component is plotted in the XZ-plane, and in Figs. 1e and 1f, in the YZ-plane for the same spheroids. For the prolate spheroid, the maxima and minima of the internal field are almost aligned along the propagation direction like a wavefront. There seems to be only some difference between the planes at the back part of the particle (Figs. 1e and 1f). For the oblate spheroid, the internal field is distinctively more different between the planes (Figs. 1c and 1e). There are two pairs of maxima separated roughly by half a wavelength, which tend to interfere constructively near the backward-scattering direction.

The parallel intensity $I_{\parallel}$, the perpendicular intensity $I_{\perp}$, the total intensity $I_{\parallel} + I_{\perp}$, and the degree of linear polarization $P = (I_{\perp} - I_{\parallel})/(I_{\perp} + I_{\parallel})$ are plotted in Figs. 2a and 2b for $c/a = 1/1.4$ and in Figs. 2c and 2d for $c/a = 1.4$. We show both the cases where the internal field is unmodified and when the longitudinal component is omitted. As can be seen, when omitting the longitudinal component, the negative polarization becomes totally positive in the mid-range scattering angles, but remains negative near the backward-scattering direction. The strong NPB for the oblate spheroid can be understood by the regular structure of the maxima in Fig. 1c. For the prolate spheroid, the NPB is weaker. It should be noted that the spheroids with sizes $x = 8$ also have very weak NPBs, especially when compared to spherical particles. This was also shown by Xie *et al.* [6].

References

[1] K. Muinonen, E. Zubko, J. Tyynelä, Yu. G. Shkuratov, and G. Videen, 'Light scattering by Gaussian random particles with discrete-dipole approximation," JQSRT 106, 360-377 (2007)

[2] J. Tyynelä, E. Zubko, G. Videen, and K. Muinonen, 'Interrelating angular scattering characteristics to internal electric fields for wavelength-scale spherical particles," JQSRT 106, 520-534 (2007)

[3] J. Tyynelä, K. Muinonen, E. Zubko, and G. Videen, 'Interrelating angular scattering characteristics to internal electric fields for Gaussian-random-sphere particles," JQSRT, in press (2008)

[4] E. Zubko, Yu. G. Shkuratov, G. Videen, and K. Muinonen, 'Effects of interference on the backscattering properties of irregularly shaped particles using DDA," Proceedings of the 9th Conference in Electromagnetic and Light Scattering by Nonspherical Particles: Theory, Measurements and Applications, 287-290 (2006)

[5] M. A. Yurkin, V. P. Maltsev, and A. G. Hoekstra, 'The discrete dipole approximation for simulation of light scattering by particles much larger than the wavelength," JQSRT 106, 546-557 (2007)

[6] Q. Xie, H. Zhang, Y. Wan, Y. Zhang, L. Qiao, 'Characteristics of light scattering by smoke particles based on spheroid models," JQSRT 107, 72-82 (2007)

The influence of the turning effect on the scattering in a layered media

A. Yu. Valkov, A. A. Zhukov, and V. P. Romanov
Saint-Petersburg State University, Russia, e-mail: alexvalk@mail.ru

A problem of light scattering by the random inhomogeneities in a layered media with large regular structure scale has been considered. The main attention has been paid to the influence of the wave turning points presence on the scattering phenomena in these systems. Our approach for normal waves and Green function calculation is based on the use of WKB-approximation far from turning points and Airy functions near them. For scattered intensity calculation we suggest the original extension of classical Kirchhoff method for the case of volume scattering and we get the expression for the scattered intensity in the far zone which takes into account the turning effect of the incident and scattered beams. Physical aspects of the results obtained have been analysed. It has been shown in particular that even a comparatively low permittivity gradient causes the noticeable redistribution of the scattered intensity between front and back hemispheres. The resulting scattering indicatrix has rather an exotic shape with sharp peaks, steps and dips with the magnitude comparable to the average intensity value.

I. INTRODUCTION

Most media with a smooth varying permittivity coefficient have random inhomogeneities of different origin causing light scattering. In this paper we consider the problem of wave scattering in a smooth layered media with large regular structure scale which significantly exceeds the wavelength. These systems have characteristic properties such as turning-point presence also as forbidden zones [1–3, 5, 6]. Wave fields near turning points are interrogated in layered media with different permittivity distributions [2, 4, 7]. More complex anisotropic systems like HLC are discussed in [8, 9] with the related forbidden zone tunneling effect [10–13]. Wave tunneling effect is especially noticeable in thin gradient films where it defines reflection and transmission coefficients according to the angle of incidence [11–13]. In this work we will investigate the influence of wave turning effect and the turning point neighborhood on the scattering phenomena that was not studied before. Using WKB-approximation for incident and scattered fields far from turning points and Airy-functions near them we find normal waves in the medium to construct general expression for the Green function in $(\mathbf{q}, z)$-representation. We are using the approach based on the Kirchhoff method provides explicit expressions for the single scattering intensity in the far zone [14–16].

II. BASIC EQUATIONS

To get rid of extra mathematical complication that is not of the fundamental nature we will consider all fields as scalars. Introducing scalar monochromatic wave $u(\mathbf{r}, t) = u(\mathbf{r}) \exp(-i\omega t)$ where ω is the circular frequency we are to solve the Helmholtz equation for the amplitude $u(\mathbf{r})$:

$$[\Delta + k^2(\mathbf{r})]u(\mathbf{r}) = 0, \tag{2.1}$$

where $k^2(\mathbf{r}) = (\omega/c)^2 \varepsilon(\mathbf{r})$, c — electromagnetic constant and $\varepsilon(\mathbf{r})$ — permittivity:

$$\varepsilon(\mathbf{r}) = \varepsilon_0(z) + \delta\varepsilon(\mathbf{r}), \quad \varepsilon_0(z) = \langle \varepsilon(\mathbf{r}) \rangle,$$

here $\varepsilon_0(z)$ is the mean permittivity of the medium changing along Oz axis, $\delta\varepsilon(\mathbf{r})$ are random permittivity fluctuations, $\langle \delta\varepsilon(\mathbf{r}) \rangle = 0$. Let us consider the Helmoltz equation in the equivalent integral form:

$$u(\mathbf{r}_\perp, z) = u_0(\mathbf{r}_\perp, z) - k_0^2 \int\limits_{V_{\text{sc}}} T_0(\mathbf{r}_\perp - \mathbf{r}'_\perp; z, z') \delta\varepsilon(\mathbf{r}'_\perp, z') u(\mathbf{r}'_\perp, z') \mathrm{d}\mathbf{r}'_\perp \mathrm{d}z', \tag{2.2}$$

where $k_0 = \omega/c$, V_{sc} — scattering volume, $\mathbf{r}_\perp = (x, y)$ is $\mathbf{r}$ component orthogonal to Oz axis, u_0 is the solution of the following non-disturbed wave equation:

$$\Delta u_0(\mathbf{r}_\perp, z) + k^2(z) u_0(\mathbf{r}_\perp, z) = 0, \quad k^2(z) = k_0^2 \varepsilon_0(z), \tag{2.3}$$

function $T_0(\mathbf{r}_\perp - \mathbf{r}'_\perp; z_1, z_2)$ used in (2.2) is the Green function of the equation (2.3). The resulting solution for u_0 in the regions I, II and III (see fig. 1a) is:

$$u_0(\mathbf{r}_\perp, z) = \exp(i\mathbf{k}_\perp\mathbf{r}_\perp)\times\begin{cases}\dfrac{A_1 e^{i\varphi_{tz}} + (B_1 - iA_1)e^{-i\varphi_{tz}}}{\sqrt{f(z)}}, & z \in \mathrm{I},\\ \sqrt{\dfrac{\pi}{p_0}}\left[(2A_1 e^{-i\pi/4} + iB_1)\times \mathrm{Ai}(p_0(z-z_t)) + B_1 e^{-i\pi/4}\,\mathrm{Bi}(p_0(z-z_t))\right], & z \in \mathrm{II},\\ \dfrac{(A_1 + iB_1/2)e^{i\varphi_{tz}} + B_1 e^{-i\varphi_{tz}}}{\sqrt{f(z)}}, & z \in \mathrm{III},\end{cases} \tag{2.4}$$

where $f(z) = f(k_\perp, z) = \sqrt{k^2(z) - k_\perp^2}$, $z_t = z_t(k_\perp)$ is wave turning point corresponding to $f(z_t) = 0$, $p_0^3 \equiv -\,\partial f^2(z)/\partial z\big|_{z=z_t}$, A_1, B_1 are arbitrary constants, $\varphi_{tz} = \varphi_{tz}(z, k_\perp) = \int_{z_t}^{z} f(z')dz'$. We also use the notation $\mathbf{k}(z) = (\mathbf{k}_\perp, k_z(z))$. To get the expression for $T_0(\mathbf{r}_\perp - \mathbf{r}'_\perp; z_1, z_2)$ we use (2.4) to construct two waves u_+ and u_- propagating respectively to $+\infty$ and $-\infty$:

$$u_+(q,z) = \begin{cases}(f(z))^{-1/2}\left\{e^{i\varphi_{tz}} - ie^{-i\varphi_{tz}}\right\}, & z \in \mathrm{I},\\ 2e^{-i\pi/4}\sqrt{\dfrac{\pi}{p_0}}\,\mathrm{Ai}\left(p_0(z-z_t)\right), & z \in \mathrm{II}\\ (f(z))^{-1/2}e^{i\varphi_{tz}}, & z \in \mathrm{III},\end{cases} \tag{2.5}$$

$$u_-(q,z) = \begin{cases}(f(z))^{-1/2}e^{-i\varphi_{tz}}, & z \in \mathrm{I},\\ e^{-i\pi/4}\sqrt{\dfrac{\pi}{p_0}}\left[i\,\mathrm{Ai}(p_0(z-z_t)) + \mathrm{Bi}(p_0(z-z_t))\right], & z \in \mathrm{II},\\ (f(z))^{-1/2}\left(ie^{i\varphi_{tz}}/2 + e^{-i\varphi_{tz}}\right), & z \in \mathrm{III},\end{cases} \tag{2.6}$$

Using (2.5) and (2.6) we get the expression for the Green function $T_0(\mathbf{q}; z, z_1)$:

$$T_0(\mathbf{q}; z, z_1) = (i/2)u_+(q, z_{\max})u_-(q, z_{\min}), \tag{2.7}$$

where $z_{\max} = \max(z, z_1)$, $z_{\min} = \min(z, z_1)$. From (2.4) and (2.7) using the Kirchhoff method we get the expression for the scattered intensity $I_\pm^{(S)}(\mathbf{k}^{(i)}, \mathbf{k}^{(s)})$:

$$\begin{aligned} I_\pm^{(s)}(\mathbf{k}^{(i)}, \mathbf{k}^{(s)}) = I^{(i)} S_\perp \frac{k_0^4}{16\pi^2 r^2}\frac{k^{(s)}}{k^{(i)}}k_z^{(i)}k_z^{(s)2} \\ \times\left|u_\pm(k_\perp^{(s)}, \pm L/2)\right|^2 \\ \times\iint_{-L/2}^{L/2} u_\mp(k_\perp^{(s)}, z_1)u_\mp^*(k_\perp^{(s)}, z_2)G(\mathbf{k}_\perp^{(s)} - \mathbf{k}_\perp^{(i)}; z_1, z_2) \\ \times u_+(k_\perp^{(i)}, z_1)u_+^*(k_\perp^{(i)}, z_2)\mathrm{d}z_1\mathrm{d}z_2, \end{aligned} \tag{2.8}$$

here I_+ and I_- correspond to the scattering in the front ($z > L/2$) and back ($z < L/2$) hemispheres respectively, $\mathbf{k}^{(i),(s)}$ are wave vectors of the incident and scattered waves, $I^{(i)} = J_0|E_0^{(i)}|^2k^{(i)}$ is the incident field intensity, $S_\perp$ — the lateral surface area of the slab and G is the correlation function:

$$G(\mathbf{k}_\perp^{(s)} - \mathbf{k}_\perp^{(i)}; z_1, z_2) = S_\perp^{-1}\left\langle\delta\varepsilon^*(\mathbf{k}_\perp^{(s)} - \mathbf{k}_\perp^{(i)}; z_1)\delta\varepsilon(\mathbf{k}_\perp^{(s)} - \mathbf{k}_\perp^{(i)}; z_2)\right\rangle. \tag{2.9}$$

The general expression (2.8) is used to find scattering intensity for different situations depending on the presence of the turning points of incident and scattered waves also as on the width of the turning point neighborhood compared to the slab width.

III. RESULTS

To illustrate the results obtained let use the linear model of the permittivity and the Gaussian for the correlation function:

$$\varepsilon(z) = \varepsilon_0 - \Delta\varepsilon z/L, \tag{3.1}$$

$$G(\mathbf{Q}; z) \equiv G(\mathbf{Q}) = G_0\exp\left(-Q^2r_c^2/2\right), \tag{3.2}$$

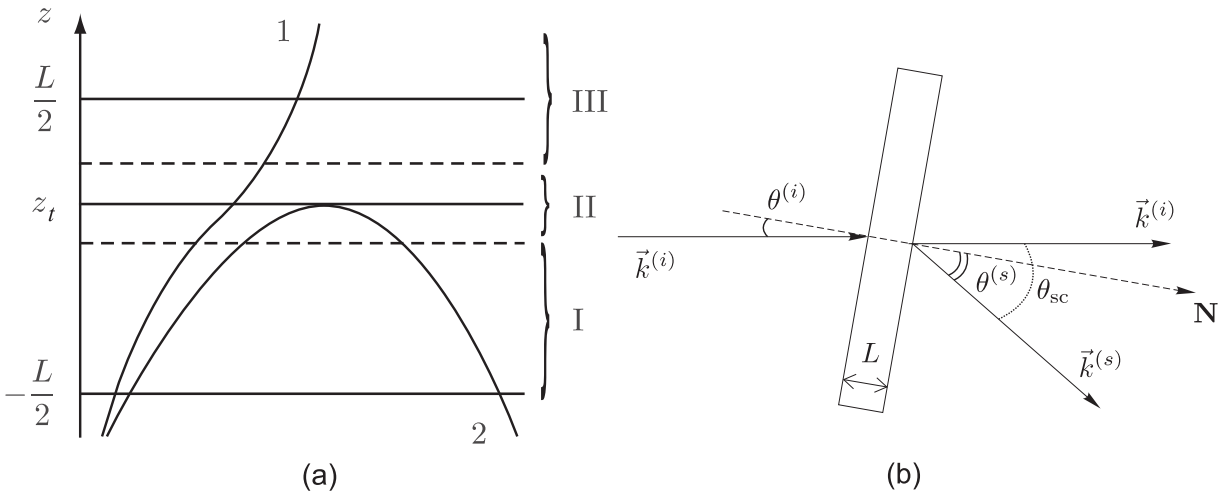

Figure 1: (a) — ray trajectories inside the slab $-L/2 \leqslant z \leqslant L/2$, 1 — without turning points, 2 — with turning point $z = z_t$; WKB-based solutions are used in I and III regions, Airy functions are used in II; (b) — scattering geometry, $\theta^{(i)}$ — angle of incidence, $\theta^{(s)}$ — angle of scattering wave output direction, $\theta_{\rm sc}$ — angle of scattering.

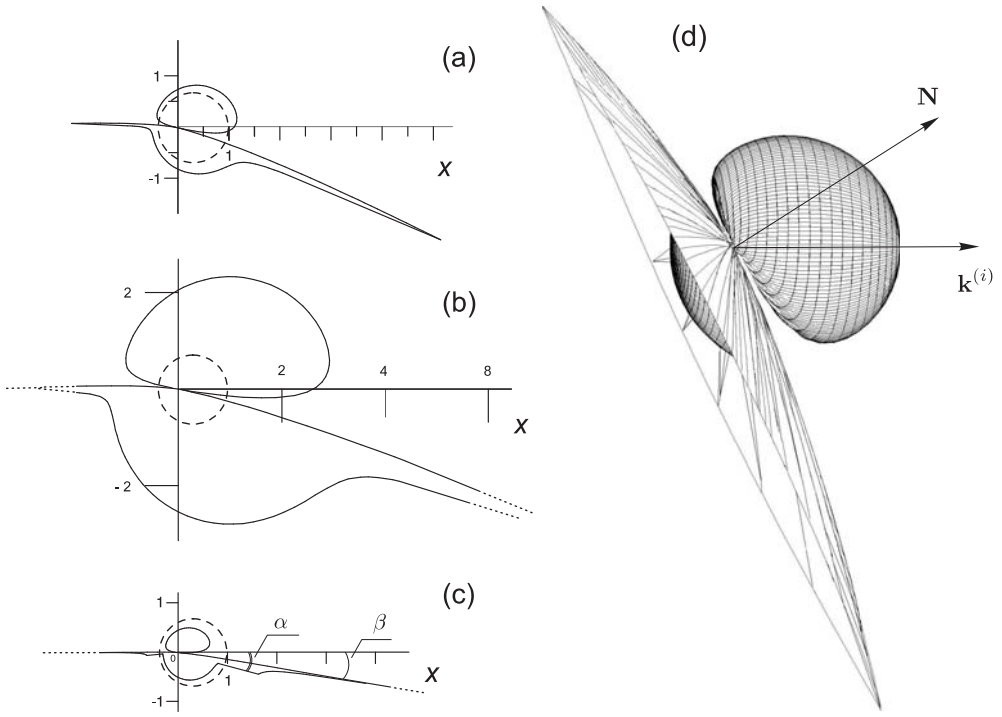

Figure 2: Scattering indicatrix for the gradient media with $\Delta\varepsilon = 0.05$ and anisotropic diffusers, $\overline{k}r_c = 1$. (a), (b), (c) — 2-D profile in the $(\mathbf{N}, \mathbf{k}^{(i)})$ plane with $\theta^{(i)}$ near the turning angle $\theta_t = 79.57°$: (a) — the incident wave has no turning points, $\theta^{(i)} = 77.4°$, (b), (c) — the incident wave has turning point, $\theta^{(i)} = 80.2°$ $\theta^{(i)} = 85.3°$ respectively, $\alpha = \theta_t - \pi/2$, $\beta = \pi/2 - \theta^{(i)}$. Dashed line — homogenous medium. OX axis is chosen in the line of $\mathbf{k}^{(i)}$. (d) — 3-D side view, $\theta^{(i)} = 28.7°$.

where L is the slab width, ε_0 — permittivity in the slab center ($z = 0$), $\Delta\varepsilon$ — total variation of ε inside the slab, r_c — correlation radius, $G_0 = \text{const}$. The scattering geometry is shown on fig. 1b. The resulting indicatrix is shown on fig. 2.

Scattering indicatrix in the layered medium even with low permittivity gradient has a complex form compared to the homogeneous medium with the same scatterer type. It has sharp steps in the back hemisphere with the amplitude comparable to the average intensity value. After the incidence angle reaches given boundary value θ_t the scattering indicatrix has extra narrow peaks with the amplitude several times greater than the mean value. Near directions orthogonal to the to the layer normal the intensity falls off very quickly in several orders of magnitude. One can observe general intensity attenuation in the front hemisphere according to its augmentation in the back hemisphere. The permittivity gradient in the anisotropic medium causes also additional changes in the total scattering cross-section.

The effects listed above are of the geometrical-optics origin. The divergence from the geometrical optics and the use of Airy functions is essential for the very thin slabs ($L \sim 10^{-5} - 10^{-4}$ cm). Also we have to use Airy functions in the

neighborhood of the intensity steps ($\theta^{(i)} = \theta_t$, $\theta^{(s)} = \pi - \theta_t$), peaks ($\theta^{(s)} = \pi - \theta^{(i)}$) and dips ($\theta^{(s)} = \pi/2$) for the arbitrary slab thickness. But in that case the divergence from the geomtrical-optics results become apparent in a very short angle intervals ($\Delta\theta \sim 0.005^\circ - 0.05^\circ$ for the steps, $\Delta\theta \sim 0.001^\circ - 0.1^\circ$ for the peaks and $\Delta\theta \sim 0.2^\circ - 2^\circ$ for the dips).

---

[1] Brilluen L., Parodi M., *Propagation des Ondes dans les Milieux Periodicues* Paris, 1956.
[2] Brekhovskikh L.M., *Waves in layered media* New York: Academic Press, 1960.
[3] L.M. Brekhovskikh, O.A. Godin, *Acoustics of Layered Media*, v. I *Plane and Quasi-Plane Waves*, v. II *Point Sources and Bounded Beams*, Berlin: Springer-Verlag, 1998,1999.
[4] Felsen L., Marcuvitz N., *Radiation and scattering of waves*, Wiley, 2003.
[5] P. Yeh, *Optical Waves in Layered Media*, Wiley, Hoboken, New Jersey, 2005.
[6] A. Yariv, Yeh P., *Optical Waves in Crystals* New York: Wiley, 1984.
[7] Ginzburg V.L., *Propagation of electromagnetic waves in plasma [in Russian]* Moscow: Nauka, 1967.
[8] E.V. Aksenova, A.Yu. Valkov, A.A. Karetnikov et al., Journal of Experimental and Theoretical Physics **126**, 1109 (2004).
[9] E.V. Aksenova, A.A. Karetnikov, A.P. Kovshik et al., Europhys. Lett. **69**, 68 (2005).
[10] E.V. Aksenova, E.V. Krukov, V.P. Romanov, Optics and Spectroscopy **101**, 1006 (2006).
[11] A. Shvartsburg, G. Petite, Eur. Phys. J. **D 36**, 111 (2005).
[12] A. Shvartsburg, V. Kuzmiak, G. Petite, Phys. Rev. **E 76**, 016603 (2007).
[13] A. Shvartsburg, G. Petite, Optics Letters **31**, 1127 (2006).
[14] E.V. Aksenova, A.Yu. Valkov, V.P. Romanov, Journal of Experimental and Theoretical Physics **72**, 124 (2004).
[15] E.V. Aksenova, V.P. Romanov, A.Y. Val'kov, Phys. Rev. **E 71**, 051702 (2005).
[16] E.V. Aksenova, A.Yu. Valkov, V.P. Romanov, Optics and Spectroscopy issue 3, **104**, 429 (2008).

Separation of Variables Method for Multilayered Particles

Alexander A. Vinokurov[1], Victor G. Farafonov[1], Vladimir B. Il'in[2]

[1] *St. Petersburg University of Aerocosmic Instrumentation, Bol. Morskaya 67, St. Petersburg, 190000 Russia*

[2] *St. Petersburg University, Universitetskij pr., 28, St. Petersburg, 198504 Russia*

tel: +7 (812) 708-3940, e-mail: alexander.a.vinokurov @gmail.com

Abstract

We present a new exact method for solving the problem of light scattering by an isolated multilayered non-spherical (axisymmetric) particle. The method is based on the separation of variables approach using the single field expansions in terms of spherical functions. We divide the fields in two parts and utilise special scalar potentials for each of them. The main feature of the method is that the dimension of systems of equations arisen does not increase with a growth of the number of the layers. Numerical results obtained for spheroids and Chebyshev particles show that the suggested method is stable for particles with 4 and more layers in which case the extended boundary condition method is known to fail.

1 Introduction

Various natural particles studied in atmosphere physics, astrophysics, biophysics, etc. are nonspherical and inhomogeneous (see, e.g., [1]). The optical methods are often most suitable for investigation of the media containing such particles. The methods are based on mathematical simulations of light scattering by simplified particle models. So far, only the model of scatterers with randomly distributed inclusions was sufficiently developed for wide applications. An alternative simple model of scatterer structure is *multilayered* particles.

Light scattering by such particles can be modeled with many methods. The universal ones (DDA, FDTD, etc. – see about these and other methods mentioned here in the review [1]) being very computational time-consuming are hardly applicable when the number of layers n is large. Another rather approximate method GMT [4] is much more perspective, but we have not found any results for $n \gg 1$. Among the exact methods (SVM, EBCM, etc.) one should start with the EBCM. The pioneer work on light scattering by layered particles [5] was rather theoretical. Further development of the method (see [6] for a review) has shown that it does not give reliable results already for $n > 3$ [7]. The SVM was applied so far only to spheroids with confocal layers [8, 9] which are particles of peculiar structure.

In this paper a version of the SVM applicable to *any* axisymmetric multilayered scatterers is developed. We use nonstandard (non-Debay) scalar potentials of the fields and expand them in the corresponding spherical functions. Some advantages of the suggested computational scheme are discussed and first numerical results are presented.

2 Theoretical Approach

Let us consider scattering of a plane wave by an isolated particle with n layers (Fig. 1). We take particles with axisymmetric layers, i.e. in the spherical coordinate system (r, θ, φ) the layer external surfaces S_i are defined by equations $r = r_i(\theta)$, $i = 1, \ldots, n$. $\boldsymbol{E}^{(i)}$ and $\boldsymbol{H}^{(i)}$ are the electric and magnetic fields inside the $(i-1)$th layer.

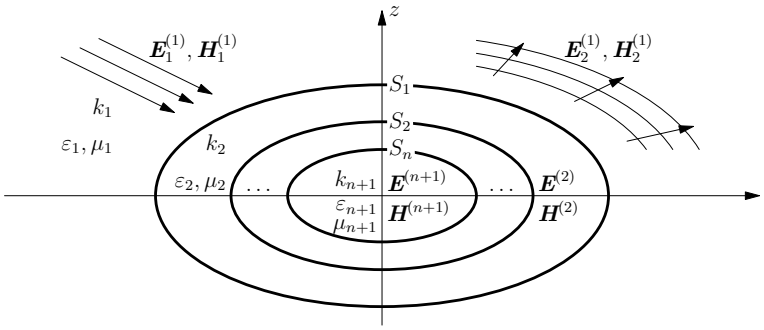

Figure 1: Cross-section of a layered particle and the notations used.

The fields $\boldsymbol{E}^{(i)}$, $\boldsymbol{H}^{(i)}$ can be represented as sums $\boldsymbol{E}^{(i)} = \boldsymbol{E}_1^{(i)} + \boldsymbol{E}_2^{(i)}$, $\boldsymbol{H}^{(i)} = \boldsymbol{H}_1^{(i)} + \boldsymbol{H}_2^{(i)}$, $i = 1, \ldots, n+1$, where $\boldsymbol{E}_1^{(i)}$, $\boldsymbol{H}_1^{(i)}$ are regular at the coordinate origin and $\boldsymbol{E}_2^{(i)}$, $\boldsymbol{H}_2^{(i)}$ satisfy the radiation condition at infinity. The fields $\boldsymbol{E}_1^{(1)}$, $\boldsymbol{H}_1^{(1)}$ and $\boldsymbol{E}_2^{(1)}$, $\boldsymbol{H}_2^{(1)}$ correspond to the incident and scattered radiation, respectively. $\boldsymbol{E}_2^{(n+1)} = \boldsymbol{H}_2^{(n+1)} = \boldsymbol{0}$.

To solve the light scattering problem one needs to find the scattered field from the Maxwell equations and the boundary conditions describing continuity of the tangential components of the fields at the scatterer boundary.

For axisymmetric scatterers, we represent all fields by sums

$$\boldsymbol{E}_s^{(i)} = \boldsymbol{E}_{s,\,\mathrm{A}}^{(i)} + \boldsymbol{E}_{s,\,\mathrm{N}}^{(i)}, \quad \boldsymbol{H}_s^{(i)} = \boldsymbol{H}_{s,\,\mathrm{A}}^{(i)} + \boldsymbol{H}_{s,\,\mathrm{N}}^{(i)}, \quad l = 1, \ldots, n, \quad s = 1, 2, \tag{1}$$

where $\boldsymbol{E}_{s,\,\mathrm{A}}^{(i)}$, $\boldsymbol{H}_{s,\,\mathrm{A}}^{(i)}$ do not depend on the azimuthal angle φ and averaging of $\boldsymbol{E}_{s,\,\mathrm{N}}^{(i)}$, $\boldsymbol{H}_{s,\,\mathrm{N}}^{(i)}$ over this angle gives zero. The light scattering problem can be solved independently for these parts of the fields [2].

To find $\boldsymbol{E}_{s,\,\mathrm{A}}^{(i)}$, $\boldsymbol{H}_{s,\,\mathrm{A}}^{(i)}$ we utilise the scalar potentials

$$p_s = E_{s,\,\mathrm{A},\varphi}^{(i)} \cos\theta, \quad q_s = H_{s,\,\mathrm{A},\varphi}^{(i)} \cos\theta, \quad l = 1, \ldots, n, \quad s = 1, 2, \tag{2}$$

where $E_{s,\mathrm{A},\varphi}^{(i)}$, $H_{s,\mathrm{A},\varphi}^{(i)}$ are the φ-components of the fields.

These potentials satisfy the scalar Helmholtz equation and can be expanded in terms of the spherical functions ($i = 1, \ldots, n+1$)

$$\begin{matrix} p_1^{(i)} \\ q_1^{(i)} \end{matrix} = \sum_{l=1}^{\infty} \begin{matrix} a_{1,l}^{(i)} \\ b_{1,l}^{(i)} \end{matrix} j_l(k_i r) P_l^1(\cos\theta)\cos\varphi, \qquad \begin{matrix} p_2^{(i)} \\ q_2^{(i)} \end{matrix} = \sum_{l=1}^{\infty} \begin{matrix} a_{2,l}^{(i)} \\ b_{2,l}^{(i)} \end{matrix} h_l^{(1)}(k_i r) P_l^1(\cos\theta)\cos\varphi, \tag{3}$$

where $j_l(k_i r)$ and $h_l^{(1)}(k_i r)$ are the spherical Bessel functions and the first kind Hankel functions, respectively, $P_l^1(\cos\theta)$ are the Legendre functions of the first kind.

Using the boundary conditions in the usual form and the potential expansions (3) we get an infinite system of linear equations relative to the expansion coefficients, e.g. for TM mode of the incident wave polarization

$$\begin{cases} \begin{pmatrix} \mathrm{A}_1^{(i)}(k_i) & \mathrm{A}_2^{(i)}(k_i) \\ \mathrm{B}_1^{(i)}(k_i) & \mathrm{B}_2^{(i)}(k_i) \end{pmatrix} \begin{pmatrix} \boldsymbol{b}_1^{(i)} \\ \boldsymbol{b}_2^{(i)} \end{pmatrix} = \begin{pmatrix} \mathrm{A}_1^{(i)}(k_{i+1}) & \mathrm{A}_2^{(i)}(k_{i+1}) \\ \mathrm{C}_1^{(i)}(k_{i+1}) & \mathrm{C}_2^{(i)}(k_{i+1}) \end{pmatrix} \begin{pmatrix} \boldsymbol{b}_1^{(i+1)} \\ \boldsymbol{b}_2^{(i+1)} \end{pmatrix}, \quad i = 1, \ldots, n-1, \\ \begin{pmatrix} \mathrm{A}_1^{(n)}(k_n) & \mathrm{A}_2^{(n)}(k_n) \\ \mathrm{B}_1^{(n)}(k_n) & \mathrm{B}_2^{(n)}(k_n) \end{pmatrix} \begin{pmatrix} \boldsymbol{b}_1^{(n)} \\ \boldsymbol{b}_2^{(n)} \end{pmatrix} = \begin{pmatrix} \mathrm{B}_1^{(n)}(k_{n+1}) \\ \mathrm{C}_1^{(n)}(k_{n+1}) \end{pmatrix} \boldsymbol{b}_1^{(n+1)}. \end{cases} \tag{4}$$

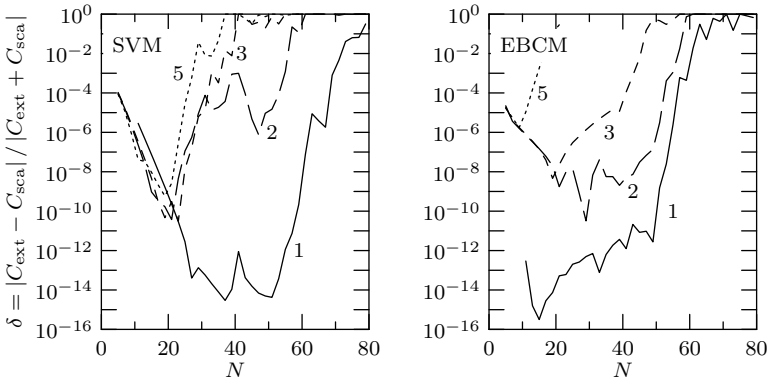

Figure 2: The dependence of accuracy measure δ on the number of terms kept in the field expansions N for 1-, 2-, 3- and 5-layered spheroids with the aspect ratios $a_i/b_i = 1.5$ and the size parameter $x_{\mathrm{V},1} = 1$. The incident radiation angle $\alpha = 45°$.

Here $\boldsymbol{b}_s^{(i)}$ are the infinite vectors containing expansion coefficients of the potentials $q_s^{(i)}$. The elements of the infinite matrices $\mathrm{A}_s^{(i)}$, $\mathrm{B}_s^{(i)}$, $\mathrm{C}_s^{(i)}$ are integrals of radial and angular functions and their derivatives, for example

$$A_{1,\,ln}^{(i)} = \int_0^{\pi} j_l(k_i r) P_l^1(\cos\theta) P_n^1(\cos\theta) \sin\theta d\theta. \tag{5}$$

Starting with the last equation, sequential elimination of the expansion coefficients can be done for all layers except for the first and $(n+1)$th ones, which gives $\begin{pmatrix} \boldsymbol{b}_1^{(1)} & \boldsymbol{b}_2^{(1)} \end{pmatrix}^{\mathrm{T}} = \begin{pmatrix} \mathrm{Q}_1 & \mathrm{Q}_2 \end{pmatrix}^{\mathrm{T}} \boldsymbol{b}_1^{(n+1)}$.As the expansion coefficients of the incident wave potentials $\boldsymbol{b}_1^{(1)}$ are known one can find the unknown coefficients for the scattered radiation $\boldsymbol{b}_2^{(1)} = \mathrm{Q}_2\mathrm{Q}_1^{-1}\boldsymbol{b}_1^{(1)}$.

In calculations truncated systems of equations are used as only N terms can be kept in the scalar potentials expansions. In the described approach the matrices Q_1, Q_2 are computed using an iterative scheme where at each step a system $N \times N$ is solved. This approach is more robust to an increase of the layer number than solving of one $(nN) \times (nN)$ system occurred in known schemes.

To find the fields $\boldsymbol{E}_{s,\,\mathrm{N}}^{(i)}$, $\boldsymbol{H}_{s,\,\mathrm{N}}^{(i)}$ we use the scalar potentials $U_s^{(i)}$, $V_s^{(i)}$, e.g. for the TM mode

$$\boldsymbol{E}_{s,\,\mathrm{N}}^{(i)} = -\frac{1}{i\varepsilon_l k_0} \nabla \times \nabla \times \left(U_s^{(i)} \boldsymbol{i}_z + V_s^{(i)} \boldsymbol{r} \right), \quad \boldsymbol{H}_{s,\,\mathrm{N}}^{(i)} = \nabla \times \left(U_s^{(i)} \boldsymbol{i}_z + V_s^{(i)} \boldsymbol{r} \right) \tag{6}$$

These potentials satisfy the scalar Helmholtz equation and can be expanded in terms of the spherical functions $(i = 1, \ldots, n+1)$

$$\begin{matrix} U_1^{(i)} \\ V_1^{(i)} \end{matrix} = \sum_{m=1}^{\infty} \sum_{l=m}^{\infty} \begin{matrix} a_{i,\,ml}^{(i)} \\ b_{1,\,ml}^{(i)} \end{matrix} j_l(k_i r) P_l^m(\cos\theta) \cos m\varphi, \quad \begin{matrix} U_2^{(i)} \\ V_2^{(i)} \end{matrix} = \sum_{m=1}^{\infty} \sum_{l=m}^{\infty} \begin{matrix} a_{2,\,ml}^{(i)} \\ b_{2,\,ml}^{(i)} \end{matrix} h_l^{(1)}(k_i r) P_l^m(\cos m\theta) \cos\varphi. \tag{7}$$

For each m we get infinite systems of linear equations relative to the potentials expansion coefficients. These systems are solved in a similar manner as above.

3 Numerical Results

We have implemented the described approach in a FORTRAN77 code. It was tested for multilayered spheroids and Chebyshev particles of different sizes and shapes by comparison with results obtained

when possible with a code based on the EBCM method [6]. Accuracy of the codes was analysed by using a relative difference of the scattering and extinction cross sections calculated for non-absorbing particles $\delta = |C_{\rm sca} - C_{\rm ext}|/(C_{\rm sca} + C_{\rm ext})$. Typical dependence of accuracy of the methods under consideration on the number of terms kept in the expansions N is shown in Fig. 2.

For homogeneous spheroids, the EBCM is known to be more effective than the SVM when the spherical functions are applied [3] because the former converges more quickly (see the solid lines on Fig. 2). However, when we increase the number of the particle layers (see the long dashed and dashed lines for 2 and 3 layers) the speed of EBCM convergence falls and accuracy of results becomes $\sim 10^{-8}$–10^{-7}. The trend of SVM convergence is the same for layered and homogeneous spheroids. The best accuracy achieved with the SVM for spheroids with 2 and 3 layers is $\sim 10^{-10}$ that provides 7–8 correct digits in the results. When the number of layers is relatively large, e.g. 5 or more (see the dotted lines in Fig. 2), the SVM still well converges and gives the same accuracy as for 2 or 3 layers, while EBCM accuracy drops to $\sim 10^{-5}$ that gives only 2–3 correct digits. Similar results were obtained for layered Chebyshev particles. More numerical examples will be presented at the conference.

Acknowledgements

The work was supported by a grant RFBR 07-02-00831. V.I. acknowledges a support by the grants RNP 2.1.1.2852 and NSh 1318.2008.2.

References

[1] M.I. Mishchenko, J. Hovenier, and L.D. Travis (eds), *Light Scattering by Nonspherical Particles* (Academic Press, San Francisco, 2000).

[2] V.G. Farafonov, V.B. Il'in, Single light scattering: computational methods. In: A. Kokhanovsky (Ed.) *Light scattering reviews*, (Springer, Berlin, 2006), pp. 125–177.

[3] V.G. Farafonov, A.A. Vinokurov, and V.B. Il'in, "Comparison of light scattering methods using the spherical basis", Opt. Spectr., **102**, 1006–1016 (2007).

[4] A. Doicu, Th. Wriedt, and Y. Eremin, *Light Scattering by Systems of Particles. Null-Field Method with Discrete Sources - Theory and Programs* (Springer, New York, 2006).

[5] B. Peterson, S. Ström, "T-matrix formulation of electromagnetic scattering from multilayered scatterers", Phys. Rev., D 10, 2670–2684 (1974).

[6] V.G. Farafonov, V.B. Il'in, and M.S. Prokopjeva, "Light scattering by multilayered nonspherical particles: a set of methods", JQSRT, **79–80**, 599-626 (2003).

[7] M.S. Prokopjeva, "Extinction and polarization of light by nonspherical inhomogeneous interstellar dust particles" (Ph.D. thesis in St.Petersburg Univ., 2005).

[8] I. Gurwich et al., "Scattering of electromagnetic radiation by multilayered spheroidal particles: recursive procedure", Appl. Opt., **39**, 470–477 (2000).

[9] V.G. Farafonov, "Light scattering by multilayer nonconfocal ellipsoids in the Rayleigh approximation", Opt. Spectr., **90**, 743–752 (2001).

Application of the discrete dipole approximation to extreme refractive indices: filtered coupled dipoles revived

Maxim A. Yurkin,[1,2] Michiel Min,[3] and Alfons G. Hoekstra[1]

[1] *Faculty of Science, Section Computational Science, University of Amsterdam, Kruislaan 403, 1098 SJ, Amsterdam, The Netherlands*
[2] *Institute of Chemical Kinetics and Combustion, Siberian Branch of theRussian Academy of Sciences, Institutskaya 3, Novosibirsk 630090, Russia*
[3] *Astronomical institute Anton Pannekoek, University of Amsterdam, Kruislaan 403, 1098 SJ, Amsterdam, The Netherlands*
tel: +31 (20) 525-7562, fax: +31 (20) 525-7490, e-mail: yurkin@gmail.com

Abstract

We compared three formulations of the discrete dipole approximation (DDA) for simulation of light scattering by particles with refractive indices $m = 10 + 10\mathrm{i}$, $0.1 + \mathrm{i}$, and $1.6 + 0.01\mathrm{i}$. These formulations include filtered coupled dipoles (FCD), lattice dispersion relation (LDR) and radiative reaction correction (RRC). We compared number of iterations (proportional to simulation time) and accuracy of final results. We showed that LDR performance for $m = 10 + 10\mathrm{i}$ is especially bad, while FCD, which we have implemented in the ADDA computer code, is a good option for all cases studied. Now these extreme refractive indices can be routinely simulated using modern desktop computers.

1 Introduction

The discrete dipole approximation (DDA) is a well-known method to calculate light scattering by arbitrary shaped inhomogeneous particles [1]. The widespread application of the DDA started with the work of Draine and coworkers [2-4], especially after release of their computer code DDSCAT to the public domain. They also systematically showed that DDA performance deteriorates with increasing refractive index m. Since then it was accepted that application of DDA is limited to a range approximately described as $|m - 1| < 2$, based on the standard formulation of the DDA including the lattice dispersion relation (LDR [4]). Recently, it has been shown that this standard DDA formulation has problems both for $|m| \gg 1$ and $\mathrm{Re}(m) \ll 1$ [5]. Such extreme m-values do appear in spectral resonances of many materials in the infrared range [5]. Accurate predictions of the spectral shape of absorption resonances are of crucial importance for the interpretation of astronomical observations. Moreover, metallic particles in the infrared have very large values of m, hence they might be the dominant source of opacity in many environments [6]. However, currently accurate methods to predict the opacity of metallic particles are lacking.

While the range of $\mathrm{Re}(m) < 1$ is poorly studied, there have been a number of attempts to improve DDA performance for large m. They include filtered coupled dipoles (FCD [7]), weighted discretization (WD [8]), integration of Green's tensor (IT [9]), Rahmani-Chaumet-Bryant formulation (RCB [10]), and surface-corrected LDR (SCLDR [11]). RCB and SCLDR require a preliminary solution of the electrostatic problem for the same particle, and IT requires a numerical evaluation of oscillatory integrals to build up the DDA interaction matrix, which is not trivial to implement and may consume a lot of computer time. WD is an efficient in decreasing shape errors [12] but it causes all boundary dipoles to have different polarizabilities, which is incompatible with current internal data structure of publicly available DDA codes such as DDSCAT and ADDA [13]. The only known drawback of FCD is that it is hard to theoretically analyze its convergence [12]. On the other hand, FCD is a good option since it is easy to implement and it does improve the performance of DDA for large m, as was shown by its authors [7,14]. It seems that the only reason why FCD, proposed 10 years ago, was not adopted by the light scattering community is that it was not included as an option in a publicly available DDA code.

In this paper we endeavor to revive FCD. For that we implement it in the ADDA code and demonstrate its performance for a number of scattering problems in comparison with LDR and radiative reaction correction (RRC [2]) formulations. We also discuss practical feasibility of DDA simulation of light scattering by particles with extreme refractive indices.

2 Methods

FCD is based on application of the sampling theorem to the volume integral equation for the electric field [7], and it effectively modifies the formula for calculation of interaction terms (i.e. off-diagonal terms of the interaction matrix). The new formula requires calculation of sine and cosine integrals, which takes some

time. However, according to our experience, this time is comparable to one iteration of the iterative solver and hence can be neglected in most cases (data not shown). The dipole polarizabilities (i.e. diagonal terms of the interaction matrix) are those of Clausius-Mossotti (CM) with $O((kd)^2)$ corrections [7].

We have implemented FCD in ADDA and used it (v.0.78.2) for all simulations presented in this paper. We tried two extreme refractive indices ($10 + 10i$ and $0.1 + i$, typical for SiC in the infrared [5]) and one moderate one ($1.6 + 0.01i$, typical for silicates in the visible). Three particle shapes were used: a sphere, a cube, and a cubical discretization of a Gaussian random field particle (GRF [15]) using 100 cubes, located on a $8\times8\times8$ grid. We used two different sizes: $kD_x = 8$ ("large") and $kD_x = 10^{-5}$ (Rayleigh regime), where k is the wavenumber and D_x is the particle length along the x-axis. For both cases orientation of the particle was fixed. We used FCD, LDR, and RRC formulations for large particles. For the Rayleigh particles LDR and RRC are both equivalent to CM – so only FCD and CM were used. For all simulations we used the QMR iterative solver [13]. However, we also tried BiCGStab in a few cases (see below). The default threshold of the iterative solver was used (10^{-5}).

For each combination of shape, size, and refractive index we used 18 different discretizations from 8 to 512 dipoles (n_x) per D_x with approximately uniform spacing on a logarithmic scale. For large and Rayleigh particles we use $y = kd|m|$ and $1/n_x$ as discretization parameters respectively. All simulations were run on Dutch compute cluster LISA (http://www.sara.nl/userinfo/lisa/description/). Since only the sphere allows for exact analytical solution, we used the extrapolation technique [16] to infer reference results for the cube and the GRF particle. Using error estimates provided by the extrapolation technique for all formulations applied to the same particle and assuming these errors to be independent, we computed a weighted average and corrected error estimates for each formulation. For spheres we also performed extrapolation to compare its accuracy relative to the exact Mie results.

3 Results and discussion

First we analyze the total number of iterations (N_{iter}) performed by ADDA, which determine the total simulation time. For Rayleigh particles FCD is faster than CM for both extreme refractive indices, while N_{iter} is only weakly dependent on the discretization (see Fig. 1 for example). Results of N_{iter} for the best discretization ($n_x = 512$) are summarized in Table 1: FCD is about 6 and 1.2 times faster for $m = 10 + 10i$ and $0.1 + i$ respectively. For large particles with any of the considered m, as well as for Rayleigh particles with $m = 1.6 + 0.01i$, all formulations show very similar N_{iter} almost independent on y, except for the following. (1) For $m = 10 + 10i$ LDR shows strange dependence of N_{iter} on y for all studied shapes (see Fig. 2 for example). This can be explained by the nature of LDR formulation, which employs corrections of order y^2. When y is not small this correction may be large and wrong, so that it not only decreases the accuracy of simulations (see below) but also strongly increases the condition number of the interaction matrix. This is not so noticeable for very coarse discretizations due to the small dimension of interaction matrix, but become prominent for $y \sim 1$. Other formulations employ corrections given in powers of kd, which is much smaller than y for this m. (2) QMR fails for very fine discretizations of cubes for both RRC and LDR and for both extreme refractive indices (data not shown). However, BiCGStab does converges for these cases showing similar N_{iter} for all formulations (except for LDR in combination with $m = 10 + 10i$).

Due to the space limitations we can not present all the accuracy results in this contribution, and show only a few representative examples. Table 2 summarizes relative errors of absorption efficiency Q_{abs} for all studied cubes, showing errors of different formulations for the best discretization, estimate of the extrapolation error (using the 5 best discretizations), and the corrected estimate of this error. One can see that for cubes with $m = 10 + 10i$ FCD is superior (1-2 orders of magnitude) to other formulations, although for Rayleigh cubes CM yields similar accuracy after extrapolation. For cubes with $m = 0.1 + i$ FCD is 60 times more accurate than CM in the Rayleigh regime and shows similar accuracy for $kD_x = 8$, but is less accurate after extrapolation. The most surprising result is for "very moderate" $m = 1.6 + 0.01i$. FCD is more than 10 times more accurate than both LDR and RRC for cubes, although after extrapolation the accuracies are similar. Such behavior has never been reported for FCD because, to the best of our knowledge, it has never been systematically applied to cubically shaped particles (i.e. those without shape errors [16]). Accuracy results for GRF, simulated only for $m = 10 + 10i$ (data not shown), are similar to the cube results for the same m.

For spheres there is generally a relatively small difference between the accuracies of different DDA formulations, while extrapolation results for FCD have the same or worse accuracy than others (data not shown). There is only one exception, shown in Fig. 3, a large sphere with $m = 10 + 10i$. This figure also

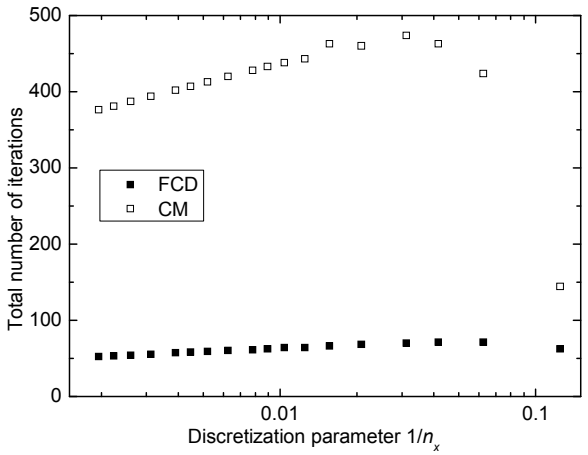

Fig. 1. N_{iter} versus $1/n_x$ for a Rayleigh cube, $m = 10 + 10i$.

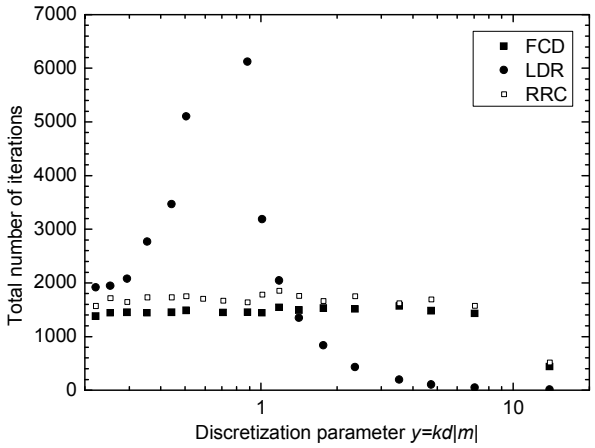

Fig. 2. N_{iter} versus y for $kD_x = 8$ sphere with $m = 10 + 10i$.

Table 1. N_{iter} for Rayleigh particles with $n_x = 512$.

	$m = 10 + 10i$			$m = 0.1 + i$	
formulation	cube	sphere	GRF	cube	sphere
FCD	52	66	82	106	86
CM	376	389	540	121	105

Table 2. Relative errors of Q_{abs} for cubes.

m	kD_x	formulation	$n_x = 512$	extr. est.	cor. est.
$10 + 10i$	$\ll 1$	FCD	8.3×10^{-4}	2.5×10^{-4}	1.2×10^{-4}
		CM	1.4×10^{-2}	1.2×10^{-4}	1.1×10^{-4}
	8	FCD	9.1×10^{-4}	3.6×10^{-5}	3.6×10^{-5}
		LDR	3.0×10^{-1}	1.5×10^{-2}	1.3×10^{-2}
		RRC	2.2×10^{-1}	3.2×10^{-2}	2.3×10^{-2}
$0.1 + i$	$\ll 1$	FCD	1.3×10^{-5}	4.6×10^{-5}	5.9×10^{-5}
		CM	7.7×10^{-4}	4.6×10^{-6}	4.6×10^{-6}
	8	FCD	1.4×10^{-4}	9.0×10^{-4}	1.3×10^{-3}
		LDR	2.4×10^{-4}	2.2×10^{-5}	1.0×10^{-5}
		RRC	1.8×10^{-4}	1.0×10^{-5}	9.7×10^{-6}
$1.6 + 0.01i$	$\ll 1$	FCD	1.7×10^{-7}	8.9×10^{-6}	1.7×10^{-6}
		CM	1.6×10^{-4}	1.4×10^{-6}	1.4×10^{-6}
	8	FCD	1.7×10^{-5}	1.9×10^{-5}	7.8×10^{-6}
		LDR	2.3×10^{-4}	8.7×10^{-6}	7.9×10^{-6}
		RRC	1.5×10^{-4}	5.4×10^{-5}	1.3×10^{-5}

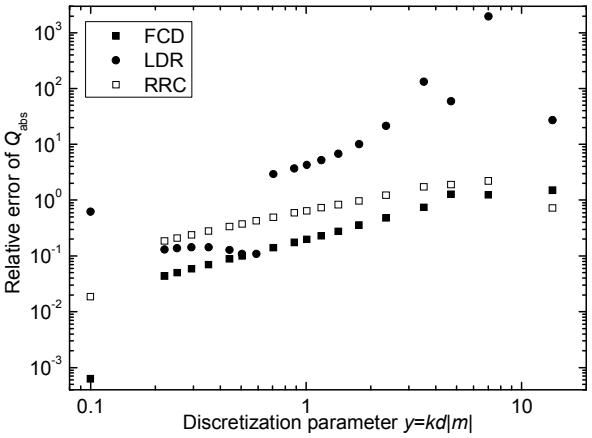

Fig. 3. Relative error of Q_{abs} versus y for $kD_x = 8$ sphere with $m = 10 + 10i$ in log-log scale. Points for $y = 0.1$ depict errors of extrapolated values (using 9 best discretizations) compared to the Mie solution.

shows typical behavior of LDR errors versus y for this m. So we can conclude that LDR is the worst possible option for $m = 10 + 10i$. The general tendency, exemplified in Fig. 3, is that when FCD is superior for $n_x = 512$ it is also superior for almost the whole studied range of FCD, although its superiority for smaller n_x may be smaller, since FCD seems to have a larger exponent in the power dependence of errors on y. The inability of FCD to improve accuracy for spheres in general is probably because shape errors, to which FCD is susceptible to the same extent, contribute most to the total errors for the studied sizes and refractive indices. Further study is required to check this hypothesis. Accuracies of extinction efficiency and angle-resolved S_{11} and $-S_{21}/S_{11}$ show the same trends as that of Q_{abs} (data not shown).

It should be noted that in some cases FCD convergence is oscillatory around the linear trend in log-log scale (data not shown), which explains relatively large errors during extrapolation of its results. However, currently there exists no easy-to-use and robust implementation of DDA extrapolation technique for arbitrary particles, i.e. performance of the extrapolation should first be tested on a class of similar problems, using some reference results. Therefore, for practical applications good accuracy of single DDA simulations seem to be more important than good potential for extrapolation.

FCD makes extreme refractive indices much more feasible for DDA simulations, but they still require extreme computer power. We do not present computational times in this paper, but only give a few guiding values. Requiring moderate accuracy of 10% in Q_{abs} (which is considered sufficient e.g. for computing an absorption spectrum of astrophysical dust), a single DDA simulation will fit into 2 GB of

memory and will take about 10 and 2 hours on 3 GHz single-core processor for single orientation of wavelength-sized particles with refractive index $10 + 10\mathrm{i}$ and $0.1 + \mathrm{i}$ respectively. However, required time can be as small as a few minutes for Rayleigh or cubically shaped particles.

3 Conclusion

We have compared three DDA formulations: FCD, LDR, and RRC for simulations of light scattering by cubes, spheres, and GRF with sizes comparable and much smaller than the wavelength, using three refractive indices: $10 + 10\mathrm{i}$, $0.1 + \mathrm{i}$, and $1.6 + 0.01\mathrm{i}$. FCD improves convergence of the iterative solver for Rayleigh particles and extreme refractive indices: it is about 6 and 1.2 times faster than CM for $m = 10 + 10\mathrm{i}$ and $0.1 + \mathrm{i}$ respectively. FCD significantly decreases discretization errors of the DDA compared to other formulations almost for all studied cases, including moderate value of m. This is clearly visible for cubes and GRF, since their results are not obscured by the presence of large shape errors. The improvement of accuracy is up to a factor 100. The only drawback of FCD is that in some cases the extrapolation technique applied to its results leads to larger errors than for other formulations. If comparing LDR and RRC, our results show that LDR is a "never use" option for $m = 10 + 10\mathrm{i}$, comparable to RRC (and generally to FCD) for $m = 0.1 + \mathrm{I}$, and better than RRC for $1.6 + 0.01\mathrm{i}$ (the latter is well-known in the literature).

FCD has been implemented in the publicly available code ADDA and is ready to be applied by the light scattering community. Although further comparative studies are definitely required, FCD is at least a very good candidate to become a default DDA formulation for day-to-day simulations. Extreme refractive indices, such as considered in this paper, can be routinely (although not quickly) simulated using modern desktop computers.

References

[1] M. A. Yurkin and A. G. Hoekstra, "The discrete dipole approximation: an overview and recent developments," J. Quant. Spectrosc. Radiat. Transfer **106**, 558-589 (2007).

[2] B. T. Draine, "The discrete-dipole approximation and its application to interstellar graphite grains," Astrophys. J. **333**, 848-872 (1988).

[3] B. T. Draine and P. J. Flatau, "Discrete-dipole approximation for scattering calculations," J. Opt. Soc. Am. A **11**, 1491-1499 (1994).

[4] B. T. Draine and J. J. Goodman, "Beyond clausius-mossotti - wave-propagation on a polarizable point lattice and the discrete dipole approximation," Astrophys. J. **405**, 685-697 (1993).

[5] A. C. Andersen, H. Mutschke, T. Posch, M. Min, and A. Tamanai, "Infrared extinction by homogeneous particle aggregates of SiC, FeO and SiO2: Comparison of different theoretical approaches," J. Quant. Spectrosc. Radiat. Transfer **100**, 4-15 (2006).

[6] F. Kemper, A. de Koter, L. B. F. M. Waters, J. Bouwman, and A. G. G. M. Tielens, "Dust and the spectral energy distribution of the OH/IR star OH 127.8+0.0: Evidence for circumstellar metallic iron," Astron. Astrophys. **384**, 585-593 (2002).

[7] N. B. Piller and O. J. F. Martin, "Increasing the performance of the coupled-dipole approximation: A spectral approach," IEEE Trans. Ant. Propag. **46**, 1126-1137 (1998).

[8] N. B. Piller, "Influence of the edge meshes on the accuracy of the coupled-dipole approximation," Opt. Lett. **22**, 1674-1676 (1997).

[9] P. C. Chaumet, A. Sentenac, and A. Rahmani, "Coupled dipole method for scatterers with large permittivity," Phys. Rev. E **70**, 036606 (2004).

[10] A. Rahmani, P. C. Chaumet, and G. W. Bryant, "Coupled dipole method with an exact long-wavelength limit and improved accuracy at finite frequencies," Opt. Lett. **27**, 2118-2120 (2002).

[11] M. J. Collinge and B. T. Draine, "Discrete-dipole approximation with polarizabilities that account for both finite wavelength and target geometry," J. Opt. Soc. Am. A **21**, 2023-2028 (2004).

[12] M. A. Yurkin, V. P. Maltsev, and A. G. Hoekstra, "Convergence of the discrete dipole approximation. I. Theoretical analysis," J. Opt. Soc. Am. A **23**, 2578-2591 (2006).

[13] M. A. Yurkin, V. P. Maltsev, and A. G. Hoekstra, "The discrete dipole approximation for simulation of light scattering by particles much larger than the wavelength," J. Quant. Spectrosc. Radiat. Transfer **106**, 546-557 (2007).

[14] N. B. Piller, "Coupled-dipole approximation for high permittivity materials," Opt. Comm. **160**, 10-14 (1999).

[15] M. Min, L. B. F. M. Waters, A. de Koter, J. W. Hovenier, L. P. Keller, and F. Markwick-Kemper, "The shape and composition of interstellar silicate grains," Astron. Astrophys. **462**, 667-676 (2007).

[16] M. A. Yurkin, V. P. Maltsev, and A. G. Hoekstra, "Convergence of the discrete dipole approximation. II. An extrapolation technique to increase the accuracy," J. Opt. Soc. Am. A **23**, 2592-2601 (2006).

Scattering of light by fluffy aggregates consisting of small and large particles

N. N. Zavyalov and N. V. Voshchinnikov

Sobolev Astronomical Institute, St. Petersburg University, Universitetskii prosp., 28, St. Petersburg, 198504 Russia
tel: +7 812-428-4263, fax: +7 812-428-7129, e-mail: Zavyalov_n@rambler.ru, nvv@astro.spbu.ru

Abstract

We study intensity and polarization of radiation scattered by fluffy aggregates. Model is porous pseudosphere with small size (Rayleigh) inclusions and inclusions of different sizes. The calculations are carried out using the discrete dipole approximation (DDA) code for several materials with complex refractive indices ranging from $1.20 + 0.00i$ to $1.75 + 0.58i$. The results are compared with the predictions of the Lorenz-Mie theory with a refractive index found from the effective medium theory based on the Bruggeman rule and the extended Mie theory for n-layered spheres. It is found that the scattering characteristics of particles with small inclusions are described by the Bruggeman–Mie theory quite well (deviations usually do not exceed $\sim 5 - 15\%$). For particles with inclusions of different sizes the satisfactory agreement between n-layered spheres and DDA computations is obtained for small and intermediate porosity.

1 Introduction

Finding the optical properties of fluffy aggregate particles is an important task for different fields of science and industry. Such particles are generally assumed to be constituents of interstellar clouds, circumstellar and protoplanetary disks, various suspensions, etc. Because the numerical methods developed for the aggregate optics calculations are rather computationally expensive, we develop "effective" models where complex particle is replaced by a simple model with similar optical properties. In papers [1] and [2] it was shown that the extinction efficiencies and other integral scattering characteristics of porous pseudospheres with small size (Rayleigh) inclusions can be well described using Lorenz-Mie theory and a refractive index found from the Bruggeman mixing rule of the effective medium theory (EMT). At the same time, the extinction of heterogeneous particles having inclusions of various sizes (Rayleigh and non-Rayleigh) are found to resemble those of spheres with a large number ($\gtrsim 15 - 20$) of different layers [1].

Here, we study angular scattering properties of particles consisting of vacuum and some material. As earlier [2], five refractive indices of materials corresponding to biological, atmospheric and cosmic particles were selected. Previous analysis of applications of different mixing rules was mainly focused on extinction efficiencies (see Refs. [3], [4] and references therein). Only a couple times intensity and polarization of scattered radiation calculated using some EMT mixing rule compared with the results of microwave analog experiments [5] and the results of DDA calculations [6] and [7].

2 Models and calculations

We consider spherical particles consisting of some amount of a material and some amount of vacuum. The amount of vacuum characterizes the particle porosity $\mathcal{P}$ ($0 \leq \mathcal{P} < 1$), which is introduced as

$$\mathcal{P} = V_{\rm vac}/V_{\rm total} = 1 - V_{\rm solid}/V_{\rm total},$$

where $V_{\rm vac}$ and $V_{\rm solid}$ are the volume fractions of vacuum and solid material, respectively. If $\mathcal{P} = 0$ the particle is homogeneous and compact. Fluffy particles also can be presented as homogeneous spheres of the

same material mass with radius $r_{\rm porous}$ and a refractive index found using an EMT. The size parameter of porous particles can be found as

$$x_{\rm porous} = \frac{2\pi r_{\rm porous}}{\lambda} = \frac{x_{\rm compact}}{(1-\mathcal{P})^{1/3}} = \frac{x_{\rm compact}}{(V_{\rm solid}/V_{\rm total})^{1/3}},$$

where λ is the wavelength of incident radiation.

The optical properties of particles with inclusions are evaluated using program DDSCAT (version 6.0) [8]. The particles ("targets" in the DDSCAT terminology) are reproduced by pseudospheres with inclusions of a fixed size or with a given distribution of inclusions over their sizes (see [1] for details). Targets with the values of $d_{\rm incl}$ ranging from 1 to 9 are considered. The inclusions of the size $d_{\rm incl} = 1$ are dipoles, while the inclusions with $d_{\rm incl} = 3, 5, 7$ and 9 consist of 27, 125, 343 and 729 dipoles, respectively. Contrary to previous calculations, the optical characteristics of pseudospheres with inclusions are averaged over 256 target orientations.

The effective models of aggregates includes the Lorenz-Mie calculations for homogeneous spheres with refractive index found from Bruggeman mixing rule and calculations for n-layered spheres.

We consider non-polarized incident radiation and analyse the angular dependence of the intensity (element S_{11} of the Müller scattering matrix) and linear polarization of scattered radiation ($P = -S_{12}/S_{11}$).

3 Results and discussion

Computations were performed for fluffy particles with size parameters $x_{\rm compact} = 1, 3$, and 10 and porosity $\mathcal{P} = 0.33$, 0.5 and 0.9. The refractive indices of compact particles are chosen to be $m_{\rm compact} = 1.20 + 0.00i$, $m_{\rm compact} = 1.33 + 0.01i$, $m_{\rm compact} = 1.68 + 0.03i$, $m_{\rm compact} = 1.98 + 0.23i$, and $m_{\rm compact} = 1.75 + 0.58i$. These values are typical of refractive indices of biological particles, dirty ice, silicate, amorphous carbon and soot in the visual part of the spectrum, respectively. The effective refractive indices calculated using Bruggeman mixing rule are given in Table 3 in [2].

Some results for aggregates with Rayleigh inclusions are shown in Figs. 1 and 2. It is seen that satisfactory agreement between the effective model and DDA computations is obtained for almost all scattering angles excluding deep minima. As usual, the agreement improves for particles with smaller size parameters, smaller values of refractive index and smaller porosity. If we are restricted to porosity $\mathcal{P} = 0.33$, the deviations in calculated intensity do not exceed $\sim 5\%$, $\sim 15\%$ and $\sim 25\%$ for $x_{\rm compact} = 1, 3$, and 10, respectively. For very porous particles (right panels in Figs. 1 and 2) the difference between the effective model and DDA computations becomes rather large for scattering angles $\Theta \gtrsim 100^\circ$ (for $x_{\rm compact} = 10$ this occurs for $\Theta \gtrsim 60^\circ$) This is not unexpected, since diffraction plays a major role for small scattering angles, and this depends primarily on the external morphology of the particle. At larger scattering angles, the internal composition plays a larger role.

Figure 3 illustrates the behaviour of angular scattered characteristics for aggregates with Rayleigh and non-Rayleigh inclusions. More or less similar behaviour of intensity and polarization takes place for porosity $\mathcal{P} = 0.33$ only. For $\mathcal{P} = 0.9$ the model of n-layered spheres gives satisfactory agreement only in the case of forward intensity and backscattering polarization. However, we expect that the deviations decrease after the averaging over size distribution because in this case, the minima become washed out (see, for example, discussion in [9]).

Acknowledgments

We are grateful to Bruce Draine and Piotr Flatau for providing DDSCAT 6.0 code. The work was partly supported by grants NSh 8542.2006.2, RNP 2.1.1.2152 and RFBR 07-02-00831 of the Russian Federation.

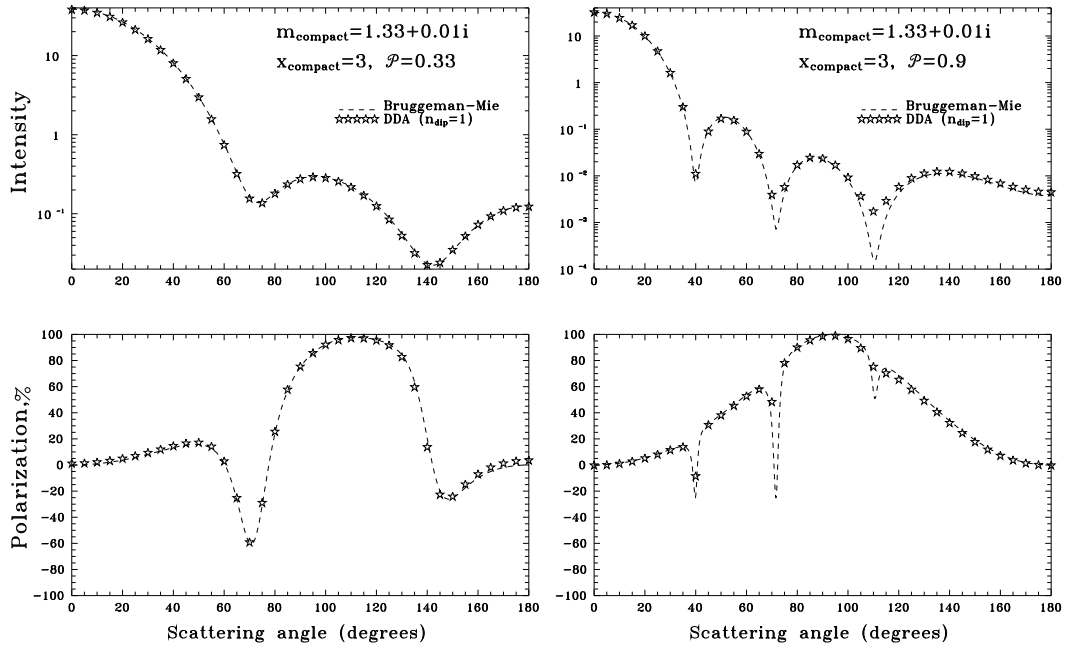

Figure 1: Intensity and polarization of the scattered radiation calculated for pseudospheres with small inclusions (DDA computations) and effective models (Bruggeman–Mie computations). The refractive indices of the inclusions are $m_{\text{compact}} = 1.33 + 0.01i$, the size parameter is $x_{\text{compact}} = 3$, the porosity of particles $\mathcal{P} = 0.33$ (left) and $\mathcal{P} = 0.9$ (right).

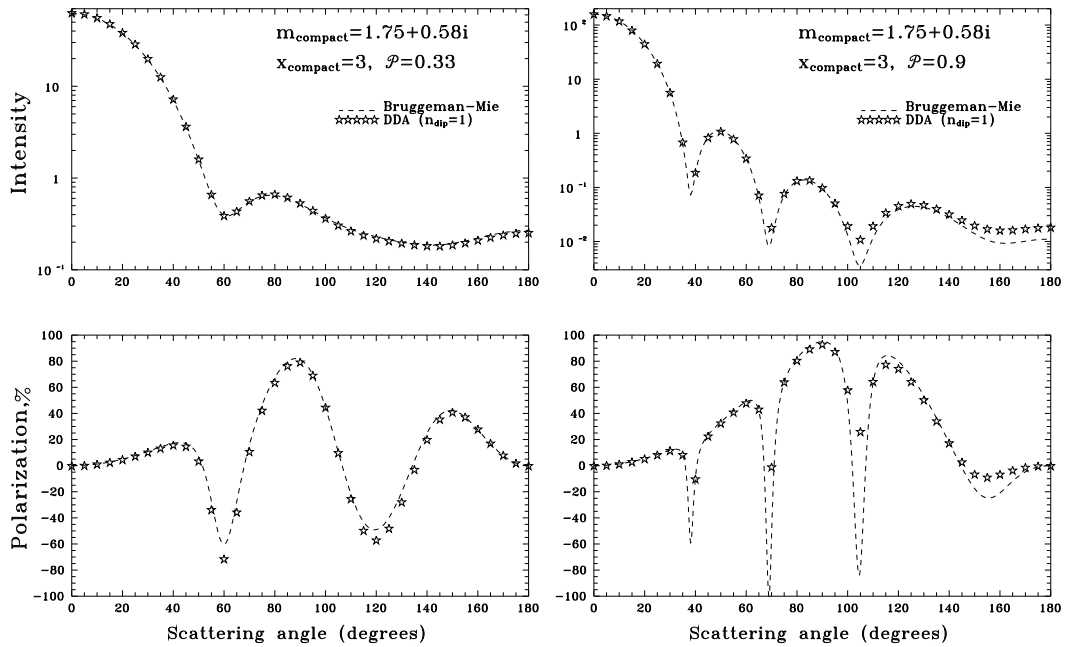

Figure 2: The same as in Fig. 1 but now for refractive index $m_{\text{compact}} = 1.75 + 0.58i$.

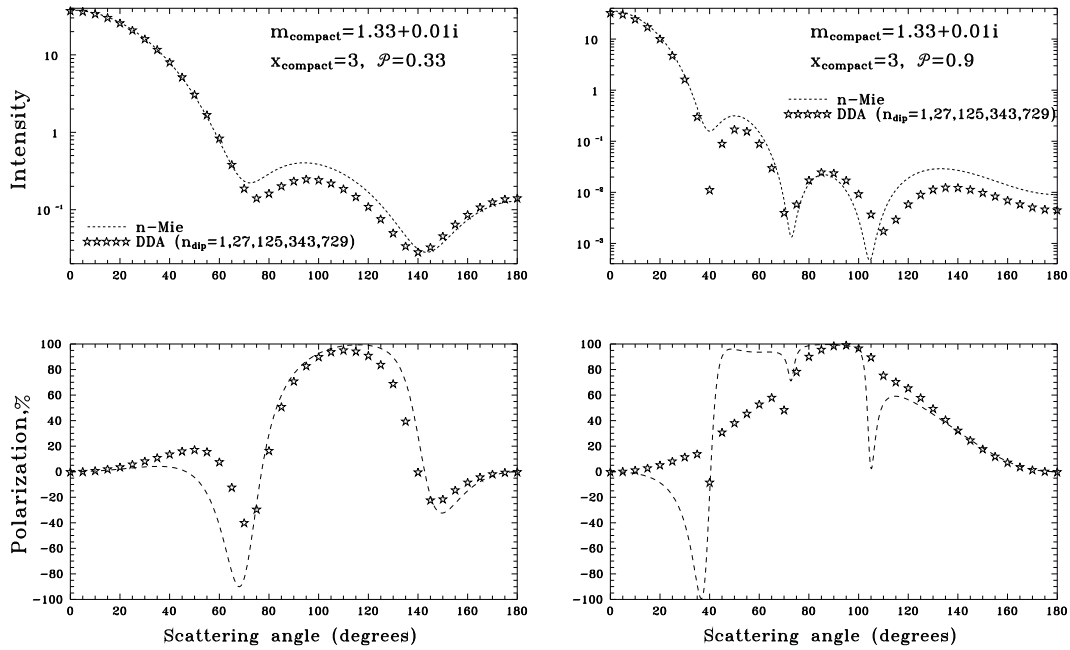

Figure 3: Intensity and polarization of the scattered radiation calculated for pseudospheres with small and large inclusions (DDA computations) and effective models (n-layered spheres). The refractive indices of the inclusions are $m_{\rm compact} = 1.33 + 0.01i$, the size parameter is $x_{\rm compact} = 3$, the porosity of particles $\mathcal{P} = 0.33$ (left) and $\mathcal{P} = 0.9$ (right).

References

[1] N. V. Voshchinnikov, V. B. Il'in, and Th. Henning, "Modelling the optical properties of composite and porous interstellar grains", Astron. Astrophys., **429**, 371–381 (2005).

[2] N. V. Voshchinnikov, G. Videen, and Th. Henning, "Effective medium theories for irregular fluffy structures: aggregation of small particles," Applied Optics, **46**, 4065–4072 (2007).

[3] N. V. Voshchinnikov, "Optics of Cosmic Dust. I", Astrophys. & Space Phys. Rev., **12**, 1–182 (2004).

[4] N. Maron and O. Maron, "Criteria for mixing rules application for inhomogeneous astrophysical grains", Monthly Notices Roy. Astron. Soc., in press ([arXiv:0712.3796]).

[5] L. Kolokolova, and B. Å. S. Gustafson, "Scattering by inhomogeneous particles: microwave analog experiments and comparison to effective medium theory", J. Quant. Spectrosc. Rad. Transfer, **70**, 611–625 (2001).

[6] M. J. Wolff, G. C. Clayton, and S. J. Gibson, "Modeling composite and fluffy grains. II. Porosity and phase function", Astrophys. J., **503**, 815–830 (1998).

[7] M. Kocifaj, and G. Videen, "Optical behavior of composite carbonaceous aerosols: DDA and EMT approaches", J. Quant. Spectrosc. Rad. Transfer, **109**, 1404–1416 (2008).

[8] B. T. Draine, and P. J. Flatau, "User Guide for the Discrete Dipole Approximation Code DDSCAT.6.0," [astro-ph/0309069] (2003).

[9] M. I. Mishchenko, L. D. Travis, and A. A. Lacis, "Scattering, Absorption, and Emission of Light by Small Particles," Cambridge University Press (2002).

Applicability of discrete-dipole approximation to conductive particles

Evgenij Zubko,[1,2] Dmitry Petrov,[2] Yuriy Shkuratov,[2] Hajime Okamoto,[1]
Karri Muinonen,[3] Hiroshi Kimura,[4] Tetsuo Yamamoto[4] and Gorden Videen[5]

[1] *Graduate School of Science, Tohoku University, Aoba, Aramakiaza, Aoba-ku, Sendai 980-8578, Japan*
[2] *Institute of Astronomy, Kharkov National University, 35 Sumskaya St., Kharkov 61022, Ukraine*
[3] *Observatory, PO. Box 14, FI-00014 University of Helsinki, Finland*
[4] *Institute of Low Temperature Science, Hokkaido University, Kita-ku North 19 West 8, Sapporo 060-0819, Japan*
[5] *Army Research Laboratory, 2800 Powder Mill Road Adelphi Maryland 20783 USA*

Abstract

We study the applicability of discrete-dipole approximation (DDA) to particles consisting of conducting materials and find that at refractive index m=1.5+1.3i DDA delivers results of reasonable accuracy over a wide range of particle sizes.

1 Introduction

The discrete-dipole approximation (DDA) is a powerful approach to compute light scattering by arbitrarily shaped particles. It has no restrictions on shape or internal structure of a target. In the DDA the target is replaced by a set of small volumes (cells) in a configuration that reproduces the original structure of the scatterer. The DDA has certain shortcomings. Most obvious is that it is a numerical technique and computationally intensive. The number of computations increases with size and refractive index. In order to provide domination of the electric dipole moment over other multipoles induced on a constituent cell, we have to decrease significantly the cell size. For instance, in the case of iron (m = 3 + 4i, at visible wavelength), the reduction is of 3 times in comparison with ice (m = 1.313 + 0i) and organic material (m = 1.5 + 0.1i).

In this paper, we show that materials having a relatively small refractive index like m = 1.5 + 1.3i can represent conducting material well in addition to having magnetic dipole and electric quadrupole moments remaining relatively small compared to the electric dipole moment for small constituent volume $x_{\rm cell} = 2\pi r_{\rm cell}/\lambda \approx 0.3$, where λ is the wavelength and $r_{\rm cell}$ is the radius of a sphere having a volume equivalent with the single constituent cell. This ratio is almost the same as in the case of dielectric material at this size parameter; thus, using refractive index of m = 1.5 + 1.3i, we can study general features of light scattering by conductive particles over a wide range of sizes.

2 Discussion of results

Using own computer implementation of DDA [e.g., 1, 2], we consider light scattering by single spheres. Spheres were generated in cubic lattice of 128 cells per side. We assume that sphere occupies only fourth part of the largest volume, when its diameter is equal to side of lattice. Such an assumption was made in order to set equal volume for sphere and agglomerated debris particles [1] generated in lattice of the same size. The size parameter of initial matrix is x=30; whereas for the sphere $x_{\rm sph}$=19.133. Note that, the size parameter of single cell is $x_{\rm cell}$=0.291, which is the largest value over all our previous studies [e.g., 1, 2]. We expect that this case is difficult for DDA analysis.

We perform four different tests which prove that DDA can be applied at the refractive index m=1.5+1.3i and size parameter of single cell as large as $x_{\rm cell}$=0.291. We compare this case with that of m=1.5+0.05i

because, at such refractive index, an angular profile of linear polarization of sphere consisting of cubic cells at x_{cell}=0.291 reveals good agreement with exact result of Mie theory (x_{sph}=19.133).

2.1 Relative contribution of magnetic dipole and electric quadrupole moments

Using Lorenz-Mie theory, we compute electric dipole, magnetic dipole, and electric quadrupole moments in the case of a single constituent cell. In the theory, these are represented, correspondingly, by scattering coefficients a_1, b_1, and a_2 [3]. At x_{cell} = 0.291 and m = 1.5 + 0.05i, $|a_1|$ = 0.004856, $|b_1|$ = 0.000058, and $|a_2|$ = 0.000023. Growth of the imaginary part of refractive index to Im(m)=1.3 changes these coefficients to: $|a_1|$ = 0.014013, $|b_1|$ = 0.000178, and $|a_2|$ = 0.000061. One can see that increasing the absorption amplifies all scattering coefficients by approximately the same factor of three. The essential point is that the relative contributions of magnetic dipole and electric quadrupole moments remain approximately the same: $|b_1|/|a_1| \approx 0.012$ and $|a_2|/|a_1| \approx 0.0045$. Thus, from general point of view, in both cases the DDA delivers numerical result of the same accuracy. Note, that in the case of iron (m = 3 + 4i) and x_{cell} = 0.291, DDA definitely fails and the relative contribution of the magnetic dipole moment is five times larger; whereas, the relative contribution of the electric quadrupole moment remains almost the same.

Another way to verify the contribution of the magnetic dipole moment has been used by Draine [4]. He considered the ratio of the magnetic dipole absorption to the electric dipole absorption

$$C_{\text{abs}}^{m} \big/ C_{\text{abs}}^{e} = 0.0111 \cdot (x_{\text{cell}})^2 ((\text{Re}(\varepsilon) + 2)^2 + \text{Im}(\varepsilon)^2) , \quad (1)$$

where Re(ε) and Im(ε) are the real and imaginary parts of the dielectric permittivity. We compute this ratio as well. At x_{cell} = 0.291, the cases of m = 1.5 + 0.05i and m = 1.5 + 1.3i reveal similar values of the ratio (1): 0.017 and 0.021, respectively. In the case of iron the ratio (1) is 0.565, i.e., about 30 times higher. Summarizing this section, we can state that the error in assuming just a dipole moment is approximately the same for materials of m = 1.5 + 1.3i and m = 1.5 + 0.05i.

2.2 Satisfaction of Maxwell equations

In order to verify that the results obtained with the DDA satisfy Maxwell equations, we consider the scattering cross-section C_{sca} calculated in two different ways. One of them is based on the Optical theorem [3] that is used to compute the cross-sections of extinction C_{ext} and absorption C_{abs}. The coefficient of extinction C_{ext} results from interference of the incident electromagnetic wave with the forward-scattered field, and the coefficient of absorption C_{abs} can be calculated directly from the field induced on the dipoles. The scattering cross-section C_{sca} is the difference between the coefficients C_{ext} and C_{abs}.

The cross-section C_{sca} also can be computed by integrating the intensity of the scattered field over a circumscribing sphere. This definition of C_{sca} takes into account mutual interference of waves scattered by all dipoles to the observation point. Both methods for computation of C_{sca} reveal principal mathematical distinctions, and most critically, these two methods can only be in agreement if the DDA algorithm satisfies Maxwell equations; hence, a comparison is a test of whether the Maxwell equations were satisfied. We compute the difference between C_{sca} obtained in these two different ways and found that for the sphere of m = 1.5 + 0.05i and x_{sph} = 19.133 (x_{cell} = 0.291), the difference is 10.603%; whereas, for the same size sphere of m = 1.5 + 1.3i a difference in C_{sca} of 10.575% is obtained. Thus, increasing Im(m) from 0.05 to 1.3 has no influence on the satisfaction of Maxwell equations using this technique.

Another point to consider is the magnitude of the difference between the two values of C_{sca} as 10.5% may be significant. By comparison, we study how much that difference might be in the case when numerical result does not satisfy Maxwell equations. We consider a sphere of x_{sph} = 19.133 and m = 1.5 + 1.3i. The total number of iterations required to achieve light-scattering properties at regular accuracy is 156, but we interrupted the process at the eleventh iteration and used the results of the first ten iterations only. In this case, the difference in C_{sca} is more than a factor of ten.

2.3 Distribution of energy of the induced field over the volume of the scatterer

Since values of the real and imaginary part of the refractive index m = 1.5 + 1.3i are similar, the material possesses conducting properties. We expect the energy to be concentrated near the particle surface and, indeed, the ratio of the skin depth to wavenumber for this refractive index is 0.385; i.e., the skin layer is thinner than the size of one constituent cell in the sphere at x_{sph}=19.133 [5].

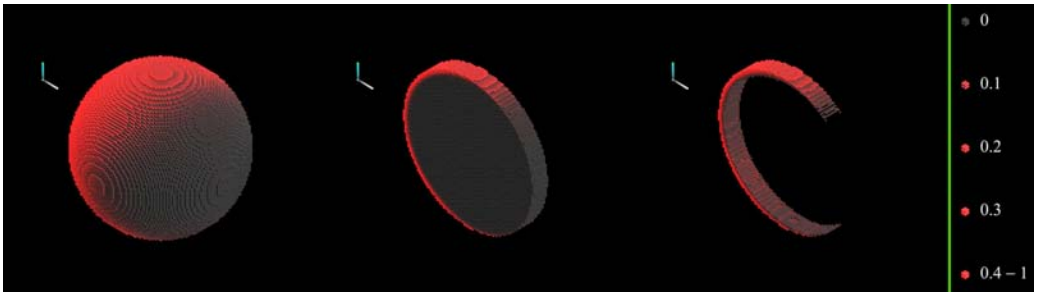

Figure 1: Distribution of energy inside the sphere at x_{sph}=19.133 and m=1.5+1.3i obtained with DDA.

In Fig. 1 we present results of DDA computations of the energy of the induced field in an x_{sph} = 19.133, m = 1.5 + 1.3i sphere. The total number of cells is 285,144 and their size parameter is x_{cell} = 0.291. On the left portion of Fig. 1, the energy distribution over the sphere exterior is shown. White and blue lines indicate the directions of propagation and the electric-field vector of the incident electromagnetic wave. The energy distribution has been normalized, so, it varies from 0 to 1. The middle of Fig. 1 presents a slice of the sphere, and on the right, we show the same slice omitting the dipoles whose induced-field energy is less than 0.01. One can see that only the outermost dipoles appear in a saturated red color; whereas, dipoles forming the next layer are already darker. The attenuation of energy between layers is about 3 times or even higher. This is in good quantitative agreement with our estimation of skin depth.

2.4 Comparison with Lorenz-Mie theory

Comparison with Lorenz-Mie theory provides a method to check the accuracy of the DDA, but we must remember there are two sources of error: violation of the Maxwell equations and an insufficient approximation of the perfect sphere by the array of dipoles. Ascertainment of the real reason for the difference between the DDA and Mie theory is not always trivial; nevertheless, we present results of such a comparison in Fig. 2 for a sphere of x_{sph} = 19.133. In the DDA simulation, the sphere is approximated by 285,144 dipoles whose x_{cell} = 0.291. On the left in Fig. 2, at m = 1.5 + 0.05i, there is a strong resemblance between the results of the DDA and Lorenz-Mie theory. Simultaneously, at m = 1.5 + 1.3i, the difference between both approaches is quite significant (see right panel in Fig. 2). However, taking into account the arguments mentioned in sections 2.1–2.3, we do not necessarily interpret that difference as a violation of the Maxwell equations, but as a discretization error. First and foremost, we note that the skin depth is smaller than the cell size. This means that the induced fields computed using the DDA are average values over the cell volumes. In turn, the discretization roughness is visible to the electromagnetic field, since both their spatial frequency components are comparable. This surface roughness increases the contribution of the outer layers and reduces that of the particle interior. This is demonstrated also in the right panel of Fig. 2, which shows the polarization response from a thin shell otherwise having the same properties. In this case the interior cannot contribute to the scattering because there is none. DDA simulations performed using smaller spheres show that the light scattering approaches that of Lorenz-Mie theory as the resolution is further increased.

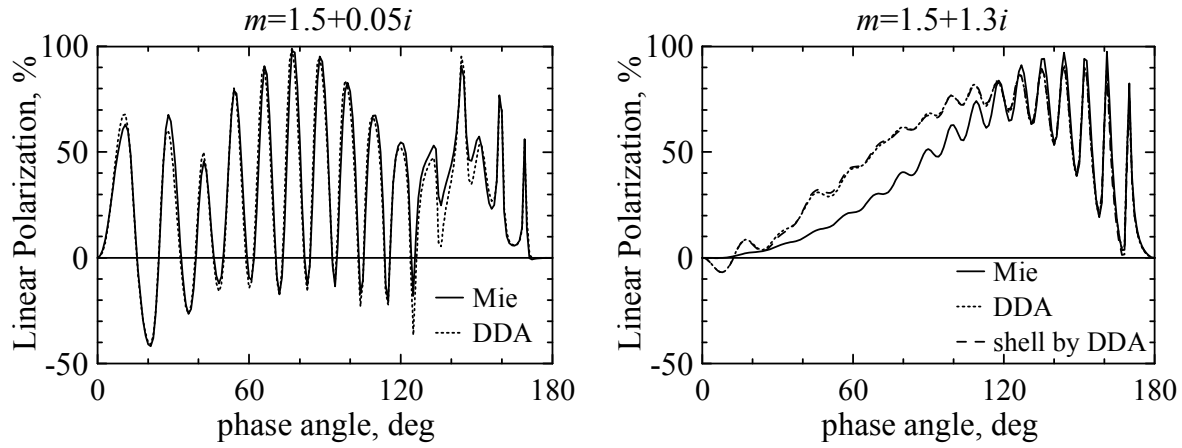

Figure 2: Degree of linear polarization as function of phase angle produced by sphere at x_{sph}=19.133.

3. Conclusion

The DDA can be applied to the study of light scattering by irregularly shaped particles having relatively high absorption, assuming a relatively small absolute value of refractive index $|m| \leq 2$. So long as the non-electric-dipole contributions remain relatively small, the DDA allows us to consider particles as large as in the case of optically soft particles (m = 1.313+0i). However, as the absorption increases the role of surface roughness is enhanced, resulting in errors in describing particle shape. Such errors should be considered especially for smooth particle systems like spheres and spheroids. When considering naturally occurring irregularly shaped particles, this roughness must be incorporated into the particle description. Note, that in many applications the surface roughness of irregularly shaped particles does not cause any problems; it might be even desirable.

Acknowledgments

This research was partially supported by a Grant-in-Aid for Scientific Research from the Japanese Society for the promotion of Science.

References

[1] E. Zubko, Yu. Shkuratov, N. Kiselev, G. Videen, “DDA simulations of light scattering by small irregular particles with various structure,” J. Quant. Spectr. Radiat. Transfer., **101**, 416–434 (2006).

[2] E. Zubko, K. Muinonen, Yu. G. Shkuratov, G. Videen, T. Nousiainen, “Scattering of light by roughened Gaussian random particles,” J. Quant. Spectr. Radiat. Transfer., **106**, 604–615 (2007).

[3] C. F. Bohren and D. R. Huffman, *Absorption and Scattering of Light by Small Particles* (Wiley, New York, 1983).

[4] B. T. Draine, “The discrete-dipole approximation and its application to interstellar graphite grains,” Astrophysical J., **333**, 848–872 (1988).

[5] M. Born and E. Wolf, *Principles of optics* (Cambridge University Press, Cambridge, 1999).

MINERAL DUST AEROSOLS

A 3D Regional Saharan Dust Transport Model, and Comparisons with Satellite Observations

J. R. Banks[1], R. G. Grainger[1], M. N. Juckes[2]

[1] *Department of Atmospheric, Oceanic, and Planetary Physics, University of Oxford, Clarendon Laboratory, Parks Road, Oxford, OX1 3PU, UK*
[2] *The British Atmospheric Data Centre, Rutherford Appleton Laboratory, Harwell Science and Innovation Campus, Didcot, OX11 0QX, UK*

Tropospheric aerosols have a significant influence on climate and have been recognised by the Intergovernmental Panel on Climate Change as the biggest source of uncertainty in understanding future climate, yet the factors controlling their spatial distribution remain unclear. Despite new observations from the UK ATSR instruments and the MODIS and MISR instruments (on NASA's Terra satellite) there are still open questions about aerosol sources, sinks, microphysical properties and the aerosol vertical distribution.

A three-dimensional dust lifting and transport model, using meteorological fields from ECMWF analyses, is used to compare predicted dust loading over the Sahara with observations from AERONET, SEVIRI, AATSR, and MISR. The model will be used to investigate the sensitivity of the predicted aerosol profiles to variations in model parameters. Processes included in the model include emission, advection, diffusion, gravitational settling, and turbulent deposition.

Light scattering and absorption properties of dust particles retrieved from satellite measurements

Rong-Ming Hu,[1] and Ranjeet Sokhi[1]

[1] *University of Hertfordshire, Centre for Atmospheric and Instrumentation Research (CAIR), College Lane, Hatfield, Herts AL109AB, United Kingdom*

tel: +44 (1707) 284052, fax: +44 (1707) 284185, e-mail: r.hu@herts.ac.uk

Abstract

We use the radiative transfer model and chemistry transport model to improve our retrievals of dust optical properties from satellite measurements. The optical depth and absorbing optical depth of mineral dust can be obtained from our improved retrieval algorithm. The solar radiative forcing of dust aerosols has also been calculated using refined optical model and radiative transfer model.

1 Introduction

Mineral dust particles are the most widespread natural and anthropogenic aerosols and play an important role in climate forcing by altering the earth's energy budget through scattering and absorption of radiation (Tegen et al., 1996; Sokolik and Toon, 1996), and changing the cloud formation (Kaufman et al., 2005). In spite of decadal efforts, the detailed information on physical, chemical and optical properties of mineral dust is still limited. Satellite remote sensors have provided rich information on aerosol optical properties in recent years (King et al., 1999; Mishchenko et al., 1999; Kaufman et al., 2002, Kahn et al., 2005). However, the uncertainties stem from simplified assumptions of dust composition, dust profile, dust mixing state and morphology used in retrieval algorithms. In this study, we use the additional information from global chemistry transport model (GEOS-Chem) to improve the results of satellite retrievals of dust aerosol optical depth (AOD) and absorbing aerosol optical depth (AAOD).

2 Methodology

The backscattered radiance measured by satellite sensors can be converted to aerosol optical properties such as AOD and aerosol effective radius. In order to estimate the dust AOD, we use the AOD data from the Moderate Resolution Imaging Spectrometer (MODIS) measurements (Chu et al, 2002, Remer et al., 2002). As the data over bright surface such as Saharan desert are rejected, we use the Multiangle Imaging Spectro-Radiometer (MISR) (Kahn et al., 2005) AOD data over these regions. The calculation of dust AOD δ_{dust} is as follows:

$$\delta_{dust}(\lambda) = \delta_{a}(\lambda) \cdot f_{dust} \quad (1)$$

Where δ_a is AOD at wavelength λ and f_{dust} is the fraction of dust aerosols. We use the aerosol fraction values generated from GEOS-Chem model (Bey et al., 2001, Park et al., 2005). The model is driven by assimilated meteorological data from the Goddard Earth Observing System (GEOS-3) at the NASA Global Modeling and Assimilation Office (GMAO). The mineral dust simulation is based on the Dust Entrainment and Deposition (DEAD) scheme Zender et al. (2003) as implemented by Fairlie et al. [2006]. The size distribution of dust aerosols is assumed to be lognormals with four size bins (Martin et al., 2003).

For dust aerosol absorption, we first retrieve the column effective aerosol single scattering albedo (ω_0) that reproduces the Total Ozone Mapping Spectrometer (TOMS) aerosol index (Torres et al., 2005), when constrained by MODIS and MISR aerosol optical depth and by relative vertical profiles from GEOS-Chem model (Hu et al., 2007). We use a Mie scattering

algorithm (Mie, 1908) for small spherical dust particles and the T-Matrix algorithm (Mishchenko et al., 1995) for large non-spherical dust particles to calculate the optical quantities. The total backscattered radiance is calculated by the vector discrete ordinate radiative transfer model VLIDORT (with polarization) (Spurr, 2007; Natraj etal., 2006). A look-up table of backscattered radiances was developed for a variety of atmospheric and surface conditions as function of all sun-satellite viewing geometries. The most likely solution is selected by a chi-squared minimization method for ambiguous solutions (Hu et al., 2002). As we assume the external mixing state of aerosol components such as sulfate, soot, mineral dust, sea salt and organics, the dust ω_0 can be calculated from the column effective ω_0 with the aerosol fractions inputted from GEOS-Chem simulations. Then we can calculate the dust absorbing aerosol optical depth (AAOD) from the dust AOD and ω_0. Finally, the solar radiative forcing of dust particles at the top of atmosphere can be calculated using radiative transfer model VLIDORT.

3 Results and discussions

The vertical profiles of dust particles are determined from the GEOS-Chem simulations. We performed dust simulation for year 2003. Figure 1 presents the vertical profiles of dust particles for different size bin at Dahkla, Western Sahara. We find the dust particles can be lifted to high level under the suitable meteorological condition. Interestingly, the peak altitudes of dust profiles for particle radius between 0.1 and 3 μm are almost same.

Figure 2 shows the dust AOD at 360 nm retrieved from MODIS and MISR during spring of 2003. The high values of AOD are seen over Sahara, Gobi and Australia deserts with strong dust emission sources. The enhancement of AOD over the part of Atlantic Ocean, East Asia, Pacific Ocean and North America is clear evidence that the dust particles are long range transported far away from source regions. The dust particles originated from seasonal dust storms are harmful to human health and create poor visibility in surrounding regions.

Figure 3 presents the dust AAOD derived from dust AOD and ω_0. High values of AAOD are found over areas driven by dust storms. As the AAOD is less sensitive to cloud contamination and aerosol humidification (Kaufman et al., 2006), it is very suitable to detect aerosol type such as dust particles. The high values of dust AAOD have been found over the Atlantic Ocean in downwind of Saharan region. Strong negative solar radiative forcing occurred over the most part of deserts and near areas (Figure 4).

The physical and chemical processes of dust formation, evolution and transport are very complicated. It is highly challenge for model simulation and satellite retrieval. Uncertainties exist in size distribution, refractive indices, morphology and mixing state of dust particles. Indeed, there is no consensus on the radiative forcing of anthropogenic dust particles in current stage. Subsequent measurements from ground-based, airborne and space-based instruments can provide more information on the optical, microphysical, chemical properties, and the temporal and spatial variation of dust particles. The combination of modeling and observation to improve our understanding of dust properties is highly recommended.

Acknowledgments

This work is supported by U.K. Natural Environment Research Council as part of Mesoscale Modelling for Air Pollution Application Network (MESONET) project and the U.K. Environment Agency of Comparison of Simple and Advanced Regional Models (CREMO) project.

References

[1] Bey I., D. J. Jacob, J. A. Logan, R. M. Yantosca, Asian chemical outflow to the Pacific: origins, pathways and budgets, *J. Geophys. Res*., 106, 23,097-23,114, 2001.

[2] Chu, D.A., Y.J. Kaufman, C. Ichoku, L.A. Remer, D. Tanre, and B.N. Holben, Validation of MODIS aerosol optical depth retrieval over land, *Geophys. Res. Lett*., 29, 10.1029/2001GL013205, 2002.

[3] Fairlie, T. D., D. J. Jacob and R. J. Park, The impact of transpacific transport of mineral dust in the United States, *Atmos. Environ.*, in press, 2007.

[4] Hu, R.-M., R.V., Martin, and T. D. Fairlie, Global retrieval of columnar aerosol single scattering albedo from space-based observations, *J. Geophys. Res.*, 112, D02204, doi:10.1029/2005JD006832, 2007.

[5] Hu, R.-M., K.S. Carslaw, C. Hostetler, L.R. Poole, B. Luo, T. Peter, S. Fueglistaler, T.J. McGee, and J.F. Burris, Microphysical properties of wave polar stratospheric clouds retrieved from lidar measurements during SOLVE/THESEO 2000, *J. Geophys. Res.*, 107, 8294, doi:10.1029/2001JD001125, 2002.

[6] Kahn, R., et al., Multiangle Imaging Spectroradiometer (MISR) global aerosol optical depth validation based on 2 years of coincident Aerosol Robotic Network (AERONET) observations. *J. Geophys. Res*., 110, D10S04, doi:10.1029/2004JD004706, 2005.

[7] Kaufman, Y.J., D.Tanre, and Boucher, A satellite view of aerosols in the climate system, *Nature,* 419, 215-223, 2002.

[8] Kaufman, Y.J., I. Koren, L. A. Remer, D. Rosenfeld, and Y. Rudich, The effect of smoke, dust and pollution aerosol on shallow cloud development over the Atlantic Ocean, *Proc. Natl. Acad. Sci. U.S.A.*, 102, 11207-11212, 2005.

[8] Kaufman, Y.J., I. Koren, Smoke and pollution aerosol effect on cloud cover, *Science*, 313, 655-658, 2006.

[9] King, M.D., Y.J. Kaufman, D. Tanre and T. Nakajima, Remote sensing of tropospheric aerosols from space: Past, present and future, *Bull. Am. Meteo. Soc*., 2229-2259, 1999.

[10] Martin, R.V., D.J. Jacob, R.M. Yantosca, M. Chin, and P. Ginoux, Global and regional decreases in tropospheric oxide emissions constrined by space-based observations of NO2 columns, *J. Geophys. Res*., 108, 4097, doi:10.1029/2002JD002622, 2003.

[11] Mie, G., Beitrage zur Optik truber Medien, speziell Kolloidaler Metallosungen. *Ann. Physik, 25*, 377-445, 1908.

[12] Mishchenko, M. I., and A. A. Lacis, B. E. Charlson, and L. D. Tavis, Nonsphericity of dust-like tropospheric aerosols: Implications for aerosl remote sensing and climate modeling, *Geophys. Res. Lett*., 22, 1077-1080, 1995.

[13] Natraj, V., R. Spurr, H. Boesch, Y. Jiang, and Y. Yung, Evaluation of errors in neglecting polarization in the forward modeling of O2 A band measurements from space, with relevance to CO2 column retrieval from polarization sensitive instruments, *JQSRT*, in press, 2006.

[13] Park, R.J., D.J. Jacob, M. Chin, and R.V. Martin, Sources of carbonaceous aerosols over the United States and implications for natural visibility conditions, *J. Geophys. Res*., 108, 4355, doi:10.1029/2002JD003190, 2003.

[14] Remer, L.A., et al., Validation of MODIS aerosol retrieval over ocean, *Geophys. Res. Lett*., 29, doi:10.1029/2001GL013204, 2002

[15] Sokolik, I. N., and O. B. Toon, Direct radiative forcing by anthropogenic airborne mineral aerosols, *Nature*, 381, 681-683, 1996.

[16] Spurr, R. J. D., VLIDORT: A linearized pseudo-spherical vector discrete ordinate radiative transfer model for forward model and retrieval studies in multilayer, multiple scattering media, *JQSRT*, in print, 2007.

[17] Tegen, I., A. A. Lacis, and I. Fung, The influence on climate forcing of mineral aerosols from disturbed soils, *Nature*, 380, 419-422, 1996.

[18] Torres, O., P.K. Bhartia, J.R. Herman, Z. Ahmad, and J. Gleason, Derivation of aerosol properties from satellite measurements of backscattered ultraviolet radiation - theoretical basis, *J. Geophys. Res., 103*, 17099-17110, 1998.

[19] Zender C. S., H. Bian, D. Newman, Mineral Dust Entrainment and Deposition (DEAD) model: Description and 1990s dust climatology, *J. Geophys. Res.*, 108 (D14)}, 4416, doi:10.1029/2002JD002775, 2003.

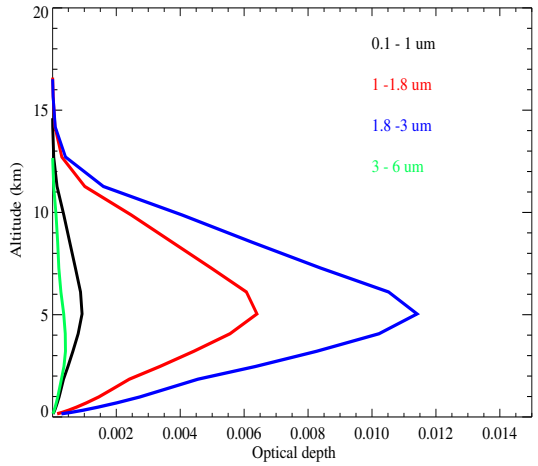

Figure1. The vertical profiles of dust particles simulated by GEOS-Chem at Dahkla.

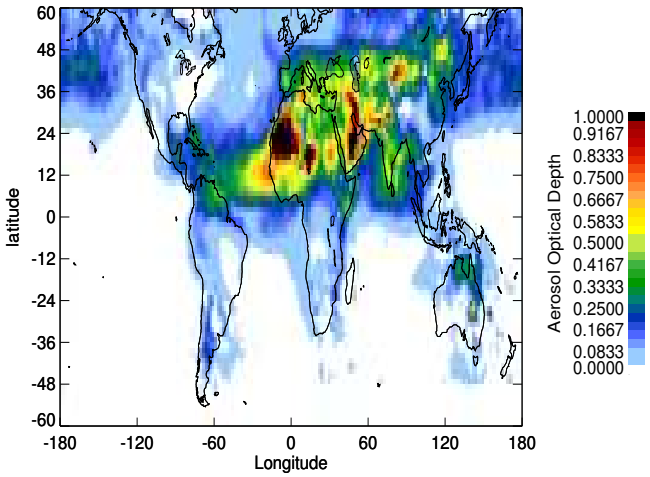

Figure 2. The dust aerosol optical depth retrieved from satellite measurements during spring of 2003.

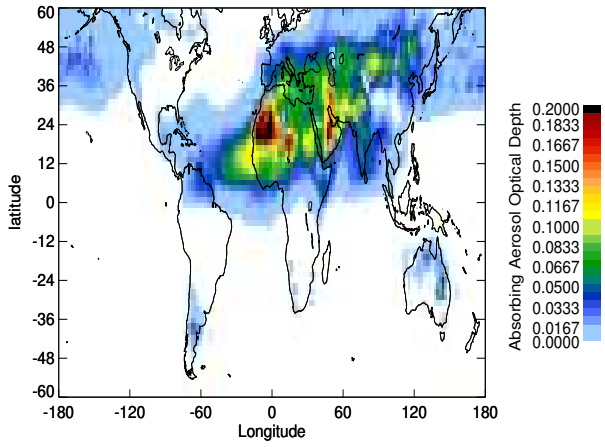

Figure 3. The dust AAOD retrieved from satellite measurements during spring of 2003.

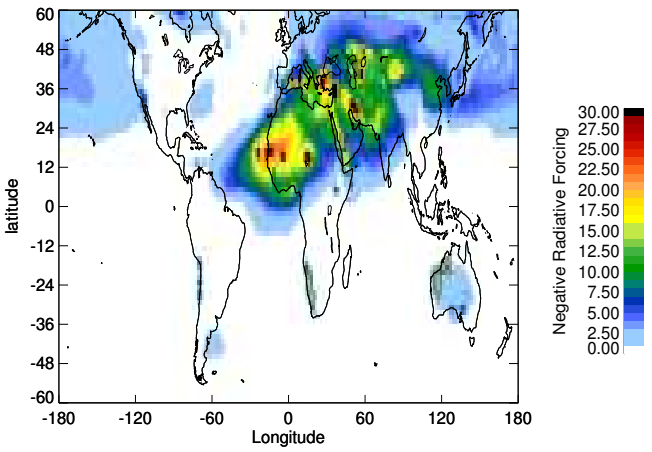

Figure 4. The solar radiative forcing (W/m^2) of dust aerosols at TOA calculated from VLIDORT during spring of 2003.

Bottom-up approach to study dielectric properties of carbon soot

R. Langlet[1], F. Moulin[1], M. R. Vanacharla[1], S. Picaud[1], M. Devel[1]

[1] *UTINAM institute, UMR CNRS 6213,*
16 route de GRAY, 25030 Besançon CEDEX, FRANCE
tel: +33 381-666476, fax: +33 381-666475, e-mail: michel.devel@univ-fcomte.fr

Abstract

Dielectric properties of various soot nanoparticles are simulated using an atomistic multi-step DDA-like approach. It is found that even for pure carbon particles, these properties clearly depend on the details of the atomic structure, especially in the visible domain.

1 Introduction

During several decades, a large quantity of pollutants have been rejected in the atmosphere among which the carbon dioxide that possess warming properties and the carbon soot that play an uncertain role in the climate change. The optical properties of soot depend widely on their location in the atmosphere and on their geometrical properties.

Atmospheric carbon soot is mainly made of carbon nanoparticles arranged in fractal clusters of variable size. These nanoparticles are characterized by spherical geometries (with diameters ranging from a few to tens of nm) and by a onion-like arrangement of small carbon clusters. In our study, we adopt a bottom-up multi-step approach in which these soot nanoparticles are modeled by random distributions of various pure carbon chemical units (C_{13}, C_{16}, C_{19}, C_{24}) on concentric spheres. We have developped a multi-step discrete dipole approximation (DDA) model, adapted to the typical geometry of the soot nanoparticles and to the use of true atomic polarizabilities[1], which is able to deal with more than 100 000 atoms (nanoparticles with 15 nm diameter, experimentally observed size) while keeping a very good accuracy compared to the exact modelisation (figure 1). The dynamical dielectric function is computed for several kinds of nanoparticles.

2 Results

The principle of the method is illustrated on the following figure (Left part). The proof of its accuracy is given on the right part of the picture.

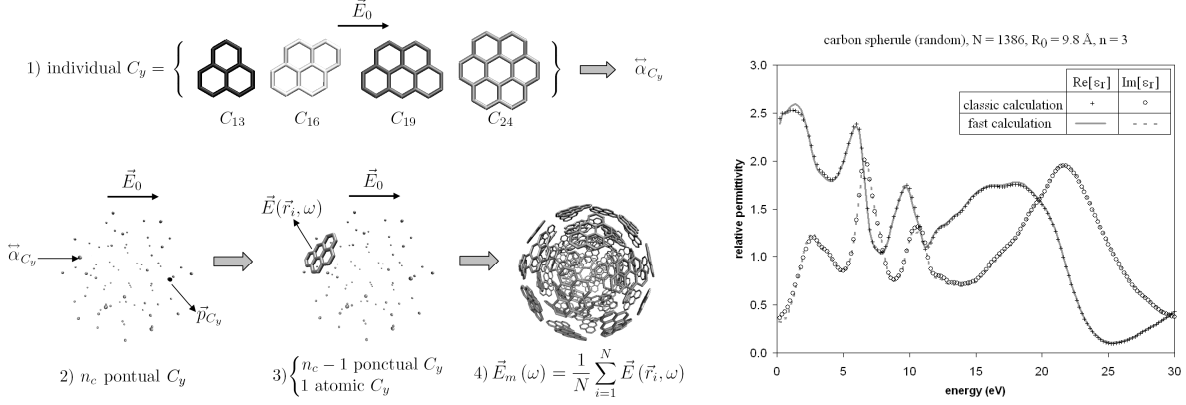

Figure 1: (Left) Description of the fast multi-step method; (Right) Example of comparison between the dielectric response of exact calculation (symbols) and simplified (fast) calculation (lines) for a carbon spherule containing 1386 atoms.

In the poster, we present results concerning nanoparticles made with various mixtures of elementary units. A first example is given below

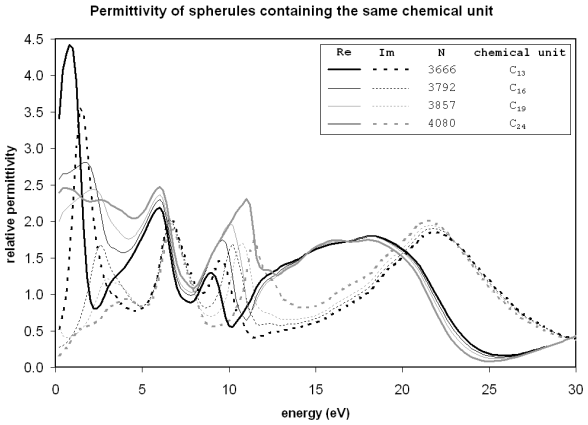

Figure 2: Examples of dielectric functions computed for carbon spherules made by different kinds of chemical units.

3 Conclusion

The results computed for our theoretical nanoparticles are of the same order of magnitude that the experimental results obtained for isolated large nanoparticles [2]. Indeed, for nanoparticles with increasing sizes the calculations highlight a saturation effect of the permittivity above 10 000 atoms.

The main results show a great dependence of the nanoparticle dielectric function on their detailed atomic structure (see figure 2), especially for optical frequencies. This confirms the possibility to gain information on the atomic structure of soot by means of EELS or optical measurements. This result also confirms the importance of studying atmospheric carbon soot in order to understand their optical and infrared effects and to give a definite balance sheet of their radiative properties.

Acknowledgments

The “Région de Franche-Comté” is thanked for its financial support for M.R. Vanacharla.

References

[1] F. Moulin, M. Devel and S. Picaud, Optical properties of soot nanoparticules, JQSRT, **109**, 1791-1801 (2008)

[2] D. Alexander, J. Anderson, P. Crozier, Improved determination of aerosol optical properties from the EEL spectrum, Microsc. Microanal. **13** (Suppl 2), 1254–1255 (2007).

Investigation into Single Scattering Properties of Airborne Saharan Dust Particles

D.S. McCall, [1] Z. Ulanowski, [1] E. Hesse, [1] C. Stopford, [1] K. Kandler, [2] P.H. Kaye, [1]

[1] *STRI, University of Hertfordshire, Hatfield AL10 9AB, United Kingdom*
[2] *Inst. fuer Angewandte Geowissenschaften, Technische Universität Darmstadt, Schnittspahnstr. 9, D-64287 Darmstadt, Germany*

Abstract

The phase functions of single mineral dust particles levitated in an electrodynamic balance have been measured. Normalized phase functions and the asymmetry parameter could be determined because nearly the full range of scattering angles was available: 0.5° to 177°. The particles have been characterized using microscopy.

1 Introduction

The importance of airborne particulates to the Earth-atmosphere radiation balance is well established. Aerosols such as Saharan dust particles have direct effects on the Earth's energy budget by scattering and absorbing radiation, and indirect effects, such as acting as cloud condensation nuclei [1]. Estimates of the amount of atmospheric dust originating from northern Africa range from 260 to 1500 x 10^6 tons per year [2]. These dust particles cause large uncertainties in assessing the effect of atmospheric aerosols on climate forcing. Therefore, it is important to obtain accurate scattering data from representative Saharan dust particles. In the past, scattering matrices of distributions of mineral dust grains have been measured [3]. Here, we use an Electro Dynamic Balance (hereafter EDB) [4] to levitate single dust grains during scattering measurements. Single dust grains are isolated and characterized by microscopy before carrying out the light scattering measurements. It is therefore possible to do a rigorous comparison with scattering models and, once data for a range of sizes is available, with remote sensing observations.

2 The Experimental Setup

The EDB has been developed for studying single microscopic particles. A single microparticle can be charged, injected into the trap and then levitated [4]. In order to randomize particle orientation during the experiment, angular instabilities and particle rotation were induced [5]. This was achieved by increasing the amplitude and decreasing the frequency of the AC-voltage. Upon illumination with a laser of wavelength 0.5145 μm, an array of 175 optical fibres placed at one degree intervals collects scattering data for scattering angles between 3° and 177°. These optical fibres pass the scattered flux to a photomultiplier, and after digitization to a computer, where scatterings pattern are recorded for different states of incident polarization, as well as for background scattering (stray light in the absence of the particle) [6]. A CCD photodiode array measures the forward scattering between approximately 0.5 and 5 degrees with angular resolution of 0.01061° per pixel [5].

3 Saharan Dust Particles

Samples of mineral dust were obtained from various sites. The sample in the example shown below was sourced from a hamada in Morocco, at 29.84957°N, 6.01508°W. This sample had been sieved to contain particles of sizes 20-75 μm. The mineralogy of the sample was identified and semi-quantified by X-ray Diffraction. The sample has a mineral content composed of quartz, albite, calcite, microcline, hematite and the clay minerals chlorite and kaolinite, with quartz, microcline and chlorite predominant. One of these particles was selected for levitation. The particle was examined under an optical microscope in different orientations to obtain size and shape information. Some particles were also examined by

scanning electron microscopy to show detail of surface structure. If the particles were to be used for scattering measurements, they would be imaged without coating. The particles were in general found to have rough surfaces as is shown in Figure 1.

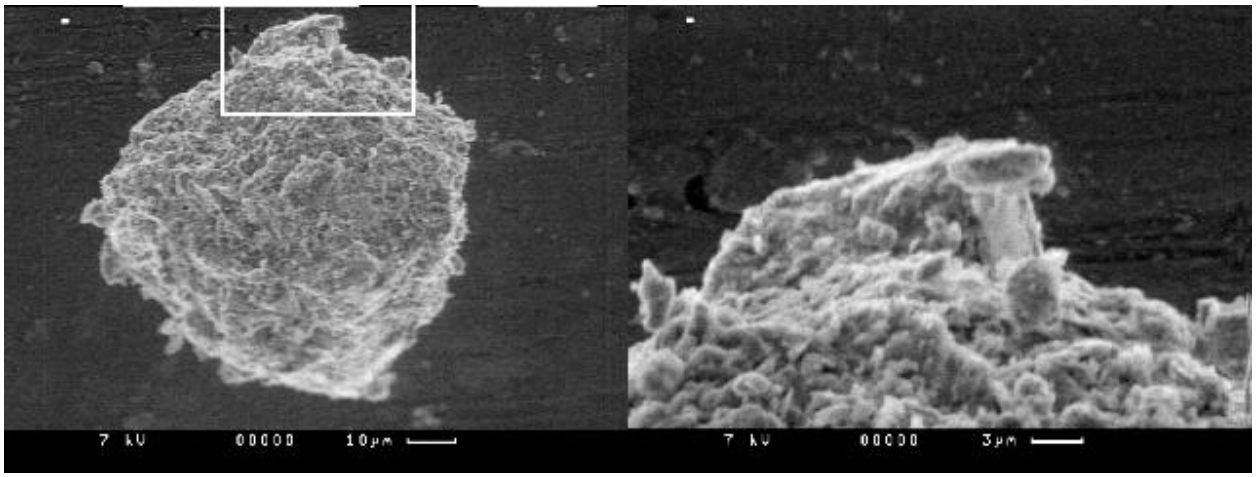

Figure 1: A dust particle as seen under the scanning electron microscope. The image on the right is a magnification of the area shown in the first image. The dust particle was not coated prior to electron microscopy.

From the optical microscopy, the selected particle was found to have the longest dimension of 37.5 µm. In the orientation of the particle seen in Figure 2.1, the measured breadth was 17.5 µm. In the orientation in Figure 2.2, the measured breadth was 21 µm.

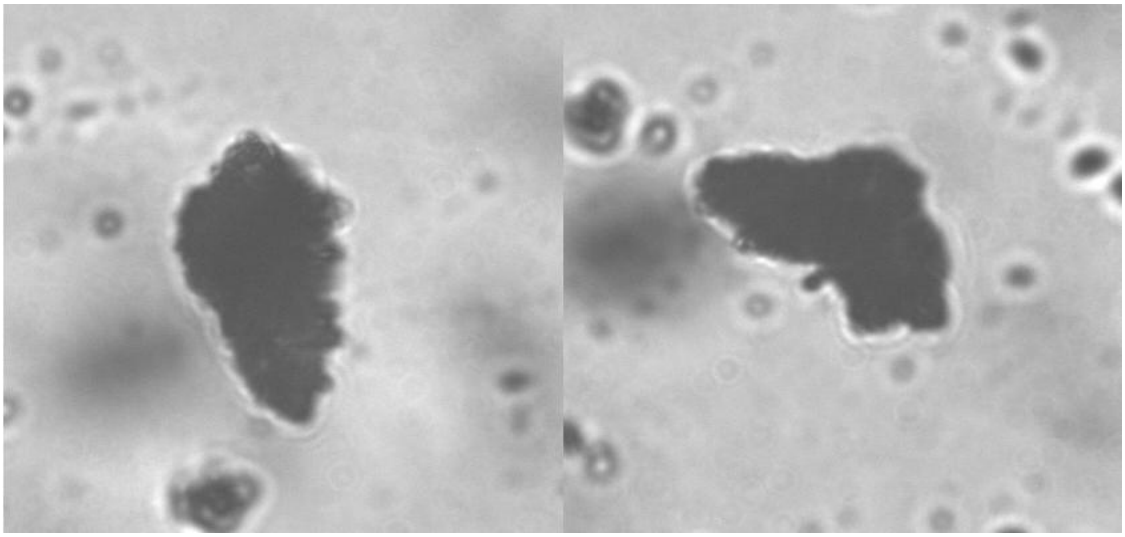

Figure 2: From left to right: 2.1 – Dust particle as seen under an optical microscope. Dimensions are approximately 17.5 µm x 37.5 µm. 2.2 – Same particle as in 1.1 turned by 90° along its long axis. The dimensions are approximately 37.5 µm x 21 µm.

4 Phase Function

Figure 3 shows the normalized phase function for the dust particle shown in Figure 2. The actual measured range of angles for this particle extends down to 0.6°. The inset in Figure 3 shows the low angle measurements made by the CCD, extending from 0.6° to 5.1°. The laser diffractometer data extends from 3° to 177°.

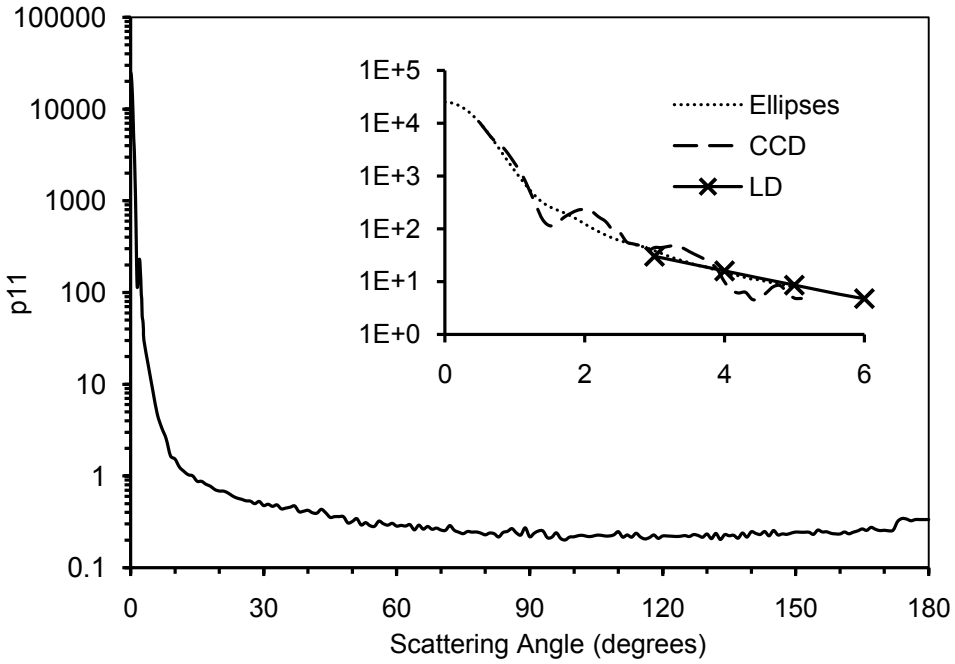

Figure 3: Normalized phase function for the dust particle shown in Figure 2. The results were extrapolated between 0° and 0.6° using diffraction on an elliptical aperture averaged over a range of radii between 9 μm and 19 μm. The inset shows the relationships between the laser diffractometer results, the CCD array results and the elliptical aperture data between 0° and 6°.

In order to complete the phase function so that it can be normalized and the asymmetry parameter can be computed, it is necessary to extrapolate the data between 0° and 0.6°. For low angles, the scattering from a particle is largely dependent on diffraction. If the particle was more spherical, it would be suitable to use Lorenz-Mie theory averaged across a range of spheres corresponding to the changing cross-section of the rotating particle. However, as the particle is highly aspherical, a suitable approach at low scattering angles is to use Fraunhofer diffraction on a collection of randomly-oriented elliptical apertures [7,5]. This can be seen in the inset in Figure 3, and allows extrapolation of the scattering data for the angles 0° to 0.6°. With the full range of scattering data, the normalized phase function has been completed as shown in Figure 3, and the asymmetry parameter has been calculated, g=0.76. The phase function has some diffraction features in the near forward scattering region, as detected by the CCD. However, the rest of the phase function is almost featureless between approximately 80° and 170° - it is almost constant. A slight increase in backscattering between 170° and 180° is observed.

5 Conclusion

The phase functions for levitated single mineral dust particles have been obtained. A laser diffractometer and a CCD have been used to capture scattering data down to as little as 0.6°. The remaining 0.6° has been extrapolated using Fraunhofer diffraction on a distribution of elliptical apertures. Having the full phase function has enabled normalization and the calculation of the asymmetry parameter, which was 0.76 for the example show here. The phase function is flat and featureless at large angles, as determined previously for distributions of mineral dust grains [3]. This result will enable comparison and rigorous verification of data generated by computer models. The Ray Tracing with Diffraction on Facets (RTDF) [8] code has already been tested for particles with curved surfaces down to size parameter 40 [9], and it could be applied to an approximation of the particle seen in Figure 1.

Acknowledgements

This work was supported by the Natural Environment Research Council (UK).

References

[1] H. Yu, Y. J. Kaufman, M. Chin, G. Feingold, L. A. Remer, T. L. Anderson, Y. Balkanski, N. Bellouin, O. Boucher, S. Christopher, P. DeCola, R. Kahn, D. Koch, N. Loeb, M. S. Reddy, M. Schulz, T. Takemura, and M. Zhou. "A review of measurement-based assessments of the aerosol direct radiative effect and forcing," Atmos. Chem. Phys. **6**, 613-666, (2006).

[2] C. Perez, S. Nickovic, J.M. Baldasano, M. Sicard, F. Rocadenbosch. "A long Saharan dust event over the western Mediterranean: Lidar, Sun photometer observations, and regional dust modeling," J. Geophys. Res. **111** D15214, (2006).

[3] H. Volten, O. Munoz, E. Rol, J.F. de Haan., W. Vassen., J.W. Hovenier., K. Muinonen, and T. Nousiainen, "Scattering matrices of mineral aerosol particles at 441.6 nm and 632.8 nm," J. Geophys. Res. **106**, 17375-17401, (2001).

[4] E. Hesse, Z. Ulanowski, P.H. Kaye. "Stability Characteristics of cylindrical fibres in an electrodynamic balance designed for single particle investigation," J. Aerosol Science **33**, 149-163 (2002).

[5] Z. Ulanowski, E. Hesse, P.H. Kaye and A.J. Baran, "Light scattering by complex ice-analogue crystals," J. Quantit. Spectr. Rad. Transfer **100**, 382-392 (2006).

[6] Z. Ulanowski, R.S. Greenaway, P.H. Kaye, I.K. Ludlow. "Laser diffractometer for single- particle scattering measurements," Meas. Sci. Technol. **13**, 292-296 (2002).

[7] Y. Kathuria. "Far-field radiation patterns of elliptical apertures and its annuli," IEEE Trans Antenn Proap **31,** 360-364 (1983).

[8] A.J.M. Clarke, E. Hesse, Z. Ulanowski, P.H. Kaye. "A 3d implementation of ray-tracing with diffraction on facets: Verification and a potential application," J. Quantit. Spectr. Rad. Transf. **100**, 103-114 (2006).

[9] E. Hesse, D.S. McCall, Z. Ulanowski, C. Stopford, P.H. Kaye. "Application of RTDF to particles with curved surfaces," Contained in this volume.

Ray-optics radiative-transfer method for scattering by inhomogeneous Gaussian random particles

Karri Muinonen,[1] Timo Nousiainen,[2] Olga Muñoz,[3] Hannakaisa Erkkilä,[2,1] and Gorden Videen[4]

[1]*Observatory, Kopernikuksentie 1, P.O. Box 14, FI-00014 University of Helsinki, Finland*
[2]*Department of Physics, P.O. Box 68, FI-00014 University of Helsinki, Finland*
[3]*Instituto de Astrofisica de Andalucia, CSIC, Camino Bajo de Huetor 50, E-18008 Granada, Spain*
[4]*Army Research Laboratory, 2800 Powder Mill Rd., Adelphi, Maryland 20783, U.S.A.*
tel: +358 9-19122941, fax: +358 9-19122952, e-mail: Karri.Muinonen@helsinki.fi

Abstract

We combine ray optics and radiative transfer to study light scattering by inhomogeneous Gaussian-random-sphere particles large compared to the wavelength of incident light. We show that incorporating diffuse scatterers in the conventional ray-optics approximation allows us to obtain improved interpretations of the scattering matrices measured experimentally for large Saharan sand particles.

1 Introduction

Natural small particles much larger than the wavelength commonly exhibit irregular overall shapes, inhomogeneous internal compositions, as well as wavelength-scale surface roughness. No exact electromagnetic methods are available for the computation of light scattering by these particles that are the primary constituents in the regoliths of atmosphereless solar-system objects and in the desert surfaces on the Earth.

Continuing the scattering studies for small solar-system particles large compared to the wavelength [1], terrestrial aerosol particles [2, 3], as well as large Saharan sand particles [4], we combine the conventional ray-optics [1] and radiative-transfer treatments [5] to compute scattering by irregular particles with either internal inhomogeneities or surface roughness in the framework of what we call the ray-optics radiative-transfer method (RR). We have shown earlier that the inhomogeneities and/or surface roughness play a crucial role in scattering by Saharan sand particles.

We apply RR to explain the experimentally measured scattering matrix of large Saharan sand particles [4]. Figure 1 shows sample images of sand particles taken using the Field Emission Scanning Electron Microscope (FESEM). The particles exhibit substantial micron-to-submicron-scale surface roughness.

Figure 1: Saharan sand particles (left [4]; particle diameters ~200 μm), surface roughness on the particles (middle; width of image ~25 μm), and a sample Gaussian-random-sphere particle (right).

2 Ray-optics radiative-transfer method

In the RR method, extinction, scattering, and absorption cross sections as well as full 4×4 scattering phase matrices are solved for through ray tracing with six different incident polarization states. Rays are traced until the flux density has decreased below a predefined tolerance or until a predefined number of reflections and/or refractions and/or diffuse scattering processes are completed. The ray-optics part—including the geometric-optics and forward-diffraction components—is based on the methods developed for Gaussian particles [1]. The radiative-transfer part relies on the multiple-scattering methods for coherent backscattering by complex random media of discrete scatterers [5].

In the radiative-transfer part, a mean free path length is specified for extinction, with an exponential probability density function following for the path length. For each diffuse scattering process, the full scattering phase matrix is accounted for, as well as the full state of polarization of the incident Stokes vector. The scattering phase matrix is specified using cubic splines (cf., [5]) for a user-defined scattering phase matrix or using an empirical Henyey-Greenstein matrix (H-G) with two parameters: the asymmetry parameter and the maximum polarization parameter. The H-G matrix is constructed from the Rayleigh matrix as follows. The Rayleigh matrix elements are divided by the Rayleigh phase function, and the resulting matrix elements are then multiplied by the H-G phase function. Finally, the 12 and 21-elements are multiplied by the maximum polarization parameter.

We utilize two different RR methods: one accounts for internal inhomogeneities with the single-scattering albedo and mean free path length as additional parameters, whereas the other one accounts for surface roughness with the single-scattering albedo and optical thickness as additional parameters. As to the former method, the diffuse scatterers are embedded in a homogeneous and isotropic medium described by a complex refractive index. As to the latter method, the diffuse scatterers constitute an optically thin plane-parallel medium on the surface of the Gaussian random sphere, assuming that the physical thickness of the medium is negligible as compared to the typical radial distance of the Gaussian sphere.

3 First results for Saharan dust particles

In order to reproduce the measured Saharan dust-particle scattering matrix, we assume the Gaussian-random-sphere geometry for our model particles and parameterize the shape with two statistical parameters: the radial-distance relative standard deviation σ and the covariance-function power-law index ν [6]. Following the statistical shape analysis of the measured dust particles, we fix $\sigma = 0.2$ and $\nu = 3.3$.

The complex refractive index of the particles is set at $m = 1.55 + i10^{-4}$ which is considered representative of the large, quartz-rich dust particles. For these preliminary simulations, we ignore the size distribution of the particles and simply use a single size parameter $x = ka = 100$, where k is the wave number and a is the mean radius of the Gaussian-random-sphere particles. In the ray optics approximation, the size affects only the diffraction peak and the absorption inside the particles, so this is not a critical simplification. The geometric-optics computations are carried out at the 633-nm wavelength for 700 sample particles with 700 rays incident on each particle in random orientation, totaling altogether 490,000 rays. Diffraction is solved for an ensemble of 100 particles.

The influence of the radiative-transfer modification on scattering is demonstrated in Fig. 2. The solid line depicts results from the traditional ray optics, dotted line from the ray optics modified by internal inhomogeneity (free path length 3.0 μm, albedo 0.9, $g = 0.1$), and the dashed line the ray optics with externally scattering surface roughness (optical depth 0.5, $g = 0.5$, albedo 0.9). Diamonds and error bars show the measured scattering matrix for comparison. Obviously, both modifications improve the performance of the traditional ray optics, especially for the polarization elements. The improvement for the phase function is more difficult to judge due to the normalization (all phase functions are set to unity at the 30° scattering

angle) that is likely to be sensitive to the absense of the size distribution in the simulations. Nevertheless, both modifications produce a flat phase function similar to the measured one.

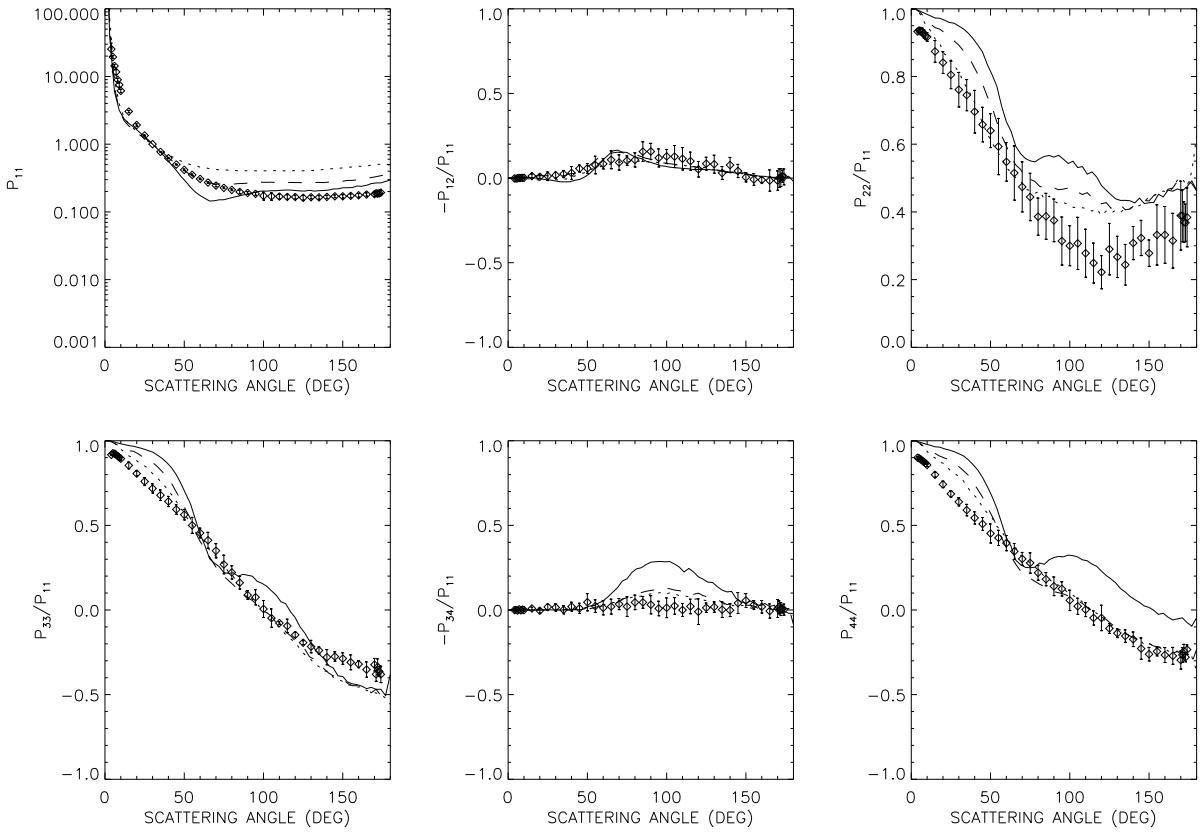

Figure 2: Comparison of simulated and measured scattering matrices for large Saharan dust particles. Traditional ray-optics results are depicted with the solid line, whereas the dashed and dotted lines present the inhomogeneity and surface-roughness modifications, respectively. Diamonds and error bars depict the measured scattering matrix [4].

It is interesting to look at the model parameters that lead to good fits between the simulations and the measurements. Obviously, both internal and external modifications benefit from high albedo. In contrast, surface modification works well with g close to unity whereas internal inhomogeneity works better with small g. A possible explanation would be that internal inhomogeneities have smaller size scales than the external surface-roughness distortions.

4 Conclusion

Ray-optics radiative-transfer methods have been developed for light scattering by inhomogeneous Gaussian-random-sphere particles large compared to the wavelength of incident light. The method involves Fresnelian reflections and refractions on the interfaces as well as diffuse scattering processes within the interior or on the surface facing free space.

The first results for large Saharan sand particles are promising. For both internal and external diffuse media, improved fits are obtained between the theoretical model and the experimental data. For example, it is possible to explain, simultaneously, the flat scattering phase function towards the backscattering direc-

tion and the neutral degree of linear polarization for unpolarized incident light. Further improvements are expected when more realistic phase matrices are used for the surface and internal scatterers. For example, phase matrices for the thin calcite flakes that are observed to cover large quartz particles in Saharan dust samples (see Nousiainen et al, present meeting) would be good candidates as surface-roughness elements; alternatively, one could use, e.g., the measured phase matrices for small particles (such as feldspar [2]).

In the future, RR can turn useful in studies of coherent backscattering by random media with Gaussian-random-sphere geometries. The method allows the assessment of the mutual significance of the coherent-backscattering (e.g., [5]) and single-scattering interference mechanisms [6, 7] in scattering by the regoliths of atmosphereless solar-system objects.

Acknowledgments

Research supported, in part, by EC Contract No. MRTN-CT-2006-033481.

References

[1] K. Muinonen, T. Nousiainen, P. Fast, K. Lumme, and J. I. Peltoniemi, “Light scattering by Gaussian random particles: ray optics approximation,” *JQSRT* **55**, 577-601 (1996).

[2] H. Volten, O. Muñoz, J. F. de Haan, W. Vassen, J. Hovenier, K. Muinonen, and T. Nousiainen, “Scattering matrices of mineral aerosol particles at 441.6 nm and 632.8 nm, *J. Geophys. Res.* **106**, 17375–17401 (2001).

[3] T. Nousiainen, K. Muinonen, and P. Räisänen, “Scattering of light by large Saharan dust particles in a modified ray-optics approximation, *J. Geophys. Res.* **108**, D1, 4025 (2003).

[4] O. Muñoz, H. Volten, J. W. Hovenier, T. Nousiainen, K. Muinonen, D. Guirado, F. Moreno, and L. B. F. M. Waters, ”Scattering matrix of large Saharan dust particles: Experiments and computations,” *J. Geophys. Res.* **112**, D13215 (2007).

[5] K. Muinonen, “Coherent backscattering of light by complex random media of spherical scatterers: Numerical solution, *Waves in Random Media* **14**(3), 365–388 (2004).

[6] K. Muinonen, E. Zubko, J. Tyynelä, Yu. G. Shkuratov, and G. Videen, “Light scattering by Gaussian random particles with discrete-dipole approximation,” *JQSRT* **106**, 360–377 (2007).

[7] J. Tyynelä, E. Zubko, G. Videen, and K. Muinonen, “Interrelating angular scattering characteristics to internal electric fields for wavelength-scale spherical particles,” *JQSRT* **106**, 520–534 (2007).

Optical modeling of thin calcite flakes using DDA

Timo Nousiainen[1], Evgenij Zubko[2], Jarkko Niemi[3], Kaarle Kupiainen[4],
Martti Lehtinen[5], Karri Muinonen[6], and Gorden Videen[7]

[1]*Department of Physics, P.O.Box 68, FI-00014 University of Helsinki, Finland*
[2] *Center for Atmospheric and Oceanic Studies, Tohoku University, Aoba, Aramakiaza, Aoba-ku, Sendai 980-8578, Japan*
[3]*Department of Biological and Environmental Sciences, P.O. Box 27, FI-00014 University of Helsinki, Finland*
[4]*Finnish Environment Institute, P.O.Box 140, FI-00251 Helsinki, Finland*
[5]*Geological Museum, P.O.Box 64, FI-00014 University of Helsinki, Finland*
[6]*Observatory, P.O.Box 14, FI-00014 University of Helsinki, Finland*
[7]*Army Research Laboratory, 2800 Powder Mill Rd., Adelphi, Maryland, 20783 USA*
tel: +358 9 191 51064, fax: +358 9 191 50860, e-mail: timo.nousiainen@helsinki.fi

Abstract

Simulations of optical properties of small calcite flakes found in Saharan dust samples are carried out using the discrete-dipole approximation. The results show that for volume-equivalent size-parameters $x_{eq} \in [1, 8]$, these particles have consistently and considerably higher asymmetry parameter than the corresponding volume-equivalent spheres. The negative polarization branch is surprisingly weak.

1 Introduction

Mineral dust is one of the radiatively most important aerosol types in the Earth's atmosphere, where it influences the radiative balance and thus the climate, but also can affect remote-sensing observations of the atmosphere. This effect is not limited to remote aerosol measurements, but can extend to other measurements like trace-gas monitoring. Consequently, there is a high demand for assessing the radiative impact of dust. Ultimately, this impact depends on their single-scattering, hereafter optical, properties. Optical modeling of dust particles is challenging because there is no precise morphological description, and hence, no theoretical light-scattering solution available, and the large variability of their sizes, shapes, and compositions complicates the problem.

We present preliminary results of our optical simulations for thin calcite flakes. The study is based on an analysis of two samples of Saharan dust, collected from the ground in two locations in Tunisia. The thin flake-like calcite particles were the most interesting particle type encountered, since these particles should be very easily lifted airborne due to their small sizes and very large surface-area-to-mass ratio. In addition, such particle shapes have not been previously considered in dust-particle modeling studies. Calcite is also strongly birefringent mineral. The optical simulations have been conducted using the discrete-dipole approximation (DDA) [1].

2 Dust samples

Two Saharan dust samples were collected from recesses able to trap airborne fine particles by Richard and Roland Pelisson of SaharaMet[1] in south Tunisia. The particles in recesses are significantly finer than particles retrieved in the open desert. Both samples were further sieved prior to the analysis, so particle diameters are smaller than approximately 0.14 mm.

[1]http://www.saharamet.com/index.html

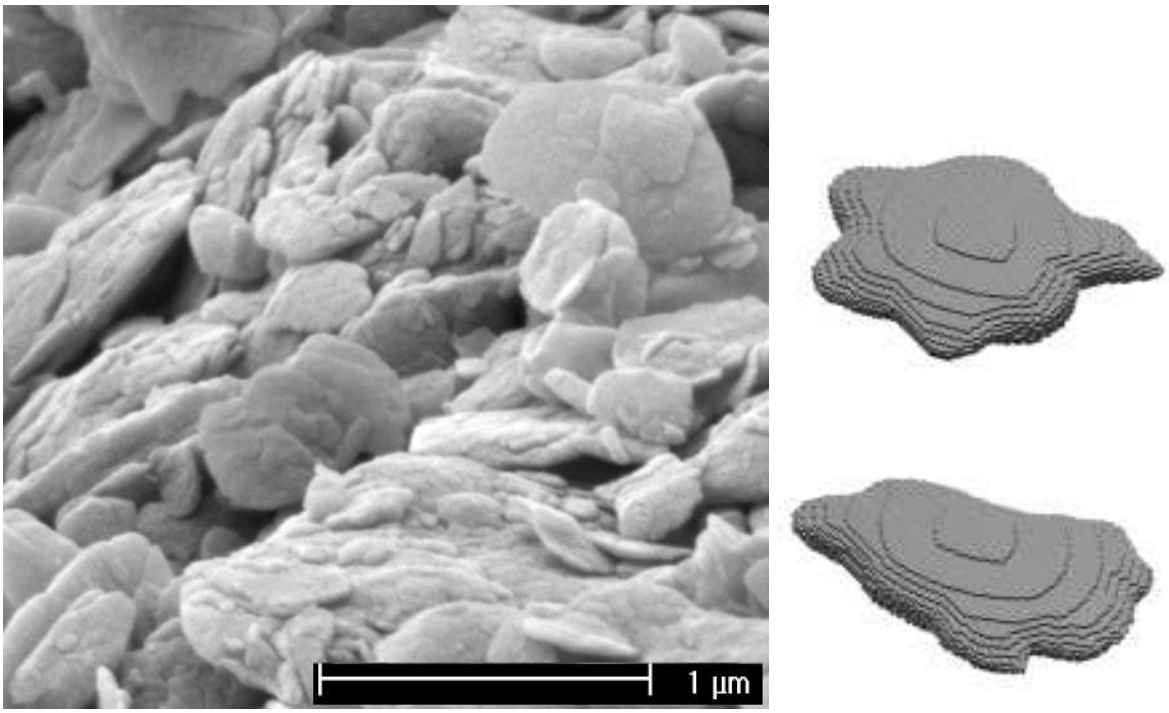

Figure 1: Small calcite flakes from one of the Saharan dust samples (left) and sample model shapes (right).

Mineralogy of the samples are assessed using X-ray diffractography and infrared spectrometry. Electron microscope images are used to analyze the particle shapes. To match the particle types with their mineralogical composition, scanning electron microscopy with energy-dispersive X-ray microanalysis is used. The samples are composed mostly of calcite, dolomite, and quartz. Furthermore, few aluminosilicate particles are present.

Example calcite flakes covering a large 100 μm quartz particle are shown in Fig. 1. Indeed, all large quartz particles in the samples are at least partially covered by calcite flakes. The flakes have radii r mostly below 1 μm and are common in both samples. In one sample nearly all submicron particles appear to be calcite flakes. The model shapes shown in Fig. 1 have an aspect ratio of approximately 6.

3 Results

Calcite belongs to a trigonal system of crystal symmetries and thus has a single optic axis [2]. Waves propagating parallel to the optic axis are subject to an extraordinary refractive index n_e; whereas, waves traveling normal to the optic axis experience an ordinary refractive index n_o. At λ = 589 nm wavelength, the refractive indices for calcite are n_e = 1.486 and n_o = 1.658, resulting in a birefringence $|n_e - n_o|$ = 0.172 [3]. The imaginary part of the refractive index is very low and here calcite is simply assumed to be nonabsorbing. It is noted that calcite is not strongly dispersive at visible and near infrared wavelengths, so the results obtained here are applicable to most radiatively important solar wavelengths.

Simulations are carried out at λ = 589 nm for volume-equivalent size parameters x_{eq} = 1, 2, 4, 6, and 8. Size parameters for circumscribing spheres are approximately twice as large. Three sets of simulations are planned: one with diagonalized dielectric tensor diag(n_e, n_o, n_o) and two based on equivalent isotropic materials. Only the two isotropic sets have been computed thus far. In the first of these, the model particles

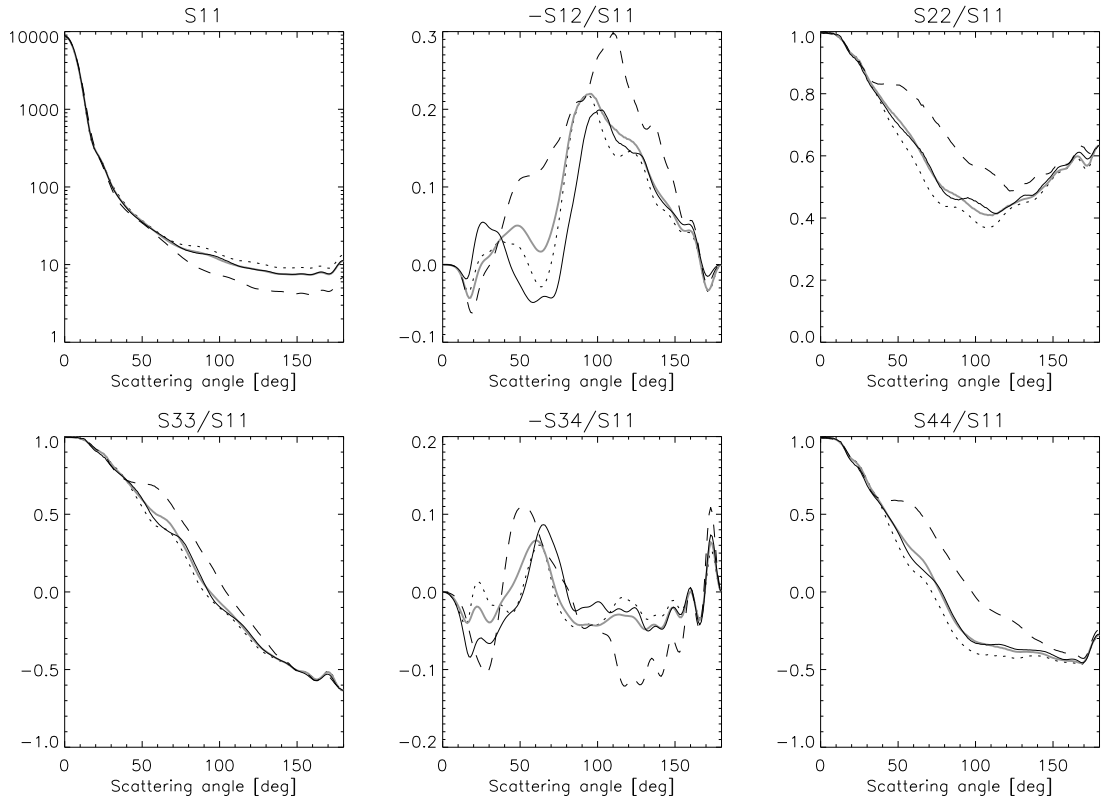

Figure 2: The non-zero independent scattering matrix elements for calcite flakes for size parameter $x_{\mathrm{eq}} = 8$. The lines correspond to m_{iso} (thin solid), n_o (dotted), n_e (dashed), and $\frac{1}{3}$-$\frac{2}{3}$ approximation (thick grey).

are assumed to have an equivalent refractive index $m_{\mathrm{iso}} = [(n_e^2 + 2n_o^2)/3]^{1/2} = 1.603$. In the second set, the so-called "$\frac{1}{3}$-$\frac{2}{3}$ approximation" is used (see e.g. [1]). In this case, one third of the particles is assumed to have $m = n_e$, and two thirds $m = n_o$; the optical properties are then averaged, weighted by the corresponding scattering cross sections. These isotropic equivalences are analogous to internal and external mixing, respectively.

The simulations are carried out for an ensemble of randomly oriented particles. The particle ensemble consists of 10 different model shapes. Although the number of orientations used for orientation-averaged results increases with x_{eq} from 729 to 2925, even 2925 orientations does not guarantee convergent random-orientation results at $x_{\mathrm{eq}} = 8$ for our model shapes. To speed up the calculations, we do not increase the number of orientations further but use different sets of orientations for different model particles. The ensemble averaging then completed also the orientation averaging.

Figure 2 shows example results for the $x_{\mathrm{eq}} = 8$ case. In general, the two isotropic analogs produce very similar results, and their agreement is better for smaller x. The negative polarization branch (NPB) is not visible for $x_{\mathrm{eq}} < 6$. The backscattering enhancement in the scattered intensity is possibly seen at $x_{\mathrm{eq}} = 2$, but for $x_{\mathrm{eq}} \geq 4$ it is clear and well-defined, narrowing as expected with increasing particle size. The scattering-matrix element S_{22} shows a narrow-angle double-lobe feature near backscattering, reminiscent of the wider double-lobe features observed in, e.g., concave-hull-transformed Gaussian-random-sphere particles (Erkkilä and Muinonen, present meeting). Again, the feature appears to correlate with the

Table 1: Asymmetry parameters for the simulated cases and corresponding spheres.

x_{eq}	m_{iso}	n_o	n_e	$\frac{1}{3}$-$\frac{2}{3}$
1	0.283 (0.210)	0.283 (0.217)	0.283 (0.198)	0.283 (0.213)
2	0.634 (0.582)	0.638 (0.561)	0.623 (0.631)	0.635 (0.577)
4	0.805 (0.642)	0.787 (0.603)	0.835 (0.761)	0.801 (0.655)
6	0.825 (0.380)	0.812 (0.269)	0.847 (0.667)	0.822 (0.444)
8	0.834 (0.643)	0.812 (0.755)	0.876 (0.466)	0.833 (0.691)

backscattering peaks and negative polarization branches.

The asymmetry parameter g for the calcite flakes and corresponding volume-equivalent spheres (in parentheses) as a function of x_{eq} are shown in Table 1. For both isotropic analogs, the flakes have higher g than the corresponding spheres. With one exception, the same holds for the n_o and n_e cases. Interestingly, the isotropic analogs match each other better in the case of flakes than for Mie spheres. Not surprisingly, the spheres are much more sensitive to x and n.

4 Discussion and conclusions

DDA simulations for calcite flakes found in Sarahan dust samples are carried out. In the simulated size-parameter range ($x_{\mathrm{eq}} \in [1, 8]$), the asymmetry parameters are consistently and considerably higher for the calcite flakes than for the corresponding equal-volume spheres and appear much less sensitive to particle size and refractive index. Both isotropic equivalences produce very similar scattering but, unfortunately, the estimates for the importance of calcite's birefringence on the optical properties are not yet available.

It is interesting to compare our results to those for Gaussian random spheres in [4]. The latter show a very strong NPB (up to -21%) which is well defined already at $x_{\mathrm{eq}} = 2$. In contrast, the NBP for the flakes is not seen below $x_{\mathrm{eq}} = 6$ and the amplitude is only a few percents. In fact, the linear polarization from flakes is much more positive overall. Such differences even for ensembles of irregular particles indicate considerable potential for remote-sensing applications. When a strong surface roughness is introduced to the Gaussian random spheres, the differences with flakes decrease substantially.

Finally, it is noted that atmospheric dust particles may attain preferred orientation in the atmosphere [5]. Due to their shape, calcite flakes would be good candidates for the responsible particles.

References

[1] B. T. Draine, "The discrete-dipole approximation and its application to interstellar graphite grains," Astrophys. J. **333**, 848–872 (1988).

[2] D. McKie, C. McKie, *Crystalline solids* (Thomas Nelson and Sons, Ltd, Exeter, UK, 1974).

[3] W. Tröger, *Optical Determination of Rock-Forming Minerals: Part I determinative tables*, 4th Edition, (E. Schweizerbart'sche verlagsbuchhandlung, Stuttgard, 1979).

[4] E. Zubko, K. Muinonen, Yu. G. Shkuratov, G. Videen, T. Nousiainen, "Scattering of light by roughened Gaussian random particles," J. Quant. Spectrosc. Radiat. Transfer **106**, 604–615 (2007).

[5] Z. Ulanowski, J. Bailey, P. Lucas, J. Hough, and E. Hirst, "Alignment of atmospheric mineral dust due to electric field." Atm. Chem. Phys. **7**, 6161–6173 (2007).

Optical modeling of mineral dust aerosol: a review

Timo Nousiainen

Department of Physics, P.O.Box 68, FI-00014 University of Helsinki, Finland
tel: +358 9 191 51064, fax: +358 9 191 50860, e-mail: timo.nousiainen@helsinki.fi

Abstract

Dust particles are uniquely and irregularly shaped particles that can be inhomogeneous, form aggregates, be composed of anisotropic materials, and have a preferred orientation. As such, modeling their light scattering is very challenging. This review takes a look at recent developments in dust particle optical modeling.

1 Introduction

Mineral dust refers to atmospheric aerosols that originate from the suspension of soil-constituting minerals. Deserts are the largest sources of mineral dust, but dust lifting occurs from all bare soil surfaces.

Dust particles are irregularly and uniquely shaped. They can be expected to be internally inhomogeneous, form aggregates, and come with a wide range of mineralogical compositions, including many anisotropic species. There is also evidence that dust particles might even obtain preferred orientations in the atmosphere [1]. Further, the atmosphere is very efficient in mixing aerosols from different sources, and dust may also mix with other atmospheric constituent to obtain e.g. sulfate, water, or ice coatings.

Mineral dust represents a great challenge for modeling light-scattering properties. Accounting for the variability of the physical properties of dust particles is in itself a challenge. Further, there is no exact analytical solution for light scattering by dust-like particles. Hence, dust optical modeling requires that one simplifies the model particles, uses non-exact methods, or both. Due to the limitations of numerical methods and the wide range of relevant particle sizes, one is often forced to use different methods at different size-parameter ranges. Testing different modeling approaches is complicated by the lack of reliable and accurate references.

Recent years have substantially improved our understanding of how these particles scatter light. Improved numerical methods, increasing computing resources, and the introduction of high-quality laboratory measurements have facilitated the modeling efforts substantially. This review provides a summary of these recent developments. Remote-sensing aspects are intentionally left out.

2 Model investigations

Pure modeling studies are convenient for investigating how certain factors, such as different physical properties of dust particles, affect scattering. The main complications are the inherent limitations of the methods used and separating the desired impact from the side effects. As examples of the latter, consider how to avoid porosity or surface roughness from affecting neither the volume nor the cross-sectional surface area.

2.1 Size dependence

The optical effects of particle anisotropies, especially those due to nonspherical shape, have been investigated for decades. These effects depend considerably on the size parameter.

When particles are smaller than the wavelength, only the largest scale nonsphericities are important, and effective medium approximations are expected to account for the possible internal inhomogeneities accurately. For wavelength-scale particles, small-scale details, such as surface roughness, become relevant. Fortunately, volume-integral methods such as the discrete-dipole approximation (DDA) allow us to investigate this transition in detail. When the size parameter further increases, the surface texture becomes the dominating factor [2,3]. This transition introduces us to one of the largest challenges in dust optical

modeling: we simply lack methods that can account explicitly for the impact of particles' wavelength-scale features when the particles themselves are considerably larger than the wavelength. While new methods are being introduced to address this at the large-particle limit (see Muinonen et al., present meeting), the intermediate size parameters remain almost uncharted territory.

2.2 Surface roughness

From results of electron microscopy, there are two types of surface roughness that often coexist. On the one hand, the particle surface itself can be rough, and on the other hand, small particles may aggregate on the surface to add roughness. There are only few studies about the optical impact of dust particles' surface roughness, but pure modeling studies for relevant refractive indices exist.

The most comprehensive treatment of roughness effects on wavelength-scale dust particles appears to be [4], where the DDA was used for Gaussian random spheres of varying roughness characteristics. The roughness tends to make the linear polarization more Rayleigh-like and positive, and the phase function smoother. Interestingly, thin-layer roughness tends to strengthen depolarization; whereas, thick-layer roughness weakens it. The impact of roughness increases with increasing particle size, consistent with results for roughened spheres [5,6]. It is interesting that an increase in the large-scale nonsphericity related to the particle shape also increases linear polarization but is not sufficient to make it positive [7].

For particles much larger than the wavelength, the overall impact of surface roughness is to strengthen side-scattering, smooth out the matrix elements, decrease linear polarization, and increase depolarization. Qualitatively, the effects are similar whether the roughness is in the wavelength-scale or larger [2,3,8].

2.3 Particle inhomogeneity

The impact of particle inhomogeneity has not been studied much. For particles much larger than the wavelength, [2] and [3] used Lambertian screens to mimic internal inhomogeneities and noted that moderate amount of inhomogeneities improved the agreement of simulations with laboratory measurements. Muinonen et al. (present meeting) obtained similar results using a generalized Henyey-Greenstein phase matrix for the internal inhomogeneities. Inhomogeneity effects for wavelength-scale particles were studied by [9] using randomly generated porosity with the DDA. Inhomogeneous mixtures of dust and sulfate/ice based on layered spheres have been considered by [10].

Interestingly, $-P_{12}/P_{11}$ tends to be mostly positive and decreases with increasing size parameter for porous particles [9]. Both observations are consistent with laboratory measurements for varying mineral dust species presented in [8], although the model particles in [9] are much more absorbing. This behavior may not be a unique feature of porosity but rather follows from the increasing complexity of model particles due to increasing the amount of porous cavities; i.e., the increase in the particle size is analogous to increasing the number of monomers in an aggregate. This view is further supported by the Rayleigh-like linear polarization of large ballistic clusters of spheres (Erkkilä and Muinonen, this meeting).

2.4 Distributions

Realistic models of atmospheric dust particles should include a number of distributions: size, shape (including roughness), and composition (including internal structure) all vary from particle to particle. So far, most studies have considered only the size and shape distributions. Distributions increase the complexity of the system, so it is not surprising that their principal impact is to smooth out various dependencies such as the angular dependence of phase matrix elements or the wavelength dependence of cross sections.

Modeling studies with dust particle distributions are many. Size and shape distributions have been considered for spheroids [e.g. 11–16], polyhedrons [15], Gaussian spheres [17], and various other random shapes [9,18,19]. Apparently only [18] accounts also for the composition distribution.

An interesting aspect of shape distributions is that the impact of shape averaging seems to depend much on the type of model particles considered. Scattering by spheroids depends considerably on the spheroids'

shape; whereas, different polyhedrons and irregular blocks of cubes seem to scatter light similarly to each other [9,15,18,19]. Further, [13] fitted scattering matrices for distributions of spheroids, polyhedrons, and cylinders, and noted that the best-fit shape distributions show very little correlation with each other. Thus, when simplified model shapes are used, the shape distributions that provide good results may not resemble in any way the actual dust particle shape distribution. Consequently, simple shape parameters such as the circularity or the aspect ratio may be of very limited use in characterizing dust particles.

3 Comparisons with laboratory data

Scattering matrices of varying dust samples measured in a laboratory provide us with very useful benchmarks for testing the applicability of different approaches for modeling dust optical properties. In this sense, one of the most interesting findings from the laboratory investigations [e.g. 8,20] is that the measured scattering matrices for different mineral and volcanic dust samples look remarkably similar albeit the considerable differences in their size, shape, and composition distributions. It is thus not surprising that the laboratory-measured scattering matrices have been reproduced to a good degree by quite diverse sets of model particles. For example, the scattering matrix of the feldspar sample measured by [8] has been more or less successfully fitted by shape distributions of spheroids, polyhedrons, and Gaussian random spheres [14,15,17]; whereas, [19] matched the scattering matrix of olivine particles using irregular cubic blocks. Gaussian random spheres also have been used successfully for two different Saharan dust samples [2,3]. Interestingly, the exact form of the shape distribution does not seem critical, except for the model of spheroids. This is likely to be connected to the high symmetry of the spheroidal particles.

The comparisons also show us that it is easier to match the measured phase function than the polarization elements with simplified model shapes. This illustrates the additional benefit of having the whole phase matrix measured in the model validation, and emphasizes how polarization elements of the matrix contain additional information about the dust particle shapes. Retrieving this shape information using simplified model shapes, however, seems very difficult.

4 Conclusions

Simplified model shapes seem adequate for reproducing measured phase functions for wavelength-scale dust particles, while their performance with the polarization elements is less satisfactory. For larger particles such shapes seem to be of limited use, since, e.g., surface-roughness effects become important.

Surface roughness and internal inhomogeneity seem to affect scattering similarly. The underlying reason may be that both transformations increase the complexity of the model particles. Indeed, dust particles and especially their ensembles show such a high degree of complexity that caustics and most interference features are effectively removed from the scattering patterns. This is very likely the reason why the laboratory-measured scattering matrices for different dust samples are so similar to each other. An interesting side effect of this is that using laboratory measurements as benchmarks may not be critically dependent (albeit highly desired) on the accurate characterization of all the physical properties of the samples.

Although our ability to model dust optical properties has increased considerably during the last decade, there is still much to be done. Obviously, more information about the dust physical properties and their global distributions is needed. In particular, not much is known about the internal inhomogeneity characteristics. Also, we obviously need to further improve and validate the light-scattering models used. This is particularly relevant for dust particles too large to be treated with DDA-type methods. Finally, there are particle types that have not been properly modeled yet. For example, closely packed irregular-particle aggregates have not been considered at all, although electron microscopy indicate such particle to be common. Coated and otherwise transformed dust types also require more realistic model treatment.

References

[1] Z. Ulanowski, J. Bailey, P.W. Lucas, J.H. Hough, and E. Hirst. Alignment of atmospheric mineral dust due to electric field. *Atm. Chem. Phys.*, **7**, 6161–6173, 2007.

[2] T. Nousiainen, K. Muinonen, and P. Räisänen. Scattering of light by large Saharan dust particles in a modified ray optics approximation. *J. Geophys. Res.*, **108**, 4025, 2003, doi:10.1029/2001JD001277.

[3] O. Muñoz, H. Volten, J.W. Hovenier, T. Nousiainen, K. Muinonen, D. Guirado, F. Moreno, and L.B.F.M. Waters. Scattering matrix of large Saharan dust particles: experiments and computations. *J. Geophys. Res.*, **112**, D13215, 2007, doi:10.1029/2006JD008074.

[4] E. Zubko, K. Muinonen, Yu. Shkuratov, G. Videen, and T. Nousiainen. Scattering of light by roughened Gaussian random particles. *J. Quant. Spectrosc. Radiat. Transfer*, **106**, 604–615, 2007, doi:10.1016/j.jqsrt.2007.01.050.

[5] C. Li, G.W. Kattawar, and P. Yang. Effects of surface roughness on light scattering by small particles. *J. Quant. Spectrosc. Radiat. Transfer*, **89**, 123–131, 2004.

[6] T. Nousiainen and K. Muinonen. Surface-roughness effects on single-scattering properties of wavelength-scale particles. *J. Quant. Spectrosc. Radiat. Transfer*, **106**, 389–397, 2007, doi:10.1016/j.jqsrt.2007.01.024.

[7] K. Muinonen, E. Zubko, J. Tyynelä, Yu. Shkuratov, and G. Videen. Light scattering by Gaussian random particles with discrete-dipole approximation. *J. Quant. Spectrosc. Radiat. Transfer*, **106**, 360–377, 2007, doi:10.1016/j.jqsrt.2007.01.049.

[8] H. Volten, O. Muñoz, J.F. de Haan, W. Vassen, J.W. Hovenier, K. Muinonen, and T. Nousiainen. Scattering matrices of mineral aerosol particles at 441.6 nm and 632.8 nm. *J. Geophys. Res.*, **106**, 17375–17401, 2001.

[9] R. Vilaplana, F. Moreno, and A. Molina. Study of the sensitivity of size-averaged scattering matrix elements of nonspherical particles to changes in shape, porosity and refractive index. *J. Quant. Spectrosc. Radiat. Transfer*, **100**, 415–428, 2006.

[10] C. Pilinis and X. Li. Particle shape and internal inhomogeneity effects on the optical properties of tropospheric aerosols of relevance to climate forcing. *J. Geophys. Res.*, **103**, 3789–3800, 1998.

[11] T. Nousiainen. Impact of particle shape on refractive-index dependence of scattering in resonance domain. *J. Quant. Spectrosc. Radiat. Transfer*, **108**, 464–473, 2007, doi:10.1016/j.jqsrt.2007.07.008.

[12] M.I. Mishchenko, L.D. Travis, R.A. Kahn, and R.A. West. Modeling phase functions for dustlike tropospheric aerosols using a shape mixture of randomly oriented polydisperse spheroids. *J. Geophys. Res.*, **102**, 16831–16847, 1997.

[13] F.M. Kahnert, J.J. Stamnes, and K. Stamnes. Using simple particle shapes to model the Stokes scattering matrix of ensembles of wavelength-sized particles with complex shapes: Possibilities and limitations. *J. Quant. Spectrosc. Radiat. Transfer*, **74**, 167–182, 2002.

[14] O. Dubovik, A. Sinyak, T. Lapyonok, B.N. Holben, M. Mishchenko, P. Yang, T.F. Eck, H. Volten, O. Muñoz, B. Veihelmann, W.J. van der Zande, J.-F. Leon, M. Sorokin, and I. Slutsker. Application of spheroid models to account for aerosol particle nonsphericity in remote sensing of desert dust. *J. Geophys. Res.*, **111**, D11208, 2006, doi:10.1029/2005JD006619.

[15] T. Nousiainen, M. Kahnert, and B. Veihelmann. Light scattering modeling of small feldspar aerosol particles using polyhedral prisms and spheroids. *J. Quant. Spectrosc. Radiat. Transfer*, **101**, 471–487, 2006. doi:10.1016/j.jqsrt.2006.02.038.

[16] P. Yang, Q. Feng, G. Hong, G.W. Kattawar, W.J. Wiscombe, M.I. Mishchenko, O. Dubovik, I. Laszlo, and I.N. Sokolik. Modeling of the scattering and radiative properties of nonspherical dust-like aerosols. *J. Aerosol Sci.*, **38**, 995–1014, 2007.

[17] B. Veihelmann, T. Nousiainen, M. Kahnert, and W.J. van der Zande. Light scattering by small feldspar particles simulated using the Gaussian random sphere geometry. *J. Quant. Spectrosc. Radiat. Transfer*, **100**, 393–405, 2006, doi:10.1016/j.jqsrt.2005.11.053.

[18] O.V. Kalashnikova and I.N. Sokolik. Modeling the radiative properties of nonspherical soil-derived mineral aerosols. *J. Quant. Spectrosc. Radiat. Transfer*, **87**, 137–166, 2004.

[19] F. Moreno, R. Vilaplana, O. Muñoz, A. Molina, and D. Guirado. The scattering matrix for size distributions of irregular particles: an application to an olivine sample. *J. Quant. Spectrosc. Radiat. Transfer*, **100**, 277–287, 2006.

[20] O. Muñoz, H. Volten, J.W. Hovenier, B. Veihelmann, W.J. van der Zande, L.B.F.M. Waters, and W.I. Rose. Scattering matrices of volcanic ash particles of Mount St. Helens, Redoubt, and Mount Spurr volcanoes. *J. Geophys. Res.*, **109**, 2004, doi:10.1029/2004JD004684.

Influence of Alignment on the Scattering Properties Atmospheric Mineral Dust

Zbigniew Ulanowski,[1] Olga V. Kalashnikova,[2] Philip W. Lucas,[1] Bertrand Berçot,[1]

[1] *Science and Technology Research Institute, University of Hertfordshire, Hatfield AL10 9AB, UK*
[2] *Jet Propulsion Laboratory, 4800 Oak Grove Dr., Pasadena CA 91109, USA*
tel: +44 1707 284604, fax: +44 1707 284185, e-mail: z.ulanowski@herts.ac.uk

Abstract

We carry out an investigation of the influence of particle alignment on the scattering properties of mineral dust layers. Our modelling indicates that in addition to modifying optical thickness, the alignment can significantly alter the scattering properties, including polarization. Influence of the alignment on remote sensing retrievals is also examined, and it is concluded that satellite and to a lesser extent sun photometry retrievals would be significantly affected.

1 Introduction

Mineral dust in the atmosphere exerts significant indirect influence on radiation by acting as a source of efficient nuclei for cloud formation, modifies both the shortwave and the longwave radiation, and is a major source of nutrients in the marine environment. There is also growing evidence that Saharan dust outbreaks may be reducing Atlantic hurricane activity. Consequently, much effort has been directed at the development of global-scale measurement of aerosol properties, including both satellite and ground-based instruments such as sun photometers and lidar [1,2].

Recent polarimetric observations of atmospheric Saharan dust have provided strong evidence for the presence of vertically aligned particles [3]. The observations, using a high-sensitivity astronomical polarimeter PlanetPol, which achieves fractional polarization sensitivities better than 10^{-6} with an absolute accuracy of about 1% [4], showed ~50 ppm excess of horizontal polarization of transmitted starlight in the presence of Saharan dust over La Palma, Canary Islands in May 2005. At present no other explanation exists for this measurement, despite extensive checks [3,5]. The alignment is thought to be due to a vertical electric field of the order of a kV/m, present probably because of dust charging. It was concluded that partial alignment of larger grains was likely to be a common feature of atmospheric mineral dust layers. For the observed case, shortwave optical thickness in the vertical direction was estimated to change by between 5 and 10% due to the alignment – a “Venetian blind effect”. It was also suggested that the electric field associated with the alignment might modify dust transport by aiding the retention of larger particles within the dust layer [3].

Here we present the results of initial investigations of the influence of the postulated alignment on the scattering properties of mineral dust layers, starting with the case of the aerosol observed over La Palma. We investigate the angular dependence of scattering and the degree of linear polarization, and examine the potential impact on remote sensing retrievals of dust properties.

2 Scattering computations

Scattering calculations were done for prolate spheroids of aspect ratio 1.5. Dust size distributions and refractive index (1.46 – *i*0.006) were obtained for the dates of the dust event from the AERONET sun photometer in Santa Cruz Level 1.5 data (http://aeronet.gsfc.nasa.gov) using the spheroidal particle retrieval method of Dubovik et al. [2]. Additional screening was applied (number of measurements > 20, zenith angle between 25 and 77°). The size distributions were combined with size-dependent orientation distributions, calculated for various electric field strengths [3], to compute elements of the scattering

matrix using the T-matrix program developed by Mishchenko [6]. Wavelength of 780 nm was used and vertical (zenith) incidence was assumed. Molecular scattering was not included.

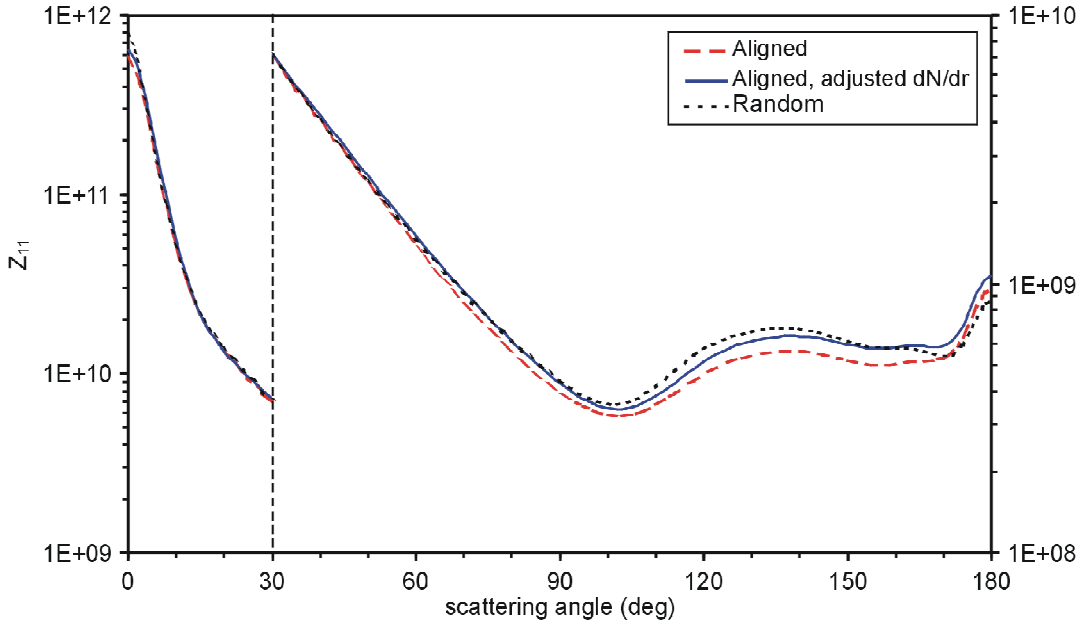

Fig. 1: Unnormalized phase functions computed for the AERONET size distribution on 4 May 2005, with (dashed line) and without the alignment (dotted line), and "aligned" phase function optimized to give best fit to the "random" (non-aligned) one by adjusting the distribution (solid line).

Figure 1 shows the phase function computed for the AERONET size distribution with and without the alignment. It can be seen that significant differences are present, mostly at larger angles. Thus partially aligned dust is estimated to scatter up to 27% less in the forward region, up to 20% less near 120°, and 10% more in backscattering, compared to non-aligned dust, during the La Palma episode. These differences may influence satellite retrievals for some viewing geometries, e.g MISR. However, most of the angular region where sun photometers operate was less strongly affected, with the exception of scattering angles towards 120°.

Since the AERONET size distribution was retrieved on the usual assumption of random alignment, we carried out a computational experiment to determine retrieval sensitivity to alignment. We computed a new phase function with the assumption of partial alignment (field strength of 1600 V/m) but with size distribution optimized to give best least squares fit between the new "partial alignement" and the old "random alignment" phase functions. While only imperfect fit could be obtained – see Figure 1 – the change in the size distribution was substantial. Both the coarse mode and the region centered on 100 nm radius were enhanced, while the mode near 400 nm radius was depleted – see Figure 2. Also, in this example the optical thickness was <0.3. Since the strength of the alignment is expected to increase with the amount of dust, and many dust episodes show higher thickness, the impact can be much greater.

Figure 3 shows the degree of linear polarization (DLP) computed for the AERONET size distribution with and without the alignment. Polarization changes due to alignment are seen to be significant, particularly at larger angles. A similar distribution optimization procedure was used to modify the DLP curves. However, in contrast to the phase function case, it was not possible to force the DLP for aligned dust to adopt a shape characteristic of the "random" DLP. This indicates that the DLP may provide a characteristic signature of alignment, although arguably not as unique as that of polarized extinction. This also suggests that mineral dust retrievals from satellite polarimeters like POLDER/PARASOL or GLORY-APS [1] may not become convergent unless alignment is assumed. In this context, it may be relevant that, qualitatively, the changes in the DLP caused by the alignment are similar in magnitude to those due

the removal of a third of the size distribution by volume, for example [7]. Since it has been argued that retrieval algorithms based on radiance measurements alone cannot provide sufficient retrieval accuracy for aerosols [8], the existence of alignment could mean that the only available option is to combine alignment-based algorithms with polarimetry. However, it appears that the main obstacle at present is the lack of fast vector radiative transfer codes capable of including aligned particles. Such codes are increasingly used in astronomy, where speed of computation is of secondary importance [9,10] but are absent from atmospheric science.

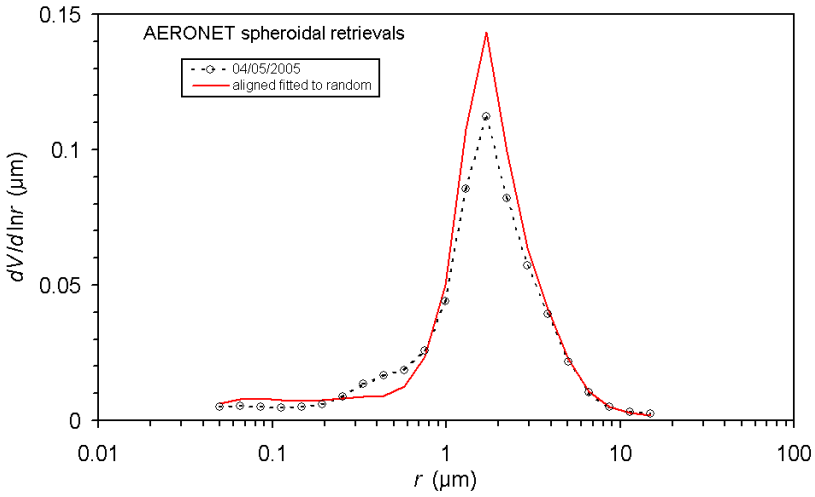

Fig. 2: AERONET size distribution for the La Palma dust on 4 May 2005 (dotted line with circles), and distribution optimized so that the “aligned particle” phase function computed from it gave best fit to the “random” (non-aligned) phase function for the original size distribution (solid line) – Fig. 2.

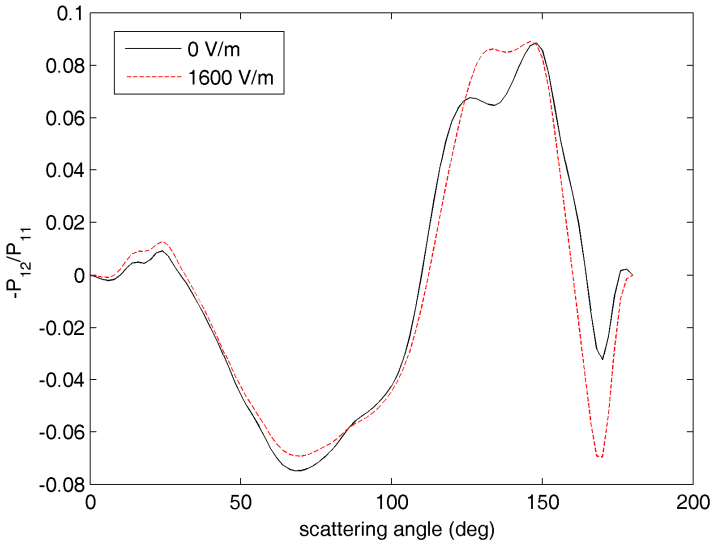

Fig. 3: Degree of linear polarization (DLP) computed for the AERONET size distribution without (0 V/m field, solid line) and with (1600 V/m field, dashed line) the alignment.

3 Conclusions

Polarimetry of transmitted starlight, showing ~50 ppm excess of horizontal polarization in the presence of

Saharan dust, indicates the presence of vertically aligned particles in the atmosphere. Significance of the alignment from the point of view of scattering properties can be summarised as follows:

- Change in optical thickness, particularly for zenith (vertical) incidence;
- Change in phase function - may affect satellite retrievals and to a smaller extent sun photometers;
- Change in polarization - may affect polarimeters, e.g. POLDER/PARASOL and GLORY-APS [1].

Consequently, if the alignment is shown to be widespread, future remote sensing retrieval algorithms for mineral dust, most notably those applied to polarimetry [8], may have to be capable of handling aligned particles.

These conclusions apply to retrievals for sun at the zenith. Also, for these preliminary studies prolate spheroids have been used, while it has been demonstrated that mixtures of prolate and oblate spheroids improve the quality of mineral retrievals from sun photometers [2]. Furthermore, a single-scattering model has been applied, in the absence of fast radiative transfer codes capable of dealing with aligned particles and polarization. Future modelling studies should address these shortcomings. Likewise, further polarimetric measurements, ideally accompanied by measurements of electrical properties and lidar sounding, are needed to answer questions concerning the precise origin, magnitude and extent of the phenomenon investigated here.

Acknowledgments

We are grateful Emilio Cuevas for maintaining the sun photometer on the Santa Cruz site and the AERONET network for providing the data.

References

[1] M.I. Mishchenko, B. Cairns, G. Kopp, et al., “Accurate Monitoring of Terrestrial Aerosols and Total Solar Irradiance: Introducing the Glory Mission,” Bull. Am. Meteorol. Soc. **88**, 677-691 (2007)

[2] O. Dubovik, A. Sinyuk, T. Lapyonok et al., “Application of spheroid models to account for aerosol particle nonsphericity in remote sensing of desert dust,” J. Geophys. Res. **111**, D11208 (2006).

[3] Z. Ulanowski, J. Bailey, P.W. Lucas, J.H. Hough, and E. Hirst, “Alignment of atmospheric mineral dust due to electric field,” Atmos. Chem. Phys. **7**, 6161-6173 (2007).

[4] J.H. Hough, P.W. Lucas, J. Bailey et al., “PlanetPol: a very high sensitivity polarimeter,” Publ. Astron. Soc. Pac. **118**, 1302-1318 (2006).

[5] J. Bailey, Z. Ulanowski, P.W. Lucas, J.H. Hough, E. Hirst, and M. Tamura, “The effect of airborne dust on astronomical polarization measurements,” Mon. Not. R. Astron. Soc. **386**, 1016-1022 (2008).

[6] M.I. Mishchenko, “Calculation of the amplitude matrix for a nonspherical particle in a fixed orientation,” Appl. Opt. **39**, 1026-1031 (2000)..

[7] Z. Ulanowski, O.V. Kalashnikova, P.W. Lucas, and B. Berçot, “Radiative Properties of Aligned Atmospheric Mineral Dust,” EGU General Assembly, Vienna, (2008).

[8] M.I. Mishchenko, B. Cairns, J.E. Hansen, et al., “Monitoring of aerosol forcing of climate from space: analysis of measurement requirements,” J. Quant. Spectrosc. Radiat. Transfer **88**, 149-161 (2004).

[9] B.A. Whitney, and M.J. Wolff, “Scattering and absorption by aligned grains in circumstellar environments,” Astrophys. J. **574**, 205-231 (2002).

[10] P.W. Lucas, “Computation of light scattering in young stellar objects,” J. Quantit. Spectr. Rad. Transfer **79-80**, 921-937 (2003).

COSMIC PARTICLES

Coherent backscattering and radar polarization ratios for Saturn's rings

Janna M. Dlugach[1], and Michael I. Mishchenko[2]

[1] *Main Astronomical Observatory of the National Academy of Sciences of Ukraine, 27 Zabolotny Str., 03680, Kyiv, Ukraine, e-mail: dl@mao.kiev.ua*

[2] *NASA Goddard Institute for Space Studies, 2880 Broadway, New York, NY 10025, U.S.A, e-mail: mmishchenko@giss.nasa.gov*

Abstract

We present the results of our analysis of the circular polarization ratios measured for the A and B rings of Saturn at a wavelength of 12.6 cm [1, 2]. We assume that the ring system is not strongly stratified in the vertical direction and use the model of vertically and horizontally homogeneous plane-parallel layer of a random particulate medium. This model accounts for the effects of polarization, multiple scattering, effect of coherent backscattering, and ring particle nonsphericity. The results of our computations performed for the ring composed of randomly oriented Chebyshev particles, spheroids, and a mixture of spheroids favor the model of nonspherical particles with small-scale surface roughness, and rule out nonspherical particles with aspect ratios significantly exceeding 1.2. They also favor average ring optical thickness values larger than 3, and particles with effective radii in the range 4–10 cm.

1 Introduction

Radar observations have played a very important role in the study of the physical nature of Saturn's rings [2-4], and polarization radar measurements have always been expected to be especially indicative of the physical properties of the ring particles and the ring structure. Note that while the existing measurements of the radar cross sections published by different authors are somewhat inconsistent (cf. [2]), the measurements of the circular polarization ratio μ_C at a wavelength of 12.6 cm by Ostro et al. [1] and Nicholson et al. [2] appear to be quite consistent and show a systematic and nearly linear increase in μ_C with increasing ring opening angle *B*. This quasi-linear angular trend in μ_C has so far defied a physically-based quantitative explanation. The point is that to perform a quantitative analysis of radar depolarization measurements, one must take into account the effects of polarization, multiple scattering, coherent backscattering (CB), and particle nonsphericity. To the best of our knowledge, this has not been done before and is, therefore, the main objective of this work.

2 Theory and computational techniques

As monostatic radar observations involve measurements of the Stokes parameters in the exact backscattering direction (towards the source of illumination), the results of such observations of particulate media can be influenced by CB. The point is that the radiation reflected by a sparse disordered medium consists of two parts. The first part comes from the incoherent multiple scattering by particles and can be described by the solution of the vector radiative transfer equation (VRTE). The second part comes from the coherent interaction of particles and is equal to zero in most scattering directions except very close to the exact backscattering direction, and this case corresponds precisely to the case of monostatic radar observations.

Mishchenko [5] showed that in the exact backscattering direction all characteristics of CB can also be rigorously expressed in terms of the solution of the VRTE. This result is very useful since it allows one to calculate different characteristics of the polarized radiation scattered in the exact backscattering direction.

Thus the analysis of radar measurements of the polarization ratio involves the following:

1. the computation of the single-scattering properties of the ring particles;
2. the computation of the diffuse Stokes reflection matrix through the explicit numerical solution of the VRTE;
3. the computation of the requisite characteristics of CB in the exact backscattering direction from the diffuse Stokes reflection matrix;
4. the computation of the circular polarization ratio.

The entire procedure is described in detail by Mishchenko [6], Mishchenko et al. [7, 8]. In this work, we use the numerically exact T-matrix method [9, 7] to compute the single scattering characteristics of ring particles. Afterwards the VRTE is solved for a homogeneous plane-parallel layer by use of a computational algorithm based on the invariant imbedding technique [10] or by means of the numerical solution of Ambartsumian's nonlinear integral equation [11]. The output of this procedure is the Stokes reflection matrix, which is then used to find the elements of the coherent reflection matrix for the exact backscattering direction according to equations (14.3.21)-(14.3.25) of [8]. The final step is to calculate the values of the circular polarization ratio using equation (14.5.15) of [8].

In this work, the nonspherical ring particles are assumed to be randomly oriented. To analyze the effects of the particle shape, we have considered the models of so-called Chebyshev particles, oblate and prolate spheroids, and shape mixtures of spheroids. The shape of Chebyshev particles with respect to the particle reference frame is given by

$$R(\theta) = r_0(1 + \varsigma T_n(\theta)), \tag{1}$$

where θ is the polar angle, r_0 is the radius of the unperturbed sphere, $T_n(\theta)$ is Chebyshev polynomial (we assume n = 6), and ς is the deformation parameter [12], which can be either positive or negative. The shape of a spheroid is specified in terms of the aspect ratio E, which is defined as the ratio of the maximal to the minimal dimension of a particle. The size of each particle is specified in terms of the radius r of the sphere having the same surface area. The probability distribution of the equivalent-sphere radii is assumed to follow the simple power law distribution characterized by the effective radius r_{eff} and effective variance v_{eff}.

3 Numerical results

We have performed extensive computations of the circular polarization ratio μ_C for a plane-parallel layer of various values of the optical thickness τ, particle effective radius $r_{eff.}$. The effective variance v_{eff} is fixed at the value of 0.2, which corresponds to a size distribution that is neither very narrow nor very wide. The model refractive index of the ring particles corresponds to water ice and is equal to 1.78+0.003i [13]. In the case of Chebyshev particles the computations were performed for various values of deformation parameter ς in the range $0 < |\varsigma| \leq 0.1$, but the results obtained for particles with deformation parameters ς and $-\varsigma$ turned out to be hardly distinguishable. Therefore, we shall show only the results for Chebyshev particles with positive values ς. In all computations made for spheroids, we assume that the aspect ratio for spheroids E is fixed at 1.5, and in the case of shape mixture of spheroids we adopted aspect ratios ranging from 1.2 to 1.8 (in steps of 0.1).

Some of the results of our extensive numerical computations are summarized in Figures 1 and 2.In both figures, we also present the average μ_C values measured for the A and B rings (dots) and the corresponding error bars.

4 Conclusion

The results of our numerical modeling of polarized radar reflectivity of Saturn's rings lead to the following conclusions.

1. The extrapolation of the values of μ_C to $B \approx 0^0$ shows the ring particles to be weakly depolarizing.
2. It is impossible to reproduce the results of radar observations without an explicit inclusion of the CB

effect. Of course, the effect of CB should have been expected to be significant since the phase angle in monostatic radar observations is by definition equal to zero. However, it was important to establish this result by explicit numerical modeling.

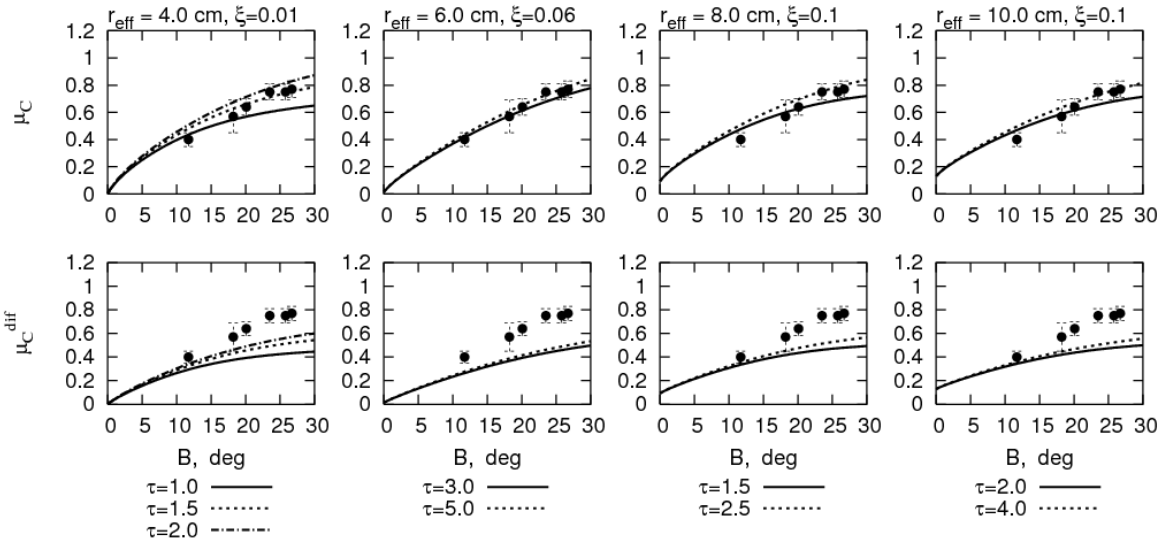

Figure 1: Circular polarization ratios μ_C and μ_C^{dif} versus ring opening angle in the case of Chebyshev particles. Dots correspond to the results of observations [1, 2].

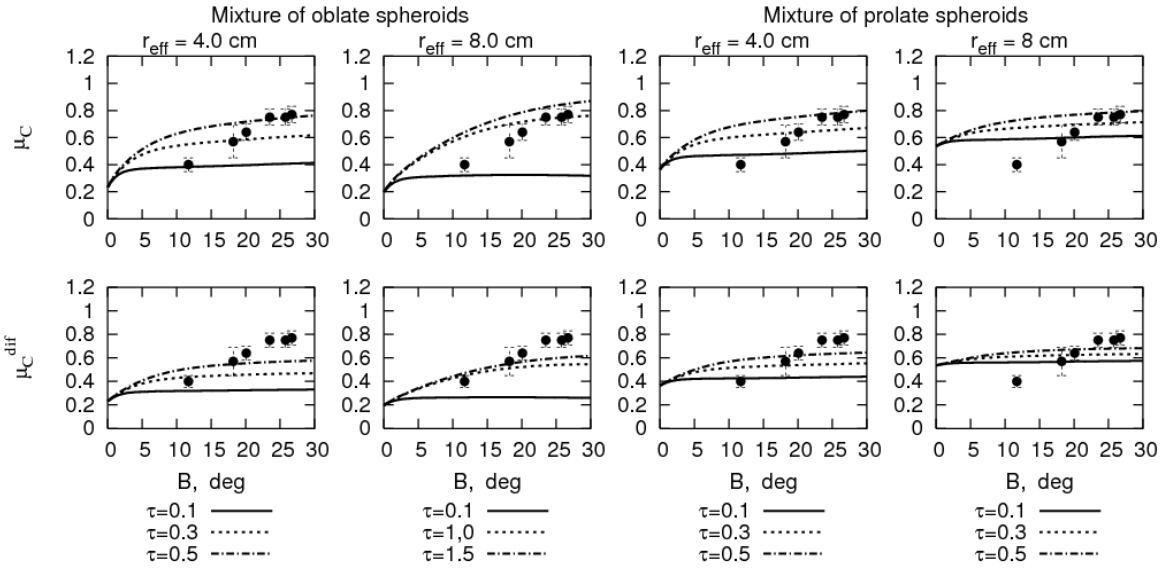

Figure 2: As in Figure 1, but for the shape mixture of spheroids

3. Our results favor the model of ring bodies in the form of particles with small-scale surface roughness (Chebyshev particles with $|\varsigma|$ < 0.15) and rule out the model of a shape mixture of spheroids. They show the large observed circular polarization ratios to be mostly the result of multiple interparticle scattering rather than the result of particle nonsphericity.

4. We obtain average ring optical thickness values to be in the range 3 or even larger. However, it can be seen that the retrieval of the optical thickness depends rather strongly on the assumed size of the error bars in the radar observations.
5. Our results favor particles with effective radii in the range 10 cm and definitely rule out effective radii significantly smaller than 4 cm. This result does not imply that ring particles with radii much smaller than 4 cm do not exist. The point is that radar observations at 12.6 cm are completely insensitive to the presence of micrometer particles.

In conclusion, we believe that additional studies are required in order to analyze all available datasets (including the existing radar measurements of polarization ratio) and to develop a physically based model of Saturn's rings.

Acknowledgments

This research was sponsored by the NASA Radiation Sciences Program managed by Hal Maring.

References

[1] S. J. Ostro, G. H. Pettengill, D. B. Campbell, "Radar observations of Saturn's rings at intermediate tilt angles", Icarus, **41**, 381–388 (1980).

[2] P. D. Nicholson, R. G. French, D. B. Campbell et al., "Radar imaging of Saturn's rings", Icarus, **177**, 32–62 (2005).

[3] R. M. Goldstein, R. R. Green, G. H. Pettengill, D. B. Campbell, "The rings of Saturn – two-frequency radar observations", Icarus, **30**, 104–110 (1977).

[4] S. J. Ostro, "Planetary radar astronomy", Rev. Mod. Phys., **65**, 1235–1279 (1993).

[5] M. I. Mishchenko, "Polarization effects in weak localization of light: Calculation of the copolarized and depolarized backscattering enhancement factors", Phys Rev, B **44,** 12597–12600 (1991).

[6] M. I. Mishchenko, "Diffuse and coherent backscattering by discrete random media – I. Radar reflectivity, polarization ratios, and enhancement factors for a half-space of polydisperse, nonabsorbing and absorbing spherical particles", JQSRT, **56,** 673–702 (1996).

[7] M. I. Mishchenko, L. D. Travis, A. A. Lacis, *Scattering, absorption, and emission of light by small particles* (Cambridge University Press, Cambridge, 2002).

[8] M. I. Mishchenko, L. D. Travis, A. A. Lacis, *Multiple Scattering of Light by Particles: Radiative Transfer and Coherent Backscattering* (Cambridge University Press, Cambridge, 2006).

[9] P. C. Waterman, "Symmetry, unitarity, and geometry in electromagnetic scattering", Phys Rev D **3**, 825–839 (1971).

[10] M. I. Mishchenko, "The fast invariant imbedding method for polarized light: computational aspects and numerical results for Rayleigh scattering", JQSRT, **43**, 163–171 (1990).

[11[W. de Rooij, *Reflection and transmission of polarized light by planetary atmospheres. PhD dissertation* (Vrije Universiteit, Amsterdam, 1985).

[12] W. J. Wiscombe, A. Mugnai, *Single scattering from nonspherical Chebyshev particles: a compendium of calculations* (NASA Ref. Publ. NASA RP-1157, 1986).

[13] S. G. Warren, "Optical constants of ice from the ultraviolet to the microwave", Appl. Opt., **23**, 1206–1225 (1984).

A new mechanism possibly explaining the circular polarization of light scattered in comets: asymmetry of the comet itself

Daniel Guirado,[1] Fernando Moreno,[1] and Michael I. Mishchenko[2]

[1] *Instituto de Astrofísica de Andalucía, CSIC, P.O. Box 3004, 18008 Granada, Spain,*
tel: +34 (958) 230-598, fax: +34 (958) 530-814, e-mail: dani@iaa.es
[2] *NASA Goddard Institute for Space Studies, 2880 Broadway, New York, NY 10025, USA.*

Abstract

A new mechanism producing circular polarization of light scattered in comets is presented. This mechanism is based neither on any intrinsic feature of the particles nor on their possible alignment, but rather on the overall geometry of the comet. Asymmetry of the whole comet around the direction of the incident light is proved to be a necessary condition for the light scattered in the comet to be circularly polarized. A Monte Carlo method is used to simulate the radiative transfer in the coma of a comet. Some results on circular polarization for an asymmetrical coma around the direction of the incident light are presented. These first results correspond to a spherical nucleus with zero albedo, and they give small values of the DCP compared to the observations. More calculations involving asymmetrical reflections from the nucleus as well as a non-spherical geometry are proposed for future work.

1 Introduction

A non-zero degree of circular polarization (DCP hereafter) has been persistently detected in light scattered by comets. A summary of some of the available observations is presented in Table 1.

Table 1: observations of DCP of light scattered in comets.

Comet	Author	Wavelength (nm)	Aperture	Phase angle (º)	DCP (%)
Halley	Morozhenko [1]	514	2.7”x81”	21.1-34.8	(-0.76±0.27)-(0.37±0.20)
Halley	Morozhenko [1]	484	2.7”x81”	21.1-34.8	(-0.05±0.15)-(0.70±0.28)
Halley	Dollfus [2]	visible*	2.1” to 107”	40.7-22.5	(-0.65±0.39)-(1.18±0.48)
Halley	Metz [3]	560	10”, 15” and 21”	66.1	(-2.2±0.1)-(0.7±0.0)
Hale-Bopp	Manset [4]	684	15.5”	40-47.4	(-0.24±0.02)-(0.20±0.04)
Hale-Bopp	Rosenbush [5]	485	10”	46	(-0.26±0.02)-(-0.06±0.06)
C/1999 S4	Rosenbush [6]	red**	15”	60.9-122.1	up to 1
C/2001 Q4	Rosenbush [7]	red**	10”	76	Up to more than 0.4

* Wide band filter centered at 500 nm and covering the whole visible spectrum.
** Wide band R filter.

Although being small, the observed DCPs significantly deviate from zero, as seen in Table 1. Observations of Hale-Bopp, C/1999 S4 and C/2001 Q4 are of better precision than those of Halley. Hence, for comparison with models, observations of Hale-Bopp and more recent comets ($\left|DCP\right|_{\max} = (0.26 \pm 0.02)\%$) should be considered more reliable than those of Halley ($\left|DCP\right|_{\max} = (1.18 \pm 0.48)\%$). We would like to note that some systematic errors might have been introduced in the observations of Halley by Metz [3], as explained by Dollfus [2].

Understanding the origin of the observed DCPs could give us information about some intrinsic features of the dust particles of the coma, or about some of the processes they are undergoing. Three mechanisms have been historically proposed to explain the circular polarization of light scattered in comets, all of them regarding the dust particles of the coma: alignment of non-spherical scatterers, asymmetry of particles even in random orientation, and optical activity of the grains. Up to now, none of them has yielded numerical results in good agreement with the observations of circular polarization. With regard to

alignment, a good review of the mechanisms that could be aligning particles is presented in [8]. Lazarian [9] shows that particles under a subsonic flux of gas are aligned with their longest axis perpendicular to the direction of the flux. Particles in comets are affected by the solar wind, but it is not definitively proved that that the interaction with this flux is the main mechanism aligning particles in comets, because other effects not yet considered could be occurring. For example, the water vapour in the coma could be ionized by the solar wind, preventing the inner particles of the coma from interacting with the outer flux. However, even if the grains in the coma are aligned with their longest axis perpendicular to the direction of the incident flux, they would still have a range of orientations by virtue of rotating about the direction of incidence. This would result in a symmetrical geometry of the dust sample around the direction of the incident light, which cannot produce circular polarization, as explained in Sec. 2. Averaging over orientations and geometries of asymmetrical particles in random orientation rapidly leads to a zero DCP, as shown in [10]. On the other hand, there are no explicit calculations of the values that the DCP can achieve if the grains of the coma were optically active. In summary, some of the proposed mechanisms are proved not to be responsible for the observed DCP, but there is no definitive conclusion yet with regard to the other mechanisms. In this work, we propose a new mechanism involving a potentially very important element of the comet that has been ignored so far: the nucleus. By virtue of its geometry, surface albedo distribution and surface sublimation rate distribution, it determines the density function of the coma as well as the polarization state of the light that is reflected after reaching its surface.

2 Necessary condition for circular polarization

Let us consider a comet which is perfectly symmetric (both nucleus and coma) around the direction of the incident light. This system possesses certain symmetries, which means that it remains invariant after certain transformations. Among these transformations are the reflection with respect to a plane through the axis of the system and the rotation by π rad about the same axis. Let us assume that the DCP observed at a certain point P_1 is right handed and consider what happens after applying both above transformations. By applying the reflection with respect to a plane through the system axis we obtain left-handed circularly polarized light in P_2, the opposite point of P_1 (see Fig. 1a). Rotating it by π rad around the axis then leads to left-handed circular polarization in P_1. As light cannot be right-handed and left-handed polarized in a certain point at the same time, we deduce that the light scattered by a perfectly azimuthally symmetrical comet around the direction of the incident light cannot be circularly polarized.

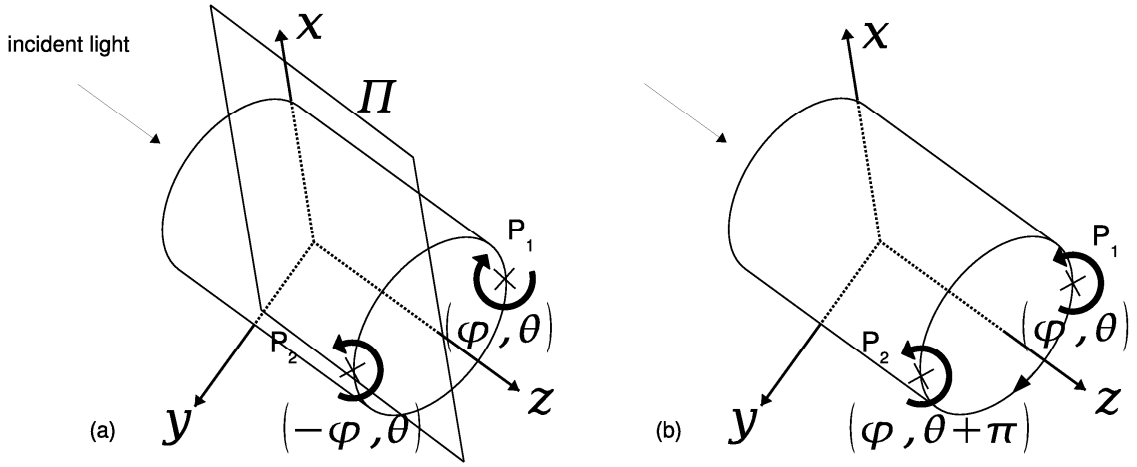

Figure1**:** Transformations of circularly polarized light observed at a certain point, under a mirror symmetry with respect to a plane through the direction of the incident light (a) and upon a rotation by π rad around the same direction (b). φ and θ are the usual cylindrical coordinates.

The symmetry around the direction of the incident light can be broken by a non-spherical nucleus, but even with a spherical nucleus it will be broken if the optical depth of the coma is different in different radial directions or the albedo of the surface of the nucleus is not uniform.

3 Monte Carlo model

Salo [11] presented a Monte Carlo model to calculate the incoming flux in the nucleus of a spherical comet. Moreno [12] described a new model based on the previous one that introduces the whole scattering matrix of the scatterers of the coma, and yields the linear polarization of the outgoing light. In order to save space, we refer to those papers for a detailed description of the models. We develop an analogous model to compute the circular polarization of the outgoing light. We use a polydisperse sample of spherical grains with a refractive index of $m = 1.6 + i0.001$ and assume the wavelength $\lambda = 0.5\mu m$. The size distribution of the sample comes from the average of measurements of real volcanic samples published in the *Amsterdam scattering database* [13]. Reflections from the nucleus are expected to be important even in the case of a uniform albedo, especially for low optical depths in the coma. Our model treats reflections in a way that the polarization state of the reflected light is calculated. This is done by using the Kirchhoff approximation with shadowing, which yields the reflection matrix analytically for a surface with smooth slopes. For definitions and more references on this method see [14].

4 Results

For simplicity, a spherical nucleus is initially assumed. Reflections from the nucleus are avoided by choosing a zero albedo in this first calculation, because further testing is still being performed of the advanced code that includes reflections. The coma is split into two hemispheres with different optical depths, in such a way that the direction of the incident light crosses the equatorial plane. We set an optical depth τ_N in one of the hemispheres and $10\tau_N$ in the other, with $\tau_N = 0.25$, 1 and 2.5. We launch 10^7 Monte Carlo packets of photons (rays), which has been proved by successive approximations to be sufficient for good statistics.

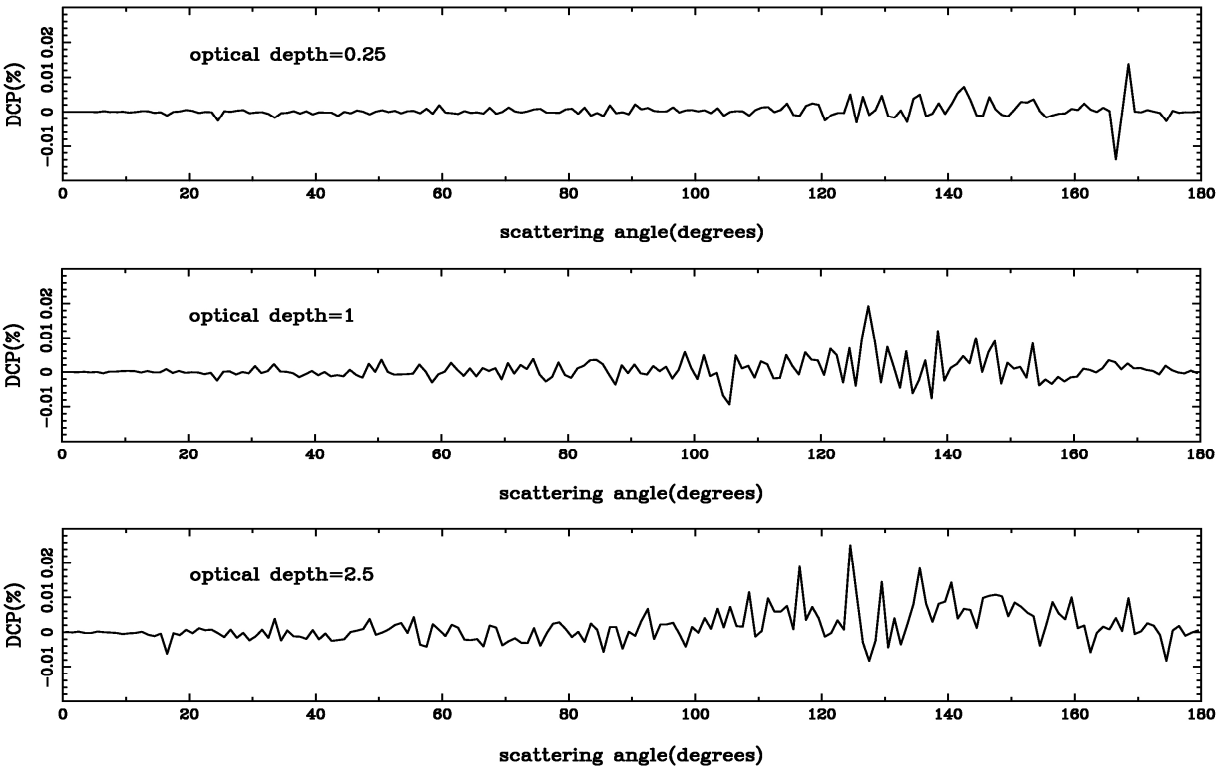

Figure 2. DCP as a function of the scattering angle for several cases in which the optical depth is $\tau_N = 0.25$, 1 and 2.5 for one of the hemispheres and is 10 times larger for the other one.

The DCP values shown in Fig. 2 are very low compared to the observations. They are in the range of the numerical noise, as we have verified by performing calculations with the same optical depths for both hemispheres of the coma.

5 Conclusions and future work

The DCP observed for light scattered in comets cannot be explained only by an asymmetry of the density function of scatterers in the coma when assuming a spherical totally-absorbing nucleus and a coma populated by spherical scatterers. More calculations involving reflections from the surface of the nucleus, a non-uniform albedo of this surface and even a non-spherical geometry must be performed in order to find out whether the large structure of the comet is the main factor responsible for the observed DCP.

References

[1] A. V. Morozhenko, N. N. Kiselev, A. L. Gural'chuk. “Circular polarization of the light from the head of Halley's comet,” Kinematika i Fizika Nebesnykh Tel **2**, 89-90 (1987).

[2] A. Dollfus and J.-L. Suchail, “Polarimetry of grains in the coma of P/Halley,” Astron. Astrophys. **187**, 669-688 (1987).

[3] K. Metz and R. Haefner, “Circular polarization near the nucleus of comet P/Halley,” Astron. Astrophys. **187**, 539-542 (1987).

[4] N. Manset and P. Bastien, “Polarimetric observations of comets C/1995 O1 Hale-Bopp and C/1996 B2 Hyakutake,” Icarus **145**, 203-219 (2000).

[5] V. K. Rosenbush, N. M. Shakhovskoj and A. E. Rosenbush, “Polarimetry of comet Hale-Bopp: linear and circular polarization, stellar occultation,” Earth, Moon and Planets, **78**, 381-386 (1999).

[6] V. Rosenbush, L. Kolokolova, A. Lazarian, N. Shakhovskoy and N. Kiselev, “Circular polarization in comets: Observations of Comet C/1999 S4 (LINEAR) and tentative interpretation,” Icarus, **186**, 317-330 (2007).

[7] V. Rosenbush, N. Kiselev, N. Shakhovskoy, S. Kolesnikov and V. Breus, “Circular and linear polarization of comet C/2001 Q4 (NEAT). Why circular polarization in comets is predominantly left-handed?,” proceeding in the Tenth International Conference on Light Scattering by Non-spherical Particles, 181-184 (2007).

[8] A. Lazarian, “Magnetic fields via polarimetry: progress of grain alignment theory,” J. Quant. Spectr. Radiat. Transfer, **79-80**, 881-902 (2003).

[9] A. Lazarian and T. Hoang, “Subsonic mechanical alignment of irregular grains,” Astrophys. J., **669**, L77-L80 (2007).

[10] D. Guirado, F. Moreno, J. W. Hovenier, “Circular polarization of light scattered by randomly built aggregates,”, in preparation.

[11] H. Salo, “Monte Carlo modelling of the net effects of coma scattering and thermal reradiation on the energy input to cometary nucleus,” Icarus, **76**, 253-269 (1988).

[12] F. Moreno, O. Muñoz, J. J. López-Moreno, A. Molina and J. L. Ortiz, “A Monte Carlo code to compute energy fluxes in cometary nuclei,” Icarus, **156**, 474-484 (2002).

[13] http://www.astro.uva.nl/scatter/SIZAVERAGEVOLC.TXT

[14] M. I. Mishchenko and L. D. Travis, “Satellite retrieval of aerosol properties over the ocean using polarization as well as intensity of reflected sunlight,” J. Geophys. Res., **102**, 16989-17013 (1997).

Comparison of Mie/EMA/T-Matrix/DDA based models with the observed interstellar extinction and other parameters

Ranjan Gupta

IUCAA, Pune 411007 India

D.B. Vaidya

Gujarat College, Ahmedabad-380006, India

Abstract.

Most of the observed extinction data is interpreted using calculations based on the Mie theory for homogeneous spherical dust grains (see e.g. Mathis et al. 1977). Recently, alternative methods based on Effective Medium Approximation (EMA); T-Matrix and Discrete Dipole Approximation (DDA) for modeling the observed interstellar extinction curve are available. We have also modeled the additional observed parameters i.e. interstellar polarization and the abundance constraints. This paper shows a comparison of these theoretical models and we conclude that the DDA based composite grain model suits best to explain all the three observed parameters viz.: interstellar extinction; polarization and also the abundance constraints.

1. Introduction

The theory for calculating the scattering, absorption and extinction parameters for homogeneous spheres was given by Mie (1908) and it is commonly used to interpret the observed scattering (extinction) in many areas e.g. meteorology, atmospheric science, astrophysics etc. Mathis et al. (1977) used this model and showed that the dust grains comprising a mixture of solid silicate and graphite spheres and a power law grain size distribution could fit the observed interstellar extinction curve (Whittet, 2003) very well. However, the collected particles from stratosphere and comet flyby missions have provided enough evidence that the real dust grains are not at all solid spheres and are rather highly non-spheroidal mixtures of various components like graphites, silicates, PAHs etc and are also highly porous in nature.

This has led many researchers in this field (including our group) to reconsider the light scattering models using Mie theory, for alternative models like EMA, T-Matrix and DDA where one could simulate the dust grains as non-spherically shaped particles with porosity added and follow a power law size distribution with various compositions. The non-spherical shape is a must to reproduce the interstellar polarization curve (Serkowski's curve – Serkowski et

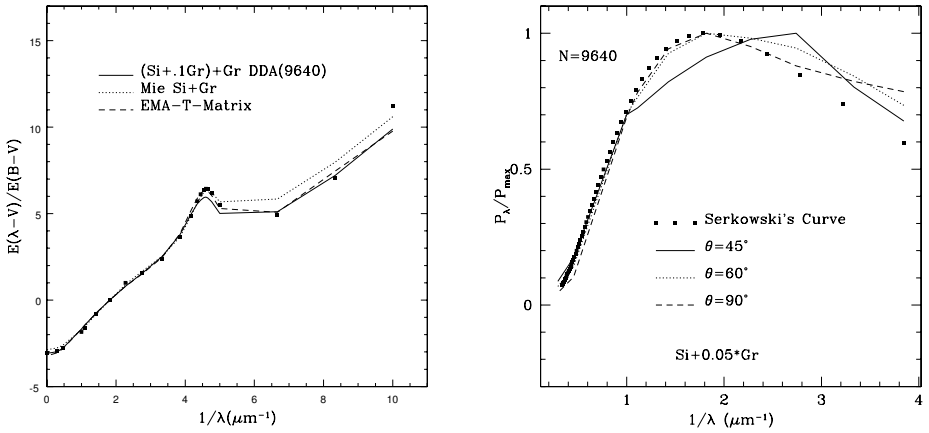

Figure 1. The left panel shows the interstellar extinction curves. The right panel shows the interstellar polarization curve.

al., 1975). Further, the abundance constraints on the maximum available carbon in the Interstellar Medium (ISM) is limited and this requires the proposed grain models to use less amount of carbon which cannot be satisfied with the Mie theory where solid grains are used. Thus porosity plays an important role in satisfying this last criterion.

2. Mie/EMA/T-Matrix and Composite DDA grain models

In the EMA the optical constants of the materials are obtained using the Maxwell-Garnet mixing rule (Bohren and Huffman, 1983). We have used the EMA to produce a simulated grain (which has vacuum as one of the components to introduce porosity) and then used the T-Matrix (Mishchenko, 2002) code to obtain the extinction efficiencies and subsequently compared the resultant extinction curve with the observed curve.

The composite DDA model is described in our recent work (Vaidya et al., 2007) where we have used a grain model consisting silicate dipoles embedded with some fraction of graphite dipoles and in addition some solid graphite grains to reproduce the interstellar extinction curve.

3. Results & Conclusions

The Figure 1 shows (on the left panel) the interstellar extinction curve models (fitting with the observed curve) by solid grains (Mie), EMA-T-Matrix and Composite DDA.

The right panel in this Figure shows the fitting of Composite DDA model produced interstellar polarization and its fitting to the Serkowski's curve.

The Table 1 depicts the abundance constraint as evaluated from the solid grains models and our composite model.

Table 1. Abundance Ratios

Abundance Ratio (ppm)	ISM	Other Models	Our Model
C/H	110	254	160
Si/H	17	32	25

In conclusion, we can say that the Composite and porous DDA grain model is able to fit the observed interstellar extinction as well as the polarization quite well and also satisfies the abundance constraint by demanding less amount of Carbon (as compared to the solid grains). With the upcoming ISRO (Indian Space Research Organization) UV missions like TAUVEX and ASTROSAT, which will have UV observing capabilities, our models will help in understanding the dust distribution in our galaxy by modeling the UV extinction observations from these satellites.

4. Acknowledgements

The authors thank the grant from the ISRO-RESPOND project
No. ISRO/RES/2/345/2007-08 under which this work has been carried out.

References

Bohren, C.F. and Huffman, D.R., 1983, in Absorption and Scattering of Light by Small Particles, John Wiley, New York.

Mathis J.S., Rumpl W., Nordsieck K.H., 1977, ApJ, 217, 425

Mie, S., Ann. Phys.,1908, 330, 377

Mishchenko, M.L., Travis, L.D. and Lacis, A.A., 2002, in Scattering, Absorption and Emission of Light by Small Particles, CUP, Cambridge, UK.

Serkowski K., Mathewson D.S. and Ford V.L., 1975, ApJ, 196, 261

Vaidya D.B., Gupta R., Snow T.P., 2007, MNRAS, 379, 791

Whittet D.C.B., 2003, in Dust in the Galactic Environments, 2nd edn. IoP Publishing, Bristol, UK.

LIGHT SCATTERING BY COSMIC PARTICLES

J. W. Hovenier,[1] and M. Min[1]

[1] *Astronomical Institute "Anton Pannekoek", University of Amsterdam*
Kruislaan 403, 1098 SJ Amsterdam, The Netherlands
tel:+31 (0)20 5257491, fax: +31 (0)20 5257484, e-mail: J.W.Hovenier@uva.nl

Abstract

We define cosmic particles as particles outside the Earth. Two types of cosmic particles can be distinguished, namely liquid and solid particles. The solid particles are often called grains or cosmic dust particles. Cosmic particles occur in a great variety of astronomical objects and environments. At light scattering conferences most attention is usually paid to Solar System bodies. The main purpose of this contribution is to provide a brief introduction to light scattering by cosmic particles, focussing on particles in the atmospheres of (exo) planets and satellites, comets and particulate surfaces. We also point out some key areas for further research.

1 Atmospheres of (exo) planets and satellites

In the atmospheres of planets and satellites liquid particles may occur in the form of clouds, hazes, fog and rain. This happens e.g. in the atmospheres of the Earth and Venus. In these cases the cloud particles are (nearly) spherical and often approximately homogeneous, so that Mie theory can be used to compute their scattering and absorption properties for arbitrary sizes, refractive indices and wavelengths.

There is, however, also a large variety of non-spherical particles in the atmospheres of planets and satellites. This is well-known for the Earth's atmosphere due to numerous studies of ice clouds and aerosols. Other examples are provided by dust storms on Mars as well as clouds and hazes in the atmospheres of giant planets like Jupiter and Saturn, which contain solid particles of condensed material [1]. In the last few decades enormous progress has been made in developing methods for computing light scattering by non-spherical particles [2-4]. By using these methods it has become clear that for all kinds of non-spherical particles Mie theory generally provides insufficient accuracy for computing their absorption and scattering properties, not only in the visible part of the spectrum, but also for larger wavelengths [5]. This means that one should be careful with accepting particle and atmospheric properties based on using Mie theory when the particles may not be spherical.

Instead of computing light scattering properties of non-spherical particles one can also employ experimental results, like the phase functions and the scattering angle dependence of other elements of the scattering matrix for various kinds of randomly oriented natural particles [see e.g. The Amsterdam Light Scattering Database at http://www.astro.uva.nl/scatter]. This holds in particular for cases in which the experimental data have been extrapolated to cover the entire range of scattering angles from 0 to 180 degrees. The laboratory measurements have shown that not only theoretical, but also experimental evidence exists that significant deviations from Mie theory can occur for non-spherical particles.

After fixing the single scattering properties, multiple scattering calculations are usually necessary before a comparison can be made with the observed brightness (intensity) and polarization of a planetary atmosphere. For this purpose several very accurate methods are available and nowadays multiple scattering calculations do not constitute a major stumble-block anymore [6,7]. But, unless the atmosphere is optically very thick, the reflected radiation can only be accurately computed when the reflective properties of the underlying surface are known. Very often one makes the physically poor assumption that the surface reflects all incident radiation isotropically and destroys all polarization, i.e. behaves like a Lambert surface. This is virtually always a very rough oversimplification. What we need is the complete (bidirectional) reflection function of the surface, if polarization is ignored, and otherwise the complete 4 by 4 (bidirectional) reflection matrix [6] for various wavelengths. Only then can we take the

interaction between the atmosphere and surface properly into account. This is a key area for further theoretical and experimental research, especially for solid surfaces.

The phase angle is the angle between the directions to the Sun and the observer, as seen from the planet or other Solar System body being observed. It varies between 0 and 180 degrees for earthbound observations of Mercury and Venus. Due to this large phase angle coverage, and a rainbow feature in the observed polarization, much information could be deduced over 30 years ago from earthbound observations of Venus about the size and composition of the (spherical) cloud particles and the altitude of the top of the main cloud deck [8]. For a long time it seemed impossible to perform a similar analysis for other planetary atmospheres in the Solar System, mainly because solid non-spherical particles are expected to dominate their reflection properties and the field of light scattering by non-spherical particles was still in its infancy. Today this is much less of a problem, but the limited range of phase angles for all planets outside the orbit of the Earth hampers the interpretation of earthbound observations in terms of particle properties and cloud structure. For such observations the maximum phase angle is about 47 degrees for Mars, 12 degrees for Jupiter and even smaller for planets at larger distances. Space research has provided observations at more phase angles and with a better spatial resolution than earthbound observations. This has made it possible to make more detailed studies of the atmospheres of planets and satellites. However, in many cases the analyses were based on the assumption that the particles scatter and absorb radiation like homogeneous spheres. Therefore, it is important to investigate with modern methods for computing scattering and absorption by non-spherical particles to what extent conclusions in the literature need to be modified. Important clues for such studies may be obtained from remote sensing retrieval of properties of aerosols in the atmosphere of the Earth based on a shape mixture of randomly oriented polydisperse spheroids. Comparison with Mie-based retrievals showed a significant improvement in particle phase functions, size distributions and refractive indices [9]. Significant errors in the retrieved aerosol optical thickness can be expected if Mie theory is used to analyze reflectance measurements for non-spherical aerosols [10].

Over 280 exopanets have been discovered so far, but not much is known about the nature of their atmospheres and surfaces. An exoplanet is a planet in orbit around a star instead of the Sun and its phase angle [angle between the directions to the star and the Earth as seen from the exoplanet] varies between 90 degrees plus or minus the acute angle between the plane of the orbit and the plane perpendicular to the line between the observer and the star. So the observable phase angle range may be considerable and several attempts have been made and are planned to observe the polarization of exoplanets. Recently the first direct detection of an exoplanet in visible polarized light was reported [11]. Whenever the phase angle range is appreciable, an analysis similar to that conducted for Venus is possible, for spherical as well as non-spherical particles [12].

2 Comets

The solid nucleus of a comet is surrounded by a cloud of particles called the coma. These particles are illuminated by the Sun and scatter light in all directions, in particular to the Earth. The time variations of the brightness of the coma, as observed from Earth, do not only depend on the variations in the distances of the comet to the Sun and the Earth, as well as the phase angle, but also on changes in the dust production rate. This makes it difficult to obtain reliable intensity phase curves, i.e. the brightness as a function of phase angle for unit distances [13].The results obtained so far indicate a distinct forward scattering peak, a flat shape at medium scattering angles and a gentle backscattering peak. These are normal features for non-spherical particles. The degree of linear polarization is a relative quantity and therefore accurate linear polarization phase curves have been obtained for a variety of comets. These curves are all bell- shaped. This means they have a broad range of positive linear polarization [vibrations perpendicular to the scattering plane dominating over the parallel vibrations] with a maximum at or near 90 degrees and weak negative polarization near small phase angles. Interpretations of these curves are usually based on single scattering computations for various kinds of particles, in particular aggregates.

But light scattering experiments and computations have shown that more compact irregular mineral particles are also good candidates for interpreting the linear polarization phase curves [14]. Circular polarization has been observed for local regions of several comae.This can be ascribed to orientation of particles and/or a predominance of particles of one kind over their mirror symmetric counterparts.The wavelength dependence of the linear polarization was called red for a long time, but in recent years some exceptions of this rule have been observed [15]. More spectropolarimetric observations and laboratory experiments will be needed to refine the characterization of cometary particles.

3 Particulate surfaces

Many bodies in the Solar System have (almost) no atmosphere. These include the Moon, most other satellites of planets and also asteroids. Their linear polarization phase curves are bell-shaped with negative polarization for small phase angles. Their intensity phase curves exhibit the so-called photometric opposition effect, i.e. a surge in brightness when the phase angle tends to zero. Explaining this and also the negative polarization at small phase angles is not easy, because the particles at the top of the surfaces of these bodies touch each other, which clearly makes the favorite assumption of independent scattering questionable. A plethora of papers and discussions at light scattering conferences have been devoted to this topic. The photometric opposition effect as well as the negative polarization at small phase angles can in principle be explained by the coherent backscattering mechanism. The gist of this multiple scattering mechanism is that the interference of waves propagating in opposite directions through the particulate medium is constructive for the exact backscattering direction and directions close to it [3, 7, 16].

Direct numerical solutions of the Maxwell equations provide an accurate quantitative approach to the problem of electromagnetic energy transport in densely packed media [17]. This is another key area for further research which seems to have a bright future given the expected increase in computer capabilities.

References

[1] R. A. West, "Scattering and Absorption by Nonspherical Particles in Planetary Atmospheres." In: Proceedings of the 8th Conference on Electromagnetic and Light Scattering by Nonspherical Particles: Theory, Measurements and Applications," edited by F. Moreno, J. J. Lopez-Moreno, O. Munoz and A. Molina, 321-324 (2005).

[2] M. I. Mishchenko, J. W. Hovenier and L. D. Travis, Light Scattering by Nonspherical Particles: Theory, Measurements, and Applications (Academic Press, San Diego, 2000).

[3] M. I. Mishchenko, L. D. Travis and A. A. Lacis, Scattering, Absorption, and Emission of Light by Small Particles (Cambridge University Press, Cambridge, 2002).

[4] G. Videen, M. I. Mishchenko, M. Pinar Menguc and N. Zakharova, Peer-reviewed Abstracts of the Tenth Conference on Electromagnetic & Light Scattering (Bodrum, 2007).

[5] M. Min, J. W. Hovenier and A. de Koter, "Shape effects in scattering and absorption by randomly oriented particles small compared to the wavelength," Astron. Astrophys. **404**, 35-46 (2003).

[6] J. W. Hovenier, C.V.M. van der Mee and H. Domke, Transfer of Polarized Light in Planetary Atmospheres : Basic Concepts and Practical Methods (Kluwer/ Springer, Dordrecht, 2004).

[7] M. I. Mishchenko, L. D. Travis and A. A. Lacis, Multiple Scattering of Light by Particles : Radiative Transfer and Coherent Backscattering (Cambridge University Press, Cambridge, 2006).

[8] J. E. Hansen and J. W. Hovenier, "Interpretation of the polarization of Venus," J. Atmos. Sci. **31**, 1137-1160 (1974).

[9] O. Dubovik, B. N. Holben, T. Lapyonok, A. Sinyuk, M. I. Mishchenko, P. Yang and I. Slutsker, "Non-spherical aerosol retrieval method employing light scattering by spheroids," Geophys. Res. Letters **29**, 54 (2002).

[10] M.I. Mishchenko, L. D. Travis , R. Kahn and R. A. West," Modeling phase functions for dustlike troposheric aerosols using a shape mixture of randomly oriented polydisperse spheroids,"JGR **102**, 16831-16847 (1997).

[11] S. V. Berdyugina, A. V. Berdyugin, D. M. Fluri and V. Piirola,"First detection of polarized scattered light from an exoplanetary atmosphere," Ap.J. **673**, L83 - L86 (2008).

[12] D. M. Stam, J. W. Hovenier and L. B. F. M. Waters,"Using polarimetry to detect and characterize Jupiter- like extrasolar planets," Astron. Astrophys. **428**, 663-672 (2004).

[13] L. Kolokolova, M. S. Hanner. A. C. Levasseur-Regourd and B. A. S. Gustafson," Physical properties of cometary dust from light scattering and thermal emission," In: "Comets II," edited by M. C. Festou, H. U. Keller and H. A. Weaver, Univ. of Arizona Press, Tucson, pp. 577-604 (2004).

[14] F. Moreno, O. Munoz, D. Guirado, and R. Vilaplana, "Comet dust as a size distribution of irregularly shaped compact particles," JQSRT **106**, 348 - 359 (2007).

[15] N. Kiselev, V. Rosenbush, L. Kolokolova and K. Antonyuk, "The anomalous spectral dependence of polarization in comets," JQSRT **109**, 1384-1391 (2008).

[16] K. Muinonen,"Light scattering by inhomogeneous media: Backward enhancement and reversal of linear polarization," Ph.D. thesis," Univ. of Helsinki (1990).

[17] M. I. Mishchenko," Multiple scattering, radiative transfer, and weak localization in discrete random media: unified microphysical approach," Rev. Geophys., **46**, RG2003, doi: 10.1029/2007RG000230.

Polarimetry of the Galilean satellites and Jupiter near opposition

Nikolai Kiselev,[1] Vera Rosenbush,[1] Fedor Velichko,[2] Sergej Zaitsev,[1]

[1] *Main Astronomical Observatory of National Academy of Sciences of Ukraine, 27 Zabolotnoho Street, Kyiv, 03680 Ukraine*

[2] *Institute of Astronomy of Kharkiv National University, 35 Sums'ka Street, Kharkiv, 61022 Ukraine*

tel: +38 (044) 526-2147, fax: +38 (044) 526-2147, e-mail: kiselev@mao.kiev.ua

Abstract

New polarimetric observations of the Galilean satellites together with available previous observations are analyzed. The causes of differences between our results and observations of other authors are discussed. It is shown that there is no second inversion point near the phase angle 0.5°. New polarimetric observations fully confirm the presence of the polarization opposition effect for the satellites Io, Europa, and Ganymede in the region of phase angles smaller than 2°.

1 Introduction

The phase-angle and wavelength dependences of polarization near opposition for different atmosphereless solar system bodies (ASSBs) are still in the focus of attention because the behavior of polarization at small phase angles is a key test for alternative models of light scattering by regolith surfaces. Nevertheless, the available polarimetric data, even for bright satellites of Jupiter, are very limited and mutually contradictory. Rosenbush et al. [1, 2] were the first to detect the secondary minimum of polarization for the high-albedo Galilean satellites Io, Europa, and Ganymede, the so-called polarization opposition effect, at very small phase angles, less than 1°, and with an amplitude of about 0.35%. To the contrary, Morozhenko [3, 4] and Chigladze [5] found for all Galilean satellites that there is an inversion point at a phase angle ≈0.5° where polarization changes sign. In this work we present new polarimetric observations of the Galilean satellites and their analysis along with an analysis of the previous observations.

2 Observations and results

New polarimetric observations of Io, Europa, Ganymede, and Callisto were carried out with a one-channel photoelectric photometer–polarimeter mounted on the 70-cm reflector of the Chuguev Observational Station of the Institute of Astronomy of the Kharkiv National University on June 5–8, 2007. The corresponding phase angles changed within the range from –0.13° to 0.62°. We used a 19″ circular diaphragm and the V filter for all observations. The following parameters of the instrumental polarization were determined from observations of polarization-free standard stars [6]: q_i = –0.066±0.010% and u_i = 0.050±0.011%. The zero-point of the position angle of the polarization plane was determined with an accuracy of 0.7° from observations of standard stars with large polarization [6]. The polarization errors for the satellites included statistical errors and errors due to the instrumental polarization and did not exceed 0.03%.

From the observations, we calculated the position angles $\theta_r = \theta - (\theta_{sca} \pm 90)$ between the polarization plane θ and that perpendicular to the scattering plane θ_{sca}. Figure 1 presents the phase-angle dependence of the angle θ_r for the satellites, including our new observations of 2007 (open circles), those of 2000 [2] (filled circles), and of 1988 [1] (open diamonds), as well as the data obtained by Morozhenko in 1986 [4] (straight crosses). One can see that our data obtained in 2007 are in a good agreement with

our data obtained during the 1988 and 2000 oppositions. In these cases, the plane of polarization for the satellites lies in the plane of scattering and θ_r is close to 90°, i.e., the degree of polarization is negative.

In accordance with θ_r, Fig. 2 presents the phase-angle dependence of polarization derived from our observations mentioned above. For comparison, the regular branches of negative polarization calculated using all published data at phase angles greater than 2° are also shown [2]. The phase-angle dependences of polarization for the leading and trailing hemispheres of Io, Europa, Ganymede, and Callisto are shown according to [2, 7].

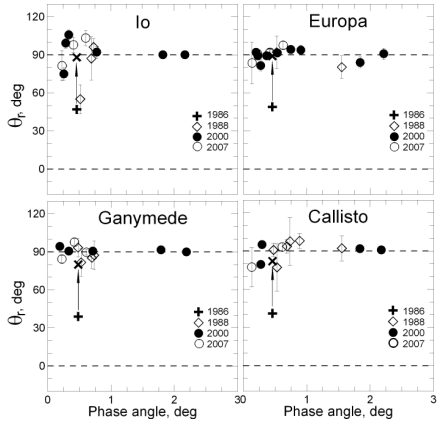

Figure 1: Phase-angle dependence of the angle θ_r for the Galilean satellites according to observations by Rosenbush et al. (1988, 2000), this work (2007), and Morozhenko (1986; straight crosses (+) are original data and oblique crosses (×) are those after correction).

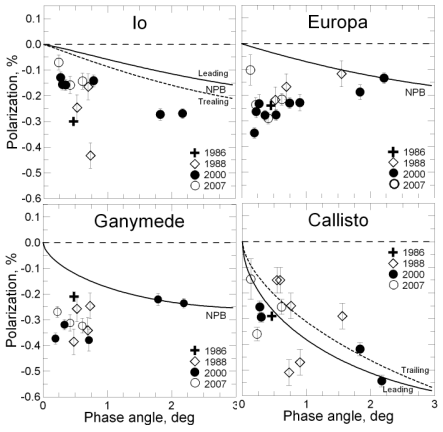

Figure 2: Phase-angle dependence of polarization for the Galilean satellites. Notation is the same as in Fig.1. The regular negative polarization branches (solid and dashed lines) are taken from [2, 7]. The data are not corrected for the longitudinal effect of polarization.

3 Discussion

The new observations fully confirm the presence of the polarization opposition effect for the high-albedo satellites Io, Europa, and Ganymede at phase angles less than 1° originally discovered by Rosenbush et al. [1]. No polarization opposition effect was found for the moderate-albedo satellite Callisto. Moreover,

our data do not confirm the statement by Morozhenko [3, 4, 8] that “the plane of polarization does not coincide with the plane of scattering and is not perpendicular to it” (cf. straight crosses in Fig. 1). To determine the plane of polarization for the satellites, Morozhenko used observations of the polar regions of Jupiter, in belief that the plane of polarization for these regions is orthogonal to the scattering plane, i.e., $\theta_r = 90°$. However, previously Chigladze [5] had found that for the Jovian polar regions the angle θ_r turns sharply at phase angles less than 1° (Fig. 3, left panel). In order to analyze this situation, we carried out observations of the polar regions of Jupiter and confirmed the observed effect (Fig. 3, right panel). Using the new value $\theta_r = 41°$ for the polar regions of Jupiter and the data obtained by Morozhenko [4] we found that the plane of polarization for satellites coincides with the plane of scattering (oblique crosses in Fig. 1).

Thus, the statements by Morozhenko [4, 8] that, on the one hand, the difference between the plane of polarization and the plane of scattering is about 45° and, on the other hand, there are large values of negative polarization (straight crosses in Fig. 2) for all four Galilean satellites at the phase angle 0.4° are essentially contradictory. Indeed, for the angle $\theta_r \approx 45°$, the degree of polarization is related to the scattering plane, i.e., the degree of negative polarization is close to zero according to the expression $P_r = P_{obs}\cos 2\theta_r$.

We have also analysed the data by Chigladze and concluded that his calculations of the scattering plane are erroneous. Therefore, we conclude that there is no second inversion point near the phase angle 0.5° for the Galilean satellites.

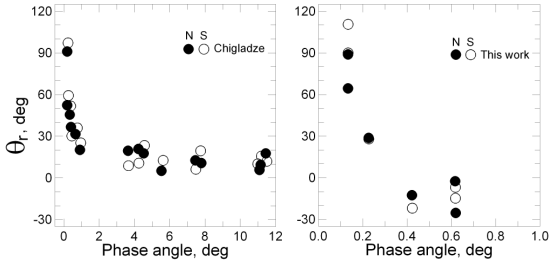

Figure 3: Change of the angle θ_r with decreasing phase angle toward opposition for the northern (full circles) and southern (open circles) polar regions of Jupiter. The left panel depicts the data by Chigladze, whereas the right panel shows our new data.

Gradie and Zellner [9] were the first to note that “the polarization of Ganymede does not vanish at zero phase angle”. But they explained this fact as “possibly the result of icy polar cups”. Rosenbush et al. [1] for the first time interpreted significant negative polarization of Io, Europa, and Ganymede at very small phase angles as the polarization opposition effect caused by the coherent backscattering mechanism. This effect was theoretically predicted by Mishchenko [10] who termed a sharp and very narrow peak of negative polarization at nearly zero phase angles as “the polarization opposition effect”. Later, the polarization opposition effect for the Galilean satellites Io, Europa, and Ganymede was confirmed by Rosenbush and Kiselev [2]. Moreover, this effect was found for other high-albedo objects such as E-type asteroids [11, 12], the satellite of Saturn Iapetus [13]; Dollfus (see in [1]) detected this effect for the A and B rings of Saturn. Thus, an entire new class of high-albedo objects exhibiting the polarization opposition effect has been identified [14].

4 Conclusion

New observations of the Galilean satellites of Jupiter in 2007 are in a good agreement with our previous observations. There is no second inversion point near the phase angle 0.5° claimed by Chigladze and Morozhenko. We have identified the causes of differences between our data and those by Chigladze and Morozhenko [3-5].

Acknowledgments

N. Kiselev and V. Rosenbush are thankful to the SOC and LOC of the ELS-XI Conference and NASA for financial support.

References

[1] V. Rosenbush, V. Avramchuk, A. Rosenbush, M. Mishchenko, *"Polarization properties of the Galilean satellites of Jupiter: Observations and preliminary analysis,"* Astropys. J. **487**, 402–414 (1997).

[2] V. Rosenbush and N. Kiselev, *"Polarization opposition effect for the Galilean satellites of Jupiter,"* Icarus. **179**, 490–496 (2005).

[3] A. Morozhenko and E. Yanovitskij, *"Investigation of physics of planets and small bodies of solar system,"* In: Main Astronomical Observatory 50 years (Y. Yatskiv, Ed.).pp. 135-163. (Naukova Dumka, Kiev) (1994).

[4] A. Morozhenko, *"Results of spectropolarimetric observations of planets and Jupiter's satellites in oppositions 1986, 1988, 1989,"* Kinem. Phys. Celest. Bodies. **17**, 45–57 (2001).

[5] R. Chigladze, " ,*"Investigations of polarimetric properties of Galilean satellites of Jupiter and planet Uranus,"* Ph.D. thesis. Abastumany Astrophysical Obs. p. 175 (1989).

[6] C. Heiles, "9286 stars: an agglomeration of stellar polarization catalogs. Astron. J. **119**, 923–927 (2000).

[7] V. Rosenbush, "The phase-angle and longitude dependence of polarization for Callisto," Icarus. **159**, 145–155 (2002).

[8] A. Morozhenko and A. Vid'machenko, In: Videen G., Yatskiv Y., Mishchenko M. (eds.), Photopolarimetry in Remote Sensing, Kluwer Acad. Publ. 369–384 (2004).

[9] J. Gradie, B. Zellner, "A polarimetric survey of the Galilean satellites," BAAS. **5**, 403–404 (1973).

[10] M. Mishchenko "On the nature of the polarization opposition effect exhibited by Saturn's rings," Astroph. J. **411**, 351–361 (1993).

[11] V. Rosenbush, N. Kiselev, V. Shevchenko, et al., "Polarization and brightness opposition effects for the E-type Asteroid 64 Angelina," Icarus. **178**, 222–234 (2005).

[12] V. Rosenbush, V. Shevchenko, N. Kiselev, et al., "Polarimetry and photometry of asteroid 44 Nysa: comparision of opposition effects in E-type asteroids," Abstracts of the Conference "200 years of Kharkov astronomy" (2008).

[13] V. Rosenbush, "The scattered light properties of small Solar System bodies," Doctor degree thesis. Main Astronomical Observatory. Kyiv (2007).

[14] M. Mishchenko, V. Rosenbush, N. Kiselev, "Weak localization of electromagnetic waves and opposition phenomena exhibited by high-albedo atmosphereless solar system objects," Appl. Opt. **45**, 4459–4463 (2006).

Deep Impact as a Light Scattering Space Experiment

Ludmilla Kolokolova,[1] Ashley King,[1] Michael A'Hearn[1]

[1] *University of Maryland, Department of Astronomy, College Park, Maryland 20742 USA*
tel: +1 (301) 405-1539, fax: +1 (301) 405-3538, e-mail: ludmilla@astro.umd.edu

Abstract

Deep Impact space mission was accomplished in July 2005 when its impactor hit the nucleus of comet 9P/Tempel 1 and produced a thick cloud of materials excavated from the nucleus interior. The ejecta cloud was studied using on board cameras and near-infrared spectrometer with a high temporal and spatial resolution. The flow of the Deep Impact ejecta across the limb of the nucleus allows us to map the optical depth and the albedo of the particles as a function of time and azimuth. The obtained maps of the optical depth and albedo support the idea of a layered structure of the comet nucleus.

1 Introduction

Comets always have been objects of special interest for planetary scientists as they are leftovers from the protosolar nebula that preserved its materials in pristine form and, thus, keep the clues to the formation of the Solar system. However, only so called "new" comets, which arrive from the edge of the Solar system, have rather untouched materials on their surface. The surface of the "old" comets, those that entered interior of the Solar system long ago and since that time have stayed at rather small heliocentric distances, has been changed under the solar radiation and bombardment by charged particles and micrometeorites. However, these changes should affect only the outer 2-3 meters of the comet nucleus, whereas the interior of the comets still should be pristine. To study these pristine materials from the comet interior was the main goal of the NASA space mission Deep Impact [1, 2]. The spacecraft reached the target body, comet 9P/Tempel 1, on July 4, 2005 and hit it with the impactor, a small vehicle specially designed to penetrate as deep as possible inside the nucleus. The impact produced a cloud of the materials excavated from the surface and interior of the comet. Hundreds of images, obtained with a high temporal and spatial resolution by the Deep Impact High and Medium resolution instruments, showed how the cloud was developing and its structure was changing with the time from the impact (Fig. 1).

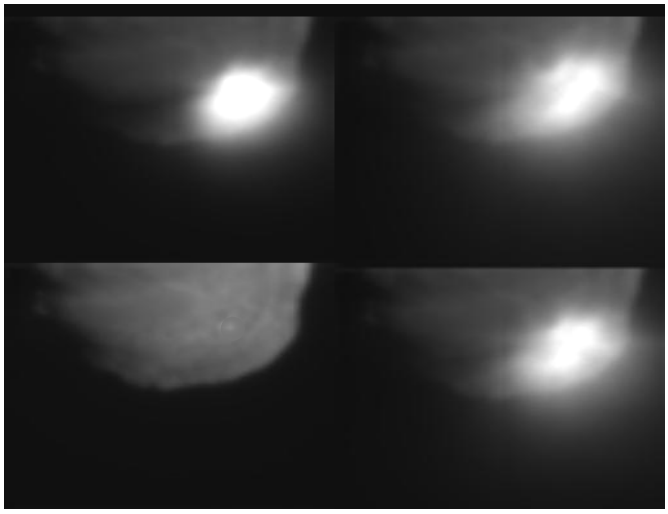

Figure 1. The nucleus of comet 9P/Tempel 1 and the ejecta cloud produced by the Deep Impact as it looked before the impact (bottom left), and 1.747 (bottom right), 3.615 (top right) and 5.482 (top left) seconds after the impact. The images were taken by the Medium Resolution Instrument (MRI). The field of view of the instrument was 0.587 degrees or 10.0 milliradians. The data were taken from [3]. The dataset has a spatial scale ~70 m/pixel and covers the time range from 0.057 seconds before impact to about 300 seconds after impact.

This paper studies the characteristics of the ejecta cloud and its dust particles at a set of locations on the limb of the nucleus (i.e. a set of directions, azimuths, in the cloud) for a range of time from the impact. This allows us to see appearance of different materials, excavated as the explosion developed, and gave us information about the internal structure of the nucleus, e.g. layering of the materials inside it. Thus, Deep Impact can be called a space experiment that allowed us to use light scattering techniques to find the properties of the materials inside comet nuclei.

2 Method

To study the change in the dust distribution in the ejecta cloud with time we used the images taken by the Deep Impact Medium Resolution Instrument (MRI). The data and the instrument description are available through the NASA Planetary Data System, PDS [3]. The images taken with the MRI have a time resolution of 65 millisec for many seconds before and after the impact and gradually greater spacing after that as the ejecta are moving more slowly. We emphasize here the data taken just before and in the first 100 seconds after the impact, thus limiting the change in geometry due to motion of the flyby spacecraft. Although the instrument had a variety of filters (the filter wheel contained two clear apertures and eight other filters, among them three narrow-band gas filters and the following dust filters: 345/6.8 nm, 526/5.6 nm, 750/100 nm, 950/100 nm; the numbers show the central wavelength and the bandpass of the filters) here we consider only the data taken with the clear filter 650/700 nm (from the data obtained with the gas filters we could conclude that within the considered time period the gas contamination was low).

Optical depth. The optical depth of the cloud was detected through the obscuration of the limb by the ejecta that can be clearly seen in the bottom images of Fig. 1. Using an image taken just before the impact (see Fig.1, bottom left image), at each point on the downrange limb of the nucleus, we measure the brightness of the limb above the background, I_b. Then on the images after the impact we measure the brightness at the same locations on the nucleus limb, I_n, and immediately out of the limb, I_c. We suppose that the dust that produces obscuration on the limb is the same as the dust just outside the limb at the same location on the limb (azimuth) and moment of time. The brightness on the limb after impact is produced by the light scattered by the ejecta dust particles and the light scattered by the nucleus and attenuated by the ejecta cloud. The latest is equal to $I_n - I_c$ and is also equal to $I_b \exp(-\tau)$ that allows us to determine the optical depth τ. The obscuration was determined on the limb of the nucleus for a variety of the points along the nucleus perimeter, i.e. for a variety of azimuths in the ejecta cloud, and for a variety of the times after the impact from 0.001 up to 105 seconds.

Albedo. In case of small optical depth, for an ensemble of particles, the average single-scattering albedo of the particles, $\omega = \sigma_{sca} / \sigma_{ext,}$ can be calculated as the ratio of the intensity of the light scattered by the ensemble to the intensity of the light lost due to the extinction by the ensemble particles. As we mentioned above, we suppose that the properties of the cloud are the same on the limb and immediately beyond the limb. This means that the geometrical thickness of the cloud, the number density of the dust particles, and their optical properties defined by their size and composition are the same in both these almost identical locations. This dust produces the optical depth τ calculated in Section 2.3.1.1 that by definition is $\tau = n \cdot l \cdot \sigma_{ext}$, where n is the number density of the particles, l is the geometrical thickness of the cloud. The same dust scatters light producing the brightness I_c, which can be defined as $I_{sun} \cdot n \cdot l \cdot \sigma_{sca(62.9^o)}$ where $\sigma_{sca(62.9^o)}$ is the scattering cross-section at the phase angle 62.9º and I_{sun} is the intensity of the sunlight at the heliocentric distance of the comet. One can see that from the expressions for optical depth and brightness it is possible to find out single-scattering albedo as $\omega = I_c/(I_{sun} \cdot \tau)$. Note, that this is not a traditional single-scattering albedo but the albedo at the phase angle of the observations that was equal to 62.9°. This means that the obtained values of albedo are smaller than the values we would obtain if we calculated the traditional single-scattering albedo of the ejecta particles. Where the optical depth is high, we use a 1D radiative transfer approach similar to the one described in [4], Chapter 3, to estimate the albedo. We present the phase function of the dust particles by the Henyey-Greenstein function and calculate the optical depth counting on the Sun light scattered/absorbed by the cloud and the one that

was transmitted through the cloud, reflected from the surface of the nucleus (whose reflectivity we know through the before-impact brightness, I_b) and then passed through the cloud again. Calculations are done for a variety of values for the Henyey-Greenstein parameter g and albedo of the particles. The best-fit solution has been found for those moments and locations in the cloud where $\tau \geq 1$ was found from our calculations described above. The best fit parameters for the optically thick parts of the cloud demonstrate low values of albedo, usually below 0.05, and a rather stable value of g that was changing within 0.68-0.7.

3 Results

Figure 2a shows the optical depth calculated as described above at several azimuths from the impact site. It plots the optical depth as color-coded symbols with time from impact starting at 0.001 (shown by the most distant from the nucleus points near the right edge of the figure) and increasing toward the impact site. Time scale in seconds is shown along the topmost profile; it indicates the mid-time for each exposure. Figure 2b shows the albedo corresponding to Figure 2a. Figure 3 shows perspective contour plots based on many more data but otherwise similar to Fig. 2. The highest frequency variations may be noise. One can see that the optical depth changed from 0 to 4.25 and albedo ranged from 0.02 to 0.25.

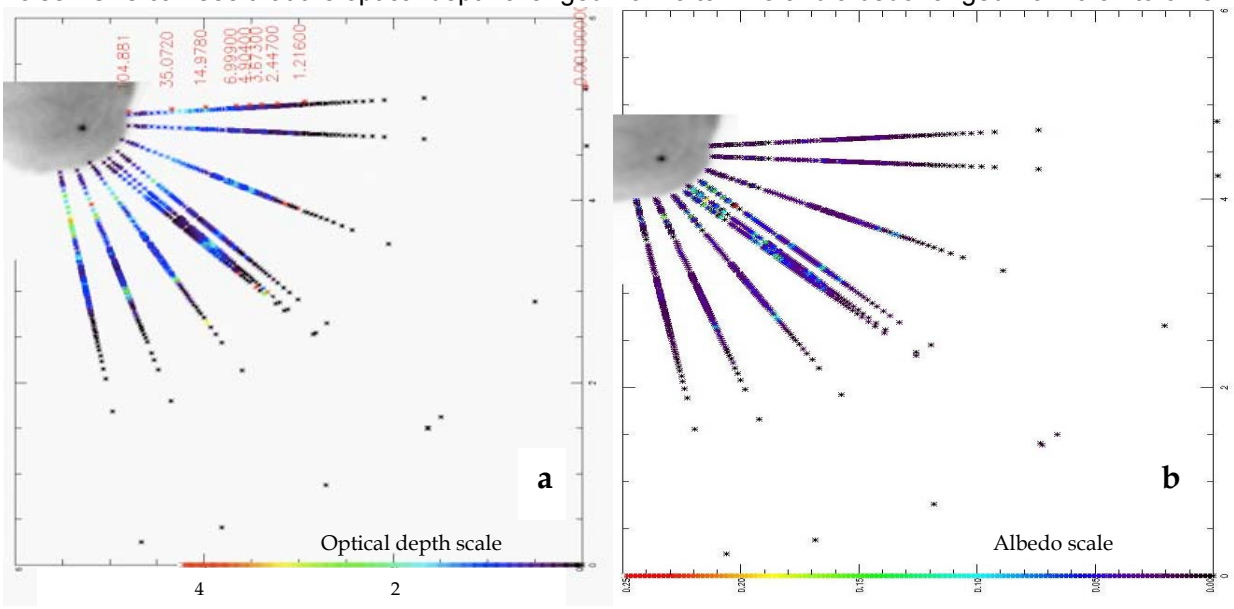

Figure 2. Optical depth (a) and albedo (b) of the ejecta at selected azimuths from the impact site as a function of time. given in seconds at the topmost profile of Fig. 2a.

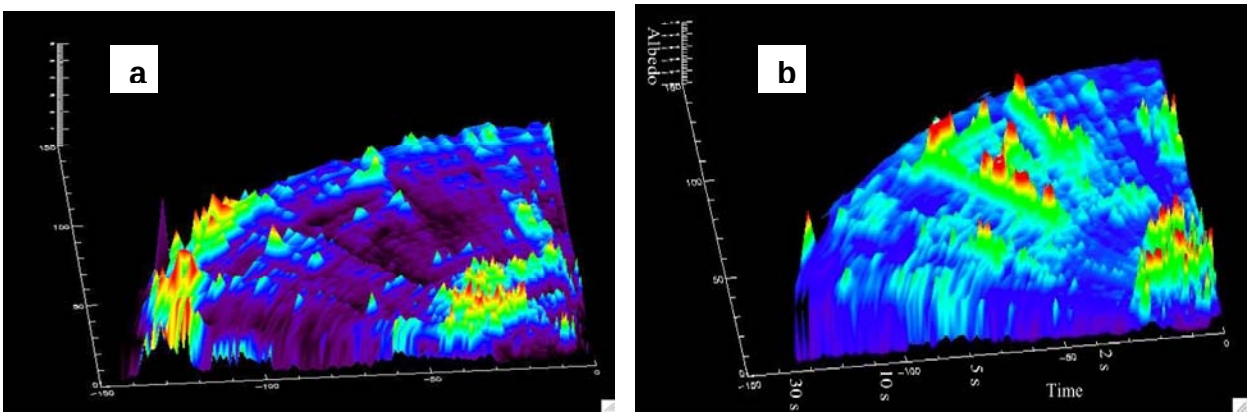

Figure 3. Perspective contour plots of an expanded dataset similar to that in Figure 2 but rotated so that one is looking away from the impact site.

4 Conclusions

The results of our calculations, even though they present just a first approximation to the problem, allow us not only to find out the structure of the ejecta cloud and estimate albedo of the dust particles but reveal some properties of the comet nucleus. Really, the optical depth as well as the particle albedo varies dramatically both with time and with azimuth around the limb. The variations with time are not monotonic. They show ups and downs indicating significant layering of the material prior to excavation. These layers may be the result of either varying material or speeds of the ejecta cloud. This is a direct evidence of the inhomogeneous, layering structure of the nucleus of comet 9P/Tempel 1 (also confirmed by other data, see [5]) that can be a general specific of the comet nuclei. The higher albedo locations are likely associated with the relatively higher preponderance of icy grains in certain downrange directions as discussed by Sunshine et al. [6]

Assuming that the ejecta material originated from subsequent layers as time progressed, we will be able to determine where these had initially been excavated from. The layering is most likely caused by sequential passes of the comets near the Sun that caused sublimation of volatiles and displacement of other materials. Information from studies such as ours will help to further understand the evolution of the comets.

The analysis of these data is continuing and we will report on the latest interpretation in terms of layering and ice-refractory mixing. The MRI allowed us to get the images of the cloud in a variety of filters. The narrow-band filters (see above) were designed to match the Hale-Bopp filter sets used for ground-based programs since 1996. We are planning to study colors of the dust and their change and correlations with the albedo to determine physical properties of the particles from different layers within the nucleus and comparing them with the colors of other comets.

Acknowledgments

Ashley King acknowledges support by NASA's Planetary Data System (PDS) College Student Investigator (CSI) program. The work was also supported by NASA grants NNX07AF93G (DDAP) and NNG05GB79G (PDS SBN). Ludmilla Kolokolova acknowledges the travel grant from the ELS-11 Organizing Committee.

References

[1] M. A'Hearn, M. Belton, W. A. Delamere, J. Kissel, K. P. Klaasen, L. A. McFadden, et al. "Deep Impact: Excavating Comet Tempel 1," Science **310,** 258-264 (2005).

[2] M. A'Hearn, M. Belton, A. Delamere, W. H. Blume "Deep Impact: A large-scale active experiment on a cometary nucleus," Space Sci. Rev. **117**, 1-21 (2005).

[3] S. McLaughlin (Ed.) DIF-C-MRI-3/4-9P-ENCOUNTER-V2.0. NASA Planetary Data System (2006).

[4] A. Kokhanovsky "Light scattering media optics: problems and solutions," Springer, Berlin (2004).

[5] P. H. Schultz, C. M. Ernst, J. B. Anderson „Expectations for Crater Size and Photometric Evolution from the Deep Impact Collision," *Space Sci. Rev*. **117**, 207-239 (2005).

[6] J. Sunshine, O. Groussin, P. Schultz, M. A'Hearn, L. Feaga, T. Farnham, K. Klaasen "The distribution of water ice in the interior of Comet Tempel 1," Icarus**, 190,** 284-294 (2007).

PLANETPOL polarimetry of the exoplanet systems τ Boo and 55 Cnc

P.W.Lucas,[1] J.H.Hough,[1] J.A.Bailey,[2] M.Tamura,[3]
E.Hirst,[1] and D.Harrison[1]

[1] University of Hertfordshire, Centre for Astrophysics Research,
College Lane, Hatfield AL10 9AB, UK
[2] Department of Physics, Macquarie University, NSW 2109, Australia
[3]National Astronomical Observatory, Osawa 2-21-2, Mitaka, Tokyo 181, Japan
tel: +44 1707 286070, fax: +44 1707 284185, e-mail: p.w.lucas@herts.ac.uk

Abstract

We present very sensitive polarimetry of τ Boo and 55 Cnc in an attempt to detect the partially polarised reflected light from the planets orbiting these two stars. τ Boo is orbited by an unusually massive hot Jupiter planet. The data show a standard deviation in the night to night average Stokes Q/I and U/I polarisation parameters of 3.45×10^{-6}. We place a 4-σ upper limit on the radius and geometric albedo, x, of τ Boo b of $x(R/1.2\ R_{Jup})^2<0.34$. 55 Cnc is orbited by a hot Neptune planet (55 Cnc e) at 0.038 AU, a hot Jupiter planet (55 Cnc b) at 0.11 AU, and at least 3 more distant planets. The fractional polarisation of this star is very stable, with a standard deviation in the night to night average Q/I and U/I parameters of 1.65×10^{-6}. This allows us to place a 4-σ upper limits of $x(R/1.2\ R_{Jup})^2<0.10$ for 55 Cnc e and $x(R/1.2\ R_{Jup})^2<0.93$ for 55 Cnc b. We conclude that τ Boo is a dark planet and that 55 Cnc e is likely to be relatively small, like GJ436b. The fact that the τ Boo data show more scatter, despite the smaller photon noise for this bright star, might be due to the spot activity detected photometrically by the MOST satellite, via the transverse Zeeman effect. However, the scatter has a low statistical significance so this is unclear. These results contrast markedly with the recent claim of a 3-σ detection of a periodic polarisation signal from HD189733 with amplitude $P=2 \times 10^{-4}$, attributed to the planet HD189733b.

1 Introduction

Since the seminal discovery of 51 Peg b by Mayor & Queloz [1] ~300 extrasolar planets have been found (eg. [2]**).** Approximately one third of these orbit very close to their central star, with semi-major axes, a<0.1~AU. The number of short period planets is increasing rapidly with the growing success of transit based searches such as SuperWASP [3] and HATNet [4], which are even more strongly biased towards such detections than the radial velocity method.

These close in planets offer the best opportunity to study the physical characteristics of the planets, as opposed to their orbital parameters. The combination of transit data and radial velocity data yields a precise planetary mass, size and density. Furthermore, recent studies with the Spitzer Space Telescope [5],[6] and the Hubble Space Telescope, e.g. [7],[8], have obtained a great deal of information about the chemical composition and pressure temperature profiles of the atmospheres of the two brightest transiting ``hot Jupiter'' planets, HD189733b and HD209458b.

These studies used infrared photometry and spectroscopy of radiation emitted by the planets and optical spectrophotometry of the transit. All required exceptionally high signal to noise data for the integrated light of the star and planet.

Polarimetry is a promising method to detect extrasolar planets in reflected light. The basic principle is that reflected light is partially polarised, whereas the direct light from stellar photospheres has negligible linear polarisation. Kemp et al.[9] measured an upper limit on the integrated linear polarisation from the solar disc of P< 2x10^{-7} in the V band. Polarimetry therefore circumvents the contrast problem associated with planets that are spatially unresolved from the central star. Hough et al.[10] described the Planetpol instrument, which was specifically constructed to achieve a sensitivity to fractional linear polarisations of order 10^{-6} by using a fast modulator system, similar in principle to that of [9]. Polarimetry with fast modulators (which induce a rapid periodic variation of the retardance of electromagnetic vibrations in orthogonal planes) permits this very high sensitivity by separating the polarised component of the incident radiation field from the unpolarised component, converting the former into a high frequency signal in the time domain.

This means that very small fractional polarisatons can be measured without the need for very precise flux measurements with the detector. Planetpol achieves photon noise limited performance so the main limitation on the polarisation sensitivity is the need to gather in excess of 10^{12} photons in order to measure fractional polarisations as low as 10^{-6}. The fast modulation is performed by Photoelastic Modulators (PEMs) operated at 20 kHz, which is fast enough to remove the effects of time varying absorption by the Earth's atmosphere.

2 Observations

All observations were made with Planetpol mounted at the Cassegrain focus of the 4.2-m William Herschel Telescope at the Roque de los Muchachos Observatory in La Palma, one of the Canary Islands. τ Boo was observed in three observing runs on 24-26 April 2004, 25-30 April 2005 and 7-8 May 2005. 55 Cnc was observed on 15-20 February 2006.

3 Results and models

We find no sign of the periodic polarisation signal expected for a planet with a short orbital period in our datasets. The data for τ Boo show a standard deviation in the night to night average Stokes Q/I and U/I polarisation parameters of 3.45×10^{-6}. The data for 55 Cnc are more stable, showing a standard deviation in the night to night average Q/I and U/I parameters of 1.65×10^{-6}.

We have constructed Monte Carlo light scattering models in order to quantify the upper limits on the radii and albedo of the planets. After running an ensemble of atmospheric models with Rayleigh scattering atmospheres or Rayleigh-like scattering by small aerosols we find that the expected polarisation signal is $2.8 \times 10^{-5} (x/0.75) (r/0.05AU)^{-2} (R/1.2RJup)^2$, where x is the geometric albedo, r is the orbital radius and R is the planetary radius. This leads to a 4-σ sensitivity limit of $x(R/1.2R_{Jup})_2 < 0.34$ for τ Boo b and a -σ sensitivity limit of $x(R/1.2R_{Jup})_2 < 0.10$ for 55 Cnc e.

4 Conclusions

We conclude from the upper limit for Boo b that it is a fairly dark planet. A non-detection at an upper limit of $x(R/1.2RJup)^2 < 0.34$ is not particularly surprising since there are a large number of molecular absorption features, eg. the KI resonant line at 770 nm, which could reduce the geometric albedo to a lower level if there is no high altitude dust layer. Dust particles could also be responsible for a low albedo, eg. if the grains are very small or composed of a relatively absorptive substance such as iron.

The strong upper limit for 55 Cne e, $x(R/1.2RJup)^2 <0.10$, is a little harder to explain in terms of a low albedo. At the time the observations were planned there were no available calculations or data concerning the likely size of very strongly irradiated Neptune mass planets. Recent calculations, e.g. [11],[12], suggest that while a wide range of sizes (0.4 RJup to ~1 RJup are possible, it is likely that hot Neptune mass planets will usually have radii <0.6RJup.

References

[1] Mayor M., Queloz D., Udry S., Harrison T.E., 2004, ApJ, 614, L81

[2] Butler R.P., Wright J.T., Marcy G.W., Fischer D.A., Vogt S.S., Tinney C.G., Jones H.R.A., Carter B.D., Johnson J.A., McCarthy C., Penny A.J., 2006, ApJ, 646, 505

[3] Pollacco et al.2006, PASP, 118, 1407

[4] Bakos et al.2004, PASP, 116, 266

[5] Knutson H.A., Charbonneau D., Allen L.E., Fortney J.J., et al.2007, Nature, 447, 183

[6] Knutson H.A., Charbonneau D., Allen L.E., Burrows A., Megeath S.T., 2008, ApJ, 673, 526

[7] Pont, Knutson, Gilliland et al. 2008, MNRAS, 385, 109

[8] Swain, Vasisht, Tinetti, 2008, astro-ph/0802.1030

[9] Kemp J.C., Henson G.D.,Steiner C.T., Powell E.R., 1987, Nature, 326, 270

[10] Hough J.H., Lucas P.W., Bailey J.A., Tamura M., Hirst E., Harrison D., Bartholomew-Biggs M., 2006, PASP 118, 1302

[11] Baraffe I., Alibert Y., Chabrier G., Benz W. 2006, A&A, 450, 1221

[12] Fortney J.J., Marley M.S., Barnes J.W., 2007, ApJ, 659, 1661

A feasible and physically realistic mechanism for polarization of cosmic dust

Kari Lumme[1] and Antti Penttilä[1]

[1] *Observatory, University of Helsinki, P.O. Box 14, FI-00014 University of Helsinki, Finland*
e-mail: Kari.Lumme@helsinki.fi

Abstract

We show that both particle-cluster and cluster-cluster aggregates of spherical constituents when integrated over a power-law size distribution, γ about -3.5, very nicely produce the general form of linear polarization observed for cosmic dust particles in cometary comae, interplanetary dust and regoliths of atmosphereless objects. Light scattering computations have been done for the submicron-sized constituents with the numerically exact codes, the superposition *T*-matrix and the DDA, with the number of constituents ranging from a few to 500. The size parameters for the largest aggregates are about 70. The suggested mechanism is fairly insensitive to the crucial parameters such as the refractive index, packing density and number of constituents and no special fine-tuning of the few parameters is needed. Also the opposition effect is quite consistent with the existing data.

1 Introduction

The nonlinear brightening and linear polarization of cosmic dust seen in the cometary comae, interplanetary dust particles and planetary regoliths of atmosphereless bodies are issues which have been known for decades. It is rather surprising that the rigorous physical explanation for them is still lacking to a rather large extent. Up to about 20 years ago the reason for the opposition effect was almost unanimously attributed to the so-called mutual shadowing. This belongs to the category of ray optics. Since then more and more attention has been shown to the strictly rigorous wave optical ideas which suggests a so-called coherent backscattering mechanism for the opposition effect. Of course mutual shadowing can still play some role but need not be explicitly accounted for in the wave optics.

Some 80 years researchers have been trying to understand why such widely different bodies in the Solar System present linear polarization as a function of the phase angle are so similar, in the first approximation only modulated with a constant. A straightforward explanation for this has never been given. Too often a huge amount of adjustable parameters are assumed and a physically questionable model accepted where the individual parameters are strictly fine-tuned.

There are some basic things which have been accepted by researchers for the CDPs (Cosmic Dust Particles). Most importantly, wave-optical methods are compulsory, CDPs are particle-cluster (PC) or cluster-cluster (CC) aggregates and the refractive index is somewhere in the range 1.5 -1.7 for the real part and 0.0001 to 0.01 range for the imaginary part.

The incentive for this work is to present a mechanism which has a minimum number of free parameters, is physically realistic, produces a decent opposition effect and in quantitative way is capable of fitting the data without those fine-tunings. Finally, we suggest how the "infinite aggregates" or regoliths could be understood based on our results for the CDPs

2 Particle geometries

Based on the collected Brownlee particles and a recently analyzed cometary particle brought by the NASA Stardust mission [1] we will use both PC and CC processes to create the scattering geometries. The existing codes to do exact light scattering for aggregates is currently limited to two possibilities, the superposition *T*-matrix (CTmat) [2] and any of the existing DDA-codes, of which we have selected the

ADDA ("Amsterdam DDA") code [3]. For a moderate number of spheres up to ~100 the CTmat is very much preferable over ADDA. This is because it provides quite exact results, which are important at large scattering angles in the negative branch of polarization. In the ADDA there are those standard fluctuations in results at a few per cent level close to the opposition geometry. For two reasons we limit ourselves to spherical constituents: because of the codes (mainly CTmat) and to avoid any extra parameters to describe the shapes of the monomers.

The often used packing codes are ballistic (a linear trajectory towards the center from a random direction) but they automatically produce about the same packing density. We used such a packing routine which selects randomly from the binomial distribution the constituent where we put the next one and which does not intersect any of the packed constituents. Varying the parameter in the distribution we get sparsely or densely packed aggregates.

To study the effect of the packing density *pD* we need the reference volume which confines the particles so that all the material is inside that volume. Often this standard volume is assumed to be a sphere which is not a good idea because it can greatly underestimate the *pD*, especially for flattened packing geometries. We prefer the convex hull which is the minimum convex enclosure for concave objects. The convex hull can easily be computed by codes provided on the Internet. In Fig. 1 we show some geometries.

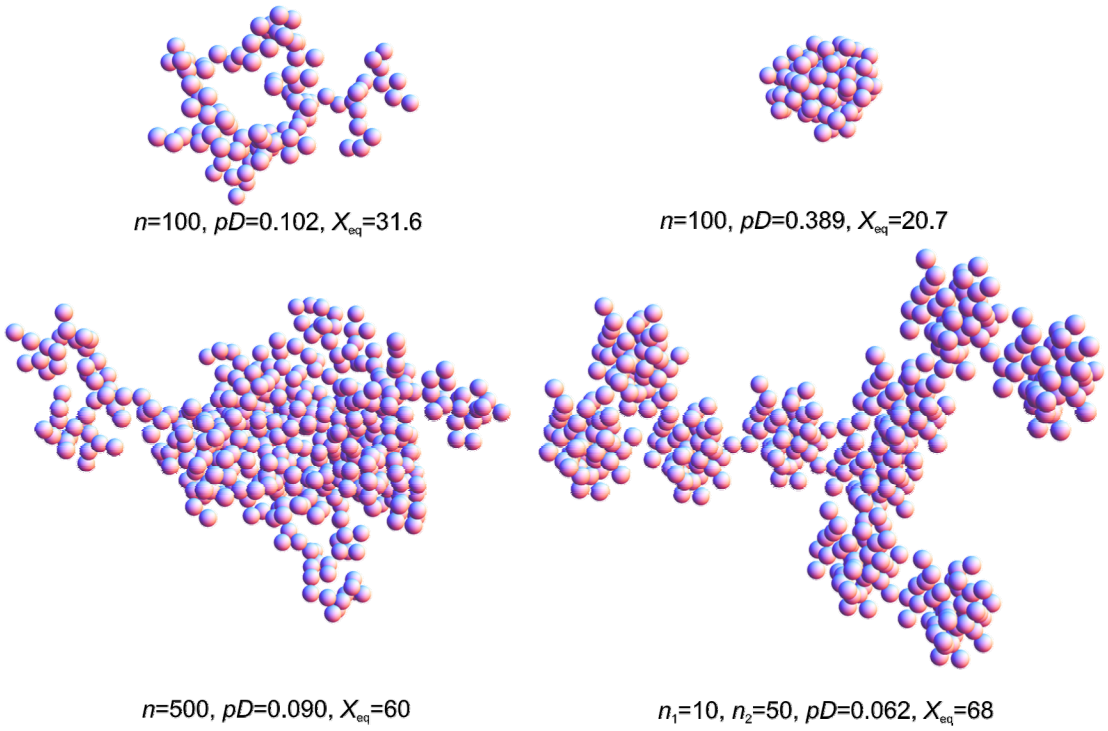

Figure 1: Our simulated packings are from top left to bottom right: PC sparse packing, PC dense packing, large sparse packing and CC packing where n_1 is the number of individual clusters and n_2 the number of constituents in a singe cluster. Here n is the total number of constituents, pD is the packing density, and X_{eq} is the volume equivalent size parameter of the aggregate.

We packed both equal-sized and power law distributed monomers and computed light scattering for both with varying upper and lower sizes. It soon became evident that a collection of aggregates which had equal-sized constituents in one aggregate but where that size varies from aggregate to aggregate had a much more stable behavior in scattering. Browsing the literature showed that the pictures of cosmic dust particle aggregates seemed to suggest this conclusion. Finally, Blum in his theoretical review about

dust agglomeration [4] considers that quite plausible. Thus, in what follows, we will assume that with a lower limit x_1 and upper limit x_2 for the size parameters (which are well defined for spherical objects) we apply the Gaussian quadrature of six points to do the integration over the interval from x_1 to x_2.

To determine the x_1 and x_2 values we had to apply the trial-and-error procedure. With the default assumption for the power-law exponent γ=-3, we iterated from the CTmat results that x_1=0.8 and x_2=3. If λ is assumed to be 0.557 μm, these numbers relate to the dominating constituents sizes r_1=0.1 μm and r_2=0.3 μm. Below the lower limit the efficiencies decrease rapidly and the increase from the power-law cannot balance it. Above the upper limit the power-law reduces the contribution greatly. The both tails have a combined effect less that about 5%. This effect is further emphasized due to the Gaussian quadrature weights which are maximal in the middle of the interval and decrease towards the end points.

3 Main results

We did the light scattering computations which are computationally expensive assuming that:

- The number of the constituents $1 \le n \le 150$ for the CTmat and n=500 for the DDA is used. The effects of increasing n either on the intensity I close to the opposition or on the polarization in the whole 180 degree range are small but almost monotonous so that the opposition effect sharpens and the polarization minimum shifts towards the opposition. Some results are shown in Fig. 2.
- The refractive index m=1.6+i 0.001 in most cases. We also studied few cases where m is in the range re(m) in (1.4, 1.7) and im(m) in (0.0001, 0.01). Once again all the changes are fairly minimal and in the expected direction.

Further:

- The effect of the packing density pD with pD=0.1 and 0.4. Quite unexpectedly the changes are small in the intensity. Polarization maximum and the inversion angle shift a little to the larger scattering angles. Therefore, we cannot draw too many conclusions on the fluffiness based on the observations. Some results are shown in Fig. 3.
- How much can the assumption about equal-sized constituents in any of the six aggregates in the interval form x_1 to x_2 be relaxed? We studied a case where we allowed the constituents to randomly vary in size by 10%. This did not change the results very much but if the change it to 20% the results rapidly started to change.
- The effect of λ when changed to 0.65 μm (when also x_1 and x_2 must be accordingly changed). Very interestingly with the same m the polarization maximum increased by about 10% but the inversion angle remained about the same. This is, of course, quite consistent with the polarization observations of high P_{max} comets (see [5]) as a function of λ.
- Finally, we checked how important is the assumption that every constituent has a touching neighbor? We increased the distance between the spheres in the six aggregates from $2x_i$ ($1 \le i \le 6$) by 10% and the results remained roughly the same but if we increase that by 20% the effects are more obvious.

To conclude from the points above we can say that the only important parameters which we can play with to fit different data sets are the power-law exponent γ, re(m) and im(m), the real and imaginary parts of m. Some of the main results are shown in Figs. 2 and 3.

4 Conclusions

We have shown that the mechanism described above is quite capable in explaining polarization observed, at least for the comets without any specific fitting of the few parameters except the exponent γ. Opposition and polarization effects of the regoliths are slightly but systematically different from those of the comets. As shown above these differences can be explained, at least qualitatively so that the regoliths behave like huge aggregates, which we cannot, yet, handle with any exact light scattering code.

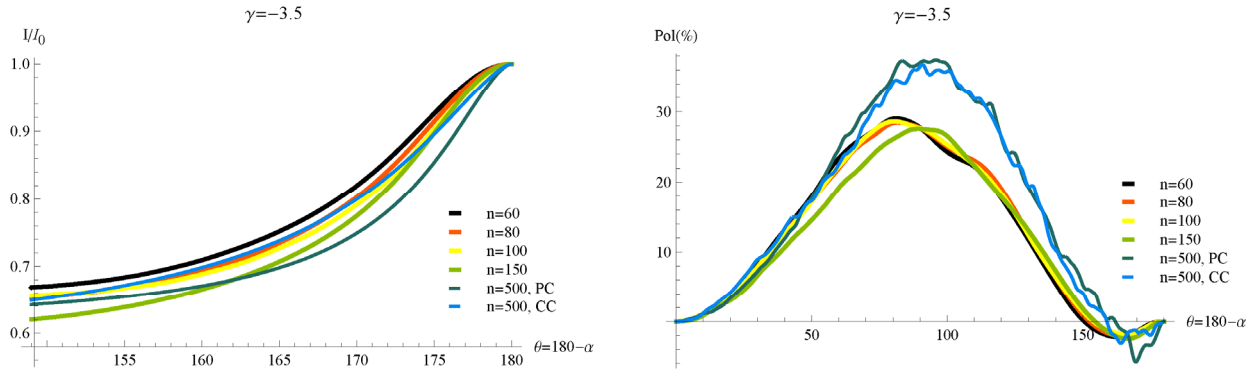

Figure 2: We can see an almost monotonous increase of the steepness of the opposition effect and how the polarization minimum shifts towards the opposition as a function of the number of the constituents. In the case of 60<*n*<150 computations are done with the CTmat and with the DDA for *n*=500 (particle-cluster, and cluster-cluster processes). In all cases *m*=1.6+*i* 0.001.

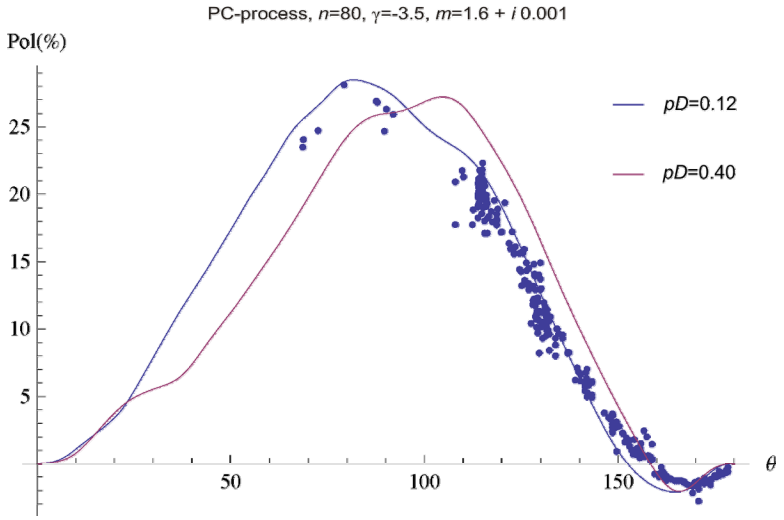

Figure 3: Intensity and polarization comparisons between two different packing densities *pD*. Polarization data for the "high P_{max}" comets is plotted with blue dots [5]. No fitting of the data has been done.

References

[1] H. Volten, O. Muñoz, J. W. Hovenier, F. J. M. Rietmeijer, J. A. Nuth, L. B. F. M. Waters, and W. J. van der Zande, "Experimental light scattering by fluffy aggregates of magnesiosilica, ferrosilica, and alumina cosmic dust analogs", Astron. Astrophys. **470**, 377–386 (2007).

[2] D. W. Mackowski, and M. I. Mishchenko, "Calculation of the *T*-matrix and the scattering matrix for ensembles of spheres", J. Opt. Soc Am A **13**, 2266–2278 (1996).

[3] M. A. Yurkin, V. P. Maltsev, and A. G. Hoekstra, "The discrete dipole approximation for simulation of light scattering by particles much larger than the wavelength", J. Quant. Spectros. Radiat. Transf. **106**, 546–557 (2007).

[4] J. Blum, "Dust agglomeration", Advances in Physics **55** (7-8), 881–947 (2006).

[5] A-C. Levasseur-Regourd, E. Hadamcik, and J. B. Renard, "Evidence for two classes of comets from their polarimetric properties at large phase angles", A&A **313**, 327–333 (1996).

Markov-Chain Monte-Carlo inversion of asteroid photometric lightcurves

Karri Muinonen and Dagmara Oszkiewicz

Observatory, Kopernikuksentie 1, P.O. Box 14, FI-00014 University of Helsinki, Finland
tel: +358 9-19122941, fax: +358 9-19122952, e-mail: Karri.Muinonen@helsinki.fi

Abstract

We present Markov-Chain Monte-Carlo inversion methods for retrieving asteroid spins and shapes from photometric lightcurves in the case of limited and/or sparsely distributed observations. In the order of increasing complexity, we utilize sphere-cylinders, axisymmetric convex shapes, and general convex shapes in the inversion. We verify the methods for the extensively observed main-belt asteroid (951) Gaspra (Galileo flyby target in 1991) and show preliminary results for the near-Earth objects 2003 MS_2 and (1981) Midas.

1 Introduction

In asteroid lightcurve inversion, the rotational period, pole, and phase (the spin state) of the object, as well as its shape and light-scattering properties are derived from disk-integrated photometric observations. Novel Markov-Chain Monte-Carlo methods (MCMC) are here studied for the inversion of asteroid spins and shapes in the case of limited numbers of and/or sparsely distributed observations.

During the last decade, considerable advances have been made in lightcurve inversion for extensively observed asteroids using convex shapes [1]. In such conventional convex inversion, the shape model is a convex polyhedron, where the free parameters are either the individual polyhedron triangle areas or the coefficients of the spherical-harmonics series describing the Gaussian curvature of the surface. Spin and shape models are derived using relative photometry by making use of the Lommel-Seeliger and Lambert scattering laws. Torppa et al. [2] report extensive results on asteroid spins and shapes using the convex inversion method. Typically, the scattering properties are taken to be homogeneous over the asteroid surface.

2 Markov-Chain Monte-Carlo inversion

We have developed three MCMC inverse methods of gradually increasing sophistigation. First, we make use of single-parameter biaxial sphere-cylinder shapes consisting of finite cylinders with hemispherical caps. By introducing suitable additional plane and cylinder elements, we obtain two-parameter triaxial sphere-cylinder-plane-element shape models [3]. We integrate analytically the disk-integrated brightnesses of the models for the combined Lommel-Seeliger and Lambert scattering law, thus efficiently reducing the computing times in the MCMC solution of the inverse problem. Second, we utilize axisymmetric convex shapes composed of a number of interconnected conical frustums. Again, we integrate the total brightnesses analytically for the conical frustums. By introducing suitable plane elements, we introduce non-axisymmetric triaxial shape models. Third, we make use of general convex shapes described using a large but finite number of triangles.

Whereas conventional lightcurve inversion consists of two parts, that is, the derivation of the normal-vector distribution and the subsequent derivation of the convex shape from the normal vectors, in the MCMC convex inversion, the convex shape solutions are directly sampled as in simplex inversion [4]). There are four parameters for the spin characteristics: the rotational period, the ecliptic longitude and latitude of the rotational pole, and the rotational phase of the object at a given time. For the general convex shape model

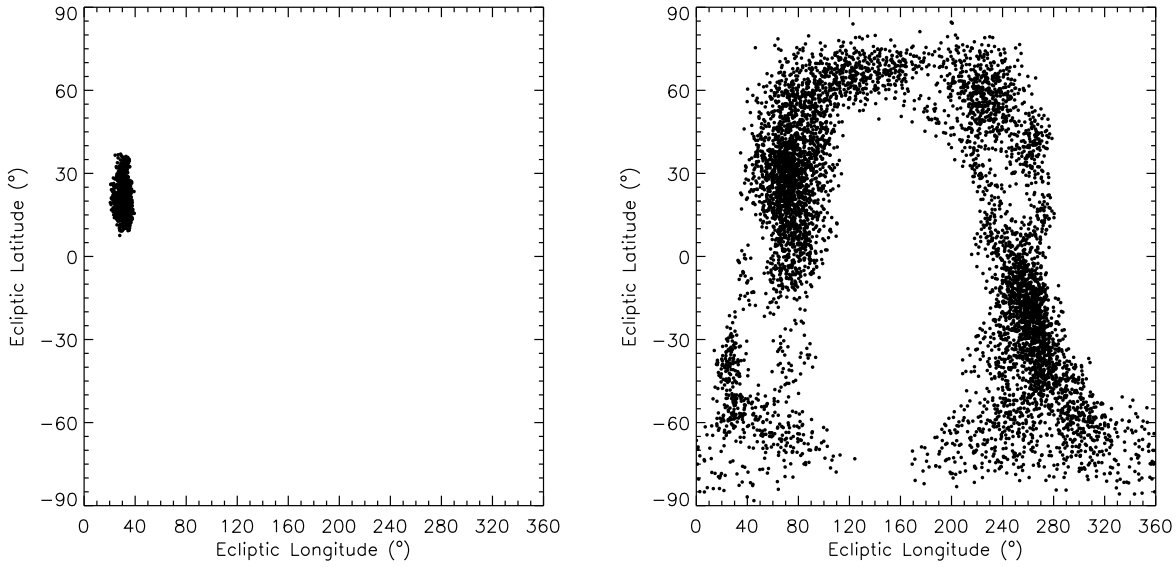

Figure 1: The MCMC sample ecliptic longitudes and latitudes of the rotational poles for (951) Gaspra (left) and (1981) Midas (right).

with K triangle rows in each octant, the shape is specified using altogether $8K^2$ triangles and $N = 4K^2 + 2$ nodes. The $3N$ Cartesian coordinates of the nodes constitute the free shape parameters. Altogether, there are $3 + 3N$ free parameters, the rotational phase becoming redundant because of the general shape model. For the sphere-cylinder and axisymmetric convex shape models, the rotational phase remains as one of the free parameters. The initialization of the sampling can be accomplished, e.g., by using prolate spheroids. For a detailed description of MCMC methods, the reader is refered to Gilks et al. [5].

The MCMC approach allows for a flexible incorporation of conditions on the shapes to be sampled. For the general convex model, at each sampling step, the convexity of the shape is verified. Solutions are constrained into a realistic regime in radial distances, that is, only radial distances within [0.3, 1.0] are presently accepted. Solutions are further constrained by the requirement that the triangle mesh be mathematically well defined.

3 First results and discussion

We apply the three MCMC inversion methods to the limited lightcurve observations of the near-Earth objects 2003 MS_2 and (1981) Midas. In both cases, we have succeeded in obtaining realistic spin and convex shape solutions within reasonable computing times. In what follows, we concentrate on the general MCMC convex inversion method and its application to (951) Gaspra and (1981) Midas.

In order to validate the MCMC convex inversion method, we apply the method to the extensive lightcurve observations of the main-belt asteroid (951) Gaspra, the target of the Galileo space-mission flyby in 1991. Figs. 1a and 2 illustrate the distributions of the pole orientation and shape: the results are in full agreement with the pole and shape resolved with the help of the Galileo mission [6] (see also [7] for pre-mission predictions).

Figure 2 shows three consequent Markov-chain sample shapes for (951) Gaspra based on 45 lightcurves from SAPC (Standard Asteroid Photometric Catalogue, `http://www.astro.helsinki.fi/SAPC/`, see references to observations therein). There are only subtle differences among the shapes illustrated. In the

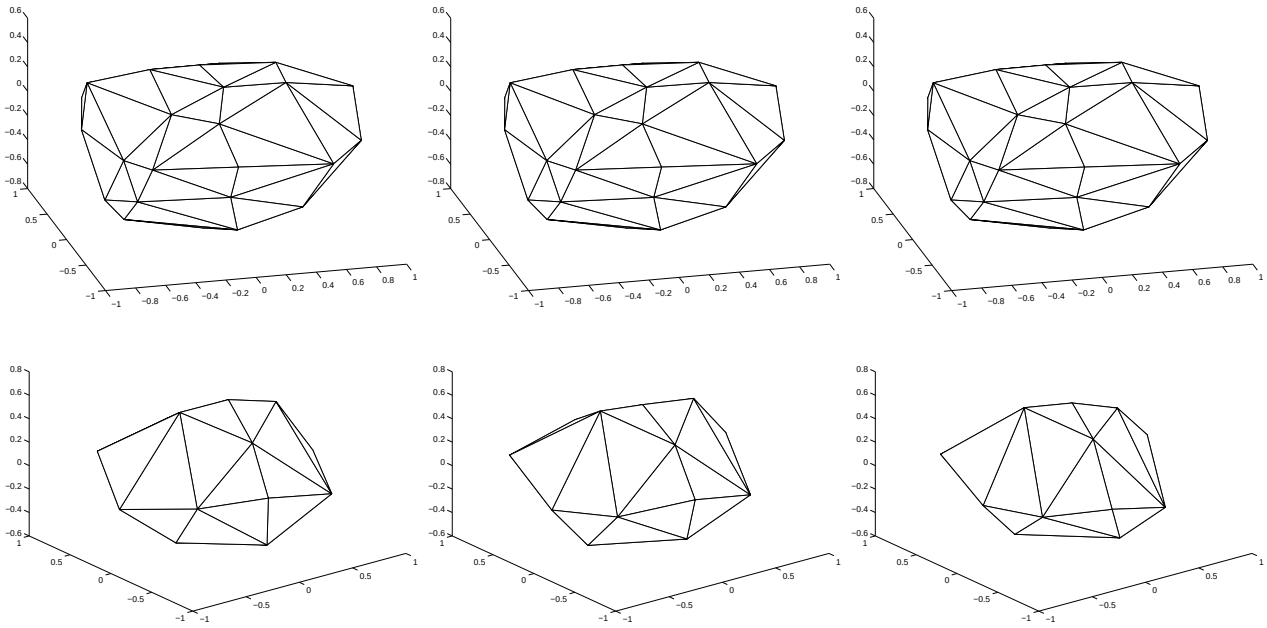

Figure 2: Three sequential MCMC sample shapes for the main-belt asteroid (951) Gaspra (top) and for the near-Earth object (1981) Midas (bottom).

present shape model, we have utilized $K = 3$, resulting in 114 shape parameters and, accounting for the spin parameters, altogether 117 free parameters in the inverse problem. The standard deviation of the observational error was set at 0.035 mag and the best-fitting MCMC sample solutions reached the rms of 0.03 mag.

Figure 2 also shows three consequent sample shapes in the MCMC chain for (1981) Midas based on altogether eight lightcurves [9, 8, 3] spanning 18 years with three differing illumination and observation geometries. For Midas, it is possible to notice the gradual deformation of the shapes in the Markov chain. We have made use of $K = 2$, that is, we have 54 shape parameters and altogether 57 free parameters in the inverse problem. Again, the best-fitting MCMC solutions resulted in rms-values of 0.03 mag.

4 Conclusion

We have developed MCMC inversion methods for deriving asteroid spins, shapes, and scattering properties from photometric lightcurve observations using few-parameter and many-parameter convex shape models. These methods are clearly more efficient than the simplex methods assessed earlier [4] With the help of the novel methods, we have successfully assessed both limited and extensive lightcurve observations of one main-belt asteroid and two near-Earth objects. There are substantial future prospects in MCMC asteroid lightcurve inversion methods, with potential application to the forecoming asteroid photometric observations by the Gaia mission (cf., [10]).

Acknowledgments

We would like to thank Dr. Johanna Torppa for numerous enlightening discussions on lightcurve inversion and for help with the observational data. We thank the Nordic Optical Telescope (NOT). Most of the NOT data utilized have been obtained using ALFOSC, which is owned by the Instituto de Astrofisica de Andalucia (IAA) and operated at the Nordic Optical Telescope under agreement between IAA and the Astronomical

Observatory of Copenhagen. Research supported, in part, by EC Contract No. MRTN-CT-2006-033481.

References

[1] M. Kaasalainen, J. Torppa, and K. Muinonen, “Optimization methods for asteroid lightcurve inversion. II. The complete inverse problem,” *Icarus* **153**, 37-51 (2001)

[2] J. Torppa, M. Kaasalainen, T. Michalowski, T. Kwiatkowski, A. Kryszczynska, P. Denchev, and R. Kowalski, “Shapes and rotational properties of thirty asteroids from photometric data,” *Icarus* **164**, 346-383 (2003)

[3] K. Muinonen, J. Torppa, J. Virtanen, J. Näränen, J. Niemelä, M. Granvik, T. Laakso, H. Parviainen, K. Aksnes, Z. Dai, C.-I. Lagerkvist, H. Rickman, O. Karlsson, G. Hahn, R. Michelsen, T. Grav, P. Pravec, and U. G. Jørgensen, “Spins, shapes, and orbits for near-Earth objects by Nordic NEON,” in *Proceedings of IAU Symposium No 236, Near-Earth Objects, our Celestial Neighbors: Opportunity and Risk* (A. Milani, G. Valsecchi, and D. Vokrouhlicky, eds., Cambridge University Press), 309-320, doi: 10.1017/S1743921307003377 (2007)

[4] K. Muinonen and J. Torppa, “Simplex inversion of asteroid photometric lightcurves, *Tenth Conference on Electromagnetic & Light Scattering*, G. Videen, M. Mishchenko, M. P. Mengüc, and N. Zakharova, Eds. (Bodrum, Turkey, June 17-22, 2007), 129-132 (2007)

[5] W. R. Gilks et al., *Markov Chain Monte Carlo in Practice*, Chapman & Hall/CRC (1996)

[6] P. Stooke, “The surface of asteroid (951) Gaspra,*Earth, Moon, and Planets* **75**, 53-75 (1996)

[7] M. A. Barucci, A. Cellino, C. De Sanctis, M. Fulchignoni, K. Lumme, V. Zappalà, and P. Magnusson, “Ground-based Gaspra modelling - comparison with the first Galileo image, *Astron. Astrophys.* **266**, 385-394 (1992)

[8] S. Mottola, G. de Angelis, M. di Martino, A. Erikson, G. Hahn, and G. Neukum, “The near-Earth objects follow-up program: First results,” *Icarus* **117**, 62-70 (1995)

[9] W. Z. Wisniewski, T. M. Michalowski, A. W. Harris, and R. S. McMillan, “Photometric observations of 125 asteroids,” *Icarus* **126**, 395-449 (1997)

[10] J. Torppa and K. Muinonen, “Statistical inversion of asteroid spins and shapes from Gaia photometry,” in *Three-Dimensional Universe with Gaia, ESA Special Publications SP-576* (C. Turon, K. S. O’Flaherty, and M. A. C. Perryman, Eds., ESA Publications Division, ESTEC, The Netherlands), 321-324 (2005)

Scalar approximation to coherent backscattering by spherical media

Karri Muinonen,[1] Hannu Parviainen,[1] Jyri Näränen,[1] and Gorden Videen[2]

[1] *Observatory, Kopernikuksentie 1, P.O. Box 14, FI-00014 University of Helsinki, Finland*
[2] *Army Research Laboratory, 2800 Powder Mill Rd., Adelphi, Maryland 20783, U.S.A.*
tel: +358 9-19122941, fax: +358 9-19122952, e-mail: Karri.Muinonen@helsinki.fi

Abstract

We present numerical computations for coherent backscattering of scalar waves by spherical random media of discrete scatterers. We make use of double Henyey-Greenstein single-scattering phase functions and assume radial optical thicknesses approaching infinity. We conclude that the scalar treatment allows for an efficient initial assessment of multiple-scattering problems.

1 Introduction

Multiple scattering in complex random media of scatterers can result in coherent backscattering that has been invoked to explain, to a considerable part, the nonlinear brightenings (opposition effects) and negative polarization branches observed for atmosphereless solar-system objects.

Coherent backscattering by plane-parallel media of spherical scatterers has been treated in [1] using numerical Monte-Carlo methods, accounting for polarization. For spherical media and Rayleigh scatterers, the methods have been applied to the polarimetric and photometric observations obtained for transneptunian objects at the Very Large Telescope of the European Southern Observatory (VLT/ESO; e.g., [2, 3]).

Monte-Carlo methods for scalar coherent backscattering were put forward already in late 1990s [4] and applied to interpret the opposition effects of icy solar-system objects [5]. These studies are extended presently by utilizing double Henyey-Greenstein single-scattering phase functions (2HG), allowing for more realistic a modeling of the single-scattering phase functions.

2 Multiple-scattering methods

In the Monte-Carlo methods for vector and scalar waves, coherent backscattering is computed alongside radiative transfer by incorporating the reciprocity relation of electromagnetic scattering at the backscattering geometry (e.g., [1]). The reciprocity relation for scalar waves is, however, significantly more straightforward than that for vector waves. The numerical methods are presently optimized by the simultaneous computation of coherent backscattering for a large number of extinction mean free paths, resulting in an efficiency increased by a factor approaching the number of different mean free paths.

The 2HG single-scattering phase function is of the form

$$\begin{aligned} P_{11}(\theta) &= w\frac{1-g_1^2}{(1+g_1^2-2g_1\cos\theta)^{\frac{3}{2}}} + (1-w)\frac{1-g_2^2}{(1+g_2^2-2g_2\cos\theta)^{\frac{3}{2}}}, \\ g &= wg_1 + (1-w)g_2 \end{aligned}$$

where g_1 and g_2 describe the forward and backward asymmetries, w is the normalized weight of the first Henyey-Greenstein function, θ is the scattering angle, and g is the asymmetry parameter of the full 2HG phase function.

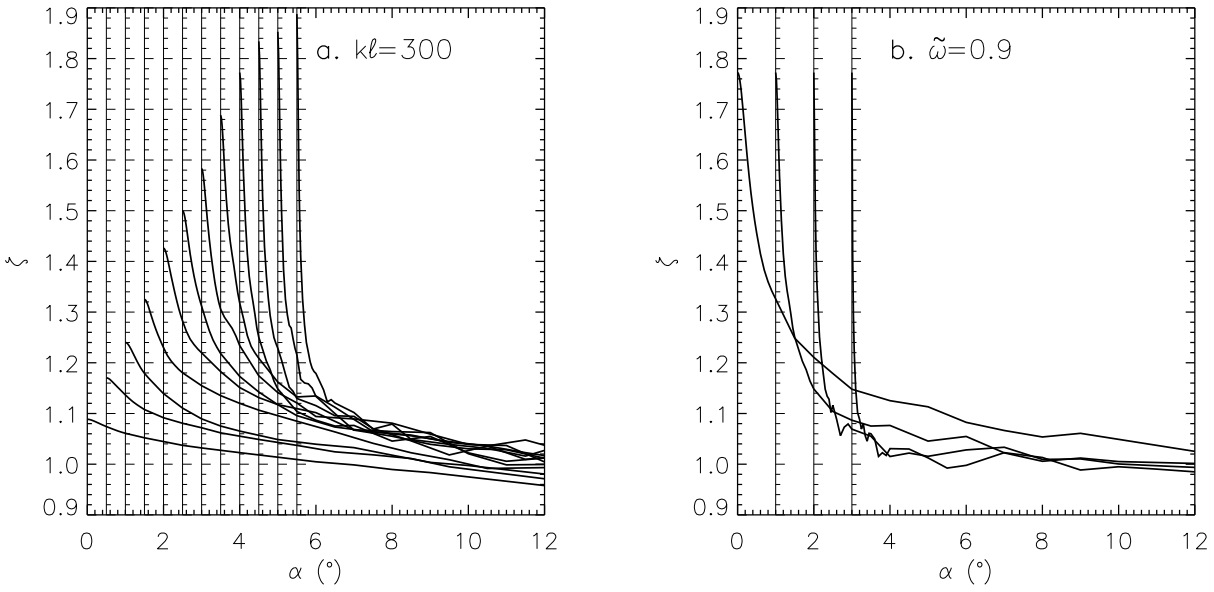

Figure 1: Enhancement factors (ζ) for spherical media of scatterers (radial optical thickness $\tau_r \to \infty$) with double Henyey-Greenstein phase functions specified by $g = 0.6$, $g_1 = 0.8$, and $g_2 = -0.2$ for varying single-scattering albedos $\tilde{\omega}$ and extinction mean free paths $k\ell$: (a) $\tilde{\omega} = 0.1$, 0.2,. . . , 0.9, 0.95, 0.97, 0.99, $k\ell = 300$ (from left to right, shifted for better illustration); (b) $\tilde{\omega} = 0.9$, $k\ell = 100$, 300, 1000, 3000 (from left to right, shifted).

We note that the multiple-scattering problem is defined by five parameters: the single-scattering albedo $\tilde{\omega}$, the three 2HG parameters w, g_1, and g_2, as well as the extinction mean free path of the medium $k\ell$ ($k = 2\pi/\lambda$ is the wave number, and λ is the wavelength).

We have compared tentatively the scalar and vector treatments for coherent backscattering by spherical media of infinite radial optical thickness in the case of Rayleigh scattering. For $\tilde{\omega} = 0.9$ and $k\ell = 300$, the enhancement factors (over the pure radiative-transfer contribution at phase angle $\alpha = 0$) are $\zeta(0) = 1.57$ and $\zeta(0) = 1.54$ for the vector and scalar cases, respectively. We consider the difference level to be acceptable in many applications, warranting further studies of scalar coherent backscattering.

3 Results and discussion

We have carried out computations with 5000 incident rays for a total of 5292 spherical media of 2HG single scatterers: the computations cover 12 single-scattering albedos $\tilde{\omega} = 0.1$, 0.2, . . . , 0.90, 0.95, 0.97, 0.99, 28 dimensionless mean free paths $k\ell = 2\pi\ell/\lambda = 30$, 40, 50, . . . , 100, 120, 140, . . . , 200, 250, 300, . . . , 400, 500, 600, . . . , 1000, 2000, 3000, . . . , 5000, 10000, and 21 2HG phase functions with $g = 0.1$, 0.2, . . . , 0.7 when $g_1 = 0.8$ and $g_2 = -0.4$, -0.2, 0.0.

The enhancement factors ζ and HWHM peak widths α_{HWHM} are shown in Fig. 1 in the case of $g = 0.6$, $g_1 = 0.8$, and $g_2 = -0.2$ for varying $\tilde{\omega}$ and $k\ell$. As is often observed for coherent backscattering, increasing $\tilde{\omega}$ and increasing $k\ell$ result in increasing $\zeta(0)$ and decreasing α_{HWHM}, respectively.

Figure 2 shows the $\zeta(0)$ and α_{HWHM} values against the geometric albedo of the spherical medium p_{MS}. In Fig. 2a, increasing $\tilde{\omega}$ is seen to result in increasing $\zeta(0)$ for three different 2HG phase functions

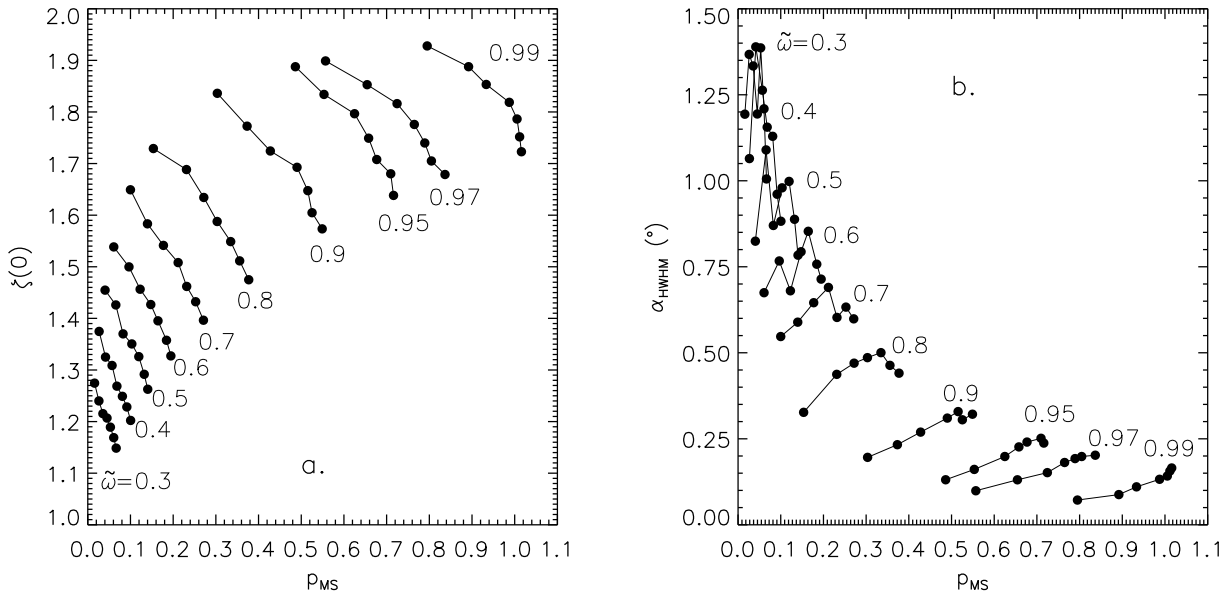

Figure 2: Coherent backscattering by spherical media ($\tau_r \to \infty$) with $k\ell = 300$: (a) backscattering enhancement factors ($\zeta(0)$) and (b) angular widths ($\alpha_{\rm HWHM}$) vs. geometric albedo ($p_{\rm MS}$) for varying $\tilde{\omega}$, $g_1 = 0.8$, $g_2 = -0.2$, and $g = 0.1$, 0.2,. . . ,0.7 ($\zeta(0)$ increases for increasing g).

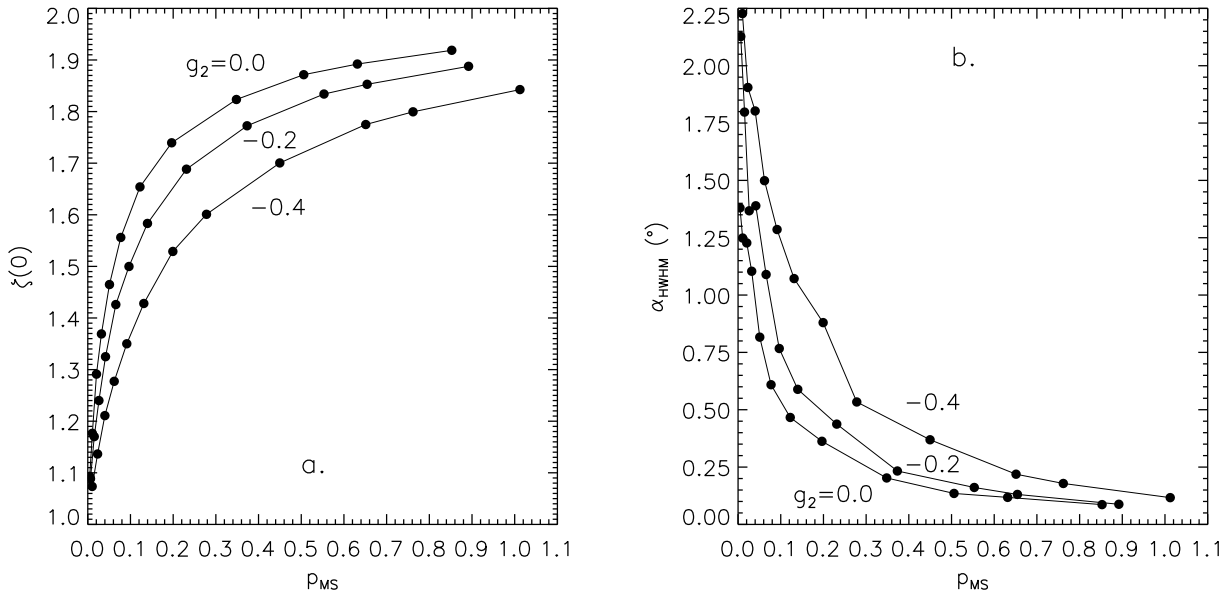

Figure 3: Coherent backscattering by spherical media ($\tau_r \to \infty$) with $k\ell = 300$: (a) $\zeta(0)$ and (b) $\alpha_{\rm HWHM}$ vs. geometric albedo ($p_{\rm MS}$) for $g_1 = 0.8$, $g_2 = -0.4$, -0.2, 0.0, and $g = 0.6$, and varying $\tilde{\omega} = 0.1$, 0.2, . . . , 0.7, 0.9, 0.95, 0.97, 0.99 (from left to right).

with coinciding asymmetry parameter $g = 0.6$. In Fig. 2b, decreasing α_{HWHM} is seen to follow for increasing $\tilde{\omega}$.

The dependence of $\zeta(0)$ and α_{HWHM} on g is illustrated in Fig. 3 for varying $\tilde{\omega}$. Based on Fig. 3a, increasing g results in decreasing p_{MS} but increasing $\zeta(0)$. Then, Figure 3b shows that increasing g decreases α_{HWHM} (at least for higher $\tilde{\omega}$, cf. the accuracy of the present numerical computation).

4 Conclusion

We have assessed the scalar approximation to coherent backscattering by optically thick spherical media of scatterers with double Henyey-Greenstein phase functions. We have verified the accuracy of the enhancement factor from the scalar treatment for Rayleigh scatterers to be at the level of 2%. In comparison to the vector treatment, the scalar one allows for faster numerical computation. With the present multiple-scattering problem, we have mapped basic trends of coherent backscattering depending on the single-scattering albedo and phase function. It is our goal to complete the computations and distribute the results to the community for potential further analyses and applications.

References

[1] K. Muinonen, “Coherent backscattering of light by complex random media of spherical scatterers: Numerical solution,” *Waves in Random Media* **14**, No. 3, 365-388 (2004)

[2] H. Boehnhardt, S. Bagnulo, K. Muinonen, M. A. Barucci, L. Kolokolova, E. Dotto, and G. P. Tozzi, “Surface characterization of 28978 Ixion (2001 KX_{76}), *Astron. Astrophys.* **415**, L21-L25 (2004)

[3] I. N. Belskaya, A.-C. Levasseur-Regourd, Y. G. Shkuratov, and K. Muinonen, “Surface properties of Kuiper-Belt objects and Centaurs from photometry and polarimetry, in *The Solar System Beyond Neptune* (M. A. Barucci, H. Boehnhardt, D. P. Cruikshank, and A. Morbidelli, Eds., University of Arizona Press, Tucson, Arizona, U.S.A.), 115-127 (2008)

[4] K. Muinonen, “Coherent backscattering of light by solar system bodies: Efficient scalar computation, *Bull. Am. Astron. Soc.* **31**, 1076 (1999) (abstract)

[5] S. Kaasalainen, K. Muinonen, and J. Piironen, “Comparative study on opposition effect of icy solar system objects, *JQSRT* **70**, 529-543 (2001)

Colorimetric behavior of photometric opposition effect

V. Psarev,[1,2] A. Ovcharenko,[1,2] Yu. Shkuratov,[1,3] G. Videen[4]

[1]*Astronomical Institute of Kharkov V.N. Karazin National University, 35 Sumskaya St, Kharkov, 61022, Ukraine*

tel. +38-057-700-5349. e-mail: pva@astron.kharkov.ua

[2]*Main Astronomical Observatory of the National Academy of Sciences, Kiev, Ukraine*

[3]*Radioastronomical institute of the National Academy of Sciences, Kharkov, Ukraine*

[4]*Army Research Laboratory AMSRD-ARL-CI-ES, 2800 Powder Mill Road Adelphi Maryland 20783 USA*

Abstract

We study the spectral behavior of the photometric opposition effect for several laboratory samples at extremely small phase angles. It is shown that in the phase angle range from 1.5° up to 0.005° the normalized color ratio I(0.63 μm) / I(0.47 μm) can vary greatly. This increases up to 25% with decreasing phase angle for red samples, and it decreases for blue materials, like blue water-color. The color ratio changes weakly for a MgO sample which is spectrally neutral. The results can be considered as an additional instrument in remote sensing of surfaces with complicated structure, in particular, for analyzing and interpreting observations of Kuiper belt objects. The spectral behavior of the opposition effect could be taken into account in taxonomy of such objects.

1 Introduction

Trans-Neptunian and Kuiper belt objects (TNOs and KBOs) attract interest because these bodies are some of the oldest bodies of the Solar system. Studying their physical properties can help us to understand their origin and the evolutionary history of the early Solar system. Hundreds of such faint celestial bodies have been observed and studied. These objects are observable from Earth at phase angles less than 2°. Photometric observations reveal a prominent brightness opposition spike that is extremely narrow. Such observations of TNOs and KBOs motivated our laboratory studies of the opposition effect at very small phase angles [1,2].

Laboratory studies demonstrate a wide range of brightness phase-slope variations at small phase angles; whereas, colorimetric analysis of this effect is in its infancy. In this study we use a laser photometer of extreme small phase angles [1,2] for colorimetric investigations in a phase-angle range varying from 0.005º - 1.5º. We study a few laboratory samples with different albedo and color ratios C(0.63/0.47 μm) = I(0.63 μm) / I(0.47 μm), where I is the normalized intensity in blue (λ = 0.47 μm) and red (λ = 0.63 μm) light.

2 Techniques of investigation

In our measurements we modify equipment from previous experiments [2]. First, we add an independent fixed-base registration channel to take into account deviations of the illuminating laser beam intensity (see Fig. 1). Second, we use a panoramic digital camera to decrease dispersion of phase-curve data. To

investigate spectral properties of laboratory samples, we use several lasers. In these experiments we have used polarized crystal lasers, a red-light laser with power 20 mW and blue-light laser with power 50 mW.

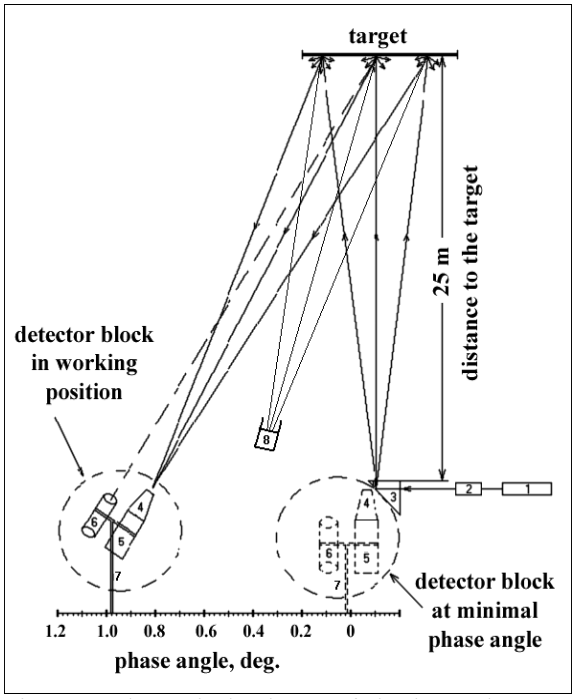

Figure 1: The optical scheme of the laser photometer: (1) laser, (2) collimator block, (3) prism of total reflection, (4) pinhole camera with polarizer-orientation control, (5) either photomultiplier or digital camera Canon EOS 400D (CMOS matrix 3888 × 2522 = 10.1 Mpx), (6) correction spyglass, (7) scrollable holder, (8) fixed base registration photometry channel

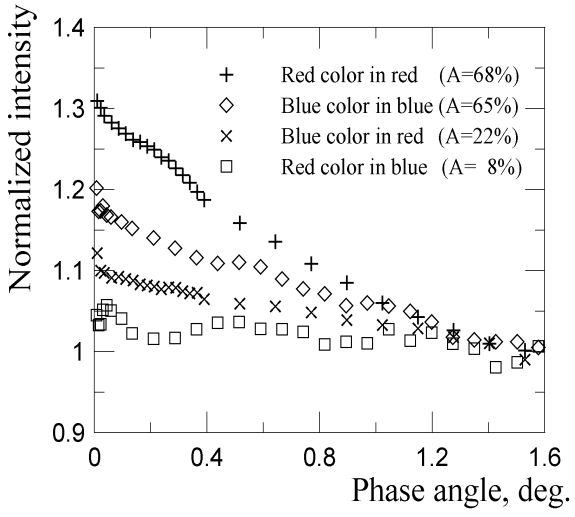

Figure 3: Photometric phase curves for red and blue laboratory samples in red and blue spectral bands

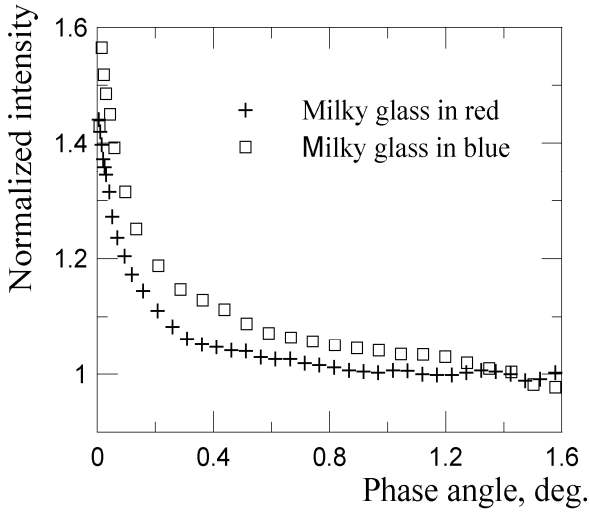

Figure 2: Photometric phase curves for milky glass laboratory sample in red and blue spectral bands

The diameter of the output light beam is 1.0 mm, and the input diameter of the receiver is 1.5 mm. This allows us to obtain a minimum phase angle of 0.005º and spatial resolution of approximately 0.004°. If we use a digital camera (Canon EOS 400D) instead of photomultiplier for registration of the backscattered light flux, the minimum phase angle is 0.003º. The diameter of the working zone on the sample surface is 3-5 cm at 25 m distance between the lighter and sample. A large prism of total reflection has been placed before the sample in order to provide operating with friable samples (powders, sands or liquids). The optical scheme of the laser photometer is shown in Fig. 1.

Each sample is measured twice at increasing and decreasing phase angles. Coincidence of these two phase curves is considered as an indicator of the reproducibility of the measurements. Any point of the phase curves is measured 30 (bright samples), 50 (samples with average albedo) or 100 (dark samples) times. Typical relative standard deviation of data for any point of the phase curve is approximately 0.5% - 1.0%.

One important consideration of our measurements is an estimate of the instrumental light background that appears due to scattering by dust in air. This factor influences all measurements, but especially those from low-albedo samples at extremely small phase angles. To take into account

this background, we make additional measurements immediately after the sample measurements using a sample shield to absorb the laser wavelength. This shield (filter) is placed so that its normal is oriented approximately 10° from the incident beam, diverting the specular reflection from the detector. This measurement provides us with a signal from the dust in air that we subtract from the signal obtained from the sample.

Laboratory samples of light scattering surfaces are prepared by sprinkling the substance on a dark substrate. The characteristic size of scattering grains for all samples was similar, of approximately one micron. We obtained photometric phase curves in red and blue spectral bands for samples with different colors, dry red and blue water-colors, MgO screen, and a milky glass plate. We have employed the last sample as a secondary photometric standard since its photometric properties are similar to those of the Halon standard [3]. We smoothed the obtained phase curves using a sliding-average procedure and then divided the phase curves obtained using red light with those obtained using blue light.

3 Results and discussion

In this section we show results of our colorimetric measurements. The albedo *A* of the samples is estimated as the ratio of light intensity from the sample to the intensity from the Halon standard at a phase angle of 1.5º. Figure 2 shows that the milky glass plate produces a very sharp opposition spike at phase angles less than 0.4° in both red and blue light. This spike is due to coherent backscattering enhancement [e.g., 4]. Figure 3 shows that the colored samples demonstrate very different behavior at small phase angles. The red sample has very different albedo *A* in blue and red wavelengths, 8% and 68%, respectively; these differences in optical properties are the primary reason for the large differences in the phase curves. The blue sample with albedo *A* of 22% and 65% in red and blue wavelengths, respectively, has a smaller albedo difference leading to smaller differences in the opposition spikes. These features become more apparent when we plot the colorimetric phase curves shown in Fig. 4. Here we present a phase trend of the ratio C(0.63/0.47 μm). It is necessary to note the high amplitude of change that approaches 25% at 0º for the red sample. The other samples show a trend in the negative direction, meaning a dominance in blue light, but the amplitudes are much smaller than that of the red sample. The spectrally neutral MgO sample shows weak phase dependence, much weaker, for instance, than the milky glass sample. This likely is due to the size of the particles composing the MgO sample that have a much wider polydispersity in spatial frequencies than that of the milky glass.

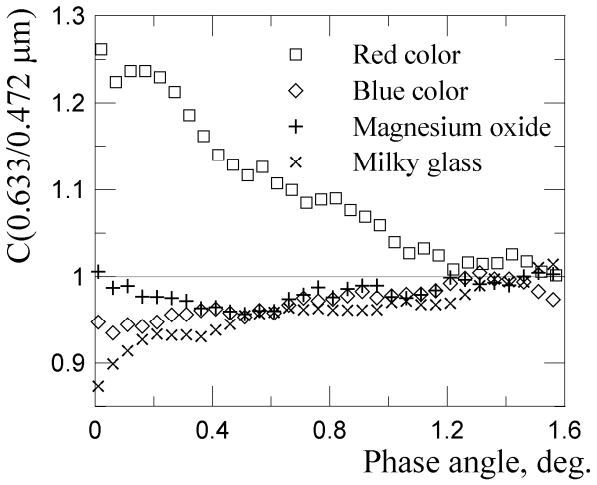

Figure 4: Colorimetric phase curves of studied laboratory samples

3 Conclusion

Our laboratory study of the colorimetric phase dependence of various samples shows significant changes of the ratio C(0.63/0.47 μm). This ratio can either increase or decrease as phase angle approach zero phase angle, depending on the sample albedo in red and blue light. Differences also can be seen in samples that are relatively neutral spectrally, for instance, between the sample of milky glass and MgO, suggesting that morphological properties also have a role in determining the color ratio. We know, for

instance, that the coherent-interference mechanism that produces enhanced backscattering is an interference phenomenon that depends on wavelength, but it also has a complicated dependence on the size and shape of the particles composing the sample. Our main conclusion is that the spectral peculiarities of the photometric opposition effect should be taken into account in different taxonometric models of Kuiper belt objects.

Acknowledgments

This work was partially supported by the Ministry of education and science of the Ukraine (Project #H/14-2002) and by CRDF grant UKP2-2897-KK-07.

References

[1] V.A. Psarev, A.A. Ovcharenko, I.N. Belskaya, Y.G. Shkuratov. Laboratory study of some opposition effect features. International Conference "The Solar System Bodies: From Optics to Geology", May 26–29, 2008, Kharkiv, Ukraine, abstract book, p.102.

[2] V. Psarev, A.Ovcharenko, Yu. Shkuratov, I. Belskaya, G. Videen. Photometry of particulate surfaces at extremely small phase angles. J. Quant. Spectrosc. Rad. Transfer. 2007. 106. 455-463.

[3] V. Weidner, J. Hsia. Reflection properties of pressed polytetrafluoroethylene powder. J. Opt. Soc. Am. 1981. 71. 856–861.

[4] Yu. Shkuratov, G. Videen, M. Kreslavsky, I. Belskaya, V. Kaydash, A. Ovcharenko, N. Opanasenko, E. Zubko. Scattering properties of planetary regoliths near opposition. In: Proceedings of the NATO Advanced Study on Photopolarimetry in Remote Sensing, Kluwer Academic Publisher, 2004, 191-208.

Atypical polarization in some recent comets

V. Rosenbush,[1] N. Kiselev,[1] L. Kolokolova,[2] S. Velichko,[3] F. Velichko,[3] K. Antoniuk,[4] S. Kolesnikov,[5]

[1] *Main Astronomical Observatory of National Academy of Sciences of Ukraine, 27 Zabolotnoho Street, Kyiv, 03680 Ukraine*
[2]*University of Maryland, College Park, USA,*
[3]*Institute of Astronomy of Kharkiv National University, Kharkiv, Ukraine,*
[4]*Crimean Astrophysical Observatory, Nauchnyj, Ukraine*
[5]*Astronomical Observatory of Odesa National University, Shevchenko Park, 65014 Odesa, Ukraine*
tel: +38 (044) 526-2147, fax: +38 (044) 526-2147, e-mail: rosevera@mao.kiev.ua

Abstract

Our polarimetric observations of recent bright comets 17P/Holmes, 8P/Tuttle, and 73P/Schwassmann-Wachmann 3 are described and analyzed. Tentative interpretation of their unusual properties is given based on aggregate model of comet dust.

1 Introduction

A large diversity of composition among comets leads to conclusion that there is no such object as a "typical comet". We present results of polarimetric observations of several recent bright comets, including 17P/Holmes and 73P/Schwassmann-Wachmann 3 (sub-fragments B and C) during theirs outbursts and 8P/Tuttle, that demonstrate a significant variety in polarimetric properties. A tentative explanation of the observations on the base of the model of cometary dust as ensemble of aggregated submicron particles is provided.

2 Observations and some results

17P/Holmes. This comet is unique. This distant inconspicuous Jupiter-family comet (with aphelion at the orbit of Jupiter and perihelion at 2.2 AU) has suddenly increased its brightness almost million-fold. On October 23-24, 2007 Comet Holmes went from magnitude 17 to magnitude 2.8 in just a few hours, doubling in brightness every half hour, presumably due to a very large ejection of gas and dust. The comet was easily seen almost all night and we could carry out its polarimetry.

On October 27–November 5, 2007 the polarimetric observations of Comet Holmes were made with a one-channel photoelectric photopolarimeter mounted at the 0.7-m reflector of the Chuguiv Observational Station (Ukraine). The filters BC (λ4845/65 Å) and WRC (λ7228/1140 Å) and 88, 33, and 20″ diaphragms were used. On November 8–22, 2007 the comet was also observed at the 1.25-m telescope of the Crimean Astrophysical Observatory, hereafter CrAO, (Ukraine) with a five-channel photoelectric photopolarimeter. The wide-band filters R (λ6860/1080 Å) and I (λ7660/550 Å) and 12″ diaphragm were used. Diaphragm was centered at a photometric nucleus and two regions of coma at the distance 6 arcmin to the north and the south of photometric nucleus. The comet was observed within the phase angle range 16.1–11.3°.

Figure 1 summarizes our observations. The typical phase-angle dependence of polarization for comets [1] is also shown there. All observed comets show very similar characteristics of negative polarization branch: position of the minimum at phase angle $\alpha_{min} \approx 10°$ with the value $P_{min} \approx -1.5\%$, and inversion angle at $\alpha_{inv} \approx 22°$. However, it is evident from Fig. 1 that the polarimetric properties of Comet Holmes are very different. The figure reveals that the absolute values of polarization were very low, regardless of the position of measured area in the coma, and smaller than for any of the previously observed comets. The degree of polarization near the minimum was approximately −1.1% in the R filter

and about ~0.5% in the I filter. According to the data in red bands (open symbols), the expected inversion angle should be about 18° which is also unusually low for comets.

The other peculiarity of Holmes' polarization is its atypical spectral trend. Even though there is not enough data to draw a firm conclusion about the typical spectral behavior of comet polarization at small phase angles, none of the previously observed comets showed such a pronounced negative spectral gradient. Comet Holmes is the first one for which it reached ~0.77 %/1000 Å near the polarization minimum.

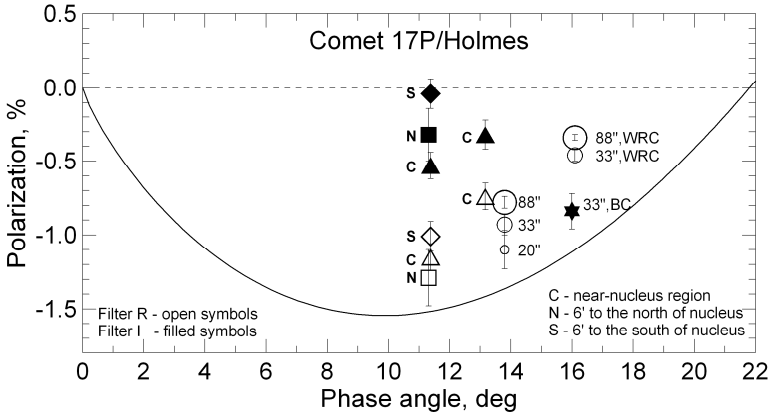

Figure 1: Phase-angle dependence of polarization for Comet Holmes in different filters and diaphragms. The typical curve of polarization for comets in the red continuum is shown by solid line.

8P/Tuttle. Previous optical studies classified this comet as "typical" in the chemical composition of its volatiles. The exceptionally favorable apparition in 2007/2008 provided a great opportunity for various observations of Comet Tuttle. Infrared observations of this comet revealed unexpectedly unusual composition of this comet [1], distinct from that of any comet observed to date.

We measured linear and circular polarization of Comet Tuttle on January 10, 2008 when the phase angle of this comet was about 68°. A one-channel photoelectric photopolarimeter mounted at the 2.6-m Shain telescope of the CrAO and R filter were used. The same method of simultaneous measurements of circular and linear polarization along the cuts as for comet C/1999 S4 (LINEAR) [2] was used.

The mean values of linear and circular (by absolute value) polarization degree along the cuts are 13.28 ± 0.36% and 0.60 ± 0.07%, respectively. Typical value of linear polarization for dusty comets at the corresponding phase angle is about 20%. As Fig. 2 shows (filled circle), polarization degree of Comet Tuttle is significantly lower than that for typical dusty comets.

73P/Schwassmann-Wachmann 3 (S-W 3). The nucleus of this comet broke into several active sub-fragments in 1995/1996 [3], which continued to disintegrate at the 2006 apparition. During this apparition two brightest remaining fragments of this comet, B and C, displayed strikingly different activity profiles. In particular, fragment B underwent several outburst events in the April-May 2006, which were also characterized by significant ejections of dusty debris, while C displayed less active behavior. Thus, most likely, fragment B was surrounded by fresher material because of frequent outbursts and fragmentation. Therefore, it was important to compare polarization for different fragments of the nucleus.

The polarimetric (aperture and CCD imaging) observations of the C, B, and G fragments of the comet were carried out in April–May 2006 when the phase angle changed from 38° to 67°. For the observations, a 1.25-m telescope with a five-channel aperture polarimeter and 0.7-m telescope with imaging polarimeter of the CrAO together with the wide-band R and I filters were used.

We found that polarization in the I filter is significantly less than that in the R filter for both nuclei B and C at all observed phase angles [4]. The degree of polarization was systematically increasing with decreasing the measured area of the coma. In general, the discrepancy in polarization of different nuclei is within the accuracy of measurements. The degree of polarization of both fragments B and C was in

agreement with the composite phase-angle dependence of polarization for dust-rich comets in the red continuum (Fig. 2).

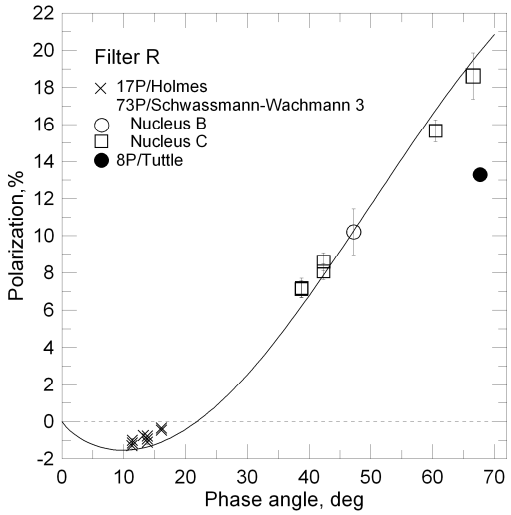

Figure 2: Polarization of comets 17P/Holmes, 73P/Schwassmann-Wachmann 3 (sub-nuclei B and C), and 8P/Tuttle in the R bands as compared with composite phase-angle dependence of polarization for dust-rich comets in the red continuum (solid line).

2 Interpretation of the observations

2.1 Negative polarization branch

It is believed that the negative polarization at small phase angles results from light scattering by aggregated dust particles in comet atmospheres. Theoretical modeling of light scattering by aggregates shows that the depth of the negative polarization branch depends on aggregate size (the number of monomers) and gets values typical for comets only if the aggregates are larger than 0.6 μm [5]. The other factor that may influence the negative polarization is the composition of particles: the negative polarization is usually more pronounced for more transparent, silicate-rich particles than for more absorptive carbon-rich ones [6]. Finally, some unusual combination of aggregated and compact particles in the dust may be the reason of comet's peculiarities since the ratio of aggregate/compact particles in the dust influences the degree of negative polarization as well as its spectral trend [7]. Due to such a complex nature of negative polarization, in case when it shows some unusual values (as at the outburst in Comet Holms) the model of the dust should be obtained based on the combination of both angular and spectral dependences of polarization together with the data of photometric, thermal, and other observations of the comet dust.

2.2 Spectral gradient of polarization

In the visual, observations usually show that the spectral gradient of polarization is positive at $\alpha > 30^{\circ}$, i.e. the values of polarization increase with the wavelength, also denoted as red polarimetric color (hereafter PC). However, for some comets, we have found an anomalous (negative) spectral dependence of polarization, namely the polarization degree in the red wavelength range is systematically less than that in the blue domain [4]. Recently, we have collected a number of evidences that this peculiarity is intrinsic in comets 21P/Giacobini-Zinner, C/1989 X1 (Austin), C/1999 S4 (LINEAR), 9P/Tempel 1. Also, we have found that comet Holmes as well as both fragments B and C of comet S-W 3 demonstrated the anomalous spectral dependence of polarization in the visible. This feature may be related to some specific properties of the dust in these comets.

The polarimetric color at small phase angles for most comets is typically almost neutral. Comet Holmes is the first comet for which atypical, i.e. blue PC, spectral dependence of polarization has been found even at small phase angles. Thus, the negative spectral gradient of polarization may be specific for some comets in both, positive and negative, polarization branches.

To interpret the data on spectral gradient of polarization, we apply our model of comet dust particles as aggregates successfully used to examine the phase dependencies of comet brightness and polarization. For ballistic cluster-cluster and particle-cluster aggregates, at $\alpha > 30^{o}$, red PC accompanied by red photometric color is typical in the visible [5, 6]. This may be explained the following way: with increasing wavelength, the monomer size parameter $2\pi r/\lambda$ gets smaller; monomers become "more Rayleigh" particles that increase their positive polarization. However, at some point, not properties of individual monomers but interaction between them becomes the dominating factor in light scattering. The strength of the electromagnetic interaction depends on the number of the monomers that the electromagnetic wave covers at a single period (on the light-path equal of one wavelength). This has two consequences. First, the interaction increases with the wavelength: the longer is the wavelength the more particles it covers. The stronger is the interaction the more depolarized becomes the light (similar to multiple-scattering effects), resulting in the negative, blue, PC. Second, the transition from individual particle effects (red PC) to the particle interaction effects (blue PC) starts at some specific combination of the size of monomers and the average distance between them (defined by the aggregate porosity). For more compact particles, this effect starts at shorter wavelengths, and they may exhibit blue PC even in the visible. This tells us that comets with blue PC may have more compact aggregates than the comets with red PC (not surprising since all listed comets are short-period, old ones). One can see that the wavelength at which the sign of the PC changes may be indicative about the porosity of the aggregates. Note that this may not work for the negative polarization (e.g. in case of Comet Holmes) where composition of the material may be the main factor that determines the spectral trend of polarization (see [6]). Since the sign of the PC depends on both the size of monomers and the porosity of aggregates, and should also depend on the spectral changes in the refractive index, more serious studies of the interplay between these three characteristics is required.

Acknowledgments

V. Rosenbush, N. Kiselev, and L. Kolokolova are thankful to the SOC and LOC of the ELS-XI Conference and NASA for financial support.

References

[1] B.P. Bonev, M.J. Mumma, Y.L. Radeva, et al., "The peculiar volatile composition of comet 8P/Tuttle: A contact binary of chemically distinct cometesimals?" Astrophys. J. Letters, in print, (2008).

[2] V. Rosenbush, L. Kolokolova, A. Lazarian, et al., "Circular polarization in comets: Observations of Comet C/1999 S4 (LINEAR) and tentative interpretation," Icarus **186**, 317-330 (2007).

[3] C.M. Lisse, M.F. A'Hearn, M.G. Hauser, et al., "Infrared observations of comet By COBE," Astrophys. J. **496**, 971-991 (1998).

[4] N. Kiselev, V. Rosenbush, L. Kolokolova, K. Antonyuk, "The anomalous spectral dependence of polarization in comets," JQSRT **109**, 1384-1391 (2008).

[5] L. Kolokolova, H. Kimura, N. Kiselev, V. Rosenbush "Two different evolutionary types of comets proved by polarimetric and infrared properties of their dust," Astron. Astrophys. **463**, 1189-1196 (2007).

[6] H. Kimura, L. Kolokolova, I. Mann, "Light scattering by cometary dust numerically simulated with aggregate particles consisting of identical spheres," Astron. Astrophys. **449**, 1243-1254 (2006).

[7] L. Kolokolova, H. Kimura, "Model of comet dust consistent with ground based observations and studies of Stardust returned samples," DPS meeting #39, #54.06 (2007).

A study of frequency and size distribution dependence of extinction for astronomical silicate and graphite grains

Ashim K Roy.[1] Subodh K Sharma.[2] and Ranjan Gupta,[3]

[1] *Physics and Applied Mathematics Unit, Indian Statistical Institute, Kolkata 700035.*
[2] *S N Bose National Centre for Basic Sciences, Salt Lake, Kolkata 700098.*
[3] *Inter University Centre for Astronomy and Astrophysics, Pune 411007.*

tel: 0091 (033) 2335 5706, fax: +0091 (033) 2335 3477, e-mail: sharma@bose.res.in

Abstract

This paper presents, in the framework of Mie theory, a parametrization of extinction spectrum curves of the silicates and the graphite grains separately in terms of minimum and maximum of sizes in a power law size distribution. These equations can be useful in a number of situations involving silicates and graphite grains. As a demonstration, average extinction spectrum of the interstellar medium will be analyzed.

1 Introduction

In a recent publication we analyzed extinction spectrum of a collection of homogeneous spherical particles of an unknown size distribution [1]. It was shown that an extinction spectrum, in general, has some easily identifiable characteristic regions where the extinction-frequency relationship can be approximated by simple empirical formulas involving first four moments of the particle size distribution. The analysis clearly showed the manner in which the essential features of the particle size distribution gets coded into its extinction spectrum. It was demonstrated that the moments could indeed be obtained from its extinction spectrum. It was assumed in this study that all particles were of same material and that their refractive index did not vary with frequency.

The purpose of this work is two fold. First, to examine the possibility of extending the ideas developed in [1] to a material whose refractive index varies with the wavelength. Our second aim is to demonstrate the applicability of these results to a multicomponent system. To this end, we choose one of the simplest model used to successfully reproduce the average interstellar extinction spectrum. It is the two component model due to Mathis et al. [2]. This model is ideally suited for our purpose. It is assumed in this model that individual grains of silicates and graphites are homogeneous spheres following power-law size distribution. The graphite component is further assumed to be consisting of parallel and perpendicular components. It is shown in this work that indeed the various regions of the extinction spectrum (for silicates as well as graphites) have information on size distribution coded in them. We present these relationships in infrared, visible, ultraviolet and far-ultraviolet wavelength domains for silicates and graphite grains separately.

2. Relevant formulas

For silicate as well as for graphite, spherical grains of size distribution $f(a) \propto a^{-3.5}$ have been assumed, where a is the radius of the sphere. With extinction coefficient, K_{ext}, defined in the standard way, we arrive at the following relations for the silicate grains by studying a large number of extinction curves:

$$K_{ext}^{sil}(IR)=2\pi N_s \bar{a^4} \nu^3 a_m \left[99.9562-111.5963\nu a_m-\frac{12.8548}{(\nu a_m)}+\frac{1.1011}{(\nu a_m)^2}\right],$$

$$K_{ext}^{sil}(V)=\frac{2\pi N_s \bar{a^4}}{a_m^2}\left[-1.995+\frac{2}{3}\left([a_m]-2.76\right)^2-[\nu]\left(-34.92+35.81[a_m]-4.85[a_m]^2\right)\right],$$

$$K_{ext}^{sil}(UV)=2\pi N_s \frac{\bar{a^4}}{a_m^{1.5}}\times 10^{2.5}\left[9.6[\nu]+\frac{0.112}{[\nu]}+0.04\nu a_m-\frac{0.92}{[\nu]a_m^{\ 2}}\right],$$

$$K_{ext}^{sil}(FUV)=1.08162\times N_s\times 10^{-10}[\nu]\left[1-1.201[\nu]+0.515113[\nu]^2-\frac{0.24}{[\nu]}\right],$$

where $[a_m]=a_m\times 10^5$, $[\nu]=\nu\times 10^{-5}$, N_s is the number of silicate grains and a_0, a_m are respectively the lower and the upper limit of the radii in the distribution. The initials IR, V, UV and FUV stand for infrared, visible, ultraviolet and far ultraviolet wavelengths. The fourth moment of the distribution $\bar{a^4}$ may also be expressed in terms of a_0 and a_m. Above empirical equations have been arrived at by studying a large number of extinction curves for power law size distribution. The values of refractive index at various wavelengths have been taken from the data base at (http://www.astro.princeton.edu/draine). These equations yield extinction efficiencies to within 5 percent of the correct efficiencies and are valid in the range $0.02\mu m<a_0<0.05\mu m$, $1.5\mu m<a_m<2.5\mu m$ for graphites and $0.04\mu m<a_0<0.06\mu m$ and $2.0\mu m<a_m<4.0\mu m$ for silicates.

For perpendicular component of graphite, we have arrived at following relations:

$$K_{ext}^{gra}(IR)=C\left[-21.4836+318.9289(\nu a_m)-606.2808(\nu a_m)^2+\frac{0.6931}{(\nu a_m)}\right]\times M,$$

where

$$M=\left[0.6646193-\frac{0.0257163}{(\nu a_m)}+\frac{0.1803948}{(\nu a_m)^2}\right],$$

and $C=2\pi N_g \bar{a^4}/a_m^2$ with N_g as the number of perpendicular graphites. Further,

$$K_{ext}^{gra}(V)=C\left[-0.9817+21.7734(\nu a_m)-9.45(\nu a_m)^2\right],$$

$$K_{ext}^{gra}(UV)=C\left[0.5836\frac{\sqrt{[a_m]}}{([\nu]-0.4622)}+1.40[a_m]\right],$$

in the range (1500-1900 Angstrom),

$$K_{ext}^{gra}(UV)=C\left[5.718[a_m]+11.902\sqrt{[a_m]}-0.602[a_m]^2-|[\nu]-0.4622|\left(30.12+5.33[a_m]-\frac{1.8}{[a_m]}\right)\right]$$
$$+C\left[\left(-250+2450[a_m]-300[a_m]^2\right)([\nu]-0.4622)^2+\left(12.225+4.11[a_m]+\frac{3.75}{[a_m]}\right)([\nu]-0.4622)\right],$$

in the UV peak region (2000-2300 Angstrom)

$$K_{ext}^{gra}(UV)=C\left[-3.33+9.1\sqrt{[a_m]}+\left(0.329\sqrt{[a_m]}/p\right)-\left(5.405+1.864[a_m]\right)p^{1/2}\right];\ p=0.4622-[\nu],$$

in the region 2400-3815 Angstrom and

$$K_{ext}^{gra}(FUV)=2\pi N_g 10^{-8}a_0^{5/2}\frac{\nu^2}{a_m^{0.265}}\left[1-\frac{0.3911}{\nu}a_m+0.1132\nu a_m\right].$$

Similar equations have been obtained for graphite parallel. Detailed results showing the accuracy of these relations and demonstration of the usefulness of these equations for interstellar medium will be presented during the conference.

References

[1] A. K. Roy, and S. K. Sharma, “A simple analysis of extinction spectrum of a size distribution of Mie particles,” J. Opt. A: Pure and Appl. Opt. **7**, 675-684 (2005).

[2] J. S. Mathis, W. Rumpl, and K. H. Nordsieck, “The size distribution of interstellar grains” ApJ. **280**, 425-433 (1977).

Cometary polarization , Sen

The analysis of cometary polarization data using Mie and other light scattering theories

Asoke K Sen and H S Das
Department of Physics,
Assam University,
Silchar 788011, India
Telephone : 91-3842270990, 9435070349, FAX 91-3842270802
Email: asokesen@yahoo.com; asokesen@bsnl.in

Abstract

Comets exhibit high (up to 25 %) amount of optical polarization when they are observed through ground based or space borne telescopes. These polarizations are caused due to the scattering of light by cometary grains. Such polarizations as observed by the authors for comet Halley and Austin in past helped to understand the composition and size distribution of cometary grains to a great extent [1, 2, 3].

In a more recent work the authors using Mie Theory compared the optical polarization data of a number of periodic and nonperiodic comets and concluded that the grains change in size as the comets get dynamically older [4]. A further work on comet Levy revealed that the observed cometary polarization values are better explained, if we assume that the grains are prolate rather than spherical [5].

However, with the present development in different light scattering codes with grains (particles) of various shapes, one can consider a more realistic grain model where cometary grains are porous and irregular. Such particles can be best represented by *aggregates* of monomers with a given size and composition . It appears from our calculations that with cometary grains as '*aggregates*' , the polarization data of comets can be better explained compared to other different shapes of grains. Recent calculations on comet Levy with such *aggregates* are presented.

1 Introduction

Comets are known to exhibit high amount of polarization, which are caused due to scattering of sunlight by dust grains present in the coma of comets. The polarization so observed through ground based or space borne telescopes, largely depend on the scattering angle. As the scattering angle becomes very high (> 160 degrees), almost all the comets exhibit negative polarization. It has been found that, the observed cometary polarization data can be explained fairly well, by assuming the grains to be Mie spheres with a specific dust size range and compositions characterized by complex refractive indices. Following a similar procedure, the authors had in past explained the observed polarization values of all the available comets (for which sufficient polarization data was available for modeling till that date) with reasonable accuracy [4] . These include eight comets both periodic and non-periodic like Halley, Hale-Bopp, Levy, Austin, Faye, Bradfield, Hykutake and Kopf. A typical fit of observed polarization values for

comet Halley in the wavelength (λ) 0.684 μm, as taken from the above work [4] is reproduced in Figure 1 below:

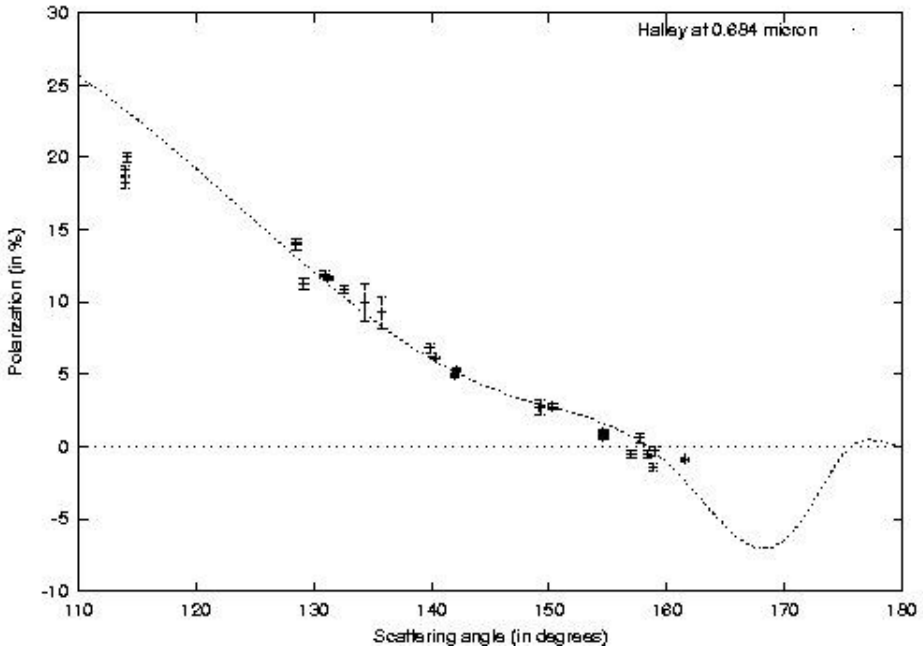

Figure 1. Observed polarization data of comet Halley at 0.684 μm, fitted against a grain model containing Mie spheres.

The sizes of cometary grains for above model calculation was taken from [6], which suggested a power law size distribution function. And the complex refractive index was used as a free parameters for modeling, which was determined as (1.386, 0.038) for best fit . This value was suggestive of dirty ice, dirty silicate types of grains among other possibilities. This attempt of fitting the observed polarization data with Mie Theory, for various sizes and compositions was repeated on other comets too in that work. And assuming that the compositions of grains don't differ between comets (with scientific justifications as explained [6]), it was also found that the grains of various comets increase in their sizes as they grow dynamically older with successive revolutions around sun.

2. aspherical grains as compared to spherical grains in comets

It seems quite reasonable to expect that the naturally occurring cometary grains can not be ideal compact spheres, as required by any Mie Theory based calculations [7]. However, till recently cometary scientists have been using such Mie particles to explain the observed polarization data as it is more convenient and direct, with fewer number of free parameters required for modeling.

In an attempt to explain the observed polarization data of comet Levy (1990XX) , we noticed that the polarization can be simulated more accurately if we assume the grains to be prolate (with aspect ratio 0.48) rather than Mie's ideal sphere [5]. This model calculation also successfully reproduced the observed negative polarization values for comet Levy, which was earlier not possible for similar comets [8].

A Chi-square minimization technique was followed for model fitting. We considered particles with different sizes and composition and a T-matrix based scattering code was executed. It was found

that the sum of square of difference between observed and calculated values of polarization becomes minimum, if we assume grains are prolate instead of being spherical. And there was complete uniqueness in the model fitting of data. Thus, one can conclude that the cometary grains are more likely to be prolate rather than spherical (at least for comet Levy) . A comparison of the simulated curves with these two types of grains, along with observed data for comet Levy at wavelength 0.485 μm is shown in Figure 2. (reproduced from [5]).

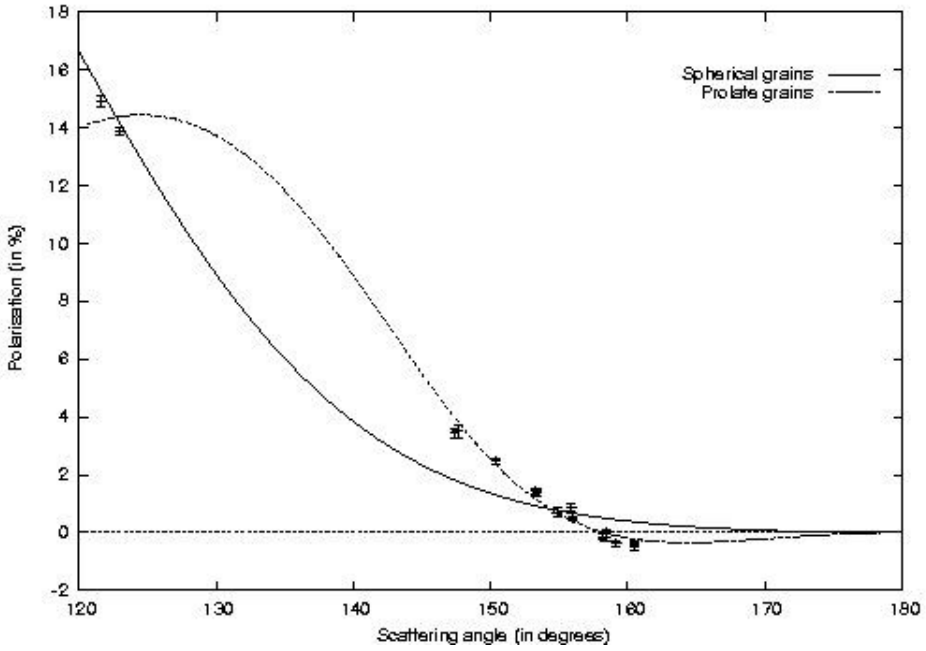

Figure 2. Comparison of simulated curves with prolate and spherical grains, along with observed data for comet Levy are shown (reproduced from [5])

3. The *aggregates* of monomers as the grains of the comets :

With the fact that the prolate grains give a better fit to the observed polarization data as seen in comet Levy, one should extend these calculations to other comets, for which fit was obtained using Mie theory. But no significant progress can be made.

However, it will be more realistic, if we can perform scattering calculations, where grains are assumed to be porous and irregular in shape. This can be done using a number of scattering techniques including DDA, *aggregates* of monomers etc. In the present work, we assume an individual grain to be an *aggregate* of several monomers and perform calculation by Superposition T-matrix method. To begin with, one can assume that all the monomers are of same size and compositions. In the simulations, these *aggregate* particles will be grown either by particle-cluster aggregation (BPCA) or BCCA (cluster-cluster aggregation). Based on the polarization data reported for comet Levy at 0.484 μm [8], a code was run with above procedures for *aggregates*. It was observed that *aggregates* made with a certain number (128) of monomers, explain the observed polarization data in a much better way as compared to Mie spheres or prolate grains. Monomers with size around 0.12 μm and refractive index (1.78, 0.052) produce polarization values which fit best to the observed data. Results from these calculations are presented in figure 3.

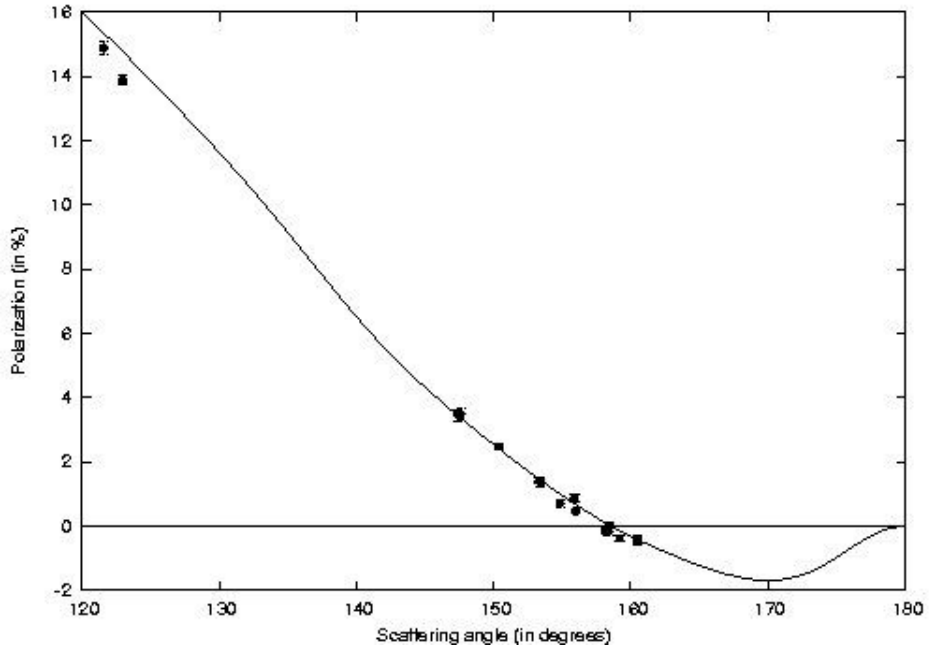

Figure 3 : Polarization data of comet Levy are compared with the theoretically simulated curve obtained using *aggregate* model of grains

4. Conclusions: With the development of better light scattering techniques, it appears that the cometary polarization data can be best explained with '*aggregate* ' grains among other shapes likes spheres, spheroids etc.

5. References:

[1] A. K. Sen, U.C. Joshi, M. R.Deshpande and C. Debiprasad C., Icarus, 86, p248 (1990)

[2] A.K.. Sen, M. R. Deshpande , U.C. Joshi, N. K. Rao , and A. V. Raveendran , A & A **242**, p496 (1991) ;

[3] A. K. Sen , U. C. Joshi , and M. R. Deshpande , MNRAS, **253**, p738 (1991)

[4] H. S. Das, A. K. Sen, A. K. and Kaul, C. L. , A&A, **423**, p373, (2004)

[5] H. S. Das and A. K. Sen, A&A, **459**, p272 (2006)

[6] E. P. Mazets , R. L. Aptekar , S. V. Golenetskii , A. Yu Guryan , A. V. Dyachkov , V. N. Ilyinskii ,V.N. Panov ,G .G Petrov, A. V. Savvin, R. Z. Sagdeev R.Z., I.A Sokolov , N.G. Khavenson , V.D.Shapiro ,V.L. Shevchenko , , Nature, **321**, p276 (1986)

[7] J. M. Greenberg and J.I Hage , ApJ, **361**, p260 (1990)

[8] D. X. Kerola and Larson S. M. Icarus, **149**, p351 (2001)

[9] G. P. Chernova, N. N. Kiselev and and K. Jockers Icarus, **103**, p144 (1993)

Composite Grains: Effect of Inclusions on Silicate Features

D.B. Vaidya

Gujarat College, Ahmedabad-380006, India

Ranjan Gupta

IUCAA, Pune 411007 India

Abstract.

We use discrete dipole approximation (DDA)to calculate the absorption efficiency of composite spheroidal grains in the spectral region $1.0 - 30.0\mu m$. The composite grains consist of host silicate spheroids and inclusions of graphite. We study the variation of the 10 and $18\mu m$ features as a function of porosity and volume fraction of the inclusions. Using the absorption efficiencies we calculate the infrared flux for the composite grains and compare the model curves with the observed LRS-IRAS data. We present the composite grain model and discuss the results.

1. Introduction

Although, cosmic dust grains are in general not homogeneous spheres, usually the observed absorption/scattering/extinction data are interpreted using calculations based on Mie theory, strictly valid for homogeneous spheres. Since there is no exact theory to study the scattering properties of the inhomogeneous (porous, fluffy, composite) grains there is a need for formulating models of electromagnetic scattering by the inhomogeneous grains. We use discrete dipole approximation (DDA)(Draine, 1988) to calculate the absorption efficiencies of the porous and composite spheroidal grains in the spectral region $1.0 - 30.0\mu m$. The composite grains consist of host silicate spheroids and inclusions of graphite. Using these results on the absorption efficiencies of the composite grains we calculate the infrared flux and study the variation in the 10 and $18\mu m$ features. We also study the effect of porosity upon the silicate features.

2. Composite grain model

We have modified the DDSCAT code (Draine and Flatau 2003) to study the scattering properties of the composite spheroidal grains. We present a composite spheroidal grain model with a host silicate spheroid, containing a large number of N dipoles, and graphite inclusions. The volume fractions of the graphite inclusions used are 10%, 20% and 30%. For a representative composite spheroidal grain model we refer (Vaidya et. al. 2007, Fig. 1). Details on the computer code and the corresponding modification to the DDSCAT code are given in Dobbie

(1999) and Vaidya et. al. (2001, 2007). Mathis (1996) has used effective medium theory (EMT) to study the composite grains.

3. Results

Figure 1 shows the absorption efficiencies (Q_{abs}) for the composite grains for 10% , 20% and 30% volume fractions of the graphite inclusions. These results show that the absorption efficiency decreases with the increase in the volume fraction of the inclusions. These results also show the shift in the wavelength of peak absorption, viz. 10 and 18μm, with the variation in the volume fraction of the inclusions . We also find the variation in the width of the features with the volume fraction of the inclusions (Figure 1a). The effect of porosity upon the features is shown in Figure 1b. Using these absorption efficiencies we calculate the infrared flux and compare the model curves with the observed IRAS (LRS) data (Figure 2).

4. Conclusions

This study on the composite grains shows that:

(i) the silicate features at 10μm and 18μm are modified with porosity and volume fraction of inclusions,

(ii) the model curves for the composite grains do not match the 18μm feature well,

(iii) Composite grain models with other inclusions; e.g. amorphous carbon or with ice - mantle, are required to be studied.

5. Acknowledgements

The authors thank the grant from the ISRO-RESPOND project
No. ISRO/RES/2/345/2007-08 under which this work has been carried out.

References

Dobbie J., 1999, PhD Thesis, Dalhousie University,

Draine B.T., 1988, Ap.J. , 333, 848

Draine B.T. and Flatau P.J.,2003, DDA code version 'ddscat6.1'

Mathis J.S., 1996, Ap.J., 472, 643

Vaidya D.B., Gupta R., Dobbie J.S and Chylek P., 2001, A & A, 375, 584

Vaidya D.B., Gupta R., Snow T.P., 2007, MNRAS, 379, 791

Whittet D.C.B., 2003, in Dust in the Galactic Environments, 2nd edn. IoP Publishing, Bristol, p. 240

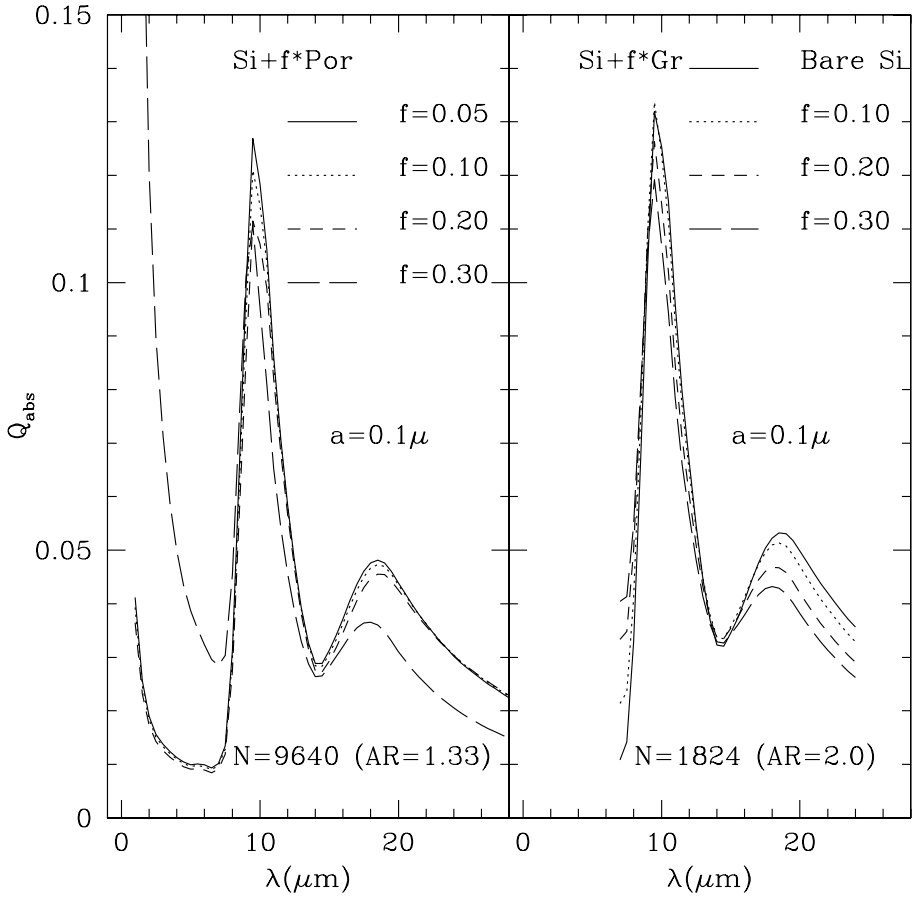

Figure 1. Absorption efficiencies of composite grains for 10%, 20% and 30% volume fractions of graphite inclusions on the left panel and the right panel shows the effect of porosity.

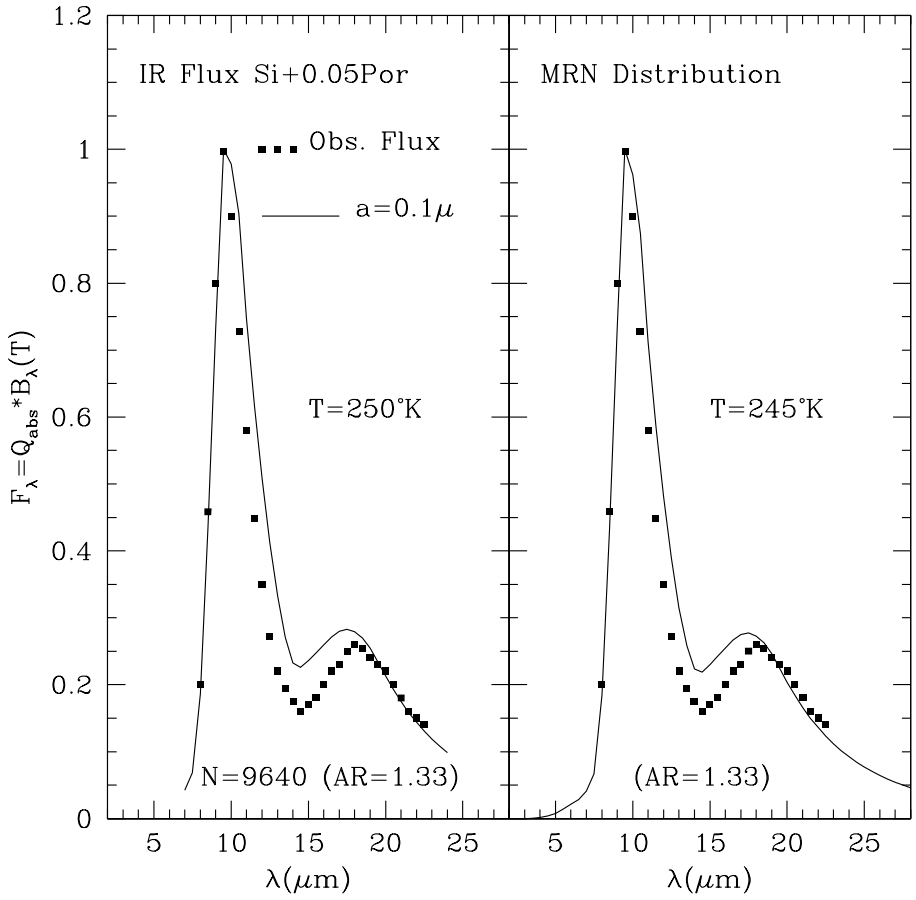

Figure 2. Comparison of model IR flux with the observed IRAS LRS data (Whittet, 2003).

How the particle size and shape influence the profile and peak position of infrared spectral ice bands of astrophysical interest

R. Vilaplana,[1] J. Cantó,[1] C. Millán[1], F. Moreno[2]

[1] *Univesidad Politécnica de Valencia, Dto. Applied Physics, Pl. Ferrandiz Carbonell, nº 2, Alcoy, Spain*
[2]*Instituto de Astrofísica de Andalucía (CSIC), C/ Camino Bajo de Huetor, nº 50, Granada, Spain*
tel: +1 (34) 96 652 84 26, fax: +1 (34) 96 652 84 09, e-mail: rovilap@fis.upv.es

Abstract

The profile and peak position of the absorption and extinction feature of dust particles are very sensitive to different factors as for example: molecular environment, temperature, irradiation history and particle size and shape. We have concentrated our attention to how the particle size and shape influence the profile and peak position of some ices of astrophysical interest. There has been research done on this subject, but it usually depends on the application. There is not an exhaustive study that fills all the gaps. We are carrying out an extensive study in order to be able to understand how this influence works. Up to date we have made calculations with spheres and aggregate of spheres for the narrow CO band at 2140 cm^{-1} and also for the two strongest bands of CO_2 at 2341 and 657.8 cm^{-1} initially by using the complex refractive index of these solid ices alone and for more realistic model. We have found that the double peak sometimes observed can also be produced by the sphere becoming similar in size or larger to the wavelength and not only by some small particles of specific shapes.

1 Introduction

Icy surfaces form mantles on the refractory dust grain cores in the interstellar medium (ISM). Different dust populations are found in the circumstellar envelopes, the diffuse and dense ISM. Starlight in part is scattered but also absorbed; and absorbed energy is reradiated by dust grains in the infrared range. A number of features appear in the infrared extinction due to molecular growth ice mantles on the refractory dust grain cores.

Most of our knowledge on the physical and chemical properties of icy grain mantles is based on the comparison between observations and laboratory experiments. The experimental infrared spectra are generally obtained from a thin film of ice formed at low temperature by gas deposition on a flat substrate. Nonetheless, in the ISM the ice mantles are deposited on the interstellar dust particles which have size and shape. On the other hand, we can also interpret astronomical observations by comparison with computational calculations. Using the optical constants of ices at low temperatures and the scattering codes we can obtain the absorption and extinction coefficients for ice particles with different shapes.

Observations show that some peak positions and their widths show variations from object to object. The CO and CO_2 have sharp bands in the infrared range and their band shape depends strongly on the ice composition [1,2,3]. For instance, the two independent solid CO components observed along most lines of sight (one narrow band generally centred at about 2140 cm^{-1} and broader one at 2136 cm^{-1}). These two bands are attributed to variations in composition and/or physical characteristics of the grain (i.e. shape, size). Laboratory studies on the shape and peak position of the solid CO and CO_2 bands in astrophysical relevant mixtures have shown that the narrow CO band at 2140 cm^{-1} occurs in mixtures dominated by non-polar molecules (CO itself, CO_2, O_2, N_2), and the broad feature is due to mixtures with polar molecules such as H_2O ice [1,2,3,4]. In these studies, computational calculations of absorption cross sections in the Rayleigh limit for various single shapes (spheres, prolate and oblate spheroids, rods, disks and core/mantle spheres) have shown that while the spheres show a single absorption feature, other homogeneous shapes show a double peak and for the core/mantle spheres the relative strength

and position of these features depend on the relative core/mantle volume and core optical properties. They have also observed that the average in size and shape generally tend to smooth the spectral structure, to shift the peak and to broaden it. The aforesaid calculations are for small particles (X<<1), however scattering effects are important when particle sizes become comparable or larger than the wavelength. They have also calculated the extinction cross sections for core/mantle models for wider size distributions and observed a broadening of the peak at lower frequencies and how a scattering peak slightly displaced from the absorption occurs [1]. These studies with core-mantle models conclude that the particle shape effects depend on the abundance of ice. Other studies carried out for non-icy solids of astrophysical interest show that the temperature effects are masked in the transmission spectra by the particle morphology effects [5,6,7]. So, an exhaustive study of the influence of the particle shape and size in the position and peak profile has a great interest for distinguishing, clearly, how this influence works.

2 Computational calculations and results

We have carried out computational calculations by using scattering codes focused on the peak profile of the narrow CO band at 2140 cm^{-1} (4.67 μm) and on the two strongest bands of the CO_2, namely the asymmetric stretching ν_3 at 2341 cm^{-1} (4.27 μm) and bending ν_2 at 657.8 cm^{-1} (15.2 μm). We have used in these calculations the optical constants of CO and CO_2 ices deposited at 12.5 K derived in the infrared spectral range with a resolution of 2 cm^{-1} by Baratta & Palumbo 1998 [8].

Owing to the non-restriction with the X of Mie calculations, our initial study is based on spheres. We have done calculations of the extinction coefficient for X from 0 to 3. Figure 1 shows the projection in a plane of the extinction coefficient of the 2140 cm^{-1} peak profile of the solid CO. The x axis represents the wavenumber in cm^{-1} and the y axis the X varying from 0 to 3. Figure 2 shows the extinction coefficients of the 2140 cm^{-1} CO peak profile versus the wavenumber in for spheres for X values of 0.25, 0.5, 1, 2 and 3.

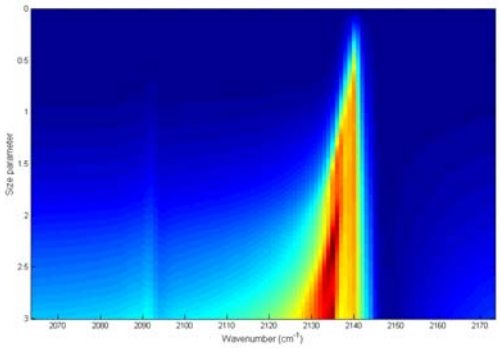

Figure 1: The projection of the extinction coefficient of the 2140 cm^{-1} peak profile of the solid CO.

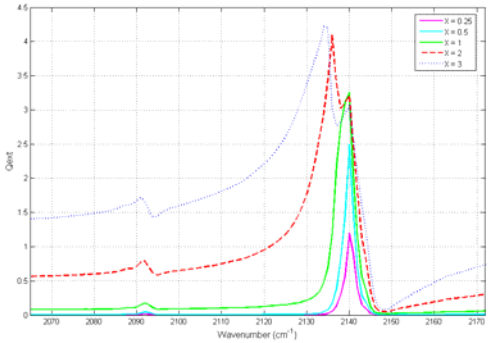

Figure 2: The extinction coefficients of the 2140 cm^{-1} CO peak profile versus the wavenumber for spheres with values of X of 0.25, 0.5, 1, 2 and 3.

These two figures show that the double peak of the solid CO, one 2140 cm^{-1} and the broader one about 2136 cm^{-1}, which have been seen in some observations and laboratory experiments with ice mixtures, could also be originated by spheres that become comparable or larger than the wavelength as well and not only for Rayleigh homogeneous spheroids of pure CO or core/mantle spheres as was shown by Tielens et al. 1991. Our calculations with spheres for the two strongest bands of the solid CO_2 show a similar behaviour as it can be seen in figure 3 and figure 4.

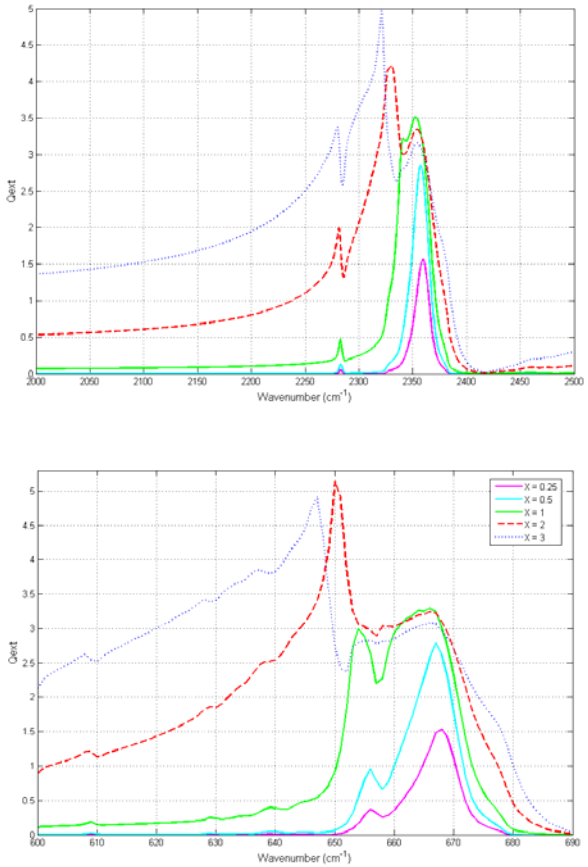

Figure 3 and figure 4: The extinction coefficients of the 2341 cm^{-1} (top) and 657.8 cm^{-1} (bottom) CO_2 peak profiles versus the wavenumber in cm^{-1} for spheres with different X values.

In order to do a more realistic study we have done calculations with the DDA code for aggregates of spheres randomly generated with a size monomer of 0.12 μm. Initially, we have considered the refractive index of the solid CO alone, later we have used a more realistic particle in two ways: the first one is a homogeneous aggregate whose refractive index was obtained by using the Maxwell-Garnett law, the second one is a heterogeneous aggregate formed by dipoles with different indexes (graphite, silicate and ice).

Figure 5 shows the extinction coefficient for different aggregates of sphere randomly generated with effective radii of 0.39, 0.52, 0.57 and 0.62 μm by using the refractive index of the solid CO alone. This figure shows that sphere aggregates of solid CO with X<<1 generate a unique peak shifted somewhat to higher wavenumbers in comparison with the peak obtained with spheres. The double peak observed with calculations with other Rayleigh homogeneous shapes does not appear with these aggregates.

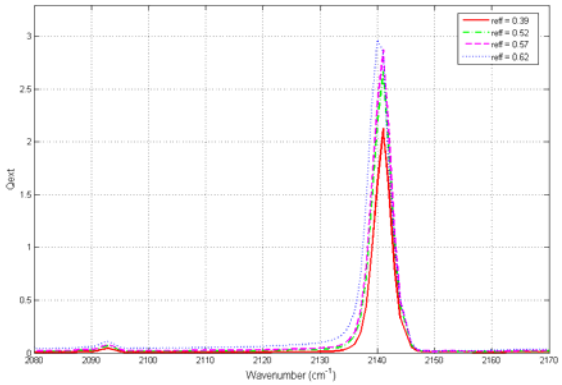

Figure 5: The extinction coefficient for different aggregates randomly generated with a size monomer of 0.12 μm for the refractive index of the solid CO.

3 Conclusion

With the calculations done up to now, two interesting results have been observed. The first one is related to the fact that particles comparable or larger to the wavelength for the two ices are considered to have given rise to a scattering peak slightly displaced from the absorption one. The second one is related to the calculations with small aggregates for solid CO alone, which give a single peak displaced somewhat with respect to the single peak obtained with spheres and which is not the case of the results obtained with small particles of specific shapes.

Acknowledgments

This work was supported by contract AYA2007-63670and AYA2007-65899 and FEDER funds.

References

1] A. G. G. M. Tielens, A. T. Tokunaga, T. R. Geballe, and F. Baas, “Interstellar solid CO: polar and nonpolar interstellar ices,” ApJ **381**, 181-199 (1991).

[2] Ehrenfreund, A. C. A. Boogert, P. A Gerakines, A. G. G. M. Tielens, E. F. van Dishoeck, “ Infrared spectroscopy of interstellar apolar ice analogs,” A&A **328**, 649-669 (1997).

[3] P. Ehrenfreund, A. C. A. Boogert, P. A. Gerakines, D. J. Jansen, W. A. chutte, A. G. G. M. Tielens, and E. F. van Dishoeck , “A laboratory database of solid CO and CO_2 for ISO,” A&A **315**, 341–344 (1996).

[4] M. E. Palumbo, A. G. G. M. Tielens, and A. T. Tokunaga, “Solid Carbonyl Sulphide (OCS) in W33A,” ApJ **449**, 674-680 (1995).

[5] Th. Henning and H. Mutschke, “Low-temperature infrared properties of comic dust analogues,” A&A **327**, 743-754 (1997).

[6] A.Tamanai, H. Mutschke, J. Blum, and R. Neuhäuser, “Experimental infrared spectroscopic measurement of light extinction for agglomerate dust grains,” JQSRT **100**, 373-381, (2006).

[7] A. C. Andersen, H. Mutschke, T. Posch, M. Min, and A. Tamanai, “Infrared extinction by homogeneous particle aggregates of SiC, FeO and SiO_2: Comparison of different theoretical approaches,” JQSRT, **100**, 4-15 (2006).

[8] G. A. Baratta and M. E. Palumbo, "Infrared optical constants of CO and CO_2 thin icy films," J. Opt. Soc. Am. **A15**, 3076-3085 (1998): http://www.ct.astro.it/lasp/optico.html

Light scattering by agglomerated debris particles composed of highly absorbing material

Evgenij Zubko,[1,2] Hiroshi Kimura,[3] Yuriy Shkuratov,[2] Karri Muinonen,[4]
Tetsuo Yamamoto,[3] and Gorden Videen[5]

[1] *Graduate School of Science, Tohoku University, Aoba, Aramakiaza, Aoba-ku, Sendai 980-8578, Japan, e-mail: zubko@caos-a.geophys.tohoku.ac.jp*
[2] *Institute of Astronomy, Kharkov National University, 35 Sumskaya St., Kharkov, 61022, Ukraine*
[3] *Institute of Low Temperature Science, Hokkaido University, Kita-ku North 19 West 8, Sapporo 060-0819, Japan*
[4] *Observatory, PO. Box 14, FI-00014 University of Helsinki, Finland*
[5] *Army Research Laboratory, 2800 Powder Mill Road Adelphi Maryland 20783 USA*

Abstract

We study the influence of material absorption on light scattering by irregularly shaped particles whose sizes are comparable with the wavelength. We find that the angular profile of linear polarization is extremely sensitive to the imaginary part of refractive index, and there are some unique features that may assist in the retrieval of physical properties of particles using remote-sensing techniques.

1 Introduction

Organic material is an abundant component of cosmic dust; for example, *in-situ* analyses of the chemical composition of cometary dust showed that about 50% of all particles contain a considerable amount of organic material [1]. Organic material can result from UV processing of interstellar ices deposited on cold dust grains, and subsequent UV and ion processing of organic residue may transform it into hydrogenated amorphous carbon [2]. Optical properties of organic material strongly depend on the dose of UV radiation and ion bombardment. For instance, at wavelength of λ = 0.5 μm, the processing of organic material in a form expected in the diffuse interstellar medium yields a refractive index m = 1.567+0.144i [2]. Heavier processing changes the refractive index to m = 1.855 + 0.45i; whereas, the refractive index of hydrogenated amorphous carbon is m = 2.27 + 0.64i [3]. Thus, organics are transient materials between dielectric and conductor materials. Study of light scattering by irregularly shaped particles composed of such material is the main purpose of our paper.

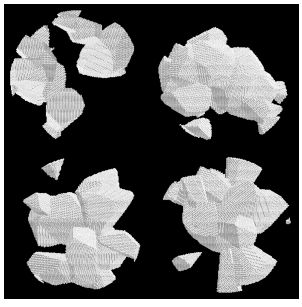

Figure 1: Images of agglomerated debris particles.

2 Model dust and its light scattering

We simulate light scattering by irregularly shaped particles using our own implementation of the discrete dipole approximation (DDA) [see, e.g., 4]. We generate irregularly shaped model particles by damaging a perfect sphere with the following algorithm. The spherical volume is filled with a regular cubic lattice that is considered as the initial matrix of the irregular particles. All cubic cells forming this initial matrix are divided into two groups: cells belonging to the surface layer and cells internal to the surface layer. The depth of the surface layer is a parameter of our model. In this work it is fixed to 0.5% of the size of the matrix. Among surface dipoles we choose randomly 100 cells that are considered as seed cells of empty space. In the set of internal dipoles, we randomly choose 21 and 20 seed cells of material and empty space, respectively. Then, step-by-step, each cell distinct from

the seed cells is marked with the same optical properties as that of the nearest seed cell. Images of four sample particles generated in this way are shown in Figure 1. As can be seen, the particles appear to be aggregates of very irregular shape. We identify such particles as agglomerated debris particles. Previously, we have studied the light scattering of some manifestations of this kind of particles [4].

We characterize the size parameter x of agglomerated debris particles by the radius of its circumscribing sphere r_{cs}, i.e. $x = 2\pi r_{cs}/\lambda$. Generally, this radius coincides with the radius of the initial matrix, or is within a few percent, so we use this value instead for simplicity. We consider a set of four size parameters x = 5, 10, 20, and 30. In the first case, the radius of the initial matrix is 16 cells, in the second it is 32 cells, and in the two last cases it is 64 cells. The total numbers of cells forming initial matrices are 17,256, 137,376 and 1,099,136. Agglomerated debris particles occupy on average approximately 26% of these volumes. Thus, agglomerated debris particles have a rather sparse structure.

The real part of the refractive index has been fixed at 1.5. Excluding the case of x = 30, the imaginary part is varied from 0 to 1.3. For the largest particles convergence cannot be reached at Im(m) = 0. For all particle sizes, a large imaginary part of refractive index does not cause any problems with convergence. For instance, in the case of Im(m) = 0.3–1.3, the number of iterations remain smaller than that of Im(m) = 0.05.

For averaging considerations, we consider a minimum of 500 particle realizations for each size parameter. More realizations are needed at larger size parameter; for example at x = 30, the average number of realizations is approximately 800. Scattering properties of each particle have been additionally averaged over 100 scattering planes, evenly distributed around the wavevector of the incoming light. Thus, fluctuations of the standard deviation of the linear degree of polarization over the entire range of phase angle α do not exceed 1%. The phase angle α is supplementary to the scattering angle θ, i.e., $\alpha = 180° - \theta$.

One essential question of this study is whether our numerical results obtained at large imaginary parts of refractive index satisfy the Maxwell equations. We have considered four independent tests in order to answer that question; each of them has confirmed that our results are reliable [5]. For instance, clearly, DDA remains valid only while an electric dipole moment of cells forming a scatterer, dominates over other multipoles. For the cells forming the largest particles (i.e., x=30), we compare the relative contributions of the magnetic dipole and electric quadrupole moments at Im(m)=0.05 and Im(m)=1.3: they remain almost the same. Another test is a comparison of values of scattering cross-section C_{sca} obtained through the Optical theorem [6] and integration of intensity of scattered light over a circumscribing sphere. In the case of x=5–20, the difference between these two values was found to vary from 0.5 to 3%; at x=30, it was of 6–7% over the entire range of imaginary parts of refractive index. We find experimentally that even the difference in C_{sca} of 10% does not mean violation of Maxwell equations. In addition, we study the distribution of the induced field energy over the particle volume and find that, at x=30 and m=1.5+1.3i, energy is concentrated in a very narrow surface layer with thickness of 3-4 dipoles; whereas in the subsurface volume there is no electromagnetic field at all. Such behavior is expected from conductors.

3 Results and discussion

In this section we present results for the two extreme sizes: x = 5 and x = 30; other cases show qualitatively similar behavior. In the discussion, we will refer to the other results as necessary. Figure 2 shows the degree of linear polarization P as a function of phase angle α and the imaginary part of refractive index Im(m). The left panel corresponds to x = 5 and the right one to x = 30. One can see that small particles show only positive linear polarization at all phase angles. Their polarization maximum increases with Im(m) and, simultaneously, it shifts toward larger phase angles. When Im(m) exceeds 0.5, the angular profile of linear polarization becomes bimodal and further increasing Im(m) makes this effect more explicit. This feature is the most pronounced in the case of the smallest particles as increasing particle size tends to wash it away. At x = 30, the second maximum is already quite inexpressive. Note, a similar bimodal profile of the polarization curve was found in laboratory measurements of hematite

particles [7]. This suggests that it may be a persistent feature of small particles having very high imaginary refractive index.

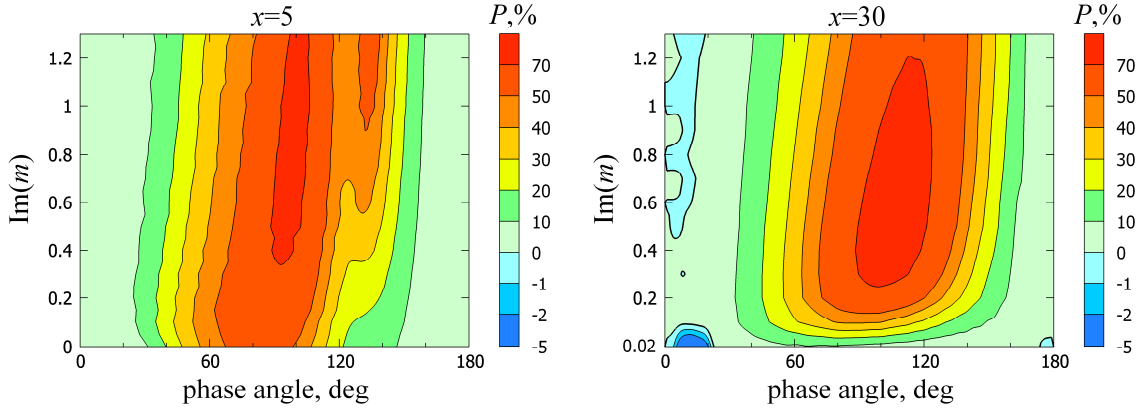

Figure 2: Degree of linear polarization as a function of phase angle α and Im(m).

At all particle sizes, the amplitude of positive polarization changes with Im(m) non-monotonically. For low absorption, the amplitude increases together with absorption until some maximum amplitude is reached. Further increasing Im(m) results in a decrease in amplitude. The inflection occurs at Im(m) ~ 1 (x = 5), 0.95 (x = 10), 0.7 (x = 20), and 0.5 (x = 30). At those inflection points, the linear polarization is as high as 70–80%.

Interestingly, the phase angle of the polarization maximum increases monotonically with Im(m). In the case of smallest particles, the position of polarization maximum shifts from 85° at Im(m) = 0 to 102° at Im(m) = 1.3. While particle size increases, the shift of the polarization maximum position becomes greater: at x = 30, it changes from 66° at Im(m) = 0.02 to 118° at Im (m) = 1.3.

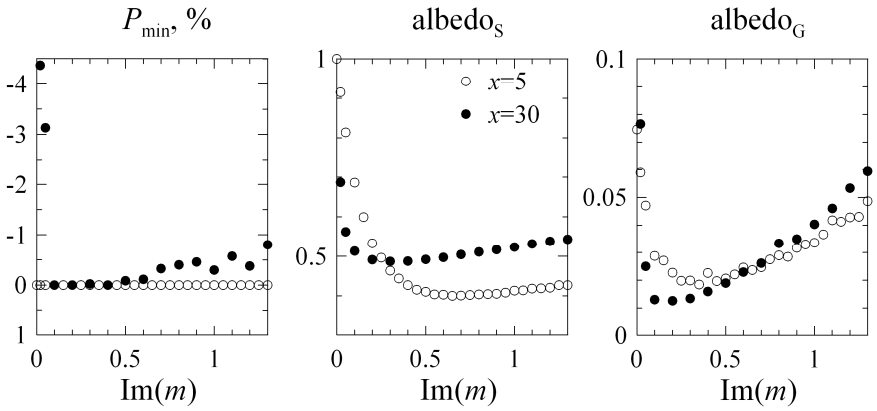

Figure 3: P_{min}, albedo of single scattering, and geometrical albedo as functions of Im(m).

While at x = 5, the particles demonstrate essentially positive polarization at all phase angles, as the size parameter increases to x = 10–30, non- and weakly-absorbing particles reveal a rather deep negative polarization branch (NPB) at small phase angles. This NPB vanishes when Im(m) exceeds values of 0.1. The effect of further growth of absorption depends strongly on particle size. At x=10, linear polarization remains positive. At x = 20, a shallow NPB appears episodically: the deepest NPB with P_{min} = -0.86% is found at Im(m) = 1.1. At x = 30, the NPB appears again at Im(m) = 0.5 and persists systematically up to the largest value of Im(m) (see Figures 2 and 3). Note that this recurrence of the NPB

is not as deep as that of the weakly absorbing particles and it often is accompanied with a small branch of positive polarization near $\alpha = 0°$ (see Figure 2).

Finally, we consider two types of albedo, namely, albedo of single scattering (middle panel in Figure 3) and geometrical albedo (right panel in Figure 3). Single-scattering albedo is the ratio of the scattering to extinction cross-sections; whereas, geometrical albedo is equal to $I(0)\cdot\pi/(k^2\cdot G)$, where $I(0)$ is the intensity of backscattering, k is the wavenumber, and G is the geometrical cross-section. As one can see in Figure 3, both kinds of albedo show a non-monotonic dependence on Im(m), and in all cases there is only one minimum. The minimum of the single-scattering albedo occurs at Im(m) = 0.65 in the case of x = 5 and at Im(m) = 0.3 in the case of x = 30. In both cases, further growth of Im(m) increases albedo slightly. At all sizes studied, albedo remains higher than 0.4, suggesting that particles comparable with wavelength cannot be too dark.

Geometrical albedo shows two essential differences from single-scattering albedo. First of all, its minimum appears much earlier: Im(m) = 0.35 and Im(m) = 0.2 at x = 5 and 30, respectively. While particle size increases, the minima positions of the single-scattering and geometrical albedos tend to converge. Another distinctive feature is that after its minimum, the geometrical albedo grows very rapidly with Im(m). For instance, at x = 5, the value of geometrical albedo at Im(m) = 1.3 already exceeds its value at Im(m) = 0.05. Simultaneously, the amplitude of the linear polarization at Im(m) = 1.3 remains much higher than at Im(m) = 0.05. Interestingly, the linear polarization maximum correlates much better with minimum of the single-scattering albedo than the geometrical albedo. It may signify that, although Umov's law (which states that the brighter the surface the lower its maximum of linear polarization) is associated with geometrical albedo [8], it may have its foundation in single-scattering albedo. We find in the case of particles comparable with wavelength that Umov's law appears to hold for both dielectric and conducting materials, but it fails for transition materials.

Acknowledgments

This research was partially supported by a Grant-in-Aid for Scientific Research from Japan Society for the promotion of Science.

References

[1] E. Jessberger, "Rocky Cometary Particulates: Their Elemental, Isotopic and Mineralogical Ingredients," Space Science Rev., **90**, 91–97 (1999).

[2] P. Jenniskens, "Optical constants of organic refractory residue," A&A, **274**, 653–661 (1993).

[3] W. W. Duley, "Refractive indices for amorphous carbon," ApJ, **287**, 694–696 (1984).

[4] E. Zubko, Yu. Shkuratov, N. Kiselev, G. Videen, "DDA simulations of light scattering by small irregular particles with various structure," J. Quant. Spectrosc. Radiat. Transfer., **101**, 416–434 (2006).

[5] E. Zubko, D. Petrov, Yu. Shkuratov, H. Okamoto, K. Muinonen, H. Kimura, T. Yamamoto, G. Videen, "Applicability of discrete-dipole approximation to conductive particles," this volume.

[6] C. F. Bohren and D. R. Huffman, *Absorption and Scattering of Light by Small Particles* (Wiley, New York, 1983).

[7] O. Muñoz, H. Volten, J. W. Hovenier, M.Min, Y. G. Shkuratov, J. P. Jalava, W. J. van der Zande, and L. B. F. M. Waters, "Experimental and computational study of light scattering by irregular particles with extreme refractive indices: hematite and rutile," A&A, **446**, 525–535 (2006).

[8] J. E. Geake and A. Dollfus, "Planetary surface texture and albedo from parameter plots of optical polarization data," Mon. Not. Roy. Astron. Soc., 218, 75–91 (1986).

LIGHT SCATTERING PROPERTIES OF CIRRUS

Light scattering properties of cirrus: A review

Anthony J. Baran[1]

[1] *Met Office, Exeter, UK*
tel: +44(0)1392884438, fax: +44(0)1392885681, e-mail: Anthony.baran@metoffice.gov.uk

Abstract

Cirrus consists of a variety of ice crystal shapes, the sizes of which can vary from less than 10 μm to over 10000 μm. The ice crystal shapes can take on a variety of geometric forms from simple hexagonal structures, such as plates and columns to simple bullets, rosettes and aggregates of these shapes. Though, depending on the presiding atmospheric conditions the ice crystals may be further perturbed to a more complex state through the process of surface roughening, deformations, and/or aerosol/air inclusions. Predicting the general radiative properties of such ice crystal ensembles so that climate models and remote sensing of cirrus may be further improved is the current challenge. In this review article current single ice crystal models and ensembles will be reviewed and tested against intensity and polarized intensity measurements. Requirements for future measurements to further constrain ice crystal models will also be discussed.

1 Introduction

Cirrus usually exists at altitudes greater than about 5 km [1] and can cover up to 30% of the earth's surface in the midlatitudes. In the tropics the spatial coverage could be as much as 70% [1, 2]. With such a spatial and temporal coverage it is hardly surprising that cirrus is a major component of the earth-atmosphere radiation balance [3-5]. However, the magnitude of the cirrus feedback is still uncertain for the following reasons. At cirrus altitudes the cloud is composed of ice crystals that are generally complex, which can exist as either single symmetric crystals such as columns and plates or non-symmetric ice crystals such as ice aggregates. Moreover, the complex ice aggregates may also have ice crystal components that are symmetric [6]. Though, it is the more complex non-symmetric ice crystals that tend to be the more common shape [7-9]. The sizes of single ice crystals may also vary over several orders of magnitude so the size parameter (ratio of spherical equivalent circumference-to-incident wavelength) can also vary significantly and take on values of less than unity or greater than 10000. With this combination of variable ice crystal complexity and size the computation of their single-scattering properties over a wide range of size parameter space is problematic because there is no one method of light scattering that can be applied to cover such a range [10]. Moreover, in order to make the light scattering problem tractable some idealized ice crystal geometry must be assumed so that T-matrix [11], Finite-Difference-Time-domain [12], Physical Optics [13], ray-tracing [14] or a combination of these methods can be applied. The idealized geometries assumed may have very different single-scattering properties resulting in different predictions for the radiative properties of cirrus thereby contributing to the uncertainty in the cirrus feedback [15].

In order to monitor the contribution of cirrus to the earth-atmosphere radiation balance there now exists a series of space-based satellites [16] that measure the radiative and hydrological contribution of cirrus to the climate system. This series of satellites called the 'A'-train uses a variety of active and passive sensors ranging from a lidar which can measure extinction and the linear depolarization ratio [17], a 94 GHz cloud-profiling radar [16], and an array of solar and infrared sensors with some of the solar sensors measuring the total and polarized reflection [18]. With such an array of sensors it is important to construct ice crystal models that can be consistently applied across a wide range of size parameter space such that the light scattering problem is tractable as well as obtaining physically consistent retrievals from the 'A'-train measurements. This further requires that the ice crystal or ensemble model must also be consistent with the cirrus microphysical and bulk properties in the form of the particle size distribution function (PSD) and ice water content (IWC). These are not only requirements for remote sensing but also for general

circulation models that predict weather and climate change [19]. The present article explores such ice crystal models and what measurements are required to further constrain them.

2 Single or ensemble ice crystal models ?

An example of the various ice crystal shapes that can exist in cirrus is illustrated by Figure 1 (a)-(b). The figure shows Stratton Park Engineering Company (SPEC) Cloud Particle Imager (CPI) probe [20] examples of midlatitude cirrus ice crystals. These images were obtained during the CAESAR (Cirrus and Anvils: European Satellite and Airborne Radiation measurements project) campaign of flying around the UK located over the sea during the Winter and Autumn of 2007 [21]. As can be seen from the figure ice crystal shapes can vary from single hexagonal ice columns, which appear in Figure 1 (a) to show

(a) (b)

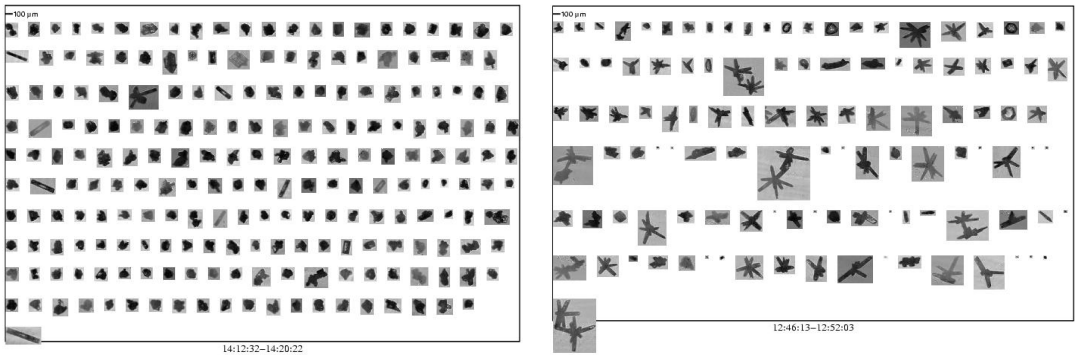

Figure 1: Ice crystal images obtained from the CPI probe during the CAESAR campaign of flying in midlatitude cirrus around the UK located over the sea during the Winter and Autumn of 2007. From Ref. [21].

evidence of inclusions to compact pristine irregulars and compact aggregated irregulars. Figure 1 (b) illustrates other examples of ice crystals such as pristine rosettes and aggregates of rosettes. The SPEC CPI samples ice crystals between maximum dimensions of 2.5 to about 2500 μm though the smallest ice crystals shown in Figure 1 (a)-(b) with maximum dimensions much less than 100 μm may appear as quasi-spherical due to the limiting resolving power of the probe. These ice crystals are often described as 'spheres' by automatic shape recognition algorithms and in light scattering calculations they are assumed to be either ice spheres [22], spheroids [23], droxtals [24], or Gaussian random spheres [25]. It is currently unknown what the actual shapes of these very small ice crystals are, though it is very important to characterize such shapes and sizes since their light scattering properties can be profoundly different [26] and can have significant impacts on cirrus radiative properties [27].

The problem Figure 1 illustrates is how to model the light scattering properties of cirrus given such a diverse range of ice crystal shape and size ? Traditionally, it has been common to assume that the radiative properties of cirrus can be modelled assuming single randomly oriented ice crystal shapes such as hexagonal ice plates, hexagonal ice columns, six or eight-branched bullet-rosettes, polycrystals [14], ice aggregates [28], or by a chain of ice aggregates [29]. Though these single ice crystal models can be made to represent the more complex ice crystals shown in Figure 1(a) – (b) by randomizing them through surface roughness, distortions or air/aerosol inclusions and these randomizations can profoundly alter their phase function properties as shown in Figure 2. The figure shows that by distorting [14] single hexagonal ice columns or plates optical features such as the 22^o and 46^o halos can be made to significantly reduce or disappear and that the phase function of the distorted hexagonal columns and plates appears similar to the inhomogeneous hexagonal monocrystal (IHM). The IHM model is a single ice crystal hexagonal column with spherical air bubble and aerosol inclusions [30]. Therefore, by randomizing ice crystals in some way (surface roughness and distortion have a similar impact on the phase function) phase functions can be made to appear featureless around the halo regions and relatively smooth.

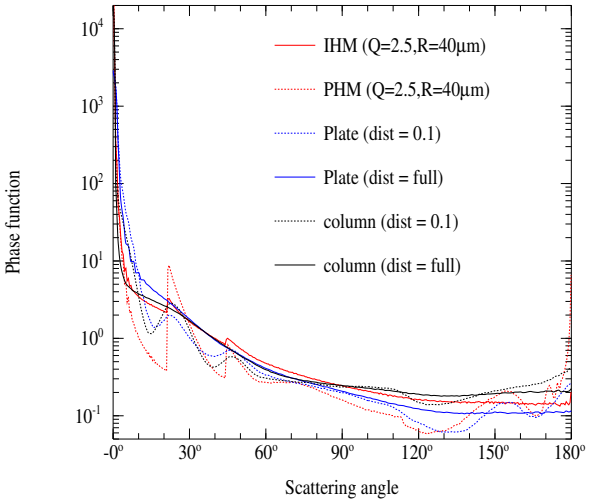

Figure 2: The phase function plotted as a function of scattering angle for a variety of single ice crystal models. The IHM of aspect ratio (Q) = 2 and width (R) = 40 μm is represented by the red line. The pristine hexagonal column (PHM) of the same aspect ratio and width is represented by the dotted red line. The hexagonal ice plate assuming a distortion of 0.1 and 0.4 (full) is represented by the dashed and full blue line, respectively. The hexagonal ice column assuming a distortion of 0.1 and 0.4 is represented by the dashed and full black line, respectively. From Ref. [30].

The question is how well do these single or randomized ice crystal models represent actual cirrus phase function properties ? The answer to this question is illustrated by Figure 3. The figure shows aircraft-based multi-angular radiometric 0.87 μm data between the scattering angles of 20° to about 125° obtained below semi-transparent cirrus [31]. The figure shows that single ice crystal models as represented by hexagonal ice columns, bullet-rosettes and ice aggregates with both small and large maximum dimensions do not represent the scattering phase function of cirrus well. However, the other two phase functions (a laboratory phase function known as the VPP [32] representing an ensemble collection of ice crystals and the analytic phase function [31]) better represent the measured cirrus phase function. The analytic phase function is a linear piecewise parameterization of the Henyey-Greenstein phase function generated by assuming some value of the asymmetry parameter and is modelled on the VPP phase function. Moreover, the total optical depth (column integrated vertical extinction), τ, predicted by each of the models is shown on the left hand-side of the figure and the mean experimental value for τ was found to be 0.75 ± 0.08. Again the phase functions representing an ensemble of ice crystals best fit the measured optical depth. Moreover, Ref. [33] finds that an ice crystal ensemble represents linear polarization measurements better than single ice crystal models such as hexagonal ice columns or hexagonal ice plates.

In terms of representing the bulk and microphysical properties of cirrus Ref. [34] found that an ice crystal ensemble model composed of droxtals, pristine hexagonal ice columns and plates, hollow columns, bullet-rosettes and ice aggregates predicted cirrus *in situ* measured ice water content (IWC) and median mass diameter better than single ice crystal models: the *in situ* measurements were obtained from a number of field campaigns covering the midlatitudes and tropics. Currently, the available aircraft-based radiometric and satellite-based evidence [35] suggests that cirrus is better represented by phase functions which are relatively featureless and flat at backscattering angles, and that ensembles of ice crystals more accurately predict IWC and cirrus microphysical properties. Further evidence for this is presented in the next section.

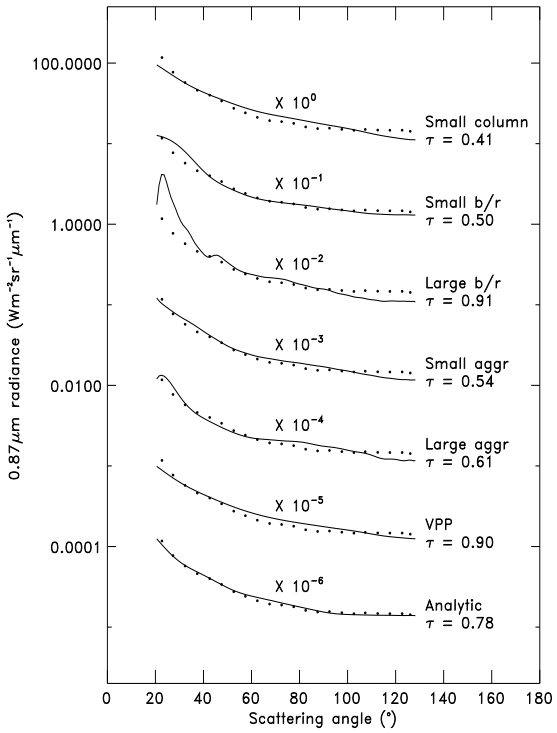

Figure 3: The measured transmitted 0.87 μm radiance plotted as a function of scattering angle. The bold dots represent the measurements. The term b/r is the bullet-rosette and aggr is the hexagonal ice aggregate described in [28]. From Ref. [31].

3 An ensemble ice crystal model: Tests against *in situ* and satellite measurements

In the previous section the cirrus scattering and bulk/microphysical properties were separated though in this section it is shown how an ensemble model of cirrus can be combined with a parameterized particle size distribution (PSD) to predict both the scattering and bulk/microphysical properties. Given the array of space-based satellite sensors that measure the radiative and hydrological contributions of cirrus it is important to unify bulk and microphysical properties with scattering predictions in a consistent manner. An ensemble cirrus model that combines cirrus PSDs with predictions of cirrus bulk and scattering properties in a self-consistent manner is described in [36]. This ensemble cirrus model is shown in Figure 4.

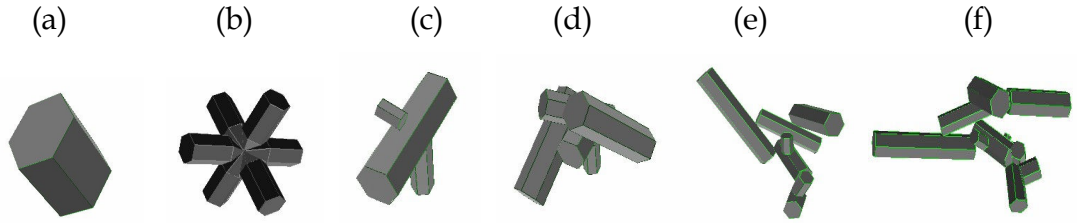

Figure 4: The ensemble model of cirrus (a) simple hexagonal ice column of aspect ratio unity (b) six-branched bullet rosette (c), (d), (e), and (f) three, five, eight and ten branched aggregates, respectively. From Ref. [36].

The figure shows that the ensemble model consists of simple hexagonal ice columns, representing the smallest ice crystals in the PSD, and six-branched bullet-rosettes. As the ice crystal size increases aggregates of hexagonal ice columns are formed by arbitrarily attaching other hexagonal elements until a chain of ten hexagonal elements is constructed; this representing the largest ice crystals in the PSD. The PSD function is generated using the parametrization described in [37], which links the IWC and cloud

temperature to a PSD. In the sub-sections that follow the ensemble model predictions of cirrus bulk/microphysical and intensity/polarization properties are tested against *in situ* and satellite measurements, respectively. The origin of the *in situ* measurements is described in [21] and the satellite intensity and polarization measurements obtained from the Polarization and Directionality of the Earth's Reflectances (POLDER) instrument are described in [36].

3.1 Testing the ensemble model against *in situ* measurements

The *in situ* measurements of IWC and volume extinction coefficient were obtained from the SPEC CPI probe during the CAESAR campaign of flying in semi-transparent cirrus around the UK [21]. The measurement uncertainties are estimated to be ±50% due to errors in sampling volume, shattering of ice crystal on the inlet of the probe and ice crystal orientation. The *in situ* volume extinction coefficient was estimated from twice the area density since the ice crystals were sufficiently large for the geometric optics approximation to be valid. The *in situ* total τ could then be estimated from the column integrated volume extinction coefficient. The ensemble model prediction of the volume extinction coefficient and τ could be estimated in a similar way given the PSD [37]. The ensemble model prediction of IWC was obtained from the integrated geometric ice crystal volume over the PSD, assuming a constant density, ρ = 0.92 gcm^{-3} and a varying density with respect to size, D, of the form, $\rho \sim D^{-1.1}$ [38]. The assumption of a varying density with respect to size was applied to ice crystals whose maximum dimensions were greater than 100 μm and this variation in density may take into account the changing ice crystal volume due to aggregation. Shown in Figure 5 are examples of the ensemble model predictions of (a) IWC and (b) volume extinction coefficient. For reasons of brevity other examples cannot be shown but the behaviour of the ensemble model for all other cases is similar [21].

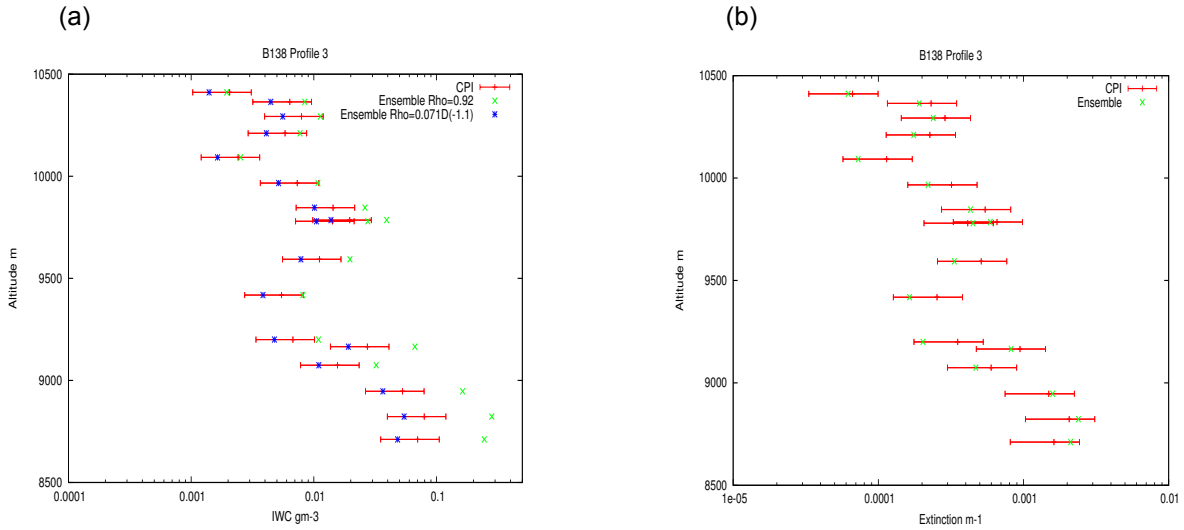

Figure 5: Examples of the ensemble models prediction of (a) IWC with the green and blue asterisks representing a constant and varying density with respect to size, respectively and (b) volume extinction coefficient represented by the green asterisks. The error bars represent the SPEC CPI measurements. From Ref. [21].

The figure shows that in the case of IWC the ensemble model can predict the CPI measurements within the experimental uncertainty for all altitudes if a varying density is assumed. Towards the lower altitudes less than about 9500 m the ensemble model assuming a constant density over predicts the IWC possibly because the larger ice crystals existing towards the bottom of the cloud may be more spatial and/or are air included. In the case of the volume extinction coefficient the ensemble model predicts the CPI measurements to generally well within the experimental uncertainties. Though in some cases the

predictions are towards the lower end of the experimental uncertainties this could be due to ice crystal shattering or an under prediction of the ice crystal number density by the parameterized PSD. These uncertainties are due to the inability of present *in situ* measurement probes/techniques to characterize ice crystals less than 100 μm in size. From Figure 5 (b) the in situ τ was estimated to be 1.05 ± 0.52 this compares to an ensemble prediction of 0.99. The total optical depth is a very important radiative property to predict if the impact of cirrus in climate change simulations is to be correctly quantified. The next sub-section examines if this ensemble model can predict the correct cirrus total and polarized solar reflectance.

3.2 Ensemble model against total reflectance and polarized reflectance measurements

In this sub-section the global 25th June 2003 POLDER measurements of total and polarized solar reflectance described in [36] are used to test the ensemble models prediction of the scattering matrix. Each of the ice crystals shown in Figure 4 is assumed to be randomly oriented and the scattering matrix from each is computed under the assumption of the geometric optics approximation [14]. In [36] it was shown that the ensemble model, if randomized using distortions and spherical air bubble inclusions, could replicate the analytic phase function shown in Figure 2. The two randomizations were applied to each ice crystal member of the ensemble and the resulting scattering matrix integrated over the PSD. The integrated ensemble model scattering matrix could then be used to simulate the POLDER total and polarized reflectances, the results of which are shown in Figure 6 (a) and (b), respectively.

(a) (b)

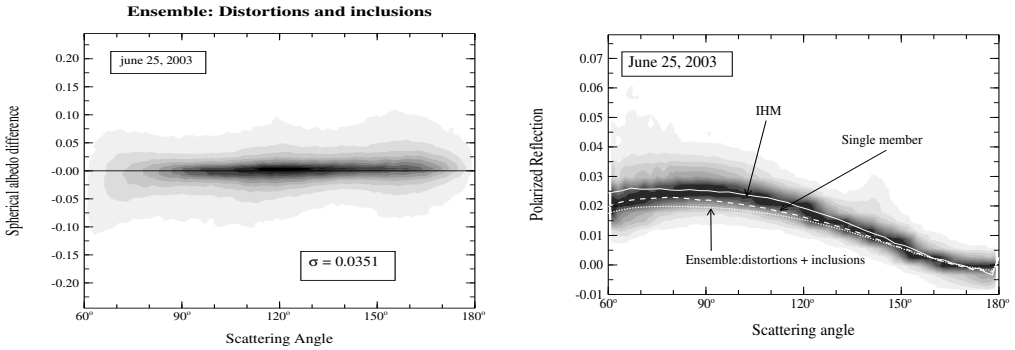

Figure 6: (a) The normalized point density of directions plotted against the scattering angle showing differences between the mean spherical albedo and the directionally averaged spherical albedo assuming the ensemble model randomized using distortions and spherical air inclusions. The mean residual spherical albedo, $\sigma = 0.0351$. (b) The polarized reflectance plotted against scattering angle showing results for the ensemble model (dotted line), single member of the ensemble (three-branched aggregate) represented by the dashed line and the IHM model (full line). From Ref. [36]

The figure shows that the ensemble model under the assumption of two randomizations is well able to predict the total solar reflectance without bias. However, in the case of the polarized reflectance the ensemble model does not follow the polarization gradient as well as the other two models, which are single ice crystal models. In the case of polarization this result is not surprising since polarization originates from towards the cloud-top and here the ice crystals are more likely to be pristine crystals rather than aggregated. However, the opposite would be true in the case of total solar reflectance. This difference between total and polarized reflectance illustrates the potential in using intensity and polarized intensity to discriminate between vertically homogeneous and inhomogeneous cirrus.

The two single ice crystal models shown in Figure 6 (b) behave, in terms of polarization between the scattering angles of 60^o to 180^o, in a similar way. Yet these two ice crystal models are geometrically very different. In order to discriminate ice crystal models further polarization measurements obtained at scattering angles much less than 60^o are required as shown by Figure 7.

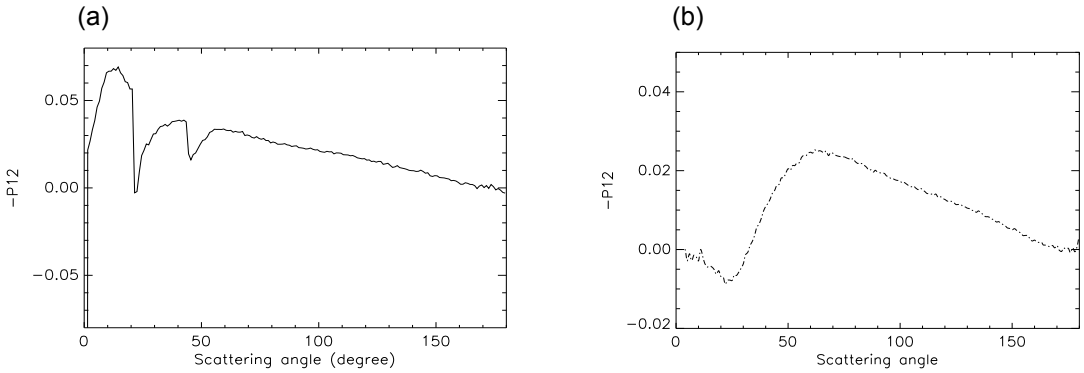

Figure 7: The –P12 element of the scattering matrix plotted as a function of scattering angle for (a) IHM and (b) the three-branched member of the ensemble under the assumed randomizations of distortions and spherical air bubble inclusions. From Ref. [36].

Figure 7 shows distinct predictions between the two models in polarization at scattering angles less than about 50^{o}. Polarization measurements at such scattering angles are required if ice crystal models are to be further constrained.

4 Conclusion

Given the array of space-based instruments that are now able to measure the contribution of cirrus to the earth-atmosphere radiation balance and to the hydrological cycle it is now important to devise cirrus ice crystal models that are able to replicate observed bulk and microphysical properties such as the IWC and volume extinction coefficient. These two parameters are fundamental to radiative transfer through cirrus; this then provides a link between the predicted cirrus bulk and microphysical properties to the general scattering matrix. Single ice crystal models are inadequate for this purpose as it has been demonstrated that they are poor at predicting the bulk cirrus properties and also their predicted phase functions do not generally describe the cirrus scattering phase function as shown by aircraft-based measurements. It is important to represent the variability of ice crystal shape through an ensemble model of cirrus which through some prior PSD can predict the bulk and microphysical as well as the general scattering properties of cirrus, thus providing a self-consistent treatment. One way forward has been presented in this review in which it was shown that such an ensemble could re-produce to within experimental uncertainty both the bulk and microphysical properties of a midlatitude cirrus case. It was also shown that the ensemble could re-produce on a global scale the general cirrus scattering properties through the total solar reflectance. A simple member of the ensemble was also shown to adequately describe the linear polarized reflectance.

However, such a model that can predict the bulk and microphysical properties to within the experimental uncertainty needs to be further constrained. This is because the experimental uncertainty is itself very large $\pm$50% due to uncertainties in the mass-dimensional relationships which are used to convert size spectra to an IWC, shattering on the inlet of the probe giving false number concentrations of the abundance of small ice crystals, uncertainties in the sampling volume of the probes, and the orientation of ice crystals. Clearly, if cirrus models are to be further constrained such uncertainties need to be eliminated by measuring directly the IWC and volume extinction coefficient without the need to assume mass-dimensional relationships or area-dimensional relationships. Better cloud probes need to be designed so that ice crystal shattering on the inlet of the probe can be removed, moreover, the shapes of such ice crystals would also need to be categorized.

Regarding space-based, ground-based and aircraft-based measurements there is a clear need for simultaneous radiometric measurements covering the electromagnetic spectrum of importance to the earth-atmosphere radiation balance and hydrological cycle. In order to achieve this, if coupled with new *in situ* probes that eliminate the above problems, then further field campaigns are required especially in the tropical and arctic regions where combined *in situ* and radiometric information is sparse. The importance of polarization measurements have also been highlighted in this review but in order to constrain

microphysical models further such measurements are needed at low scattering angles, especially around the halo regions. Polarization combined with intensity measurements could also provide information on the inhomogeneity of cirrus on a global scale.

Clearly, there is much more to be done if the representation of cirrus in general circulation models is to be further improved since these clouds can be a natural greenhouse source; only by improving the understanding of cirrus light scattering properties can confidence in climate change simulations be increased.

Acknowledgments

The University of Manchester is thanked for the provision of the CPI data, in particular Dr P. Connolly and Hazel Jones. The FAAM facility is also thanked for the provision of flight data during the CAESAR campaign. The University of Lille is thanked for the provision of the POLDER data.

References

[1] D. P. Wylie and W. P.Menzel, “Eight years of cloud statistics using HIRS.” J. Climate, **12**, 170 184 (1999).

[2] C. J. Stubenrauch, A. Chédin, G. Rädel, N. A. Scott, and S. Serrar, S, “Cloud properties and their seasonal and diurnal variability from TOVS Path-B.” J. Climate, **19**, 5531-5553 (2006).

[3] J. M. Edwards, S. Havemann, J.-C.Thelen, and A. J. Baran, “A new parametrization for the radiative properties of ice crystals: Comparison with existing schemes and impact in a GCM.” Atmos. Res., **83**, 19-35 (2007).

[4] L. Donner, C. J. Seman, B. J. Soden, R. S. Hemler, J. C. Warren, J. Strom, and K. N. Liou, “Large-scale ice clouds in the GFDL SKYHI general circulation model.” J. Geophys. Res. **102**, 21745-21768 (1997)

[5] J. E. Kristjánsson, J. M. Edwards, and D. L. Mitchell, “The impact of a new scheme for the optical properties of ice crystals on the climate of two GCMs.” J. Geophys. Res. **105**, 10063-10079 (2000).

[6] M. T. Stoelinga, J. D. Locatelli, and C. P. Woods, “The occurrence of ‘irregular’ ice particles in stratiform clouds.” J. Atmos. Sci., **64**, 2740 – 2750 (2007).

[7] A. J. Heymsfield, and L. M. Miloshevich, “Parametrizations for the cross-sectional area and extinction of cirrus and stratiform ice cloud particles.” J. Atmos. Sci. **60**, 936-956 (2003).

[8] A. Korolov, G. A. Isaac, and J. Hallett, “Ice particle habits in stratiform clouds,” Q. J. R. Meteorol. Soc. **126**, 2873-2902 (2000).

[9] G. M. McFarquhar, and A. J. Heymsfield, “Microphysical characteristics of three anvils sampled during the central equatorial Pacific experiment.” J. Atmos. Sci., **53**, 2401-2423 (1996).

[10] A. J. Baran, “On the scattering and absorption properties of cirrus cloud.” Jour. Quantit. Spectrosc and Radiat. Trans., 89, 17-36 (2004).

[11] S. Havemann, A. J. Baran, and J. M. Edwards, “Implementation of the T-matrix method on a massively parallel machine: a comparison of hexagonal ice cylinder single-scattering properties using the T-matrix and improved geometric optics methods”. J. Quant. Spectrosc. Radiat. Trans**, 79 80**, 707-720 (2003).

[12] P. Yang, K. N. Liou, M. I. Mishchenko, B. C. Gao, “Efficient finite-difference time-domain scheme for light scattering by dielectric particles: application to aerosols”, Appl. Opt. **39**, 3727-3737 (2000).

[13] P. Yang, and K. N. Liou, "Geometric-optics-integral-equation method for light scattering by nonspherical ice crystals" Appl. Opt. **35**, 6568-6584 (1996).

[14] A. Macke, J. Mueller and E. Raschke, "Single-scattering properties of atmospheric ice crystals", J. Atmos. Sci, **53**, 2813-2825 (1996).

[15] K. N. Liou and Y. Takano, "Light scattering by nonspherical particles: Remote sensing and climatic implications." Atmos. Res., **31**, 271-298 (1994).

[16] G. L. Stephens, D. G. Vane, R. J. Boain, G. G. Mace, K. Sassen, Z. E. Wang, A. J. Illingworth, E. J. O'Connor, W. B. Rossow, S. L. Durden, S. D. Miller, R. T. Austin, A. Benedetti, C. Mitrescu, "The cloudsat mission and the a-train – A new dimension of space-based observations of clouds and precipitation." Bull. Amer. Met. Soc., **83**, 1771-1790 (2002)."

[17] H. M. Cho, P. Yang, G. W. Kattawar, S. L. Nasiri SL, Y. X. Hu, P. Minnis, C. Trepte, D. Winker, " Depolarization ratio and attenuated backscatter for nine cloud types: Analyses based on collocated CALIPSO lidar and MODIS measurements." Optics Express, **16**, 3931-3948 (2008).

[18] M. Doutriaux-Boucher, J.-C. Buriez, G. Brogniez, L.-C. Labonnote, and A. J. Baran, "Sensitivity of retrieved POLDER directional cloud optical thickness to various ice particle models," Geophys. Res. Lett, **27**, 109-112 (2000).

[19] S. F. Iacobellis, G. M. McFarquhar, D. L. Mitchell, R. C. J. Somerville, "The sensitivity of radiative fluxes to parameterized cloud microphysics." J. Climate, **16**, 2979 – 2996.

[20] R. P. Lawson, B. A. Baker, C. G. Schmitt, and T. L. Jensen, "An overview of microphysical properties of Arctic clouds observed in May and July during FIRE.ACE." J. Geophys. Res., **106**, 14989-15014 (2001).

[21] A. J. Baran, P. J. Connolly, and C. Lee, "Testing an ensemble model of cirrus ice crystals using in situ measurements of ice water content, volume extinction coefficient and ice crystal effective dimension obtained in the midlatitudes." Submitted to the Quart. Jour. Roy. Meteor. Soc. (2008).

[22] G. M. McFarquhar, A. J. Heymsfield, A. Macke, J. Iaquinta, and S. M. Aulenbach, "Use of observedice crystal sizes and shapes to calculate the mean-scattering properties and multispecrtral radiance." CEPEX April 4 1993 case study, J. Geophy. Res. **104**, 31763-31779 (1999).

[23] G. M. McFarquhar, P. Yang, A. Macke and A. J. Baran, "A new parameterization of single-scattering solar radiative properties for tropical anvils using observed ice crystal size and shape distributions." J. Atmos. Sci., **59**, 2458–2478 (2002).

[24] P. Yang, B. A. Baum, A. J. Heymsfield, Y. X. Hu, H.-L. Huang, S.-C. Tsay, and S. Ackerman, "Single-scattering properties of droxtals." J. Quant. Spectrosc. Radiat. Transfer **79-80**, 1159-1180 (2003).

[25] T. Nousiainen and G. M. McFarquhar, "Light scattering by quasi-spherical ice crystals", J. Atmos. Sci, **61**, 2229 – 2248 (2004).

[26] Z. Ulanowski, E. Hesse, P. H. Kaye and A. J. Baran, "Light scattering by complex ice-analogue crystals." J. Quant. Spectr. Rad. Transfer, 100, 382-392 (2006).

[27] D. L. Mitchell, P. Rasch, D. Ivanova, G. McFarquhar, T. Nousiainen, "Impact of small ice crystalassumptions on ice sedimentation rates in cirrus clouds and GCM simulations", Geophys. Res. Lett. 35, L09806 (2008).

[28] P. Yang, and K. N. Liou, "Single-scattering properties of complex ice crystals in terrestrial atmosphere", Contrib. Atmos. Phys. **71**, 223-248 (1998).

[29] A. J. Baran, and L. C. Labonnote, “On the reflection and polarization properties of ice cloud.” J.Quant. Spectrosc. Radiat. Transfer **100**, 41-54 (2006).

[30] C.-Labonnote, L., G. Brogniez, F. Parol, P. François, F. Thieuleux, and A. J. Baran, “Using multi-angular polarised measurements from POLDER3/PARASOL for ice cloud microphysics purpose.” International Symposium of "A-Train Lille 2007,” France, 22-25 October (2007).

[31] A. J. Baran, P. N. Francis, L.-C. Labonnote, and M. Doutriaux-Boucher, “A scattering phasefunction for ice cloud: Tests of applicability using aircraft and satellite multi-angle multi-wavelengthradiance measurements of cirrus.” Quart. J. Roy. Meteorol. Soc., **127**, 2395-2416 (2001).

[32] O. A. Volkovitskiy, L. N. Pavlova, and A. G. Petrushin, “Scattering of light by ice crystals.” Atmos.Ocean. Phys., **16**, 90-102 (1980).

[33] K. N. Liou, *An introduction to atmospheric radiation* (Academic Press, Oxford, 2002).

[34] B. A. Baum, A. J. Heymsfield, P. Yang P., and S. T. Bedka, “Bulk scattering properties for theremote sensing of ice clouds. Part I. Microphysical data and models.” J. App. Met. **44**, 1885-1895 (2005).

[35] W. H. Knap, L.-C. Labonnote, G. Brogniez, and P. Stammes, “Modeling total and polarized reflectances of ice clouds: evaluation by means of POLDER and ATSR-2 measurements.” Appl. Opt., **44**, 4060-4073 (2005).

[36] A. J. Baran, and L.-C. Labonnote, “A self-consistent scattering model for cirrus. I: The solar region.” Quart. Jour. Roy. Metsoc. **133**, 1899-1912 (2007).

[37] P. R. Field, A. J. Heymsfield, and A. Bansemer, “Snow size distribution parameterization for midlatitude and tropical ice cloud.” J. Atmos. Sci. **64**, 4346-4365 (2007).

[38] S. Y. Matrosov, “Retrievals of vertical profiles of ice cloud microphysics from radar and IR measurements using tuned regressions between reflectivity and cloud parameters.” J. Geophys. Res. **104**, 16741-16753 (1999).

Specular component of light scattered by preferably oriented nonspherical particles

Anatoli Borovoi,[1] Natalia Kustova,[1] and Ariel Cohen [2]

[1] *Institute of Atmospheric Optics, pr. Akademicheski 1, Tomsk 634055, Russia*
tel: +07-3822-492864, fax: +07-3822-492086, e-mail: borovoi@iao.ru
[2] *Hebrew University of Jerusalem, Safra Campus 1, Jerusalem 91904, Israel,e-mail:cariel@cc.huji.ac.il*

Abstract

Bidirectional phase function for a fluttering plate is studied. This function is used for interpretation of light pillars watched in the atmosphere. Possibilities to retrieve particle parameters from these patterns are discussed.

1 Introduction

Appearance of a specular component in scattered radiation is a general phenomenon that occurs in different fields of optics. Thus, light scattered by a rough surface (for example, by a matt top of a table) reveals often a distinct specular component because the surface resembles a dull mirror. This is the mirror that creates the specular component. A rippling water surface often produces well-known glitter paths from the sun and the moon that correspond to the specular component, too. In the atmosphere, sun and moon pillars watched on the sky are the specular components created by ice crystals of cirrus clouds when they are preferably oriented in the horizontal plane [1]. Analogously, horizontally oriented snowflakes in the near-ground layer produce light pillars seen over ground-based sources of light [2], and so on.

All properties of the specular component are governed by simple and evident laws of geometric optics. Therefore, the specular component is connected with microphysical parameters of a scattering medium by rather simple equations. And vice versa, because of simplicity of these equations, the specular component proves to be a promising tool for retrieving certain microphysical parameters of scattering media.

In particular, in the atmospheric optics, there is an urgent problem to know radiative properties of ice crystal particles when they reveal their preferably horizontal orientation (e.g., [3]). These radiative properties are strongly dependent on oscillation of particle orientations near the horizontal plane that is called flutter. However, both theoretical and experimental data concerning the flutter are very poor. Recently, the flutter has been studied experimentally by a rather complicated and non-efficient technique of scanning polarization lidar [4, 5]. In this contribution, we show that the flutter can be studied by more efficient and obvious methods based on the specular component.

2 Phase function of a fluttering plate

In the case of ice crystal particles preferably oriented in the horizontal plane, the specular component is created by light reflection from the lower horizontally oriented facets of the crystals. A contribution of the upper horizontally oriented facets can be easy taken into account, too. Here we neglect this contribution for brevity. Thus, the problem is reduced to calculation of the phase function (or scattering matrix) for a reflecting plate with fluttering orientation. As far as we know, this problem has not yet been considered by anyone even in the geometric optics approximation. In this section, we fill in this gap.

Assume a plate of the area of *s* is fluttering near the horizon. Denote its normal by the unit vector $\mathbf{N}$. Then the flutter is determined by the probability density function $p(\mathbf{N})$ with the normalization $\int p(\mathbf{N})d\mathbf{N} = 1$. Intensity of scattered (i.e. reflected within geometric optics) light at a fixed orientation of the plate is described by the equations:

$$I(\mathbf{n} \mid \mathbf{N}, \mathbf{m}) = (\mathbf{m} * \mathbf{N})R(\mathbf{m}, \mathbf{N})s\delta(\mathbf{n} - \mathbf{n}') \qquad (1)$$

$$\mathbf{n}' = \mathbf{m} - 2(\mathbf{m} * \mathbf{N})\mathbf{N} \qquad (2)$$

where the unit vectors **m** and **n** indicate the incident and scattering directions, respectively; the asterisk denotes a scalar product; *R* is the reflection coefficient that can be easy found for a given polarization of incident light due to the Fresnel equations; δ is the Dirac delta-function; and Eq.(2) determines the reflecting or scattering direction. The function **n′**(**N**) of Eq. (2) makes a mapping of particle orientations **N** into scattering directions **n′** and the function **N**(**n′**) corresponds to the inverse mapping.. Then an average of Eq. (1) with the weight function *p*(**N**) yields explicitly the desired differential cross-section of the fluttering plate

$$< I(\mathbf{n} \mid \mathbf{m}) >= \int I(\mathbf{n} \mid \mathbf{N}, \mathbf{m}) p(\mathbf{N}) d\mathbf{N} = (\mathbf{m} * \mathbf{N}(\mathbf{n})) R(\mathbf{m}, \mathbf{N}(\mathbf{n})) sp(\mathbf{N}(\mathbf{n})) \left(D\mathbf{N} / D\mathbf{n} \right) \qquad (3)$$

Here the factor (*D***N**/*D***n**) is the Jacobian of the mapping **N**(**n**) that is known analytically. The normalized quantity $< I(\mathbf{n} \mid \mathbf{m}) > / \int < I(\mathbf{n} \mid \mathbf{m}) > d\mathbf{n}$ is called the bidirectional phase function.

The flutter considered means small deviations of particle normals **N** from the normal $\mathbf{N}_0$ directed to the zenith. Therefore the scattered light of Eq. (3) at a fixed incident direction **m** is a finite spot localized near the center $\mathbf{n}_0 = \mathbf{n}'(\mathbf{N}_0)$. It is natural to assume the flutter having axial symmetry about the vertical, i.e. the distribution *p*(**N**) is reduced to the function *P*(β) of the azimuth angle $\beta = \arccos(\mathbf{N}_0 * \mathbf{N})$ with the normalization $\int_0^{\pi} P(\beta) \sin \beta d\beta = 1/2\pi$ where the tilts β run in the interval [0, *F*], *F* is the maximum flutter angle. In this case, for the vertical illumination $\mathbf{m} = \mathbf{N}_0$, the scattered spot $<I(\mathbf{n})>$ is a circle with the zenith radius Δθ = 2*F*. If the incident angle $\theta_0 = \arccos(\mathbf{N}_0 * \mathbf{m})$ increases, the zenith size of the spot relative to its center $\mathbf{n}_0$ remains the same Δθ = 2*F* while its azimuth size is compressed as $\Delta\varphi \approx (\sin 2F) \cos\theta_0$. Fig. 1 illustrates these regularities.

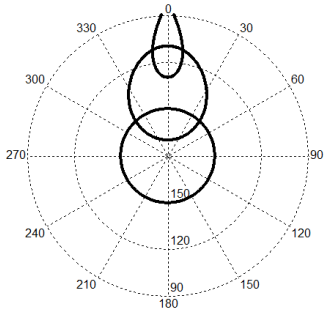

Figure 1: Contours of the phase function on the scattering direction hemisphere at the maximum flutter angle of *F* = 15º and the incident angles of θ_0 = 0º, 40º, and 80º

In the case of the vertical illumination $\mathbf{m} = \mathbf{N}_0$, Eq. (3) is simplified as

$$< I(\theta) >= const R(\theta/2) P(\theta/2) \quad \text{where } \theta = \pi - \arccos(\mathbf{N}_0 * \mathbf{n}) \qquad (4)$$

In Eq. (4), the angular structure of the scattered spot is directly expressed in terms of the probability density function for flutter *P*(β).

3. Light pillars in the sky and over the ground.

Light pillars appearing in the sky and over ground-based light sources can be effectively described by the phase function considered above. Note that these phenomena of specular scattering were discussed by a majority of previous authors [1, 2] directly on the base of geometric optics. Such a direct approach is not convenient for an analytical study of the phenomena. In this presentation, we use the phase function

conception well-known in optics of scattering media that allows us to work out a simple and strict theory of specular scattering.

The light pillars seen in the sky correspond to light emitted by either the sun or the moon and scattered by ice crystal of cirrus when the ice crystals occur to be horizontally oriented. In this case, both a light source and an observer are positioned at practically infinity from scattering particles. Therefore, it is just the phase function of the previous section at a fixed incident direction that is watched in the sky. This conclusion leads to an evident proposal to retrieve the flutter probability distribution $P(\beta)$ from the light intensity measured along a diameter of the scattered spot due to Eq. (4). For crude estimations, the zenith angular size $\Delta\theta = 2F$ of the scattered spot can be used to find directly the maximum flutter angle F. In the case of slant illumination, when the spot is elongated, the measurements along the longest diameter are the best. Such measurements can be easy managed for ground-based experiments, too. On the contrary to the complicated and hardly reliable technique of scanning polarization lidar used for studying the flutter [4, 5], a continuous light source and a CCD detector [6] can be effectively used for this purpose.

The light pillars appearing over ground-based sources prove to be more complicated for using them for similar inverse problems. Consider light intensity seen by an observer over a ground-based point light source. Assume the source is situated at the origin **O** of a coordinate system where **R** denotes a position of an observer. Then an observer watches the 2D pattern Q(**R**, **Ω**) where **Ω** is observation direction. According to the well-known radiative transfer equation, the ray intensity $Q(\boldsymbol{R}, \boldsymbol{\Omega})$ is the following integral in the single-scattering approximation

$$Q(\mathbf{R},\boldsymbol{\Omega}) = \int_0^\infty I_0 \mid \mathbf{R} - \boldsymbol{\Omega} l \mid^{-2} \exp[-\tau(\mathbf{0}, \mathbf{R} - \boldsymbol{\Omega} l)) - \tau(\mathbf{R} - \boldsymbol{\Omega} l, \mathbf{R})] < I(\boldsymbol{\Omega} \mid (\mathbf{R} - \boldsymbol{\Omega} l) / \mid \mathbf{R} - \boldsymbol{\Omega} l \mid > dl \quad (5)$$

where I_0 is a power of the source, τ (**R**, **R′**) is the optical depth between two points in space, and the main integrand is the differential cross section of Eq. (3). We have calculated the integral numerically and two qualitative conclusions have been obtained. First, transversal profiles of the light patterns are weakly dependent on height where the pillar is observed. This is the reason that the patterns looks like pillars. An example of the calculated pattern Q(**R**, **Ω**) is presented in Fig.2. Second, the angular structure of the pillars is weakly dependent on distance between the source and an observer. Unlike Eq. (4), the patterns Q(**R**, **Ω**) depends on certain integral transformation of the desired flutter probability density $P(\beta)$. Nevertheless, certain possibilities to use the patterns Q(**R**, **Ω**) for the inverse scattering problems exist and they will be discussed.

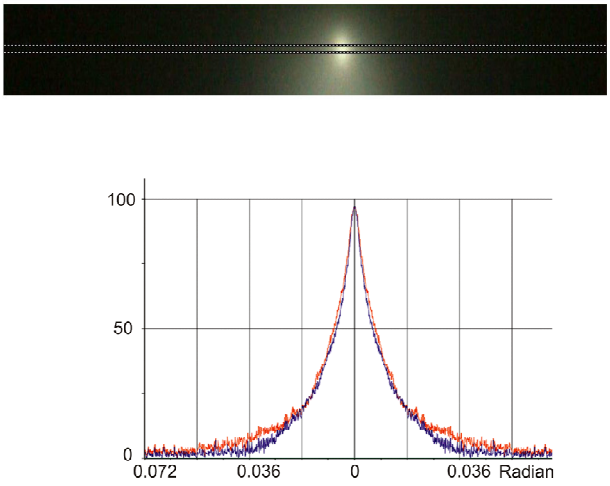

Figure 2: The specular spot and its digitization along diameter in the red (upper) and the blue (lower).

4. Diffraction in the specular component

In practice, diffraction spreads the angular functions of Eqs. (3)-(5) obtained in the geometric optics approximation. If the angular widening is essential, these equations can be generalized by use of the Fraunhofer diffraction equations. Vice versa, this widening can be used for retrieving particle sizes along with their flutter. Such a possibility was realized by us experimentally [6]. Here preferably oriented ice crystals in the atmosphere were illuminated in the vertical direction by a floodlight beam. We prove that the angular radius of the spot is equal approximately to

$$\Delta\theta \approx F + \lambda / D \tag{6}$$

where λ is wavelength and D is the average diameter of the plates. Therefore measurements of the angular width $\Delta\theta$ at two wavelengths allow us to retrieve both the maximum flutter angle F and the average horizontal diameter D. Fig. 2 shows a case where we obtained $F \approx 0.4^{o}$ and $D \approx 17\mu$.

5 Conclusion

We have considered the main properties of the specular component of scattered radiation along with the possibilities to retrieve some parameters of scattering media from the specular component. Though we discussed a particular case of light pillars occurring in the atmosphere, appearance of the specular components is a general physical phenomenon. In particular, the same properties should appear in light reflection from soils and blankets of snow, not saying of light reflection from a rippling water surface, in light scattering by aligned biological structures, and so on

Acknowledgments

This research is supported by the Russian Foundation for Basic Research under the grant 06-05-65141 and by the International Association for the Promotion of Cooperation with Scientists through the New Independent States of the Former Soviet Union (INTAS) under the grant 05-1000008-8024.

References

[1] A.J. Mallmann, J.H. Hock, R.G. Greenler, "Comparison of Sun pillars with light pillars from nearby light sources," Appl. Opt. **37**, 1441-1449 (1998).

[2] K. Sassen, "Polarization and Brewster angle properties of light pillars," JOSA **A4**, 570-580 (1987).

[3] Y.Hu, M. Vaughan, Z. Liu, B. Liu, P. Yang, D. Flittner, B. Hunt, R. Kuehn, J. Huang, D. Wu, S. Rodier, K. Powell, C. Trepte, D. Winker, "The depolarization-attenuated backscatter relation: CALIPSO lidar measurements vs. theory," Opt. Express **15**, 5327-5332 (2007)

[4] V. Noel, G. Roy, L. Bissonnette, H. Chepfer, P. Flamant, "Analysis of lidar measurements of ice clouds at multiple incidence angles," Geophys. Res. Lett. **29**, 014828 (2002)

[5] V. Noel, K. Sassen, "Study of planar ice crystal orientations in ice clouds from scanning polarization lidar observations," J. Appl. Meteorol. **44**, 653-654 (2005)

[6] A. Borovoi, V. Galileiski, A. Morozov, A. Cohen, "Detection of ice crystal particles preferably oriented in the atmosphere by use of the specular component of scattered light," Opt. Express **16**, 7625-7633 (2008)

Application of RTDF to particles with curved surfaces

E. Hesse, D.S. Mc Call, Z. Ulanowski, C. Stopford,
and P.H. Kaye

University of Hertfordshire, Centre for Atmospheric and Instrumentation Research, Hatfield, Hertfordshire, UK.
tel: +44 (0) 1707 286170, fax: +44 1707 284185, e-mail: e.hesse@herts.ac.uk

Abstract

The applicability of RTDF is extended to particles with curved surfaces. This allows tests against *T*-matrix calculations for larger size parameter and modeling of light scattering by more realistic particle shapes, such as ice crystals with rounded edges.

1 Introduction

The importance of ice and mixed-phase clouds to the earth-atmosphere radiation balance and climate is well established. However, despite extensive study, there is still a large uncertainty over the radiative properties of these clouds. This is partly due to inadequate theoretical models of light scattering by the constituent ice crystals of realistic shapes and sizes.

Computations of light scattering properties for non-spheroidal particles based on exact methods like the Separation of Variables (SVM) Method, e.g. [1], *T*-matrix [2,3], Discrete Dipole Approximation (DDA) [4] have upper size parameter limits of applicability, depending on the method and the complexity of particle shape. This leaves a size parameter range that is covered neither by exact methods nor by Geometric Optics (GO). A modified Kirchhoff approximation (MKA) method has been introduced [5] to calculate far fields from classical Geometric Optics (GO) results, which encouraged the development of the Improved GO model [6]. The latter is, however, computationally expensive. For moderate values of the size parameter the Finite Difference Time Domain (FDTD) method can be used [7] but it too, puts severe demands on computational resources. Thus, despite its limitations, Geometric Optics (GO) combined with projected-area diffraction, e.g. [8], is still the most widely used model for moderate to large size parameters. Recently, diffraction on facets was introduced into a ray tracing model (Ray Tracing with Diffraction on Facets, RTDF) [9-11]. This method maintains the flexibility and computational efficiency of GO while producing much improved results. Given the rapid and flexible computation offered by ray-tracing based models, it is possible to create 2D light scattering patterns for even very complex crystals. Such patterns provide much more information than azimuthally averaged scattering data such as a phase function. In contrast to standard GO, the RTDF model can produce such patterns for fixed as well as averaged random orientation. 2D scattering patterns have been correctly predicted by the RTDF model [10], and it is therefore expected to become a suitable tool for particle characterization, in particular since cloud probes now exist that characterize ice particles on the basis of 2D scattering patterns (e.g. [12]). A large proportion of ice crystals have curved as well as planar surface components, e.g. due to the onset of sublimation or melting. Other atmospheric particles, like Saharan dust, are irregular. Their surfaces could be approximated as multifaceted objects. In this paper, the RTDF model is used to model scattering by 'hybrid' particles, the surface of which has both planar and curved components. RTDF phase functions of circular cylinders are compared with *T*-matrix [13], which is an analytical technique, and GO combined with projected area diffraction [8]. The effect of rounded edges on 2D scattering patterns of hexagonal columns is demonstrated.

2 Method and results

The RTDF model combines ray tracing with diffraction on flat facets. The model calculates diffraction using an approximation for the far-field direction of the Poynting vector. The angle of diffraction of a reflected or refracted ray is calculated from the ray's proximity to the facet edges [11]. In the following, curved surfaces will be approximated by arrays of planar facets. As an example, the lateral surface of a circular cylinder will be approximated by a succession of thin stripes. The approximation of a curved surface will improve with the number of plane facet elements, avoiding artificial sharp edges and therefore reducing artefact structures in the angular distribution of scattered light. A decrease of the angle between surface normals of neighbouring facets needs to be accompanied by a reduction of diffraction at these facets. In the following, the far field deflection angle φ_o calculated by RTDF [11] is multiplied by the sine of the angle γ between the normals of the neighbouring facets under consideration, if $\gamma < 90°$.

$$\begin{aligned} \varphi &= \varphi_o \sin\gamma \quad && \forall\ 0 < \gamma < \pi/2 \\ \varphi &= \varphi_o && \forall\ \pi/2 < \gamma < \pi \end{aligned} \tag{1}$$

This ensures that no diffraction takes place between coplanar facets. Full far field diffraction is applied between facets with normals which include an angle of 90° or larger.

The RTDF results are compared with computations using *T*-matrix [13,14], which is an analytical technique, and GO combined with projected area diffraction [8]. Fig. 1 shows randomized phase functions for a circular cylinder with refractive index 1.311 for size parameters $x = 2\pi a_{sph}/\lambda$ equal to 40, 80 and 120, where a_{sph} is the radius of a sphere with equivalent surface area. The aspect ratio of the column $L/2a$ is 1, where L is the column length and $2a$ its diameter.

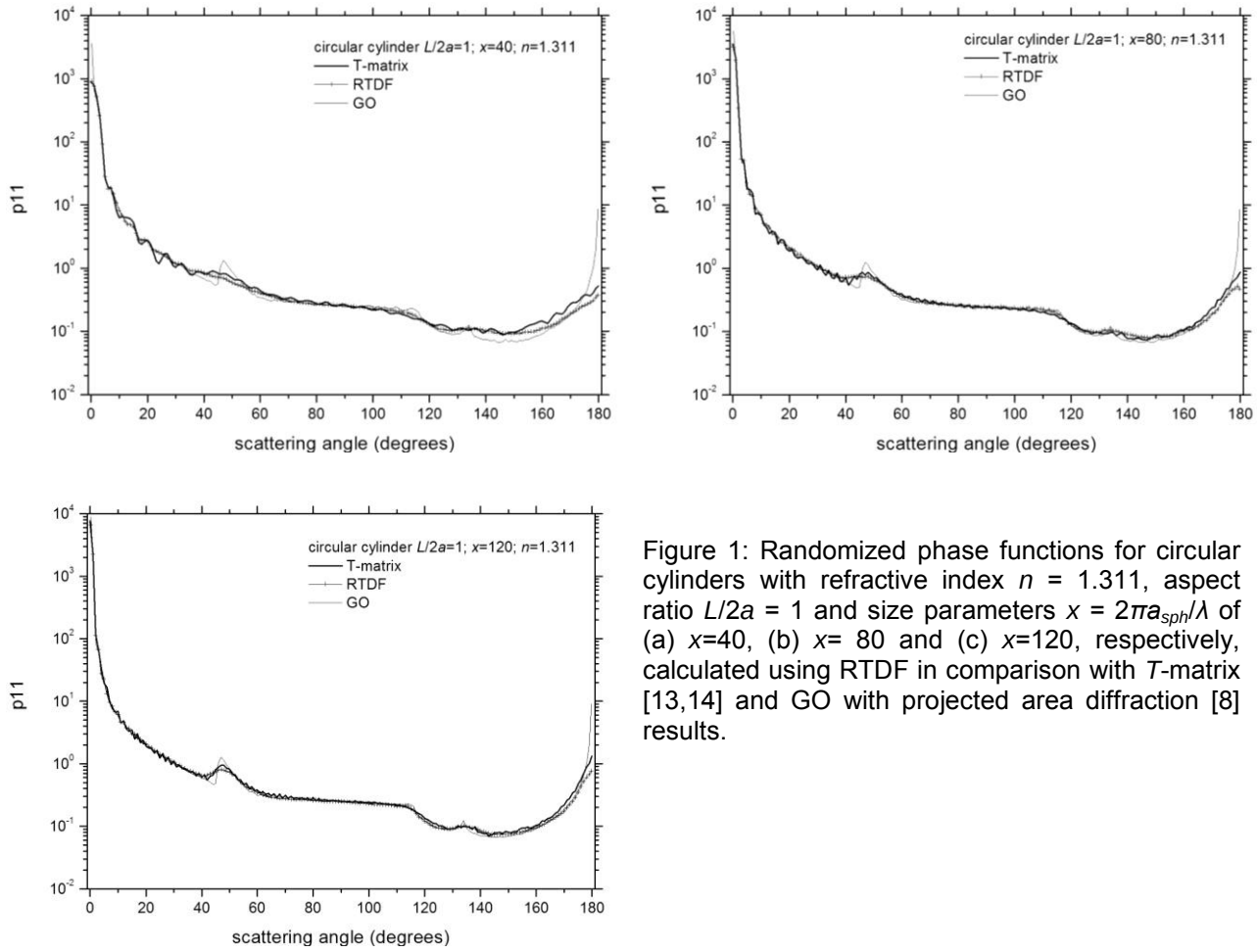

Figure 1: Randomized phase functions for circular cylinders with refractive index n = 1.311, aspect ratio $L/2a$ = 1 and size parameters $x = 2\pi a_{sph}/\lambda$ of (a) x=40, (b) x= 80 and (c) x=120, respectively, calculated using RTDF in comparison with *T*-matrix [13,14] and GO with projected area diffraction [8] results.

The RTDF results approximate the *T*-matrix calculations much better than GO over the whole angular range, and in particular in near exact forward and backscattering, in the halo region, and in the backscattering region. In agreement with the *T*-matrix calculations [13], the RTDF results show that size parameter 40 is too small to produce a pronounced 46° halo. Diffraction features appear slightly wider in RTDF than in the *T*-matrix results due to the approximation of diffraction during internal reflection and refraction steps by far field values (multiplied by sin γ according to eq.(1)), currently implemented in the RTDF model [11].

Fig. 2a shows 2D scattering patterns calculated for a hexagonal column of size parameter $2\pi a/\lambda$, where a is the edge length of the basal facet, aspect ratio $L/2a=3$ and orientation described by Euler angles α=0°, ß=70°, γ=10°, as seen from the perspective of the incident beam. Fig. 2b shows the pattern for the same column but with rounded long edges of the prism facets. The circumscribing circle has a radius of 0.956 a. Rounded edges are approximated by a succession of eight thin facets, each of which covers an angular segment of 1° around the long axis of the particle.

The main feature in both scattering patterns is the bright arc through forward scattering. In Fig. 2a three bright spots are situated on the arc. The central one is essentially due to rays entering through facet 4 and leaving through facet 7 (see Fig. 2a for facet numbers). The two outer ones are due to refraction through 60° prisms, entering through facets 5 and 3 respectively, and leaving through facet 7. The additional bright spots along the arc in Fig. 2b are due to rays passing through edge facets. The double features left and right of the central bright spot are due to rays entering through facet 4 and leaving through the (rounded) edge between facets 6 and 7, and rays entering at the edge between facets 3 and 4 and leaving through facet 7, respectively. The splitting of these spots is due to the approximation of the curved edge by a discrete number of plane facets. In Figs. 2a and b, the central spot on the arc is connected to one bright spot almost directly above, corresponding to refraction through facets 1 and 7. In Fig 2b, an additional bright spot slightly to the left of the previous one is due to rays refracted through facet 1 and the edge between facets 6 and 7. Below each of the three maxima on the arc in Fig. 2a is another intensity maximum due to more complicated ray paths entering through facet 5, 4, and 3, respectively. (The central lower maximum is stronger than the outer ones due to contributions by external reflection from facet 1.) In Fig. 2b we find corresponding maxima to each intensity maximum along the arc caused by ray paths through edge facets.

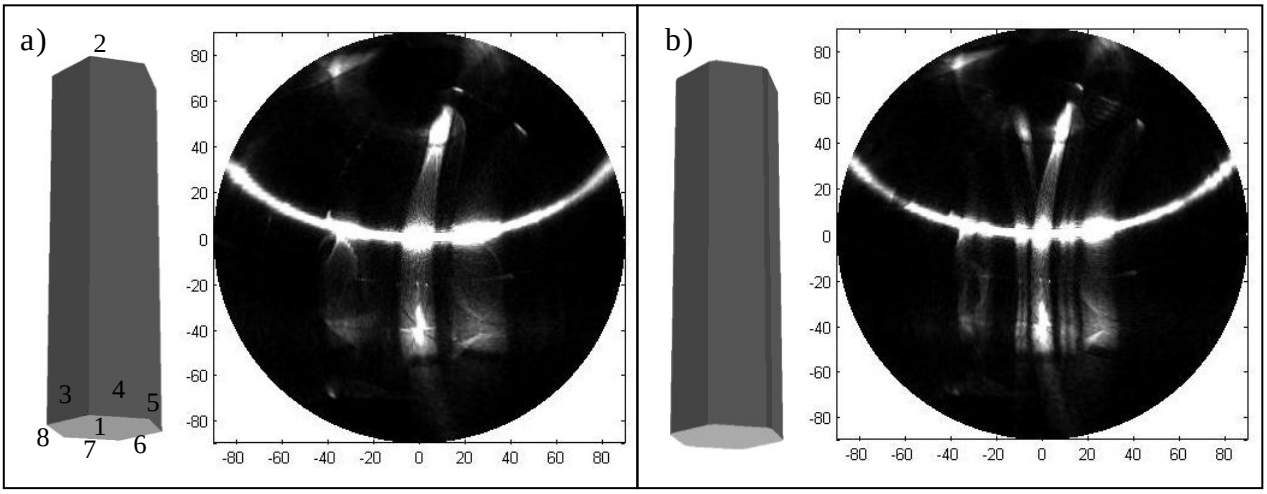

Figure 2: a) Orientation of a hexagonal column (α=0°, ß=70°, γ=10°) from the point of view of the incident light and scattering pattern projected into the forward facing hemisphere; the facets are numbered as shown. b) Schematic and scattering pattern for the same column as in Fig. a), but with rounded long edges of the prism facets.

3 Conclusion

The RTDF model has been developed further to approximate curved surfaces by an array of planar facets and taking into account the angle between surface normals when calculating diffraction during ray-tracing.

The enhanced RTDF model has been tested against *T*-matrix results for circular cylinders. The RTDF results approximate the *T*-matrix calculations much better than GO over the whole angular range, and in particular in near-exact forward and backscattering, and in the halo region. The modification of 2D scattering patterns by rounded edges in comparison to pristine crystals has been demonstrated for a hexagonal column. The expansion of the applicability of the RTDF model towards particles with curved surfaces and 'hybrid particles', which have plane as well as curved surfaces is potentially useful for the calculation of the scattering properties of ice crystals of realistic shapes and comparison with experimental data.

Acknowledgment

This research was supported by the Natural Environment Research Council of the UK.

References

[1] T. Rother, K. Schmidt, S. Havemann, "Light scattering on hexagonal ice columns", J Opt Soc Am A **18**, 2512-2517 (2001).

[2] M.I. Mishchenko, G. Videen, V.A. Babenko, N.G. Khlebtsov, T. Wriedt, "T-matrix theory of electromagnetic scattering by particles and its applications: a comprehensive reference database", J Quantit Spectrosc Radiat Transf **88**, 357-406 (2004).

[3] M.I. Mishchenko, G. Videen, V.A. Babenko, N.G. Khlebtsov, T. Wriedt, "Comprehensive T-matrix reference database: A 2004-06 update", J Quantit Spectrosc Radiat Transf **106**, 304-324 (2007).

[4] M.A. Yurkin, A.G. Hoekstra, "The discrete dipole approximation: An overview and recent developments", J Quantit Spectrosc Radiat Transf **106**, 558-589 (2007).

[5] Muinonen K. "Scattering of light by crystals: a modified Kirchhoff approximation", Appl Opt **28**, 3044-3050 (1989).

[6] P. Yang, K.N. Liou "Geometric-optics-integral equation method for light scattering by nonspherical ice crystals", Appl Opt **35**, 6568-6584 (1996).

[7] P. Yang, K.N. Liou. In: Mishchenko MI, Hovenier JW, Travis LD, editors. *Light scattering by nonspherical particles*, (New York: Academic Press, 1999. p. 173-221).

[8] A. Macke, J. Mueller, E. Raschke, "Single scattering properties of atmospheric ice crystals", J Atmos Sci **53**, 2813-2825 (1996).

[9] E. Hesse, Z. Ulanowski, Scattering from long prisms using ray tracing combined with diffraction on facets. J Quantit Spectrosc Radiat Transf. **79-80C**, 721-732 (2003)

[10] A.J.M. Clarke, E. Hesse, Z. Ulanowski and P.H. Kaye, "A 3D implementation of ray-tracing with diffraction on facets: Verification and a potential application", J Quantit Spectrosc Radiat Transf **100**, 103-114 (2006).

[11] E. Hesse, "Modelling diffraction during ray-tracing using the concept of energy flow lines", J. Quantit. Spectrosc. Radiat. Transf. **109**, 1374–1383 (2008).

[12] P.H. Kaye, E. Hirst, R.S. Greenaway, Z. Ulanowski, E. Hesse, P.J. DeMott, C. Saunders, P. Connely, "Classifying atmospheric light scattering by spatial light scattering", submitted to Optics Letters.

[13] M. I. Mishchenko, A. Macke, "How big should hexagonal ice crystals be to produce halos?", Appl. Opt. **38**, 1626-1629 (1999).

[14] M.I. Mishchenko and L.D. Travis, "Capabilities and limitations of a current FORTRAN implementation of the T-matrix method for randomly oriented, rotationally symmetric scatterers", J. Quant. Spectrosc. Radiat. Transfer **60**, 309-324 (1998).

A light scattering instrument for investigating cloud ice microcrystal morphology

Paul Kaye,[1] Edwin Hirst,[1] Zbigniew Ulanowski,[1] Evelyn Hesse,[1]
Richard Greenaway,[1] and Paul deMott[2]

[1] *University of Hertfordshire, Centre for Atmospheric and Instrumentation Research, Hatfield, Hertfordshire, U.K.*
[2] *Dept. of Atmospheric Science, Colorado State University, Fort Collins, CO 80523-1371, USA.*

tel: +44 (0)1707 284173, fax:+44 (0)1707 284185, e-mail: p.h.kaye@herts.ac.uk

Abstract

We describe an optical scattering instrument designed to assess the shapes and sizes of microscopic atmospheric cloud particles, especially the smallest ice crystals that can profoundly affect cloud processes and radiative properties yet cannot be seen clearly using in situ cloud particle imaging probes. The new instrument captures high-resolution spatial light scattering patterns from individual particles down to ~1 μm in size passing through a laser beam. Its significance lies in the ability of these patterns to provide morphological data for particle sizes well below the optical resolution limits of current probes.

1 Introduction

Clouds influence climate through radiative (scattering and absorption of solar and thermal radiation) and other physical processes that impact on the Earth's radiation budget and alter the magnitude of the climate change. Such cloud feedbacks are a source of significant uncertainty in climate models. Indeed, the Intergovernmental Panel on Climate Change (IPCC 2007) reiterated their view that 'cloud feedbacks remain the largest source of uncertainty' [1]. These uncertainties are especially acute for ice or mixed-phase clouds (the latter comprising both ice crystals and super-cooled droplets) since the radiative properties of such clouds are radically dependent upon the relative abundance of crystals and droplets, their size spectra and, in particular, the diverse crystal shapes present [2]. To be able to understand the radiative transfer properties of ice and mixed phase clouds, therefore, a detailed knowledge of the particles' shapes and sizes is required [3]. This is especially true for the smallest ice crystals (sub-20 μm) for which there is evidence of widespread abundance in cirrus clouds [4,5]. Detailed knowledge of these crystals is also crucial to space-borne remote sensing for the retrieval of cirrus properties [5].

A currently used instrument for capturing in-situ cloud ice crystal morphological data is the Cloud Particle Imager, CPI [6]. This uses pulsed laser illumination to capture real images of cloud particles on a CCD (charge coupled device) camera. It provides extremely valuable data for particles larger than ~25 μm, but below this, diffraction, optical aberrations, and constrained depth-of-field make detailed assessment of particle shape impractical. To gain insight into the shapes and structures of cloud particles smaller than this, an alternative approach must therefore be employed.

2 Spatial light scattering

Any discrete particle will scatter light spatially in a pattern dependent on its size, shape, orientation and internal structure (and on the wavelength and polarization of the incident light). These patterns are not bound by depth-of-field and optical resolution constraints common to imaging systems and can therefore yield data on particle shapes for much smaller particles (~ wavelength of the incident light). We have previously employed this approach in the Small Ice Detector (SID1) [8], a wing-mounted probe that employs six discrete optical detectors arranged around a laser beam to capture the azimuthal distribution of light scattered by individual cloud particles passing through the beam. Since spherical droplets scattered equally to all detectors whilst non-spherical ice crystals produced unequal responses, discrimination between these particle classes can be readily achieved. However, with such limited spatial resolution, the light scattering data can reveal little about each crystal's actual shape and structure.

3 Particle Phase Discriminator, PPD1

In contrast, the new Particle Phase Discriminator instrument (PPD1) is capable of capturing high-resolution spatial light scattering patterns from individual atmospheric ice crystals down to ~1 μm in size. The instrument has been designed for use in either an atmospheric research aircraft, drawing ambient atmospheric air through specially designed fuselage ports, or with laboratory-based cloud simulation chambers. A wing-mounted variant of the instrument has also been developed.

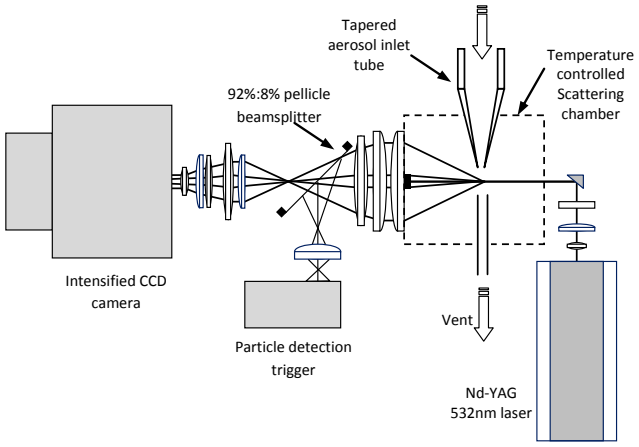

Figure 1. Schematic of PPD1 ice crystal scattering instrument

The instrument, shown schematically in Fig. 1, employs a gated intensified charge coupled device camera (ICCD) to record particle light scattering patterns with single photon sensitivity across 582x582 pixels. In operation, particle-laden sample air flows through a tapered thermally-controlled nozzle at typically 15 l min^{-1} (~80 ms^{-1}), although a much wider range of flow rates can be accommodated. The sample flow has a diameter of ~ 2.5 mm when it exits the nozzle and crosses the beam from a 150 mW 532 nm Nd-YAG laser (Crystalaser Inc., Reno, NV). The beam has an elliptical cross-section of 4.5 mm width and 120 μm depth and is circularly polarized to minimize polarization-dependent variations in the captured particle scattering patterns.

Receiving optics collect the scattered light over scattering angles from 6º to 25º, sufficient to encompass the classic 22º halo scattering from hexagonal ice particles. This light is then split 92:8 by a pellicle beamsplitter, the smaller proportion being directed to a photomultiplier module (Hamamatsu H6779) to allow both estimation of the particle size and to trigger the scattering pattern capture on the ICCD camera (Photek Ltd., East Sussex, UK). The estimated particle size is expressed, as with many conventional optical particle counters (OPCs), as the size of a spherical particle of known refractive index that would produce the same signal as the particle in question. For particles of regular geometric form, such as spherical droplets, ice columns, or platelets, a more accurate determination of particle size may be achieved from theoretical inversion of the captured scattering pattern images (see below).

The scattering pattern acquisition rate is ~20 s^{-1} (50 s^{-1} in burst mode). All other particles passing through the scattering volume are counted and sized (as described above) with the data transmitted at user-defined intervals (typically 100 ms) to a host computer in the form of 16-channel size histograms. Fig. 2 illustrates some of the numerous classes of scattering pattern captured in preliminary experiments at the University of Manchester Icing Cloud Chamber, a 10m fall tube in which ice cloud properties and crystal growth can be studied over temperatures down to -50°C.

The top row shows scattering images from water droplets of increasing size from 3.5μm to 22 μm (determined by comparison with Mie Theory); row 2 illustrates classical scattering from hexagonal ice columns, exhibiting the bright 22º halo spot; row 3 may originate from freezing droplets exhibiting one or more ice facets, as observed experimentally for larger droplets up to ~100 μm by Takahashi and Mori [9]; row 4 corresponds to hexagonal ice platelets; row 5 images exhibit features that they may result from

partially sublimated platelets in which the sharp crystal apices have become rounded.

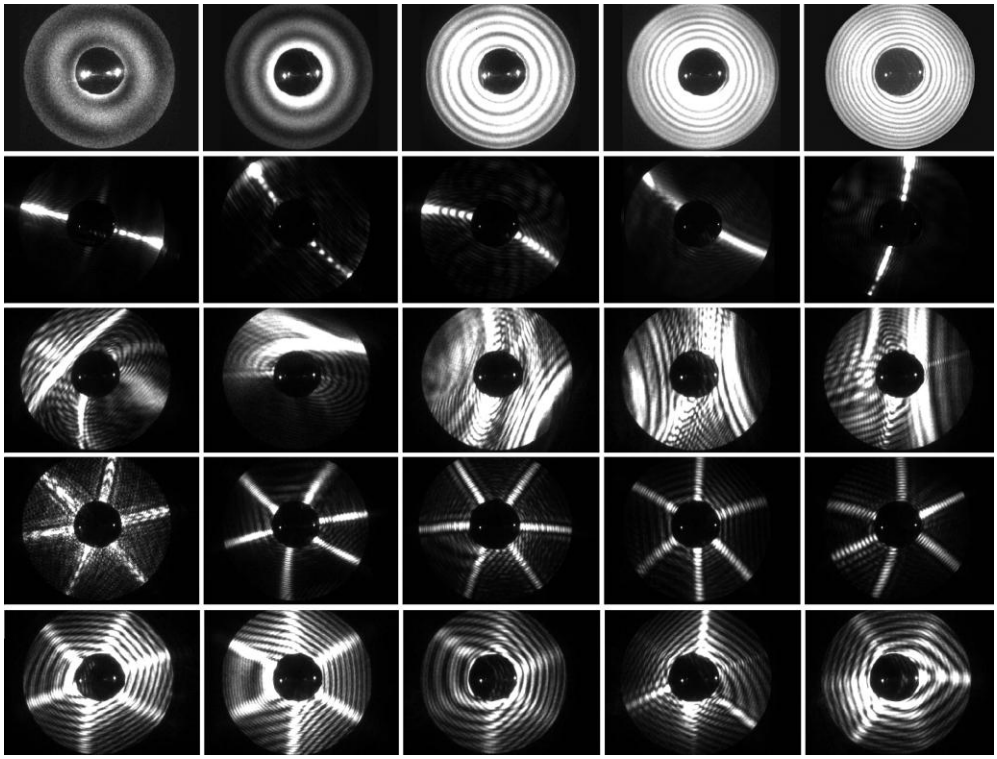

Figure 2. Droplet (top row) and ice crystal scattering patterns.

The scattering pattern images offer unique insights into the diverse habits of cloud ice crystals too small to be resolved by current cloud probes. However, whilst conventional pattern recognition methods may be readily used to group recorded images into broad ice habit classes such as those indicated in Fig. 2, more detailed theoretical inversion of the patterns is required to yield quantitative morphological data. This challenge is currently being addressed by the authors and others through both advancements in modeling [10,11] and by reference to scattering from known particles such as ice analogs [12,13]. Fig. 3 illustrates this modeling approach, showing two experimental patterns from Fig.2, each with its best-fit theoretical interpretation derived using Ray Tracing and Diffraction on Facets (RTDF) theory [10,11], and the corresponding particle shape and orientation (assuming beam direction into paper). The first corresponds to a hexagonal ice column 16 μm length and 7 μm across flats; the second, to a hexagonal ice platelet, 10 μm height and 43 μm across flats. The RTDF theory is still under development but already allows good assessment of size as well as shape for both pristine and complex ice crystals such as rosettes, despite not yet replicating some finer interference features of the experimental patterns.

4 Conclusion

We anticipate that advancement of theoretical scattering models will ultimately allow inversion of patterns for even imperfect (but realistic) ice crystals having rounded facets and/or rough surfaces. Until this is achieved, we are undertaking the parameterization of patterns from such morphologies by comparison with scattering patterns from ice crystal analogs of accurately known shape and structure [13]. With the ongoing improvement in inversion and interpretation of the scattering patterns, we hope that the resulting, previously unattainable, data on microscopic cloud particle shape, size and relative abundance will aid understanding of these particles' roles in cloud microphysical and radiative processes, and ultimately their effect on climate.

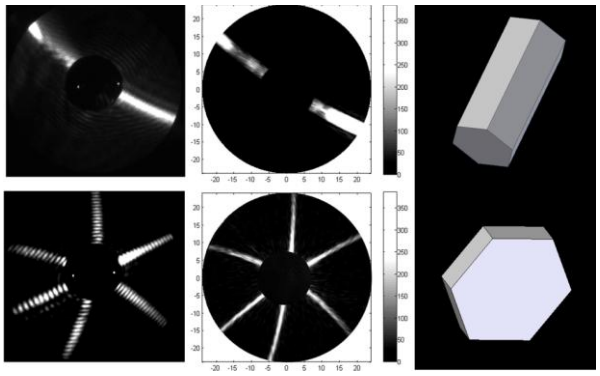

Figure 3. Experimental scattering pattern (left) with matching RTDF theory and corresponding crystal shape for ice column and ice platelet.

References

[1] IPCC Fourth Assessment Report -WG1 (Cambridge, 2007).

[2] C. Prabhakara, D. P. Kratz, J. M. Yoo, G. Dalu, and A. Vernekar, "Optically thin cirrus clouds – radiative impact on the warm pool", J. Quant. Spectrosc. Ra. Trans. **49**, 5, 467-483 (1993).

[3] W. P. Arnott, Y. Y. Dong, and J. Hallett, "Role of small ice crystals in radiative properties of cirrus: A case study, FIRE II, November 22 1991", J. Geophys. Res., **99**, D1, 1371-1381 (1994).

[4] J-F. Gayet, F. Auriol, A. Minikin, J. Ström, M. Seifert, R. Krejci, A. Petzold, G. Febvre, and U. Schumann, "Quantitative measurement of microphysical and optical properties of cirrus clouds", Geophys. Res. Lett. **29**, 2230 (2002).

[5] P. Yang, B. A. Baum, A. J. Heymsfield, Y. X. Hub, H.-L. Huang, S-C. Tsaye, S. Ackerman, "Single scattering properties of droxtals", J. Quantit. Spectr. Rad. Transf. **79–80**, 1159–1169 (2003).

[6] R. P. Lawson, A. V. Korolev, S. G. Cober, T. Huang, J. W. Strapp, G. A. Isaac, "Improved measurements of the drop size distribution of a freezing drizzle event". Atmos. Res. **48**, SI JUN., 181-191 (1998).

[7] Z. Ulanowski, P. Connolly, M. Flynn, M. Gallagher, A.J.M. Clarke and E. Hesse, "Using ice crystal analogues to validate cloud ice parameter retrievals from CPI ice spectrometer data". In Proceedings of 14th Int. Conf. Clouds Precipit., (ICCP, 2004), pp.1175-1178.

[8] E. Hirst, P. H. Kaye, R. S. Greenaway, P. Field and D. W. Johnson, "Discrimination of micrometre-sized ice and super-cooled droplets in mixed-phase cloud", Atmos. Environ. **35**, 1, 33-47 (2001).

[9] C. Takahashi and M. Mori, "Growth of snow crystals from frozen water droplets" Atmos. Res. **82**, 385–390 (2006).

[10] A. J. M. Clarke, E. Hesse, Z. Ulanowski & P. H. Kaye, "A 3D implementation of ray tracing combined with diffraction on facets: Verification and potential application", J. Quantit. Spectr. Rad. Transf. **100 (1-3)**, 103-114 (2006).

[11] E. Hesse, "Modelling diffraction during ray-tracing using the concept of energy flow lines", J. Quantit. Spectr. Rad. Transf. **109**, 1374-1383 (2008).

[12] Z. Ulanowski, E. Hesse, P. H. Kaye, A. J. Baran and R. Chandrasekhar, " Scattering of light from atmospheric ice analogues", J. Quantit. Spectr. Rad. Transf. **79-80C**, 1091-1102 (2003).

[13] Z. Ulanowski, E. Hesse, P.H. Kaye & A.J. Baran, "Light scattering by complex ice-analogue crystals", J. Quantit. Spectr. Rad. Transf. **100 (1-3),** 382-392 (2006).

Using multi-angular total and polarized POLDER-3/PARASOL reflectance measurements for ice cloud microphysics purpose

Laurent C.-Labonnote,[1] Gérard Brogniez,[1] Frédéric Parol,[1] Phillipe François,[1]
François Thieuleux,[1] and Anthony J. Baran[2]

[1] Laboratoire d'Optique Atmosphérique, University of Lille,
Bât. P5, 59655 Villeneuve d'ascq, France
[2] Met. Office, Exeter, United Kingdom
tel: +33(0)320336190, fax: +33(0)320434342, e-mail: labon@loa.univ-lille1.fr

Abstract

In this paper we exploit the multi-viewing polarized and total reflected light measurement capability of the space-based POLDER-3/PARASOL instrument to test different ice cloud microphysical models. In particular, their capabilities to reproduce the angular signature of total and polarized reflected light from cirrus. Two methods are presented: The first one exploits the directional spherical albedo to find the model that minimizes its angular variation; the second method makes use of polarized reflectance in order to find the model that best reproduces its directional behaviour.

1 Introduction

Cirrus clouds generally occur at altitudes greater than 6 km and permanently cover nearly 30% of the globe [1]. Their impact on the earth radiation budget is identified as a major unsolved problem in climate research [2], since a number of physical parameters are involved (position of the cloud, vertical variation of ice crystal shape and size, distribution of ice mass within the cloud,…). It is therefore essential to constrain those parameters in order to better represent the cirrus cloud radiative effect in climate models.
One way is to use measurement from space of reflected light above ice cloud. This has been done for a long time from different instruments and allows the retrieval, for example, of their microphysical properties as well as optical thickness or cloud-top pressure [3]. In this study we propose to make use of multi-angular total and polarized reflectances simultaneously measured by the space-based POLDER-3/PARASOL [4] instrument to infer ice cloud microphysical properties and to get some indication about their macro-physical properties.

2 The POLDER-3 instrument

POLDER-3 (POLarization and Directionality of the Earth's Reflectances) is a multi-directional and multi-spectral polarimeter. The latest version of the instrument was launched in December 2004 and is part of the 'A-train' onboard the satellite platform PARASOL. It has a large field of view ranging from +/- 43^o across track and +/- 51^o along track. POLDER-3 has channels centered at 0.443, 0.490, 0.565, 0.670, 0.763, 0.765, 0.865, 0.910 and 1.02 µm. Three of them are polarized (0.490, 0.670 and 0.865 µm) and are utilized in our study. The instrument can sample a given pixel from up to 16 viewing directions covering scattering angles between 60^o and 120^o.

3 Microphysical models

Up to 18 different single randomly oriented ice cloud microphysical models are tested in this study. It is now well established that ice cloud particles are very diverse and complex [5]. To reproduce them we built our microphysical models database for a large variety of shape and degree of heterogeneity. The shapes tested range from the simple hexagonal ice plate and ice column to more elaborate single and six branch

bullet rosette [6] and a chain aggregate [7]. Moreover previous studies have demonstrated that the best phase functions to apply for cirrus remote sensing are generally featureless and flat at backscattering angles [8]. We therefore included models with different degree of inhomogeneity or randomization to generate featureless phase function. Finally, models used in MODIS and the POLDER algorithm [9][10] for retrieving ice cloud properties were also included in the data base. Table 1 summarizes the characteristic of each microphysical model.

4 Using multi-viewing measurements in total light

4.1 Spherical Albedo Difference (SAD) test

Cirrus cloud optical thickness is expressed equivalently in terms of cloud spherical albedo assuming a black underlying surface. From POLDER-3 multi-viewing measurements it is therefore possible to get a directional spherical albedo for each cloudy pixel, and use it to test our microphysical models. The so-called “best-fit” model is the one that minimizes the angular variation of the difference between the directional value and averaged value of spherical albedo. More details about this test and ice cloud pixel filtering can be found in the following paper [7].

Table 1: Ice cloud microphysical models used in this study. The randomization parameter means degree of roughness (full is roughness + air bubble inclusion).

Models	Randomization	Size distribution	numbering
Chain aggregate	0.1	No	0
	0.3	No	1
	full	No	2
Six branch bullet	0.1	No	3
	0.3	No	4
	full	No	5
Hexagonal plate	0.1	No	6
	full	No	7
Single bullet	0.1	No	8
	0.2	No	9
	full	No	10
Hexagonal column	0.1	No	11
	full	No	12
IHM	air bubble	No	13
PHM	0	No	14
Modis (D=10µm)	0	Yes	15
Modis (D=70µm)	0	Yes	16
Modis (D=130µm)	0	Yes	17

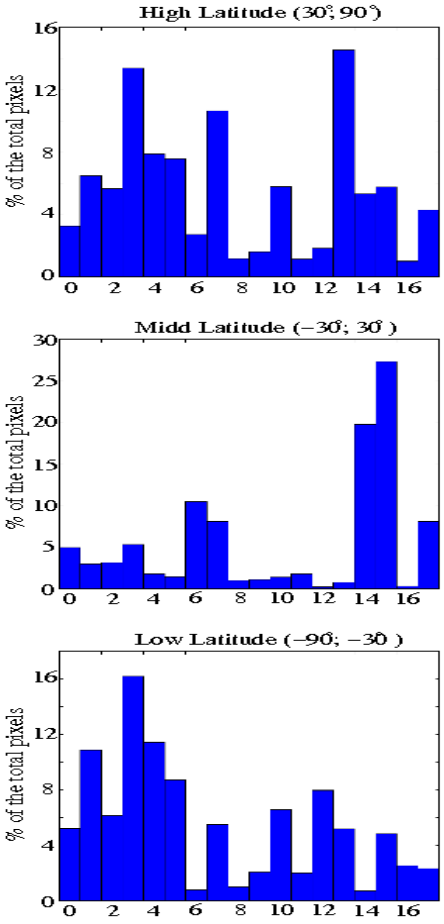

Figure 1: Histogram of selected microphysical model from SAD test, for three latitudinal bands and a one day Parasol orbiting on April 11th 2007. The abscissa axis corresponds to the model numbering of table 1.

4.2 Results

We applied the SAD test over all selected ice cloudy pixels for one day of POLDER-3 measurements on April 11th 2007 using the ice cloud microphysical models defined in Table 1. The model that gives the

lowest standard deviation in terms of the spherical albedo difference was selected and labeled as the "best-fit model". Results are summarized in Figure 1.

We can see from this figure that a unique model is not able to describe the angular behavior of reflected light from all ice clouds obtained during one day of measurements. As a matter of fact, the "best-fit" model varies with the season and latitude. For example IHM (model 13) and six branched bullet rosette (model 3) seems to be the more representative of ice cloud particles at higher latitudes than in the tropics, whereas MODIS (model 15) shows the opposite behavior.

The conclusion inherent in this section is that although the majority of cirrus clouds are described by some level of randomization there are some which are best described by pristine models, in the tropics for example. Therefore, we need to use heterogeneous as well as more homogeneous microphysical models with different shape and randomization characteristics to be able to catch the angular signature of the majority of cirrus clouds measured in total light. Not shown here but for some cirrus cloud no microphysical models were able to describe the angular behavior of reflected light, this could be due to some spatial heterogeneity problem or other microphysical models not considered in Table 1.

5 Using multi-viewing measurements in polarized light

The goal of this section is to understand the relation between total and polarized light. Does the information become redundant or complementary, if complimentary then how to use it? We are trying through some examples to give some thought on different situations detected during one day POLDER-3 measurements.

Here the microphysical model selection is accomplished as follow. First, for each microphysical model we compute the reflected polarized light from an adding-doubling code [11]. Second, we apply a simple least square method to find the microphysical model that minimizes the difference between the measurement and forward model.

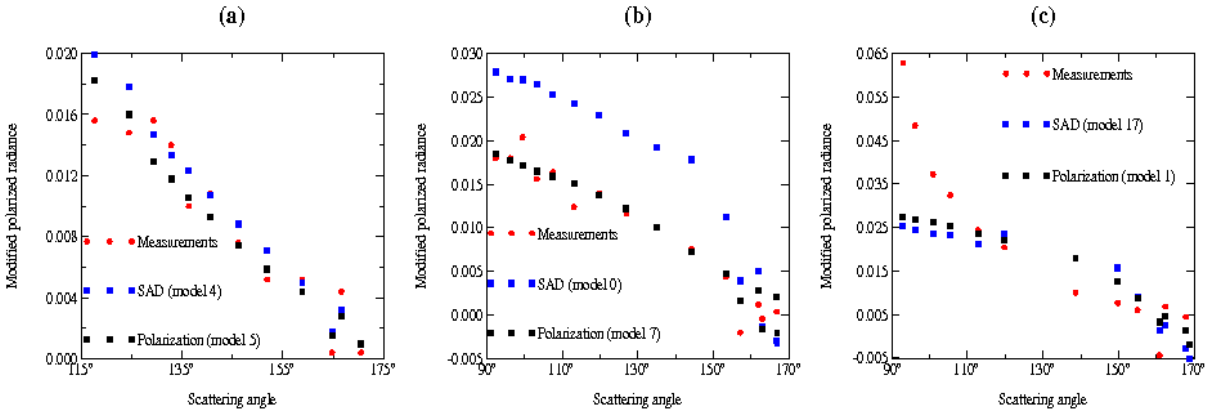

Figure 2: Polarized reflectance as a function of scattering angle for 3 ice cloudy pixels. Red dot stand for measurements, blue and black squares present the forward model computation using the microphysical model given by respectively the SAD test and polarization.

In figure 2 we have plotted the polarized reflectance computed with the best microphysical model retrieved by: (i) the SAD test (blue squares), and (ii) the polarization test (black squares). POLDER-3 measurements are also plotted (red circle) as a function of scattering angle. Three main cases can be encountered and are illustrated in this figure. First, both the SAD and polarization test give the same microphysical model with a low standard deviation which means that we should be in presence of a rather homogeneous cirrus cloud (fig. 2a). Second, SAD and the polarization test gives different microphysical models with rather low standard deviation for both which means that the cirrus cloud should be vertically heterogeneous (because polarization and total light are sensitive to different part of the cloud) (fig. 2b). Third, nothing is working, i. e. we get a high standard deviation value, which means that either the cloud is too heterogeneous horizontally or the microphysical model database is not representative of the cirrus cloud (fig. 2c).

6 Conclusion

For the first time cirrus cloud is studied using simultaneous multi-viewing measurements of total and polarized light. A set of ice cloud microphysical models with different shapes and degree of heterogeneity are used to mimic the difference between measurement and forward model of the reflected total and polarized light over cirrus cloud. Because total and polarized light are sensitive to different part of the cloud, we expect to get complementary information. We therefore elaborate two different algorithms, one that makes use of the total light and a second that utilizes polarized light only, in order to get the microphysical model that best reproduces their angular behavior. Results show that we run into different cases: (i) both algorithms agreed on the microphysical model suggesting a rather homogeneous cirrus cloud, (ii) distinct microphysical model were selected indicating that we may be in presence of vertically heterogeneous cloud, (iii) both selected model do not catch the angular signature pointing towards either the microphysical models considered are insufficient or there is some macro or microphysics heterogeneity effects.

References

[1] D. P. Wylie, W. P. Menzel, H. M. Woolf, and K. L. Strabala, “Four years of global cirrus cloud statistics,” J. Climate, **7**, 315-335 (1994).

[2] G. L. Stephens, S. C. Tsay, P. W. Stackhouse, and J. P. Flateau,”The relevance of the microphysical and radiative properties of cirrus clouds to climate and climate feedback,” J. Atmos. Sci., **47**, 1742-1753 (1990).

[3] D. K. Lynch, K. Sassen, D O’C. Starr and G. L. Stephens, *Cirrus* (Oxford University press, 2002)

[4] D. Tanré, A. Lifermann and the PARASOL team, “The PARASOL mission, Satellite Observations of Tropospheric Trace Gases and Aerosols”, IGACtivities. Newsletter, **35**, 35-37 (2007).

[5] R. P. Lawson, B. Baker, B, Pylson and Q. Mo, “In situ Observation of the Microphysical properties of Wave, Cirrus, and Anvil Clouds. Part II: Cirrus Clouds,” J. Atmos. Sci., **63**, 3186-3203 (2006).

[6] A. Macke, J. Muller and E. Raschke, “Single scattering properties of atmospheric ice crystals”, J. Atmos. Sci., **53**, 2813-2825 (1996).

[7] A. J. Baran and L. C.-Labonnote, “On the reflection and polarization properties of ice cloud”, JQSRT, **100**, 41-54 (2006).

[8] A. J. Baran, P. N. Francis, L.-C. Labonnote, and M. Doutriaux-Boucher, “A scattering phasefunction for ice cloud: Tests of applicability using aircraft and satellite multi-angle multi-wavelengthradiance measurements of cirrus.” Quart. J. Roy. Meteorol. Soc., 127, 2395-2416 (2001).

[9] B. Baum, A. J. Heymsfield, P. Yang and M. Thomas, “Bulk scattering models for the remote sensing of ice clouds. Part I: Microphysical data and models”, J. Appl. Meteor., **44**, 1885-1895 (2005).

[10] L. C.-Labonnote, G. Brogniez, J.-C. Buriez, M. Doutriaux-Boucher, J. F. Gayet and A. Macke, « Polarized light scattering by inhomogeneous hexagonal monocrystals. Validation with ADEOS/POLDER measurements”, J. Geophys. Res., **106**, 12139-12153 (2001).

[11] J. F. D. Haan, P. B. Bosma and J. W. Hovenier, “ The adding method for multiple scattering calculations of polarized light”, Astron. Astrophys., **183**, 371-391 (1987).

Solar scattering on oriented crystals in cirrus clouds around the specular direction

Claire Lavigne[1], Antoine Roblin[1], Patrick Chervet[1]

[1] *Onera, the French Aerospace Lab*
Theoretical and Applied Optics Department
Chemin de la Hunière, 91761 Palaiseau cedex, France
tel: +33 169 93 63 33, fax: +33 169 93 63 45, e-mail: claire.lavigne@onera.fr

Abstract

Solar scattering on oriented cirrus crystals near the specular reflection direction is modelled using a mix method combining geometrics optics and diffraction effects. Different potential sources of phase function broadening around the specular direction, such as multiple scattering, solar disk or tilt effects, are studied by means of a Monte Carlo method. Finally the radiance detected by an airborne sensor located a few kilometres above the cirrus cloud and pointing in the specular scattering direction is evaluated and compared to the level obtained with the usual assumption of random crystal orientation.

1 Introduction

Radiative transfer in the atmosphere is influenced significantly by the scattering and absorption of radiation by ice clouds. With measurements from lidar [1], from satellite [2,3] or in situ [4], it has been pointed out that ice crystals are often preferentially oriented with their long axis in the horizontal plane. Usually, radiative properties studies of cirrus clouds assume a random orientation of ice crystals. This leads to simplifications for the optical properties and for the radiative computations. The random orientation hypothesis enables to reproduce the well-known halos (for example the 22° halo in visible wavelength) but it can't model a class of rare halos due to aligned crystals [5] and subsun phenomenon. The subsun is the sharp specular reflection of sunlight in the glint direction by horizontally oriented ice plates. Simulations show that subsuns are produced by the reflection of sunlight from either horizontal or swinging ice crystals [6,7]. Various sources of solar glint broadenings can be identified. First, the dispersion of plate's orientation will lead to an increase of the apparent cloud surface which reflects the sun irradiance, compared to a perfectly specular horizontal surface. Secondly, the single scattering phase function in the direction corresponding to specular reflection is characterized by a width which is directly related to the crystal size. Finally, if a photon is scattered more than one time, its reflection angle will be different from the original glint angle.
This paper deals with scattering by a cirrus layer made up of oriented crystals. A method is proposed to estimate the phase function of an oriented crystal around the direction of specular reflection, whatever its size. Impact of the different sources of signal broadening is evaluated. The signal reflected by a cirrus cloud and detected by an airborne sensor is finally compared to the one obtained in case of the usual random crystal orientation assumption.

2 Phase function of an oriented crystal around the specular scattering direction

The scattering phase function of a crystal is calculated in this paper by use of a mix between geometric optics considerations described by Fresnel laws and diffraction theory. In this way accurate results are obtained whatever the size parameter of the particle is.

1.1 Phase function of an horizontal crystal

Each crystal is treated as a reflecting surface whose reflectivity β is computed using Fresnel laws. The diffraction pattern is approximately computed by using a circular aperture with the same area as the projected particle area. A diffraction phase function P_{diff} is obtained from the solid angle normalization of the diffracted intensity. The scattering phase function P_{scat} around the specular direction is equal to the diffraction phase function apart from a renormalization factor:

$$P_{scat} = \beta P_{diff} \tag{1}$$

The scattering phase function obtained by Eq. (1) in the specular direction plane, has been compared to an exact one calculated by a T-matrix code [8] at two wavelengths in the visible and infrared domain and for two solar zenith angles. As an example, the phase function is shown in Fig. 1 at a wavelength of 3.7 µm and a solar zenith angle of 50°. General agreement between results from both methods is very good for all calculated cases. Peaks due to diffraction are quite well reproduced by the T-matrix method too.

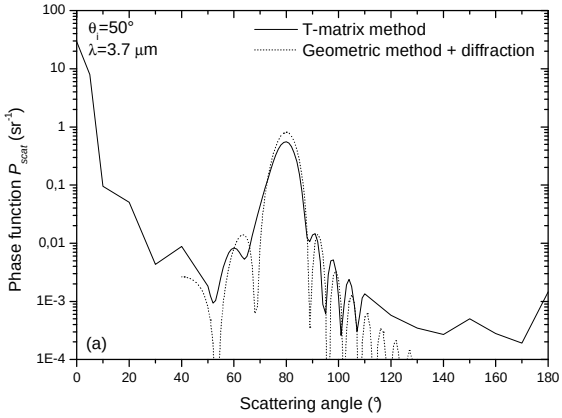

Figure 1 : Comparison between the phase function calculated around the direction of specular reflection by the T-matrix method [8] and our method taking into account diffraction effect and geometric considerations for a solar zenith angle equal to 50°, at a wavelength of 3.7 µm and for a disk with size parameter of 34.

1.2 Phase function of swinging crystals

Ice crystals aren't perfectly horizontally aligned because of turbulence effects during their fall in the atmosphere. They present small flutter angles, lower than 3° in most cases [3]. Crystal tilts are supposed to follow a Gaussian distribution [9]. The phase function of a swinging crystal has been calculated by a Monte Carlo model taking into account 3×10^5 crystal orientations obeying the Gaussian distribution. Results are presented in Fig. 2 for two particles radius equal to 20 and 150 µm for λ=3.7 µm. For a particle with moderate radius of 20 µm, the effect of crystal diffraction appears to be largely more important than the one due to crystal orientation. In that case, taking only into account diffraction is enough to correctly describe the phase function of a swinging crystal. For larger particles, broadening around the direction of specular reflection can be explained neither by diffraction effect alone nor by only fluctuations in crystal orientation. Both contributions have to be taken into account to evaluate properly the particle phase function.

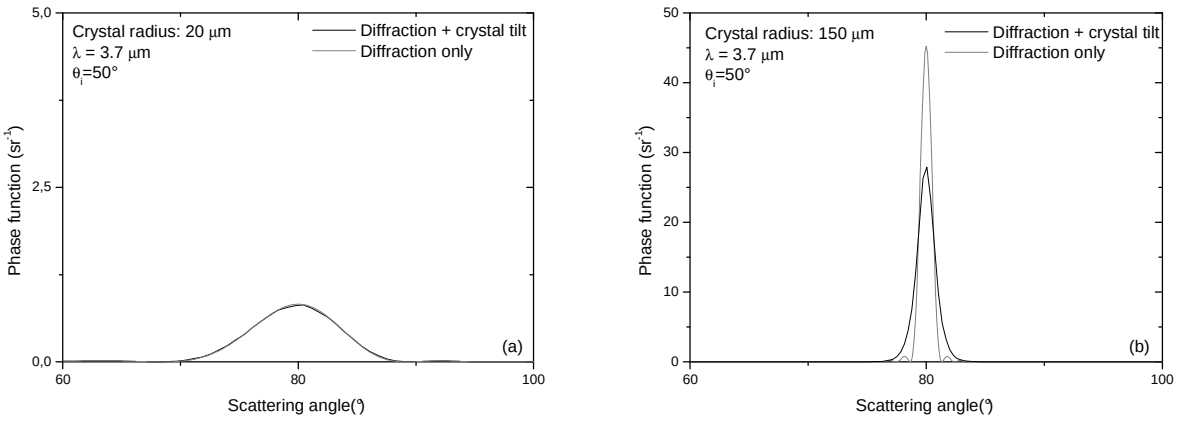

Figure 2 : Comparison between crystal phase functions in the plane of specular reflection taking into account tilt and diffraction effects for particles with radius equal to (a) 20 μm (b) 150 μm at a wavelength of 3.7 μm. The solar zenith angle is taken to be 50°.

2 Specular reflected radiance detected by an imager

In case of a cloud layer, the distribution of the scattered signal around the direction of specular reflection can be enlarged by tilt effects but also by multiple scattering and solar disk. Impact of both contributions has been evaluated showing that they can be neglected to a first approximation. Since no specific size distributions are available for oriented crystals, scattering properties have been averaged over a size distribution *N(r)* of Fu [10].

The radiance L_{scat} scattered by the cloud from direction θ_i to θ_r is given by:

$$\frac{\partial L_{scat}(\theta_i,\theta_r)}{\partial \tau'} = \beta \times I_{sun} \cos\theta_i \times T_{atm} \times P\left(N(r),\theta_i,\theta,\varphi=\pi\right) \qquad (2)$$

τ' is the optical thickness of the specular cloud layer, θ_i is the sun zenith angle, I_{sun} the solar irradiance, T_{atm} is the atmospheric transmission between the sun and the cloud and $\theta=\pi-\theta_i-\theta_r$ is the scattering angle and *P* is the phase function of the specular cloud layer.

The radiance detected by an airborne sensor located a few kilometres above a cirrus cloud and pointing in the specular scattering direction is obtained from Eq. (2). Results calculated at the centre of the Field Of View for a cirrus cloud altitude equal to 11 km and a sensor located three kilometres above are shown in Table 1. They are compared to the random oriented particles case. For both solar zenith angles, scattered radiance is largely higher when oriented crystals are included in the cloud. Radiances calculated for the two kinds of particles differ from more than three orders of magnitude. Solar reflection on a cirrus cloud can have a dramatic effect on the signal received by a sensor. It can become totally blind to other light sources.

Table 1: Comparisons between the radiance obtained at the centre of the sensor taking into account oriented and non oriented crystals at a wavelength equal to 3.7 μm.

Solar zenith angle	Solar scattered radiance for oriented crystals ($W\times sr^{-1}\times cm^{-2}\times cm$)	Solar scattered radiance for non oriented crystals ($W\times sr^{-1}\times cm^{-2}\times cm$)
θ_i=10°	2×10^{-8}	2×10^{-11}
θ_i=50°	5×10^{-8}	3×10^{-11}

3 Conclusion

A new method which takes into account diffraction effect in the specular direction has been developed to calculate the phase function of on oriented ice crystal. Comparisons with results obtained by a T-matrix code show a very good agreement. Impact of crystal tilt has been evaluated by use of a Monte Carlo method.
Scattering by a cirrus layer made up of several crystal sizes has been examined too. Influence of different potential sources of signal broadening around the specular direction has been evaluated showing that multiple scattering and solar disk width can be neglected.
The radiance detected by a sensor pointing in the direction of specular scattering has been calculated and a dramatic increase of the signal can be observed in comparison with the non oriented particles case. Calculations presented in this paper are limited to the specular scattering plane. It should be useful to evaluate the angular width of the phase function around the specular direction but relative to the azimuth angle.

Acknowledgments

The authors would like to thank M. Mishchenko for making his T-matrix code publicly available.

References

[1] Platt C.M.R., N.L. Abshire, and G.T. McNice, “Some Microphysical Properties of an Ice Cloud from Lidar Observation of Horizontally Oriented Crystals”, J. Appl. Meteor. **17**, 1220–1224 (1978).

[2] Chepfer H.; Brogniez G.; Goloub P.; Breon F.M.; Flamant P.H, “Observations of horizontally oriented ice crystals in cirrus clouds with POLDER-1/ADEOS-1”, J. Quant. Spect. Radi. Transf. **63**. 521-543 (1999).

[3] Noel V. and Chepfer H., “Study of ice crystal orientation in cirrus clouds based on satellite polarized radiance measurements”, J. Atmos. Sci. **61**, 2073-2081 (2004).

[4] Ono A., “The Shape and Riming Properties of Ice Crystals in Natural Clouds”, J. Atmos. Sci. **26**, 138–147 (1969).

[5] Tape W. and G. P. Konnen, “A general setting for halo theory”, Appl. Opt. **37**, 1434-1434 (1999).

[6] Bréon F-M and Dubrulle B., “Horizontally oriented plates in cirrus clouds”, J. Atmos. Sci. **61**, 2888-2898 (2004).

[7] Lynch, D.K., Gedzelman, S.D. and Fraser, A.B., “Subsuns, Bottlinger’s Rings and Elliptical Halos”, Appl. Opt. **33**, 4580-4589 (1994).

[8] Mishchenko M. I., “Calculation of the amplitude matrix for a nonspherical particle in a fixed orientation”, Appl. Opt. **39**, 1026-1031 (2000).

[9] Noel V. and Sassen K., “Study of planar ice crystal orientations in Ice Clouds from sacking polarization lidar observations” Journal of applied meteorology **44**, 653-664 (2005).

[10] Fu Q., “An accurate parameterization of the solar radiative properties of cirrus clouds for climate models” Journal of Climate **9**, 2058-2081 (1996).

Initial investigation into using Fourier spectra as a means of classifying ice crystal shapes

C. Stopford,[1] Z. Ulanowski,[1] E. Hesse,[1] P.H. Kaye,[1] E. Hirst,[1]
M. Schnaiter,[2] and D. McCall[1]

[1] *University of Hertfordshire, Centre for Atmospheric & Instrumentation Research, Hatfield, Hertfordshire, AOL10 9AB, United Kingdom*
[2] *IMK-AAF, Forschungszentrum Karlsruhe, 76344 Eggenstein-Leopoldshafen, Germany.*
tel: +44 (0) 1707-284174, fax: +44 (0) 1707-284185, e-mail: c.stopford@herts.ac.uk

Abstract

Fast Fourier Transforms of azimuthal light scattering patterns are investigated as a method for classifying cirrus cloud ice crystals. Small Ice Detector Mk. 2 data is compared to modelled reference data of various aspect ratio, size and basal indentation.

1 Introduction

Characterization of the shape of cloud ice crystals is important with respect to their effect on radiative forcing in the atmosphere. Due to the small size of the crystals, direct imaging suffers from resolution constraints [1]. Because of this, few instruments are capable of recording useful information regarding the smaller particles. Small Ice Detector Mk. 2 (SID-2) relies on light scattering from individual particles, and so can observe particles in the 1μm-50μm size range. The detector consists of 24 azimuthally arranged elements collecting information between 9° and 19.8°, with a further 3 elements spanning the 5.5°-9° range (though the latter are not considered in this investigation.)

A computational model has been developed at the University of Hertfordshire to include diffraction on facets in a ray tracing model [2][3]. This model allows generation of scattering patterns from crystals with known morphology and orientation, which can then be compared with measurements. A reference database of patterns from various crystal sizes, basal indentations and aspect ratios has been developed for this purpose. A laboratory rig has also been assembled to measure the scattering pattern from ice analogue crystals (crystals with similar optical properties to ice but stable at room temperature [4]) in known orientations, for scattering angles from 5° to 120°. Modelled patterns are then compared to imaged patterns from the analogues for verification purposes.

2 Reference database

The Ray Tracing with Diffraction on Facets (RTDF) model was used to create a database of patterns for crystals with known shape. Each crystal is a hexagonal prism, with variable size, aspect ratio and degree of basal indentation. Basal indentation refers to an indentation of the hexagonal basal facets. This indentation takes the form of a hexagonal pyramid extending from each of the basal facets towards the centre of the crystal. The complete set is comprised of modelled data from crystals of 9 sizes (4.5μm, 7μm, 11μm, 16μm, 23μm, 27μm, 32μm, 35μm, & 40μm), each with a range of 5 aspect ratios (length:diameter 8:1, 3:1, 1:1, 1:3, 1:8), and 8 degrees of basal indentation (0%, 5%, 10%, 17%, 25%, 33%, 41% & 49% of the total length) over 80 evenly spaced orientations - a total of 28800 individual patterns. For the computation, a cluster of 40 processors was used, for duration of 32 hours, so expansion of the reference data is feasible. The model has been compared to imaged scattering patterns from ice analogue crystals suspended in a custom built laboratory rig. Before inclusion in the database, each computed 2D scattering pattern is reduced to its equivalent SID-2 response, the modulus of the fast Fourier transform (FFT) calculated and normalised to the zero order coefficient – figure 1 [6].

Figure 1, from left to right – 2D scattering pattern from modelled column (rings represent area recorded by the SID-2 detector), polar plot of square root intensity of SID-2 pattern, normalised FFT spectrum of polar plot

3 Test of FFT fitting as a method of crystal classification

FFT fitting is performed by finding the smallest RMS difference between the FFT spectrum of a subject particle and reference FFT spectra.

To test the fitting as a viable method of crystal classification, a further set of crystals was modelled, of the same aspect ratio and basal indentation, but a different range of sizes. This was then fitted to the database, and the error for each fitting inspected. The error is defined as the sum of the distances separating the fit from the expected bin (in three dimensions of Aspect Ratio, Basal Indentation and Size) multiplied by the number of particles in that bin – Eq (1).

$$Error = \sum_{1}^{\#Bins} \frac{\sqrt{\Delta AR^2 + \Delta BI^2 + \Delta Sz^2} \times Size\ of\ Bin}{Number\ of\ Patterns} \quad (1)$$

Initial investigations showed that three reference sizes (4.5μm, 11μm and 23μm) provided a poor fitting for a set of modelled test crystals. To increase the accuracy, an additional two sizes (7μm and 11μm) were added to the reference data, which improved the fitting considerably – Figure 2. This indicates that the FFT patterns are heavily dependent on size as well as aspect ratio and basal indentation, even when normalised.

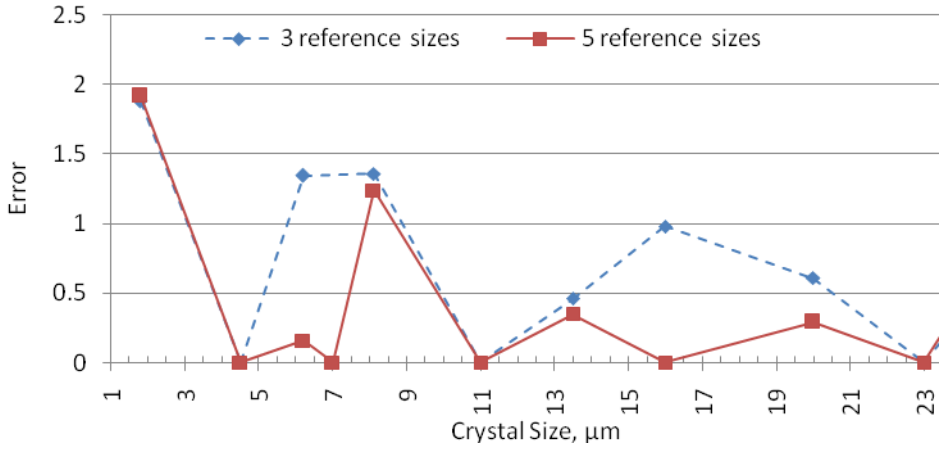

Figure 2. Comparison of fitting error between modelled test crystals over a range of sizes and the reference database before (3 reference sizes) and after (5 reference sizes) the addition of two crystal sizes to the reference database.

Because of the size dependence the error in fitting will increase as crystal sizes extend beyond the range of reference sizes. Expanding the database below 2.3μm is currently not feasible since the RTDF model becomes inaccurate for two dimensional scattering below this point.

4 Laboratory scattering measurements

Scanning electron microscopy has been employed to obtain precise dimensions of analogue crystals to enable comparison between modelled and experimental data. Once measured, crystals were placed in the scattering rig, and their scattering patterns imaged. The crystals were rotated in order to get a range of patterns from known orientations. Crystals were then modelled for use with the RTDF program, and scattering patterns were produced. Comparison of the imaged and modelled patterns shows a good fit.

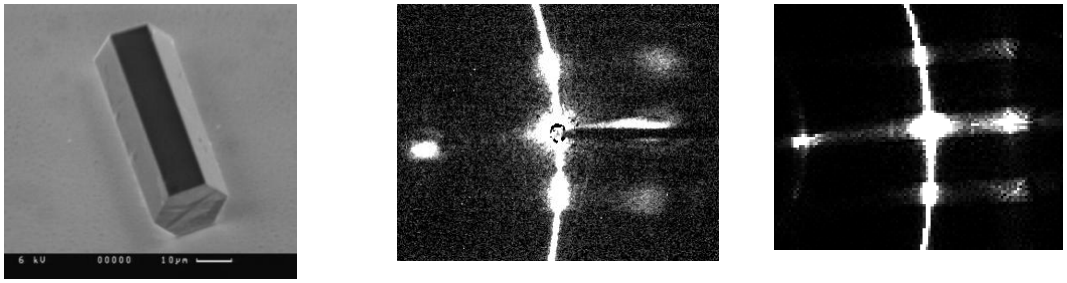

Figure 3 (left) Scanning Electron Microscope image of 2:1 aspect ratio ice analogue column, (middle) experimental 2D scattering pattern from ice analogue column with long axis at 40° to incident beam. Note that the dark line from the centre of the image to the right is a rod supporting the crystal on a glass plate, (right) RTDF modelled 2D scattering pattern of equivalent crystal.

5 Application of fitting data to SID-2 experimental data from a cloud chamber

During the HALO-01 campaign at the AIDA cloud chamber [5], small ice crystals were produced and recorded by numerous instruments, including SID-2. During experiment 18 flat plates were observed by the PHIPS imaging probe [7], which is in agreement with the FFT fitting of SID-2 data from that experiment - Figure 4. In addition, IR spectroscopy indicates a presence of 1:1 ratio compacts around 11μm as seen in the SID-2 data. FFT fitting is limited to a maximum RMS of 0.046, which includes approximately 50% of the data from the experiment.

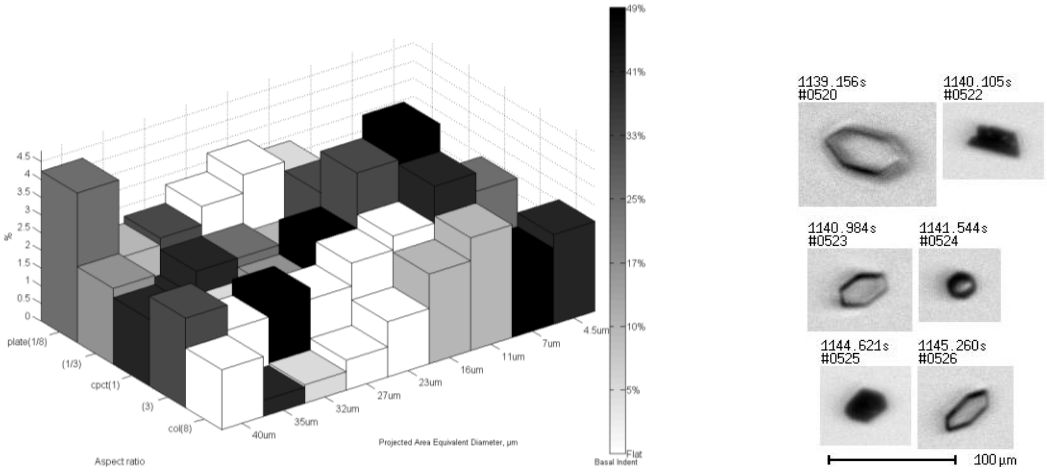

Figure 4 (left) – Best fits of FFT spectra of data recorded by SID-2 at HALO-01 campaign at the AIDA cloud chamber (right) – PHIPS data from the same time period shows large plates

6 Conclusions

A set of reference scattering patterns was computed using the RTDF model. These were verified by comparing them to experimental scattering patterns from ice analogues. Retrieval of crystal shape from azimuthal scattering patterns from SID-2 cloud probe data was investigated by least squares fitting of the patterns to the reference set. FFT was used to remove the dependence of scattering patterns on rotation about the axis of the SID-2 detector. The fitting method is shown to be able to recover crystal aspect ratio and depth of basal indentation while being dependent on size.

Acknowledgements

Natural Environment Research Council and the European ACCENT network provided funding for this work.

References

[1] Z. Ulanowski, E. Hesse, P.H. Kaye, and A.J. Baran, “Light scattering by complex ice-analogue crystals,” J. Quantit. Spectr. Rad. Transf. **100**, 382-392 (2006)

[2] E. Hesse, A. J. M. Clarke, Z. Ulanowski and P. H. Kaye, “Light scattering by ice crystals modelled using the Ray Tracing with Diffraction on Facets method,” EGU General Assembly, Vienna (2007).

[3] A. J. M. Clarke, E. Hesse, Z. Ulanowski, and P. H. Kaye, “A 3D implementation of ray tracing combined with diffraction on facets,” J. Quantit. Spectr. Rad. Transf. **100**, 103-114 (2006)

[4] Z. Ulanowski, E. Hesse, P. H. Kaye, A.J. Baran, R. Chandrasekhar, “Scattering of light from atmospheric ice analogues,” J. Quantit. Spectr. Rad. Transf. **79-80C**, 1091-1102 (2003).

[5] O. Möhler, P. R. Field, P. Connolly, S. Benz, H. Saathoff, M. Schnaiter, R. Wagner, R. Cotton, M. Krämer, A. Mangold, A.J. Heymsfield, “Efficiency of the deposition mode ice nucleation on mineral dust particles,” Atmos. Chem. Phys. **6**, 3007–3021 (2006).

[6] Z. Ulanowski, C. Stopford, E. Hesse, P. H. Kaye, E. Hirst, and M. Schnaiter, “Characterization of small ice crystals using frequency analysis of azimuthal scattering patterns,” Proc. 10th Int. Conf. on Electromagnetic & Light Scatt., Bodrum, 225-228 (2007).

[7] R. Schoen, M. Schnaiter, Z. J. Ulanowski, & O. Moehler, “Ein neuartiges Geraet zur beruehrungsfreien Abbildung von Eiskristallen,” 70th Ann. Meeting German Physical Society, Heidelberg (2006).

AEROSOLS
(REMOTE SENSING FROM GROUND, AIRCRAFT AND SPACE)

Depolarization by Aerosols: Entropy of the Amsterdam Light Scattering Database

Shane R Cloude,

AEL Consultants,
26 Westfield Avenue, Cupar, Fife, KY15 5AA, Scotland, UK
tel:+44 1334 650761, e-mail: aelc@mac.com

Abstract

In this paper we apply, for the first time, an entropy analysis to measured scattering matrices from the Amsterdam light scattering database. We select four important examples of aerosols from this database and use them to demonstrate differences in entropy between the particle clouds. These differences are further investigated by analyzing the polarized behavior of the matrices via a single parameter, the alpha angle. We conclude as to the potential for discriminating different aerosols on the basis of their entropy/alpha signatures.

1 Introduction

Understanding the scattering behavior of aerosols is important for climate studies and better understanding of cloud microphysics. Such interpretations are however made complicated by the shape and size irregularities of aerosol particles, making formal analysis very difficult. For this reason extensive use has been made of laboratory measurements of the scattering matrix, as provided for example by the Amsterdam light scattering database (ALSD) (http://www.astro.uva.nl/scatter/). While extensive analysis of these data sets has already been carried out [1], here we provide a novel approach designed to expose more clearly the underlying depolarization behavior of such particles. This approach is based on the concept of scattering entropy, as described in [2]. We first briefly summarize the methodology used and then show some sample results to illustrate the utility of this new method.

2 Depolarization and Scattering Entropy

As shown in [2,3], depolarization by any system of particles can be conveniently formulated as an eigenvalue decomposition of the 4 x 4 complex Hermitian coherency matrix [T], which is related in a 1-1 mapping to the conventional 4 x 4 real scattering matrix [F], itself relating Stokes vectors of incident and scattered beams [4]. In the important special case of a cloud formed by combinations of reciprocal particles with a plane of symmetry, the scattering and coherency matrices are then related as shown in equation 1.

$$[F]=\begin{bmatrix} f_{11} & f_{12} & 0 & 0 \\ f_{12} & f_{22} & 0 & 0 \\ 0 & 0 & f_{33} & f_{34} \\ 0 & 0 & -f_{34} & f_{44} \end{bmatrix} \Leftrightarrow [T]=\begin{bmatrix} t_{11} & t_{12} & 0 & 0 \\ t_{12}^{*} & t_{22} & 0 & 0 \\ 0 & 0 & t_{33} & 0 \\ 0 & 0 & 0 & t_{44} \end{bmatrix}$$

$$\left.\begin{aligned} t_{11} &= \tfrac{1}{2}(f_{11}+f_{22}+f_{33}+f_{44}) \\ t_{22} &= \tfrac{1}{2}(f_{11}+f_{22}-f_{33}-f_{44}) \\ \Rightarrow t_{33} &= \tfrac{1}{2}(f_{11}-f_{22}+f_{33}-f_{44}) \\ t_{44} &= \tfrac{1}{2}(f_{11}-f_{22}-f_{33}+f_{44}) \\ t_{12} &= f_{12}-if_{34} \end{aligned}\right\} \Rightarrow [T]=(2+1)+[0+3] \qquad \text{- (1)}$$

We can then use these relations to calculate [T] for all data sets in the ALSD. Using the notation of [3], we note from equation 1 that the most general polarizing (..)/depolarizing [..] decomposition of such systems can be characterized by 6 parameters in a 2:1:0:3 cascade. Importantly we note that such symmetric systems have zero eigenvector parameters associated with depolarization. Hence the principal eigenvector of [T] can be entirely associated with polarized behavior of the system, with a scattering strength given by the largest eigenvalue of [T]. The principal eigenvector has only two complex elements and hence corresponds to diagonal 2x2 amplitude matrices. A general polarized eigenvector can then be parameterized in terms of two angles, α and δ, as shown in equation 2

$$(2+1) \rightarrow \sqrt{\lambda_{\max}} \begin{bmatrix} \cos\alpha \\ \sin\alpha e^{i\delta} \end{bmatrix} \qquad \text{- (2)}$$

Note that $\alpha = \delta = 0$ corresponds to the identify amplitude matrix and so any departure of these parameters from this point represents a departure from trivial scattering behavior. There remain 3 sub-eigenvalues that fully characterize the types of depolarization that can occur around this polarized system. While it is possible to classify directly in this eigenvalue space, it is often more convenient to use secondary parameters derived from the eigenvalues and more closely related to the degree of polarization as widely used in Stokes algebra. The most important such parameter is the scattering entropy H as defined in equation 3, where λ_i are the (real) eigenvalues of [T] [2,3].

$$H = -\sum_{i=1}^{4} P_i \log_4 P_i \qquad 0 \le H \le 1, \qquad P_i = \frac{\lambda_i}{\sum \lambda} \qquad \text{- (3)}$$

$$\underline{e}_{\max} = \begin{bmatrix} e_1 & e_2 & 0 & 0 \end{bmatrix}^T, \quad |\underline{e}| = 1 \Rightarrow \alpha = \cos^{-1}(|e_1|)$$

From the dominant normalized eigenvector of [T], $\underline{e}_{max}$, we can then estimate the alpha parameter as shown. This then gives us a clear idea of the nature of the polarized scattering component, which we expect to vary with scattering angle and particle shape and size. We now turn to consider application of these ideas to the ALSD.

3 Characterization of Aerosol particles

Details of the size distribution and material composition of all particles can be found on the ALSD web site (http://www.astro.uva.nl/scatter/) and here we select only four examples for illustration. We further restrict attention to a single wavelength (red laser with λ = 632.8nm). We select feldspar, red clay and two volcanic ash types, Lokon and Pinatubo, as these were found to exhibit limiting behavior patterns in terms of their depolarization properties. Figure 1 shows SEM photographs of the selected sets, illustrating the diversity of shape and particle size to be considered. Note in particular that the Lokon sample contains large particles, the SEM image has a 10x reduction in magnification for this sample compared to the others.

4 Results

Figure 2 shows results for these four samples. In a) we show the trace of the coherency matrix [T] (sum of eigenvalues), which equals the well-known phase function [1]. We notice the generally smooth behavior, with a larger level of scattering from the Lokon ash, especially in the backscatter hemisphere. In b) we show the corresponding normalized eigenvalue spectra (P_i in equation 3) for these samples. Here we show the four ordered eigenvalues in black, red, green and blue for each of the four samples, using the following symbols (* = feldspar, + = red clay, □ = Pinatubo and ◊ = Lokon). We note the following features:

1) The scattering in the forward direction is strongly polarized, with a clear dominant eigenvalue generating over 90% of the scattered power for scattering angles out to 20-40 degrees. The strongest depolarization on the other hand occurs for a scattering angle in the backscatter hemisphere, the exact value of which differs from sample to sample.
2) The samples fall into two clear categories. For any given scattering angle, the feldspar and Pinatubo ash are both more polarized than the red clay and Lokon ash.

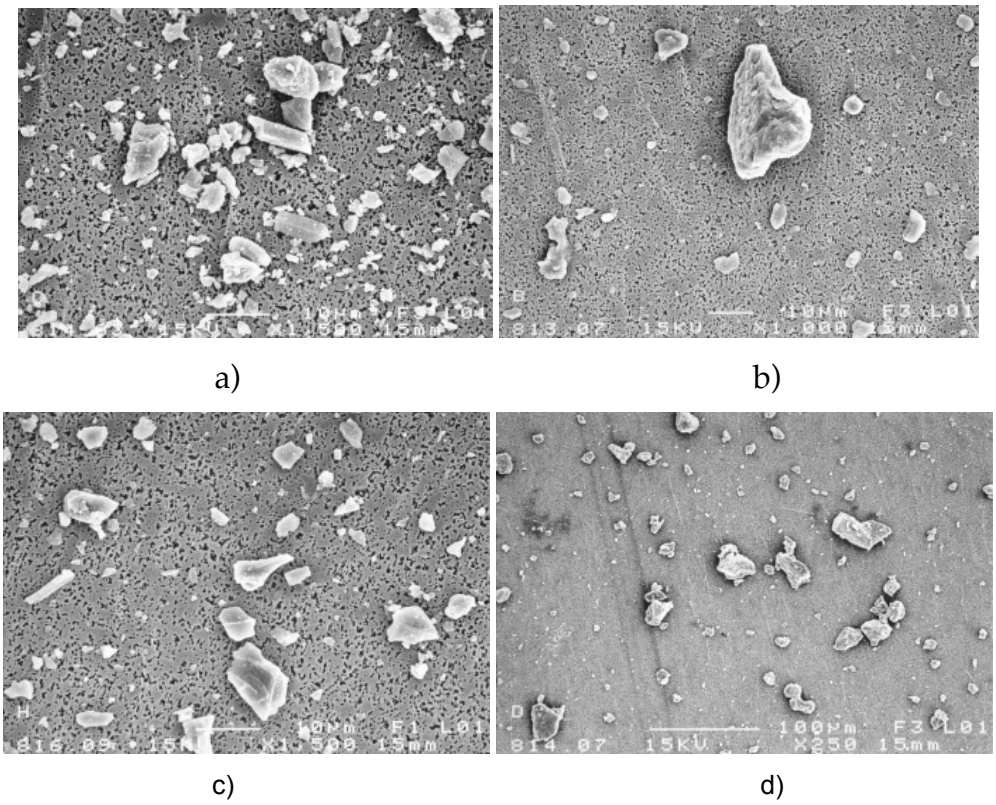

Figure 1: SEM images of the four aerosol samples used in this study, a) feldspar, b) red clay c) Pinatubu ash, d) Lokon ash, white bars are 10μm in a),b) and c) but 100μm in d)

This behavior is confirmed in the entropy variation, as shown in c). Here we see that the entropy is lowest (most polarized) for the feldspar and highest (least polarized) for the Lokon ash. Finally, the alpha angle is shown in d) and here we see a typical variation for particle clouds, with zero for forward scattering (with an amplitude matrix given by the 2 x 2 identity) and diag(1,-1) for backscatter, corresponding to $\alpha = 90^o$ [2]. For Rayleigh scattering, α equals 45^o for a 90^o scattering angle (the amplitude matrix for a dipole). We see however that the scattering angle for which α is 45^o actually varies from sample to sample.

5 Conclusions

In this paper we have applied the entropy formalism to experimental measurements from the Amsterdam light scattering database for the first time. Our results indicate that there is interesting structure in these data sets, which can be used to shed light on the nature of depolarization by aerosols.

Acknowledgments

We would like to acknowledge Hester Volten and colleagues for supporting the Amsterdam Light Scattering database and for their help in converting the data sets to coherency form.

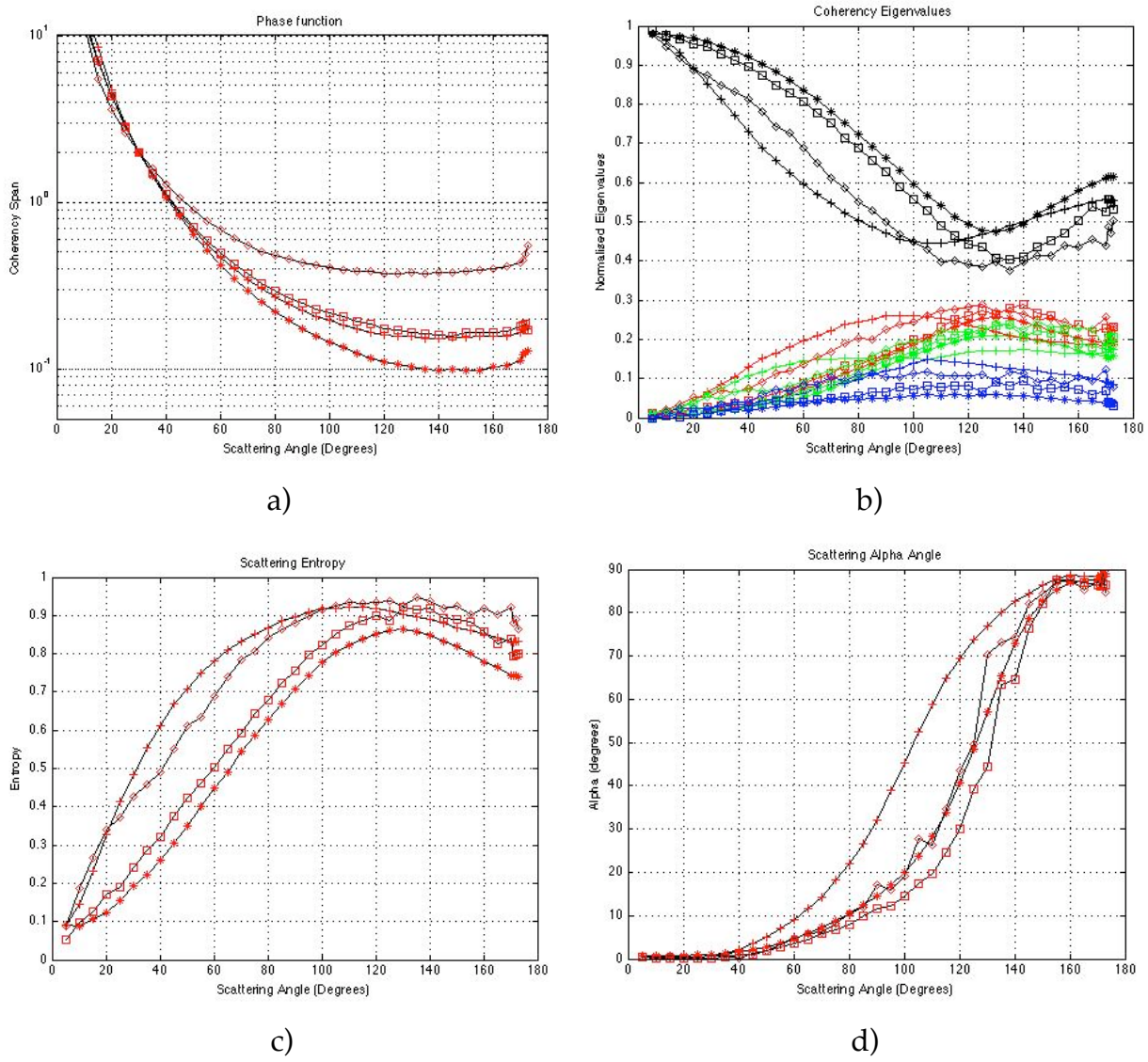

Figure 2: Entropy/alpha analysis of four particle sets (* = feldspar, + = red clay, □ = Pinatubo and ◊ = Lokon), a) is coherency span, b) is normalized eigenvalue spectra, c) is entropy and d) is alpha angle

References

[1] H. Volten, Muñoz O, Rol E, de Haan JF, Vassen W, Hovenier JW, Muinonen K, Nousiainen T., "Scattering matrices of mineral particles at 441.6 nm and 632.8 nm", Journal of Geophysical Research, **106**, 17375-17401, (2001)

[2] S.R Cloude, E. Pottier , "The Concept of Polarisation Entropy in Optical Scattering", Optical Engineering, Volume 34, No. 6, ISSN 0091-3286, pp 1599 - 1610, (1995)

[3] S R Cloude, "Polarization Symmetries in Electromagnetic Scattering", Proceedings of 10th Symposium on Electromagnetic and Light Scattering, Bodrum, Turkey, June (2007)

[4] M I Mishchenko, J W Hovenier, L D Travis, (Eds) "*Light Scattering by Nonspherical Particles: Theory, Measurements and Applications*", Academic Press, (2000)

Retrieval of Aerosol Optical Depth in Vicinity of Broken Clouds from Reflectance Ratios: A Novel Approach

E. Kassianov, M. Ovtchinnikov, L.K. Berg, S. A. McFarlane, C. Flynn

Pacific Northwest National Laboratory, USA

tel: +1 (509) 372-6535, fax: +1 (509) 372-6168, e-mail: Evgueni.Kassianov@pnl.gov

Abstract

A novel method for the retrieval of aerosol optical depth (AOD) under partly cloudy conditions has been suggested. The method exploits reflectance ratios, which are not sensitive to the three-dimensional (3D) effects of clouds. As a result, the new method provides an effective way to avoid the 3D cloud effects, which otherwise would have a large (up to 140%) contaminating impact on the aerosol retrievals. The one-dimensional (1D) version of the radiative transfer model has been used to develop look-up tables (LUTs) of reflectance ratios as functions of two parameters describing the spectral dependence of AOD (a power law). The new method implements an innovative inversion for simultaneous retrieval of these two parameters and, thus, the spectral behavior of AOD. The performance of the new method has been illustrated with a three-stage model-output inverse problem. First, the 3D properties of cumulus clouds and aerosols are generated by a Large-Eddy Simulation (LES) model. Second, synthetic reflectances at 470, 660, and 870 nm are simulated. Finally, we apply developed LUTs to convert synthetic reflectance ratios (470, 660 nm) and (470, 870 nm) into retrieved values of AOD at three wavelengths (470, 660, and 870 nm), and compare retrieved and true AOD values. Results of the model-inverse problem suggest that a new retrieval has the potential for accurate (~15%) estimation of AOD in the presence of broken clouds.

1. Introduction

The three-dimensional (3D) radiative effects may cause large uncertainties of satellite aerosol retrievals under partly cloudy conditions [1,2]. For example, analysis of multi-year aerosol statistics derived from the MODerate-Resolution Imaging Spectroradiometer (MODIS) data in clear patches of cloud fields suggests that aerosol product may be in error (up to 140%) as a result of 3D cloud-induced enhancement of clear sky reflectance [3]. To take into account such enhancement, a simple parameterization has been suggested [4]. Here we introduce an approach [5], that provides an effective way to avoid the 3D cloud effects, and we illustrate its performance with a model-output inverse problem.

2. Approach

For clear patches of broken fields, the 3D reflectance R_{3D} can be expressed as

$$R_{3D}(\lambda) = R_{1D}(\lambda) + \Delta R_{3D}(\lambda). \quad (1)$$

Here, $R(\lambda)$ is the reflectance at wavelength λ with the subscripts “3D” and “1D” indicating values obtained on the basis of 3D and one-dimensional (1D) RT calculations, respectively. The difference between 3D and 1D reflectances, ΔR_{3D}, is the cloud-induced enhancement. Similar to R_{1D}, ΔR_{3D} is

spectrally dependent [3]. In contrast to R_{1D}, ΔR_{3D} is a function of cloud optical properties. In particular, ΔR_{3D} increases with cloud optical depth [3]. Since cloud optical properties are almost spectrally independent, clouds largely scatter (reflect) the same amount of light regardless of the wavelength. Thus, we assume that relative enhancement $\Delta R_{3D}(\lambda)/R_{1D}(\lambda)$ depends only slightly on wavelength as well. As a result, we have

$$\rho_{3D}(\lambda_1,\lambda_2) \approx \rho_{1D}(\lambda_1,\lambda_2), \tag{2}$$

where $\rho(\lambda_1,\lambda_2)$ is the ratio of reflectances $R(\lambda_1)$ and $R(\lambda_2)$ at two wavelengths λ_1 and λ_2. Eq.(2) means that the reflectance ratio is not sensitive to the 3D cloud effects and therefore can be used to estimate aerosol optical depth τ_a.

The reflectance ratio depends on two values of aerosol optical depth $\tau_a(\lambda_1)$ and $\tau_a(\lambda_2)$. Thus, we have one known (ratio) and two unknowns. By selecting an additional wavelength, we obtain an open system with two *constraints* and three *unknowns*. We close the system by approximating the spectral dependence of τ_a using a power law, which has two parameters:

$$\tau_a(\lambda) = \beta \lambda^{-\alpha} \tag{3}$$

Once the parameters α and β are derived from the reflectance ratios $\rho_{3D}(\lambda_1,\lambda_3)$ and $\rho_{3D}(\lambda_2,\lambda_3)$, Eq.(3) can be used to estimate $\tau_a(\lambda)$.

3. Model-Inverse Problem

To illustrate the potential for the suggested approach, we use 3D fields of aerosol and clouds obtained from the Large-Eddy Simulation (LES) with explicit microphysics. The LES simulations are performed for typical conditions observed during the Cloud and Land Surface Interaction Campaign (CLASIC) (http://www.arm.gov/publications/programdocs/doe-sc-arm-0703.pdf) conducted during the summer of 2007. We calculate reflectances using a Monte Carlo method. In particular, we simulate aircraft observations at three wavelengths (470, 660, and 870 nm) with 0.05 km horizontal resolution. Figure 1 shows that for clear pixels located far away from clouds and their shadows the difference between 3D and 1D reflectances can be as large as 15% as indicated by the red color. This magnitude is consistent with previous studies [3]. In contrast to the reflectances, the 3D and 1D reflectance ratios are comparable (within 3%) for the majority of clear pixels (Figure 1d). Thus, the reflectance ratio is less sensitive to 3D cloud effects than reflectances themselves.

We develop look-up tables of AOD (Figure 2a,b) and corresponding 1D reflectance ratios (Figure 2c,d) as functions of two parameters α and β. Isolines of the developed ratio values are nearly orthogonal (Figure 2c,d). As a result, a *unique* solution of these two parameters (α and β) can be obtained. To illustrate performance of the retrieval, we assume that calculated reflectance ratios represent observations. Then we apply the look-up tables and retrieve two parameters (α and β) from which we derive AOD. Finally, we compare retrieved and true values of AOD (Figure 3): for the majority of clear pixels, the difference does

not exceed 15%. Compared to pixel-based differences, the domain-averaged ones are smaller (within 3%). Similar agreement is obtained for other wavelengths (470 and 870 nm).

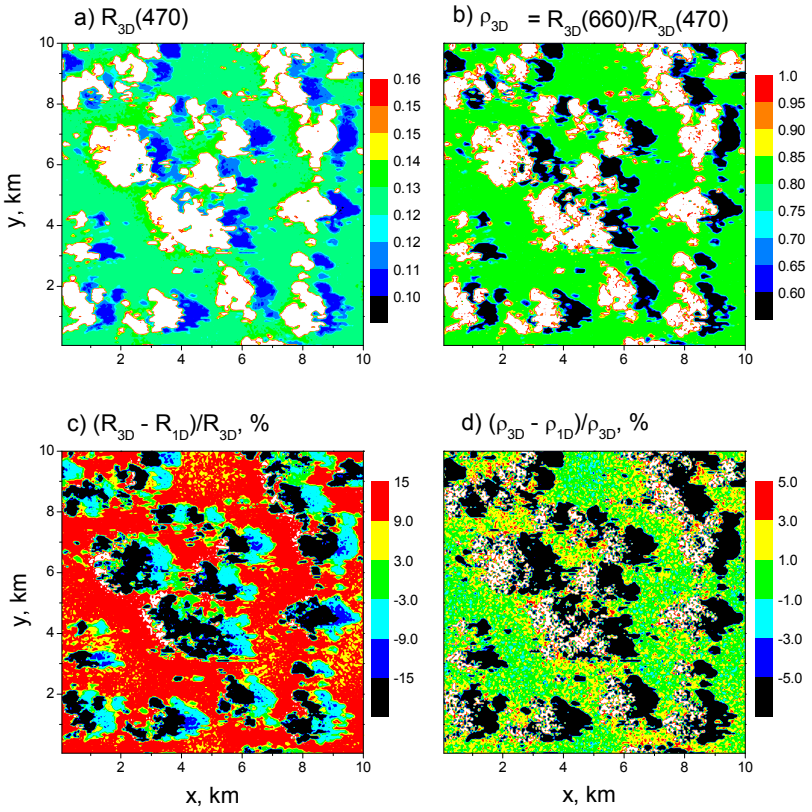

Figure 1. Simulated (a) 3D reflectance at 470 nm, (b) 3D reflectance ratio (660,470 nm), and relative difference between 3D and 1D (c) reflectances at 470 nm, (d) reflectance ratios (660,470 nm).

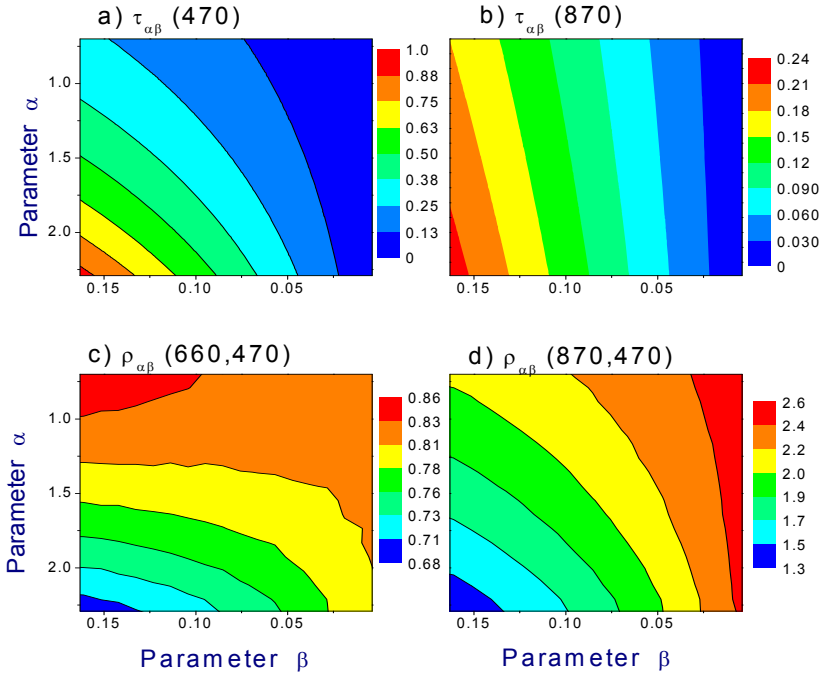

Figure 2. Look-up tables of (a,b) model AODs at 470 and 870 nm, (c,d) 1D reflectance ratios (660, 470 nm) and (870, 470 nm) in terms of parameters α and β.

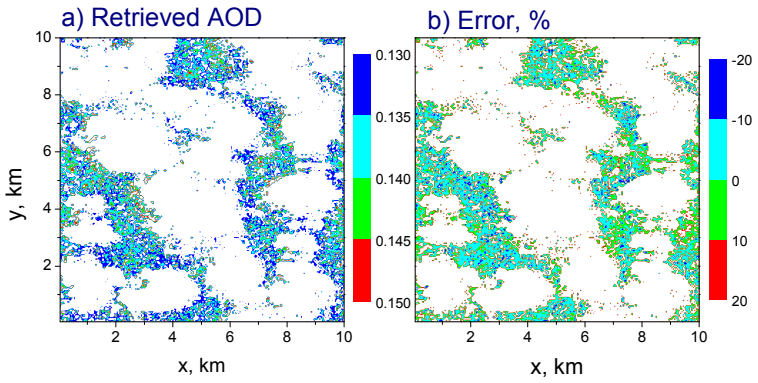

Figure 3. (a) Retrieved AOD (660 nm), and (c) corresponding differences between retrieved and true values of AOD. Here the white color represents clouds and their shadows.

4. Summary

We propose a new approach for retrieving AOD under partly cloudy conditions. This approach is based on ratios of the reflectances at different wavelengths and provides an effective way to avoid the 3D cloud effects. Weak spectral variability of cloud optical properties in the visible spectral range is the reason why the 3D cloud effects caused by surrounding clouds may be proportional at different wavelengths. Thus, by using the ratio of reflectances the 3D cloud effects can be removed. Results of the model-inverse problem suggest that for the majority of clear pixels the error in the retrieved value of AOD is within 15%, while the domain-averaged values of AOD can be retrieved more accurately (~3%). Our preliminary study demonstrates that NASA Earth Observing System (EOS) instruments (e.g., MODIS) may have the potential for accurate estimation of AOD under partly cloudy conditions using this new approach.

Acknowledgments

This work was supported by the NASA through the Radiation Sciences Program and the Office of Biological and Environmental Research (OBER) of the U.S. Department of Energy (DOE) as part of the Atmospheric Radiation Measurement (ARM) Program. The Pacific Northwest National Laboratory (PNNL) is operated for the DOE by Battelle Memorial Institute under contract DE-AC06-76RLO 1830.

References

[1] Zhang, J., J. Reid, and B. Holben, “An analysis of potential cloud artifacts in MODIS over ocean aerosol optical thickness products”, Geophys. Res. Lett. **32**, L15803 (2005).

[2] Yang, Y., and L. Di Girolamo, “Impacts of 3-D radiative effects on satellite cloud detection and their consequences on cloud fraction and aerosol optical depth retrievals”, J. Geophys. Res. **113**, D04213 (2008).

[3] Wen, G., A. Marshak, R. F. Cahalan, L. A. Remer, and R. G. Kleidman, “3D aerosol-cloud radiative interaction observed in collocated MODIS and ASTER images of cumulus cloud fields”, J. Geophys. Res. **112**, D13204 (2007).

[4] Marshak, A., G. Wen, J. A. Coakley Jr., L. A. Remer, N. G. Loeb, and R. F. Cahalan, “A simple model for the cloud adjacency effect and the apparent bluing of aerosols near clouds”, J. Geophys. Res. **113**, D14S17 (2008).

[5] Kassianov E. and M. Ovtchinnikov, “On reflectance ratios and aerosol optical depth retrieval in the presence of cumulus clouds”, Geophys Res Lett, L06807 (2008).

Estimation of BDRF models for soil and vegetation terrestrial surfaces using RSP airborne data

Pavel Litvinov,[1] Otto Hasekamp,[1] Brian Cairns[2]

[1]*SRON Netherlands Institute for Space Research,*
Sorbonnelaan 2, 3584 CA Utrecht, The Netherlands
[2]*Department of Applied Mathematics and Applied Physics, Columbia University*
New York, USA
tel: +31 (030) 2538573, e-mail: P.Litvinov@sron.nl

Abstract

The models of BDRF for soil and vegetation types of terrestrial surfaces have been estimated. RSP airborne data on low altitude over land and models which take into account single and multiple scattering are used for these purposes. It is concluded that single scattering gives main contribution in polarization for soil, whereas for vegetation types of terrestrial surfaces contribution of multiple scattering may be noticeable.

1 Introduction

One of the very important problem in remote sensing is related with description of Bidirectional Reflection Function (BDRF) for different kinds of terrestrial surfaces. Due to big variety of the Earth surfaces this problem is very complicated. The BDRF models for water surfaces are comparably quite good developed for different spectral regions [1],[2]. But for soil and vegetation types of terrestrial surfaces the different models of BDRF are often required for different wavelengths. At present time creation of BDRF models for optical and infrared regions is very important for the problem of aerosol retrievals over land, where accurate description of reflection properties of the Earth surfaces is essential.

Different models have been proposed for BDRF for soil and vegetations types of terrestrial surfaces (see, for example, [3],[4]). In general BDRF can be presented as follows:

$$\mathbf{R}(\mathbf{n}_v, \mathbf{n}_{inc}) = \mathbf{R}_1(\mathbf{n}_v, \mathbf{n}_{inc}) + \mathbf{R}_{mult}(\mathbf{n}_v, \mathbf{n}_{inc}) \ , \quad (1)$$

where $\mathbf{R}_1(\mathbf{n}_v, \mathbf{n}_{inc})$ corresponds to single scattering and $\mathbf{R}_{mult}(\mathbf{n}_v, \mathbf{n}_{inc})$ takes into account multiple scattering in a medium ($\mathbf{n}_v, \mathbf{n}_{inc}$ are unit vectors in the direction of viewing and incident correspondingly). A lot of models of BDRF for vegetation as well as for soil assume that contribution of multiple scattering is not considerable and just single scattering is taken into account [3]. Other theoretical models consider contribution of $\mathbf{R}_{mult}(\mathbf{n}_v, \mathbf{n}_{inc})$ as Lambertian term, which contributes correspondingly just into intensity (matrix element $R_{11}(\mathbf{n}_v, \mathbf{n}_{inc})$) but not into polarization and does not depend on illumination and scattering conditions [4]. There are also models based on radiative transfer theory which take into account contribution of multiple scattering in intensity as well as in polarization [5]-[7].

Here we estimate the models of BDRF which take into account polarization and try answering the question how is considerable the contribution of multiple scattering into polarization for soil and vegetation types of terrestrial surfaces. For this purposes we have considered theoretical models, which take into account contribution of single and multiple scattering in polarization, and used them for interpretation of RSP polarization measurements.

2 Data of RSP measurements

We used RSP data obtained during ALIVE measurement campaign performed in Oklahoma (USA) in September of 2005 [8]. RSP instrument measures intensity and polarization at wide range of viewing zenith angles in 9 spectral bands 410-2250 nm. There are several flights in ALIVE campaign which

present measurements at low altitude over the land (about 200-300 m). These measurements provide good opportunity for testing different models of BDRF for the Earth surfaces.

Soil and other non-vegetated surfaces have much smaller spectral contrast between the red and near-infrared bands. Follow to [8] we used this fact to distinguish soil and vegetations types of surfaces and carry out averaging of intensity and polarization over different realizations (scans). We used data of two different flights over the similar types of surfaces but at different time during the same day [8]. Thus the data for these flights are obtained for different illumination and scattering geometries and are related in average with same types of soil and vegetation surfaces.

3 Estimation of theoretical models

If the single scattering is produced by inhomogeneities differently oriented relatively incident and scattered directions (for example, by chaotically oriented leaves for vegetation surfaces, by chaotically oriented nonspherical particles of soil etc) or by facets with Fresnel's reflection, $\mathbf{R}_1(\mathbf{n}_v, \mathbf{n}_{inc})$ can be presented as follows [1],[2],[7]:

$$\mathbf{R}_1(\mathbf{n}_v, \mathbf{n}_{inc}) = \mathbf{L}(\eta_v)\mathbf{F}(\vartheta)\mathbf{L}(\eta_{inc}) f(\mathbf{n}_v, \mathbf{n}_{inc}), \tag{2}$$

where $\mathbf{L}(\eta_v)$ and $\mathbf{L}(\eta_{inc})$ are Stokes rotation matrix for angles η_v and η_{inc} [7], $\mathbf{F}(\vartheta)$ is averaged over orientations of inhomogeneities scattering matrix (for facets with Fresnel's reflection $\mathbf{F}(\vartheta)$ is the Fresnel's reflection matrix), ϑ is a scattering angle defined in scattering plane ($\cos\vartheta = \cos\vartheta_v \cos\vartheta_{inc} + \sin\vartheta_v \sin\vartheta_{inc} \cos(\varphi_v - \varphi_{inc})$, ϑ_{inc}, ϑ_v are zenith incident, zenith viewing angles, φ_{inc}, φ_v are azimuth angles of incident and viewing directions), and $f(\mathbf{n}_v, \mathbf{n}_{inc})$ is a function of zenith incident, zenith viewing angles and azimuth angles of incident and viewing directions (for the Gaussian random rough surface $f(\mathbf{n}_v, \mathbf{n}_{inc})$ depends also on properties of the Gaussian surface).

Thus, taken into account that $\mathbf{F}(\vartheta)$ for chaotically oriented and mirror symmetric particles has block-diagonal shape, the Stocks parameters Q and U of scattered radiation can be written as follows (incident radiation is supposed to be unpolarized):

$$Q(\mathbf{n}_v, \mathbf{n}_{inc}) = F_{21}(\vartheta)\cos\eta_v f(\mathbf{n}_v, \mathbf{n}_{inc}), \tag{3}$$

$$U(\mathbf{n}_v, \mathbf{n}_{inc}) = F_{21}(\vartheta)\sin\eta_v f(\mathbf{n}_v, \mathbf{n}_{inc}). \tag{4}$$

Thus in single scattering approximations for different wavelength λ_1 and λ_2 we have:

$$K(\lambda_1, \lambda_2, \vartheta) = \frac{\sqrt{Q_{\lambda_1}^2 + U_{\lambda_1}^2}}{\sqrt{Q_{\lambda_2}^2 + U_{\lambda_2}^2}} = \frac{F_{21}(\lambda_1, \vartheta)}{F_{21}(\lambda_2, \vartheta)}. \tag{5}$$

Function $K(\lambda_1, \lambda_2, \vartheta)$ in single scattering approximation and for chaotically oriented inhomogeneities depends just on the wavelength and scattering angle. Since for different illumination and scattering conditions (different sets of ϑ_{inc}, ϑ_v, φ_{inc}, φ_v) the same ϑ can be obtained, function $K(\lambda_1, \lambda_2, \vartheta)$ in single scattering approximation must be the same for different sets of ϑ_{inc}, ϑ_v, φ_{inc}, φ_v but with the same ϑ. This is not the case when multiple scattering contributes considerably in $K(\lambda_1, \lambda_2, \vartheta)$ or if inhomogeneities have rather preferable than chaotic orientation and non block-diagonal $\mathbf{F}(\vartheta)$. To demonstrate this we carried out several calculations and compared them with RSP measurements of the Stocks parameters Q and U for two different flights. Illumination and scattering geometry for the first flight: $\varphi'_{inc} \approx 137^0$, $\vartheta_{inc} \approx 42^0$, $\varphi'_v \approx 92^0$, $-40^0 \le \vartheta_v \le 60^0$. Illumination and scattering geometry for the second flight: $\varphi'_{inc} \approx 250^0$, $\vartheta_{inc} \approx 62^0$, $\varphi'_v \approx 46^0$, $-60^0 \le \vartheta_v \le 40^0$. For both flights $\varphi_{inc} = 2\pi - \varphi'_{inc}$; $\varphi_v = 2\pi - \varphi'_v$ ($\vartheta_v < 0$); $\varphi_v = \pi - \varphi'_v$ ($\vartheta_v \ge 0$). Further on the figures the solid curves will correspond to the Illumination and scattering geometry for the first flight and the dashed ones will correspond to the geometry for the second flight.

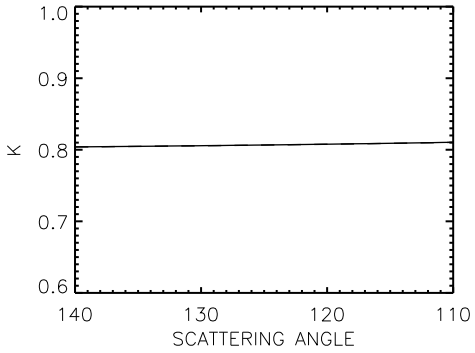

Figure 1: Angular dependence of $K(\lambda_1,\lambda_2,\vartheta)$ for the model of Fresnel's reflection by facets.

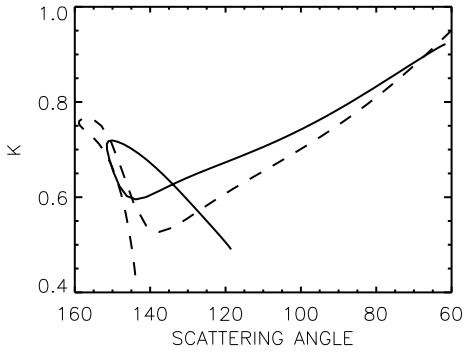

Figure 2: Angular dependence of $K(\lambda_1,\lambda_2,\vartheta)$ obtained using VRTE.

Fig. 1 presents results of calculation of $K(\lambda_1,\lambda_2,\vartheta)$ when just single scattering by facets with Fresnel's reflection is taken into account. The refractive index is considered to be wavelength dependent ($m_{\lambda_1}=1.5$, $m_{\lambda_2}=1.6$). For the considered flights different illumination and scattering condition can give the same value of ϑ. In single scattering approximation $K(\lambda_1,\lambda_2,\vartheta)$ is the same for both flights with the same ϑ (see Fig. 1).

Fig. 2 presents results of calculation of $K(\lambda_1,\lambda_2,\vartheta)$ obtained on the basis of the vector radiative transfer theory [7]. The medium is considered to be semi-infinite medium of small spherical particles without resonances in angular dependences of $F_{21}(\vartheta)$. The size parameters and the refractive indexes of the particles of the medium depend on wavelength ($x_{\lambda_1}=1.5$, $m_{\lambda_1}=1.5$; $x_{\lambda_2}=1.$, $m_{\lambda_2}=1.6$). The viewing angle for this calculations was: $-90^0 \le \vartheta_v \le 90^0$. Fig. 2 demonstrates different angular dependence of $K(\lambda_1,\lambda_2,\vartheta)$ for the two flights for the same values of scattering angle ϑ, which is due to contribution of multiple scattering.

Figs. 3, 4 present angular dependence of $K(\lambda_1,\lambda_2,\vartheta)$ obtained from RSP measured data for the two flights. Fig. 3 corresponds to soil types of surfaces and Fig. 4 corresponds to vegetation types of surfaces. Each figure contains two plots. One of them corresponds to $K(\lambda_1,\lambda_2,\vartheta)$ with $\lambda_1=470\,\text{nm}$ ('blue' band) and $\lambda_2=670\,\text{nm}$ ('red' band), another one corresponds to $K(\lambda_1,\lambda_2,\vartheta)$ with $\lambda_1=670\,\text{nm}$ ('red' band) and $\lambda_2=864\,\text{nm}$ ('near-infrared' band). The difference in angular dependences of $K(\lambda_1,\lambda_2,\vartheta)$ for the two flights more noticeable for vegetation than for soil.

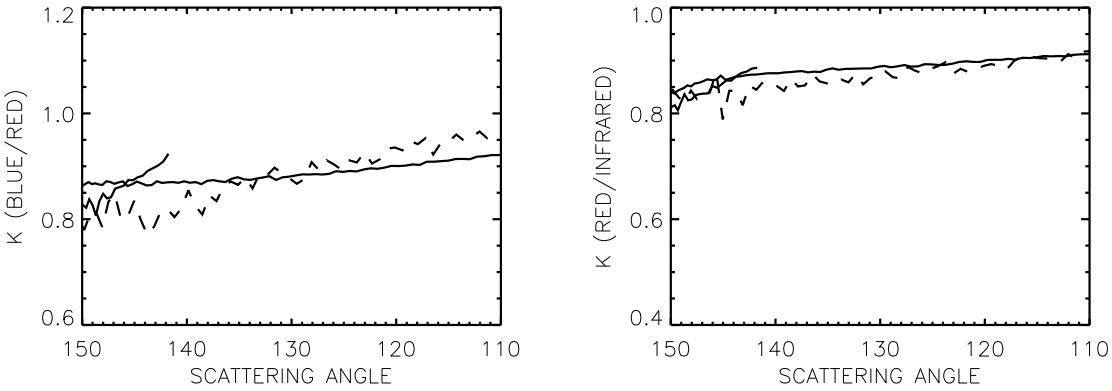

Figure 3. Angular dependence of $K(\lambda_1,\lambda_2,\vartheta)$ from RSP measurements of soil types of surfaces.

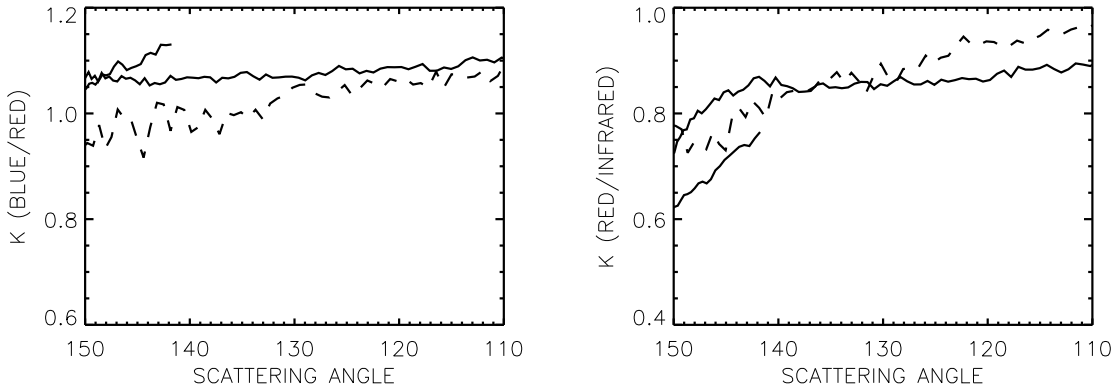

Figure 4. Angular dependence of $K(\lambda_1, \lambda_2, \vartheta)$ from RSP measurements of vegetation types of surfaces.

4 Conclusion

Obtained results demonstrate slight dependence of the relation (5) for soil types of surfaces on the illumination and scattering geometry when scattering angle is the same. On the basis of the theoretical considerations we conclude that this is due to the fact that for soil contribution of multiple scattering in polarization can be not as considerable as contribution of single scattering, whose polarization characteristics can be presented by Eqs. (3), (4).

For vegetation types of terrestrial surfaces the relation (5) depends quite noticeably on the illumination and scattering geometry. There are at least to possible reasons of this. The first one can be that the reflection from leaves is not Fresnel's reflection as it is usually supposed in models of BDRF for vegetation. In this case single scattering by not chaotically but preferably orientated leaves can give the dependence of the relation (5) on the illumination and scattering geometry at the same scattering angle. Another reason can be related to contribution of multiple scattering between different leaves.

We plan to carry out similar considerations for other flights related to other regions to further check these results.

Acknowledgments

We thanks M. Mishchenko for his radiative transfer code, which has been used to obtain results of Figure 2.

References

[1] L. Tsang, J.A. Kong, R.T. Shin, *Theory of Microwave Remote Sensing* (Wiley, New York, 1985).

[2] M.I. Mishchenko, L.D. Travis, Journal of Geophysical Research. **102**,16989-17013 (1997).

[3] F.-M. Breon, D.Tanre, P. Lecomte and M. Herman, IEE Transactions on Geoscience and Remote Sensing. **33**, 487-499 (1995).

[4] R.J.D. Spurr, JQSRT. **83**, 15-46 (2004).

[5] L. Tsang, J.A. Kong, K-H. Ding, *Scattering of electromagnetic waves. Advanced topics* (Wiley ,New York, 2001).

[6] M.I. Mishchenko, J.M. Dlugach, E.G. Yanovitskij, N.T. Zakharova, JQSRT. **63**, 409-432 (1999).

[7] M.I. Mishchenko, L.D. Travis and A.A. Lacis, *Multiple Scattering of Light by Particles. Radiative Transfer and Coherent Backscattering* (Cambridge University Press, 2006).

[8] K.D. Knobelspiesse, B. Cairns, C.B. Schaaf, B. Schmid, M.O. Roman, Remote Sensing of Enviroment (2008, submitted).

Monte Carlo ray tracing technique for light scattering by particles with non-spherical inclusions

Maya Mikrenska and Pavel Koulev,

Institute of Mechanics,

Acad. G. Bonchev str., bl. 4, Sofia 1113, Bulgaria
tel: + (359) 2979-6466, e-mail:mikr@imbm.bas.bg

Abstract

A simple and computationally advantageous algorithm for simulation of light scattering by large particles with multiple cubical inclusions is developed. The proposed method is based on ray tracing and direct simulation Monte Carlo. The computational model is applied to examine the effect of multiple scattering inside the host particle and absorption properties of the inclusions on the scattering phase function.

1 Introduction

The study of light scattering by inhomogeneous micro particles is motivated by the great importance of the problem for astronomy, atmospheric science, climatology, oceanography, optical particle sizing, etc. For example, water droplets in the atmosphere that contain insoluble inclusions are of essential interest for climatology.

The first calculations for sphere with concentric inclusion have been done by Aden and Kerker [1], and later extended by Toon and Ackerman [2] for multilayered sphere. The theory of light scattering by spherical particle containing one non-concentric spherical inclusion has been developed by Borghese et al. [3] and Videen et al. [4]. The T-matrix method has been applied by Wried and Doicu [5] for a great variety of particles including inhomogeneous particles. The multiple multipole method code for inhomogeneous particles has been developed by Hafner and Bombolt [6]. Monte Carlo ray tracing combined with Mie theory has been used by Mishchenko and Macke [7] for large particles with multiple spherical inclusions.

The main goal is to developed Monte Carlo ray tracing technique for numerical simulation of light scattering by large particles with non-spherical inclusions. In this paper we present some first results from the application of the algorithm for the study of effects of absorption of light due to the non-transparency of the inclusions and multiple scattering inside the particle on the scattering phase function.

2 Model description

We consider spherical dielectric particles containing absorbing cubical inclusions with given size distribution and number density under the following assumptions: The inclusions have arbitrary orientations; of the inclusions the wavelength is much smaller than the particle size as well as than the inclusions sizes so that the geometric optics is applicable; the inclusions are disposed within a concentric sphere with radius equal to the radius of the host particle decreased by four times mean radius of the inclusions that ensure the validity of Snell's law and Fresnel's formulas; the distance between internal inclusions must be larger than a few times their radii in order to act as independent scatterers.

Radiation absorbing is realized according to Beer-Lambert law

$$I = I_0 e^{-\alpha z}, \tag{1}$$

where $\alpha = \frac{4\pi k}{\lambda}$ is the absorption coefficient, I is the light intensity , I_0 is the initial light intensity, z is the propagation depth (path length), k is the extinction coefficient, and λ is the wavelength.

For the simulation of light scattering by large particles with multiple inclusions we use Monte Carlo ray tracing algorithm. The present computational technique is an extension of the method for single light scattering by cubes [8] and rounded cubes [9, 10]. We use direct simulation Monte Carlo method to trace out of the photon paths for a great number of photons in accordance with geometric optics laws. As a result of each photon-host particle interaction both of the following chains of elementary events are possible: an external reflection; a refraction (the photon gets into the particle), followed by one or more internal reflections combined with single or multiple scattering by the inclusions (internal scatterers) and finally by absorption or refraction (the photon gets out of the host particle). For the internal scatterers we apply the algorithm for a photon path tracing at single scattering by cube. In contrast to the spherical shape, the cubic shape of the inclusions presume occurrence of total internal reflections inside the inclusion. The total internal reflection in an inclusion is possible in case that refractive index of the inclusion is greater than the refractive index of the host particle. Otherwise, the total internal reflection is possible in the inclusion "exterior". The free path *fp* of the photon at multiple scattering is determined by means of the mean free path *mfp* as follows:

$$fp = -\log(1-rand)*mfp, \quad (2)$$

where *rand* is a random number, uniformly distributed in [0,1].

For each photon-optical interface interaction Snell's law determines the possible propagation direction and the changes of parallel and orthogonal to the scattering plane light intensities are calculated by means of Fresnel's formulas. The coefficients in Fresnel's formulas are used as probabilities for the choice of the outcome of the photon – optical interface interaction: reflection or transmission (refraction). The weighted outcomes of tracing of all launched photons are summed and the final result for scattering phase function is calculated.

3 Results and discussion

A series of numerical experiments is provided in order to examine the influence of inclusions density and the imaginary part of the refractive index of the internal scatterers on the scattering phase function. The number of launched photons in all experiments varies from 1.10^7 to 5.10^7.

At first, the proposed computational model is applied for numerical simulation of light scattering by spherical particle with radius r_s =100 μm and refractive index n = 1.33 (water at wavelength of 590 nm) containing cubic inclusions of NaCl with uniform distribution of the size (sides of the cubes s = 2r = 10 μm) and refractive index n = 1.544+0.001i. It should be noted that the computational algorithm allows calculating whatever size distribution of the internal scatterers. Figure 1 shows the dependence of the scattering phase function on the mean free path or number density, respectively. For comparison, the scattering phase function of a homogeneous sphere (r_s =100μm and n = 1.33) is also included in the picture. The intensity of the scattered light decreases in the phase angle interval [0, 42^0] and conversely, increases for phase angles in the interval [42^0, 150^0]) when mean free path length decreases. Probably this effect is due to the non-zero value of the internal scatteres and the multiple scattering inside the host particle.

The next numerical experiment is aimed to study the effect of non-zero imaginary part of the refractive index k of the inclusions on the scattering phase function. The host particle is sphere again (r_s = 100μm and n = 1.33). The inclusions are cubes with real part of the refractive index 1.544 and r = 5 μm. Mean free path length is set to 20r. As shown in Fig. 2 the intensity of the scattered light increases in the phase angle interval [42^0, 150^0] when k increases. Computations show that in this interval the same effect as the

effect of multiple scattering is observed. However, the increase of absorption does not lead to significant effect at backscattering.

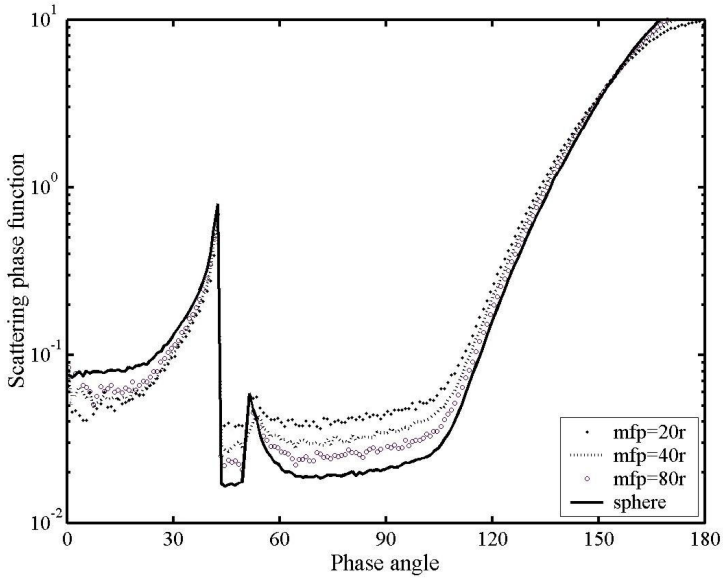

Figure 1: Effect of the mean free path on the scattering phase function.

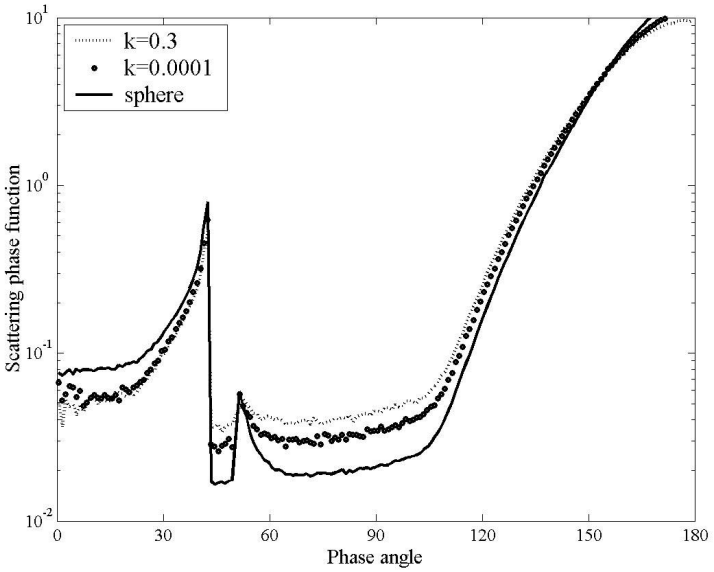

Figure 2: Effect of absorbing properties of the inclusions on the scattering phase function.

3 Conclusion

The developed computational model is capable to simulate light scattering by large particles with multiple inclusions with cubic shape and random orientation. The model is applied to study the influence of the inclusion concentration and extinction coefficient on the scattering phase function. For validation of the model the numerical results should be compared with other theoretical and experimental results.

Acknowledgments

This research is supported by Bulgarian NSF, grant TN-1521/2005.

References

[1] A. L. Aden and M. Kerker, “Scattering of electromagnetic waves from two concentric spheres”, J. Appl. Phys. **22**, 1242 –1246 (1951).

[2] O. B. Toon and T. P. Ackerman, “Algorithms for the calculation of scattering by strati ed spheres”, Appl. Opt. **20**, 3657 –3660 (1981).

[3] F. Borghese, P. Denti, R. Saija,and O. I. Sindoni, “Optical properties of spheres containing a spherical eccentric inclusion”, J. Opt. Soc. Am. A **9**, 1327 –1335 (1992).

[4] G. Videen, D. Ngo, P. Chylek, and R. G. Pinnick, “Light scattering from a sphere with an irregular inclusion”, J. Opt. Soc. Am. A **12**, 922 –928 (1995) .

[5] T. Wriedt and A. Doicu, “Novel software implementation of the T-matrix method for arbitrary con gurations of single and clusters of composite nonspherical particles”, In:Fifth Conference on Electromagnetic and Light Scattering by Nonspherical Particles:Theory,Measurements,and Applications,(Dalhousie University,Halifax, Nova Scotia,Canada, 2000).

[6] C. Hafner and K. Bomholt, *The 3D Electrodynamic Wave Simulator*, (Chichester, Wiley,1993).

[7] M. I. Mishchenko and A. Macke, “Asymmetry parameters of the phase function for isolated and densely packed spherical particles with multiple internal inclusions in the geometric optics limits”, J. Quant. Spectrosc. Radiat. Transfer Vol. **57**, No. 6, 161-194 (1997).

[8] M. Mikrenska, P. Koulev and E. Hadamcik, Direct simulation Monte Carlo of light scattering by cube, Comptes Rend. Acad. Bulg. Sci., **57**, 11, 39-44 (2004).

[9] M. Mikrenska, P. Koulev, J.-B. Renard, E. Hadamcik, and J.-C. Worms, “Direct simulation Monte Carlo ray tracing model of light scattering by a class of real particles and comparison with PROGRA2 experimental results”, J. Quant. Spectrosc. Radiat. Transfer **100**, 256-267 (2006).

[10] M. Mikrenska, P. Koulev, E. Hadamcik, J.-B. Renard, J.-C. Worms, Direct simulation Monte Carlo of light scattering by rounded cubes, Comptes Rend. Acad. Bulg. Sci., **58,** 3, 275-280 (2005).

Modeling polarization radar echoes of hydrometeors using Discrete-Dipole Approximation

Jani Tyynelä,[1,2] Timo Nousiainen,[2] Sabine Göke,[2] and Karri Muinonen[1]

[1] *Observatory, PO. Box 14, FI-00014 University of Helsinki, Finland*
[2] *Department of Physics, University of Helsinki, Finland*
email: jktyynel@mappi.helsinki.fi

Abstract

We study the applicability of the discrete-dipole approximation when modelling radar echoes for hydrometeors. We use homogeneous ice/water spheres and ice spheres coated with different amounts of water to compare to Mie scattering.

1 Introduction

When interpreting polarization radar measurements for weather forecasts and other remote sensing purposes, radar scattering models of precipitating particles provide a realistic, physical base for the inversion problem. Understanding how particles of different shape, size, and phase affect the observed radar quantaties gives a general idea how sensitive certain observables are for the inversion. In this study, we investigate the practical limits of the Amsterdam Discrete Dipole Approximation (ADDA; Yurkin *et al.*, 2000) for modeling ice and water particles of various sizes in the C-band (frequency of 5.6 Ghz).

2 Discrete-dipole approximation

The discrete-dipole approximation (DDA) is a numerical method for simulating electromagnetic scattering from wavelength-scale particles. The particle is divided into a cubic lattice of dipoles, i.e., small, sub-wavelength parts that behave as dipoles, when subject to electromagnetic waves. The electric fields for each dipole in the particle interior are found from a group of equations (e.g., Draine and Flatau, 1994), which depend on the refractive index m, the interdipole distance d, and the wavenumber k of the incident electric field. The scattered far-field is obtained by summing the induced electric fields and their phases in each dipole site.

There are, however, certain criteria that need to be accounted for. First, the number of dipoles that are used should be large enough so that both the particle shape and its scattering characteristics can be correctly simulated. Second, the interdipole distance should be small compared to the wavelength. For calculating radar cross sections, $|m|kd < 0.05$ is recommended by Teschl and Randeu (2007). For C-band radar, according to the criteria, the size of the dipoles must be about $d < 0.24$mm for ice ($m \approx 1.79 + i0.0002$, at 0°C), and $d < 0.05$mm for water ($m \approx 8.34 + i2.23$, at 0°C). Third, the size of the particle compared to the wavelength is, for practical reasons, limited. The maximum number of dipoles is determined by the available memory in a computer. For modern superclusters, it is of the order of 100 million dipoles corresponding to a grid of about 460^3 dipoles. In addition, the convergence of the equation solvers is also limited. The developers of ADDA have tested the convergence as a function of the refractive index and the size parameter $x = kr$ (see the ADDA manual, freely available). For size parameters $x < 1.0$ (radar frequencies), the convergence should be good, when $|m| < 2.0$. For larger m, it is unclear, since the testing was limited to $|m| < 2.0$. For the simulations done in this study, there was no convergence issues.

3 Simulations

The DDA calculations were done on a supercluster at the Finnish Center for Scientific Computing (CSC). The Amsterdam DDA was chosen for modeling. The computational grid is 32^3 dipoles for homogeneous ice particles and 128^3 dipoles for homogeneus water particles and coated particles. For water particles, the computations are also made for a grid of 384^3 dipoles just for checking purposes.

Spheres are used in order to compare the results to the exact Mie theory. For the calculations, eight different radii ($r = 0.5$, 1.0, 1.5, 2.0, 2.5, 3.0, 3.5, and 4.0mm) and two different compositions (ice and water) are used for the homogeneous spheres. For the water-coated ice-spheres, we use same radii as for homogeneous spheres and three ratios of water/ice radii $r_{water}/r_{ice} = 0.98$, 0.94, and 0.9, which correspond to approximately 6%, 17%, and 27%, of total water content, respectively.

4 Results

In Fig. 1, we plot the backscattering (σ_b) and extinction cross sections (σ_e) of spherical ice particles for the DDA calculations, the exact Mie theory, and the Rayleigh approximation as a function of particle radius. As can be seen, both the DDA and the Rayleigh approximation fit well to the exact theory for the whole range of sizes studied. The maximum relative error is 12.9% for σ_b and 5.9% for σ_e.

In Fig. 2, we plot σ_b and σ_e of spherical water particles. The extinction cross sections of DDA fit well to the Mie theory, but the backscattering cross sections deviate non-monotonically from the Mie theory, following more closely the Rayleigh approximation. The maximum relative error is about 66% for σ_b and 5.2% for σ_e. When the grid size is increased to 384^3, there is little improvement for the backscattering cross section. The maximum relative errors in the Rayleigh approximation are 54.6% for σ_b and 66.7% for σ_e.

In Figs. 3 - 5, σ_b and σ_e are plotted for water-coated ice-spheres using the DDA calculations, the exact theory, and the Rayleigh approximation. As can be seen, for very low water content $r_{water}/r_{ice} = 0.98$ (Fig. 3) the DDA fits well in both σ_b and σ_e, but the Rayleigh approximation starts to deviate. The maximum relative error is 36.6% for σ_b and 12.6% for σ_e. For medium water content $r_{water}/r_{ice} = 0.94$ (Fig. 4), the DDA also starts to deviate from the Mie theory, especially for larger sizes. It is still better than the Rayleigh approximation, and the maximum relative error is 46.2% for σ_b and 32.8% for σ_e. For high water content $r_{water}/r_{ice} = 0.9$ (Fig. 5), the DDA fits almost as poorly as the Rayleigh approximation. The maximum relative error is 122.2% for σ_b and 30.0% for σ_e.

5 Discussion and conclusions

When modeling ice particles like hail for radar scattering at the C-band, even the Rayleigh approximation seems to be good enough for both spherical and non-spherical particles. For pure water particles like raindrops, relative errors as high as 66% were found in the backscattering cross sections, and therefore also in some observable radar parameters, though the errors were smaller for smaller particle sizes. Using DDA for calculating σ_b for raindrops is questionable, even when using very large grids. Calculating σ_e with DDA is, on the other hand, a lot more precise. For particles with ice/water mixture, like snow and graupels, the applicability of DDA is still unclear. For water content of 27%, there was already a significant deviation from the exact theory. We plan to study, how the increasing water content affects the cross sections by using clusters of ice and water spheres. Another possibility is to use numerical methods like the generalized point-matching method (GPMM; Morrison and Cross, 1974) for raindrops. Also, since most radar algorithms assume the Rayleigh approximation, the possibility of errors in the observables should be kept in

mind, when observing particles containing water.

Acknowledgments

The authors like to thank Antti Penttilä for his help on running ADDA in a supercluster.

References

[1] M. A. Yurkin, V. P. Maltsev, and A. G. Hoekstra, 'The discrete dipole approximation for simulation of light scattering by particles much larger than the wavelength," JQSRT 106, 546-557 (2000)

[2] B. T. Draine, P. J. Flatau, 'Discrete-dipole approximation for scattering calculations," J. Opt. Soc. Am. A 11, 1491-1499 (1994)

[3] F. Teschl, W. L. Randeu, 'The DDA for modeling the scattering of radar waves by liquid and frozen precipitation particles," Proceedings of the DDA-Workshop, 23. March, Bremen, 25-29 (2007)

[4] J. A. Morrison, M. J. Cross, 'Scattering of a plane electromagnetic wave by axisymmetrix raindrops," Bell Syst. Tech. J. 53, 955-1019 (1974)

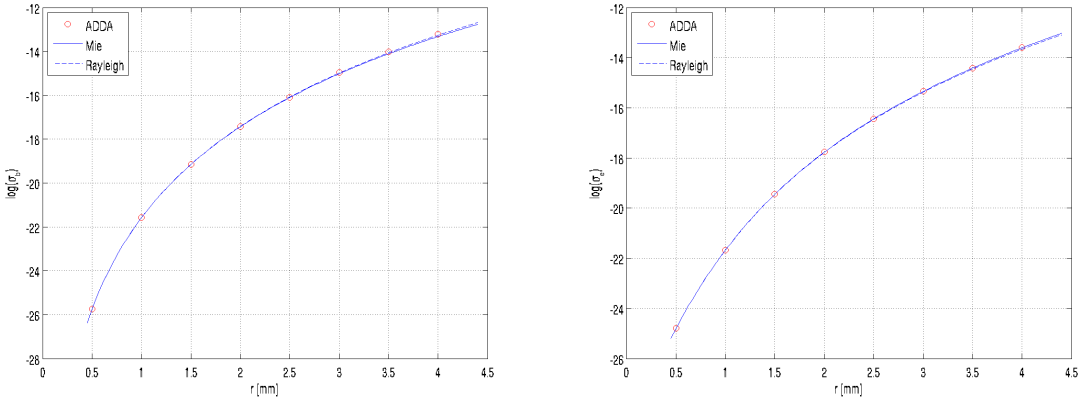

Figure 1: The logarithm of the backscattering (left) and extinction (right) cross-sections of homogeneous ice spheres as a function of radius for the DDA calculations (red dots), the exact Mie theory (blue solid line) and the Rayleigh approximation (blue dashed line).

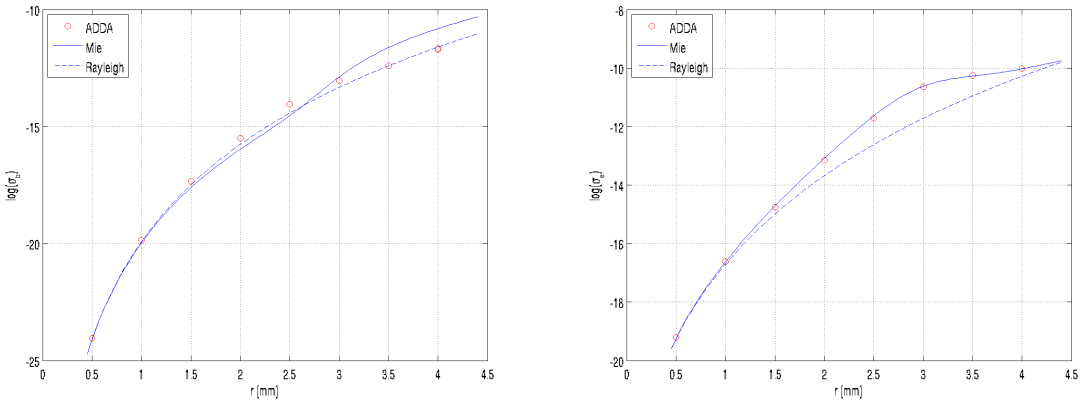

Figure 2: Same as in Fig. 1, but for homogeneous water spheres.

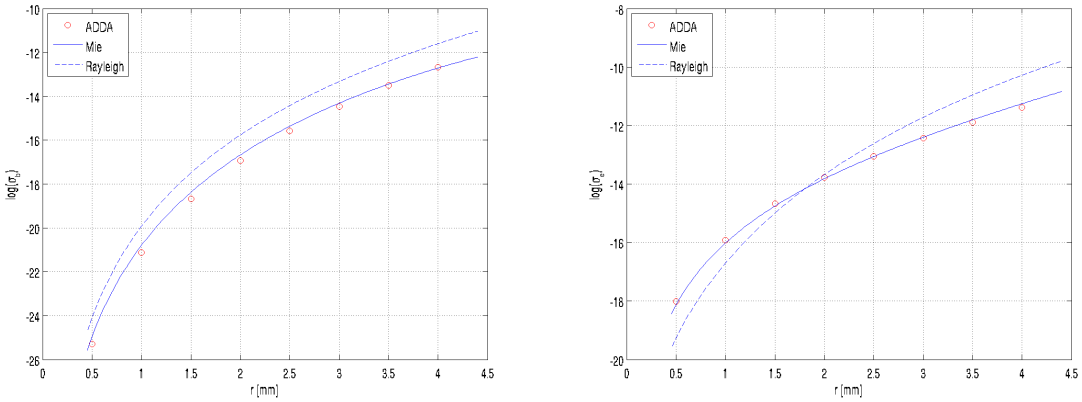

Figure 3: Same as in Fig. 1, but for water-coated ice-spheres with water/ice radii $r_{water}/r_{ice} = 0.98$.

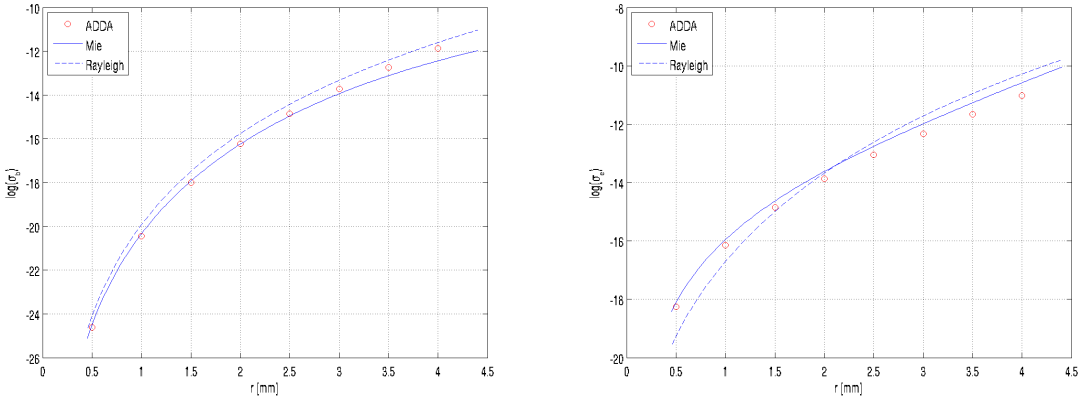

Figure 4: Same as in Fig. 1, but for water-coated ice-spheres with water/ice radii $r_{water}/r_{ice} = 0.94$.

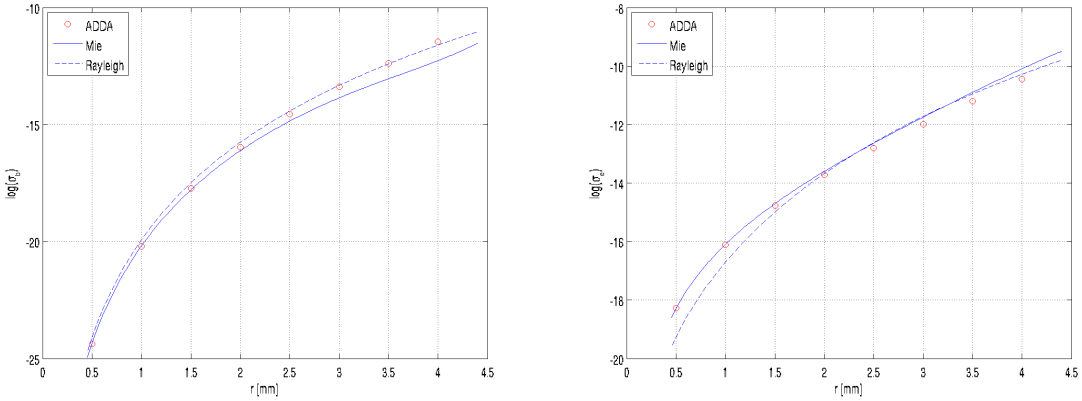

Figure 5: Same as in Fig. 1, but for water-coated ice-spheres with water/ice radii $r_{water}/r_{ice} = 0.9$.

SCATTERING FROM BIOLOGICAL PARTICLES

Modeling of light scattering by human erythrocyte

Elena Eremina

Bremen University, Badgasteiner Str. 3, 28359 Bremen, Germany
Phone: +49-421-218-3583, fax: +49-421-218-5378, e-mail: eremina@iwt.uni-bremen.de

Abstract.
In this work light scattering by a single red blood cell (erythrocyte) is modeled using the Discrete Sources Method (DSM). Due to the biconcave shape of the human erythrocyte there are different approaches to model it. In this work we take shape models used before as well as new one, obtained by a surface evolver code. Numerical results and their discussion will be presented at the conference.

1. Introduction

Light scattering by blood cells is recently of great interest in different biological and medical applications. Between other blood cells the erythrocyte is one of the most important, due to its high contamination in blood and the role it plays for hemoglobin transport over the body. In particular, studying of light scattering by erythrocytes is a suitable method for the detection of some blood diseases. An important topic for medical applications is the reconstruction of erythrocyte's properties, such as shape and refractive index from its measured scattering characteristics. For solving this problem mathematical modeling must be applied. Unlike other blood cells, erythrocyte has an advantage for modeling, as it has no internal structure and can be modeled as homogeneous object with a certain refractive index. In the same time its large size and biconcave shape complicate the calculation of its scattering behavior or make it even impossible for some scattering methods.

To simplify erythrocyte modeling often simplified shapes like spheres, oblate discs or spheroids are used to approximate a real shape. Together with simple shape approaches there are different shape models to approximate the real biconcave shape of the erythrocyte. Recently it has been shown, that simple shape models do not satisfyingly reproduce the light scattering by real erythrocyte [1,2], so the use of the more complicated artificial shape models seems to be neseccary.

In this work the light scattering by different shape models is investigated based on DSM [3]. Numerical results and their detailed discussion will be presented at the conference.

2. Mathematical model

Let us consider scattering in an isotropic homogeneous medium in R^3 of an electromagnetic wave by a local homogeneous penetrable obstacle D_i with a smooth boundary. We introduce a cylindrical coordinate system (z,θ,φ) where z is the axis of symmetry of the particle and θ_i is the incident angle with respect to z. Then the mathematical statement of the scattering problem can be formulated in the following form

$$\nabla\times\mathbf{H}_{e,i}=ik\varepsilon_{e,i}\mathbf{E}_{e,i},\ \nabla\times\mathbf{E}_{e,i}=-ik\mu_{e,i}\mathbf{H}_{e,i}\ \text{in}\ D_{e,i},\quad D_e:=R_3/\overline{D_i}, \tag{1}$$

$$\mathbf{n}_P\times\left(\mathbf{E}_i(P)-\mathbf{E}_e(P)\right)=\mathbf{n}_P\times\mathbf{E}^0(P),\quad \mathbf{n}_P\times\left(\mathbf{H}_i-\mathbf{H}_0\right)=\mathbf{n}_P\times\mathbf{H}^0(P),\quad P\in\partial D \tag{2}$$

together with the Silver-Muller radiation condition for the scattered field at infinity.

Here $\{\mathbf{E}^0,\mathbf{H}^0\}$ is the exciting field, $\mathbf{n}_P$ is the outward unit normal vector to ∂D, index *e* marks the external domain D_e, $k=\omega/c$, ε,μ are permittivity and permeability, $\mathrm{Im}\,\varepsilon_e,\mu_e\le 0$ (time dependence for the fields is chosen as $\exp\{j\omega t\}$) and the particle surface is smooth enough $\partial D\subset C^{(1,\alpha)}$. Then the above boundary-value problem is uniquely solvable.

The DSM is based on the conception of an approximate solution. The approximate solution is constructed as a finite linear combination of Discrete Sources (DS) which are dipoles and multipoles deposited in a supplementary domain inside the particle with certain amplitudes. Usually the axis of symmetry of the particle is used for such a domain. In the case of an oblate particles like erythrocytes,

disks or oblate spheroids it is not always possible to use the axis of symmetry [4]. For this purpose an analytical continuation to a complex plane is constructed. More detailed information can be found in [2]. The deposition of DS in a complex plane allows reducing calculation errors and time of computations. In frame of DSM the approximation solution is constructed for every polarization separately.

The approximate solution for the P-polarized wave accepts the form:

$$\begin{pmatrix} \mathbf{E}_{e,i}^{N} \\ \mathbf{H}_{e,i}^{N} \end{pmatrix} = \sum_{m=0}^{M} \sum_{n=1}^{N_m^{\zeta}} \left\{ p_{mn}^{e,i} \mathbf{D}_1 \mathbf{A}_{mn}^{1,e,i} + q_{mn}^{e,i} \frac{j}{\varepsilon_{\zeta}} \mathbf{D}_2 \mathbf{A}_{mn}^{2,e,i} \right\} + \sum_{n=1}^{N_0^{\zeta}} r_n^{e,i} \mathbf{D}_1 \mathbf{A}_n^{3,e,i}; \qquad (3)$$

$$\mathbf{D}_1 = \begin{pmatrix} \frac{j}{k\varepsilon_{e,i}\mu_{e,i}} \nabla \times \nabla \times \\ -\frac{j}{\mu_{e,i}} \nabla \times \end{pmatrix}, \qquad \mathbf{D}_2 = \begin{pmatrix} \frac{1}{\varepsilon_{e,i}} \nabla \times \\ \frac{j}{k\varepsilon_{e,i}\mu_{e,i}} \nabla \times \nabla \times \end{pmatrix}.$$

The approximation solution for the case of a S-polarized excitation is constructed in a similar way and has the form:

$$\begin{pmatrix} \mathbf{E}_{e,i}^{N} \\ \mathbf{H}_{e,i}^{N} \end{pmatrix} = \sum_{m=0}^{M} \sum_{n=1}^{N_m^{\zeta}} \left\{ p_{mn}^{e,i} \mathbf{D}_1 \mathbf{A}_{mn}^{1,e,i} + q_{mn}^{e,i} \frac{j}{\varepsilon_{\zeta}} \mathbf{D}_2 \mathbf{A}_{mn}^{2,e,i} \right\} + \sum_{n=1}^{N_0^{\zeta}} r_n^{e,i} \mathbf{D}_2 \mathbf{A}_n^{3,e,i} \qquad (4)$$

More details can be found in [2].

The constructed approximate solutions (3), (4) satisfy Maxwell equations (1) and radiation conditions for the scattered fields at infinity. The unknown vector of amplitudes of DS

$$\mathbf{p}_m = \left\{ p_{mn}^{e,i},\ q_{mn}^{e,i},\ r_n^{e,i} \right\}_{n=1}^{N_{e,i}^{m}},$$

is to be determined from the transmission conditions (2). As it was mentioned above, DS are situated in a complex plane adjoined to the symmetry axis of the particle. The approximate solutions (3) and (4) are finite linear combinations of Fourier harmonics with respect to the φ angle variable. Therefore, after resolving the plane wave excitation into Fourier series with respect to the φ angle we reduce the two-dimentional approximation problem enforced at the particle surface to a set of 1-dimensional problems at the particle generatrix. For solving these problems the General Matching-Point Technique is applied, more details can be found in [5].

The exactness of the result is provided by stabilization of the scattering diagram and a-posterior residual calculation.

After DS amplitudes have been determined the far-field pattern $\mathbf{F}(\theta,\varphi)$ can be computed as:

$$\frac{\mathbf{E}(\mathbf{r})}{\left|\mathbf{E}^0(\mathbf{r})\right|} = \frac{\exp(-jk_e r)}{r} \mathbf{F}(\theta,\varphi) + o\left(\frac{1}{r}\right), \qquad \text{where } r \to \infty. \qquad (5)$$

The components of the vector $\mathbf{F}(\theta,\varphi)$ can be found in [2].

For experimental studies of lights scattering by blood cells Scanning Flow Cytometers (SCF) are used. The SFC permits measurements of the angular dependency of light scattering intensity in a wide angle range from 5 to 100 degrees. The design and basic principles of the SFC are described in [6]. The output signal of the SCF is proportional to the following combination of Mueller matrix elements [7]:

$$I_s(\theta) = \int_0^{2\pi} \left(S_{11}(\theta,\varphi) + S_{14}(\theta,\varphi) \right) d\varphi. \qquad (6)$$

The Mueller matrix elements are connected with far-field pattern elements [8] and can be easily computed as a combination of elementary functions [2].

Another important light scattering characteristic is the differential scattering cross-section (DSC), which can be calculated on the base of far-field pattern components as follows:

$$\mathrm{DSC}^{P,S} = \left| F_{\theta}^{P,S}(\theta,\varphi) \right|^2 + \left| F_{\varphi}^{P,S}(\theta,\varphi) \right|^2. \qquad (10)$$

3. Numerical results and discussion.

In papers [2,9] different shape models of erythrocyte have been investigated. In this work we concentrated on two of them: the experimental shape model suggested by Skalak and shape based on Cassini ovals. Additionally we took into account the shape calculated by Surface Evolver Code (SEC), which calculates the shape profile based on the potential minimum for given volume and surface. This approach promises to deliver the most realistic shapes. The SEC gives an additional advantage as it allows the calculation of a shape profile for every volume, what is especially important for erythrocyte under osmotic lysis. Exemplary numerical results and their discussion will be presented at the conference.

Conclusion

In this work we used DSM to analyse light scattering by analysed erythrocyte based on different shape models. We compared a new SEC approach to model erythrocyte shape with previously used models. Numerical results and their discussion will be presented at the conference.

Acknowledgement

We gratefully acknowledge funding of this research by Deutsche Forschungsgemeinschaft (DFG) and the Russian Foundation for Basic Research (RFBR).

References

1. Eremina E., Hellmers J., Eremin Y., Wriedt T.: Different shape models for erythrocyte. Light scattering analysis based on the Discrete Sources Method. JQSRT 102 (2006) 3.
2. Eremina E., Eremin Y., Wriedt T.: Analysis of light scattering by different shape models of erythrocyte based on Discrete Sources Method. Opt. Comm. 244 (2005) 15.
3. Eremin Yu.A.: The Method of Discrete Sources in electromagnetic scattering by axially symmetric structures. J. Comm. Technology and Electronics. 45 (2) (2000) 269.
4. Doicu A., Eremin Yu., Wriedt T. Acoustic and Electromagnetic Scattering Analysis using Discrete Sources. Academic Press, London, 2000.
5. Voevodyn V., Kuznetsov A. Matrices and calculations. Science, Moscow, 1982, in Russian.
6. Maltsev V.P. Scanning flow cytometry for individual particle analysis. Rev. Sci. Instrum. 71 (2000) 243.
7. Maltsev V.P., Semyanov K.A. Characterisation of Bio-Particles from Light Scattering VSP; Utrecht, Boston, 2004.
8. Bohren C.F. and Huffman D. R. Absorption and scattering of light by small particles. Wiley, New York,1983.
9. Wriedt T., Hellmers J., Eremina E., Schuh R.: Light scattering by the erythrocyte: Comparison of different methods. JQSRT 100 (2006) 444.

Light scattering study of tropical fresh water diatoms

Ankur Gogoi[1], Alak K. Buragohain[2], Amarjyoti Choudhury[1], Gazi A. Ahmed[1]

[1]*Optoelectronics and Photonics Research Laboratory, Department of Physics, School of Science and Technology, Tezpur University*
[2]*Department of Molecular Biology and Biotechnology, School of Science and Technology, Tezpur University*
Tezpur-784028, Assam, India

Abstract

Laser light scattering characteristics of tropical fresh water diatoms and their siliceous frustules have been measured as a function of scattering angle at 543 nm, 594 nm and 632 nm wavelengths by using an indigenously designed and fabricated laboratory light scattering instrument. The instrument incorporates an array of sixteen highly sensitive static Si detectors that measured scattered light signals from 10^0 to 170^0 in steps of 1^0. A comparative analysis between the results obtained by using the three different incident wavelengths was done.

1 Introduction

Scattering and absorption of light from biological organisms, with diameter ranging from nanometer to micrometer, distributed in different continuous media or matrix is a subject of intensive research at the present time. The scattering properties of such organisms are determined not only by their bulk optical properties and the medium but also by their shape, size, density, scattering angle and polarization state of the incident and scattered light [1]. It is very important to study the angular scattering dependency of such particulate matter as such results help to investigate the nature of the scattering particle and to understand the propagation of light through a medium containing the scatterer [2]. From the instrumentation point of view, a number of different experimental setups have been made in the past to investigate the scattering behavior of small particles. In 1950, Kerker and VKL Mer developed a method using either the polarization ratio or the phase angle of the scattered light as a function of the scattering angle to extract size information [3]. Since that time several techniques and different approaches have been taken with greater or lesser success by various workers to design instruments for the experimental observation of scattered light and determine the scattering matrix elements [4 – 8]. A sophisticated, fully computerized setup to investigate laser light scattering was built successfully in 1980s by P. Stammes, F. Kuik, and H. Volten, at the Department of Physics and Astronomy, Free University, Amsterdem [5, 6]. The setup was subsequently improved and extended by J. W. Hovenier [8, 9]. Some more simplified and advanced experimental setups are described by B. Barkey, M. T. Valentine et al. etc [9, 10]. Many laboratory measurements and theoretical approaches on light scattering by biological organisms have also been carried out during the last few years [2, 12, 13].

In this paper, we report the design and fabrication of a laboratory light scattering instrument that successfully measured the light scattering behavior of some fresh water diatoms.

2. Experimental Section

2.1 Scattering setup

A laser based setup was designed to study the light scattering characteristics of small particles. The schematic diagram of the experimental setup is shown in figure 1. The setup essentially consists of a laser source, controlled sample holders, photodetector arrangements, data acquisition systems and

associated instrumentation. The system can measure scattered light signals from 10^0 to 170^0 in steps of 1^0.

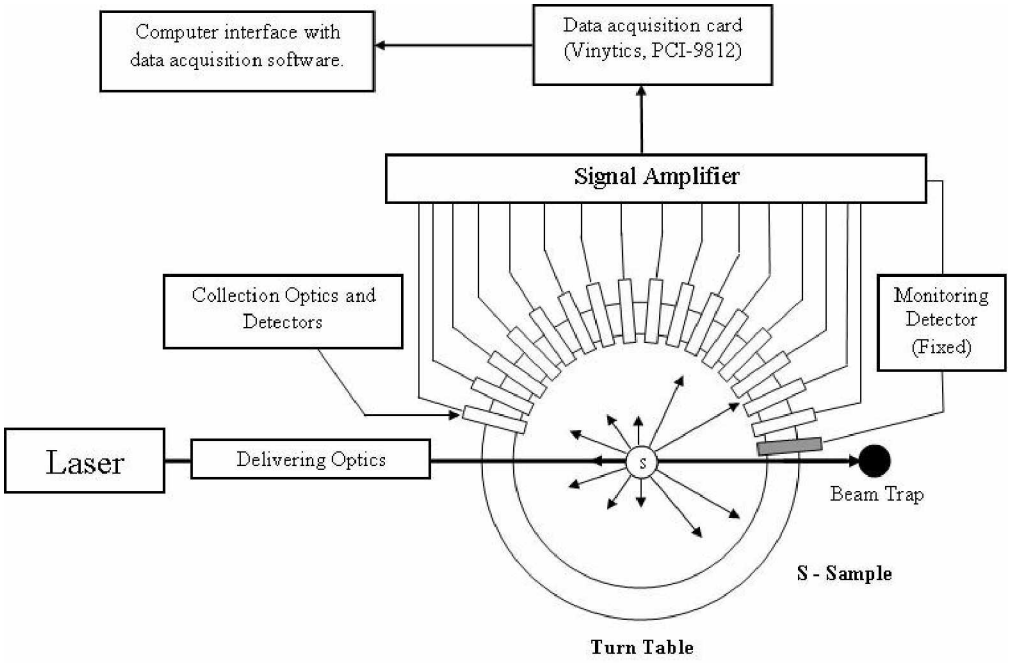

Figure 1: Design of the experimental setup

The whole set up is covered by a black polished metallic enclosure to cutoff electromagnetic noise and beam stops are placed at strategic points to minimize the intensity of stray reflections.

2.2 Culture of diatoms

Diatoms were collected from fresh water and cultures were grown by using fresh water “WC” media proposed by Guillard and Lorenzen. The protocol was slightly revised by doubling the composition of sodium meta silicate and lowering the ph from 7 to 6.2, hence making it more acidic. The diatoms were grown in both the solid and liquid media. Figure 2 shows the solid and liquid culture of diatoms. The external organic matrix covering their siliceous frustules was removed by following the procedure used by Mario De Stefano and Luca De Stefano [14]. Light scattering properties of diatoms before and after removal of the organic matrix were measured.

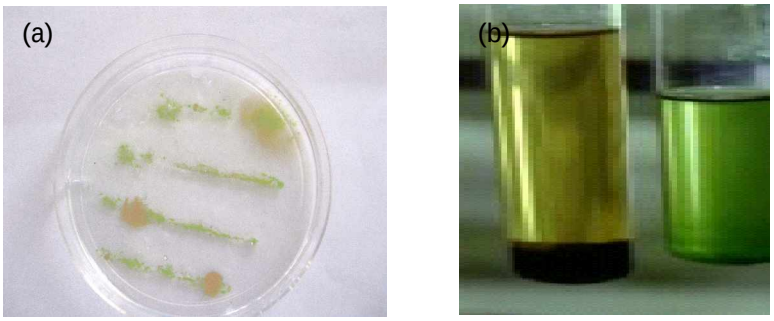

Figure 2: (a) Solid and (b) liquid culture of diatoms

2 Results

In the present work, we studied the light scattering properties of diatoms at 543 nm, 594 nm and 632 nm laser wavelengths. Photoluminescence (PL), scanning electron microscopy (SEM) technique was employed to observe the luminescence and physical morphology of the diatoms. The photoluminescence spectra of the diatoms were found to have broad peak at 430 nm under 325 nm laser excitation wavelength (figure 3). Figure 4 shows the SEM picture of a fresh water diatom frustule. It was also observed that the light scattering behavior of the diatoms and their siliceous frustules significantly varies for the three different incident wavelengths.

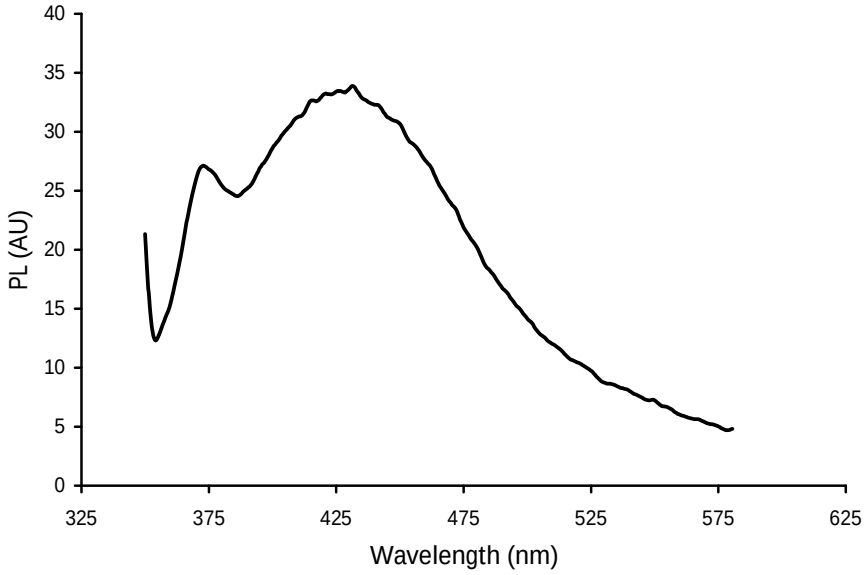

Figure 3: Photoluminescence spectra of the diatoms under 325 nm laser excitation wavelength

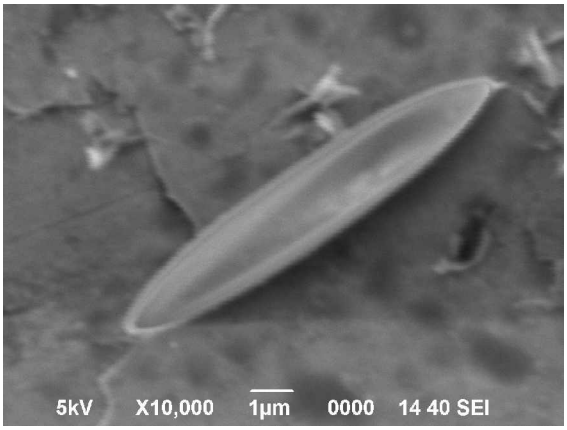

Figure 4: Scanning electron micrograph of a freshwater diatom frustule. Scale 1µm.

3 Conclusion

In this paper we report the design and fabrication of a low cost, light weight and miniaturized light scattering instrument which uses an array of 16 highly sensitive Si detectors. Using the setup, light scattering behavior of tropical fresh water diatoms has been studied as a function of scattering angle.

As the instrument has proved itself to be quite suitable for performing light scattering experiments on small particulate matter, extensive investigations will be further carried out on other aerosols and hydrosols.

References

[1] C. F. Bohren and D. R. Huffman, *Absorption and Scattering of Light by Small Particles* (Wiley, New York, 1983).

[2] M. S. Quinby-Hunt, A. J. Hunt, K. Lofftus and D. Shapiro, "Polarized-Light Scattering Studies of Marine Chlorella", Limnology and Oceanography, Vol. 34, No. 8, 1587-1600 (1989).

[3] Kerker and VKL Mer, "Particle Size Distribution in Sulfur Hydrosols by Polarimetric Analysis of Scattered Light", Journal of the American Chemical Society, Vol. 72, 3516, 1950.

[4] B. S. Pritchard and W. G. Elliott, "Two instruments for atmospheric optics measurements", J. of Optical Society of America, vol. 50, no. 3, 191-202 (1960).

[5] A. J. Hunt and D. R. Huffman, "A new polarization-modulated light scattering instrument", Rev. Sci. Instrum., vol. 44, No. 12, 1753-1762, December 1973.

[6] M. I. Mishchenko, J. W. Hovenier, and L. D. Travis eds. *Light Scattering by Nonspherical Particles: Theory, Measurements, and Applications* (Academic Press, San Diego, Calif., 2000).

[7] M. I. Michenko, L. D. Travis, A. A. Lacis. Scattering absorption and emission of light by small particles. Cambridge University Press, 2002.

[8] O. Muñoz, H Volten, J. W. Hovenier, M. Min, Y. G. Shkuratov, J. P. Jalava, W. J. Van der Zande and L. B. F. M. Waters, "Experimental and computational study of light scattering by irregular particles with extreme refractive indices: hematite and rutile" Astronomy & Astrophysics, 446, 525-535, (2006).

[9] J. W. Hovenier, H Volten, O. Muñoz, W. J. Van der Zande, L. B. F. M. Waters, "Laboratory studies of scattering matrices for randomly oriented particles: potentials, problems, and prospectives" J. of Quantitative Spectroscopy and Radiative Transfer, 79-80, 741-755, (2003).

[10] B. Barkey and K. N. Liou, "An analog light scattering experiment of hexagonal icelike particles. Part I: Experimental apparatus and test measurements", J. of the Atmospheric Sciences, Vol. 56, 605-612 (1999).

[11] M. T. Valentine, A. K. Popp, and D. A. Weitz, "Microscope-based static light-scattering instrument", Optics Letters, Vol. 26, No. 12 (2001).

[12] Maxim A. Yurkin,, Konstantin A. Semyanov, Valeri P. Maltsev and Alfons G. Hoekstra,"Discrimination of granulocyte subtypes from light scattering: theoretical analysis using a granulated sphere model", Optics express, Vol. 15, No. 25, 16561-16580 (2007).

[13] H. W. Rich and F. M. M. Morel, "Availability of well-defined iron colloids to marine diatom *Thalassiosira weissflogii*", Limnol, Oceanogr., 35 (3), 652-662 (1990).

[14] Mario De Stefano and Luca De Stefano, "Nanostructures in Diatom Frustules: Functional Morphology of Valvocopulae in Cocconeidacean Monoraphid Taxa", J. of Nanoscience and Technology, vil. 5, 15-24, 2005.

Phase function of helical particles at normal and oblique angles of incidence

Moshe Kleiman,[1] Ioseph Gurwich,[1,2] and Nir Shiloah[1]

[1] *Israel Institute for Biological Research, P. O. Box 19, Ness-Ziona 74100, Israel*
[2] *ELOP, P. O. Box 1166, Rehovot 76110, Israel*
tel: +972 8-9381-654, fax: +972 8-9381-664, e-mail: moshekl@iibr.gov.il

Abstract

The electro-magnetic scattering by a helical particle is extended to the case of oblique incidence. The phase functions of scattered radiation for normal and oblique incidence and for different values of helix parameters are presented.

1 Introduction

A possibility of treating the problem of electro-magnetic scattering by a helical particle using a Fourier approach was recently demonstrated [1]. The suggested formalism is based on the representation of a helical particle as a thin, non-homogeneous membrane with periodical boundary conditions. It has been shown that in this case one can use a calculation procedure developed for a multi-layered (hollow) cylinder [2] to determine all Fourier (diffraction) orders of the scattered field.

Several numerical examples presented in [1] show the resonant behavior of scattering by a long helix at sufficiently high frequencies (for normal incidence the helix pitch should be greater than the incident wavelength). It was shown how this resonant scattering, which is associated with periodic structure of the helical particle, is affected by helix parameters (pitch and radius). In the present work we investigate the phase function of scattered radiation for normal and oblique incidence and for different values of helix parameters.

2 Oblique incidence

For normal incidence the first diffraction peak appears at a wavelength equal to the helix pitch [1]. Fig. 1 shows the shift of the first diffraction peak with the change of the incidence angle. The position of the peak is shifted to lower frequencies with a decrease of the incidence angle.

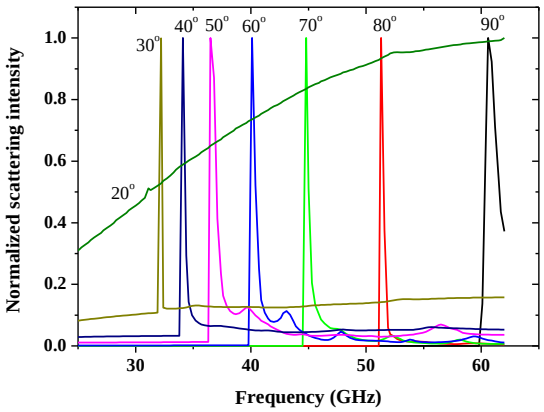

Figure 1: Frequency shift of the first diffraction peak as a function of the incident angle.

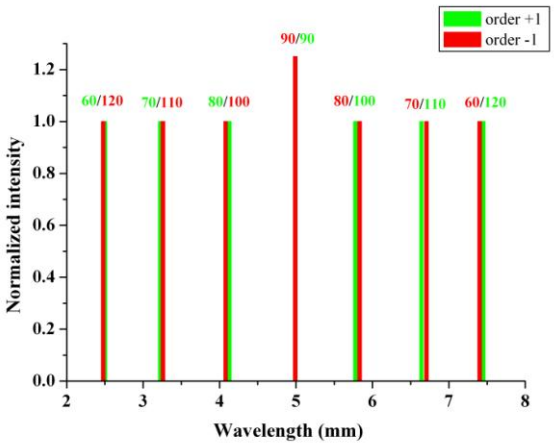

Figure 2: The first diffraction peak positions at different incident angles for +1 and -1 orders.

At very low angles of incidence the diffraction peak disappears and scattering by a helix became similar to that by a long fiber.
Since this resonant feature of electromagnetic scattering by a helix is associated with periodic structure of the helical particle (and is similar to scattering by a grating), we consider separately the scattering of different diffraction orders. Fig. 2 shows the separation in the position of the first diffraction peak for +1 and -1 diffraction orders for incident angles smaller and larger than normal incidence. The fact that for +1 order the peaks at angles below 90^0 appear at the same positions as the peaks for -1 order at symmetrical angles above 90^0 (and vice versa) is an additional proof of the consistence of our calculations. Fig. 3 shows the scattering intensity of a helix at given frequency. One can see the symmetry in the peak positions for angles in the range of $\pm 30^0$ around normal incidence. When incident angles deviate more than 30^0 from the normal, the symmetry in the peaks positions disappears.

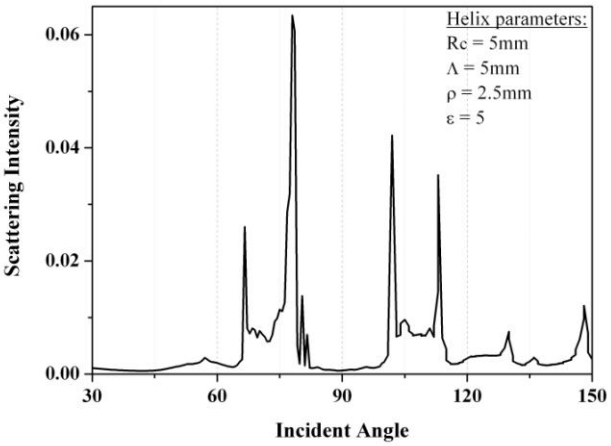

Figure 3: The scattering intensity as a function of incidence angle at frequency 100 GHz.

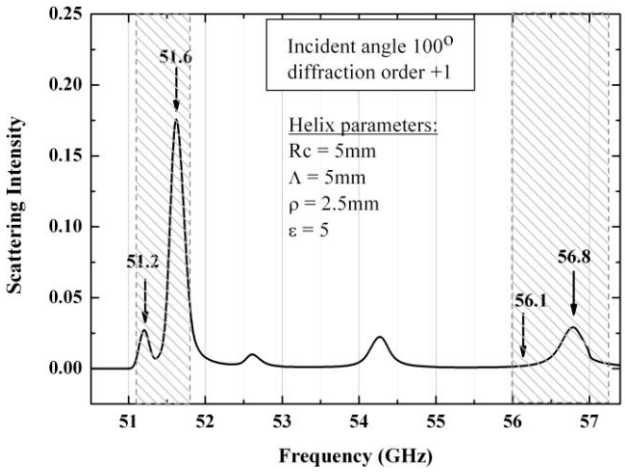

Figure 4: The +1 order scattering intensity as a function of frequency at 100^0 incident angle.

3 Phase function

Fig. 4 presents the scattering intensity as a function of frequency for +1 diffraction order and incident angle of 100^0. In this case the first diffraction peak appears at the frequency 51.2 GHz, the second peak at 51.6 GHz and so on. Here we investigate the behavior of the phase function at different diffraction peaks.

The phase function contours in the frequency range that covers the first two peaks is shown in Fig. 5 separately for polarization planes parallel (pl) and perpendicular (pr) to the polarization plane of the incident radiation. In addition, the phase function at the exact peak frequencies is presented as well, above and below these contours. Fig. 6 presents the same information for the frequency range from 56 to 57.3 GHz and the phase function at the fifth diffraction peak (56.8 GHz) and at 56.1 GHz just before this peak. One can see that at the peak frequencies the phase function is very regular and symmetrical around the scattering angle of 90^0. In the parallel polarization plane (pl) the phase function always has maximum values in the forward and backscattering directions, while in the perpendicular polarization plane (pr) there is always a minimum at these scattering angles. At the first peak (51.2 GHz) there are two maxima and three minima in the (pr) plane and two minima and three maxima in the (pl) plane. At the second peak (56.8 GHz) the number of minima and maxima in each scattering plane is increased by 1. This sequence of increase by 1 the number of maxima and minima every next peak continues farther, and at the fifth peak (56.8 GHz) it is increased by 4 relatively to the first peak.

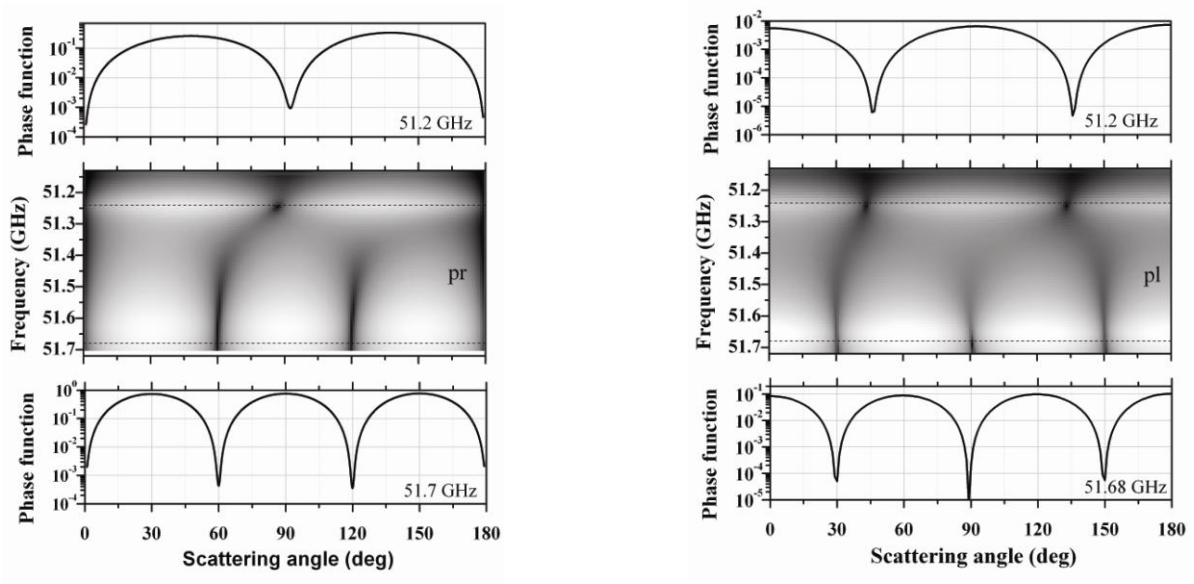

Figure 5: The phase function contours in frequencies range 51.1 to 51.7 GHz for the polarization planes parallel **(pl)** and perpendicular **(pr)** to the incident wave polarization.

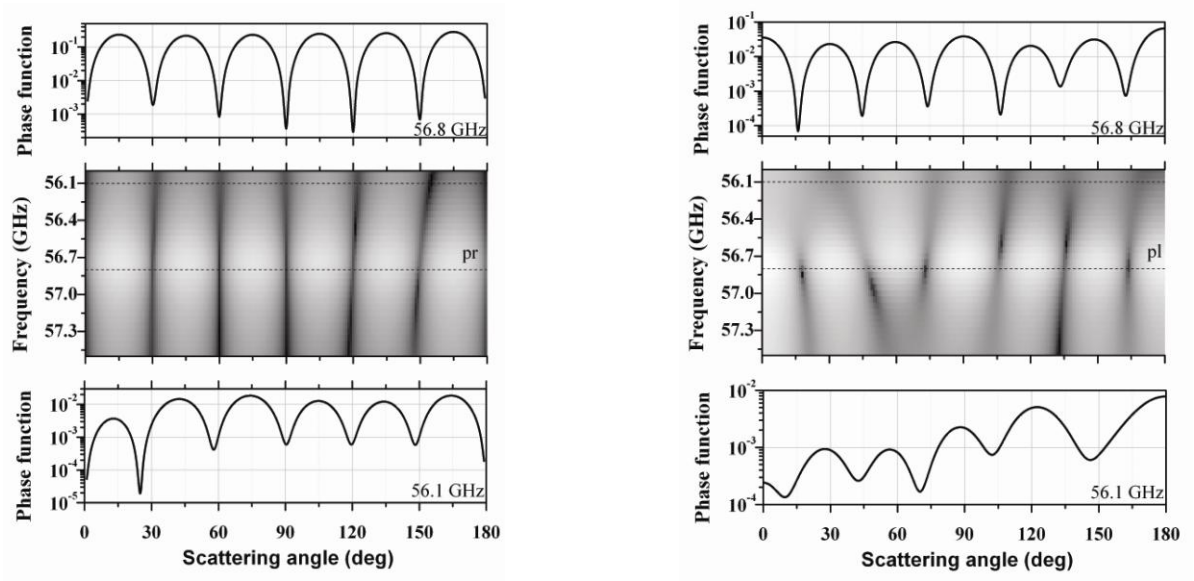

Figure 6: : The phase function contours in the frequency range 56.0 to 57.3 GHz for the polarization planes parallel **(pl)** and perpendicular **(pr)** to the incident wave polarization.

To explain this behavior of the phase function at the diffraction peaks we present in Fig. 7 the a_n and b_n coefficients for this case. The a_n coefficients contribute to the scattering in the perpendicular polarization plane and the b_n coefficients to the scattering in the parallel polarization plane. From Fig. 7 it is clear that the main contribution to the first diffraction peak comes from a_2 and b_2, to the second diffraction peak comes from a_3 and b_3 coefficients, and so on. At the fifth peak the a_6 coefficient is dominant in the

perpendicular polarization plane, while there is considerable contribution to b_6 from the lower orders in the parallel polarization plane. Therefore the symmetry of the phase function is pronounced more strongly in the perpendicular polarization plane. Between the peaks there is not any significant domination of a given coefficient and therefore the phase function does not maintain the symmetry (like at 56.1 GHz in Fig. 6).

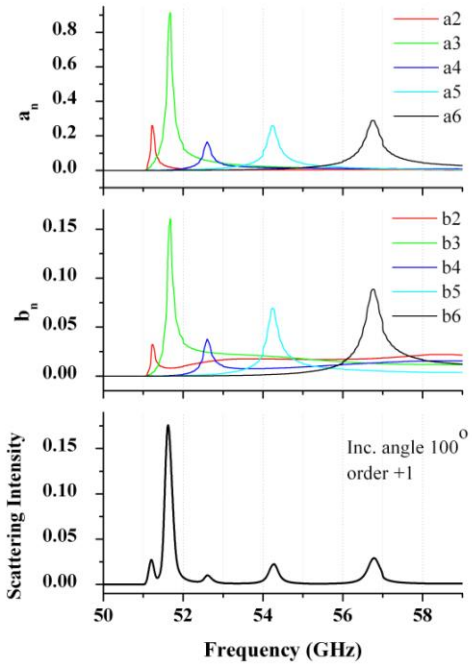

Figure 7: The a_n and b_n coefficients for +1 diffraction order as a function of frequency at 100^0 incident angle.

6 Summary

- The scattering of electromagnetic radiation by a long helix at sufficiently high frequencies (i.e., for normal incidence the helix pitch should be greater than incident wavelength) shows the resonant behavior.
- For oblique incidence the position of the first diffraction peak is shifted to lower frequencies with a decrease in the angle of incidence.
- At very low incident angles the diffraction peak disappears and scattering by a helix becomes similar to one by a long fiber.
- At the peak frequencies the phase function has a very regular form and is symmetric around the scattering angle of 90^0. This behavior of the phase function is associated with a_n and b_n coefficients.

References

[1] I. Gurwich, M. Kleiman, and N. Shiloah, “Scattering from a long helix: Theory and simulation”, JQSRT. **109**, 1392–1403 (2008).

[2] I. Gurwich, M. Kleiman, and N. Shiloah, “The recursive algorithm for electromagnetic scattering by tilted infinite circular multi-layered cylinder”, JQSRT. **63**, 217–29 (1999).

Incoherent light transport in anisotropic media: application to human red blood cells

Moumini Nadjim,[1] Baravian Christophe,[1] Jérôme Dillet,[1]

[1] *Laboratoire d'Energétique et de Mécanique Théorique et Appliquée,*
2, avenue de la Forêt de HayeBP 160 • F-54504 Vandœuvre lès Nancy
e-mail: nadjim.moumini@ensem.inpl-nancy.fr

Abstract

We use incoherent light transport to characterize anisotropic media composed by deformable particles. To describe this phenomenon, we resolve the boltzman radiative transfer by Monte Carlo simulations and Waterman's T-matrix approach on prolate ellipsoids. From this, we measure the elastic modulus of red blood cells in physiological conditions (40% in volume fraction).

1 Introduction

We can distinguished two kind of anisotropic random media. The first one is composed by many oriented fibbers inside like dentin or tissue brain. The second one is composed bycollectively oriented deformable particles like suspended red blood cells. A new optical technique based on incoherent light transport is used to investigated the deformability of red blood cells under external shear without dilution. Baravian et *al* [1] observed with this technique an anisotropic backscattering image when the red blood cells are under shear and concluded that this anisotropy is due to the deformation of red blood cells.
Thanks to Monte Carlo simulations based on Waterman's T-matrix approach introduced by M. MIshchenko [2,3] for the light scattering by a single non-spherical particle, we are able to determine the deformability of particle from the backscattering image. In fact, we resolve with the Monte Carlo simulations rigorously the boltzman radiative transfer equation [4] for a random media where the particles are oriented in the same direction and are deformable.
In this study, we firstly present our experimental device and the different red blood cells used to perform our experiments. In the second part, we will present the Monte Carlo simulations based on Waterman's T-matrix approach. And finally, we will present an example of application to human red blood cells deformation.

2. Experimental setup and Methods:

Experimental setup

The experimental set-up in Figure 1a is based on a laser (λ=635 nm) focused at the medium surface thanks to a system of mirrors. The laser beam radius is equal to 75 µm and with an Adimec MX12P CCD camera (12 bits, 1 Megapixels); we collect the backscattered light far from the laser impact. The collected image size of backscattered light is equal to 10 mm and is very large compared to the laser beam impact. This optical system is embedded on a Physica MCR300 rheometer. With this system, it is possible to perform incoherent light transport experiment and rheological experiments at the same time. All the experiments have been performed in climatized room at 20°C. Many images are acquired and averaged in order to decrease numerical noise and speckles. From the barycenter of the image, we first realize an angular average intensity integration and we obtain from this average image the radial intensity distribution I(ρ) in Figure 1b. The radial intensity distribution in Figure 1b is fitted using the semi-infinite diffusion model to obtain the measurement of the length transport l^* and the absorption length l_a [1]. The intensity is multiplied by l^{*2} and the radius ρ is divided by l^*. Several red blood cells (concentrated 40% in volume fraction) are prepared. Four no aggregating blood samples are used in this study, one with deformable discoid cells, one with deformable spherical cells and two samples with no deformable discoid and spherical cells. The human red blood cells samples are in normal physiological conditions (40% in volume fraction).

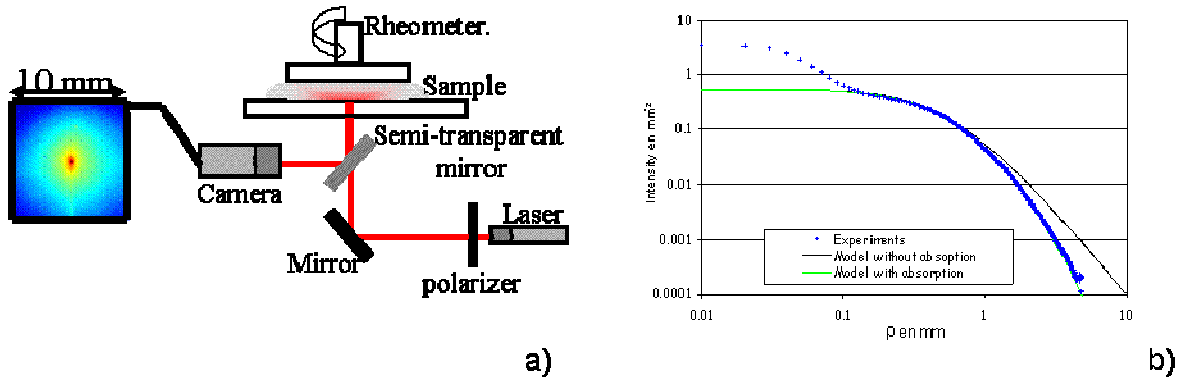

Figure 1:a) Experimental set-up b) fitted experimental data and diffusion model for deformable discoids at 50 s^{-1} (l^*=0.375 mm, l_a=14mm).

Principle of Monte Carlo simulations

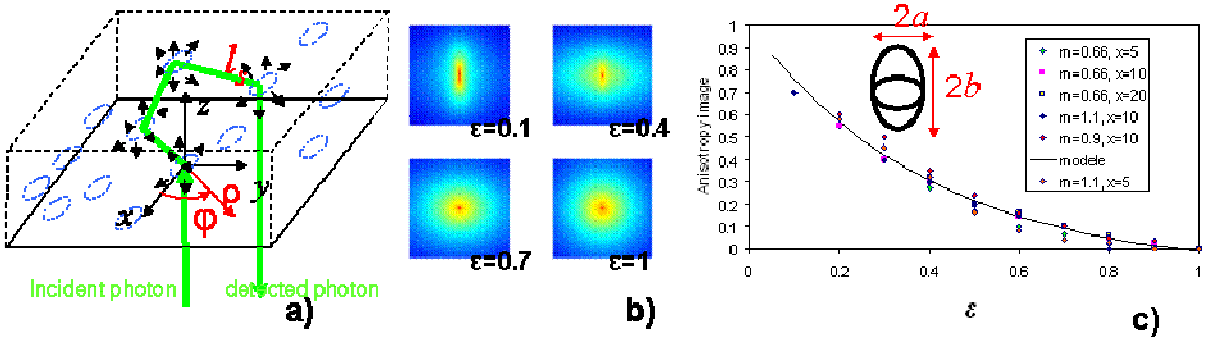

Figure 2: a) scheme of the Monte Carlo simulations b) Backscattering images obtained by Monte Carlo Simulation m=1.1 x=10 c) anisotropy image versus form factor $\varepsilon=a/b$.

Waterman's T-matrix approach solves the Maxwell equations for interactions between a non spherical particle (radius a and optical refractive index n_p) and a plane electromagnetic wave (wavelength λ) in a surrounding medium (optical refractive index $n_{m)}$. This theory uses three parameter, the size parameter $x=2\pi\, n_m\, a/\lambda$, the optical parameter $m=n_p/n_m$ and the form factor a/b (length a and width b). In the case of collection of particles, the light propagation depend on the volume fraction of particles Φ. Then, the propagation of light is characterized by the scattering length $l_s(\xi)$ and the phase function $p(\xi,\theta,\varphi,\varepsilon)$ (φ azimutal angle, θ angle between incident photon direction and scattering photon direction, ξ angle between incident photon direction and orientation of particle). These quantities are obtained with the T-matrix approach. The light propagation is modeled using the radiative transfer equation :

$$\vec{s}.\nabla\vec{L}(r,s)=\left(\frac{1}{l_s(\xi)}+\frac{1}{l_a}\right)\vec{L}(\vec{r},\vec{s})+\frac{1}{2\pi l_s(\xi)}\int_{4\pi}p(\vec{s},\vec{s}')\vec{L}(\vec{s},\vec{s}')d\Omega \qquad (1)$$

$\vec{L}(\vec{r},\vec{s})$ is the radiance ($W\,m^{-2}\,sr^{-1}$), $p(\vec{s},\vec{s}')$ is the normalized probability phase function. This equation has not yet an analytical solution for an anisotropic random media like suspended red blood cells sample and requires a numerical solution using Monte Carlo simulations. In Figure 2 b), we obtained 2-D backscattered image by superposition of 10^7 photons. Each photon is described by its position in space. We launch photon packets vertically into the sample at the origin of the coordinate systems. The normalized distance between two scattering events is sampled according to d=- $l_s(\xi)$ln(1-rand) with rand

$\in [0,1[$ is a uniform random number. At the scattering event the photon selected a direction define by θ and φ according to normalized probability phase function $p(\vec{s},\vec{s}')$ calculated by the T-matrix approach. The Monte Carlo simulations shows that for a particle size > 10, the anisotropy of the image define by Equ. 3 does not depend on the refractive index m and the particle size x. Then, from the anisotropy of the image, we directly get the deformation of the particles using Figure 2c.

3. Application to human red blood cells deformations

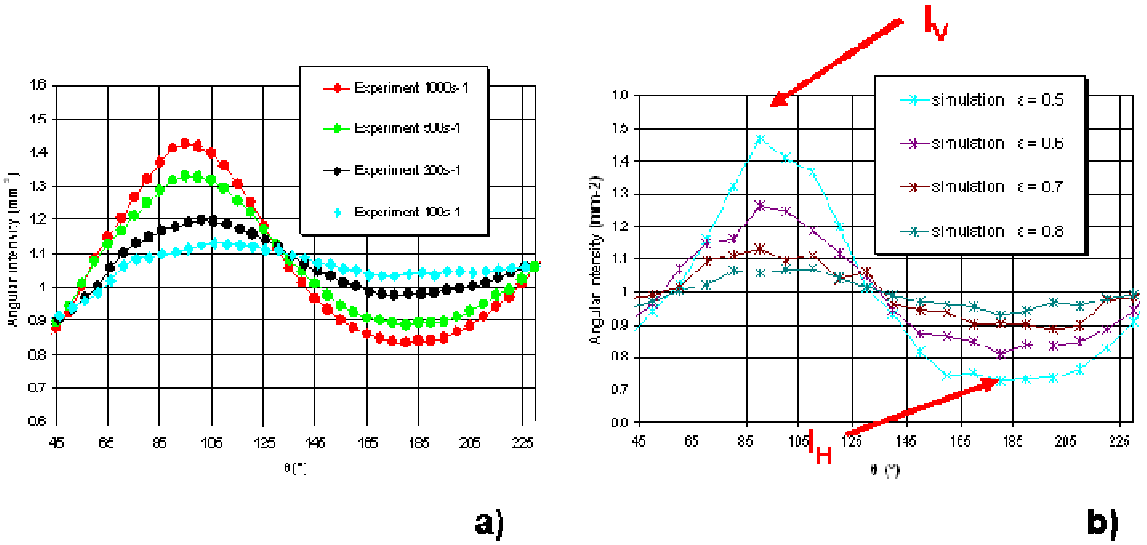

Figure 3: a)Intensity amplitude measured at $l^*/2$ for different shear rate b)Intensity amplitude obtained at $l^*/2$ for different Monte Carlo simulations

To study the deformability of the red blood cells, we performed a constant shear stress experiments. The anisotropy of the image is defined by (see figure 3b):

$$Al = \frac{I_V - I_H}{I_V + I_H} \tag{3}$$

In Figure 3b, we show angular variation of light intensity measured at a radius equal to $l^*/2$ from the barycenter of the image. In Figure 4b, we observe the evolution of the backscattered image with the shear rate. We noticed that this one become more and more anisotropic when the shear rate increased. The backscattered image is deformed with increasing shear as shown by the difference between the image obtained at a given shear rate minus the one at 10s-1 in Figure 4c). We compare the experimental oscillations to some oscillations obtained by Monte Carlo simulations. We determine the deformation of red blood cells using Figure 2c and compare with the results obtained by Schauf et *al* [6] (open symbols) in Figure 4a. From Figure 4a, we calculate an elastic modulus for red blood cells around 6.6 µN/m close to 5 µN/m measured on individual cells [7].

4 Conclusion

In conclusion, we have shown in this study that our experimental device based on incoherent light transport can be used to determine the form factor of oriented anisotropic particles. This technique applies to any sufficiently turbid media and proposes a complementary tool scattering methods used in diluted conditions.

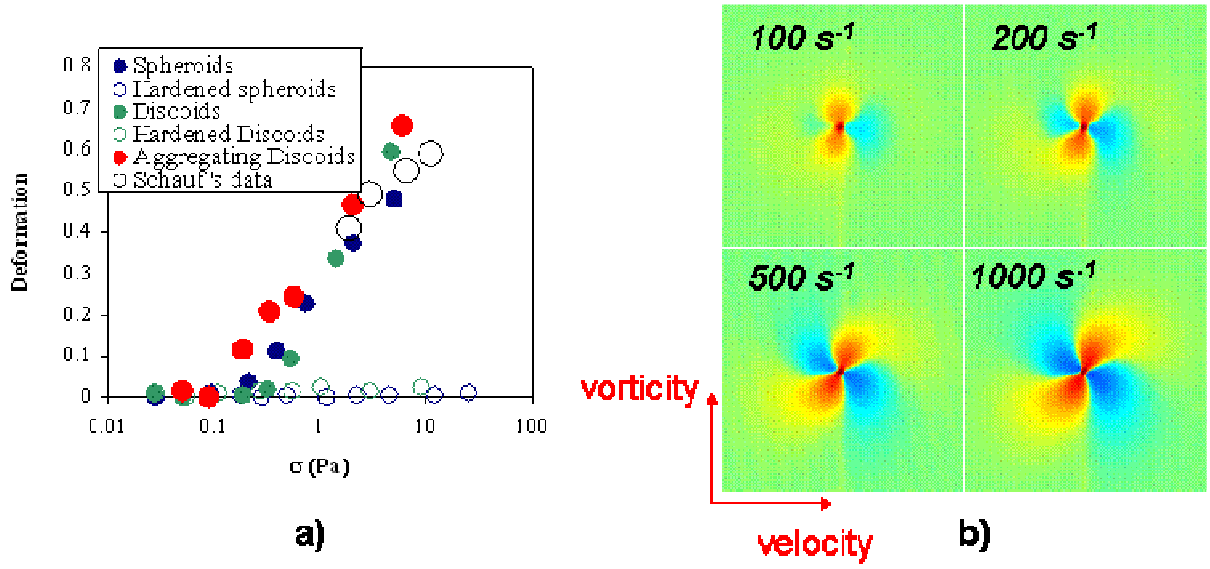

Figure 4 a) Deformation measured for different samples at various shear stresses b) Differences between images at different shear rates and the image at 10s-1.

References

[1] C.Baravian,F.Caton, J.Dillet, J.Mougel,G.Toussaint, and P.Flaud, “Incoherent light transport in an anisotropic random medium: A probe of human erythrocyte aggregation and deformation”, Phys. Rev. E **71**,066603(2007).

[2] M. I. Mishchenko, “Calculation of the amplitude matrix for a non spherical particle in fixed orientation,” Appl. Opt. **39**, 1026-1031 (2000)

[3] M. I. Mishchenko., L. D. Travis,and A. A. Lacis, *Multiple Scattering of Light by Particles: Radiative Transfer and Coherent Backscattering*,(Cambridge University Press, Cambridge2006).

[4] A. Ishimaru, *Wave Propagation and Scattering in Random Media* (IEEE Press, New York, 1997).

[5] R. Haskell, L. Svaasand, T. Tsay, T. Feng, M. McAdams, and B. Tromberg, "Boundary conditions for the diffusion equation in radiative transfer," J. Opt. Soc. Am. A **11**, 2727- (1994).

[6] B. Schauf, B. Aydeniz, R. Bayer and D. Wallwiener, “The laser diffractoscope-a new and fast system to analyse red blood cell flexibility with high accuracy”,Lasers Med. Sci. **18** (2003).

[7] S. Hénon, G. Lenormand, A. Richert and F.Gallet, “A new determination of the shear modulus of the human erythrocyte membrane using optical tweezers”,Lasers Med. Sci. **18** (2003).

Ray-wave approximation for calculation of laser light scattering by a transparent dielectric spheroidal particle

Alexander V. Priezzhev, Sergei Yu. Nikitin, Andrei E. Lugovtsov

Lomonosov Moscow State University, Physics Department and International Laser Center, Leninskye Gory, b. 1, str. 62, Moscow, 119991, Russia
tel: +7 (495) 939-2612, fax: +7 (495) 939-3113, e-mail: avp2@phys.msu.ru

Abstract

Theoretical model is presented for the calculation of light scattering by transparent dielectric spheroidal particles with sizes much larger than the wavelength. In this model, the light incident onto the particle and the light propagating inside the particle are represented by sets of rays while the scattered light – by a set of spherical waves emitted by different elements of the particle surface (ray-wave approximation - RWA). It is shown that RWA is comparable in precision with the discrete-dipole approximation but significantly exceeds the latter in the calculation time for the particles with size parameters higher than 50.

1 Introduction

Light scattering theory for homogeneous spheres of arbitrary size was developed by Gustav Mie one hundred years ago. Since then the exact and approximate solutions for layered dielectric and conducting spherical and non-spherical particles were derived and analyzed by many authors [1]. Spheroids are of particular interest among non-spherical particles: they have a canonical shape and can be studied via well established approaches. For a spheroidal particle, an exact solution was obtained by S. Asano and G. Yamamoto in a very complicated form [2]. The review of different methods of light scattering by small particles including spheroids is given in [1].

Our interest in spheroidal particles is based on modeling biological particles, red blood cells (RBC) in particular. Being complicated in shape these particles have an intrinsic property of deformation and orientation in shear flows, as well as reversible aggregation in a concentrated suspension like blood with formation of linear associates called rouleaux [3,4]. Exact calculation of scattering phase functions for such cases, important for clinical diagnostic applications, is a tough problem. The widely used approximation by equivolumed spheres in many cases is too rough and yields high errors in solving practical problems, like light propagation in flowing blood, blood cells flow cytometry, etc. [5]. Modeling deformed (elongated) RBC and RBC aggregates by spheroids of different sizes and aspect ratios seems to be a much better choice. This is also true for many other biological cells like bacteria, algae, etc. Thus elaboration of a fast procedure for calculating scattering phase functions for such particles is a hot issue.

In our previous work [6], light scattering by large homogeneous spheroidal particles with complex refractive index was studied in the frames of geometric optics approximation (GOA). In this work we develop a new ray-wave approximation (RWA), which presumably yields more precise results than GOA but is similarly low time consuming. The validity of this approximation is discussed.

2 Methods

Consider a transparent spheroidal particle with refractive index m_2 suspended in a medium with refractive index m_1. The particle is illuminated with a light beam with wavelength λ. We need to calculate the angular distribution of light intensity scattered by the particle.

Let us represent light beam incident onto the particle by a set of partial light beams. Each partial beam is characterizes by a central ray, direction of propagation $\vec{\kappa}$, complex amplitude *E,* and the cross-section

area $\Delta S_{\perp}$. The interaction of the partial beam with the particle is described by the geometric optics laws and the Fresnel's formulas.For each beam incident onto the particle surface we calculate the coordinates of the point of intersection of its central ray with the particle surface, the directions of the reflected and refracted beams and their amplitudes. While doing so we consider only those incident beams which central rays intersect the particle surface. The beams that do not satisfy this condition are not considered in further calculations. When performing the procedure of ray-tracing we account for a sufficient number of internal "reflections-refractions" which is determined by the relative refractive index. The partial light beams out-going from the particle are considered as sources of elementary spherical waves. The resulting scattered field on the observation sphere is calculated with the help of the diffraction integral of Kirhgoff. A somewhat similar approach was proposed earlier in reference [7].

2.1 Calculation of the diffraction integral

The area of a surface element of the particle illuminated by a partial wave is

$$\Delta S = \frac{\Delta S_{\perp}}{\left|\vec{\upsilon}\vec{\kappa}\right|},$$

Where $\vec{\upsilon}$ is the unit vector of the normal to the particle surface in point M, in which the central ray of the given beam intersects the particle surface. A refracted and a reflected beams characterized by similar parameters appear as a result of an elementary event of reflection and refraction. The sross-section areas of these beams are given by the formulas:

$$\Delta S_{1\perp} = \Delta S \cdot \left|\vec{\upsilon}\vec{\kappa}_1\right|, \Delta S_{2\perp} = \Delta S \cdot \left|\vec{\upsilon}\vec{\kappa}_2\right|,$$

where $\vec{\kappa}_1$ и $\vec{\kappa}_2$ - unit vectors of the directions of the reflected and refracted beams.

Partial beams outgoing from the particle are denoted by index "*j*". Let ΔS_j - be the area of the surface element of the particle, through which the partial beam with index "j" exits from the particle. Each such beam is considered as a source of an elementary spherical light wave on the particle surface. Then the diffraction integral can be written as a sum of field amplitudes of partial beams

$$E(P) = \sum_j \Delta E_j(P).$$

Here $\vec{E}(P)$ - complex amplitude of the electric field intensity at the detection point P on the detection sphere, and

$$\Delta E_j(P) = \frac{i}{\lambda} E_j(M) K_j \Delta S_j \frac{\exp(-ik\rho)}{\rho}$$

- elementary scattered field, M - exit point of the beam on the particle surface,

$$K_j = \frac{1}{2}(\vec{\nu}, \vec{\kappa}_j) + \frac{1}{2}(\vec{\nu}, \vec{\rho}_0),$$

ρ - distance from point M to point P, $\vec{\rho}_0$ - unit vector directed from point M to point P, $k = 2\pi/\lambda$ - wave number. Values $\vec{E}_j(M)$, having the meaning of complex amplitudes of partial light beams (plane waves) can be calculated with the help of the formulae presented in reference [6].

2.2 Scattering cross-section

The scattering cross-section σ is defined as the ratio of light power incident onto the particle to its intensity $\sigma = P_0 / I_0$. In numerical calculations this value can be determined from the formula

$$\sigma = N \cdot \Delta S_{0\perp},$$

where N - number of partial beams, incident onto the particle, $\Delta S_{0\perp}$ - area of the cross-section of the partial beam incident onto the particle.

2.3 Light scattering phase function

This function characterizing the angular distribution of the scattered light intensity is defined by the formula

$$f(\theta,\varphi) = \frac{I(\theta,\varphi)}{I_0}\frac{4\pi R_0^2}{\sigma},$$

where θ,φ - spherical angular coordinates of the observation point, $I(\theta,\varphi)$ - intensity of the scattered light at the observation point, I_0 - incident light intensity, R_0 - radius of the detection sphere, σ - scattering cross-section. The phase function normalization condition is

$$\frac{1}{4\pi}\int_0^{2\pi} d\varphi \int_0^{\pi} f(\theta,\varphi)\sin\theta d\theta = 1.$$

This condition determines the light energy conservation in the process of light scattering by a transparent particle and can be used for controlling the precision of calculations.

3 Results

Figure 1 shows an example of calculation of the dependences of the relative intensity of the scattered light on the scattering angle for two basic orientations of a spheroidal particle with diameter 6.5 μm and

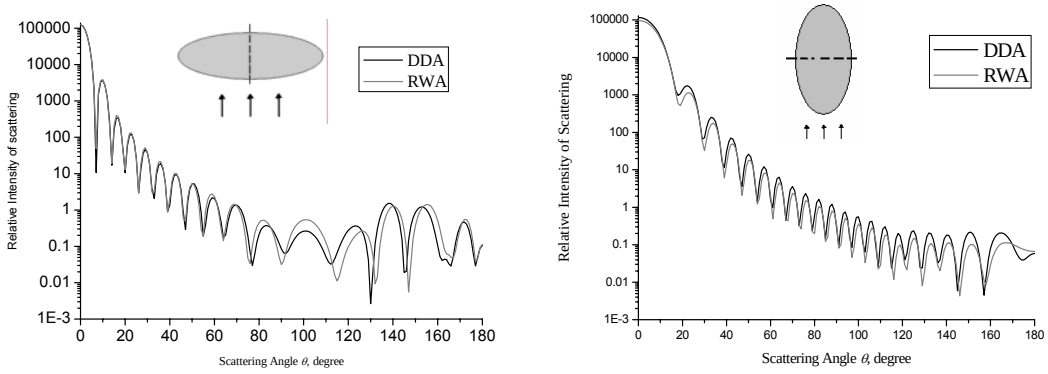

Figure 1: Diagrams of light scattering by a spheroid illuminated along its symmetry axis obtained in RWA and DDA. Spheroid semiaxes *a* = 3.25 μm, *b* = 1.15 μm; relative refractive index *m* = 1.05; particle size parameter $4\pi a/\lambda \approx 65$.

thickness 2.3 μm. The relative refractive index of the particle $m = m_2 / m_1 = 1.05$, wavelength $\lambda = 0.633 \mu m$. The spheroid symmetry axes are shown with broken lines, and the arrows show direction of the incident beam. The scattering plane coincides with the figure plane. The number of partial beams was taken 10^6 and 15 internal reflections were accounted for. The observation sphere radius was chosen 100 μm which corresponds to the far field of scattering.

For comparison, the narrow lines show the results of calculation performed in the frames of dipole-dipole approximation (DDA) [8]. Nice correspondence of the results obtained with different approaches. Calculations performed for different sizes and refractive indices show that RWA in many cases ensures much higher calculation rate than DDA. For example, for a spheroid with size parameter 85 and relative refractive index 1.33 the calculation time using a conventional personal computer in case of RWA is 20 min while in case of DDA – around 3 hours.

3 Conclusion

Ray-wave approximation offers a possibility of relatively fast calculations of scattering diagrams for transparent dielectric spheroidal particles which size parameter highly exceeds the light wavelength. The presented calculation algorithm is comparable in precision with dipole-dipole approximation however significantly exceeds the latter in calculation rate for particles with size parameter higher than 50. This algorithm is perspective for fast practical calculations of light scattering diagrams by such biological particles as red blood cells and their aggregates.

Acknowledgments

The work was supported by the Russian Foundation for Basic Research (grants 06-02-17015, 07-02-01000 and 08-02-91760_AF).

References

[1] M.I. Mishchenko, J. Hovenier, and L.D. Travis (eds), *Light Scattering by Nonspherical Particles*, (Academic Press, San Francisco, 2000).

[2] S. Asano, G. Yamamoto, “Light scattering by a spheroidal particle” Applied Optics, **14**, 29-49 (1975).

[3] A.N. Yaroslavsky, A.V. Priezzhev, J. Rodrigues, I.V. Yaroslavsky, H. Battarbee, “Optics of blood”. In V.V. Tuchin (ed), *Handbook on Optical Biomedical Diagnostics*, chapter 2 (SPIE Press, Bellingham, 2002).

[4] A.V. Priezzhev, N.N. Firsov, J. Lademann, “Light scattering diagnostics of red blood cell aggregation in whole blood samples”. In: V.V. Tuchin (ed), *Handbook on Optical Biomedical Diagnostics*, chapter 11 (SPIE Press, Bellingham, 2002).

[5] A. Hoekstra, V. Maltsev and G. Videen (eds), *Optics of Biological Particles*, (NATO Science Series, Springer, Dordrecht, 2007).

[6] A.E. Lugovtsov, A.V. Priezzhev, S.Yu. Nikitin, “Light scattering by arbitrarily oriented optically soft spheroidal particles: Calculation in geometric optics approximation”, Journal of Quantitative Spectroscopy Radiative Transfer, **106**(1-3), 285-296 (2007).

[7] Ravey J.-C., Mazeron P. “Light scattering in the physical optics approximation; application to large spheroids”, Journal of Optics (Paris), **13**(5), 273-282 (1982).

[8] M.A. Yurkin, V.P. Maltsev, A.G. Hoekstra, “The discrete dipole approximation for simulation of light scattering by particles much larger than the wavelength”, Journal of Quantitative Spectroscopy and Radiative Transfer, **106**(1-3), 546-557 (2007).

Description of a BioFluorescence Optical Particle Counter

Oliver Ryan,[1] Russell Greaney,[1] S. Gerard Jennings,[1] Colin D. O'Dowd,[1]
[1] *School of Physics & Centre for Climate and Air Pollution Studies, Environmental Change Institute, National University of Ireland, Galway, University Road, Galway, Ireland*
tel: +353 (91) 495413, fax: +353 (91) 494584, e-mail: oliver.ij.ryan@nuigalway.ie

Abstract

A bioaerosol fluorescence detection system is being constructed using an ellipsoid reflector based optical particle counter. The flux measuring device is to size submicron marine aerosol particles down to 50 nm in diameter. It will simultaneously non-destructively excite and detect fluorescence from organic matter contained in the aerosol. Chlorophyll-a is the primary fluorophor target, used as a marker for detecting phytoplankton (or derivatives thereof) in the particles. The device will aid the quantification and identification of this organic material contained in marine aerosol, providing improved inputs into climate models and air quality assessments.

1 Introduction

O'Dowd et al. [1] found that submicrometer marine aerosol contained a significant fraction of organic matter and that this fraction is associated with the seasonality of plankton biological activity as determined from satellite ocean-colour products. When plankton activity is high, the chemical composition of the aerosol is dominated by organic matter that possesses characteristics similar to organic matter found at the ocean surface.

Laser induced fluorescence will probe the organic content of marine aerosols through excitation of fluorescence of chlorophyll-a contained in the phytoplankton. In-vivo chlorophyll-a has a main broad absorbance peak at ~440 nm and two main fluorescence peaks at ~670 nm and ~720 nm. The aerosol is probed with a laser that has a wavelength in the range of 400 – 460 nm to allow for maximum absorption and induce a maximum yield of fluorescence.

The instrument will stimulate and collect a total fluorescence signal from each probed aerosol particle in order to determine the ratio of elastic scattered light at laser wavelength to fluoresced light. Simultaneously it will allow particle sizing through collection of the elastically scattered laser light, and a flux measurement by counting the particles that pass.

A 405 nm 50mW CW laser induces the chlorophyll-a fluorescence. This choice of wavelength will enable scattering measurements to infer diameters of down to 50 nm, while still stimulating chlorophyll-a at high efficiency. The energy output of 50 mW is sufficiently high to reliably induce the fluorescence, based on existing experimental data available in the literature, e.g. [2-4].

The fluorescence quantum yield is very low for chlorophyll-a in phytoplankton, ranging from 2% to 7% [5] or 0.6 - 3% [6]. The fluorescence yield depends on, for example, type of phytoplankton, light exposure history, other absorbing pigments in the phytoplankton, competing energy processes, available nutrients and surrounding medium [7, 8]. The fluorescence signature also has a very short lifetime on the order of nanoseconds making the fluorescence output almost simultaneous to the elastic scattered light signal. This necessitates the use of highly sensitive photomultiplier tubes (PMTs) to maximise data signal-to-noise.

2 Instrument Layout

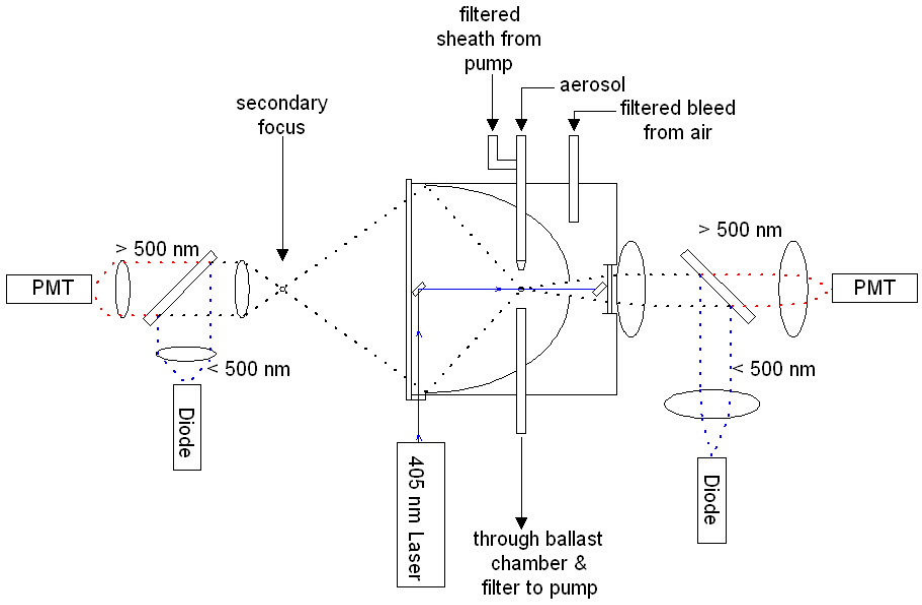

Figure 1: A schematic layout of the instrument.

Figure 1 depicts the layout of the optical particle counter instrument, based on a design by Kaye *et al.* [9]. A diaphragm pump draws air through the exhaust tube at a rate of ~3.9 L/min, and supplies the filtered sheath air at ~2.4 L/min. The filtered bleed is independently managed with a valve and its flow rate (~0.8 L/min) is balanced against the sheath and aerosol flow rates to produce a smooth non-turbulent aerosol flow (~0.7 L/min). The filtered bleed flow helps maintain a laminar aerosol flow and also allows better clearing of the chamber of rogue particles. The ballast chamber helps smooth the flow produced by the diaphragm pump. Also when the pump is switched off the lower pressure in the ballast chamber helps to continue pulling any remaining aerosol particles out of the chamber in an effort to keep it clean.

The input nozzle design is shown in Figure 2. The aerosol particles are drawn through the sample tube of 0.8 mm inner diameter (1.2 mm outer diameter) that is centred along the sheath flow tube of 3.4 mm inner diameter. The nozzle cap (with a 1 mm diameter hole in its peak) causes the sheath air to hydrodynamically focus the aerosol particles into a non-turbulent laminar stream of ~0.6 mm diameter. This stream is directed through the ellipsoid reflector primary focus where particles scatter the incident laser light (Fig. 3).

Figure 3 shows the nozzles positioned either side of the primary focus of the reflector. The laser is visible due to forced diffusion of smoke in the chamber. The laser intersects the aerosol flow (passing from left to right) producing a bright spot of scattered light. The dark ring is the filtered sheath flow. Different nozzles were used at various stages of flow testing to examine the effects of nozzle design on flow stability.

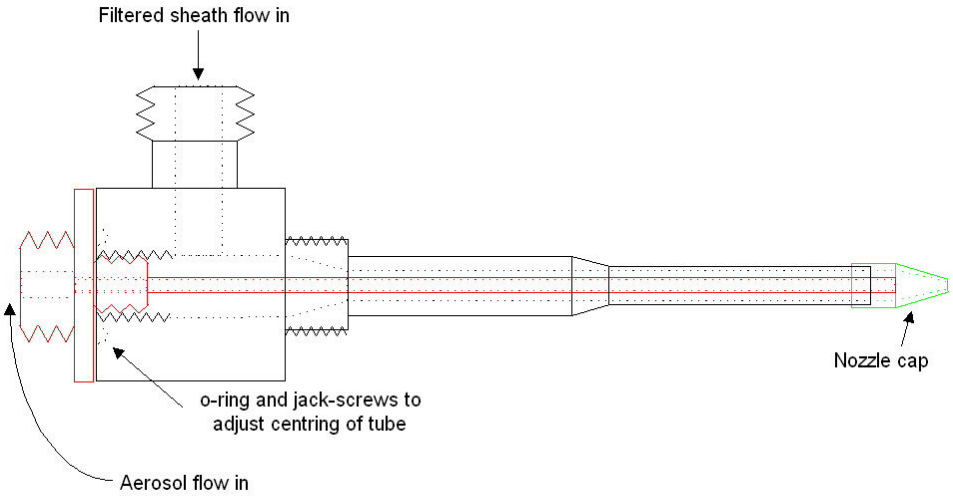

Figure 2: The input nozzle passes aerosol particles through a tube, of 0.8 mm and 1.2 mm inner and outer diameters, respectively. This is centred inside the sheath flow tube of inner diameter 3.4 mm. The nozzle cap has a 1 mm diameter hole at its end through which the particles emerge in a laminar flow of ~0.6 mm diameter.

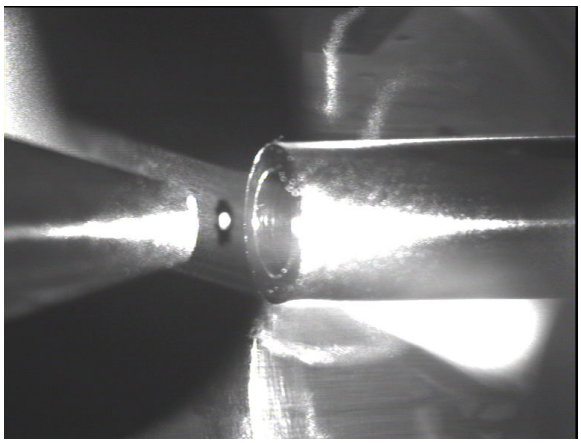

Figure 3: Input and exhaust nozzles positioned either side of the primary focus of the ellipsoid reflector. Aerosol flow is from left to right. The laser line is visible due to the forced diffusion of smoke in the instrument. The bright spot is the intersection of the laser with a smoke-filled aerosol flow. The dark ring surrounding this bright spot is the filtered sheath flow.

The ellipsoid reflector has a protected silver coating to maximize collection of the scattered 405 nm laser light as well as having high collection efficiency for the chlorophyll-a fluorescence. The laser, focused by a cylindrical lens to a sharp vertical line ~0.5 mm by 2 mm (Fig. 3), is directed by fixed mirrors to the primary focus of the reflector, where it perpendicularly intersects the aerosol flow, and further to a laser dump. High f-number aspheric lenses are used to collect and collimate the scattered light from the primary and secondary foci, for forward and back scattered measurements respectively, as well as any fluorescence. High efficiency dichroic (long pass) mirrors split the collimated beam at an edge wavelength of 500 nm, passing the scattered light to photodiodes, and the weaker fluorescent emission to highly

sensitive Hamamatsu PMTs. Dedicated electronics amplify the four detector signals which are simultaneously sampled by a National Instruments analog-to-digital card. Labview is used to display and store the signal data.

2 Discussion

Calibration and testing of the instrument is currently underway and will produce both sizing and fluorescence measurements. The calibration includes using an aerosol generating system (TSI atomizer and classifier) to supply (ammonium sulphate) particles of known diameter (from 20 nm to 300 nm) to the OPC to calibrate the photodiodes' scattered light signals. Chlorophyll-a powder will be used with the generator to produce chlorophyll particles of known diameter to calibrate the PMT signal output. After validation the instrument will be brought for chlorophyll detection trials on the Atlantic coast at the Mace Head atmospheric research station.

Acknowledgments

Thanks to Paul Kaye for the nozzle cap design and very helpful discussions. This project is funded through the Research Frontiers Programme of SFI, award no. 05/RF/GEO009.

References

[1] C.D. O'Dowd, M.C. Facchini, F. Cavalli, D. Ceburnis, M. Mircea, S. Decesari, S. Fuzzi, Y.J. Yoon, and J-P. Putaud, Biogenically-driven organic contribution to marine aerosol, Nature 431, 676-680, 2004.

[2] A.M. Chekalyuk, F.E. Hoge, C.W. Wright, and R.N. Swift, Short-pulse pump-and-probe technique for airborne laser assessment of Photosystem II photochemical characteristics, Photosynthesis Research, 66, 33-44, 2000.

[3] Z. Kolber, and P.G. Falkowski, Use of Active Fluorescence to Estimate Phytoplankton Photosynthesis in Situ, Limnol. Oceanogr. 38(8), 1646-1665, 1993.

[4] V.V. Fadeev, D.V. Maslov, D.N. Matorin, R. Reuter, and T.I. Zavyalov, Some peculiarities of fluorescence diagnostics of phytoplankton in coastal waters of the Black Sea, EARSeL eProceedings, 1, 205-213, 2000.

[5] M.P. Lizotte, and J.C. Priscu, Natural fluorescence and quantum yields in vertically stationary phytoplankton from perennially ice-covered lakes, Limno. Oceanogr. 39(6), 1399-1410, 1994.

[6] G.H. Krause, and E. Weis, Chlorophyll Fluorescence and Photosynthesis – The Basics. Annual Rev. Plant Physiol. and Plant Mol. Biol. 42, 313-349, 1991.

[7] R.J. Olson, and E.R. Zettler, Potential of flow cytometry for "pump and probe" fluorescence measurements of phytoplankton photosynthetic characteristics, Limnol. Oceanogr., 40(4), 816-820, 1995.

[8] T. Jakob, U. Schreiber, V. Kirchesch, U. Langner, C. Wilhelm, Estimation of chlorophyll content and daily primary production of the major algal groups by means of multiwavelength-excitation PAM chlorophyll fluorometry: performance and methodological limits, Photosynthesis Research, 83, 343-361, 2005.

[9] P. H. Kaye, J. E. Barton, E. Hirst, and J. M. Clark, Simultaneous light scattering and intrinsic fluorescence measurement for the classification of airborne particles, Applied Optics, 39, 3738-3745, 2000.

Continuous bio-aerosol monitoring in a tropical environment using a UV fluorescence and light scattering instrument.

Warren R. Stanley,[1] Paul H. Kaye,[1]
Virginia E. Foot,[2] Stephen J. Barrington,[2] Martin Gallagher,[3] and Andrew Gabey[3]

[1] University of Hertfordshire, Science and Technology Research Institute, Hatfield, Herts, AL10 9AB, UK
tel: +44 (0)1707 284173, fax: +44 (0)1707 284185, e-mail: p.h.kaye@herts.ac.uk
[2] Defence Science and Technology Laboratory, Porton Down, Salisbury, Wilts. SP4 0JQ, UK
tel: +44 (0)1980 613639, fax: +44 (0)1980 613987
[3]University of Manchester, School of Earth, Atmospheric and Environmental Sciences, Manchester M13 9PL.

Abstract

This paper describes an instrument designed to achieve the continuous monitoring of ambient bio-aerosol concentrations. The instrument is a compact, relatively low-cost, UV aerosol spectrometer that monitors and classifies the ambient aerosol by simultaneously recording from individual airborne particles both a 2×2 fluorescence excitation-emission matrix and multi-angle spatial elastic scattering data. The former can indicate the possible presence of specific biological fluorophores within the particle whilst the latter provides an assessment of particle size and shape. Taken together, these parameters can facilitate discrimination between biological and non-biological particles and potentially allow classification of biological particle types. Example measurements are given illustrating magnitude and temporal fluctuations in the biological fraction of aerosol within the Borneo tropical rain forest.

1 Introduction

Sensors that are able to provide continuous real-time monitoring for potential bio-aerosol hazards are required in both civilian and military environments. Where real-time response and reagent-free operation are required, techniques based on the measurement of optical and/or spectroscopic properties of individual airborne particles can offer advantages. In general, the greater the number of such parameters measured, the higher the level of detection confidence and the lower the risk of false-positive detection.

Whilst most bio-aerosol detectors/monitors have to-date been developed to meet the growing potential threat of deliberate bio-hazard release, there is growing interest in their deployment in the fields of atmospheric and climate research. Biological particles such as bacteria and pollen are known to be very efficient ice nucleators [1] and thus can influence cloud microphysical and radiative processes. However, their role remains poorly understood, in part through the lack of quantitative data relating to bio-aerosol fluxes and distributions in the atmosphere.

During the Summer of 2008, a major atmospheric research field campaign is being undertaken in Borneo as part of the ACES (Aerosol Cycle in the Earth System) experiment [2].This experiment is primarily concerned with understanding the fundamental processes involved in the formation of aerosols from the chemical processing of natural hydrocarbons emitted from forested regions. However, the campaign initially lacked instrumentation to monitor the temporal behaviour of bio-aerosol concentrations, and as a

consequence, a prototype bio-aerosol sensor developed by the authors for the UK DSTL (Defence Science and Technology Laboratory) was commissioned for inclusion in the study.

2 The prototype FAB sensor

This sensor, referred to as Fluorescence Aerosol Bio-sensor (FAB), is the latest version of a series of prototype real-time biological particle monitors [3,4]. It continuously samples ambient air at a rate of ~2.35 l/min through a delivery system that filters ~2.1 l/min of the air and re-introduces this as a sheath around the remaining ~250 ml/min sample flow. Particles within this sample flow column are aerodynamically constrained to single file as they intersect the beam from a continuous-wave 635 nm diode laser. Each individual particle, down to ~0.5 μm in size, produces a scattered light pattern that is recorded by a multi-channel photodetector used to derive particle shape and size information (see below). The scattered light signal also provides a trigger signal to initiate the sequential firing (~10 μs apart) of two xenon discharge tube sources that irradiate the particle with UV pulses centred upon ~280 nm and ~370 nm wavelength, optimal for excitation of the common bio-fluorophores tryptophan and NADH respectively. For each excitation wavelength, fluorescence is detected across two bands (300-400nm and 420-650nm) embracing the peak emissions of the same two bio-fluorophores. These data are summarised in Table 1. Particle classification may be achieved by evaluating these spatial scatter and fluorescence data to appropriately 'position' the particle within multiparameter space. Particles are measured at rates up to ~125 particles/s (limited by the xenon recharge time), corresponding to all particles for concentrations up to ~2.5×10^4 particles/l.

Table 1: Summary of FAB data parameters.

Source	Data parameter
Laser diode, 635 nm	Forward scattered light in four spatial regions. Side-scatter at 90º +/- 36º.
Xenon 1 @ 280 nm	Fluorescence in band ~300-400 nm. Fluorescence in band ~420-650 nm.
Xenon 2 @ 370 nm	Fluorescence in band 300-400 nm is discarded since the elastically scattered light at xenon 2 excitation wavelength saturates the detector. Fluorescence in band ~420-650 nm.

The forward scattered light from each particle is captured by a quadrant photomultiplier detector that covers the scattering angle range Θ = 6 - 25º; $\varnothing$ = 0 - 360º. The quadrant is orientated at 45º to the direction of the sample airflow through the laser beam, such that elongated particles (that tend to align axially with the airflow as a result of the aerodynamic confinement) scatter predominantly to the horizontally-opposed pair of quadrants. An *Asymmetry Factor, Af,* for each particle is determined by evaluating the root-mean-squared variation in the azimuthal light distribution received by the four quadrant detector elements. This is scaled such that a spherical particle (that scatters equally to all four quadrants) has an asymmetry factor of 0, whilst elongated particles such as fibres have an Af approaching 100. The sum of the four detector outputs is used in an estimate of particle size (spherical equivalent size for non-spherical particles), based on scattering intensities from known calibration microspheres.

Preliminary Results

There are numerous potential methods of combining the multiple data parameters obtained with this instrument in order to achieve particle characterisation and discrimination between different particle types. Typically, unknown particles are positioned within a multiparameter space defined by their fluorescence, size, and shape (Af) values, and classified by comparison with results from know particle types (vegetative bacteria and bacterial spores, pollens, fungal spores, etc). These will be described in more detail in the presentation.

By example here, we provide in Fig.1 the results of a simple discrimination between particles deemed biological and those deemed non-biological on the basis of the magnitude of their fluorescence signals in the two detection bands listed above. The 'biological particle' threshold for each fluorescence band (assuming appropriate particle size and Af values) was set arbitrarily in this case to 2.5*st.dev of baseline data. (The baseline data is the fluorescence signal level recorded when each xenon tube is deliberately fired in the absence of a particle. This signal level results from a number of sources including background fluorescence in the instrument scattering chamber, possible sub-0.5µm particles in the sample airstream, fluorescence filter breakthrough, etc).

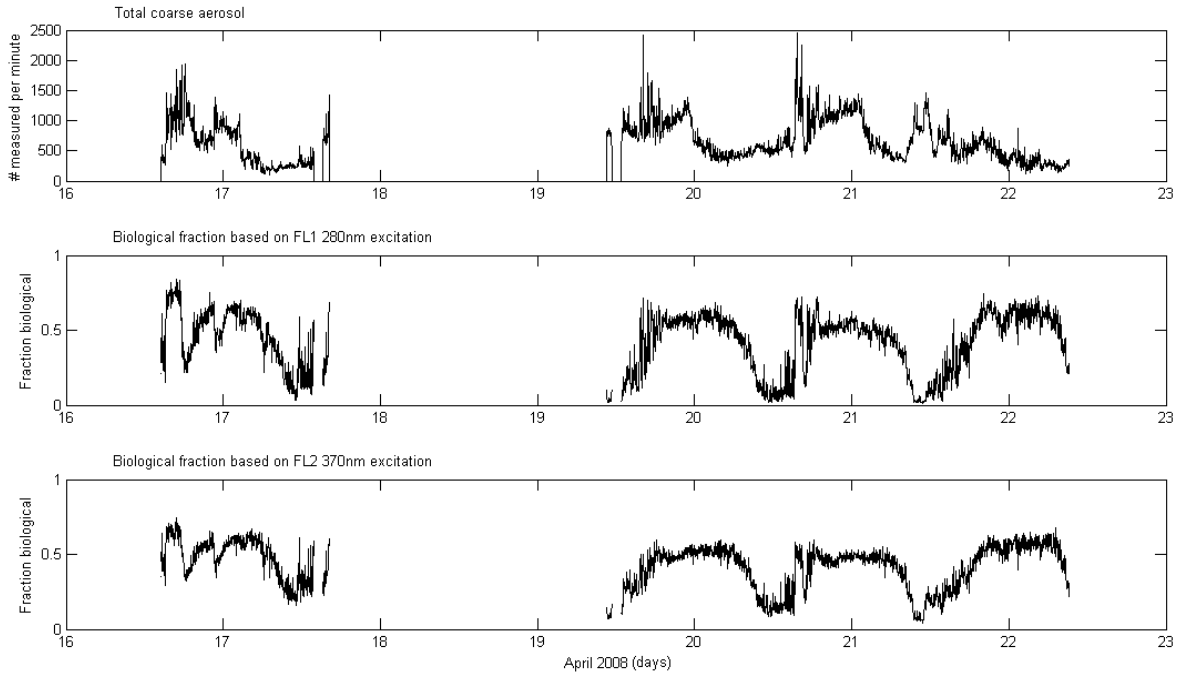

Figure 1: FAB sensor data recorded in ACES tropical rain forest campaign.

The bio-aerosol data presented in Fig. 1 were recorded with the FAB instrument at an elevation of 1.7m from the forest floor in the South-East Asian tropical rain forest. The clear diurnal cycles of increased proportions of biological particles during the night periods are consistent with predictions of nocturnal pollen release/sporulation at the location. Sunset and sunrise are around 6.30am and 6.30pm. (The gaps on the data are a result of 'power-outs' at the monitoring station).

Figure 2 shows a diurnal average of these data, comparing the number of particles deemed biological with those deemed non-biological. Decreased proportions of biological particles around mid-day are again evident, whilst detail in the periodic cycle of the fluorescence data could potentially arise from different pollenating species. (Further data analysis is being carried out to investigate this possibility).

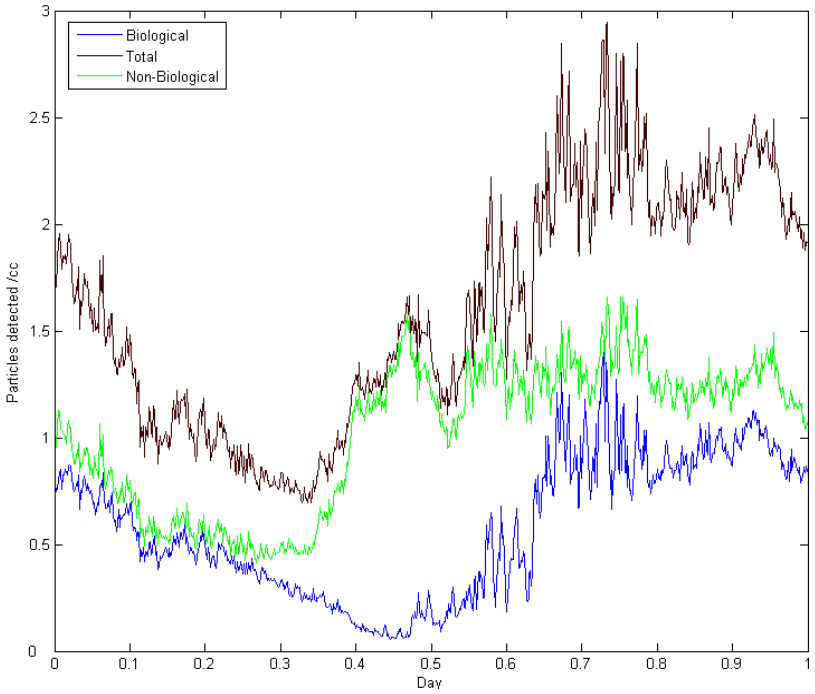

Figure 2: Diurnal average of biological and non-biological aerosol recorded in ACES Week 1. (0 on the x-axis corresponds to midnight)

4 Conclusion

These results are just one example that shows the ability and potential of the multiparameter bio-aerosol sensor to assist in the detection and characterisation of bio-aerosol both naturally occurring and produced by human activity. The rain forest deployment is part of an ongoing process of detailed characterisation of the FAB instrument involving both laboratory and field experiments with aerosols of bacteria, pollens, fungal spores, biological simulants, and a variety of non-biological materials. It is anticipated that these results will ultimately provide it with the capacity to efficiently classify the biological components of ambient environmental aerosols in real-time.

Acknowledgments

ACES campaign sensor data was provided by Dr. Martin Gallagher and Andrew Gabey of Manchester University. This work has been supported by the Defence Science & Technology Laboratory, Porton Down, U.K.

References

[1] G. Vali, *Nucleation and Atmospheric Aerosols,* 271-279 (Pergamon, 1996).

[2] See http://ncasweb.leeds.ac.uk/appraise/ .

[3] P. H. Kaye, E. Hirst, V. E. Foot, J. M. Clark, and K. L. Baxter, “A low-cost multi-channel aerosol fluorescence sensor for networked deployment,” in Optically Based Biological and Chemical Sensing for Defence. J. C. Carrano and A. Zukauskas, eds. Proc. SPIE 5617, 388-398 (2004).

[4] P. H. Kaye, W. R. Stanley, E. Hirst, E. V. Foot, K. L. Baxter and S. J. Barrington, “Single particle multichannel bio-aerosol fluorescence sensor,” Opt. Express **13**, 3583-3593 (2005).

Study of light scattering by a granulated coated sphere – a model of granulated blood cells

Maxim A. Yurkin,[1,2] David de Kanter,[1] and Alfons G. Hoekstra[1]

[1] *Faculty of Science, Section Computational Science, University of Amsterdam, Kruislaan 403, 1098 SJ, Amsterdam, The Netherlands*
[2] *Institute of Chemical Kinetics and Combustion, Siberian Branch of the Russian Academy of Sciences, Institutskaya 3, Novosibirsk 630090, Russia*
tel: +31 (20) 525-7562, fax: +31 (20) 525-7490, e-mail: yurkin@gmail.com

Abstract

We performed extensive simulations of light scattering by granulated coated sphere model using the discrete dipole approximation and varying model parameters in the ranges of sizes and refractive indices of granulated blood cells. We compared these results with predictions of Maxwell-Garnett effective medium theory and independent scattering approximation. Extinction efficiency and Mueller matrix element S_{11}, averaged over azimuthal angles, are accurately described by one of the approximations, except for the intermediate range of polar angles. We discuss dependence of S_{11} on granule diameter for any fixed angle, showing a distinct maximum, with respect to the solution of the inverse light scattering problem.

1 Introduction

Many naturally occurring particles from biological cells to astrophysical dust can be characterized by a matrix with multiple inclusions (granules). Rigorous simulation of light scattering by such particles requires computationally intensive algorithms: superposition T-matrix method [1] (applicable only to certain geometries), the finite difference time domain method (FDTD) [2] or the discrete dipole approximation (DDA) [3]. A number of approximate theories also exist, such as effective medium theories (EMTs) [4-7]. Most researchers who studied granulated particles are concerned with astrophysical or atmospheric applications [1,5-8], while our main application – light scattering by biological cells – is a much less studied field.

Biological cells, when suspended in liquid, have an important advantage with respect to the light scattering simulation [9]. Their relative refractive index is close to unity. This accelerates the rigorous methods and improves the accuracy of the EMTs and other approximate theories. FDTD simulation of light scattering by biological cells was performed in a number of manuscripts by Dunn and coworkers (summarized in [10]). However, only the dependence on the volume fraction and not on the size of the granules was studied. Recently we have performed a systematic study of light scattering by a granulated sphere in the size and refractive index range of human granulated leucocytes (granulocytes) [11]. We explained the difference of depolarization side scattering signals measured by a flow cytometer between different subtypes of granulocytes and proposed approximate methods to quickly calculate these signals.

Granulocytes are the most numerous type of leukocytes, consisting of three subtypes: neutrophils, eosinophils, and basophils. They participate in protection of the host against infectious agents including parasites, inflammations, and allergy conditions [12]. Their morphology, e.g. number or volume fraction of granules, can be an indicator of certain pathological conditions. The Scanning flow cytometer (SFC) allows fast measurement of angle-resolved light scattering patterns (LSPs) [13], which potentially contains enough information to characterize cell morphology.

In this paper we extend our previous simulations [11] including a cell nucleus. We perform extensive DDA simulations varying all parameters of the model. To analyze results we concentrate on simulated LSPs and test the accuracy of two approximate methods: Maxwell-Garnett EMT [14] and independent scattering approximation (ISA).

2 Methods

An optical model used for simulations is shown in Fig. 1. It consists of spherical cytoplasm with concentric spherical nucleus. The remaining cytoplasm is randomly filled with spherical granules up to volume fraction f. Diameters and refractive indices of cytoplasm, nucleus and granules are D_c, D_n, D_g and m_c, m_n, m_g respectively. All values of model parameters (except D_g) used for simulations are given in Table 1. Wavelength λ corresponds to the wavelength of 0.66 μm semiconductor laser in buffer saline (refractive index 1.337). All refractive indices are taken relative to the same medium. Values of m_c and m_g are the same as used in our previous study [11], and values of m_n correspond to literature data [15]. Imaginary part of all refractive indices is assumed to be zero. Values of f, D_c and D_n/D_c cover the range of all leukocytes, including monocytes and lymphocytes. For non-granulocytes, granules in our model may represent either cell organelles, e.g. mitochondria, or real granules that appear under certain physiological conditions. We have changed a single parameter at a time, fixing all other at their default values. In total 13 sets of parameters, given in Table 1, were used. For each of these sets we performed simulations for all D_g from the list: 0.075, 0.1, 0.125, 0.15, 0.175, 0.2, 0.225, 0.25, 0.275, 0.3, 0.325, 0.35, 0.375, 0.4, 0.45, 0.5, 0.6, 0.7, 0.8, 0.9, 1, 1.2, 1.4, 1.6, and 2 μm, except those that cannot fit into the cytoplasm with specified f (e.g., for the default set of parameters D_g up to 0.8 μm were used).

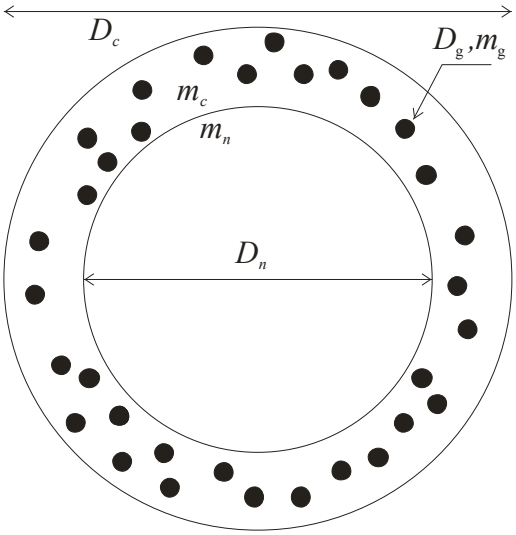

Fig. 1. A granulated coated sphere model. Shown parameters are diameters and refractive indices of cytoplasm, nucleus, and granules.

Table 1. Parameters of the model used for simulations. Values of D_g are given in the text.

f	D_c, μm	D_n/D_c	m_g	m_n	m_c	λ, μm
0.02	6	0.4	1.1	1.05	1.015	0.4936
0.05	8*	0.6	1.15	1.08*		
0.1*	11	0.8*	1.2*			
0.2	14					
0.3						

* default value for the parameter.

For each unique set of parameters including D_g we have performed 10 simulations for different random placements of the granules. Afterwards we computed mean and standard deviation (SD) of each scattering quantity. In this contribution we analyze extinction efficiency Q_{ext} and angle dependencies of Mueller matrix element S_{11}. The latter is first averaged over the azimuthal angle, so it corresponds to the LSP measured by SFC [13] as a function of polar angle θ. All simulations were performed with ADDA v.0.77 using built-in granule generator, 12 dipoles per wavelength, and the default settings of the iterative solver [16]. All simulations were run on the Dutch compute cluster LISA.*

We have also employed approximate methods to model light scattering by the same particles. First, we used Maxwell-Garnett EMT to replace granulated cytoplasm by a homogeneous spherical layer. Second, we used ISA, i.e. take the sum of scattering quantities (such as Mueller matrix or extinction cross section) of the coated sphere without granules and all granules, considered independently. Both approximate models are easily simulated using the Mie theory.

3 Results and discussion

Here we present only part of the results of analysis of the simulated data and our first conclusions. More details will be presented at the conference. Fig. 2 shows the dependence of Q_{ext} on D_g for different f, including EMT result. Also Q_{ext} do deviate from EMT result with increasing D_g, the difference is within 10% for all shown points. On contrary, ISA is completely wrong for prediction of Q_{ext} showing much steeper dependence on D_g (data not shown).

* http://www.sara.nl/userinfo/lisa/description/

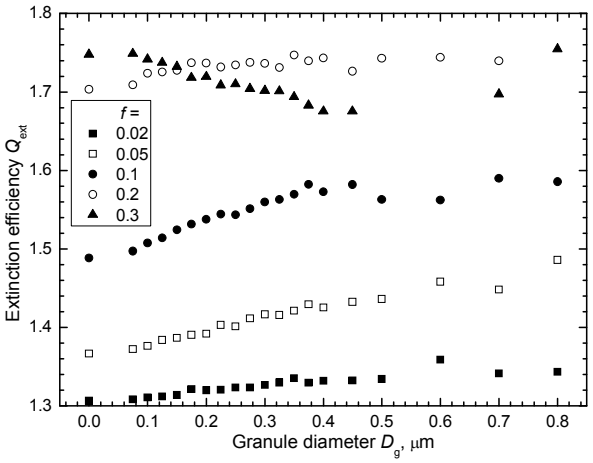

Fig. 2. Q_{ext} versus D_g for different f. Other parameters are set to the default values (see text). Values for $D_g = 0$ are computed using EMT.

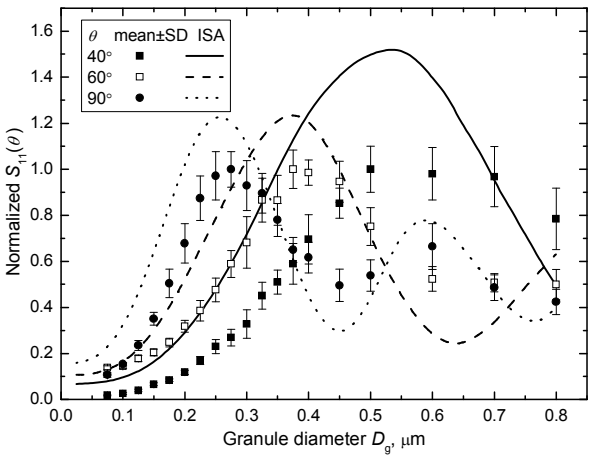

Fig. 3. $S_{11}(\theta)$ (averaged over φ and normalized over maximum DDA result for this θ) versus D_g for different θ. Other parameters are set to the default values.

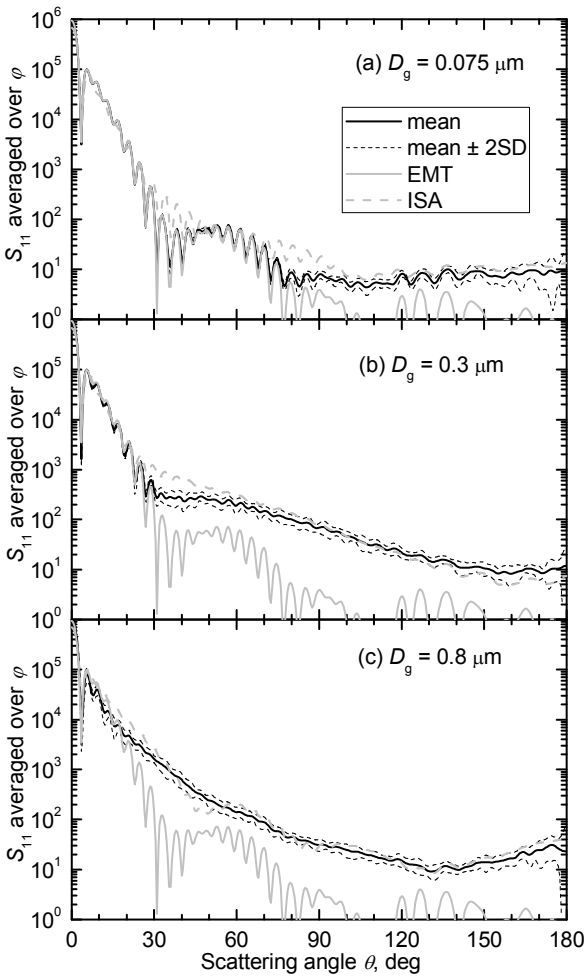

Fig. 4. S_{11} (averaged over φ) versus scattering angle θ simulated using DDA (mean values and ± 2SD range are shown), EMT and ISA for three values of D_g. Other parameters are set to the default values.

Three representative examples of LSPs are shown in Fig. 4 for the default set of parameters and $D_g = 0.075$, 0.3, and 0.8 μm. One can see that EMT is a good approximation for relatively small angles, and ISA is within 2×SD from DDA simulations for relatively large angles. However, there always exist a range of angles, where none of the tested approximations are accurate enough. This range moves towards smaller angles with increasing D_g. In other words, interaction between granules and coated sphere is negligible for large angles and is well described by EMT for small angles. In the intermediate range a more sophisticated approximation should be used. A possible candidates is Rayleigh-Debye-Gans approximation [14], which differs from ISA only in consideration of interference of fields scattered by different constituents. The interference may decrease overestimation of scattered intensity by ISA for intermediate angles.

Another interesting feature of light scattering by granulated particles is dependence of S_{11} on D_g for any fixed θ, showing a distinct maximum. An example is shown in Fig. 3 for the default set of parameters and $\theta = 40°$, 60°, and 90°, where DDA results (mean ± SD) is compared with ISA. One can see that ISA is overall rather inaccurate, but it well describes the position of the peaks, i.e. D_g for which $S_{11}(\theta)$ reaches maximum. This means that this position is largely determined by the dependence of single granule scattering intensity on size, although there is significant interference decreasing the peak amplitude. The fact that peak position decreases with increasing θ agrees with general notion of diffraction. Moreover, in

combination with satisfactory accuracy of ISA it potentially allows “deconvolution” of contribution of granules with different D_g to LSP, which is a subject of future research.

4 Conclusion

We performed extensive DDA simulations of light scattering by granulated coated sphere model varying model parameters in the ranges of sizes and refractive indices of granulated blood cells. We compared these results with predictions of Maxwell-Garnett effective medium theory (EMT) and independent scattering approximation (ISA). EMT predicts values of extinction efficiency with accuracy within 10%, and accurately describes values of averaged over azimuthal angles Mueller matrix element S_{11} (light scattering pattern measured by a scanning flow cytometer) for relatively small polar angles θ. On contrary, ISA is a good approximation of $S_{11}(\theta)$ for relatively large θ. Intermediate range of θ, which moves towards smaller θ with increasing granule diameter (at fixed volume fraction), is not described accurately by any of the two approximations.

Dependence of S_{11} on granule diameter for any fixed θ contains a peak, which position decreases with increasing θ. This allows one to approach inverse problem of determining granule sizes from light scattering patterns. Moreover, ISA accurately predicts positions of these peaks, but not their amplitudes.

References

[1] M. I. Mishchenko, L. Liu, D. W. Mackowski, B. Cairns, and G. Videen, "Multiple scattering by random particulate media: exact 3D results," Opt. Express 15, 2822-2836 (2007).

[2] A. Taflove and S. C. Hagness, Advances in Computational Electrodynamics: the Finite-Difference Time-Domain Method, 3rd ed., (Artech House, Boston, 2005).

[3] M. A. Yurkin and A. G. Hoekstra, "The discrete dipole approximation: an overview and recent developments," J. Quant. Spectrosc. Radiat. Transfer 106, 558-589 (2007).

[4] P. Chylek, G. Videen, D. J. W. Geldart, J. S. Dobbie, and H. C. W. Tso, "Effective medium approximations for heterogeneous particles," in Light Scattering by Nonspherical Particles, Theory, Measurements, and Applications, M. I. Mishchenko, J. W. Hovenier, and L. D. Travis, eds. (Academic Press, New York, 2000), pp. 273-308.

[5] L. Kolokolova and B. A. S. Gustafson, "Scattering by inhomogeneous particles: microwave analog experiments and comparison to effective medium theories," J. Quant. Spectrosc. Radiat. Transfer 70, 611-625 (2001).

[6] N. V. Voshchinnikov, V. B. Il'in, and T. Henning, "Modelling the optical properties of composite and porous interstellar grains," Astron. Astrophys. 429, 371-381 (2005).

[7] N. V. Voshchinnikov, G. Videen, and T. Henning, "Effective medium theories for irregular fluffy structures: aggregation of small particles," Appl. Opt. 46, 4065-4072 (2007).

[8] K. Lumme and J. Rahola, "Light-scattering by porous dust particles in the discrete-dipole approximation," Astrophys. J. 425, 653-667 (1994).

[9] A. G. Hoekstra and P. M. A. Sloot, "Biophysical and biomedical applications of nonspherical scattering," in Light Scattering by Nonspherical Particles, Theory, Measurements, and Applications, M. I. Mishchenko, J. W. Hovenier, and L. D. Travis, eds. (Academic Press, New York, 2000), pp. 585-602.

[10] A. K. Dunn, "Modelling of light scattering from inhomogeneous biological cells," in Optics of Biological Particles, A. G. Hoekstra, V. P. Maltsev, and G. Videen, eds. (Springer, London, 2006), pp. 19-29.

[11] M. A. Yurkin, K. A. Semyanov, V. P. Maltsev, and A. G. Hoekstra, "Discrimination of granulocyte subtypes from light scattering: theoretical analysis using a granulated sphere model," Opt. Express 15, 16561-16580 (2007).

[12] Wintrobe's Clinical Hematology, 11th ed., J. P. Greer, J. Foerster, and J. N. Lukens, eds. (Lippincott Williams & Wilkins Publishers, Baltimore, USA, 2003).

[13] V. P. Maltsev and K. A. Semyanov, Characterisation of Bio-Particles from Light Scattering, (VSP, Utrecht, 2004).

[14] C. F. Bohren and D. R. Huffman, Absorption and scattering of Light by Small Particles, (Wiley, New York, 1983).

[15] A. K. Dunn, "Modelling of light scattering from inhomogeneous biological cells," in Optics of Biological Particles, A. G. Hoekstra, V. P. Maltsev, and G. Videen, eds. (Springer, London, 2007), pp. 19-29.

[16] M. A. Yurkin, V. P. Maltsev, and A. G. Hoekstra, "The discrete dipole approximation for simulation of light scattering by particles much larger than the wavelength," J. Quant. Spectrosc. Radiat. Transfer 106, 546-557 (2007).

PARTICLE LEVITATION AND LABORATORY SCATTERING

Experimental study of collective resonances in gold nanoparticle arrays

Baptiste Auguié, William L. Barnes

School of Physics, University of Exeter,
Stocker Road, Exeter, Devon, EX4 4QL, UK
Phone: +44 1392 264187, email: ba208@exeter.ac.uk

Abstract

We present experimental evidence of sharp spectral features in the optical response of 2-dimensional arrays of gold nanorods made by electron-beam lithography. The resonance involves an interplay between the excitation of plasmons localised on the particles, and diffraction resulting from the scattering by the periodic arrangement of gold nanoparticles. We investigate this interplay through a systematic study, varying the particle size, aspect ratio, and interparticle spacing, and observing the effect on the position, width, and intensity of the sharp spectral feature.

1 Introduction

Nanoparticles of noble metals, gold and silver in particular, have been the subject of many detailed studies due to their unique optical properties [1]. In particular this is because they can support plasmon modes known as localised surface plasmon resonances (LSPR) [2]. For multiple nanostructures there is the possibility of coherent interaction between modes through multiple scattering. Light incident on a regular array as considered in this work is scattered by the particles in all directions. Of particular interest here is the light that is scattered so as to propagate in the plane of the particles. Such light will undergo multiple scattering by the regularly spaced particles provided its wavelength is matched with the periodicity of the array. This geometric resonance results in a strong interference which, when it occurs in the same spectral range as the LSPR, may lead to a dramatic modification of the measured optical extinction. It appears that this effect was first predicted by Markel [3] and followed up by Schatz and co-workers [4].

Here we report measurements from regular arrays of gold nanorods that exhibit the expected sharp features in extinction. We explore the role of array period, particle size and particle shape on the spectral lineshape. These experimental trends are qualitatively explained with a simple coupled dipole modeling.

2 Results

A set of extinction spectra is shown in figure 1 for a fixed particle size and varying particle separation. Several features are apparent from these curves: i) as the periodicity is varied, a sharp interference pattern sweeps through a broad resonance (the “isolated localised plasmon resonance” with a typical width of 100 nm), ii) a clear correlation between the sharp extinction peak and the array pitch exists, iii) the area under the extinction curve appears to be constant, as suggested by a sum rule for extinction [5].

When studying the sharp feature and its dependency on the different parameters, it is useful to try to de-correlate the effect of particle separation, particle volume, and particle aspect ratio. By using a range of samples so as to give a wide spread of particle sizes we were able to obtain the extinction from two particles of different aspect ratio that had the same volume. The use of a polariser allows us to additionally compare the two in-plane axes for a given particle. The comparison is shown in figure 2. The more elongated particles exhibit a red-shifted resonance along the long axis, the short axis being blue-shifted. As expected the particle volume alone is not sufficient to uniquely determine the observed spectral features, both of the main

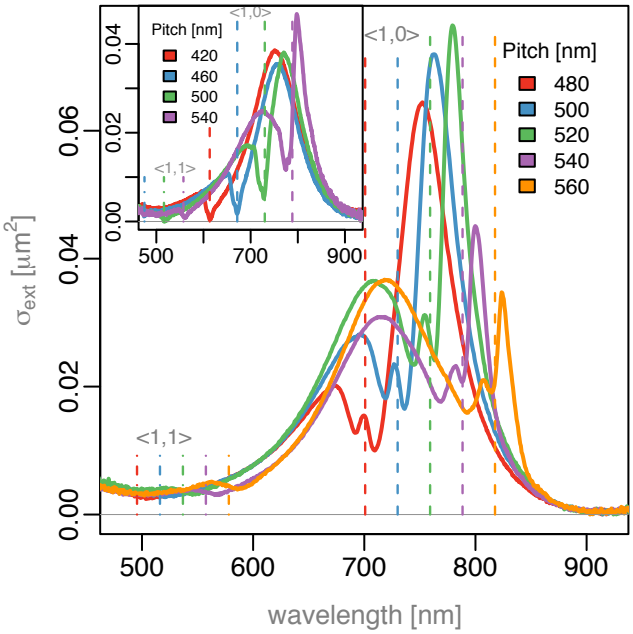

Figure 1: Extinction spectra for several gold nanoparticle arrays, normalised by the occupancy. The average particle size was 123 nm×85 nm×35 nm. Inset (nominal particle size: 120 nm×90 nm×35 nm): when the diffraction edge is on the blue side of the main resonance, a much weaker effect is observed. Interestingly, complete transmission can be obtained near the diffraction edge, see especially the curve for 420 nm pitch in the inset.

resonance and even more strikingly of the diffractive peak. The peak (and to a lesser extent the overall spectrum) is much more intense for the case of the higher aspect ratio particle, at a constant volume and constant particle separation. In these measurements, the peak intensity is mainly dictated by the proximity of the diffraction edge to the LSP resonance, which in turn is determined by the particle polarizability, a function of both the volume and aspect ratio. In fact, we expect that the radiative coupling between particles will depend on the overlap between the propagating field and the mode associated with the localised plasmon resonance. This coupling is the scattering cross-section of the particles, which can also be thought of as a probability of interaction between a propagating photon and the LSPR.

3 Conclusion

We have shown experimental evidence for the narrow spectral features that have been predicted in the literature for several years now, by using gold nanorods. The periodic arrangement of nanorods introduces an interference feature close to the diffraction edge, and its position with respect to the localised plasmon resonance was varied by changing the particle separation. We found that arrays made by electron-beam lithography can be made with sufficient control for this diffractive coupling to be both very pronounced and well controlled.

References

[1] Uwe Kreibig and Michael Vollmer. Optical properties of metal clusters. *Springer*, Jan 1995.

[2] CL Haynes and RP Van Duyne. Nanosphere lithography: A versatile nanofabrication tool for studies of size-dependent nanoparticle optics. *Journal of Physical Chemistry B*, 105(24):5599–5611, Jan 2001.

[3] VA Markel. coupled-dipole approach to scattering of light from a one-dimensional periodic dipole structure. *Journal of Modern Optics*, 40(11):2281–2291, Jan 1993.

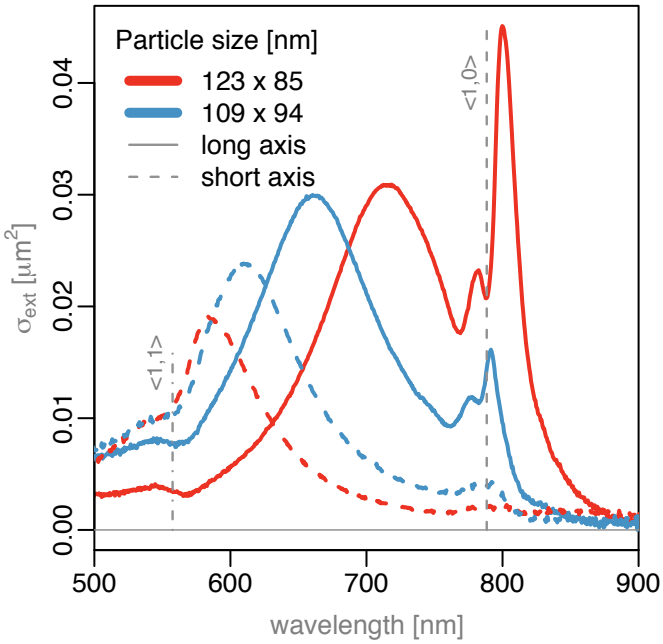

Figure 2: Extinction, normalised by the occupancy for two polarisation states (long-axis: solid lines, short-axis: dashed lines). The colors refer to two arrays of particles for which the particle volume is approximately constant, but the particles have different aspect ratios.

[4] Shengli Zou, Nicolas Janel, and George C Schatz. Silver nanoparticle array structures that produce remarkably narrow plasmon lineshapes. *The Journal of chemical physics*, 120(23):10871–5, Jun 2004.

[5] E Purcell. On the absorption and emission of light by interstellar grains. *The Astrophysical Journal*, Jan 1969.

Theoretical determination of the radiation force for a spherical particle illuminated by a focused laser beam

R.R. Dorizzi[1] and Z. Ulanowski[2]

[1] *Department of Physics, Astronomy and Mathematics, University of Hertfordshire, College Lane, Hatfield, Herts AL10 9AB, UK*

[2]*Science and technology Research Institute, University of Hertfordshire, College Lane, Hatfield, Herts AL10 9AB, UK*

tel: +44 (0) 1707-286124, fax : +44 (0) 1707-284256, e-mail: r.r.dorizzi@herts.ac.uk

Abstract

Trapping forces on dielectric spheres in single beam laser tweezers are computed. A focused beam description based on an exact solution of Maxwell's equations is compared to the 5th order Gaussian beam approximation due to Barton and Alexander. Forces on water droplets suspended in air and on polystyrene spheres suspended in water, exerted by beams focused to varying degree, are calculated. It is demonstrated that the 5th order approximation is accurate for almost paraxial beams (numerical aperture NA<0.25), as compared to the exact treatment. However, for strongly focused beams the 5th order approximation breaks down. Thus it is established that accurate beam description is vital for modeling optical traps, since in order to hold a particle effectively in a single beam trap a strongly focused beam is required.

1 Introduction

Starting with the experiments of Ashkin in 1970 [1] it became possible to use laser beams to trap a variety of particles, including living cells [2], organelles within cells [3] and even larger objects like the giant amoeba [4]. There are various types of such "laser tweezers" in use, including single and the multi beam ones. It is the aim of this work to present a theoretical model of single beam laser tweezers which uses a computational method developed by Barton *et al*. [5]. Since the model presented in [5] is based on the electromagnetic (EM) field derived from the 5th order Gaussian beam approximation [6], the accuracy of the results obtained using this model is uncertain. Hence in order to test the accuracy of the results, we replace the 5th order approximation by EM fields that are exact solutions to Maxwell's equations [7]. Very recently another model has been presented by Mazolli *et al*. [8], which is based on the Debye-type integral representation of the laser beam as a superposition of plane EM waves. The main difference between Mazolli *et al*. [8] and Barton *et al*. [5] as well as the model presented here is that Mazolli *et al*. [8] take truncations of the beam by the focusing lens into account. This is not the case in the model of Barton *et al*. [5] and the model presented here.

2 Theory and results

Lorenz [9] and Mie [10] formulated a theory with which the EM fields inside and outside a sphere can be calculated, when a plane incident wave is scattered by the sphere. Barton *et al*. [5] have used this theory, generalised to an arbitrary incident field, to compute radiation forces and torques exerted on a spherical particle. Ulanowski and Jones [11] have written a set of computer programs to model the trapping forces as derived by Barton *et al*. [5] for real relative refractive indices *n*, which is adequate for calculating the trapping forces for nonabsorbing particles. Here the programs are used with Barton's 5th order beam approximation, and the exact solutions to Maxwell's equations presented by Dorizzi [7], based on the order 01 from the family of scalar, non-paraxial beam solutions derived by Ulanowski and Ludlow [12]. The latter is referred to as the "exact" treatment. Both treatments are used to calculate the trapping forces, exerted by beams focused to varying extent, on water droplets suspended in air (Fig. 1 and 2), and on polystyrene spheres suspended in water (Fig. 3).

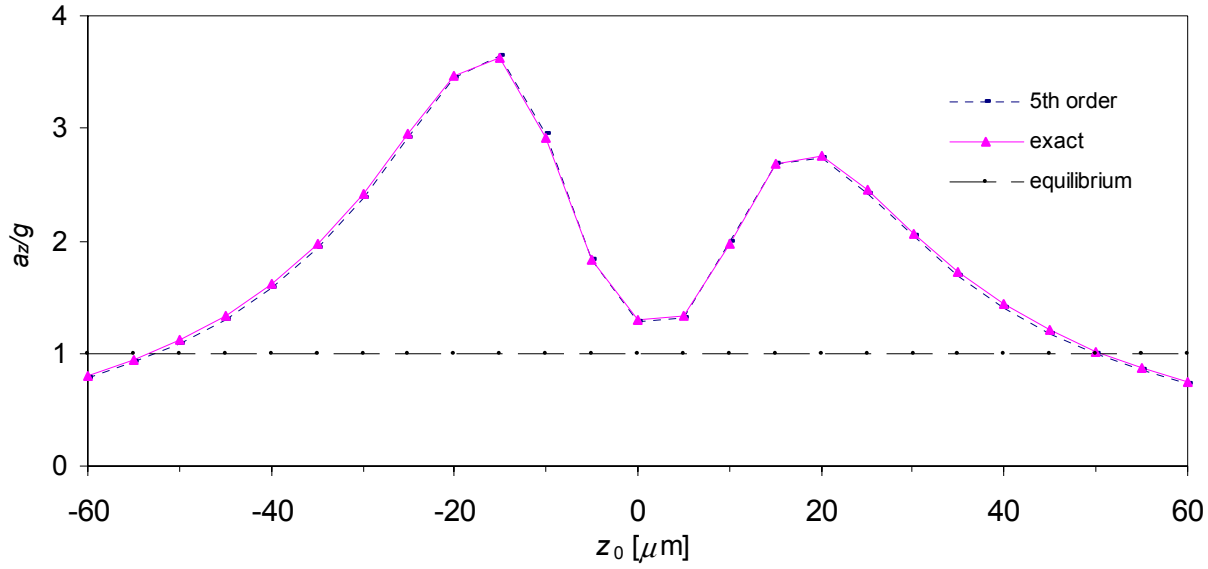

Fig. 1. Comparison of the restoring acceleration based on the 5th order Gaussian beam approximation (doted curve) and the "exact" treatment (solid curve), along the propagation axis for optical levitation of a water droplet in air, using a focused, linearly polarised laser beam, diameter of water droplet d=4.96 μm, n=1.334, wavelength λ=0.5145 μm, beam waist radius w_0=1μm, NA≈0.246 and beam power P=3.5 mW.

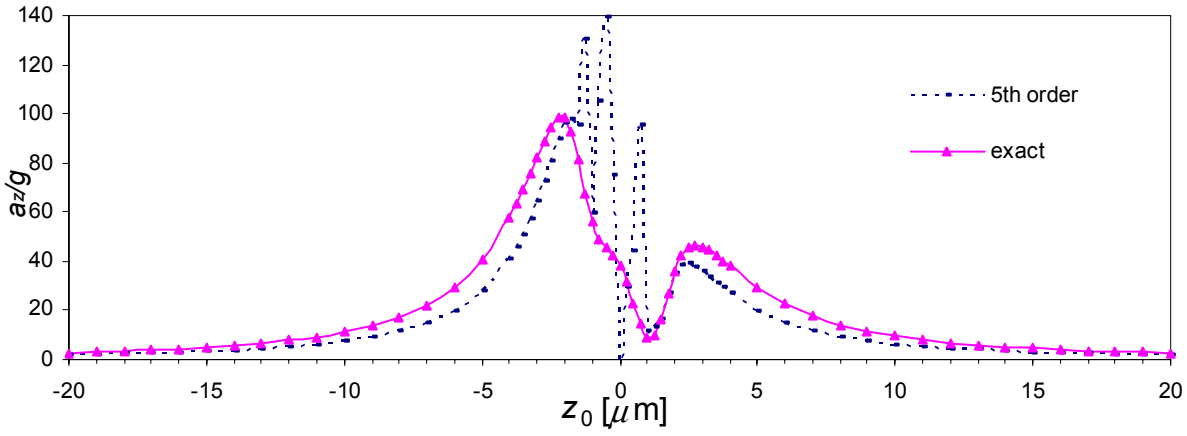

Fig. 2. Comparison of the restoring acceleration based on the 5th order approximation (doted curve) and the "exact" treatment (solid curve), along the propagation axis for optical levitation of a water droplet in air, using a focused, linearly polarised laser beam, d= 2 μm, λ_0 = 0.5145 μm, w_0=0.231μm, and P=3.5 mW.

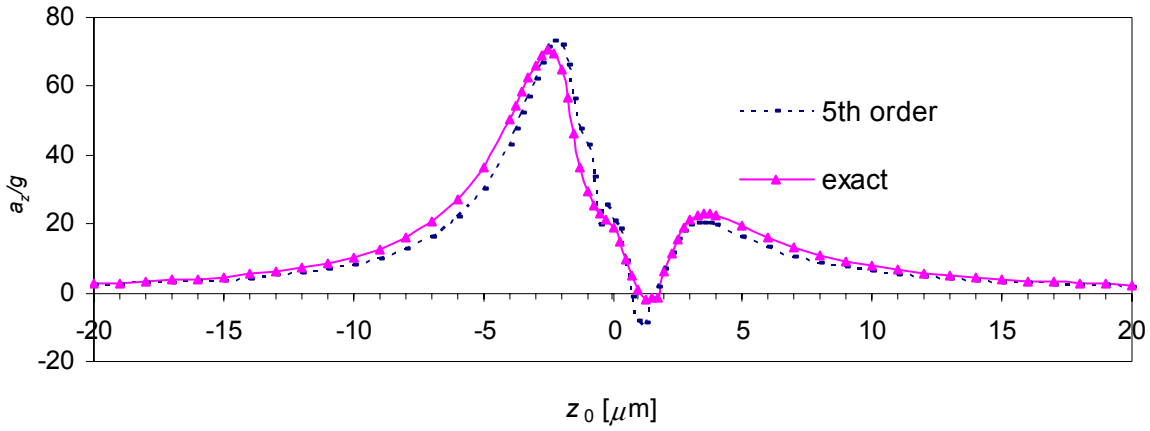

Fig. 3. Comparison of the restoring acceleration based on the 5th order Gaussian beam approximation (doted curve) and the "exact" treatment (solid curve), along the propagation axis for optical trapping of a polystyrene sphere in water, using a focused, linearly polarised laser beam, d = 2.0 μm, λ_0 = 0.5145 μm, w_0=0.231μm, P= 3.5 mW.

3 Discussion

Optical trapping forces have been calculated using the method presented by Barton *et al.* [5], which is valid for arbitrary EM fields. Fig. 1 shows that the trapping forces calculated using the 5th order approximation are accurate for a nearly paraxial Gaussian beam (NA=0.246), when compared to the exact treatment. The RMS error in this case is 1.4%. However, for strongly focused beams the 5th order approximation becomes unreliable: we observe in Fig. 2 a breakdown of the approximation when trapping a water droplet in air. From Fig. 3 it can be seen that when trapping a polystyrene sphere in water the 5th order approximation does not break down completely, but there is an RMS error of 48%. It has thus been established that it is important to have a focused laser beam description that is accurate under non-paraxial conditions, since in order to trap a particle effectively the laser beam needs to be strongly focused.

References

[1] A. Ashkin, "Acceleration and trapping of particles by radiation pressure," Phys. Rev. Lett. **24**, 4, 156-159 (1970).

[2] Y. Tadir, W. H. Wright, O. Vafa et al., "Micromanipulation of sperm by laser Generated optical trap," Fertil. Steril. **52**, 870-873 (1989).

[3] S. M. Block, D. F. Blair, and H. C. Berg, "Compliance of bacterial flagella measured with optical tweezers," Nature **338**, 514-518 (1989).

[4] A. Ashkin, K. Schütze, J. M. Dziedzic, U. Euteneuer, and M. Schliwa, "Forces generated of organelle transport measured in vitro by an infrared laser trap," Nature **348**, 346-348 (1990).

[5] J. P. Barton , D. R. Alexander, and S. A. Schaub, "Theoretical determination of net radiation forces and torque for a spherical particle illuminated by a focused laser beam," J. Appl. Phys. **66**, 10, 4594-4602 (1989).

[6] J. P. Barton, and D. R. Alexander, “Fifth-order corrected EM field components for a fundamental Gaussian beam,” J. Appl. Phys. **66**, 7, 2800-2802 (1989).

[7] Dorizzi, R. R., “Computation of Forces exerted on a Microparticle by a Laser Beam,” PhD thesis, University of Hertfordshire (2004).

[8] A. Mazolli, P. A. Maia Neto, and H. M. Nussenzveig, ”Theory of trapping forces in optical tweezers,” Proc. R. Soc. Lond. A, **459**, 3021-3041 (2003).

[9] L. Lorenz, “Sur la lumière réfléchie et réfractée par une sphère transparente,” in *Oeuvres Scientifiques de L. Lorenz, revues et annotées par H. Valentiner* (Librairie Lehmann et Stage, Copenhagen 1898).

[10] G. Mie, “Beiträge zur Optik trüber Medien, speziell kolloidaler Metal-Lösungen,” Ann. Phys. **25**. 377-445 (1908).

[11] N. T. Jones, “Modelling laser entrapment forces on microspheres,” MSc project report, University of Hertfordshire (1994).

[12] Z. Ulanowski, and I. K. Ludlow, “Scalar field of non-paraxial Gaussian beams,” Opt. Lett. **25**, 1792-1794 (2000).

Polarized-surface-wave-scattering system (PSWSS) for characterization of nanoparticles

Mathieu Francoeur, Mustafa M. Aslan, and M. Pinar Mengüç

University of Kentucky, Department of Mechanical Engineering,
Radiative Transfer Laboratory, 322 RGAN bldg., Lexington, KY 40506, USA
e-mails: mfran0@engr.uky.edu, menguc@engr.uky.edu

Abstract

We described an experimental procedure for online and non-intrusive characterization of nanoparticles (5-100 nm) via evanescent wave scattering. We found that the main experimental difficulties are to obtain samples for proper calibration of the scattering measurements, and the high ratio noise to signal.

1 Introduction

Non-intrusive and online characterization of nanoparticles (5-100 nm) is a challenging problem. Current techniques such as AFM, SEM, and TEM allow visualization of nanoparticles, but with the disadvantages of being expensive, cumbersome, intrusive, and able to provide only static measurements. A characterization framework via polarized light scattering has been successfully developed for particles larger than about 100 nm; in this technique, propagating visible light is incident upon particles in suspension, and Mueller matrix elements are measured [1]. This experimental approach cannot however be readily applied to nanoparticles with 5 to 100 nm in size, since typical wavelengths of light are too large. We therefore recently proposed an experimental framework based on the same paradigms than described above, with the particularity that particles to be characterized are deposited on a surface and illuminated via evanescent waves created by total internal reflection (TIR). We developed mathematical models for light scattering by spherical particles on a surface [2], performed a sensitivity analysis [3], and starts the development of an inversion algorithm [4]. These numerical studies have shown the feasibility of characterizing nanoparticles via evanescent wave scattering.

Given the outcome of the theoretical investigation, an experimental apparatus, called the “polarized-surface-wave-scattering system” (PSWSS), has been built in order to measure experimentally the Mueller matrix elements from nanoparticles illuminated by evanescent waves. The objective of this communication is to describe the details of the PSWSS, and to expose the main difficulties related to the measurement of evanescent wave scattering by nanoparticles.

2 Description of the PSWSS

The purpose of the PSWSS is to measure far-field scattered light by nanoparticles deposited on a surface. More particularly, the change of intensity and state of polarization of light after scattering is measured and used to infer properties of the scatterers such as size, size distribution, shape, and level of agglomeration. The PSWSS is presented in Fig. 1.

As shown in Fig. 1(a), light emerging from a 20 mW He-Ne laser source (632.8 nm) passes through an optical chopper (OCh) modulating the signal at a fixed reference frequency f_{ref}; the OCh is connected to both reference and measurement lock-in amplifiers (Stanford SR830 DSP) in order to discard any light source with frequency other than f_{ref}. The incident beam is separated into two streams via a beam splitter (BS). One part is send directly toward a H6780-04 Hamamatsu photomultiplier tube (PMT1) connected to the reference lock-in amplifier; this signal is used to normalize all data in order to cancel potential temporal fluctuations of the laser source and/or fluctuations coming from vibrations in the system. The output signal of the lock-in amplifier is send to a CPU via a PCIM-DAS1602/16 data acquisition card, and data are collected and stored via a Labview visual interface (VI). The remaining part of the incident beam

emerging from the BS is focused into a fiber collimator (FC) via a lens (L1), passes through an optics fiber (OC), and emerges on the incident leg of the PSWSS (left leg) at an angle of incidence θ_0 greater than the critical angle for TIR θ_c. The angle θ_0 is set via the movement of the translational stage (controlled by a step motor) along *z*. Displacement of the translational stage induces simultaneous translations of the left and right legs of the PSWSS along the *x*-direction, and then allows the control of θ_0.

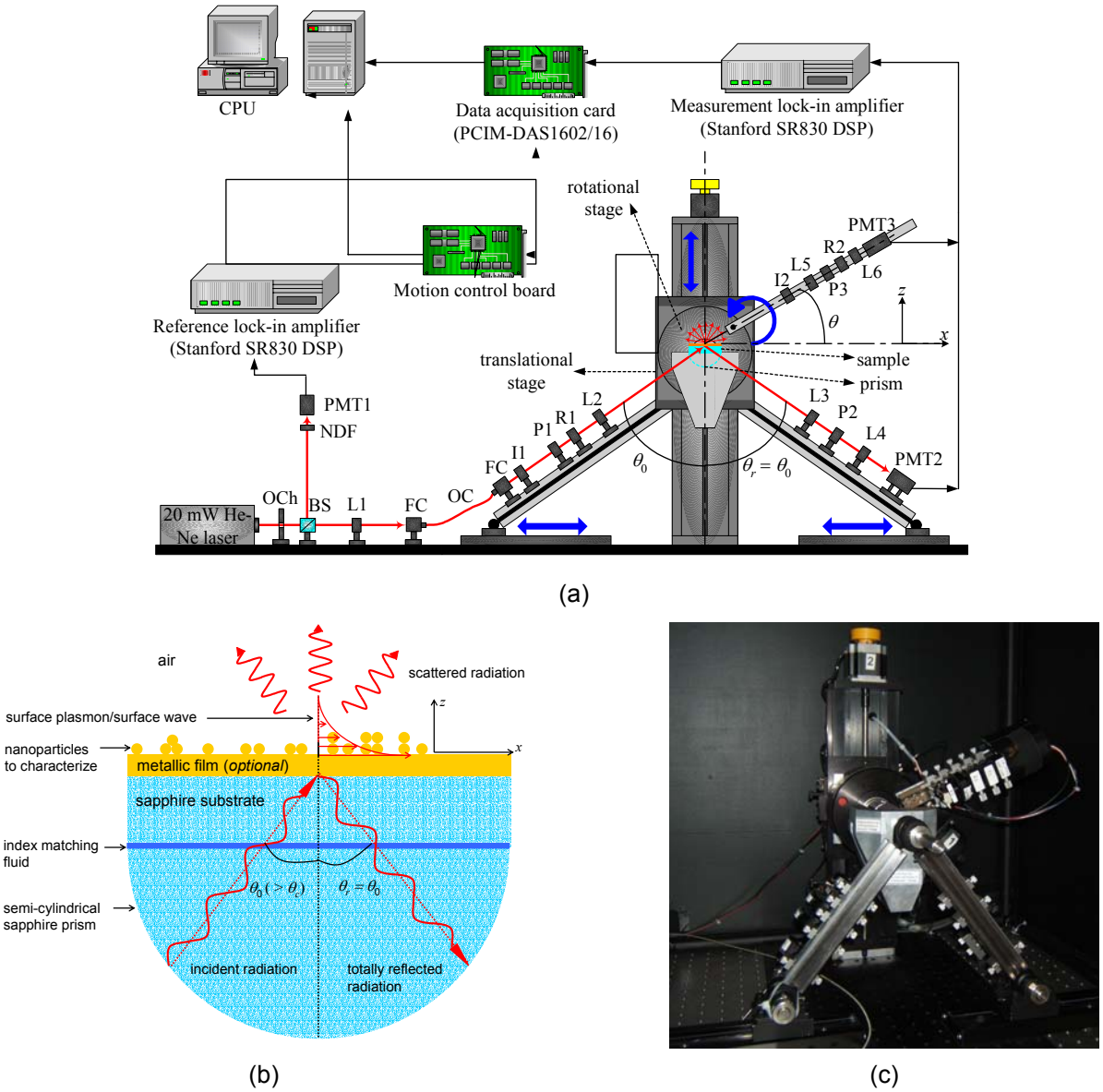

Figure 1: (a) Schematic of the PSWSS (BS: beam splitter; FC: fiber collimator; I: iris; L: lens; NDF: neutral density filter; OCh: optical chopper; PMT: photomultiplier tube; P: polarizer; R: retarder). (b) Sample-prism multilayered system. (c) Picture of the PSWSS.

The beam emerging from the FC then passes through a set of optical components (I1, P1, R1), and is focused at the interface sample-air via a biconvex lens (L2). The beam reflected at angle θ_r (=θ_0) is collected via PMT2 located on the reflected leg (right leg) of the PSWSS before passing through L3, P2, and L4. PMT2 is connected to the measurement lock-in amplifier, and the signal is stored in the CPU via the data acquisition card and the Labview VI. Scattered evanescent waves by nanoparticles are collected

in the far-field via PMT3 located on a rotating arm. The rotating arm is attached to a rotational stage, controlled by a step motor, and allows measurements for angle θ from 25° to 145°. Before being collected by PMT3, the scattered signal passes through I2, P3, and R2, and is focused via two lenses (L5, L6); scattered signals are stored in the CPU in the same way than for the reflectance measurements.

The prism-sample multilayered system is shown in Fig. 1(b). A semi-cylindrical sapphire prism (diameter of 25 mm) with a refractive index of 1.7659 at 632.8 nm is used to generate TIR. Nanoparticles to be characterized are coated on circular sapphire windows with diameter of 12.75 mm and thickness of 1 mm. An interstitial fluid (Cargille, series M) matching the index of refraction of sapphire in the visible spectrum is used between the prism and the window. The sapphire window can also be coated with a thin metallic film (about 10-100 nm) before deposition of particles; in that case, the evanescent electromagnetic field created by TIR couples with the free electrons of the metal and give rise to surface plasmon-polaritons (SPP) which are also evanescent waves [5]. Using the appropriate conditions for surface plasmon-polaritons resonance (SPR), the strength of the evanescent wave field at the sample-air interface can be amplified, and thus the far-field scattered light can increase by few orders of magnitudes [5]. To ensure the parallelism of the surfaces, pressure is applied between the sample and the prism via a sample holder. Also, as shown in the picture of the PSWSS (Fig. 1(c)), a protection box covers the PSWSS to prevent corruption of the signal by external light sources and to prevent potential deterioration of the PMTs. Note that black masks are used to hide the bottom part of the PSWSS from PMT3 to avoid collection of light reflected off the optical components.

Reflectance measurement is complementary in the PSWSS and can be useful to evaluate the extinction coefficient from the sample. Also, measurements of reflectance around the SPR angle can allow imaging of the sample. The scattering measurements is the backbone for characterization of nanoparticles, and we developed a procedure to measure six Mueller matrix elements, namely M_{11}, M_{12}, M_{22}, M_{33}, M_{34}, and M_{44}. These elements are experimentally evaluated via six independent sets of measurements using different orientations of polarizers and retarders on the incident and scattered sides. These orientation angles are chosen in order to obtain M_{ij} elements with low sensitivity to perturbations of the experimental conditions.

3 Experimental difficulties with the PSWSS

Calibration of the reflectance measurement is straightforward and has be done by measuring the reflected light around the SPR angle of samples coated with Au thin metallic films (20-50 nm). For calibration of the scattering measurements, sapphire windows coated with spherical nanoparticles is the best option for direct comparison with numerical predictions. We found that the biggest challenge is the quality control of the samples. We tried a simple technique where a droplet of solution containing nanoparticles is deposited and dried on sapphire windows. This process does not allow any control of nanoparticles dispersion, and crystal salt (contained in the solution) dried on the window disturbs the scattering patterns (observed via SEM imaging). We also tried to chemically attach nanoparticles on sapphire windows [6]; SEM images have revealed that very few nanoparticles have been attached to the substrate. The other drawbacks of this approach are the long time devoted to sample preparation, and the poor control of nanoparticles dispersion. We are currently working with a laboratory in France that is investigating an optimal way to make deposition of spherical nanoparticles on sapphire windows.

Scattered light from nanoparticles (5-100 nm in size) is very low, and it is consequently necessary to use highly sensitive detection devices. However, this has the disadvantage of increasing the ratio noise to signal to a point where it becomes very difficult to measure evanescent scattered light. We found that this noise, that we called “background light” is due to imperfect TIR at the sample-air interface. Light entering in the semi-cylindrical prism is always incident at 90° (see Fig. 1(b)). However, since the beam has a finite diameter, part of the beam is not incident at 90°, and this may causes multiple reflections inside the prism leading to a background propagating light detectable only when highly sensitive detection devices are used. A way to decrease this background light is to decrease the beam diameter as much as possible via

biconvex and biconcave lenses (note that light emerging from the FC is collimated). With the space limitation of the PSWSS, the beam diameter has been reduced to 165 μm, but this was insufficient to obtain an acceptable ratio noise to signal. The other option is to use a plano-convex cylindrical lens and to focus the light at the point where reflection occurs. This procedure has reduced the background light significantly, but the ratio noise to signal is still poor. For example, we have estimated that between 90 and 95% of the far-field collected signal was due to background light using samples coated with 15 nm and 40 nm Au spherical nanoparticles (without metallic film).

In theory, when using a plano-convex lens, the background light should be zero if all optical components are perfectly aligned. Currently, optical components in the PSWSS have to be aligned manually which make the process tedious; we are considering to re-design a part of the PSWSS to allow high accuracy alignment of the optical components. Another way to decrease the ratio noise to signal is to coat the substrate with thin metallic film in order to excite SPP; we are in the process of preparing samples with highly smooth Ag surfaces. For calibration of the PSWSS, we are also preparing sapphire windows coated with particles larger than 100 nm; indeed, by increasing particle size, far-field scattered light will increase, and the ratio noise to signal will decrease. After calibration of the PSWSS, we will gradually decrease particle size to the point where it is impossible to obtain good results due to a bad ratio noise to signal; this systematic analysis will help us to define the resolution limit of the first generation of the PSWSS.

4 Concluding remarks

We described an experimental system, called the PSWSS, for online and non-intrusive characterization of nanoparticles via evanescent wave scattering. The purpose of this communication was to expose our progresses in developing the system, and point out the main difficulties, which are the sample preparation (for calibration) and the high ratio noise to signal due to an imperfect TIR. We hope that this abstract will lead to discussions with colleagues and will help us to improve the current version of the system.

Acknowledgments

MF is grateful to the NSERC (ES D3 scholarship), to the Graduate School of University of Kentucky (Dissertation year fellowship), and to the organization committee of ELS XI for covering travel and conference expenses.

References

[1] M. Kozan, J. Thangala, R. Bogale, M. P. Mengüç, and M. K. Sunkara, “In-situ characterization of dispersion stability of WO3 nanoparticles and nanowires,” J. Nanopart. Res. **10**(4), 599-612 (2008).

[2] P. G. Venkata, M. M. Aslan, M. P. Mengüç, and G. Videen, “Surface plasmon scattering by gold nanoparticles and two-dimensional agglomerates,” ASME J. Heat Transfer **129**, 60-70 (2007).

[3] M. Francoeur, P. G. Venkata, and M. P. Mengüç, “Sensitivity analysis for characterization of gold nanoparticles and agglomerates via surface plasmon scattering patterns,” J. Quant. Spectrosc. Radiat. Transfer **106**, 44-55 (2007).

[4] R. Charnigo, M. Francoeur, M. P. Mengüç, A. Brock, M. Leichter, and C. Srinivasan, “Derivatives of scattering profiles: tools for nanoparticle characterization,” J. Opt. Soc. Am. A **24**(9), 2578-2589 (2007).

[5] H. Raether, *Surface Plasmons on Smooth and Rough Surfaces and on Gratings* (Springer-Verlag, New York,1988).

[6] N. Nath, and A. Chilkoti, “A colorimetric gold nanoparticles sensor to interrogate biomolecular interactions in real time on a surface,” Anal. Chem. **74**, 504-509, (2002).

Light scattering by fluffy aggregates (PROGRA^2 experiment) Different materials and sizes

E. Hadamcik,[1] J.-B. Renard,[2] A.C. Levasseur-Regourd,[1] J. Lasue,[1] G. Alcouffe,[3]

[1]*UPMC Univ. Paris 06, UMR 7620 (Service d'aéronomie), 91371 Verrières le Buisson, France*
[2]*LPCE/CNRS, 45071 Orléans, France*
[3]*Univ. Versailles St-Quentin, Service d'aéronomie, 91371 Verrières le Buisson, France*

tel: +33 1 64474335, fax= +33 1 69202999, email: edith.hadamcik@aerov.jussieu.fr

Abstract

This paper describes linear polarization results on low density agglomerates of different sizes. The constituent grains are in the submicron to micrometer size ranges. Some are made of bare silica or organics materials while others are silica coated by a black carbonaceous compound. The results obtained for Titan's aerosols analogues (organic materials, submicron-sized grains) are compared to in-situ light scattering results.

1 Introduction

Aggregates seem to be a major component of cosmic dust (e.g. cometary particles, Titan's aerosols). Asteroidal and cometary nuclei surfaces are layers of loosely connected grains made of fragmentary debris produced by e.g. meteoritic impacts (regolith) or by the gaseous species evaporation [1].

This work follows some previous light scattering (mainly linear polarization) studies on fluffy particles with micron and submicron-sized grains. The phase curves obtained for transparent bare silica or coated by a dark organic mantle were compared to numerical simulations [2,3]. Some other samples were mixtures of fluffy aggregates (silica and carbon black) in different ratios or size distributions [4].

Two instruments are used: PROGRA^2-vis for levitating particles studied in the visible spectral domain (543.5 nm and 632.8 nm) and PROGRA^2-surf for particles deposited on a surface in the same spectral domain. The average phase angle range is [6-150]° with a minimum value of 5° and a maximum value of 170° [5]. PROGRA^2-vis is an imaging polarimeter. The particles (micron-sized or fluffy aggregates) are lifted by a slight air-draught in a vial in the laboratory conditions. The first PROGRA^2-surf instrument uses photodiodes. The incidence angle and the emergence angle can be changed. Two configurations are preferentially used: a mirror configuration (incidence angle = half phase angle) and a normal incidence.

In the present study the constituent grains in the aggregates have submicron to micron sizes. Comparison of the results as a function of the constituent grain sizes and as a function of the agglomerates sizes will be considered for the different samples (transparent and dark).

2 Samples

The constituent grains of the aggregates are mainly spherical but some samples can be made of irregular or crystal-like grains. The silica micrometer-sized grains are bare or coated by an organic mantle (Sicastar-black®), mixtures of them differing by their composition (size and ratio) are studied. Samples made by the same constituent grains are measured: (1) in levitation for agglomerates with sizes smaller than 5 μm (LSA) and for large agglomerates of about 100 μm (LLA); (2) deposited on a surface for huge cm-sized agglomerates (HDA). These huge agglomerates were prepared by random deposition of single grains [6]. Tenth of micrometers constituent grains made in radio-frequency methane-nitrogen plasma (PAMPRE experiment, [7]) are made of organic materials (C-N-H) and called tholins. They are studied as large agglomerates (average 50 μm diameter) and the results are compared to Huygens / DISR / Titan's aerosols results [8]. Figure 1 presents some SEM images of the samples.

3 Results

3.1 Spherical micron-sized grains (Silica and Sicastar-black®)

Partly for numerical simulation purposes, spheres are used to try and better understand the internal interactions inside the agglomerates with increasing sizes. Figure 2 presents the polarization phase curves for the three kinds of agglomerates. For small agglomerates made of a few spheres only, the oscillations of the Mie scattering are present. The phase curve for the large agglomerates (LLA) of

transparent spheres presents a possible small negative branch at phase angles smaller than 20°, a polarization spike around (25-30)°, a bell-shaped branch up to 130° and an increase of polarization for large phase angles. The internal interactions between the transparent grains seem to decrease the negative branch at small phase angles, and smooth the phase curve between 40° and 130°. For HDA, the interactions between the transparent grains become important and the polarization value for phase angles between 30° and 120° is close to zero with small amplitude oscillations (Hadamcik et al., 2006).

For agglomerates (LSA) of coated spheres with a black mantle, the oscillations decrease as compared to transparent spheres and disappear for large agglomerates (LLA); the phase curve is smooth with a shape similar to the one obtained for irregular particles. Surprisingly though, for the huge deposited agglomerates (HDA) of coated spheres, the phase curve present oscillations with maxima and minima corresponding to those obtained for the small agglomerates or single spheres. The amplitude of the oscillations decreases as the phase angle increases, it may come from surface irregularities. The polarization is mainly dominated by single scattering for the coated HDA huge deposited agglomerates.

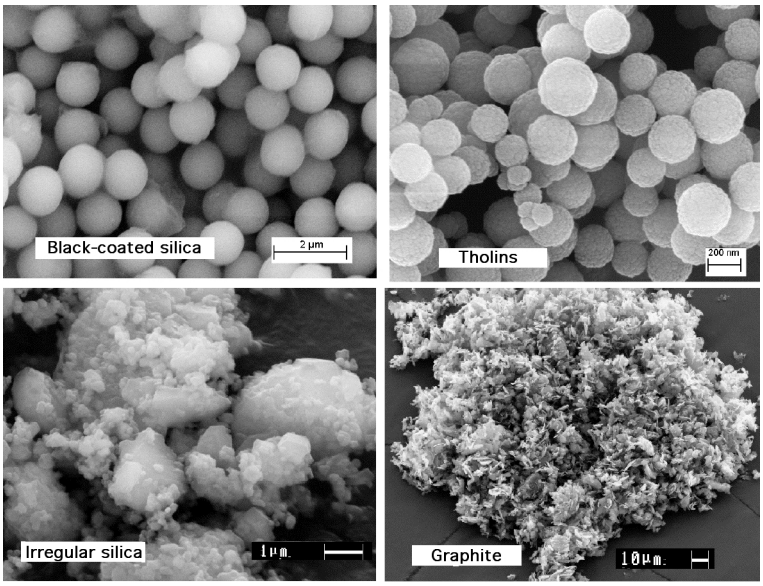

Figure 1: SEM images of some samples

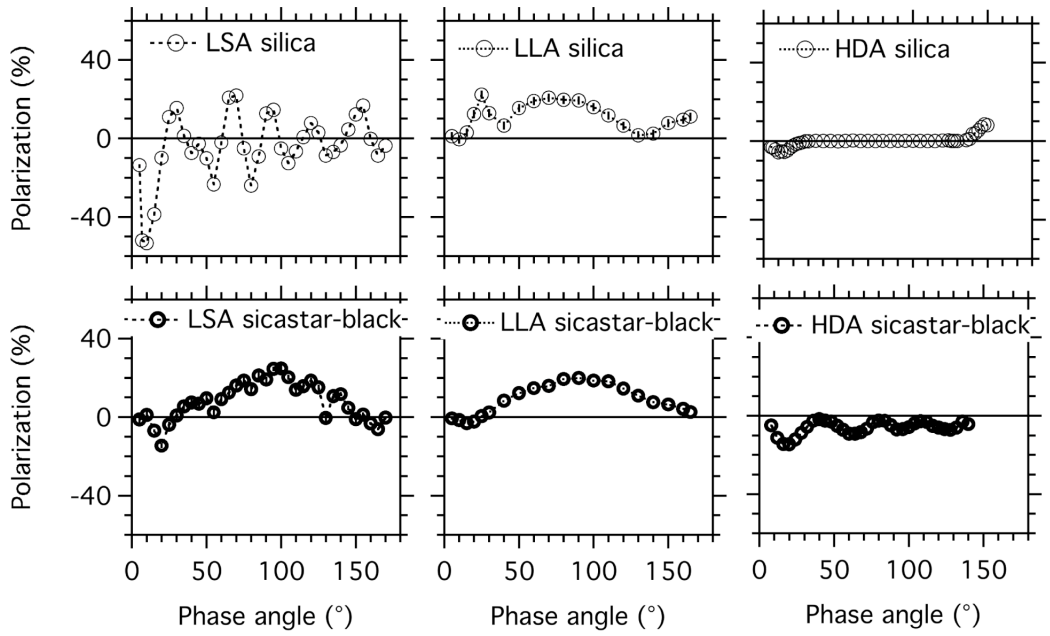

Figure 2: Silica 1.45 μm and Sicastar (core 1.31 ± 0.015 μm, carbonaceous coating 0.04 μm)

When the size of the silica core for the coated spheres decreases (1.25 ± 0.1 μm), the oscillations are more important in the case of LLA agglomerates (Fig. 3a). The phase curve obtained for a mixture of 99 % coated spheres and 1 % bare silica (about 1.5 μm spheres) present also oscillations but a difference in polarization appears clearly as compared to the coated spheres (Fig. 3a). On the same figure, the phase curve for the bare spheres is also presented.

3.2 Micron-sized irregular silica and graphite

Figure 3b presents the influence of 1% graphite in LSA of irregular silica grains. The maximum polarization value increases of about 5 %, due to the presence of graphite.

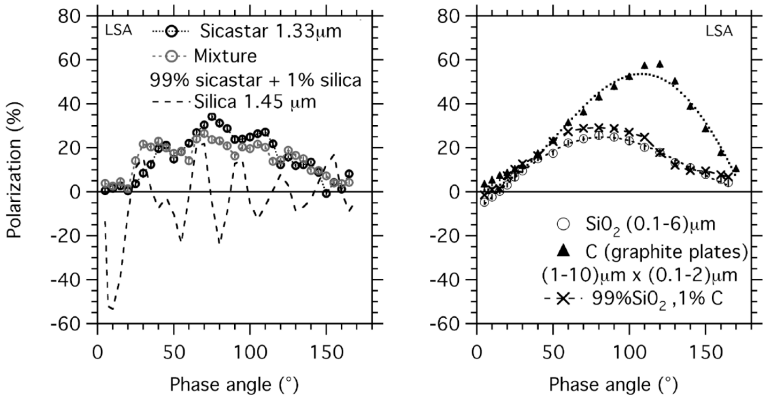

Figure 3 Levitating small aggregates and their mixture with just 1% of one of the component
(a) Spheres: bare silica and black-coated (core 1.25 ± 0.01 μm, black coating 0.04 μm)
(b) Irregular particles

3.3 Submicron-sized grains (tholins)

Analogues of Titan's aerosols are produced in the gas phase by a radio-frequency plasma technique in methane-nitrogen mixtures by the PAMPRE experiment. Depending on the experimental conditions the particles produced there from have different physical properties. One important difference between these particles is the average size of the grains in the range [0.05-1.4] μm. The other important difference is the colour of the tholins from clear brown to dark brown. The lifted particles are fluffy agglomerates with an average size of [50-100] μm. On Fig. 4, close to 90° phase angle, the maximum polarization measured on the phase curves are compared to the results of in-situ DISR/Huygens observations [8]. To obtain the smaller grains, the same conditions were used except the reduced plasma duration. The other samples are produced in different conditions. As can be seen in Fig. 4a, the fits in red and green wavelength domains respectively are mainly dependent on the size of the grains. Dark or clear materials absorb more the green light than the red light (Quirico, personal communication).

The DISR observations and laboratory measurements yield comparable results but in the experiment the size of the particles reaches hundreds of micrometers. The spectral gradient in polarization is negative for the analogues; it is similar to the observed one and can be due to a higher absorption in green than in red.

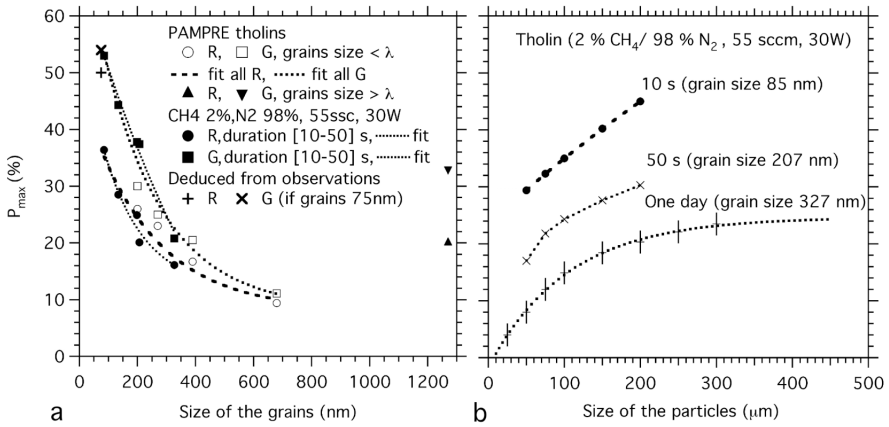

Figure 4: P_{max} vs size for tholins made in a 2% CH_4 + 98% N_2 plasma (dark brown).

(a) grains, (b) agglomerates

Figure 4b presents the variations of P_{max} as a function of the agglomerates size. P_{max} increases when the size increases up to a maximum value for each constituent grain size and stabilizes. This behaviour is similar to those observed for compact particles (size larger than the wavelength) and was observed for fluffy carbon soot [9]. Internal interaction between the grains is limited by the absorption.

4 Conclusion

These experiments point out some general parameters of the phase curves allowing to retrieve physical properties of the particles from the light they scatter. The agglomerates size influence is emphasized for different materials and size of the grains. These results are of interest for the interpretation of astronomical light scattering observations in terms of evolution of the particles in a cometary coma and in an atmosphere, also for comparison with regoliths.

Acknowledgements
The authors acknowledge Stephan Bozensztajn (UPMC Univ. Paris 06/LISE) for the SEM images, J. Blum and R. Schraepler for the huge agglomerates, G. Cernogora and C. Szopa for the tholins, A. Lebacle for the air-draught measurements.
This work was partially founded by CNES. We acknowledge CNES and ESA for the microgravity flights.

References

[1] A.C. Levasseur-Regourd, E. Hadamcik, J. Lasue, :"Interior structure and surface properties of NEOs: What should be understood to mitigate potential impacts," Adv. Space Res. **37**, 161-168 (2006).

[2] E. Hadamcik, J.-B. Renard, J. Lasue, A.C. Levasseur-Regourd, J. Blum, R. Schraepler, "Light scattering by low density agglomerates of micron-sized grains with the PROGRA^2 experiment," J. Quant. Spectrosc. Rad. Transfer **106**, 74-89 (2007).

[3] J. Lasue, A.C. Levasseur-Regourd, E. Hadamcik, J.-B. Renard, "Light scattering by coated spheres: experimental results and numerical simulations," J. Quant. Spectrosc. Radiat. Transfer **106**, 212-224 (2007).

[4] E. Hadamcik, J.-B. Renard, A.C. Levasseur-Regourd, J. Lasue, "Light scattering by fluffy particles with the PROGRA^2 experiment: Mixtures of materials," J. Quant. Spectrosc. Rad. Transfer **100**, 143-156 (2006).

[5] J.-B. Renard , J.C. Worms, T. Lemaire, E. Hadamcik, N. Huret, "Light scattering by dust particles in microgravity: polarization and brightness imaging with the new version of the PROGRA^2 instrument," Appl. Opt. **41**, 609-618 (2002).

[6] J. Blum, R. Schraepler, "Structure and mechanical properties of high-porosity macroscopic agglomerates formed by random ballistic deposition," Phys. Rev. Let. **93**, 1155031-2 (2004).

[7] C. Szopa, G. Cernogora, L. Boufendi, J.J. Correia, P. Coll, "PAMPRE: A dusty plasma experiment for Titan's tholins production and study," Planet. Space Sci. **54**, 394-404 (2006).

[8] M.G. Tomasko and 39 colleagues, "Rain, winds and haze during the Huygens probe's descent to Titan's surface," Nature **438**, 765-778 (2005).

[9] J.-B. Renard, D. Daugeron, P. Personne, G. Legros, J. Baillargeat, E. Hadamcik, J.C. Worms, "Optical properties of randomly distributed soot: improved polarimetric and intensity scattering functions," Appl. Opt. **44**, 591-596 (2005).

Size characteristics of surface plasmons and its manifestation in scattering properties of metal particles

K. Kolwas, A. Derkatchova, W. Bazhan

Institute of Physics, Polish Academy of Sciences, Al. Lotników 32/46, Warszawa, Poland

tel: +48 (22) 843 66 01 3319, fax: +48 (22) 843 09 26, e-mail: Krystyna.Kolwas@ifpan.edu.pl

Abstract

The change of the scattering properties of metal spherical particles with size is discussed in the context of plasmon (i.e. collective surface free-electron oscillations) resonances. Plasmon frequencies and plasmon damping rates of sodium, gold and silver spherical particles are studied within rigorous size dependent modeling. Predictions concerning size characteristics for dipole and quadrupole plasmons are compared with the results of light scattering experiments using sodium spherical droplets (our results) and gold and silver particles in suspension (other authors [6]). We also study the depolarizing properties of single, trapped nonspherical particle.

1 Introduction

The possibility of exciting and observing collective surface charge oscillations (plasmons) in metallic nanospheres, as well as in nanostructured metals of other shapes is a subject of interest in nanophotonics, biophotonics, sensing, biochemistry and medicine.

In many applications, size characteristics of surface plasmon excitations are crucial. It is well known, that the plasmon resonance frequency in metal spheres differs from $\omega=\omega_p\sqrt{3}$, the value known as "Mie resonance" for the ideal free-electron spherical particle that is smaller than the light wavelength. Though it is widely known, that plasmon resonance frequency is size dependent, there is only little direct data describing the size characteristics of surface plasmon resonances. Similarly, there is only little data describing higher multipolarity plasmons and their size dependent radiative and effective dumping rates (e.g.[1,2]).

In this report, we combine the formalism of the classical Mie scattering theory and the concept of collective electron oscillations, and we analyze the manner the plasmon resonances manifest in some measured quantities such as the scattering cross section or intensity of light scattered in orthogonal polarization geometries. We treat the metal sphere filled with free conduction electrons as a cavity with size-dependent eigenfrequencies ω_l, l =1,2,3,… of the optically excitable plasmons. $\omega_l(R)$ define the frequencies of the field, which can resonantly excite collective electron oscillations (plasmons) in a sphere of radius R. The size-dependent radiative losses of the excited plasmon modes are also studied. The discussion is concentrated on size characteristics of the plasmon oscillations and damping rates and their manifestations in some measured quantities in far and near field.

In our experiments on light-induced free sodium particles, we studied the smooth change of their sizes with time up to a macroscopic droplet of the order of light wavelength. The reported light scattering experiments are of two types: one involving a cloud of condensing sodium spherical droplets [3] and a second one, using single solid particles of nonspherical shape [4]. We study the manifestation of plasmon dipole and quadrupole plasmon resonances in scattered far-field intensities as well as the depolarization characteristics of oblate particle.

2 Mie scattering theory and the eigenvalue problem for the sphere

Mie scattering theory deals with the problem of the continuity of the tangent component of the total (incident + scattered) electromagnetic field while the eigenvalue problem is formulated in absence of external fields. In spite Mie scattering theory does not deal with the problem of the surface electron density oscillations (surface plasmons), although usually peaks in the absorption cross-sections or scattering spectra are interpreted as a manifestation of resonances due to the excitation of (dipole) plasmons.

We described plasmon excitations as the elementary, intrinsic property of a spherical nanostructure embedded in a dielectric medium that can manifest in the optical response to the external electromagnetic field at characteristic, size dependent resonance frequencies, usually in a complex manner.

2.1 Electromagnetic eigenmodes for the metal sphere (plasmons)

The system considered is a homogeneous, nonmagnetic metal sphere of optical properties described by the frequency dependent dielectric function $\varepsilon_{in}(\omega)$ of known analytic form, and its dielectric surrounding of properties described by ε_{out}. We look for the electromagnetic modes that can be excited at the interface. Boundary condition for the conservation of the normal component of the electric displacement field implies creation of the polarization charges at the boundary, due to the collective response of free electrons to TM polarized mode of the electromagnetic field. Conditions for the existence of TM mode is derived from the continuity relations at the spherical boundary [5,1,2]. It can be solved numerically in respect to complex values of $\omega = \Omega_l(R)$ with the sphere radius R treated as an outside parameter [1,2]. The real part of radius dependent $\Omega_l(R) = \omega'_l(R) + i\omega''_l(R)$ defines surface plasmon oscillation frequencies $\omega'_l(R)$

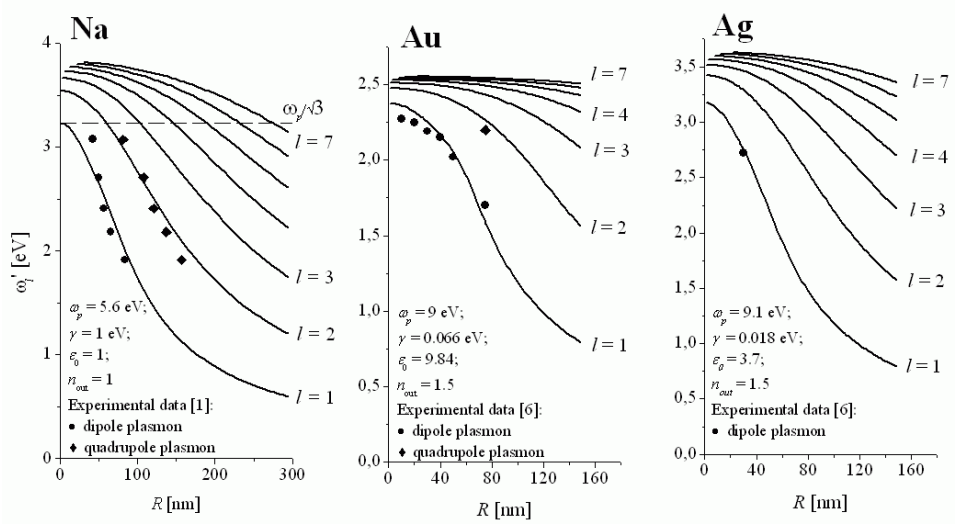

Figure 1. Multipolar plasmon resonance frequencies as a function of particle radius for sodium, gold and silver (solid lines) compared with experimental results for the dipole (l=1) and quadrupole (l=2) resonance frequencies.

for a mode l and the imaginary part $\omega''_l(R)$ defines damping frequencies (damping times) of free-electron oscillations in that mode. It should be stressed that the solutions of the dispersion relation exist only if $\omega''_l(R) \neq 0$; plasmon oscillations at spherical boundary are always damped (at least) due to radiation of free-electron oscillations. Figures 1 (solid lines) illustrate the obtained size dependence of multipolar plasmon oscillations for sodium (the best free-electron metal) as well as for gold and silver suspension of particles.

2.2 Manifestation of plasmon excitations in measured quantities (Mie scattering theory)

We discuss some consequences of resonant excitation of several multipolar (not only a dipole) plasmons that takes place for a light field of given frequency ω. In particular we show, that with increasing particle size, individual multipolar plasmon contributions with low l become better spectrally resolved, as demonstrated in Fig.1. As we believe, this effect favors visibility of more maxima in the scattering spectra of larger particles [6]. We discuss:

1. Manifestation of plasmon excitations in scattering, extinction and absorption cross sections,
2. Manifestation of plasmon excitation in light scattered under orthogonal polarization geometry.

The surface plasmon resonance contribution of given l to the measured light intensity depends (for given particle size) on the quantity, that is measured as well as on the scattering angle and polarization geometry. The measured signals are proportional to the total light intensity, resulting from the interference of both: the scattered and the incoming light fields. The fields scattered by a sphere are inevitably composed of both the TM and TE electromagnetic components of different polarity l, while the resonant plasmon contribution of given l is of TM polarization only. The TE contributions of eddy currents are also size dependent and increases monolithically with R. Therefore, the spectral position of the maximum of the measured signal does not necessarily point to the position of a plasmon resonance.

3 Scattering experiments on sodium particles

The technique of sodium particle production with light is described in more detail in [3]. It allows studies of particle aggregation dynamics from a microparticle up to a macroscopic droplet of size comparable to the light wavelength. We study elastically scattered light of linearly polarized laser light beams of several wavelengths in two orthogonal polarization geometries (Fig.2a) in two types of the experiments involving a cloud of sodium scattering spherical droplets [3] or single trapped solid particle of nonspherical shape [4].

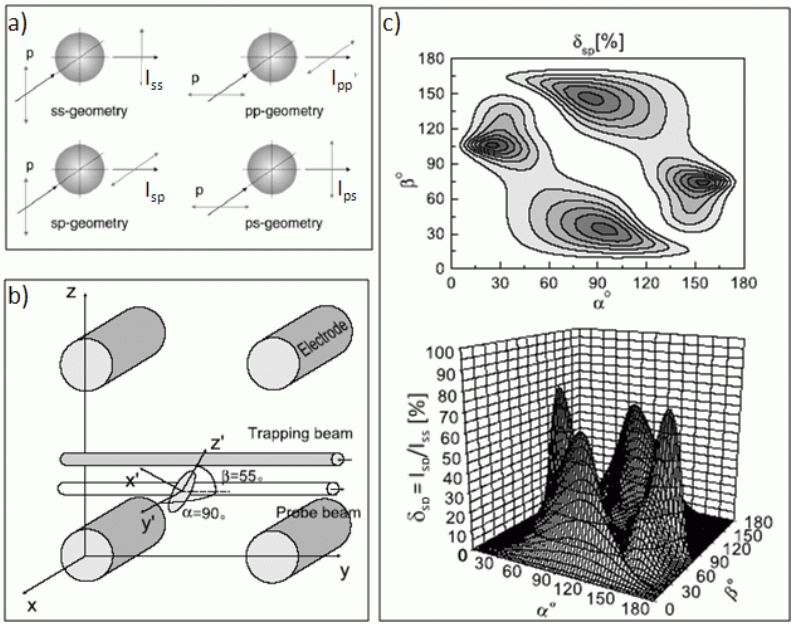

Figure 2. a) Polarization geometries of the scattering experiment with sodium particles induced by light [3,4], b) Orientation of a spheroidal particle in the electrodynamic trap, c) Three-dimensional map illustrating the dependence of the depolarization coefficient at λ_{scat}=647nm on the Euler angles α and β for a prolate spheroidal particle with refractive index 0:418 $\pm i$2:661 and effective radius 200 nm.

3.1 Identification of plasmon resonances in light scattered by light induced spherical sodium droplets

Determination of particle size and relative particle concentration dynamics is performed with use of Mie scattering theory (retardation included). From temporal dependence of particle concentration and radius R being the fit parameters, we can derive experimental intensities per unit surface, scattered by a single particle in orthogonal polarization geometries as a function of droplet radius. From these date we derive the positions of dipole and quadrupole plasmon resonances excited in particles of different radii [1]. Fig.1a (dots and diamonds) illustrates how the maxima in the intensities change with light frequency ω, and how they match the expected dipole and quadrupole plasmon resonance frequencies resulting from solving the eigenvalue problem for a sphere of given R (Fig.1a, solid line)).

3.2 Depolarization of light by single levitated sodium particle of nonspherical shape

Single sodium particles trapped in an electro-optical trap showed the unexpectedly strong depolarizing abilities [4]. To explain qualitatively the large depolarization effect, spheroidal shape of the particle was assumed and the T-matrix method (TMM) was applied to study the corresponding scattered intensities and the resulting depolarization rates. We used the TMM Fortran code [7]. The adjustable parameters of the theory are: the refractive index of the particle, the Euler angels α and β, defining the orientation of the spheroid, the size parameters a and b of the spheroid defining its semi-axis lengths. The Euler angels used in simulations are α=90^o and β=55 ^{o}, the values corresponding to the particle orientation in the trap [4]. Figs. 2c shows, that effective depolarization takes place when prolate spheroidal particle posses the effective radii smaller than the scattered light wavelength, and the larger the asphericity, the stronger the depolarization effect, as expected.

Acknowledgments

This work was partly supported by the Polish State Committee for Scientific Research (KBN), grant no 1P03B11729.

References

[1] A. Derkachova, K. Kolwas, “Size dependence of multipolar plasmon resonance frequencies and damping rates in simple metal spherical nanoparticles”. Eur. J. Phys. ST, **144**, 93 (2007)

[2] K. Kolwas, A. Derkachova, S. Demianiuk, “The smallest free-electron sphere sustaining multipolar surface plasmon oscillation,” Comp. Mat. Sci., **35**, 337 (2006).

[3] S. Demianiuk, K. Kolwas, “Dynamics of spontaneous growth of light-induced sodium droplets from the vapour phase,” J. Phys. B, **34**, 1651-71 (2001).

[4] W. Bazhan, K. Kolwas, M. Kolwas, “Depolarization of light scattered by a single sodium nanoparticle trapped in an electro-optical trap,” Opt. Com., **211**, 171-81 (2002).

[5] R. Fuchs, P. Halevi, *Basic Concepts and Formalism of Spatial Dispertion,* in *Spatial Dispertion in Solids and Plasmas (North-Holland, 1992)*

[6] C. Sönnichsen, T. Franzl, T. Wilk, G. von Plessen, J. Feldmann, “Plasmon resonances in large noble-metal clusters,” New J. Phys. **4**, 93 (2002)

[7] M.I. Mishchenko, L.D. Travis, J. Quant. Spectrosc. Radiat. Transfer **60**, 309 (2000).

Torque on Laser-driven Microrotor Fabricated by Two-photon Photo-polymerization

Vincent L. Y. Loke, Theodor Asavei, Timo A. Nieminen, Marco Barbieri,

Norman R. Heckenberg and Halina Rubinsztein-Dunlop

School of Physical Sciences, The University of Queensland,
Queensland, Australia
tel: +61 (7) 3365-3463, fax: +61 (7) 3365-1242, e-mail: loke@physics.uq.edu.au

Abstract

A trapping beam can be used to exert torque on a micron sized object via the orbital angular momentum transfer from the beam. We fabricate the micron sized objects using the two-photon photo-polymerization. By measuring the rotational frequency of the trapped object and the change in beam circular polarization we can determine the total orbital torque. We calculate the optical torque via DDA and the counteracting hydrodynamic torque via FEM simulations, and find good agreement between the predicted rotation frequency and the measured results.

1 Introduction

Optical tweezers [1], in the form of a tightly focused laser beam, can be used to trap microscopic particles with sizes ranging from 25 nm to 10 μm. Forces, due to the exchange of linear momentum between the laser beam and the trapped particle, on the order of pN can be exerted on the trapped particles with a few miiliwatts of laser power. Light can carry angular momentum and the resulting microscopic torques [2,3] on trapped object would be on the order of pN•μm due to optical angular (spin and/or orbital) momentum transfer.

It also possible to apply torque to a micro object using a beam without angular momentum; but this relies of the object's geometry (e.g. figure 1b) and how it scatters the incident beam. In this paper, we will only treat the case where the microrotor (figure 1a) is rotated by a beam with spin and orbital angular momentum.

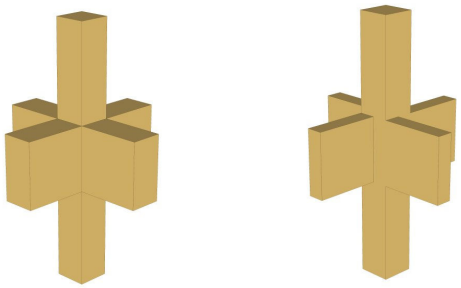

a) b)

Figure 1: a) Cross rotor b) Offset cross rotor.

2 Photopolymerization Fabrication Process

A femtosecond pulse laser is used to cure, via two photon polymerization [4], a 3D portion of resin enclosed in a cover slip (figure 2b) which sits on a computer controlled stage that translates in 3

dimensions. The input for the stage controller comprises a bitmap file that contains 2D pixel slices of required micro object; the structure is cured one layer at a time. The uncured portion is washed way with acetone.

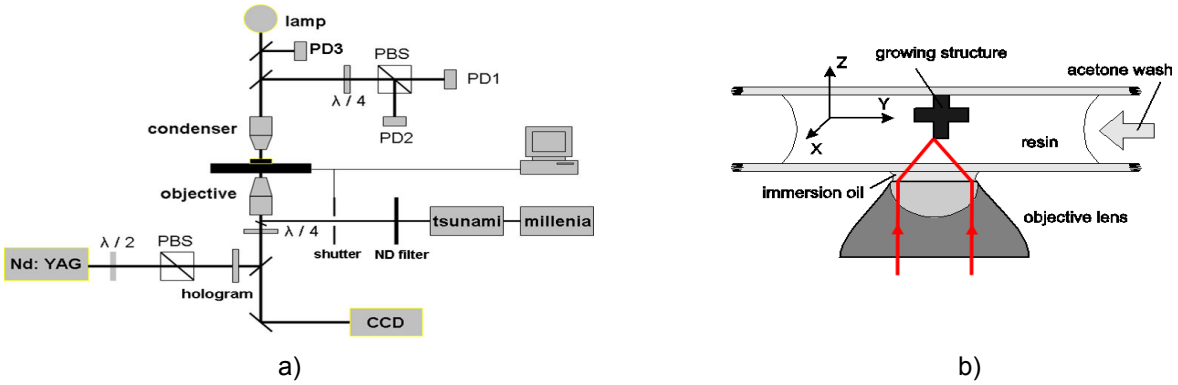

Figure 2: a) Schematic diagram of the photo-polymerization setup for fabrication of microstructures combined with an optical tweezers setup for optical trapping of the microstructures and torque measurements b) The objective lens and the cover slip enclosure containing the growing structure.

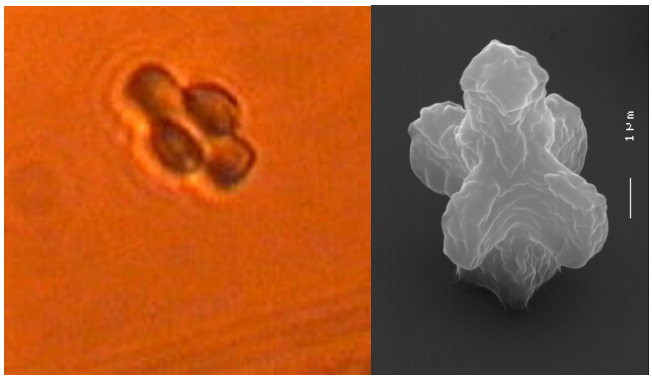

Figure 3: The finished micro rotor seen under the optical (left) and electron (right) microscopes.

2 Optical torque

The micro rotors are trapped and rotated using an Nd:YAG fiber laser in inverted optical tweezers. The incident beam is transformed from the TEM_{00} Gaussian beam to the LG02 mode using a computer generated hologram [5]. The incident angular momentum is controlled using a quarter wave plate. Orbital and spin angular momentum are transferred to the microrotor near the focus of the beam. The rotation rate is in the order of 1 Hz for 20mW at the focus.

By measuring the rotation rate and the change in polarization of the beam, the torque, in units of $\hbar$ per photon, can be calculated [6,7]

$$\tau = \Delta\sigma P / \omega \qquad (1)$$

where $\Delta\sigma$ is the change in coefficient of circular polarization, P is beam power and ω is the beam angular frequency.

3 Viscous Drag

The fluid flow field around the rotating microstructure and hence the drag torque was calculated using hydrodynamic simulations based on the Navier-Stokes equation for the case of a Newtonian fluid. We used partial differential equation solver package based on finite element numerical (FEM) analysis to solve Laplace's equations for the fluid flow velocity potential.

Typical graphical outputs of the program [8] are shown in Fig. 4 where the flow field around the rotating object is simulated as well as the shear stress field (the shear force acting per unit area) which is used to calculate the torque.

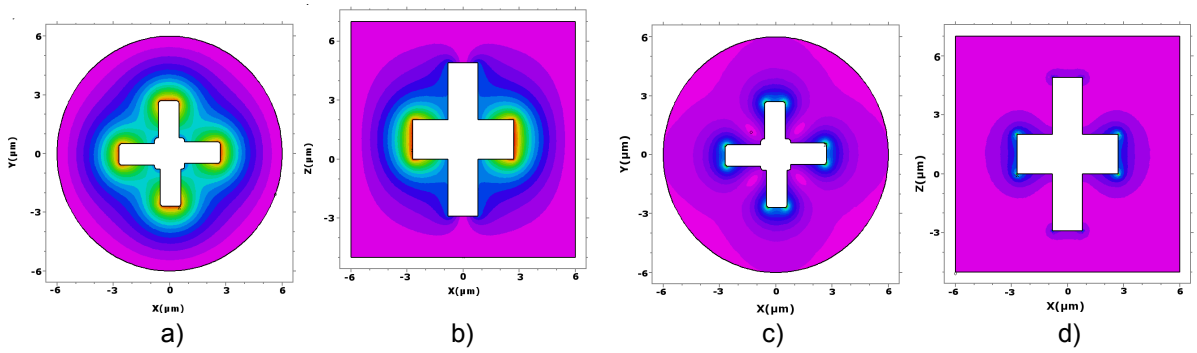

Figure 4: Typical graphical outputs of the FlexPDE program. Cross sections through XY (a) and XZ (b) planes respectively of the simulated flow field around the rotating particle. Similarly the cross sections through the same planes for the shear stress field are depicted in (c) and (d) respectively.

4 Results and Discussion

The orbital torque was found by plotting the rotation frequency (measured from the signal e.g. figure 8) as a function of the measured spin torque per photon for the three degrees of polarization. Due to the symmetry of the micro rotor, the measured signal has a clear 4-fold signature meaning that the rotation frequency of the structure is a quarter of the signal frequency. In steady rotation we can equate the total orbital torque to the drag torque but in opposing directions. The total orbital torque was $\tau_o = \Delta\sigma_o P/\omega$ = 4.8 ± 0.7 pN•μm. The simulated drag torque for the rotating structure at 2.75 Hz in linearly polarized light was τ_d = 5.4 pN•μm, which is within 10% error of the experimental value.

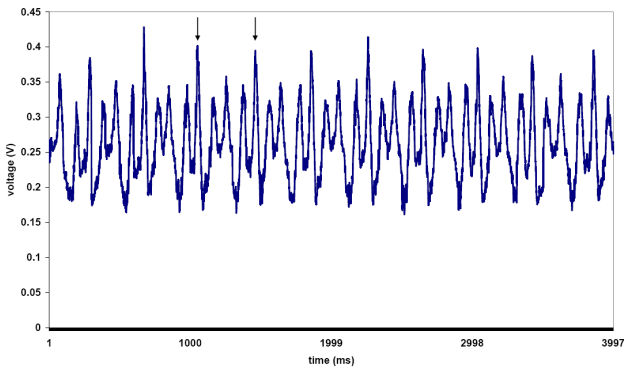

Figure 5: A typical photodiode signature measuring the rotation frequency of the trapped microstructure. The rotation period is marked by the two arrows and shows the 4-fold symmetry characteristic of the rotor.

In conclusion, we showed that the total optical torque exerted on micrometer sized objects rotating in an optical trap could be measured accurately by optical means, with an orbital angular momentum transfer ten times higher than the torque generated by the spin angular momentum. In the same time the hydrodynamic simulations of the counteracting drag torque show good agreement with the experimental results.

We also can model the microrotor and calculate the optical torque, via the DDA T-matrix method [9,10] or by calculating the intensity gradient and Poynting vector at each dipole [11].

References

[1] A. Ashkin, J. M. Dziedzic, J. E. Bjorkholm, and S. Chu, ``Observation of a Single-Beam Gradient Force Optical Trap for Dielectric Particles'', Opt. Lett. 11, 288 (1986).

[2] J. H. Poynting, Proc. R. Soc. London, Ser. A 82, 560 (1909).

[3] R. A. Beth, Phys. Rev. 50, 115 (1936).

[4] S. Maruo, O. Nakamura, and S. Kawata, Opt. Lett. 22, 132 (1997).

[5] H. He, N. R. Heckenberg, and H. Rubinsztein-Dunlop, ``Optical particle trapping with high order doughnut beams produced using high efficiency computer generated holograms'', J. Mod. Opt. 42, 217 (1995).

[6] T. A. Nieminen, N. R. Heckenberg, and H. Rubinsztein-Dunlop, ``Optical measurement of microscopic torques'', J. Mod. Opt. 48, 405 (2001).

[7] S. Parkin, G. Knoener, T. A. Nieminen, N. R. Heckenberg, H. Rubinsztein-Dunlop, ``Measurement of the total optical angular momentum transfer in optical tweezers'', Optics Express 14, 6963 (2006).

[8] FlexPDE 5.0 User Guide (PDE Solutions Inc., Antioch, CA, USA, 2005).

[9] V. L. Y. Loke, T. A. Nieminen, Theodor Asavei, N. R. Heckenberg, H. Rubinsztein-Dunlop, ``Optically driven micromachines: design and fabrication'', Proc. 10th Conference on Electromagnetic and Light Scattering, Bodrum, Turkey, G. Videen, M. Mishchenko, M. P. Mengüç, and N. Zakharova (Eds.), 2007.

[10] V. L. Y. Loke, T. A. Nieminen, N. R. Heckenberg, H. Rubinsztein-Dunlop, ``Exploiting symmetry and incorporating the T-matrix in the discrete dipole approximation (DDA) method'', Proc. DDA workshop, Institut für Werkstofftechnik, Bremen, 2007.

[11] Y. Harada, T. Asakura, ``Radiation forces on a dielectric sphere in the Rayleigh scattering regime'', Optics Communications, Vol. 124, No. 5-6, 529-541, 1996.

Characterising the Optical Properties of Aerosol Particles by Cavity Ringdown Spectroscopy

Rachael E.H. Miles, Svemir Rudić, Eyad Al-Samra, Andrew J. Orr-Ewing, and Jonathan P. Reid

University of Bristol, School of Chemistry, Cantock's Close, Bristol, BS8 1TS, UK
tel: +44 (0117) 3317417, e-mail: Rachael.Miles@bristol.ac.uk

Abstract

The study of the optical properties of aerosol, in particular their scattering and absorption as a function of particle composition, size, phase and illumination wavelength, is of considerable interest due to the influence of aerosol particles on radiative forcing and climate change. Measurements, using cavity ringdown spectroscopy, of the size parameter dependence of the extinction efficiency for benchmark systems of a spherical scatterer (polystyrene beads) and a non-spherical scatterer (dry NaCl crystals) are reported. The effect of the aerosol charging efficiency on the NaCl particle size distribution is explicitly considered. Promising agreement with theoretical values based on Mie scattering theory is observed for both benchmark systems.

1 Introduction

In 2007, the IPCC [1] reported the level of scientific understanding of the radiative forcing effect of aerosol as medium to low, with a 1.7 W m^{-2} uncertainty in the magnitude of the negative forcing due to total atmospheric aerosol loading. In order to accurately model future climate change, it is imperative that significant improvements in this knowledge base are made.

The optical properties of individual aerosol particles govern their interaction with radiation and depend on both physical and chemical characteristics, including particle size, composition, mixing state and phase. Particles can attenuate radiation through both scattering and absorption, with the sum of the two processes referred to as extinction.

The extinction efficiency, Q_{ext}, defined in Eq. (1), is the ratio of the extinction cross-section of a particle, σ_{ext}, to its geometrical cross-section, σ_{geom}.

$$Q_{ext} = \sigma_{ext}/\sigma_{geom} \quad (1)$$

This quantity relates the 'effective' cross-section a particle presents to incoming radiation with its geometrical cross-section, and can be significantly greater than, or much less than, unity [2]. A knowledge of the extinction efficiency of a particle is necessary for calculation of the single scattering albedo, ω, on which the radiative forcing effect of aerosol is modeled.

The variation in extinction efficiency with the dimensionless ratio of the particle circumference and illumination wavelength, known as the size parameter, can be modeled using Mie scattering theory [3]. The value of the extinction efficiency at a given size parameter depends on the complex refractive index of the particle, itself a function of particle composition and illumination wavelength.

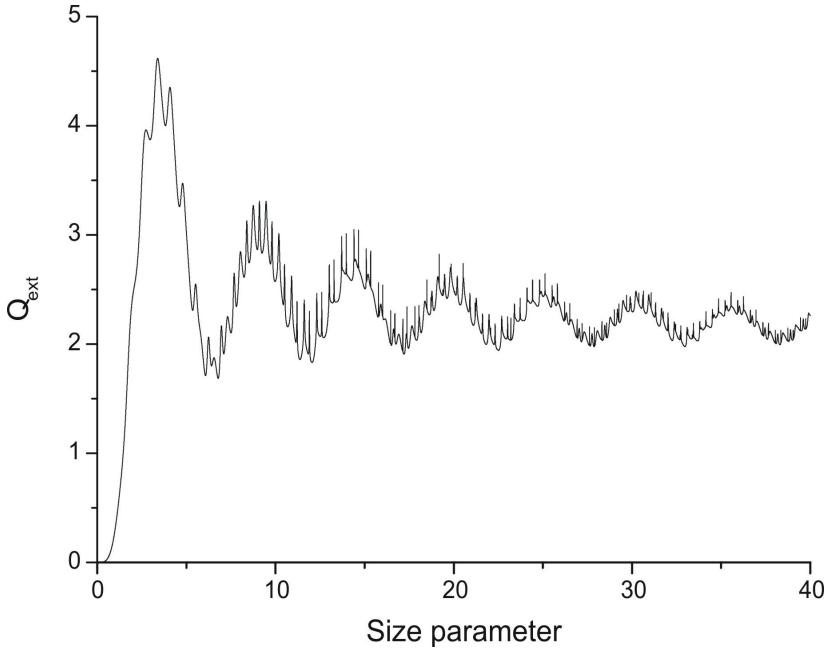

Figure 1: Extinction efficiency as a function of size parameter $x = \pi d/\lambda$, where d = particle diameter and λ = illumination wavelength, modeled for a dielectric sphere with refractive index 1.5947+1e-9i, illuminated with 560 nm radiation.

2 Experimental technique

Cavity ringdown spectroscopy is a well established technique developed by O'Keefe and Deacon [4]. Historically used for gas phase absorption measurements, its use of long sampling path lengths gives it high sensitivity and it has become an increasing popular method by which to investigate aerosol extinction [5-9].

A high finesse cavity able to support a laser light pulse (Continuum Panther OPO, lasing range 410 nm to 2.5 μm) for tens of micro seconds is formed between two highly reflective mirrors (Layertec, R = 99.98% at λ = 560nm, radius of curvature = 1m). The reflectivity of the mirrors allows the light pulse to propagate between them several thousand times, with a small amount of light transmitted out of the cavity with each mirror pass. The intensity of light within the cavity is found to decay exponentially with time, with the ringdown time, τ_o, defined as the time taken for the light intensity within the cavity to fall to 1/e of its original value.

With the introduction of aerosol into the cavity, a shorter ringdown time, τ, is observed as there are losses due to scattering and absorption of the light by aerosol, as well as mirror losses. The difference in the ringdown times between an empty cavity and one containing aerosol can be used to calculate the dimensionless loss per pass, A.

$$A = L/c(1/\tau - 1/\tau_0) \quad (2)$$

where L is the cavity length and c is the speed of light.

The loss per pass can be used to calculate the extinction efficiency of the particles in the cavity if their geometrical cross-section, number density, N, and length they occupy in the cavity, l, is known.

$$A = \sigma_{geom} Q_{ext} N l \tag{3}$$

In this work, accurate size selection of the particles is performed prior to the ringdown cavity using a differential mobility analyzer, DMA (GRIMM Vienna type). This is an electrostatic classifier capable of selecting aerosol of one mobility fraction from a polydispersed size distribution. The number density of particles leaving the cavity is recorded by a condensation particle counter, CPC (GRIMM Series 5:400). Aerosol is generated using a constant output atomizer (TSI 3076) from an aqueous solution of the aerosol medium.

This study reports on the optical properties of two benchmark aerosol systems of sub-micron, spherical, non-absorbing aerosol particles (polystyrene beads) and sub-micron, non-spherical, non-absorbing aerosol particles (dry NaCl crystals).

3 Results

The size parameter dependence of the extinction efficiency was probed experimentally by separately varying the polystyrene bead diameter and the illumination wavelength. Initial measurements were performed using 560 nm wavelength pulsed laser light, with the extinction efficiency determined for each particle diameter from the variation in aerosol extinction coefficient with particle number concentration. Experiments were repeated with pulsed laser light varying in the wavelength range 540 nm to 570 nm, demonstrating the ability of the technique to resolve fine changes in the extinction efficiency over a narrow size parameter range. Results were found to be in good agreement with theoretical predictions based on Mie scattering theory.

Preliminary investigation of light extinction by dry NaCl crystals has shown promising agreement between the extinction coefficients derived experimentally and theoretical models. The effect of the aerosol charging efficiency on the particle size distribution passed by the DMA has been explicitly considered, as has the instrument transfer function.

References

[1] *Climate Change 2007 – The Physical Science Basis*: Contribution of Working Group I to the Fourth Assessment Report of the IPCC (Cambridge University Press, Cambridge, 2007)

[2] J. H. Seinfeld and S. N. Pandis, *Atmospheric Chemistry and Physics: From Air Pollution to Climate Change* (Wiley, New York, 2006)

[3] P. W. Barber and S. C. Hill, *Light Scattering by Particles: Computational Methods: v. 1* (World Scientific Publishing Co Pte Ltd, 1989)

[4] A. O'Keefe and D. A. G. Deacon, "Cavity ring-down optical spectrometer for absorption-measurements using pulsed laser sources," Rev. Sci. Instrum. 59(12), 2544-2551, (1988).

[5] A. W. Strawa, R. Castaneda, T. Owano, D. S. Baer and B. A. Paldus, "The measurement of aerosol optical properties using continuous wave cavity ring-down techniques," J. Atm. Ocean. Technol. 20, 454-465 (2003).

[6] V. Bulatov, M. Fisher and I. Schechter, "Aerosol analysis by cavity-ring-down laser spectroscopy," Anal. Chim. Acta 466, 1-9 (2002).

[7] A. Pettersson, E. R. Lovejoy, C. A. Brock, S. S. Brown and A.R. Ravishankara, “Measurement of aerosol optical extinction at 532 nm with pulsed cavity ring down spectroscopy,” J. Aerosol Sci. 35, 995-1011 (2004).

[8] S. Rudić, R. E. H. Miles, A. J. Orr-Ewing and J. P. Reid, “Optical properties of micrometer size water droplets studied by cavity ringdown spectroscopy,” Applied Optics 46(24), 6142-6150 (2007).

[9] A. A. Riziq, M. Trainic, C. Erlick, E. Segre and Y. Rudich, “Extinction efficiencies of coated absorbing aerosols measured by cavity ring down aerosol spectrometry,” Atmos. Chem. Phys. 8(6), 1823-1833 (2008).

Laboratory measurements of scattering matrix elements of randomly oriented Mars analog palagonite particles

Olga Muñoz,[1] Hester Volten,[2], Joop Hovenier,[2] Erik Laan,[2,3]
Ted Roush,[4] and Daphne Stam,[5]

[1] *Instituto de Astrofísica de Andalucía, CSIC, Camino Bajo de Huétor 50, Granada 18008, Spain*
[2] *Astronomical Institute 'Anton Pannekoek', UvA, Kruislaan 403, 1098 SJ, Amsterdam, The Netherlands*
[3] *TNO Science & Industry, Stieltjesweg 1, 2600 AD, Delft, The Netherlands*
[4] *NASA Ames Research Center, MS 245-3, Moffet Field, CA 94035-1000, USA*
[5] *DEOS Aerospace Engineering, Technical University Delft, Kluyverweg 1, 2629 HS, Delft, The Netherlands*
tel: +34 958 121311, fax: +34 958 814530, e-mail: olga@iaa.es

Abstract

We present laboratory measurements for Martian analog particles, consisting of palagonite. We measured all elements of the scattering matrix as functions of the scattering angle from 3 to 174 degrees at a wavelength of 632.8 nm. The results may be used in studies of the Martian atmosphere.

1 Introduction

Dust from the Martian surface is regularly swept up by winds and becomes suspended in the atmosphere of Mars, sometimes covering the whole planet. These airborne dust particles scatter and absorb solar radiation and are therefore very important for the thermal structure of the thin Martian atmosphere.

The material palagonite is believed to occur on Mars with considerable abundances in the form of dust particles, both on the surface and in the atmosphere (e.g. [1,2,3]). The scattering properties of these dust particles are an important diagnostic tool containing essential information about the nature of the grains. Unfortunately, numerical techniques alone are not adequate to simulate efficiently light scattering by particles with realistic shapes and internal structures. Therefore, light scattering experiments are crucial for determining the scattering properties of real particles. We present laboratory measurements of the angular distributions of scattering properties of randomly oriented Martian analog palagonite particles. The material palagonite is believed to be a reasonable, but not perfect, analog for the abundant Martian surface and atmospheric dust particles.

2 Sample characteristics

Palagonite is a fine-grained weathering product of basaltic glass. It has a refractive index that is typical for silicate materials, namely about Re(m)=1.5 and Im(m) in the range 10^{-3} -10^{-4} [4]. The irregular shapes of the palagonite particles are illustrated in Figure 1. This Martian analog material is described more extensively by Banin et al. [5] (palagonite sample 91-16).

The measured size distributions of the palagonite particles used in this study are illustrated in Figure 2 (see [6] for the definitions of the size distributions). The effective radius and variance are, respectively, 4.5 micrometer and 7.3.

3 Experimental Method

We studied the palagonite particles with an experimental setup that can determine the full scattering matrix as a function of scattering angle θ. A detailed description of the set-up has been given by Hovenier

[7] and Hovenier et al. [8]. One advantage of measuring all 6 non-vanishing elements of the scattering matrix instead of only one or two is that systematic experimental errors can be quickly observed, identified and removed. Another advantage is that the results can be used for multiple scattering calculations with polarization included.

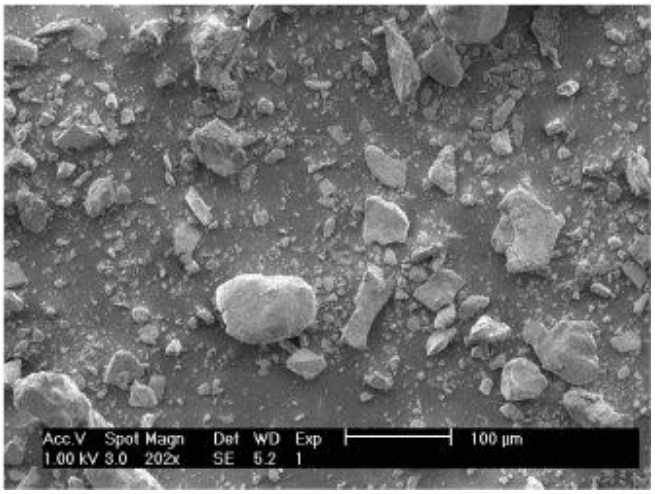

Figure 1: Scanning electron microscope (SEM) image of palagonite particles. We note that SEM images generally give a good indication of the typical shapes of the particles, but not necessarily of the sizes.

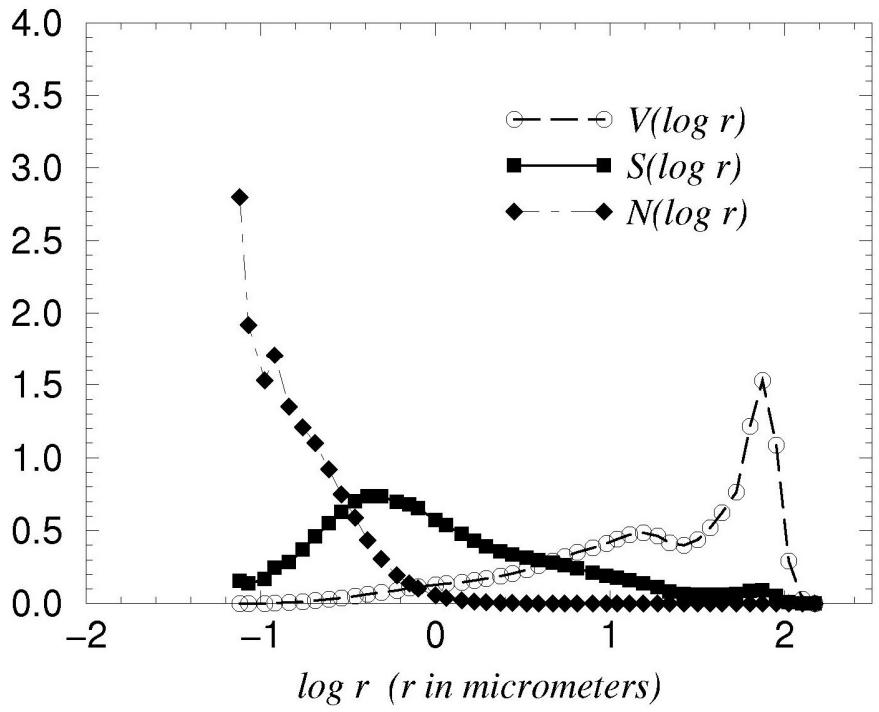

Figure 2: Measured size distributions of palagonite particles. We show V(log r), S(log r) and N(log r) i.e. the volume, projected surface and number distributions, respectively, as a function of log r where r is expressed in micrometers.

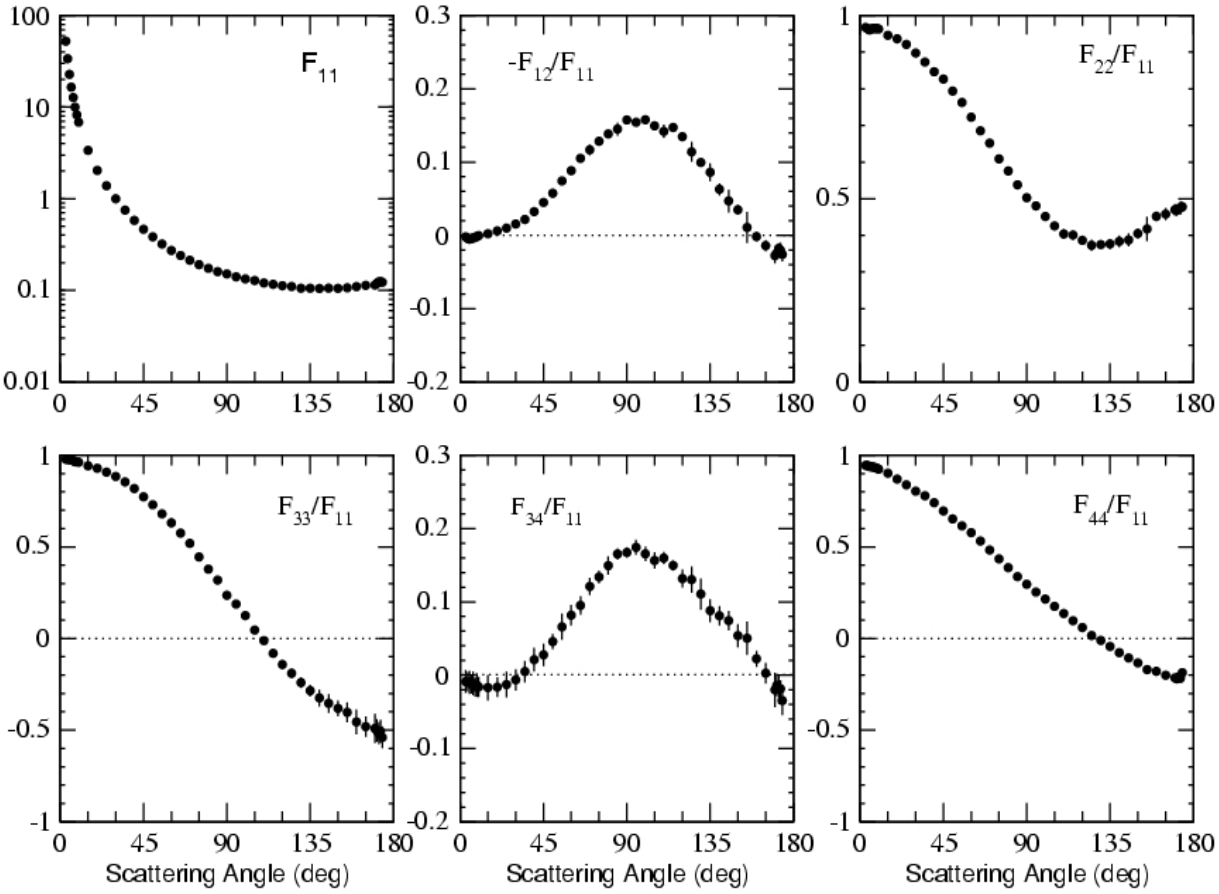

Figure 3: Measurements of the scattering matrix elements as functions of the scattering angle for randomly oriented micron-sized dust particles of Martian analog palagonite at a wavelength of 632.8nm. The scattering function is normalized to unity at 30 degrees. Experimental errors are shown by error bars or within the size of the symbols.

4 Results

Fig. 3 shows results of measurements for palagonite. We measured scattering matrix elements of the scattered light as functions of the scattering angle. The palagonite particles present a scattering behavior quite similar to that of (terrestrial) irregular mineral aerosol particles (e.g. [9,10,11]). It has a scattering function $F_{11}(\theta)$ that ranges over almost three orders of magnitude for the angles covered in the measurements, being strongly peaked towards smaller angles. It has a rather flat side-scattering and backscattering behavior. The degree of linear polarization for unpolarized incident light, $-F_{12}(\theta)/F_{11}(\theta)$, shows a characteristic bell shape, and a negative branch for large scattering angles. The scattering matrix element ratio $F_{22}(\theta)/F_{11}(\theta)$, is often used as a measure for the nonsphericity of the particles, since for spheres this function is 1 at all scattering angles. This is clearly not the case for the Martian analog particles, the deviation from 1 is large at large scattering angles, with a maximum of about 0.6. Also the matrix scattering element ratios $F_{33}(\theta)/F_{11}(\theta)$, and $F_{44}(\theta)/F_{11}(\theta)$ are not identical, as would be expected for

spheres. In contrast they show the typical behavior for nonspherical particles where the scattering matrix element ratio $F_{44}(\theta)/F_{11}(\theta)$, is greater than $F_{33}(\theta)/F_{11}(\theta)$, at large scattering angles. The shallow bell-shape found for $F_{34}(\theta)/F_{11}(\theta)$, is also commonly found for irregularly shaped silicate particles.

5 Conclusion

The results may be used in theoretical work and for studies of the Martian atmosphere. The data can be found in tabular form in the Amsterdam Light Scattering Database at www.astro.uva.nl/scatter.

References

[1] Johnson JF, PR Christensen, PG Lucey, “Dust coatings on basaltic rocks and implications for thermal infrared spectroscopy of Mars," Journal of Geophysical Research, **107**, 10.1029/2000JE001405 (2002).

[2] Christensen PR, JL Bandfield, RN Clark, KS Edgett, VE Hamilton, T Hoefen, HH Kieffer, RO Kuzmin, MD Lane, MC Malin, RV Morris, JC Pearl, R Pearson, TL Roush, SW Ruff, and MD Smith, “Detection of crystalline hematite mineralization on Mars by the Thermal Emission Spectrometer: Evidence for near-surface water," Journal of Geophysical Research, **105**, 9623-9642 (2000).

[3] Bandfield JL, “Global mineral distributions on Mars," Journal of Geophysical Research, **107**, 10.1029/2001JE001510 (2002).

[4] Clancy RT, SW Lee, GR Gladstone, WW McMillan, and T Roush, “A new model for Mars atmospheric dust based upon analysis of ultraviolet through infrared observations from Mariner 9, Viking, and Phobos," Journal of Geophysical Research, **100**, 5251-5263 (1995).

[5] Banin A, FX Han, I Kan, and A Cicelsky, “Acidic volatiles and the Mars soil”, Journal of Geophysical Research, **102**, 13341-13356 (1997).

[6] Volten H, O Muñoz, JW Hovenier, JF de Haan, W Vassen, WJ van der Zande, LBFM. Waters, “WWW scattering matrix database for small mineral particles at 441.6 nm and 632.8 nm”, Journal of Quantitative Spectroscopy and Radiative Transfer, **90**, 191-206, 2005

[7] Hovenier JW, “Measuring scattering matrices of small particles at optical wavelengths," in *Light Scattering by Non-Spherical Particles*, edited by MI Mishchenko, JW Hovenier, and LD Travis, pp. 355-365, Academic, San Diego (2000).

[8] Hovenier JW, H Volten, O Muñoz, WJ van der Zande and LBFM Waters, Laboratory studies of scattering matrices for randomly oriented particles. Potentials, problems, and perspectives, Journal Quantitative Spectroscopy and Radiative Transfer," **79-80**, 741-755, (2003).

[9] Volten H, O Muñoz, E Rol, JF de Haan, W Vassen, JW Hovenier, K Muinonen, T Nousiainen, “Scattering matrices of mineral particles at 441.6 nm and 632.8 nm," Journal of Geophysical Research, **106**, 17375-17401 (2001).

[10] Muñoz O, H Volten, JF de Haan, W Vassen, JW Hovenier, “Experimental determination of scattering matrices of olivine and Allende meteorite particles, Astronomy and Astrophysics," **360**, 777-788 (2000).

[11] Muñoz O, H Volten, JW Hovenier, B Veihelmann, WJ van der Zande, LBFM Waters, WI Rose “Scattering matrices of volcanic ash particles of Mnt. St. Helens, Redoubt, and Mount Spurr volcanoes”, Journal of Geophysical Research, **109**,10.1029/2004JD004684,2004.

Symmetry, scattering, and the optical measurement of angular momentum

Timo A. Nieminen, Theodor Asavei, Vincent L. Y. Loke, Simon J. Parkin, Norman R. Heckenberg, and Halina Rubinsztein-Dunlop

Centre for Biophotonics and Laser Science, School of Physical Sciences, The University of Queensland, Australia
tel: +61 (7) 3365-2422, fax: +61 (7) 3365-1242, e-mail: timo@physics.uq.edu.au

Abstract

A variety of different techniques have been suggested and demonstrated for the alignment or rotation of particle in optical tweezers. Although these methods are diverse, employing specially shaped particles, birefringent particles, multiple or special types of , or other methods, the fundamental principle, that optical torque results from the exchange of electromagnetic angular momentum between the trapping beam and the particle, remains the same. The symmetry of the particle and the beam play a central role in this. We discuss the role of symmetry in the application of optical torque in laser traps, and methods for the optical measurement of the angular momentum of the scattered light, and hence the optical torque exerted on the particle. All-optical measurement of the optical torque is important for the practical application of optical torque, for example for optically-driven micromachines and their use in lab-on-a-chip devices and other instruments.

1 Introduction

The application of the angular momentum of light to the alignment and rotation of microscopic particles in optical traps [1] has attracted significant attention [2]. Partly, this has been aimed at enabling enhanced manipulation with optical tweezers, but considerable effort, and corresponding progress, has been made in the direction of practical optically-driven micromachines [3]. In all of these cases, the optical torque results from the exchange of angular momentum between the trapping or driving beam and the particle or micromachine. The symmetry of the particle plays a central role in this, and is therefore of great importance for the design of particles or devices for rotation. We discuss the role of symmetry below.

An important point for practical applications of optical torque is that it is possible to measure optical angular momentum by optical means. This can allow a range of quantitative uses of optically-driven micromachines. Notably, it is simple to measure the spin angular momentum of light [4], which allows birefringent objects to be used, for example, for viscometry [5]. The optical measurement of orbital angular momentum presents a much greater challenge, and we discuss this below.

2 Electromagnetic angular momentum and symmetry

The vector spherical wavefunctions (VSWFs), used in Lorenz-Mie theory [6] and the T-matrix description on scattering by a particle [7], can be used as a basis set for the electromagnetic field:

$$\vec{E} = \sum_{n=0}^{\infty} \sum_{m=-n}^{n} a_{nm}\vec{M}_{nm} + b_{nm}\vec{N}_{nm}, \tag{1}$$

where a_{nm} and b_{nm} are the expansion coefficients of the fields, or mode amplitudes. Apart from the division into TE and TM modes, the VSWFs are described by a radial mode index n and an azimuthal mode index m. Of particular note is that the azimuthal mode index m gives the z-component of the angular momentum of the field. If we choose units such that the total power is equal to

$$P = \sum_{n=0}^{\infty} \sum_{m=-n}^{n} |a_{nm}|^2 + |b_{nm}|^2, \tag{2}$$

then the z-component of the angular momentum is equal to

$$J_Z = \sum_{n=0}^{\infty} \sum_{m=-n}^{n} m\left(|a_{nm}|^2 + |b_{nm}|^2\right), \tag{3}$$

which is equivalent to an angular momentum of $m\hbar$ per photon. In general, this will include contributions from both spin and orbital angular momentum [8]. This angular momentum results from the phase variation of $\exp(\mathrm{i}m\Phi)$.

Noting that any object, regardless of its shape, is periodic with respect to rotation about the z-axis (for an object completely devoid of symmetry, the period will be 2π), we can characterize any object in terms of the order of its discrete rotational symmetry. If we have a VSWF mode of azimuthal order m incident on a particle of p-th order rotational symmetry, the periodicity of the particle means that the scattered modes will have azimuthal orders of $m.$, $m \pm p$, $m \pm 2p$, $m \pm 3p$, and so on. This is a consequence of Floquet's theorem, and is essentially the rotational equivalent of the scattering of a plane wave into a discrete spectrum of plane waves by a grating.

This has a number of important consequences for the application of optical torque. Firstly, an axisymmetric object (in which case we have p = 0) will not change the angular momentum per photon; a torque will only result if the number of photons changes, such as through absorption. This is generally not a useful technique for optical rotation, due to the resultant heating.

Secondly, elongated objects (p = 2) will affect the polarization of light. An incident plane wave or Gaussian beam along the z-axis will have azimuthal modes m = ±1, being, in the general case, superpositions of left and right circularly polarized components. As the mode indices differ by 2, the rotational symmetry of the particle will result in coupling between them, and such objects can change the polarization of the light. In effect, the objects act as if they are birefringent (which is termed *form birefringence* [9]). However, the torque available due to form birefringence is low, typically about 0.05ħ per photon, or less [10].

Therefore, we wish to consider ways to generate higher torques. One way to do so is to make use of orbital angular momentum, which leads us to the third point, namely the effect of higher-order rotational symmetry (p > 2). Since the spin angular momentum is limited to ħ per photon, and the particle will produce scattered modes with m > 1, such a particle can act to generate orbital angular momentum.

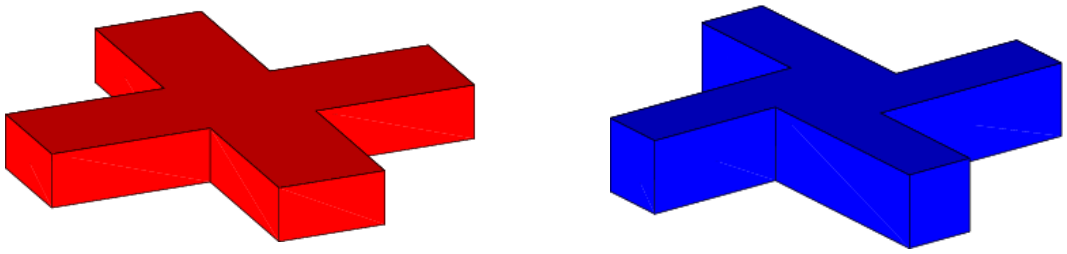

Figure 1: Structures with higher-order rotational symmetry. The left-hand object can be rotated by beams carrying orbital angular momentum, and the right-hand object, which is chiral, can be rotated by Gaussian beams.

Figure 1 shows the type of structures that can be rotated. If a symmetric structure such as the left-hand one is illuminated by a Gaussian beam or plane wave, scattering into left and right handed orbital angular momentum modes will be equal, and no torque will result. Therefore, an illuminated beam carrying orbital angular momentum is required. In this case, a Laguerre-Gauss $LG_{0,2}$ beam would be

ideal, since scattering would couple this to an $LG_{0,-2}$ beam. The direction of rotation can be controlled by varying the handedness of the incident orbital angular momentum. On the other hand, we may wish to rotate an object with a Gaussian beam. A chiral object will provide the required asymmetry between scattering into left and right handed modes [11].

3 Optical measurement of angular momentum

There is an important practical distinction between the spin and orbital angular momenta of light: the spin angular momentum can be found via measurement of the Stokes parameters [8]. However, as noted above, using orbital angular momentum can allow much higher torques. What then, is the prospect of optical measurement of orbital angular momentum? This is a problem that has received recent attention, due to the interest in using orbital angular momentum to encode information [12]. In principle, the orbital angular momentum can be measured. For example, a hologram of the type used to produce laser beams carrying orbital angular momentum as a mode analyzer [13-14]. However, it is very difficult to use methods like this in combination with optical tweezers.

Noting that the torque acting on a particle will consist of contributions from both spin and orbital angular momentum, and when the particle is freely rotating in a fluid with angular velocity Ω, the viscous drag torque must be equal in magnitude to the optical torque, we can write the total torque as

$$T_{total} = T_{spin} + T_{orbital} = D\,\Omega, \tag{4}$$

where D is an unknown constant of proportionality (the viscous drag coefficient)The spin contribution, T_{spin}, can be measured with relative ease [4]. As noted above, the orbital contribution will depend on the spatial structure of the beam, and will be largely insensitive to the polarization of the driving beam. The polarization of the beam can be readily changed, without affecting the beam otherwise, and therefore, the spin contribution can be altered, leaving the orbital component the same. Since equation (4) contains two unknown quantities, the orbital torque $T_{orbital}$ and the drag coefficient D, measurement of the spin torque and rotation rate for two different incident polarizations yields two distinct equations from which both unknown quantities can be found. While only two measurements are required, it is a sensible precaution against error to make three, for left and right circularly polarized, and linearly polarized beams. A set of such measurements is shown in figure 2 [15].

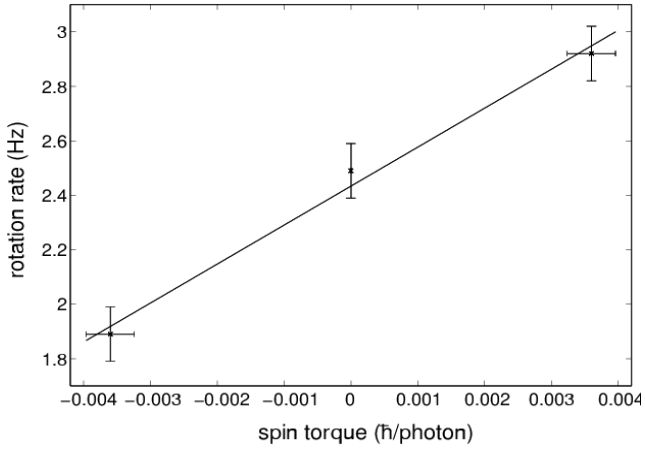

Figure 2: Measurement of orbital angular momentum by using different incident polarizations to allow the determination of the viscous drag torque [15].

4 Conclusion

We have outlined the relationship between symmetry and optical torque, and some of the implications for the design of optically-driven micromachines. In addition, we have described a method that can be used

for the measurement of the total optical torque acting on such devices, including the contribution from orbital angular momentum.

References

[1] A. Ashkin, "History of optical trapping and manipulation of small-neutral particle, atoms, and molecules," IEEE J. Selected Topics Quantum Electronics **6**, 841-856 (2000).

[2] S. Parkin, G. Knöner, W. Singer, T. A. Nieminen, N. R. Heckenberg, and H. Rubinsztein-Dunlop "Optical torque on microscopic objects," pp. 525-561 in M. W. Berns and K. O. Greulich (eds), *Laser Manipulation of Cells and Tissues* (Elsevier, Amsterdam, 2007).

[3] T. A. Nieminen, J. Higuet, G. Knöner, V. L. Y. Loke, S. Parkin, W. Singer, N. R. Heckenberg, and H. Rubinsztein-Dunlop, "Optically driven micromachines: progress and prospects," Proc. SPIE **6038**, 237-245 (2006).

[4] T. A. Nieminen, N. R. Heckenberg, and H. Rubinsztein-Dunlop, "Optical measurement of microscopic torques," J. Mod. Opt. **48**, 405-413 (2001).

[5] S. J. Parkin, G. Knöner, T. A. Nieminen, N. R. Heckenberg, and H. Rubinsztein-Dunlop, "Picoliter viscometry using optically rotated particles," Phys. Rev. E **76**, 041507 (2007).

[6] H. C. van de Hulst, *Light Scattering by Small Particles* (Wiley, New York, 1957).

[7] P. C. Waterman, "Symmetry, unitarity, and geometry in electromagnetic scattering," Phys. Rev. D **3**, 825-839 (1971).

[8] J. H. Crichton and P. L. Marston, "The measurable distinction between the spin and orbital angular momenta of electromagnetic radiation," Elec. J. Differential Eq. **Conf. 04**, 37-50 (2000).

[9] M. Born and E. Wolf, *Principles of Optics* (Cambridge University Press, Cambridge, 1997).

[10] A. I. Bishop, T. A. Nieminen, N. R. Heckenberg, and H. Rubinsztein-Dunlop, "Optical application and measurement of torque on microparticles of isotropic nonabsorbing material," Phys. Rev. A **68**, 033802 (2003).

[11] T. A. Nieminen, S. Parkin, T. Asavei, V. L. Y. Loke, N. R. Heckenberg, and H. Rubinsztein-Dunlop, "Optical vortex trapping and the dynamics of particle rotation," pp. 195-236 in D. L. Andrews (ed), *Structured Light and Its Applications: An Introduction to Phase-Structured Beams and Nanoscale Optical Forces* (Academic Press, San Diego, 2008).

[12] G. Gibson, J. Courtial, M. J. Padgett, M. Vasnetsov, V. Pas'ko, S. M. Barnett, and Sonja Franke-Arnold, "Free-space information transfer using light beams carrying orbital angular momentum," Opt. Express **12**, 5448-5456 (2004).

[13] M. V. Vasnetsov, J. P. Torres, D. V. Petrov, and L. Torner, "Observation of the orbital angular momentum spectrum of a light beam," Opt. Lett. **28**, 2285-2287 (2003).

[14] S. J. Parkin, T. A. Nieminen, N. R. Heckenberg, and H. Rubinsztein-Dunlop, "Optical measurement of torque exerted on an elongated object by a noncircular laser beam," Phys. Rev. A **70**, 023816 (2004).

[15] S. Parkin, G. Knöner, T. A. Nieminen, N. R. Heckenberg, and H. Rubinsztein-Dunlop, "Measurement of the total optical angular momentum transfer in optical tweezers," Opt. Express **14**, 6963-6970 (2006).

Particle Levitation and Laboratory Scattering

Dr. Jonathan P. Reid
School of Chemistry, University of Bristol, Bristol, BS8 1TS, UK
j.p.reid@bristol.ac.uk
http://www.chm.bris.ac.uk/~chjpr/

Light scattering has been used for many decades as a laboratory tool for characterising aerosol particles *in situ*, allowing detailed measurements of the changes in particle size, phase, shape or composition during physical or chemical transformations. When coupled with techniques for trapping and manipulating particles, the transformation can be probed over timescales of seconds to days.

Millikan was the first to demonstrate the feasibility of making measurements on single water droplets in 1909, extending this to accurate measurements of the elementary charge on an electron with less volatile oil droplets using a Millikan condenser or electrostatic balance. Over the nine decades that have followed, there have been many developments and refinements in the design of electrostatic traps. Further, in 1970 Ashkin demonstrated that single particles can be levitated optically using radiation pressure to balance the gravitational force exerted on a particle. These complementary approaches for particle trapping have been used extensively to examine mass and heat transfer in evaporating droplets, to perform measurements of light scattering and absorption from single particles, to characterise the equilibrium size and phase behaviour of multicomponent aerosol and to study the progress of chemical reactions.

More recently, it has been shown that that a single-beam gradient force optical trap (optical tweezers) can be used to manipulate arrays of up to 12 aerosol particles simultaneously. Achieving such precise control over multiple droplets provides unique opportunities to probe interparticle interactions and aerosol coagulation, and to perform comparative measurements of aerosol hygroscopicity and dynamics.

In this talk, we will review the opportunities provided by electrostatic and optical methods for isolating particles and for characterising the optical, chemical and physical properties of single and multiple particles.

INDUSTRIAL AND ENVIRONMENTAL APPLICATIONS

Extended Zero-Forward Scattering Condition by Nanoparticles

B. García-Cámara, F. González, F. Moreno and J.M. Saiz

Grupo de Óptica, Departamento de Física Aplicada, Universidad de Cantabria
Avda de los Castros s/n, 39005, Santander, (SPAIN)
tel: +34 942201868, fax: +34 942201402, e-mail: garciacb@unican.es

Abstract

Nanostructured metamaterials can open new and interesting possibilities in nanophotonics. One of these, which constitutes the heart of this research, is the possibility of governing the direccionality of the scattered light. In this work, we extend the zero-forward condition proposed by Kerker et al. [1] for dipole-like particles to finite size particles in the nanometric range. Also, the possibility of extending this condition to other directions in the scattering plane is performed.

1 Introduction

The new engineered materials or metamaterials [2] have allowed to create systems with optical properties "à la carte" including unconventional ones, as for example, the double-negative or left-handed materials [3]. This kind of materials presents interesting characteristics in electromagnetic scattering behavior that are the basis for applications like the superlensing [4], hyperlensing [5] or the electromagnetic cloaking [6]. This research topic is in continuing evolution with the objective of generalizing it to the whole electromagnetic range, in particular to the visible part of the spectrum [7]. In pursuing this idea, other important challenge is to try to reduce to the nanometric range the size of the systems with these non-natural properties. The possibility of choosing the optical properties of nanostructures could be an important step in the design of new treatments, tools or techniques for life sciences and engineering applications. Some of the pioneers in combining metamaterials and nanostructures were Kerker et al. [1]. In their work, they studied the scattered light by dipole-like particles [8] with values for ε and μ positive or negative and obtained a condition of zero light scattering in either the forward or backward directions. This was the first step in the idea of selecting the directionality of the light using nanostructures with suitable combinations of ε and μ. In this framework, Engheta [9] presented a design of nanocircuits with light using nanostructures of metamaterials. More recently [10], we studied Mie resonances in the scattered light by small particles for arbitrary values of the optical constants (ε, μ).
With this contribution, we want to go deeper in the study of governing the scattering light direction by extending the zero-forward condition proposed by Kerker et al [1] to finite size particles in the nanometric range using the Mie theory described in [10]. Also, we will present results for the generalization of the zero-forward condition to other scattering directions.

2 Zero-Forward Scattering Condition

Kerker et al. [1] made a study of the light scattering by spherical and very small particles with whatever values for the electric permittivity (ε) and magnetic permeability (μ), discovering some new features, as the zero-forward scattering condition. They used an approximate Mie theory for very small particles. To apply this approximation, two conditions must be fulfilled: i) $x<<1$ and ii) $|m|x<<1$ where m is the refractive index of the particles relative to the surrounding medium and x is the size parameter defined as $x=2\pi R/\lambda$, where R is the radius of the particle and λ is the incident wavelength [8]. Under these conditions, the particle scatters as a dipole and the first two terms of the Mie expansion (electric and magnetic dipolar

terms) can reproduce accurately the electromagnetic scattered light. The scattered intensity can be written as

$$I_1 = \frac{\lambda^2}{4\pi^2 r^2}\left|\tfrac{3}{2}(a_1\pi_1(\cos\theta)+b_1\tau_1(\cos\theta))\right|^2 \sin^2\phi$$
$$I_2 = \frac{\lambda^2}{4\pi^2 r^2}\left|\tfrac{3}{2}(a_1\tau_1(\cos\theta)+b_1\pi_1(\cos\theta))\right|^2 \sin^2\phi \quad (1)$$

In Eq. (1), I_1 and I_2 are the polarized components of the scattered intensity (with the electric field perpendicular and parallel to the scattering plane, respectively), r is the distance to the observer, a_1 and b_1 the two first Mie coefficients, π_1 and τ_1 are the angular functions described in ref [8], and θ and ϕ are the polar angles defining the scattering direction. Under the conditions pointed out previously, the a_1 and b_1 Mie coefficients can also be simplified as

$$a_1 = \frac{2i}{3}x^3\left(\frac{\varepsilon-1}{\varepsilon+2}\right)$$
$$b_1 = \frac{2i}{3}x^3\left(\frac{\mu-1}{\mu+2}\right) \quad (2)$$

Using these assumptions, Kerker et al. [1] established that if the optical constants of the particle verify the condition

$$\varepsilon = \frac{4-\mu}{2\mu+1} \quad (3)$$

the scattered intensity in the forward direction ($\theta=0^o$) is zero because $a_1=-b_1$. Also, they demonstrated that if $\varepsilon=\mu$ the scattered intensity is zero in the backward direction ($\theta=180^o$). Here, we must remark that Eq. (3) present an important exception for $\varepsilon=\mu=-2$ [11].

2 Results

The zero-forward scattering condition proposed by Kerker et al. [1] is limited to dipole-like particles ($R\rightarrow 0$). If we want to extend these results to small particles of finite size, some changes must be introduced. We consider a range of sizes $R\in[0.001\text{-}0.05]\lambda$. This would correspond to nanometric particles in the visible range. For this particle size range and arbitrary values for the optical constants, more terms of the Mie expansion are needed. In a previous paper [10], we established that for this range of sizes, the two first orders of the Mie expansion (a_1, b_1, a_2 and b_2) are sufficient. Under the condition given by Eq. (3), forward scattering is zero only for dipole-like particles ($R\rightarrow 0$); for finite size particles, forward scattering presents a minimum. In Fig.1 we show the evolution of the minimum-forward scattering, in the negative-negative range for the optical constants, as the particle size increases. For this, we used the two first orders of the Mie expansion and the complete expressions for the scattering coefficients. As can be seen, the forward minimum shifts slightly from Kerker's condition as particle size increases. These curves can be fitted to an equation equivalent to Eq. (3) with its coefficients depending on the particle size

$$\varepsilon = \frac{a(R)-b(R)\mu}{c(R)\mu+d(R)} \quad (4)$$

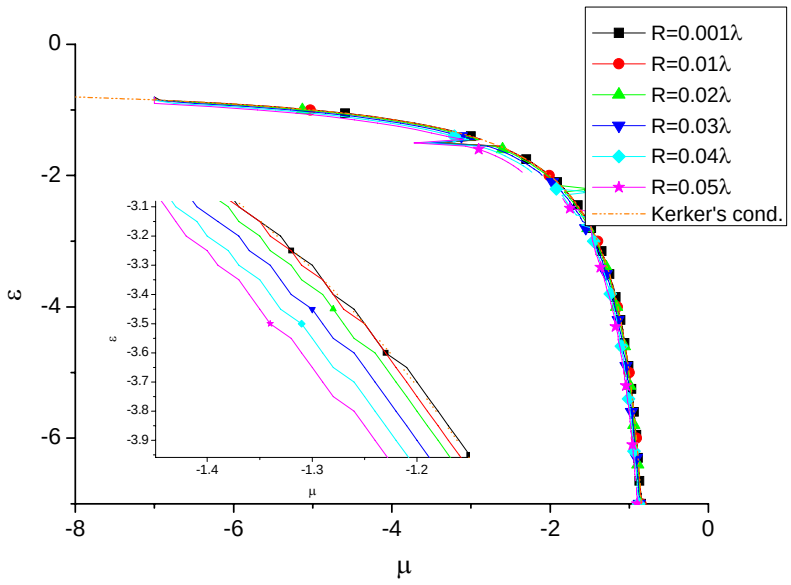

Figure 1: Pairs of ε–μ for which the forward scattering by a spherical particle is minimum for several values of the particle size. Eq. (3) ($R \rightarrow 0$) is also plotted (dashed line) for comparison. Inset: zoom of the figure for a better observation of the evolution.

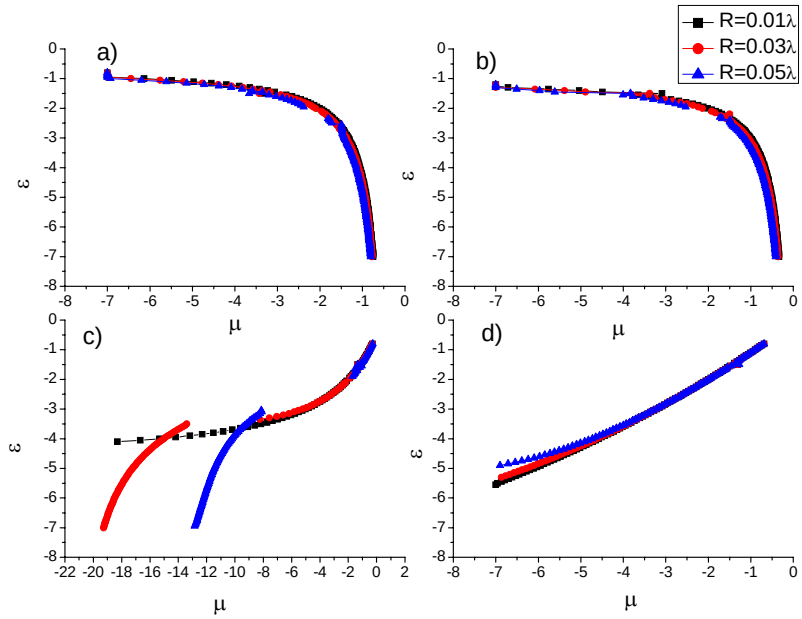

Figure 2: Pairs of ε–μ for which light scattering by a spherical particle is minimum at (a) 30º, (b) 60º, (c) 120º and (d) 150º and for three values of the particle size.

This study can be extended to other scattering angles. In particular, we have searched for the minimum in the scattered light intensity at other scattering angles different from either 0º or 180º. In Fig. 2, we plot the pairs of the optical constants (in the negative-negative range) that produce a minimum in the scattering directions: (a) *30º*, (b) *60º*, (c) *120º* and (d) *150º*.

Acknowledgments

This research was carried out with the financial support of the Ministry of Education of Spain under the project FIS2007-60158. Braulio García-Cámara wishes to thank to the University of Cantabria for his Ph.D. grant.

References

[1] M. Kerker, D.-S. Wang and C.L. Giles, “Electromagnetic scattering by magnetic spheres”, J. Opt. Soc. Am. **73**, 765-767 (1983)

[2] J.B. Pendry, A.J. Holden, D. J. Robbins and W.J. Stewart, “Magnetics from conductors and enhanced nonlinear phenomena”, IEEE Trans. Microwave Theory Tech **47**, 2075-2084 (1999)

[3] V. Shalaev, “Optical negative-index metamaterial”, Nat. Photonics **1**, 41-48 (2007)

[4] J. B. Pendry, “Negative refraction makes a perfect lens”, Phys. Rev. Lett. **85**, 3966-3969 (2000)

[5] D. Shuring and D.R. Smith, “Sub-diffraction imaging with compensating bilayers”, New J. Phys. **7**, 162-176 (2005)

[6] J.B. Pendry, D. Schuring and D.R. Smith, “Controlling electromagnetic fields”, Science **312**, 1780-1782 (2006)

[7] C. M. Soukoulis, S. Linden and M.Wegener, “Negative refractive index at optical wavelength”, Science **315,** 47-49 (2007)

[8] C. F. Bohren and D. R. Huffman, *Absorption and Scattering of Light by Small Particles* (Wiley, New York, 1983).

[9] N. Engheta, “Circuits with Light at Nanoscales: Optical Nanocircuits Inspired by Metamaterials”, Science **317**, 1698-1702 (2007)

[10] B. García-Cámara, F. Moreno, F. González, J.M. Saiz and G. Videen, “Light Scattering Resonances by Small Particles with Electric and Magnetic Properties”, J. Opt. Soc. Am. A **25**, 327-334 (2008)

[11] B. García-Cámara, F. González, F. Moreno and J.M. Saiz, “Exception for the Zero Forward Scattering Theory”, submitted to Opt. Lett.

Industrial and environmental applications of light scattering

Miroslaw Jonasz

MJC Optical Technology, 217 Cadillac Street, Beaconsfield, QC, Canada
Tel.: +1 514 695 4132, Fax: +1 514 695 3315, E-mail: m.jonasz@mjcopticaltech.com

Abstract

Light scattering has industrial applications that range from diagnostics and process control to the defining of products' properties. With the emergence of environmental consciousness, light scattering has also found important applications in environmental research.

1 Introduction

It can be argued that light scattering is one of the most ubiquitous physical processes. In practical terms, light scattering participates in the process of the very seeing of our environment. Although light scattering involves matter in any form, the scope of this review will be limited to matter in a form of “particles”.

2 Light scattering as a diagnostic and monitoring tool

Light scattering by particles of a dispersion converts each particle to a miniature light source which can be detected against a dark background. This is the basis of many light scattering-based techniques of determining the content and properties of a dispersion-like product or of the environment. People have been using light scattering in this way to visually evaluate the particle content of a medium for millenia.

The scattering of light reduces the apparent contrast of an object observed across a layer of a turbid medium. Such a contrast decays exponentially with the layer thickness at a rate that depends on the medium's particle load. At certain distance, the object vanishes, swamped by light backscattered by the medium. This is the basis of the Secchi disk technique [1] widely used in water quality testing due to its simplicity and low cost. The complex mechanism of the object disappearance [2] as well as the reliance on natural lighting and the judgment of an observer, cause significant errors in the medium's particle load determined this way. However, removing such factors by “objectively” measuring light scattering *in-situ* offers a surprisingly minor improvement because the scattering of light by particles in a turbid medium depends in a complex manner on their size distribution, compositions, shapes, and structures, generally in that order of significance. Hence, accurate relationship between the particulate load of a medium and light scattering is reduced to a medium-specific correlation between the scattering properties of the medium and its particulate load.

The complex dependence of light scattering on the properties of particles is the basis of much more specific diagnostic techniques. Let us consider, for example, the particle “size”, a fuzzy property given that many particles have irregular shapes. In respect to light scattering this property falls between the diameter of a volume-equivalent sphere (particles small relative to the wavelength of light) and a diameter of a projection-area-equivalent circle (the large particles). Very accurate light-scattering-based techniques permit the determination of the diameter and refractive index of single dielectric sphere from angular [3] and spectral [4] light scattering. However, the complexity of instrumentation and problems with the interpretation of results for nonspherical particles have limited the reach of these techniques. A simpler technique of laser diffractometry [5], which determines the particle size distribution for a dispersion from the angular pattern of the forward-scattered light has instead gained a considerable popularity. This technique relies on the particle size being the dominant factor that affects such light scattering pattern.

Laser diffractometry yields relatively repeatable results, due to averaging over many particles which results in a high signal-to-noise ratio, and (in principle) requires no calibration. By considering the particle size alone, the angular scattering pattern can be expressed as an integral of the particle size distribution of a dispersion weighed by a particle size-dependent kernel. Integral equations of this type (Fredholm equations) are common in applied physics. Hence, intense effort has been devoted to develop solution algorithms that minimize sensitivity to measurement errors [6]. The particle size- and angle-dependent kernel of that equation is generally taken to be the diffraction pattern of a disk, although a kernel defined with the Mie theory [7] improves the accuracy of the particle size distribution retrieval for dispersions of spherical particles with a known refractive index. Particle nonsphericity may cause artifacts which can be minimized by using an empirical kernel [8].

In contrast to laser diffractometry, the single-particle light scattering-based techniques examine one particle at a time. Although this makes the measurement of light scattering more difficult due to a low signal, it also offers an unprecedented level of detail in particle characterization [9]. These techniques have had most success in the characterization of spheres [10], but they have also found profound pragmatic applications for nonspherical particles. Indeed, a multi-angle light scattering measurement for each particle generates a point in a multi-dimensional space. Points representing like-particles congregate in certain regions of that space which can be outlined with clustering algorithms. Each such region represent the presence and quantity of particles of a specific type.

Advanced single-particle techniques require complex and hardly portable instruments. This stems partly from a need to consistently “fly” particles along the same part of the light beam, which is presently achieved by sophisticated sheath-fluid flow systems. Recent advances in sheatless flow-cell design [11] along with the miniaturization of the sensing cell open the possibility of making a truly portable and inexpensive single-particle instruments.

3 Light scattering as a means of defining an industrial product

Paints, coatings, and stained glass provide the quintessential examples of how light scattering is used to define properties of an industrial product. It is the intense and multiple light scattering [12] which hides the base surface under merely a several μm thick paint layer [13]. Typically, particles of titanium oxide (TiO_2) are used as scatterers, due to its high refractive index (n = ~2.7, [14]). The optimum size of TiO_2 particles in a polymer binder (n = 1.5) is ~0.2 μm, with a relatively narrow particle size distribution. Aggregation considerably reduces the efficiency of these particle as scatterers in the visible [15] and is minimized by the use of surfactants. Paints find important applications in reducing the solar heat load [16] as well as in solar energy conversion, either as black [13] and non-black coatings [17] in solar heating devices, or as a superior back-surface reflector for thin-film solar cells [18].

Particle-based chemical and physical sensors are an important emerging application of light scattering which is based on either whispering-gallery modes (WGMs) of a dielectric microsphere [19] or on the surface plasmon resonance (SPR) in noble metal nanoparticles [20]. A dielectric microsphere is an extremely good resonant cavity for visible light ($Q \sim 10^9$). This allows one to measure very small changes either in its refractive index relative to that of the surrounding medium or its size. Removal of a single molecular layer was detected [21], and the detectability of single large protein molecules with such sensors was predicted [22]. The small size of the microsphere makes it an excellent “point” sensor [23] of the relative refractive index (and factors that inflence it).

Effects of the SPR in metallic nanoparticles have been known to humanity for millenia, as proven by the existence of artifacts such as the Roman Lycurgus cup made of dichroic glass, and medieval stained glass, produced with noble metal colloids. These effects even gave an impetus to the development of the Mie theory [7]. Caused by the collective oscillation of free electrons excited by light, the SPR significantly increases the absorption/scattering by a metal nanoparticle in a relatively narrow wavelength range, albeit much larger than those of WGMs. Location of that range and its width depend on the relative particle size, the particle structure, and morphology [20]. Much research in this field has been supported by the Mie

theory [7] or its extension for coated spheres [24], although the effects of particle-shape and complex structure have to be evaluated by other methods [25].

The SPR in noble metal nanoparticles has lead to their use as markers in medical diagnostics [26] because the optical cross sections of such particles are orders of magnitude greater than those of conventional, fluorescent-dye molecular markers. The noble-metal nanoparticle markers are also much more stable, small enough to enter cells, and are generally found to be non-toxic [27] albeit this issue, along with mechanisms of removal of these particles from cells is intensely researched. Another major application, in medical therapy, is due to the high absorption cross sections of metal nanoparticles. Hence, these nanoparticles can be used to destroy targeted cells either by “slow” heating [26] or by explosions induced with ultrashort laser pulses [28].

4 Conclusion

Light scattering continues to find important use in many aspects of industrial activities of humanity.

Acknowledgments

The author wishes to thank Paul H. Kaye for inspiring this review.

References

[1] J. E. Tyler, "The Secchi disc," Limnol. Oceanogr. **13**, 1-6 (1968).

[2] W. Hou, Z. Lee, and A. D. Weidemann, "Why does the Secchi disk disappear? An imaging perspective," Opt. Express **15**, 2791-2802 (2007).

[3] V. V. Berdnik and V. A. Loiko, "Particle sizing by multiangle light-scattering data using the high-order neural networks," J. Quantit. Spectrosc. Radiat. Transfer **100**, 55-63 (2006).

[4] P. Chýlek, V.Ramaswamy, A. Ashkin, and J. M. Dziedzic, "Simultaneous determination of refractive index and size of spherical dielectric particles from light scattering data. Appl. Opt. **22**, 2302-2307 (1983).

[5] D. L. Black, M. Q. McQuay, and M. P. Bonin, "Laser-based techniques for particle size measurement: A review of sizing methods and their industrial applications," Prog. Energy Combust. Sci. **22**, 267-306 (1996).

[6] S. Twomey, "*Introduction to the Mathematics of Inversion in Remote Sensing and Indirect Measurements* (Elsevier, Amsterdam, 1977, 237 pp).

[7] G. Mie, "Beitrage zur Optik trüber Medien speziell kolloidaler Metallösungen," Ann. Phys. **25**, 377-445 (1908).

[8] Y. C. Agrawal, A. Whitmire, O. A. Mikkelsen, and H. C. Pottsmith, "Light scattering by random shaped particles and consequences on measuring suspended sediments by laser diffraction," J. Geophys. Res., **113**, C04023, 11 pp.

[9] P. H. Kaye, N. A. Eyles, I. K. Ludlow, and J. M. Clark, "An instrument for the classification of airborne particles on the basis of size, shape and count frequency," Atmos. Environm. **25A**, 645-654 (1991).

[10] D. H. Tycko, M. H. Metz, E. A. Epstein, and A. Grinbaum, "Flow-cytometric light scattering measurements of red blood cell volume and hemoglobin concentration," Appl. Opt. **24**, 1355-1365 (1985).

[11] G. K. Goddard, C. K. Sanders, J. C. Martin, G. Kaduchak, and S. W. Graves, "Analytical performance of an ultrasonic particle focusing flow cytometer," Analyt. Chem. **79**, 8740-8746 (1985).

[12] P. Kubelka and F. Munk, "Ein Beitrag zur Optik der Farbanstriche," Z. Tech. Phys. **12**, 593-601 (1931).

[13] M. Klanjsek Gunde and Z. Crnjak Orel, "Absorption and scattering of light by pigment particles in solar-absorbing paints," Appl. Opt. **39**, 622-628 (2000).

[14] J. Rams, A. Tejeda, and J. M. Cabrera, "Refractive indices of rutile as a function of temperature and wavelength," J. Appl. Phys. **82**, 994-997 (1997).

[15] J.-C. Auger, R. G. Barrera, and B. Stout, "Scattering efficiency of clusters composed by aggregated spheres," J. Quantit. Spectrosc. Rad. Transfer **79-80**, 521-531 (2008).

[16] A. K. Bendiganavale and V. C. Malshe, "Infrared reflective inorganic pigments," Rec. Pat. Chem. Eng. **1**, 67-79 (2008).

[17] Z. Crnjak Orel, M. Klanjsek Gunde, and M. G. Hutchins, "Spectrally selective solar absorbers in different non-black colours," Sol. Energy Mat. Sol. Cells **85**, 41-50 (2005).

[18] O. Berger, D. Inns, A. G. Aberle, "Commercial white paint as back surface reflector for thin-film solar cells," Solar Energy Mat. Solar Cells **91**, 1215-1221 (2007).

[19] V. S. Ilchenko and A. B. Matsko, "Optical resonators with whispering-gallery modes – Part II: Applications," IEEE J. Sel. Top. Quantum Electron. **12**, 15-32 (2006).

[20] K.-S. Lee and M. A. El-Sayed, "Gold and silver nanoparticles in sensing and imaging: Sensitivity of plasmon response to size, shape, and metal composition," J. Phys. Chem. B **110**, 19220-19225, (2006).

[21] I. M. White, N. M. Hanumegowda, and X. Fan, "Subfemtomole detection of small molecules with microsphere sensors," Opt. Lett. **30**, 3189-3191 (2005).

[22] S. Arnold, M. Khoshsima, I. Teraoka, S. Holler, F. Vollmer, "Shift of whispering gallery modes in microspheres by protein adsorption", Opt. Lett. **28**, 272–274 (2003).

[23] P. Zijlstra, K. van der Molen, and A. P. Mosk, "Spatial refractive index sensor using whispering gallery modes in an optically trapped microsphere," Appl. Phys. Lett. **90**, 161101 (2007).

[24] A. L. Aden and M. Kerker, "Scattering of electromagnetic waves from two concentric spheres," J. Appl. Phys. **22,** 1242-1246 (1951).

[25] C. Noguez, "Surface plasmons on metal nanoparticles: The influence of shape and physical environment," J. Phys. Chem. C **111**, 3806-3819 (2007).

[26] C. Loo, A. Lin, L. Hirsch, M.-H. Lee, J. Barton, N.Halas, J. West, R. Drezek, "Nanoshell-enabled photonics-based imaging and therapy of cancer," Technol. Cancer Res. Treatm. **3**, 33-40 (2004).

[27] R. Shukla, V. Bansal, M. Chaudhary, A. Basu, R. R. Bhonde, and M. Sastry, "Biocompatibility of gold nanoparticles and their endocytotic fate inside the cellular compartment: a microscopic overview," Langmuir **21**, 10644-10654 (2005).

[28] R. R. Letfullin, C. Joenathan, T. F. George, V. P. Zharov, "Laser-induced explosion of gold nanoparticles: potential role for nanophotothermolysis of cancer," Nanomed. (Future Med. Ltd.) **1**, 473-480 (2006).

Depolarized light scattering spectra from gold nanorods and nanosphere clusters

Nikolai Khlebtsov,[1,2] Boris Khlebtsov,[1] Vitaly Khanadeev,[2]
Andrei Mel'nikov,[1] and Timofey Pylaev[1]

[1] *Institute of Biochemistry and Physiology of Plants and Microorganisms, Russian Academy of Sciences, 13 Prospekt Entuziastov, Saratov 410049, Russia*
[2] *Saratov State University, Russia*
tel: +7 (8452) 970-403, fax: +7 (8452) 970-383, e-mail: khlebtsov@ibppm.sgu.ru

Abstract

We report on depolarized light scattering spectra (DLSS) from suspensions of gold nanorods and gold nanosphere clusters in terms of the depolarized ratio Ivh/Ivv measured from 400 to 900 nm. For separated nanorod samples, we observed unprecedented DLSS, with a resonance maximum of about 0.5 located between the short- and the long-wavelength extinction peak. These unusual depolarization ratios are between 1/3 and 3/4 theoretical limits established for small dielectric and plasmon-resonant needles, respectively. The measured extinction and depolarization spectra are in excellent agreement with T-matrix simulations based on TEM data. For silver nanorods, our T-matrix simulations predict multiple-peak DLSS and unique depolarization ratios exceeding the upper dipolar limit (3/4) because of multipole depolarization contributions. Finally, we present the experimental and simulated data for DLSS of 15-nm colloidal gold clusters obtained by addition of pyridine to the initial single-particle sols.

1 Introduction

The anisotropic optical properties of metal nanoparticles and nanostructures are of great interest for potential biological or chemical sensing applications [1] and for tracking of individual receptors within single living cells [2]. If colloidal nonspherical particles are preferentially oriented by an external field, they exhibit anisotropic optical properties [3]. Moreover, even for randomly oriented particles, there remain some principal differences between light scattering from nanospheres and that from nanorods or clusters. When randomly oriented nonspherical particles are illuminated by linearly polarized light, the cross-polarized scattering intensity I_{vh} occurs [4], whereas for spheres, this quantity equals zero. It is convenient to characterize the depolarized light scattering by the ratio $\Delta_{vh} = I_{vh} / I_{vv}$, where the subscripts "v" and "h" stand for vertical and horizontal polarization with respect to the scattering plane. According to the theory of light scattering by small particles [4], the maximal value of the depolarization ratio Δ_{vh} cannot exceed 1/3 and 1/8 for dielectric rods and disks with positive values of the real and imaginary parts of dielectric permeability. However, it has recently been shown [5] that the dielectric limit of 1/3 does not hold for plasmon-resonant nanorods whose theoretical depolarization limit equals 3/4.

As far as we are aware, the only experimental verification of the inequality $\Delta_{vh} > 1/3$ has been provided for a single He–Ne laser wavelength [5], and no experimental observation of depolarized light scattering spectra with resonance values $\Delta_{vh} > 1/3$ has ever been reported. Besides, there have been no accurate comparisons of measured and exactly calculated depolarization spectra from gold nanorods (GNRs) and nanosphere clusters (NCs). The primary goal of this work was to fill these gaps.

2 Experimental section

Figure 1 shows a home-made setup for DLSS measurements in the analog or the photon-counting mode. The extinction spectra were recorded with Specord BS-250 and S-300 spectrophotometers (Analytik Jena, Germany). TEM characterization was made with a Libra-120 microscope (Carl Zeiss, Germany).

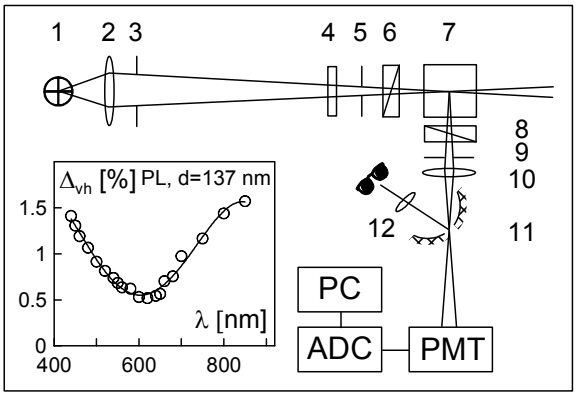

Figure 1: Experimental setup. The numbers represent a halogen lamp (*1*), achromatic lenses (*2*, *10, 12)*, iris diaphragms (*3, 5, 9*), interference filters (*4*), a four-sided 1-cm rectangular non-fluorescent-quartz cuvette (*7*), polarization prisms (*6*, *8*), and a spherical mirror with a pin hole diaphragm (*11*) (0.1, 0.5, or 1.5 mm in diameter). The symbols represent the photomultiplier PMT, the analog-to-digital converter ADC (L-Card Ltd., Russia), and the personal computer PC. Mirror (*11*) and lens (*12*) allow for visual control of scattering volume imaging with respect to the pin hole. The inset shows depolarization spectra measured for a 137-nm polystyrene latex (PL) suspension. This plot represents the upper estimate of the sum of the instrumental and latex depolarization ratios.

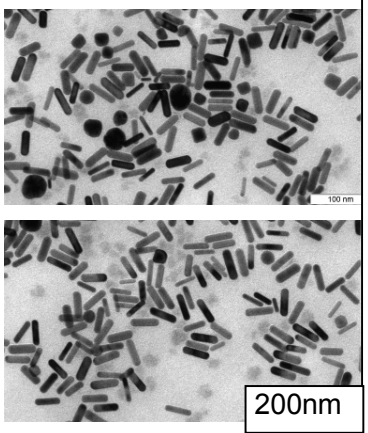

Figure 2: TEM images of GNRs before (top) and after (bottom) separation in a stepwise glycerol gradient.

Au nanorods NR-670, NR-740, and NR-780 (designated according to the longitudinal resonance wavelengths) were synthesized by the seed-mediated growth method, with minor modifications to the concentrations of the reagents [6]. Colloidal gold (CG; 15 nm) particles were fabricated by citrate reduction of $HAuCl_4$. Aggregation of CG sols was initiated by addition of pyridine to the initial CG sol (20 μL of 10 mM pyridine solution + 2 mL of 0.29 mM CG sol). To stop the aggregation, 200 μL of 0.1 mM sodium dodecyl sulfate (SDS) was added to the CG + pyridine mixture.

The main difficulty in observing high Δ_{vh} is related to particle heterogeneity. That is why all previously reported depolarization ratios were less than 0.3–0.35 for GNRs [5] and less than 0.1–0.25 for silver colloids [7]. Indeed, the depolarization resonance band is shifted to the short wavelengths, where the scattering intensity from rods is strongly decreased. On the other hand, byproduct particles may give an appreciable contribution to copolarized, but not cross-polarized, intensity, leading to a significant decrease in the measured depolarization ratio. Here, we used a separation procedure [8] to improve the quality of as-prepared samples (Fig. 2).

3 Results and discussion

The extinction spectra of the NR-780 sample before and after separation (Fig. 3a) differ in both the major resonance location (800 nm before and 780 nm after separation) and the resonance peak A_2 / A_1 ratio, which increases from 3.5 to 4.4. The depolarization spectrum in Fig. 3b demonstrates an evident resonance band between 550–750 nm with an unprecedented maximal depolarization ratio of about 50%. The error bars represent standard deviations for three independent experimental runs, including a photon-counting run for the smallest pin-hole diaphragm (0.1 mm). Thus, Fig. 3b can be considered to be the first strong evidence for depolarized resonance light scattering with extra-high ratios exceeding the dielectric-needle limit [4] of 1/3. Additional information about the NR-670 and NR-740 samples, best-fitting procedures, comparison with TEM, and discussion of DLSS physics can be found elsewhere [6].

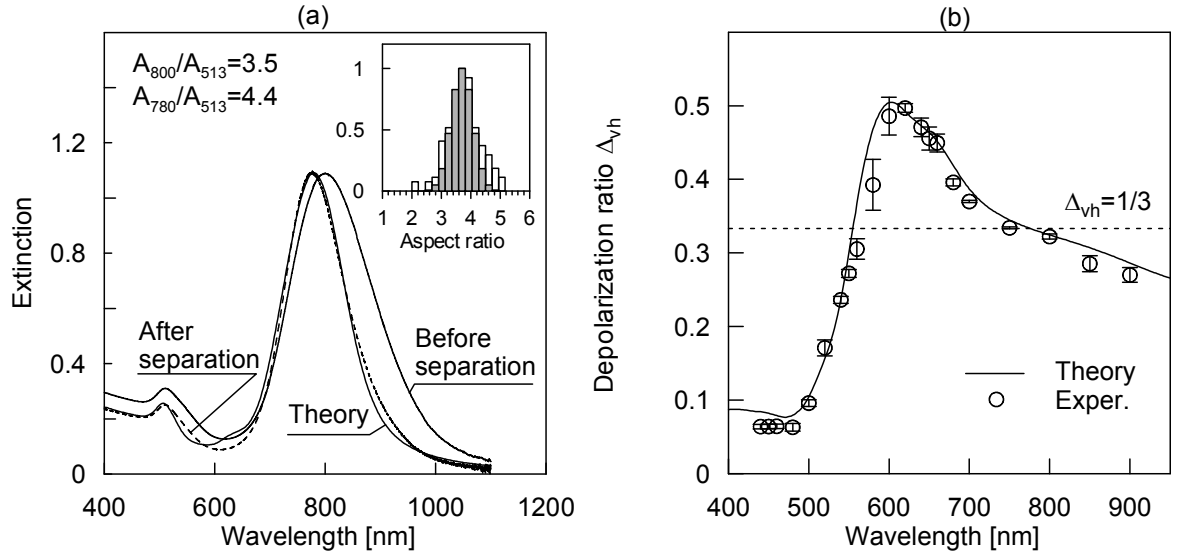

Figure 3: (a) Extinction spectra of the NR-780 sample before and after separation, together with T-matrix calculations based on TEM and best-fitting data. The inset shows a comparison of TEM aspect distribution (light columns) with normal best-fitting distribution (dark columns). (b) Experimental and simulated depolarization spectra. The error bars correspond to three independent runs, with analog and photon-counting data included. The dashed line shows the dielectric-needle limit of 1/3.

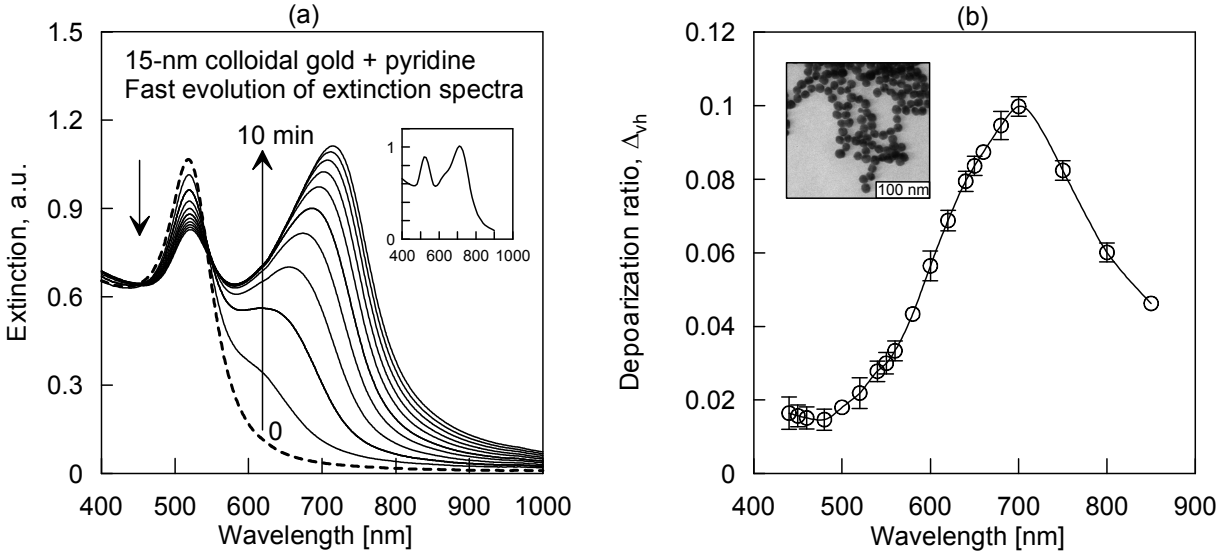

Figure 4: (a) Temporal evolution of the extinction spectra of a 15-nm CG sol after addition of pyridine. The inset shows the simulated extinction spectrum averaged over 15 statistical configurations of 100-particle ballistic clusters. (b) The depolarization spectra of a sample with stopped aggregation (after 10 min). The inset shows a TEM image of a typical CG + pyridine cluster.

Figure 4 shows the temporal evolution of the extinction spectra of a 15-nm CG sol and the depolarization spectra of a sample with the maximal red-shifted resonance peak (aggregation was stopped after 10 min). In general, both experimental spectra are in reasonable agreement with the multiparticle Mie solution for sphere clusters (see, e.g., the inset in Fig. 4a). The physical origin of the cluster DLSS is related to the short linear-chain fragments that are clearly seen in Fig. 4b.

4 Conclusion

To summarize, we have demonstrated unprecedented depolarization spectra of GNRs with the resonance maximum between 1/3 and 3/4 theoretical limits established for small dielectric and plasmon-resonant needles, respectively. These experimental observations are in excellent agreement with exact T-matrix simulations based on TEM data for particle sizes and shapes. In some analogy with the multipole nanorod extinction spectra [9], the presence of an extra-high resonance band is a signature of a high-quality preparatory procedure that will guide other researchers in determining the homogeneity of their samples with anisotropic particles. The depolarization spectra can be quite informative, including their application to nanobiotechnology, as recently demonstrated in an elegant study by Aaron et al. [2]. Finally, we have observed quite appreciable DLSS from CG clusters that can be considered to be a new promising tool to probe the internal anisotropy of random fractal aggregates built from CG particles.

Acknowledgments

This work was partly supported by grants from RFBR (nos. 08-02-00399a, 08-02-01074a, and 07-02-01434-a). BK was supported by grants from the President of the Russian Federation (no. MK 2637.2007.2), INTAS YS Fellowship (no. 06-1000014-6421), the Russian Science Support Foundation, and RFBR (nos. 07-04-00301a and 07-04-00302a).

References

[1] J. Sung, M. Sukharev, E. M. Hicks, R. P. Van Duyne, T. Seideman, and K. G. Spears, “Nanoparticle spectroscopy: Birefringence in two-dimensional arrays of L-shaped silver nanoparticles,” J. Phys. Chem. C **112**, 3252-3260 (2008).

[2] J. Aaron, E. de la Rosa, K. Travis, N. Harrison, J. Burt, M. José-Yakamán, and K. Sokolov, “Polarization microscopy with stellated gold nanoparticles for robust, in-situ monitoring of biomolecules,” Opt. Express **16**, 2153-2167 (2008).

[3] S. P. Stoylov, *Colloid Electro-Optics: Theory, Techniques, and Applications* (Academic Press, London, 1991).

[4] M. Kerker, *The Scattering of Light and Other Electromagnetic Radiation* (Academic Press, New York, 1969).

[5] N. G. Khlebtsov, A. G. Melnikov, V. A. Bogatyrev, L. A. Dykman, A. V. Alekseeva, L. A. Trachuk, and B. N. Khlebtsov, “Can the depolarized light scattering ratio be greater than 1/3”? J. Phys. Chem. B **109**, 13578-13584 (2005).

[6] B. N. Khlebtsov, V. A. Khanadeev, and N.G. Khlebtsov, “Observation of extra-high depolarized light scattering spectra from gold nanorods,” J. Phys. Chem. C (2008, submitted).

[7] N. Calander, I. Gryczynski, and Z. Gryczynski, “Interference of surface plasmon resonances causes enhanced depolarized light scattering from metal nanoparticles,” Chem. Phys. Lett. **443**, 326-330 (2007).

[8] A. V. Alekseeva, V. A. Bogatyrev, L. A. Dykman, B. N. Khlebtsov, L. A. Trachuk, A. G. Melnikov, and N. G. Khlebtsov, “Preparation and optical scattering characterization of Au nanorods, and their application to a dot-immunogold assay,” Appl. Opt. **44**(29), 6285-6295 (2005).

[9] E. K.Payne, K.L. Shuford, S. Park, G. C. Schatz, and C. A. Mirkin, “Multipole plasmon resonances in gold nanorods,” J. Phys. Chem. B **110**, 2150–2154 (2006).

Applying the *Sh*-matrices approach to small lenses with spherical surfaces

Dmitry Petrov,[1] Yuriy Shkuratov,[1] Gorden Videen[2]

[1]*Astronomical Institute of Kharkov V.N. Karazin National University. 35 Sumskaya St, Kharkov, 61022, Ukraine, phone +38-057-707-50-63,* petrov@astron.kharkov.ua
[2]*Army Research Laboratory AMSRD-ARL-CI-ES, 2800 Powder Mill Road Adelphi Maryland 20783 USA*

Abstract

The introduction of the *Sh*-matrices in the *T*-matrix method allows one to separate the shape-dependent parameters from size- and refractive-index-dependent ones. In many cases this allows an analytical calculation of the corresponding surface integrals. In this manuscript we derive and analyze the analytical solution for lenses with spherical surfaces at different thickness.

1 Introduction

In the *T*-matrix method the incident and scattered electric fields are expanded in series of vector spherical wave functions, and then a relation between the expansion coefficients of these fields is established by means of a *T*-matrix [1]. *T*-matrix elements allow for the separation of the influence of illumination/observation parameters and inner properties of a scattering object such as its size and shape parameters, and refractive index. Our modification of the extended boundary condition method (EBCM) of the *T*-matrix approach consists of a separation of the contributions of the different inner parameters of the scattering object using the shape, or *Sh* matrices [2-5]. We apply the *Sh*-matrices approach to study the scattering properties of small lenses. This can be useful for the design and optimization of miniaturized optical systems.

2 Particle model

We calculate *Sh*-matrices (see details in [2-5]) for lenses with spherical surfaces of the same diameter but different thickness. The shape of the lenses is described by the following equation:

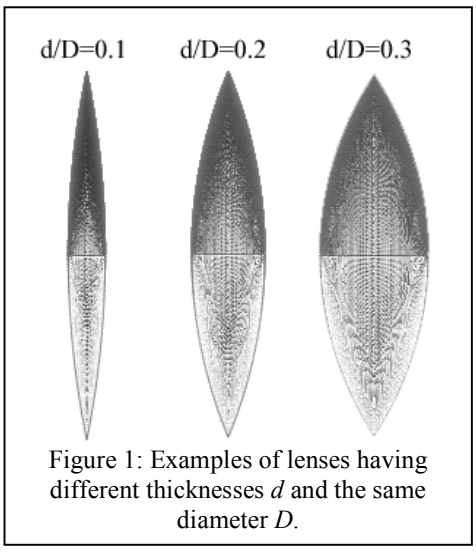

Figure 1: Examples of lenses having different thicknesses *d* and the same diameter *D*.

$$R_0(\theta) = \frac{\sqrt{\xi^2 - (\sin\theta)^2} - \left|1 - 2\left[\cos\left(\frac{\theta}{2}\right)\right]^2\right|}{\xi - 1}, \qquad (1)$$

where

$$\xi = \frac{D^2 + d^2}{D^2 - d^2}, \qquad (2)$$

where D is the lens diameter and d is the lens thickness. The polar angle θ is measured from the z axis that passes through the sphere centers. The spherical coordinate system is

centered at the position equidistant from the sphere centers. Examples of lenses having different thicknesses d and the same diameter D could be seen in Fig. 1. Further we treat these values in terms of the size parameter, e.g., $D = 2\pi D_0/\lambda$, where D_0 and λ are the diameter and wavelength given in μm.

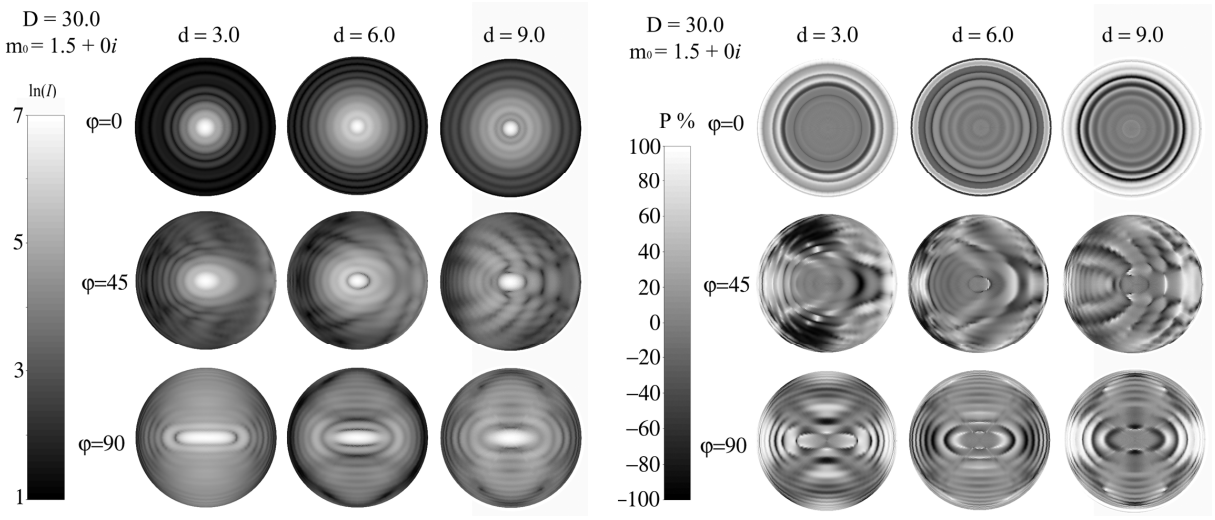

Figure 2: Maps of the forward-scattering hemisphere intensity (left panel) and polarization degree (right panel) for lenses with spherical surfaces at several fixed orientations of the lens axis relative to the direction of wave propagation (φ = 0° is the case when the incident light is parallel to the major particle axis). The refractive index of particles and size parameter is $m_0 = 1.5+0i$ and $D = 30.0$.

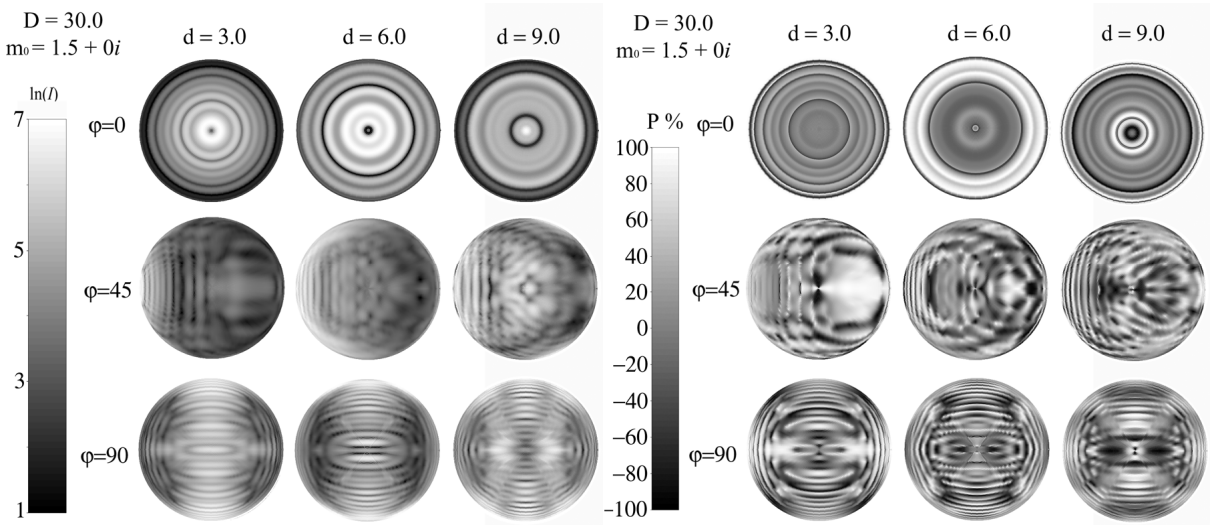

Figure 3: The same as in Fig. 2 but for the backward-scattering hemisphere.

We calculate maps of the spatial distribution in the forward and backward hemisphere for intensity (Figs. 2-3, left panel) and the degree of linear polarization (Figs. 2-3, right panel) of light scattered by lenses with $D = 30.0$ and different thicknesses ($d = 3.0$; 6.0; 9.0). The lenses are considered in fixed orientation for different angles of light incidence φ. The cases φ = 0° (light falls along the axis of the

particle), φ = 45°, and φ = 90° correspond respectively to the first, second, and third rows in Figs. 2 and 3. The refractive index of the lenses is $m_0 = 1.5+0i$. As can be seen, the scattering pattern strongly depends on lens thickness. We also note that the flatter the lens, the more prominent the forward scattering. In the backward scattering domain, the lens at $d = 9.0$ shows a prominent backscattering enhancement and deep negative polarization branch at small phase angles.

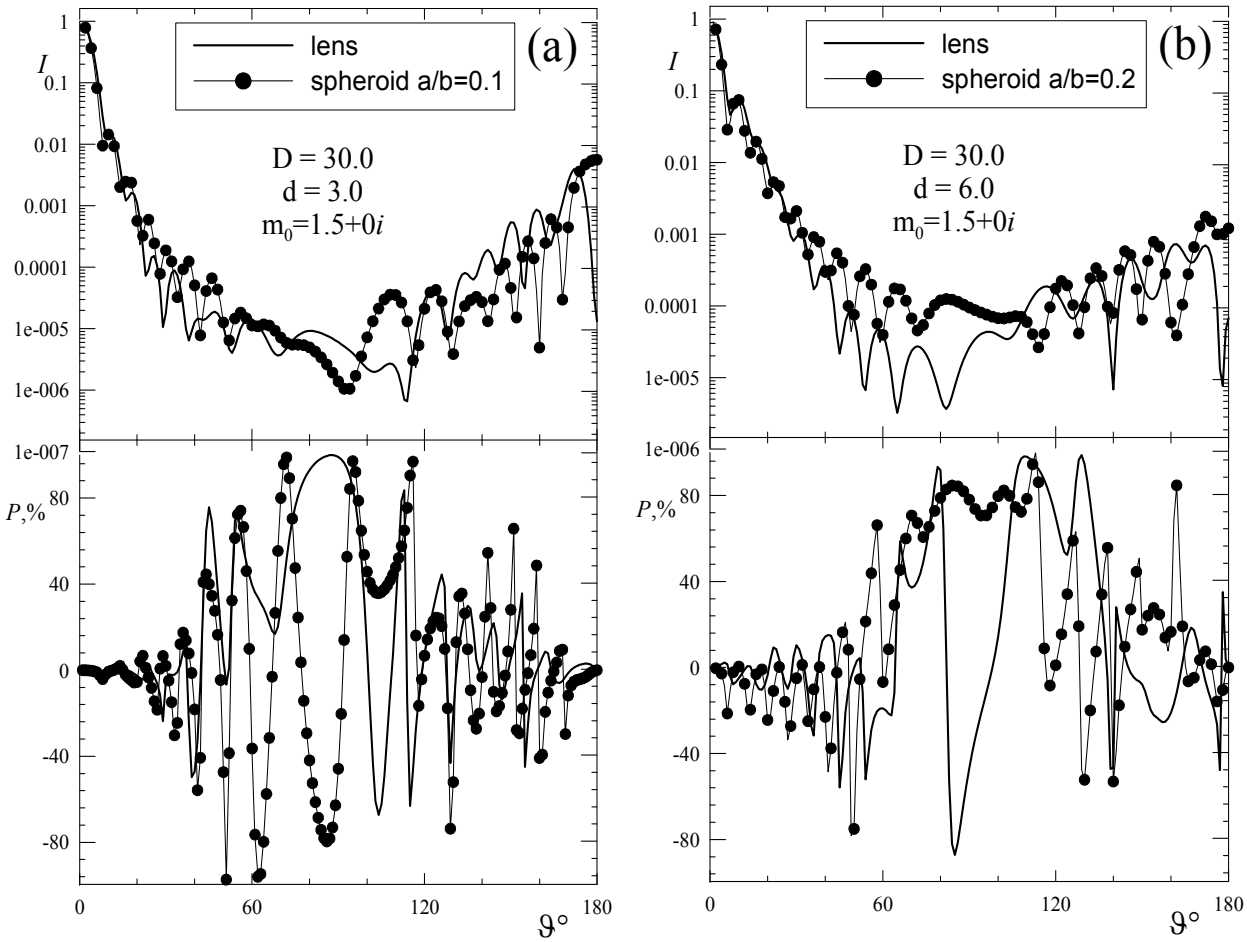

Figure 4: Phase dependences of intensity and polarization degree averaged over orientation for spherical lenses at different thickness $d = 3.0$ (a); 6.0 (b). For comparison we carry out the same calculations for a spheroid at the same d/D ratio. The refractive index is $m_0 = 1.5+0i$.

We also calculate the phase dependences of intensity and polarization degree averaged over orientation for the lenses. For comparison we carry out the same calculations for a spheroid at the same d/D ratio. In spite of the very similar shapes of these particles, the scattering patterns are noticeably different, especially near θ = 90º (see Fig. 4).

We study the effect of d/D ratio on the intensity and degree of linear polarization of the lenses averaged over orientation in Fig. 5. Calculations are carried out for different thickness $d = 3.0$; 6.0; 9.0 at at $D = 30.0$. The refractive index is $m_0 = 1.5+0i$. As can be seen, the most prominent backscattering enhancement effect is observed for the curves corresponding to the lens with $d = 9.0$. We note that this lens produces the deepest negative polarization branch at fixed orientation as well.

4 Conclusion

In the framework of the *Sh*-matrix method, we have found an analytical light-scattering solution for micro-lenses of different thickness. Figure 2 shows maps of the forward-scattering intensities and polarizations for the lenses described by Eq. (1) with different values of *d* at fixed orientations. As can be seen a contrast interference pattern is observed small values of *d/D*.

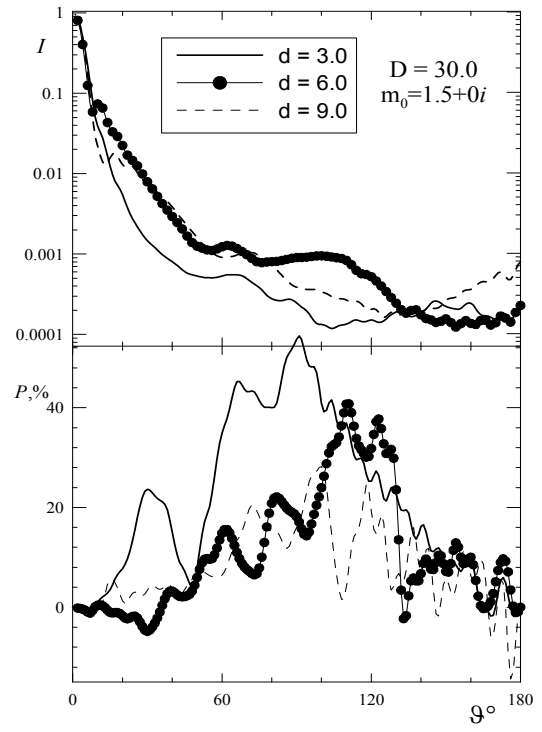

Figure: 5. Normalized intensity and degree of linear polarization for a lens with $D = 30.0$. Calculations are carried out for different thickness $d = 3.0$; 6.0; 9.0 at $m_0 = 1.5+0i$.

References

[1] M. I. Mishchenko, L. D. Travis, D. W. Mackowski, "T-matrix computations of light scattering by nonspherical particles: a review", J. Quant. Spectrosc. Rad. Transfer, **55,** 535–575. (1996).

[2] D. Petrov, E. Synelnyk, Yu. Shkuratov and G. Videen, "The *T*-matrix technique for calculations of scattering properties of ensembles of randomly oriented particles with different size," J. Quant. Spectrosc. Rad. Transfer **102**, 85-110. (2006).

[3] D. V. Petrov, Yu. G. Shkuratov, G. Videen, "Analytical light-scattering solution for Chebyshev particles," J Opt Soc Am A; Vol. 24, Issue 4, pp. 1103-1119 (2007).

[4] D. Petrov, Yu. Shkuratov, E. Zubko, G. Videen, "*Sh*-matrices method as applied to scattering by particles with layered structure," J. Quant. Spectrosc. Rad. Transfer, 106:437–454; (2007).

[5] D. Petrov, G. Videen, Yu. Shkuratov, M. Kaydash, "Analytic *T*-matrix solution of light scattering from capsule and bi-sphere particles: Applications to spore detection," J. Quant. Spectrosc. Rad. Transfer, 108:81-105; (2007).

Laser diffraction particle size distributions – a practical review of robustness of Mie theory solutions to the inverse scattering problem

Alan F Rawle Ph.D[1], Paul Kippax Ph.D[2]

[1] *Malvern Instruments Inc., 117 Flanders Road, Westborough, MA 01581-1042, U.S.A*
[2] *Malvern Instruments Ltd., Grovewood Road, Enigma Business Park, Malvern, Worcestershire, WR 14 1XZ, United Kingdom*
tel: + 1 (508) 768-6400, fax: + 1 (508) 768-6403, e-mail: alan.rawle@malvern.com

Abstract

A major industrial/commercial application of Mie theory is in light scattering equipment used for particle size distribution measurement of dry powders, suspensions or emulsions. The application of Mie Theory, coupled with advances in optical design, has enabled the measurement of particles over a very wide dynamic range, typically from 0.1 to 3000 micrometers [1]. This has delivered many benefits in terms of product understanding and quality control. However, the application of Mie Theory requires users to specify the optical properties (refractive index and absorption) of the components being measured. Much misunderstanding exists regarding the robustness of the calculated particle size distributions to these parameters, with users electing to use various assumptions rather than apply Mie Theory. This paper explores the routes by which end-users can become aware of the impact of using Mie Theory correctly and provides some practical rules relating to the selection of the optical properties for materials as diverse as glass beads and Pernod emulsions.

1 Introduction

A standard usage of Mie theory in industrial scenarios is that of generation of particle size distributions by measuring the angular dependence of the light scattered by the particulate system. Often referred to as laser diffraction, Low Angle Laser Light Scattering (LALLS) or (unfortunately) Fraunhofer diffraction, the industrial technique was first developed in the 1970's for the measurement of sprays [2]. Since then, it has been applied to a wide range of industrial processes, and can provide information over a range from 0.1 – 3000μm [1]. The generation of a particle size distribution relies on the well-known ill-conditioned problem of deconvolution of the observed angular dependence of light scattering of the particulate system, rather than the generation of a predicted scattering pattern from known sizes and shapes of particles with given optical properties. The texts and programs of Bohren and Huffman [3] and van der Hulst [4] are standard in this area and have been used and adapted for many years by laser diffraction instrument manufacturers. In the small ($d < \lambda/10$) and large size ($d > 40\lambda$) ranges, where the relative refractive index (RRI) is reasonably high (> 1.05), then the approximations of Rayleigh and Fraunhofer can be used, as the differences between the predictions made by these models and the more exact Mie theory tend to be minimal or acceptable [1]. The fact that these approximations may not be usable over all size regions is poorly understood by end users of such equipment. Micronized materials (1 – 20μm), especially those in suspension, where the RRI approaches unity, is one particular area of difficulty for such users. The tendency is to use the Fraunhofer approximation in such circumstances where knowledge of the correct properties is not immediately available or takes time to discover. This approximation covers a limited angular range (forward scattering) whereas the typical optical set-up for Mie theory involves evaluation over an extended angular range.

The most common difficulty for a newcomer to Mie theory relates to the input of the correct optical properties (the real and imaginary/absorptive components of the refractive index; 'optical constants' is inappropriate as they rarely are!) and investigating any impact that incorrect values may have on the end result. Consequently, results are often displayed in an inadequate format or conflicts arise between supplier and user of materials because different or incorrect optical properties or approximations have been used. This can be compounded by lack of understanding of the differences between the volume- or mass-based results reported by laser diffraction systems compared to the number-based distributions which tend to be reported by techniques such as image analysis and microscopy [5].

2 Practical Rules

When considering the application of laser diffraction and the use of Mie Theory to generate accurate results, the following general rules need to be taken into account.

Above and beyond anything else, the scattering data upon which any size calculations are based must be repeatable, reproducible and robust, otherwise results will simply be a self-fulfilling prophesy of "garbage in is garbage out". The material being measured must be in a dispersed form to avoid ambiguity with respect to the imaginary/absorptive part of the RI, which would be expected to vary with agglomerate or aggregate presence, as opposed to single discrete particles.

The robustness of the solution to small, sensible and systematic changes in the RI should be examined if the real part of the RI is in doubt or subject to variation [6]. This will give a guide as to the importance of the RI and how much additional information needs to be sought. It is not advisable to use default values supplied by the manufacturer or approximations such as Fraunhofer unless the robustness of these solutions has been explored. For example, the Fraunhofer approximation (typically, Reference [1], where $d > 40\lambda$ of 25μm for a He-Ne laser at 0.6328μm) may be robust for a large material prior to micronization, but this may not be the case afterwards.

If possible, it is preferable always to use a measured value of the real part of the RI, as, if there is an unambiguous real part of the RI, users are then only left with the issue of determining the imaginary component. In general, the real part of RI is required only to 2 decimal places, unless the RRI is close to unity. The imaginary part of RI is required to an order of magnitude (factor of 10) and is less easily measured. However, this parameter can only be zero for homogeneous, transparent spheres, as the surface roughness/structure of irregularly-shaped transparent materials can lead to an effective apparent increase in absorption (See section 6.6.3 in [1]). Colored materials will usually show a higher absorptive component than white or transparent materials, dependant on the wavelength of the light source used in the laser diffraction measurement. Obtaining the absorption spectrum for such materials can help with determining the magnitude of the imaginary component.

Solutions should be in line with expectation based on prior knowledge or evidence from other techniques. Optical property selections which give rise to more than one mode in the solution should be investigated carefully, especially where the minimum between the modes is at some harmonic of the laser wavelength (for example at 1.2μm for a He-Ne laser; λ = 0.6328μm), as this is often indicative of poor optical property selection. Most open and closed circuit particulate manufacturing processes give rise to an approximately lognormal or truncated lognormal respectively and seldom produce multiple size modes. As such, where multiple modes are reported by the laser diffraction analysis, the technique of converting the volume-based distribution to a number-based distribution, followed by comparison with the results obtained using microscopy, can allow some possible solutions to be rejected.

Comparison of the results obtained using wet dispersion with those obtained using dry dispersion can sometimes allow unreal solutions to be rejected, although care must be taken to ensure that the state of dispersion achieved is similar in each case.. If a material is birefringent, then the shape of the material (in particular the aspect ratio) will define if flow-alignment occurs during measurement. This then will allow selection of the required RI dependent on the appropriate axes [7].

The value of the real part of the RI can be obtained via references, measured or estimated, but should never be ignored. Sources include:

- Literature values (e.g. CRC, Handbook of Optical Constants): here (n + ik) values are available for metals and other materials. In addition, web-based resources such as Google and luxpop.com can be useful.
- RI's can be measured using a range of different techniques (immersion liquids [8], Becke lines [9], extrapolation of solution to 100% solids on an Abbé refractomer [10], ellipsometer (thin films typically), differential polarization interferometry (DPI). In addition, the volume-concentration reported by the laser diffraction system can be used to verify any selections (see below).
- Empirical estimations can be made, based on the density [11-13] or molar refractivity [14] of the material being measurement. In addition, it may be possible to calculate the RI by extrapolating from the known properties of homologous materials [15].

For small particles, the intensity of scattering, I, is proportional to $V^2\lambda^{-4}$ (Rayleigh), but absorption is proportional to $V\lambda^{-1}$ (Beer-Lambert) [16]. Thus, as particles become smaller, absorption becomes more important than scattering and the RI becomes less important than the imaginary coefficient. The RI is more important for larger particles (say 0.5 - 25μm). Above 25μm then changes in RI do not usually make major changes in result unless $n_1 \sim n_2$.

3 Results

Three examples are given of the research employed in deciding the validity of the optical constants in calculating particle size distributions using the technique of laser diffraction. In each case, the quality of the initial intensity-angular plot generated by the laser diffraction system (Mastersizer, Malvern Instruments, Malvern, Worcestershire, UK) on a dispersed system of particles was established by taking multiple measurements. Acceptable data was defined as that where the measured scattering intensity varied by less than 1% over the entire angular range of detection.

3.1 Lead bisilicate

A powdered sample of lead bisilicate was submitted to the Malvern Instruments' laboratories for particle size analysis by the dry dispersion route, and was described as a 'proprietary' material for which no optical properties could be supplied. The CAS number (65997-18-4) on the supplied MSDS sheet identified it as lead bisilicate ($PbO.2SiO_2$). The Gladstone-Dale (GD) constants for PbO and SiO_2 are 0.15 and 0.21 respectively [7].

A Google search indicated an average density of 4.8 g/cm^3 for lead bisilicate. Thus, based on a composition of 65% PbO and 35% SiO_2, we can calculate a mixed GD constant of:

(0.65 X 0.15) + (0.35 X 0.21) = 0.171.

Thus, the RI for this material can be estimated as:

RI = 1 + (0.171 X 4.8) = 1.821.

As the material is colored and irregular then a high value of the imaginary component (0.1 or 1.0) is indicated. This was fixed at 0.1 for the robustness study described below.

A robustness study, based on small, systematic and sensible changes to the optical properties used in the Mie model, gave the following particle size distributions (Figure 1), indicating robustness of the result to quite significant changes in the optical properties. This arises for 3 reasons:

- The high relative refractive index (RRI) - the measurements were conducted in air.
- The size of the material being significantly larger than d ~ λ.
- The narrowness of the particle size distribution

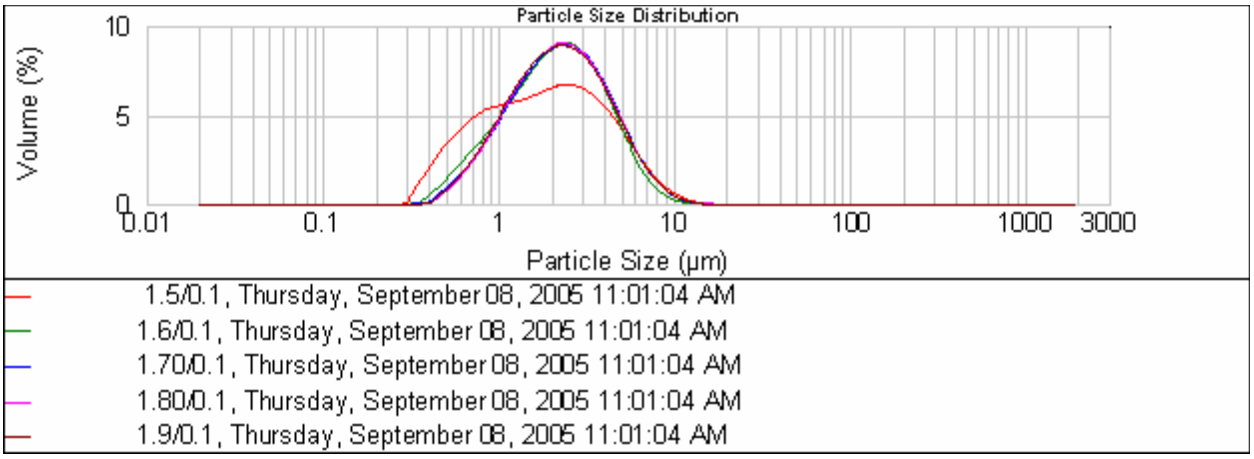

Figure 1: Changes in apparent particle size distribution caused by varying the real part of the RI for lead bisilicate, $PbO.2SiO_2$

The figure shows that significant deviations are only seen for inappropriate values of 1.50 for the real part of the RI (note the unexpected inflexion just above 1μm for this plot) and that over the range 1.60 – 1.90 the plots virtually overlap. Subsequent literature work indicated a value of 1.72 – 1.74 for the RI of $PbO.2SiO_2$.

3.2 NBS1003b

NBS1003b is a certified, spherical and transparent glass bead standard produced by NIST. The real part of the RI is stated (1.52) while the imaginary component is equated to that of a transparent, homogeneous sphere (0). Even though the median size approaches 40μm, there is significant secondary scattering in the intensity-angle profile due to the transparency of the particles (Figure 2).

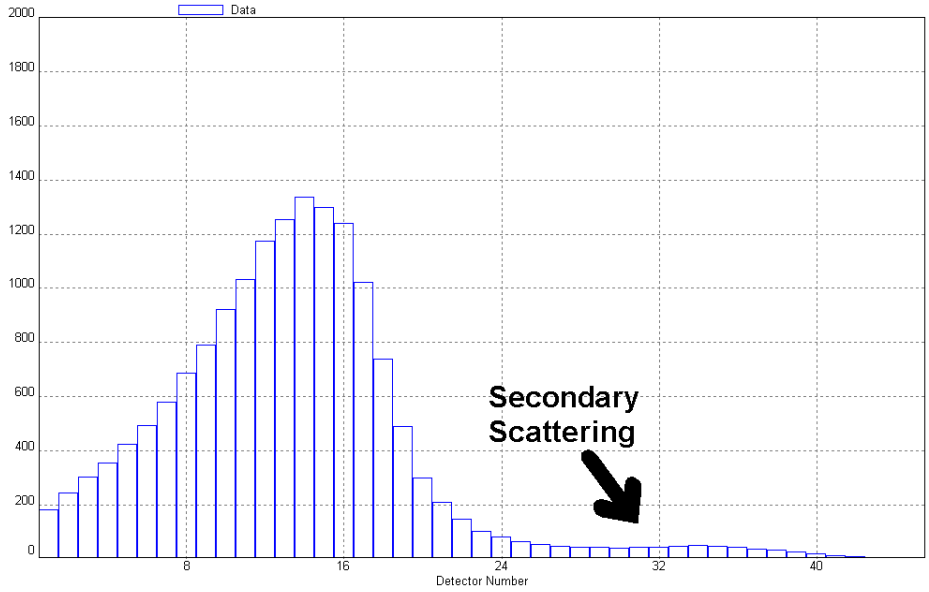

Figure 2: Intensity per detector shown as a function of detector number for the NBS1003b glass spheres using the Malvern Mastersizer. As the detector number increases, so the angle of detection increases logarithmically.

Deconvolution of the above scattering pattern using the Fraunhofer approximation (Figure 3) gives rise to an apparent subset of smaller particles with a mode of around 1μm. The presence of this mode was justified on the basis that a single small particle could be seen under the microscope and thus the Fraunhofer approximation was 'more sensitive to smaller material'. Analysis using the Mie model based on the optical properties stated above shows only a single peak (Figure 3).

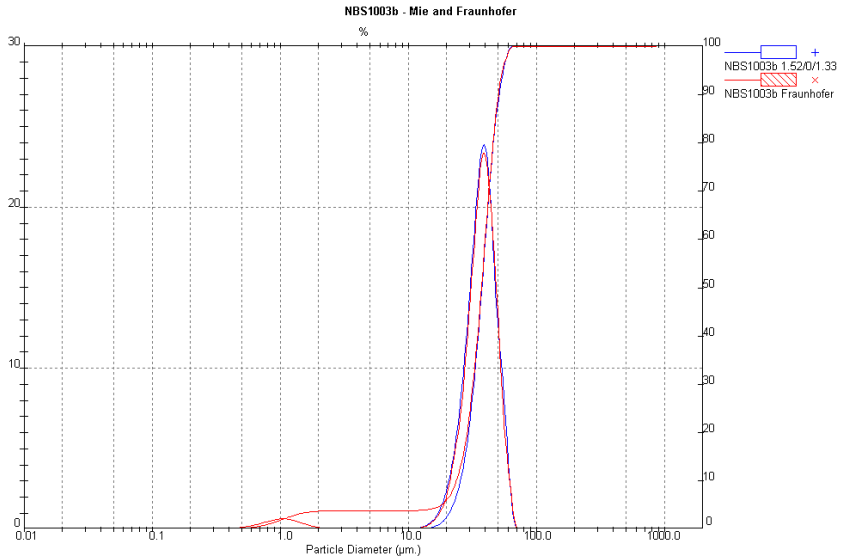

Figure 3: NBS1003b particle size distributions reported using the Fraunhofer approximation and Mie Theory (RI = 1.52, Imaginary RI = 0).

The question here is whether the amount of fine material reported within the 1μm mode (2% by volume) when using the Fraunhofer approximation is reasonable or not. In this circumstance, we can convert the volume-based results shown in Figure 3 into number distributions [17] and carry out a comparison with microscopy. This conversion shows that, by number, the vast majority of the particles would appear to be around 1μm in size, if the Fraunhofer approximation was correct, with the ratio of 1μm to 40μm particles being approximately 32000:1 (Figure 4). However, analysis of the material using microscopy reveals that the majority of the particles are around 40μm in size, and that no 1μm material is observed (Figure 4).

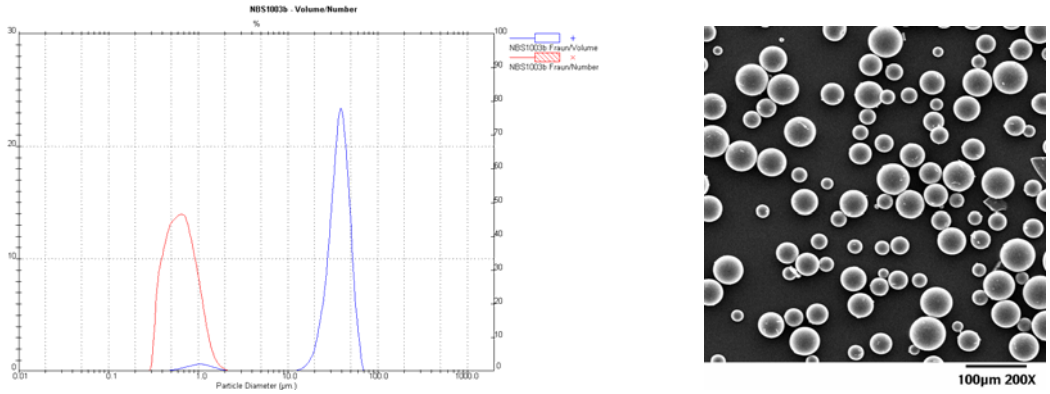

Figure 4 NBS1003b: Volume to number conversion of the Fraunhofer generated particle size distribution and an electron micrograph (Courtesy: Dr. James Kelly, NIST) of the material.

By comparison, conversion of the Mie-based result to a number distribution shows a slight shift downwards in the main mode of the distribution, in line with the narrowness of the distribution (Figure 5) and in agreement with the micrograph results.

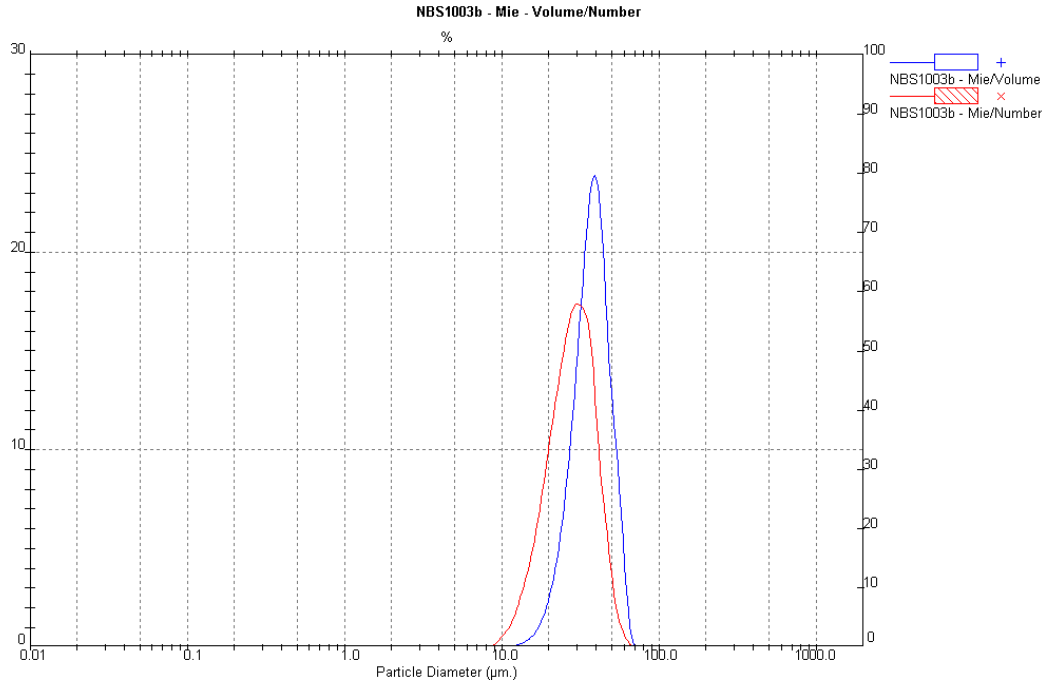

Figure 5: NBS1003b Volume-number conversion of the Mie generated particle size distribution.

In this case, the use of the Fraunhofer approximation in a situation where a significant wide-angle, secondary scattering response is observed (arising from light passage directly through the particles and interfering with that 'classically' diffracted at the contours of the particles) generates a false subset of apparently smaller particles when incorrectly interpreted. Note that this is observed in a system of particles in the 40µm range, which is substantially larger than the 40λ (or 25µm) quoted in ISO13320-1 [1] as being the lower limit for the Fraunhofer approximation.

3.3 Pernod

Pernod is a yellow, encapsulated (gum acacia) emulsion of aniseed oil (anethole) in water. The RI of the oil phase was measured as 1.56 by Abbé refractometer, a value confirmed by the CRC Handbook (Ed. R C Weast, 56th Edition, page C-162, 1975-1976). An initial study using an imaginary refractive index component of between 0.001 and 0.1 (standard for a white emulsion) gave an unexpected bimodal peaking, at approximately 200nm. The minimum at 0.6µm approximately coincides with the wavelength of illumination (He-Ne laser at 632.8nm), another common indicator of inadequate optical modeling (Figure 6). Based on the literature density value of 0.985g/cm^3 and the given starting concentration, a known volume concentration of 0.0009% obtained by dilution was measured.

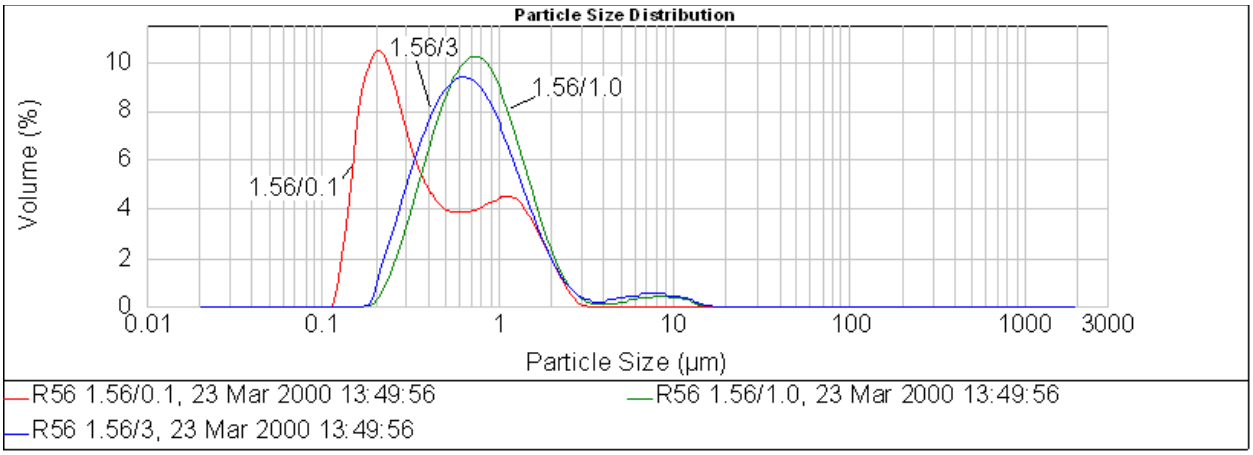

Figure 6: Particle Size distributions in relation to optical properties (Fixed real part of RI = 1.56)

The calculated volume concentration, c, is obtained by combination of Beer-Lambert law and Mie theory [18]:

$$c = \frac{100 \log_e(1 - \text{Obscuration})}{\frac{-3}{2} b \sum \frac{V_i Q_i}{d_i}}$$

where: Obscuration = (1 – transmission) and the other symbols have their customary meaning. Q_i, the scattering extinction, is calculated from Mie theory.

The known volume concentration can be compared against the calculated volume concentration. The residual (least squares minimization of the observed and calculated light scattering) can also be examined. See Table 1 below.

Table 1: Calculated volume concentrations and residuals for diluted Pernod using different imaginary values of the RI

RI	Absorption	Calculated volume concentration (%)	Weighted residual
1.56	0	0.0072	2.617
1.56	0.1	0.0022	7.204
1.56	1	0.0011	1.958
1.56	3	0.0008	1.9

It can be seen that good agreement is obtained between the calculated and known volume concentrations when the imaginary component of the RI is set to 1 or 3. This gives similar particle size distributions; in line with those seen by microscopy (occasional large particles in the 10µm range). The residual error is also minimized at these values. It is to be noted that the optimal imaginary values (1 or 3) are enormous values in comparison to bulk values and almost certainly reflect the inherent color (and light absorption) of the material combined with another interfacial layer (the gum acacia) causing light loss.

4 Discussion

It is possible to ignore the use of Mie Theory when applying the laser diffraction technique, and decide to use the approximations which are available. Users often opt to do this due to the perceived difficulties associated with obtaining the optical properties required when applying Mie Theory. However, the examples shown here suggest that the use of approximations is to be actively discouraged, when more-rigorous scattering models such as Mie Theory are available. In all events, the effect of modifying the input optical constants needs investigation and the selection of the utilized properties justified scientifically. Indeed, the determination of reasonable optical properties is not too difficult if all evidence and practical measurement is brought to the table. Personal communication with the FDA indicates that they are seeking more rigorous method development for particle size analyses using light scattering and thus the effect of the utilized optical properties needs examining and justification. This paper has indicated just a few of the routes used by experienced scientists in answering the question: “Is this end result of a particle size distribution reasonable or not?”

Even with the advances brought about in the capabilities of laser diffraction systems through the application of Mie Theory, there are still some that would argue: “Who cares what the RI is? We only require comparative data.” However, such an attitude can lead to unexpected problems. For instance, one UK manufacturer of milled materials approached Malvern Instruments for advice relating to the removal of fine particles from their process. They had installed an expensive hydrocyclone on their manufacturing process to remove fine particles reported by their laser diffraction system. Investigation showed that these fines were ‘generated’ in the analytical laboratory (not the process), where the Fraunhofer Approximation had been applied to laser diffraction analysis of the milled material.

5 Conclusion

Mie theory is a powerful tool in obtaining particle size distributions from powders, suspensions and emulsions. The end-user of commercial laser diffraction equipment should be aware of the optical properties used in the theory and should examine the robustness of the solutions to small, systematic and sensible modifications to these properties if more exact measured parameters are not available.

Acknowledgments

The author would like to thank all his colleagues in the Malvern Instruments family for their help, advice and friendliness over nearly two decades. Without this interaction he would certainly have been doing something completely different and certainly less enjoyable.

References

[1] ISO13320-1:1999 *Particle size analysis -- Laser diffraction methods -- Part 1: General principles* Document available as of: 1999-11-11 Available from http://www.iso.org (126SFR April 2008)

[2] J Swithenbank, J M Beer, D S Taylor, D Abbot, G C McCreath *A Laser Diagnostic Technique for the Measurement of Droplet and Particle Size Distribution* Progress in Astronautics and Aeronautics, Vol. 53, Experimental Diagnostics in Gas Phase Combustion Systems, Edited by B. T. Zinn, New York: American Institute of Aeronautics and Astronautics, 1977, 421-447(1977)

[3] C F Bohren and D R Huffman, *Absorption and Scattering of Light by Small Particles* (Wiley, New York, 1983)

[4] H C van de Hulst, *Light Scattering by Small Particles, Dover Publications,* (Mineola, NY, 1982)

[5] A F Rawle, *The Basic Principles of Particle Size Analysis* Malvern Instruments Application Note (Malvern, England, 1993)

[6] A F Rawle, Chapter 3.2 *'Particle Morphology and Characterization in Preformulation'* in *Preformulation Solid Dosage Form Development*, Vol. 159, Moji Christianah C. Adeyeye (Editor), Harry G. Brittain (Editor) ISBN: 0824758099, (Informa Healthcare, 2008)

[7] E S Larsen, H Berman, *The Microscopic determination of the nonopaque minerals* Second Edition, United States Department of the Interior Geological Survey Bulletin 848 (United States Government Printing Office Washington, 1934)

[8] For example, Cargille Laboratories (http://www.cargille.com/refractivestandards.shtml) has well over 150 immersion liquids spanning the range from 1.30 to 2.31 approximately

[9] N H Witchell A N Witchell *Elements of Optical Mineralogy*, Second Edition Part III Determinative Tables. Note: Parts I and II deal with "Principles and Methods" and "Description of minerals" respectively (New York John Wiley & Sons Inc, 1929)

[10] H Saveyn, D Mermuys, O Thas and P Van der Meeren, *Determination of the Refractive Index of Water-dispersible Granules for Use in Laser Diffraction Experiments*, Particle and Particle Systems Characterization, 19, 426-432 (2002). Originally presented at Partec, Nürnberg, Germany in March 2001

[11] J H Gladstone, T P Dale, *On the influence of temperature on the refraction of light*, Phil. Trans. 887, (1858)

[12] J H Gladstone, J Dale, *Researches on the refraction, dispersion, and sensitiveness of liquids* Philosophical Transactions of the Royal Society 153, 317 – 343, (1863)

[13] A Mandarino, *The Gladstone-Dale relationship Part IV: The compatibility concept and its application* Can. Min. Vol. 19, 441-450, (1981). See also: http://webmineral.com/help/Gladstone-Dale.shtml

[14] ChemSketch is a Freeware package (for research purposes) available from Advanced Chemistry Development, Inc., 110 Yonge Street 14th Floor, Toronto, Ontario, M5C 1T4, Canada. See: http://www.acdlabs.com. Conditions may apply for commercial use or where the number of atoms exceeds 50. Version 11 appears to be the latest release (April 2008).

[15] R Mehra *Application of refractive index mixing rules in binary systems of hexadecane and heptadecane with n-alkanols at different temperatures* Proc. Indian Acad. Sci. (Chem. Sci.), Vol, 115, No. 2, April 2003, 147 – 154, (2003)

[16] R Tilley *Colour and the Properties of Materials* ISBN 0-471-85197-3 (John Wiley and Sons, 2000)

[17] T Hatch, and S P Choate, *Statistical description of the size properties of non-uniform particulate substances*, J. Franklin Inst. 207, 369 – 387, (1929).

[18] ISO/DIS 13320 *Particle size analysis -- Laser diffraction methods* Under development in ISO Technical Committee TC 24/SC 4 and revises ISO13320-1:1999 (Reference [1] above). This Draft International Standard (DIS) is available from http://www.iso.org (64SFr, April 2008)

Analysis of High Order Resonances in Metallic Nanoparticles by Polarimetric Techniques

B.Setién, B.García-Cámara, F.González, F.Moreno and J.M. Saiz

Grupo de Óptica. Departamento de Física Aplicada. Universidad de Cantabria
Avda de los Castros s/n, 39005, Santander, SPAIN
tel: +34-942201868, fax: +34-942201402, e-mail:beatriz.setien@alumnos.unican.es

Abstract

The presence of scattering modes of higher order than the dipolar one, produce changes in the intensity and polarization of the scattered light by metallic nanoparticles. In this work, we study the spectral evolution of the linear polarization degree, P_L, of the scattered light by metallic nanoparticles when quadrupolar (or higher order) modes appear. In particular at 90º scattering angle, we show that the measurement of P_L can give information about particle size and optical properties of the surrounding medium.

1 Introduction

Light scattering by small particles has become an important topic because it constitutes a non-invasive technique that is crucial in fields like Biology or Medicine [1]. The case of metallic nanoparticles is especially relevant due to the possibility of exciting localized surface plasmon resonances (LSPR). LSPR's are collective oscillations of the conduction electrons at a resonant frequency [2] that produce an important enhancement of the local electromagnetic field around the particle This phenomenon makes metal nanoparticles to be the basis of applications like: biosensing (nanorulers or nanosensors) [3] and lithography [4]. It is well-known that the spectral properties of LSRP's excited on a metallic particle depend on size, shape and optical properties of the particle and its surrounding medium [5]. In particular, as particle size increases, resonances shift and broaden. Also, resonances of higher order appear. Furthermore, when the refractive index of the surrounding medium changes, the spectral properties of the LSPR's also change.
The appearance of higher order scattering modes as the particle size increases, produces changes in the polarization of the scattered radiation and consequently, the dipolar scattering behaviour starts to lose its dominance. The objective of this work is to show the influence of the variations of the size of the nanoparticles and of the surrounding medium in the polarimetric properties of the scattered light. In particular the influence on the spectral linear polarization degree (P_L) measured at ***90º*** (angle at which differences from the dipolar behavior are better appreciated).

2 Theory

LSPR's are usually analyzed using the multipolar expansion of Mie theory [6]. For very small particles, only the two first terms of that expansion (dipolar terms) makes the main contribution, but as particle size increases, more terms must be considered [7]. These higher order terms can excite new resonances that perturb the typical "eight-shape" spatial distribution of the scattered light by a dipole when it is illuminated with an incident wave whose electric field has only parallel component to the scattering plane. In particular, the influence of the presence of multipolar modes can be observed through the analysis of the polarimetric properties of the scattered light. In this work, we use the linear polarization degree to analyze these properties. The linear polarization degree (P_L) is defined as

$$P_L = \frac{I_\perp - I_{//}}{I_\perp + I_{//}} \qquad (1)$$

$I_{//}$ and $I_\perp$ being the scattered intensities with the electric field parallel and perpendicular to the scattering plane, respectively. When the particle can be considered as a scattering dipole, $I_{//}$ ***=0*** at θ_s***=90º*** and the

linear polarization degree is equal to 1. When multipolar orders are excited, their effect is superimposed to the dipolar scattering and at *90°* scattering angle $I_{//}$ and P_L become different from 0 and 1, respectively.

3 Results

In Fig. 1a), we show the scattered intensity by a silver [8] sphere at θ*=90° (*I_s*(90°))* as a function of the incident wavelength, for different particle sizes. As can be seen, for small sizes, only a peak appears corresponding to the dipolar resonance. When particle size increases, this resonance broadens and suffers a red-shift. Also, a new peak appears at lower wavelengths due to the quadrupolar contribution.

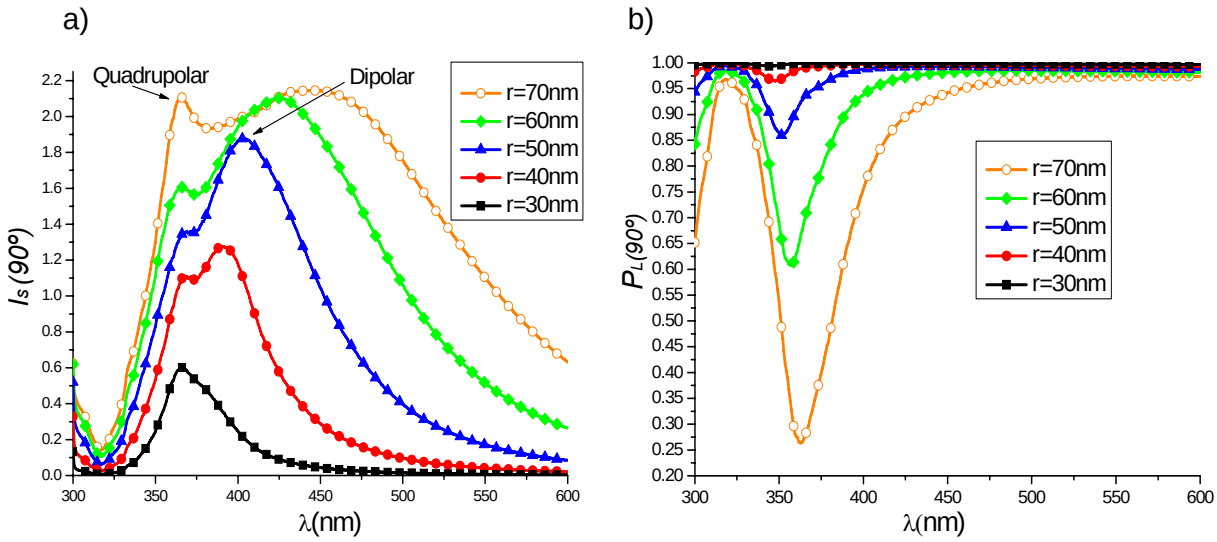

Figure 1.a) Scattered intensity, *(I_s (90°))* and b) Linear polarization degree, *P_L(90°)* by a silver spherical particle as a function of the incident wavelength for several sizes.

In Fig. 1b), we plot *P_L(90°)* for the same range of wavelengths as in Fig. 1a). We can observe that P_L reaches a minimum around the corresponding wavelength for which the quadrupolar resonance is excited. This minimum depth increases as particle size increases. Also, it shifts slightly to the red with increasing particle size.

Fig. 2 shows the evolution of the values of the minima of *P_L(90°)* with particle size. From these results, the main consequence is that the measurement of P_L at a convenient wavelength may provide with additional tools for particle size determination.

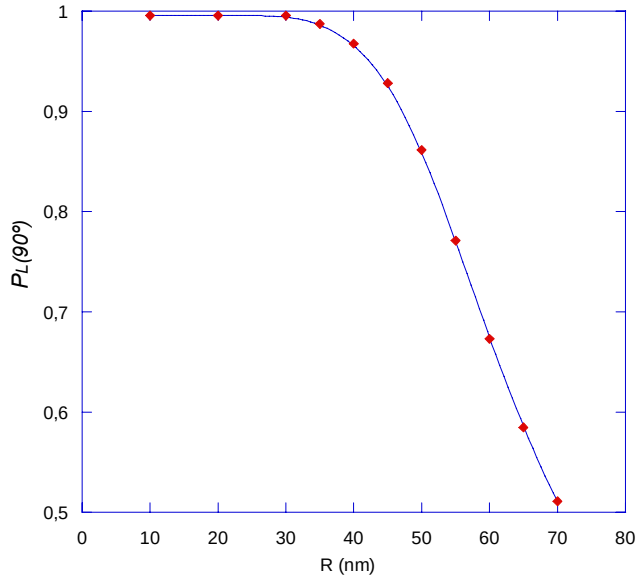

Figure 2. Evolution of the values of the minimum of the linear polarization degree, P_L *(90º),* as a function of particle size.

Following a similar analysis as before, it is possible to find the spectral evolution of P_L*(90º)* when the surrounding refractive index (*n'*) changes. This is shown in Fig. 3 for a silver particle of *R=50 nm*. The inset of this figure represents how the minimum of P_L evolves linearly as a function of *n'*.

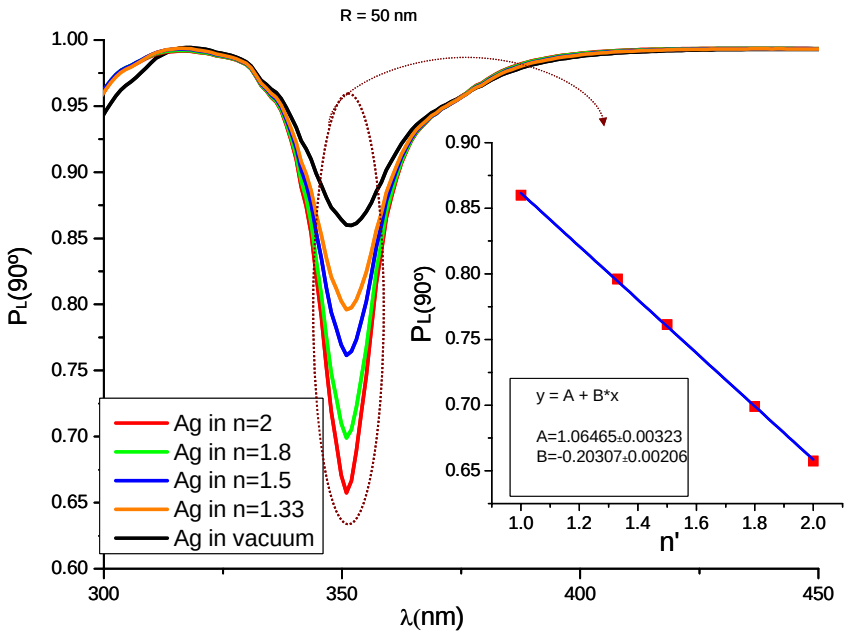

Figure 3. Spectral evolution of the linear polarization degree, P_L *(90º),* for a silver particle with *R=50 nm* for several values of the refractive index of the surrounding medium (*n'*). Inset: linear fit of the evolution of the minimum values of P_L as *n'* changes.

3 Conclusions

In this work we have shown how the determination of the spectrum of the linear polarization degree of the scattered light by metallic nanoparticles at a scattering angle of *90º* provides with information about the presence of scattering modes of higher order than the dipolar one. Among the most important consequences of this study is that the spectral measurement of $P_L(90º)$ can give information about both the size of the particles and the refractive index of the surrounding medium.

Acknowledgments

This research was supported by the Ministry of Education of Spain under the project FIS2007-60158. Braulio García-Cámara wishes to thank to the University of Cantabria for his Ph.D. grant.

References

[1] K. Aslan, J.R. Lakowicz and C. D. Geddes, “Plasmon light scattering in biology and medicine: new sensing approaches visions and perspectives”, Current Opinion in Chemical Biology, **9**, 538-544 (2005)

[2] P.N. Prasad, *Nanophotonics* (Wiley-Interscience, 2004)

[3] J. N. Anker, W. P. Hall, O. Lyandres, N. C. Shan, J.Zhao and R.P. Van Duyne, “Biosensing with plasmonic nanosensors”, Nat. Materials **7**, 442-453, (2008)

[4] X. Wei, X. Luo, X. Dong, and C. Du, “Localized surface Plasmon Nanolithography with Ultrahigh Resolution”, Opt. Exp. **15**, 14177-14183 (2007)

[5] K. L. Kelly, E. Coronado, L.L.Zhao and G. Schatz, “The Optical Properties of Metal Nanoparticles: The influence of Size, Shape and Dielectric Environment”, J.Phys. Chem. B **107**, 668-677 (2003)

[6] C. F. Bohren and D. R. Huffman, *Absorption and Scattering of Light by Small Particles* (Wiley, New York, 1983).

[7] B.García-Cámara, F. Moreno, F. González, J.M. Saiz and G. Videen, “Light Scattering Resonances by Small Particles with Electric and Magnetic Properties”, J. Opt. Soc. Am. A **25**, 327-334 (2008)

[8] E. D. Palik, *Handbook of Optical Constants of Solids* (Academic Press INC. Florida, 1985).

Simulation of Polarization-Sensitive Optical Coherence Tomography images by Monte Carlo method

Boris Veksler,[1] Mikhail Kirillin,[2] Vladimir Kuzmin,[3] and Igor Meglinski[1]

[1] Cranfield Health, Cranfield University, Cranfield, MK43 0AL, UK,
[2] University of Oulu, Optoelectronics and Measurement Techniques Laboratory, P.O. Box 4500, 90014, Oulu, Finland,
[3] St-Petersburg Institute of Commerce and Economics, 194021 St-Petersburg, Russia
e-mail: b.veksler@cranfield.ac.uk

Abstract

We introduce new Monte Carlo (MC) method for simulating Optical Coherence Tomography (OCT) images of complex multi-layered turbid scattering media. We demonstrate, for the first time of our knowledge, the use of MC technique to imitate 2-D polarization-sensitive OCT images with non-planar boundaries of layers in the medium like a human skin. The simulation of polarized low coherent optical radiation is based on the vector approach generalized from the iterative procedure of the solution of Bethe-Saltpeter equation. The performances of the developed method are demonstrated both for conventional and polarization-sensitive OCT modalities.

1 Introduction

Since Wilson and Adam [1] first introduced Monte Carlo (MC) method into the field of laser-tissue interaction this technique has been used extensively in a number of studies of photon migration for diverse optical diagnostic applications [2–5], including Optical Coherence Tomography (OCT) [6–8]. Since recently MC technique has been widely used to simulate coherent phenomena of multiple scattering [9–11] and the changes of polarization of optical radiation scattered within the biological media [12–14]. Typically, within the MC algorithms the state of the polarization and its evolution during the propagation is described in framework of Stokes-Mueller or Jones formalism [12–14].

In current research, we introduce new MC technique that is able imitating 2-D PS-OCT images of complex multi-layered turbid scattering media avoiding implementation of Stokes-Mueller and/or Jones formalism. The concept of the approach is based on the development of a unified MC program as a natural extension for the most popular standard MC code [2].

2 Materials and methods

Follow this we consider propagation of photon packets along each possible trajectory within the medium. Free photon path between two successive scattering events is governed by Poisson distribution: $f(l_i) = \mu_s \exp(-\mu_s l_i)$, and defined as: $l_i = -\mu_s^{-1} ln\xi$, where ξ is the probability that the mean free path l is no less than l_i; arbitrary ξ value is chosen in the [0, 1] interval using a random number generator; μ_s is the scattering coefficient: $\mu_s = l^{-1}$. A new direction of the photon packet after each scattering event is determined by Henyey-Greenstein scattering phase function [2], originally developed to approximate Mie scattering of light from particles with size comparable to the wavelength of the incident light. This expression is characterized by so-called anisotropy factor g which is equal to mean cosine of the scattering angle θ, $g = \overline{\cos\theta}$ ($g \in [0,1]$, with $g = 0$ corresponding to the isotropic scattering). A consideration of light scattering within an absorbing medium ($\mu_s l \neq 1$) requires a proportional reduction of the statistical weight W of each photon packet according its trajectory [15]: $W = W_0 \exp(-\sum_{i=1}^{N} \mu_a l_i)$, where W_0 is the initial photon packet weight, μ_a is the absorption coefficient of the medium, N is the number of experienced scattering events.

The photon packets fitting the given detection criteria [8], including size, numerical aperture and detector position are taken into account. Completing the tracing of the photon trajectories for a large number of photons N_{ph} (typically $N_{ph}\sim10^7$) OCT signal is calculated as a convolution of distribution of the detected photons over their optical pathlengths $L=\sum_{i=1}^{N} l_i$ with the envelope of coherence function [16]:

$$I(z)=2\sum_{i=1}^{N_{ph}}\sqrt{W_r W_s(L_j)}\exp\left[-\left(\frac{z-L_j}{l_{coh}}\right)\right], \quad (1)$$

where W_r and W_s are the total weights of the detected photon packets from reference arm and scattering medium, respectively, l_{coh} is the coherence length of probing laser radiation and z is the depth.

Using a combination of the MC technique and the iteration procedure of the solution of Bethe-Salpeter equation [10], it has been shown that simulation of the optical path of a photon packet undergoing *N* scattering events directly corresponds to the *N-th* order ladder diagram contribution. In this correspondence we generalized the above mentioned MC technique for the direct simulation the evolution of polarization vector for each photon packet. The polarization is described in terms of the polarization vector $\vec{P}$ undergoing a sequence of transformations after each scattering event [17], and all the photon packets are weighted in accordance with the polarization state. In Rayleigh and Rayleigh-Gans approximations the polarization vector of the scattered wave $\vec{P_i}$ is transformed upon the *i-th* scattering such that [17]:

$$\vec{P_i}=-\vec{e_i}\times\left[\vec{e_i}\times\overrightarrow{P_{i-1}}\right]=[\hat{I}-\vec{e_i}\otimes\vec{e_i}]\overrightarrow{P_{i-1}}, \quad (2)$$

where $\vec{e_i}$ is the unit vector aligned along the trajectory element of a photon packet after the *i-th* scattering event.

2 Results

The performances of this extended computational approach for simulating 2D conventional OCT and PS-OCT images are shown in Fig.1 for the skin model with non-planar layers [4,16] (see Fig.1a): Upper stratum corneum (average thickness 0.02 *mm*), Lower stratum corneum (0.18 *mm*), Epidermis (0.2 *mm*), Dermis with upper plexus (0.2 *mm*), Reticular dermis (0.8 *mm*) and Dermis with lower plexus (0.6 *mm*). The optical properties of the layers are: μ_s: 35, 5, 10, 10, 7, 12 (mm^{-1}); μ_a: 0.02, 0.015, 0.02, 0.1, 0.7, 0.2 (mm^{-1}); *g*: 0.9, 0.95, 0.85, 0.9, 0.87, 0.95; and refractive index *n*: 1.54, 1.34, 1.4, 1.39, 1.4, 1.39, respectively.

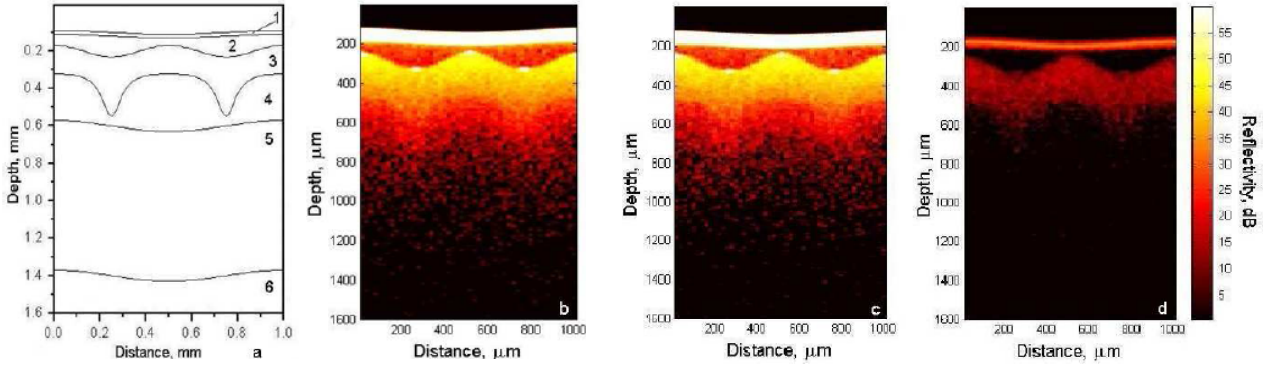

Figure 1: Schematic presentation of skin model used in the simulation (a). 2-D images obtained for convention OCT (b), and for co- and cross- polarized OCT modalities: (c) and (d), respectively.

The source-detector parameters are chosen in accordance with the parameters of the OCT system described in [18]: wavelength λ = 900 *nm*, l_{coh} = 15 *μm* and numerical aperture 0.2. In order to simulate OCT images the sequential A-scans are simulated with the defined 20 *μm* transversal scanning step.

The results of simulation of 2D OCT and PS OCT images for both co- and cross-polarized modes are presented in Fig.1 (b-d). OCT image obtained in co-polarized mode (see Fig.1c) is similar to the OCT image obtained for the convention OCT (Fig.1b), whereas intensity of the image obtained in cross-polarized mode (see Fig.1d) is much lower compare to co-polarized (Fig.1c). This is due to the origin of the OCT signal formed mostly by so-called 'snake' or low scattering order photons [22]. Therefore, contribution of the photon packets depolarized due to multiple scattering in the formation of final OCT image is relatively small in upper layers, and significantly rises for deep layers.

3 Conclusion

Based on the generalization of iterative procedure of the solution of Bethe-Saltpeter equation a new vector based MC approach has been developed. For the first time using MC technique we have imitated 2D OCT and PS OCT images of skin model with non-planar layers' boundaries. The performances of the developed method are shown both for conventional and polarization-sensitive OCT modalities.

Current approach allows considerably simplify simulation of polarized low coherent optical radiation propagation within turbid scattering media avoiding implementation of Stokes-Mueller and/or Jones formalism, with the substantial reducing of the computational resources. In a similar manner this approach can be applied for circular polarization allowing to avoid a cumbersome calculation of the Mueller matrix.

The technique can provide detailed information on polarization propagation within/outside the medium, score various physical quantities simultaneously. The technique will find a number of straightforward applications related to the non-invasive diagnostics of various disperse random media, including biological tissues, polymers, liquid crystals and others.

Acknowledgments

Authors acknowledge the support of UK BBSRC (project ref. no.: BBS/B/04242), NATO (project: PST.CLG.979652), GETA graduate school and Tauno Tönning Foundation, Finland.

References

[1] B. C. Wilson and G. Adam, "A Monte Carlo model for the absorption and °ux distributions of light in tissue," Med. Phys. 10, 824 (1983).

[2] L.-H. Wang, S. L. Jacques, L.-Q. Zheng, "MCML - Monte Carlo modeling of photon transport in multi-layered tissues," Comput. Methods Prog. Biomed. 47, 131 (1995).

[3] L. H. Wang, "Mechanisms of ultrasonic modulation of multiply scattered coherent light: a Monte Carlo model," Opt. Lett. 26, 1191 (2001).

[4] I. V. Meglinsky, S. J. Matcher, "Modeling the sampling volume for the skin blood oxygenation measurements," Med. Biol. Eng. Comput. 39, 44 (2001).

[5] D. Boas, J. Culver, J. Stott, and A. Dunn, "Three dimensional Monte Carlo code for photon migration through complex heterogeneous media including the adult human head, "Opt. Express 10, 159 (2002).

[6] Q. Lu, X. Gan, M. Gu, and Q. Luo, "Monte Carlo Modeling of Optical Coherence Tomography Imaging through Turbid Media," Appl. Opt. 43, 1628 (2004).

[7] A. Tycho, T. M. Jorgensen, H. T. Yura, and P. E. Andersen, "Derivation of a Monte Carlo Method for Modeling Heterodyne Detection in Optical Coherence Tomography Systems," Appl. Opt. 41, 6676 (2002).

[8] J. M. Schmitt and K. Ben-Letaief, "Efficient Monte Carlo simulation of confocal microscopy in biological tissue," J. Opt. Soc. Am. A 13, 952 (1996).

[9] L. F. Rojas-Ochoa, D. Lacoste, R. Lenke, P. Schurtenberger, F. Scheffold, "Depolarization of backscattered linearly polarized light," J. Opt. Soc. Am. A 21, 1799 (2004).

[10] I. V. Meglinski, V. L. Kuzmin, D. Y. Churmakov and D. A. Greenhalgh, "Monte Carlo Simulation of Coherent Effects in Multiple Scattering," Proc. Roy. Soc. A 461, 43 (2005).

[11] V. L. Kuzmin, I. V. Meglinski, "Coherent effects of multiple scattering for scalar and electromagnetic fields: Monte-Carlo simulation and Milne-like solutions," Opt.Commun. 273, 307 (2007).

[12] S. Bartel and A. H. Hielscher, "Monte Carlo Simulations of the Diffuse Backscattering Mueller Matrix for Highly Scattering Media," Appl. Opt. 39, 1580 (2000).

[13] X. Wang and L. V. Wang, "Propagation of polarized light in birefringent turbid media: A Monte Carlo study," J. Biomed. Opt. 7, 279 (2002).

[14] J. C. Ramella-Roman, S. A. Prahl, S. L. Jacques, "Three Monte Carlo programs of polarized light transport into scattering media: part I," Opt. Express 13, 4420 (2005).

[15] D. Y. Churmakov, I. V. Meglinski, D. A. Greenhalgh, "Influence of refractive index matching on the photon diffuse reflectance," Phys. Med. Biol. 47, 4271 (2002).

[16] M.Yu. Kirillin, A. V. Priezzhev, R. Myllylä, "Effect of coherence length and numerical aperture on the formation of OCT signals from model biotissues," Proc. SPIE, 6534, 65340H (2007).

[17] A. Ishimaru, Wave Propagation and Scattering in Random Media, 1 and 2 (Academic Press, 1978).

[18] M.Yu. Kirillin, E. Alarousu, T. Fabritius, R. Myllylä, A. V. Priezzhev, "Visualization of paper structure by optical coherence tomography: Monte Carlo simulations and experimental study," JEOS:RP, 2, 07031 (2007).

[19] V. L. Kuzmin, I. V. Meglinski, "Multiple scattering and intensity fluctuations in optical coherence tomography of randomly inhomogeneous media," J. Exp. Theor. Phys., 105, 285 (2007)

Retrieval of complex refractive index and size distribution of spherical particles from Dual-Polarization Polar Nephelometer data

Christophe Verhaege, Valery Shcherbakov, Pascal Personne

Laboratoire de Météorologie Physique, UMR/CNRS 6016, Université Blaise Pascal,
24 avenue des Landais, 63177 Aubière cedex, France
tel: +33 (0)4.70.02.20.73, fax: +33 (0)4.70.02.20.94, e-mail: verhaege@moniut.univ-bpclermont.fr

Abstract

An algorithm to retrieve complex refractive index and size distribution of spherical particles from Dual-Polarization Polar Nephelometer data is presented. The retrieved characteristics are in the expected ranges and in good agreement with the nature of particles and the specifications of the aerosol generators.

1 Introduction

The knowledge of microphysical and optical characteristics of aerosols is of importance for modeling the radiative balance of Earth's atmosphere, understanding the cloud life cycle, and remote sensing of tropospheric aerosols. The long term objective of the Dual-Polarization Polar Nephelometer (D2PN) [1] designed at Laboratoire de Météorologie Physique is to develop a database of optical and microphysical characteristics of aerosols and to test inverse codes against it.

The Dual-Polarization Polar Nephelometer is a device to measure the parallel and perpendicular polarized components of light scattered by an ensemble of aerosol particles. Measurements are made in the range of scattering angles from 10° to 169° with step of 1°. An inverse method was employed to retrieve complex refractive index and size distribution of spherical particles on the base of D2PN data.

In the first part, the retrieval code is briefly described. Then some main results are discussed.

2 Retrieval code

It is generally recognized that the aerosol complex index of refraction can be retrieved along with the size distribution from scattering measurements. Most of the methods are based on the Lorenz-Mie theory (see, e.g., Bohren and Huffman [2]), that is, aerosols are modeled as spherical particles. For example, Tanaka et al. [3] used the lookup table method to retrieve the refractive index and size distribution on the base of the measured parallel and perpendicular components of scattered light. Zhao et al. [4] and Zhao [5] used an inversion of measured Stokes parameters to determine the properties of ensembles of particles. Jones et al. [6] inverted the absolute intensity measurements of a 15 channels polar nephelometer to retrieve both the real part of the refractive index and the size distribution. Barkey et al. [7] used genetic algorithms to find out the real part of refractive index on the base of nephelometer measurements.

On the other hand, there are limitations on retrieval of complex refractive index $m = n + i\chi$ of spherical particles from scattering measurements [1]. In the case of the low absorbing particles $\chi \le 10^{-4}$, measurement errors substantially reduce the sensitivity to the imaginary part of the refractive index and only the range of the imaginary part can be estimated. When the absorption of particles is high $\chi > 0.5$, only the microphysical characteristics and the imaginary part can be retrieved. When the absorption of particles is moderate, i.e., $10^{-4} \le \chi \le 0.5$, the real and imaginary parts of the refractive index can be deduced along with the microphysical parameters. Thus, D2PN experimental data can be used to retrieve aerosol characteristics.

For inversion of the D2PN data, we employed the following code. When a value of the refractive index is assigned, a code, based on the method developed by Dubovik et al. (see, e.g., [8]), is used to retrieve

the particle size distribution. The dependence of kernel matrices on the real n and imaginary χ part of the refractive index is considered through the look-up table, that is, the kernel matrices were precomputed in grid points of $m = n + i\chi$, which cover for sure the whole range of expected values. The lookup table covers the range from 1.1 to 1.9 for n and from 1E-10 to 1E+1 for χ. The real-part range is divided into 40 intervals with the linear steps of 0.02. The imaginary-part range is divided into 50 steps intervals with logarithm. For each value of the refractive-index grid, a size distribution is retrieved. The value of $m = n + i\chi$ is derived using the condition of minimum of the root mean squared relative errors. The corresponding size distribution is considered as the retrieved one.

3 Results of retrieval of refractive index and size distribution

In this section, four representative examples of inversion of D2PN data are presented. All examples deal with unnormalized phase functions. The results obtained with parallel and perpendicular components of scattered light are close to those ones presented in the following.

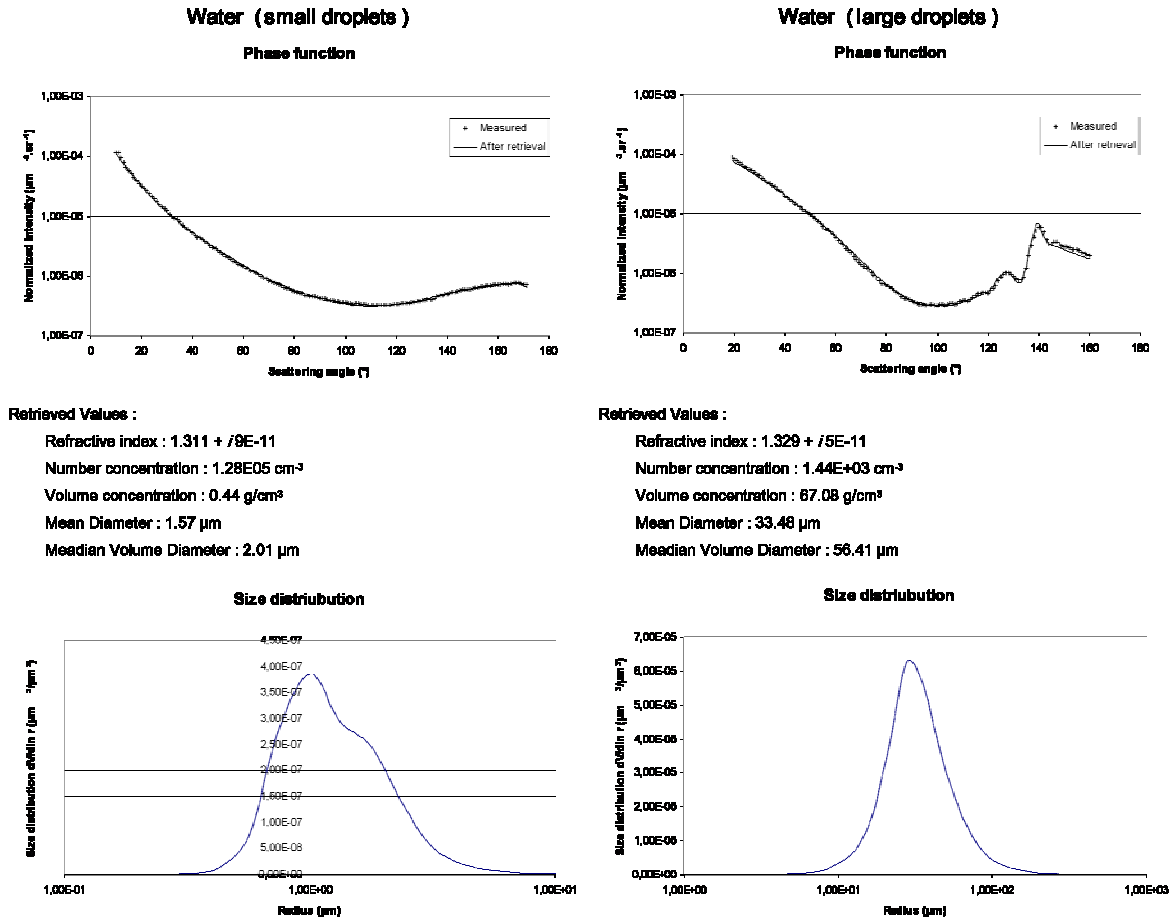

Figure 1. Ensembles of water droplets produced with two different generators. The left panels correspond to the small droplets case and the right ones are for big particles. The upper panels show the measured and retrieved phase functions. The bottom panels represent the retrieved size distributions. The estimated values of refractive index, number and volume concentration, mean diameter, median volume diameter are shown in the middle of the figure.

3.1 Examples of retrieval for two different size distribution of water droplets

The algorithm above was applied to measured phase functions of two populations of water droplets (figure 1). The populations differ in the size distribution. In the first case, a liquid aerosol generator produced small droplets; and in the second case, large droplets were generated. As it is seen on the upper panels of Figure 1, the phase function of small droplets is quite smooth. For the large droplets, the phase function has two pronounced peaks that correspond to the primary and secondary rainbows.

The true value of the refractive index of water is 1.329 + i 1.25E-7 for a wavelength of 800 nm [9]. In the case of large droplets, the retrieved value of the real part of the refractive index is perfect (1.329). For small particles, the estimated value is 1.311. This value is within the error bars that correspond the D2PN measurement errors. In the both cases, the imaginary part of the refractive index is within the expected range of values (less than 1E-4) of low absorbing particles.

For these two cases, the retrieved size distribution (see the bottom panels) and integral parameters are in accord with the specifications of the generators of particles. According to the specifications, the first generator produces particles with a mean diameter of 1.55 μm and the second one generates droplets with a mean diameter of 29 μm.

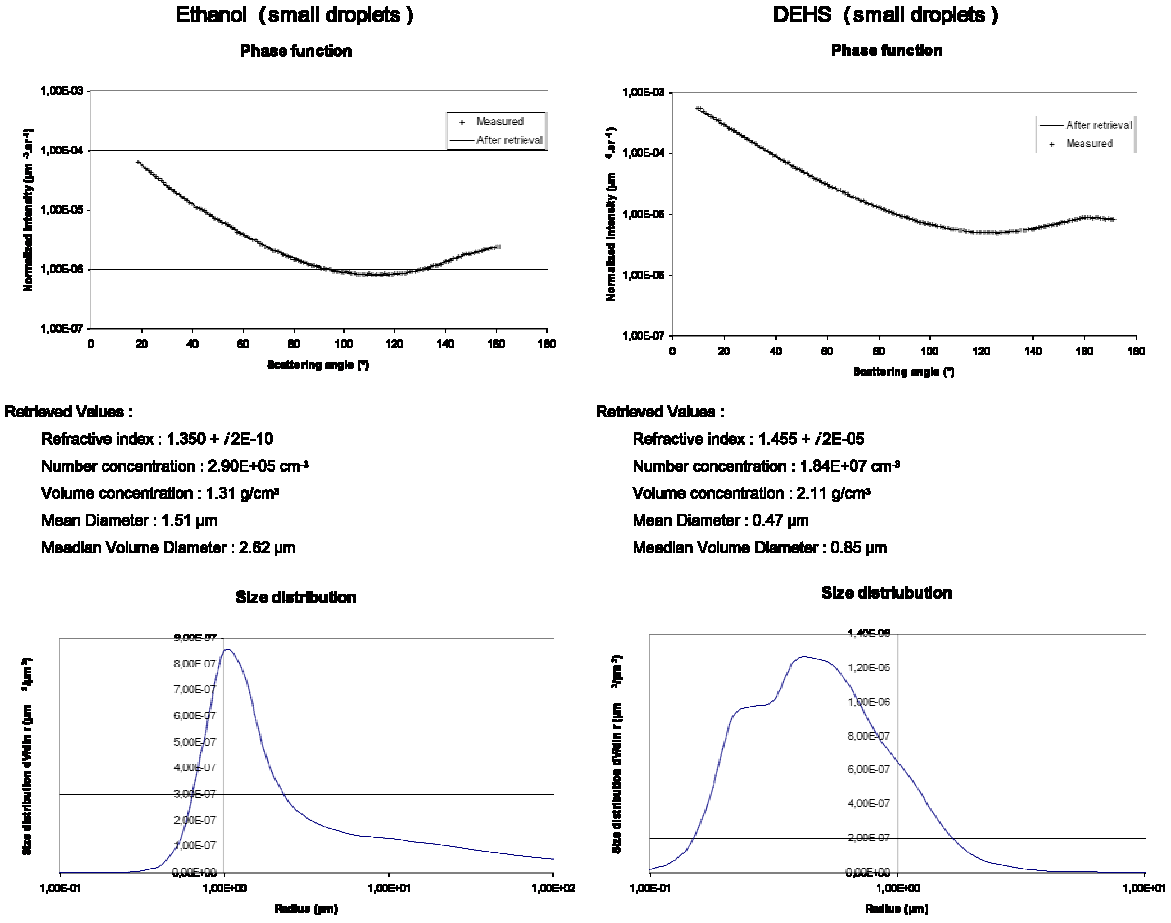

Figure 2. Ensembles of droplets produced with the same generator but from two different liquids. The left panels correspond to the ethanol and the right ones are for the DEHS. The upper panels show the measured and retrieved phase functions. The bottom panels represent the retrieved size distributions. The estimated values of refractive index, number and volume concentration, mean diameter, median volume diameter are shown in the middle of the figure.

3.2 Examples of retrieval for two different kinds of particles

In order to confirm the sensitivity of D2PN data to the refractive index value, we performed measurements for ensembles of droplets produced with the same generator but from two different liquids. The first liquid was the ethanol (the real part of the refractive index is of 1.362, low absorbing) and the second one was the DEHS (Di-Ethyl-Hexyl-Sebacate, the real part of 1.452, low absorbing). As it is seen on the upper panels of Figure 2, the both measured phase functions are smooth and like that one on the left panel of Figure 1. Nevertheless, the estimated values of n are significantly different. The retrieved real part of the refractive index of DEHS is in good agreement (1.455 against 1.452). In the case of ethanol, the difference between the estimated and exact values is within the error bars. Another time integral parameters are in accord with the specifications of the generator of droplets. The difference in the retrieved size distributions may be attributed to distinct liquid volatility features.

4 Conclusion

D2PN data along with the employed inversion algorithm provide possibility to estimate the complex refractive index and size distribution of ensembles of spherical particles. All retrieved parameters are in the expected ranges and in good agreement with the nature of particles and the specifications of the generators. It is promising to adapt the inverse method developed by Dubovik and colleagues [10] to retrieve complex refractive index and size distributions of spherical aerosols and ensembles of prolate and oblate particles from D2PN data.

References

[1] Verhaege Ch., V. Shcherbakov, P. Personne, “Limitations on retrieval of complex refractive index of spherical particles from scattering measurements”, JQSRT, in press, (2008).

[2] Bohren C. F. and D. R. Huffman, *Absorption and Scattering of Light by Small Particles* (Wiley, New York, 1983).

[3] Tanaka M., T. Takamura, T. Nakajima, “Refractive Index and Size Distribution of Aerosols as Estimated from Light Scattering Measurements”, J. Climate Appl. Meteorol. **22**, 1253-1261 (1983).

[4] Zhao F., Z. Gong, H. Hu, M. Tanaka, T. Hayasaka, “Simultaneous Determination of the Aerosol Complex Index of Refraction and Size Distribution from Scattering Measurements of Polarized Light”, Appl. Opt. **36**, 7992-8001 (1997).

[5] Zhao F., “Determination of the Complex Index of Refraction and Size Distribution of Aerosols from Polar Nephelometer Measurements”, Appl. Opt. **38**, 2331-2336 (1999).

[6] Jones M. R., K. H. Leong, M. Q. Brewster, B.P. Curry, “Inversion of Light-Scattering Measurements for Particle Size and Optical Constants: Experimental Study”, Appl. Opt. **33**, 4025-4041 (1994).

[7] Barkey B, S. E. Suzanne, A. Chung, “Genetic Algorithm Inversion of Dual Polarization Polar Nephelometer Data to Determine Aerosol Refractive Index”, Aerosol Science and Technology **41**, 751-760 (2007).

[8] Dubovik O., “Optimization of Numerical Inversion in Photopolarimetric Remote Sensing”. In: Videen G, Y. Yatskiv, M. Mishchenko, editors, *Photopolarimetry in Remote Sensing* (Dordrecht, Netherlands: Kluwer Academic Publishers, p. 65-106, 2004).

[9] D’Almedia G. A., P. Koepke, E. P. Shettle, *Atmospheric aerosols. Global climatology and radiative characteristics* (A. Deepak publishing, Hampton Virginia, 1991).

[10] Dubovik O. et al. “Application of spheroid models to account for aerosol particle nonsphericity in remote sensing of desert dust”, J. Geophys. Res., 111:D11208 (2006).

Author Index